PROCEEDINGS OF INTERNATIONAL SYMPOSIUM ON EMERGING DEVELOPMENTS AND INNOVATIVE APPLICATIONS OF RELIABILITY ENGINEERING AND RISK MANAGEMENTS, TAIPEI, TAIWAN, OCT30 -NOV. 3, 2022

EDIARR2022

International Symposium on Emerging Developments and Innovative Applications of Reliability Engineering and Risk Managements (EDIARR2022)

Proceedings

Edited by

Shi-Shuenn Chen
Distinguished Professor,
National Taiwan University of Science and Technology, Taiwan

Alfredo H-S. Ang
Emeritus Chair Professor, University of California, Irvine, USA

Publication Date: December, 2022

Published by: National Taiwan University of Science and Technology (Taiwan Tech)
Address: No. 43, Sec. 4, Keelung Rd., Taipei 106, Taiwan, R.O.C.
E-mail : tbtc@mail.ntust.edu.tw
Website: http://www.ntust.edu.tw

ISBN: 978-986-98537-5-0 (pbk)

Table of Contents

Organized Sessions

Session Topic: MA1: Resilience/Risk/Reliability Assessment Methods for Infrastructure

Session Topic: WA1: Structural health monitoring and safety evaluation

Session Topic: WA2: Reliability-Based Maintenance, Management, Life-Cycle Design and Performance of Infrastructures

Preface

International Symposium on Emerging Developments and Innovative Applications of Reliability Engineering and Risk Managements, held on 30 October-3 November 2022, is organized by the National Taiwan University of Science and Technology (Taiwan Tech) in Taipei, Taiwan.

The performance reliability and safety of built infrastructure systems are issues that are of major concern to all disciplines of engineering. Since such issues are common and important in all disciplines of engineering, the international symposium is organized to address many of the relevant issues related to major infrastructure systems. As engineers, our mission is to improve the public safety, facilitate the economic growth, and protect the environment as well as eco systems. With this international symposium, we hope to strengthen the consensus of all sectors of government, academy, industry, and research institutions.

This Symposium contains 14 keynote speeches, 5 organized sessions, and 1 special session from many parts of the world, including USA, Mexico, Denmark, Australia, Japan, Korea, Singapore, Taiwan, etc. The special session will be the reconnaissance report on seismic damage caused by the 2022/Sep earthquakes in Mexico and Taiwan presented by the Mexican Society for Earthquake Engineering and the National Center for Research on Earthquake Engineering of Taiwan. The total number of participants from the government, the academia and the industry are expected to be more than 200.

The Symposium is held under the sponsorship of the Ministry of Education, the Ministry of Science and Technology, the Taiwan Tech, and a number of supporting organizations. In particularly, the faculty and staff of the Department of Civil and Construction Engineering and Taiwan Building Technology Center (TBTC) are responsible for the Secretariat of the Symposium.

Finally, I would like to express my sincere gratitude to all the keynote speakers, the session organizers, the authors, the sponsors, and the participants for their contributions; to the members of the Steering Committee, the International Scientific Committee, and the Local Organizing Committee for their devoted time and efforts that makes EDIARR2022 a successful event.

Prof. Shi-Shuenn Chen
Symposium Chair

Organizing Committees

Steering Committee

Prof. Shi-Shuenn Chen	Former President & Director of TBTC, Taiwan Tech, Chair
Mr. Jeou-Rong Yan	Deputy Minister of Public Construction Commission, Executive Yuan, Co-Chair
Mr. R.J. Wang	Director, Architecture and Building Research Institute, Ministry of the Interior, Co-Chair
Prof. I-Tung Yang	Former Chairman, Department of Civil and Construction Engineering, Taiwan Tech, Co-Chair
Prof. Alfredo. H-S. Ang	University of California, Irvine, USA
Prof. Kuo-Wei Liao	Department of Engineering for Sustainable Environment, National Taiwan University
Prof. Chien-Kuo Chiu	Chairman, Department of Civil and Construction Engineering, Taiwan Tech
Prof. Rwey-Hua Cherng	Department of Civil & Construction Engineering, Taiwan Tech
Prof. Min-Yuan Cheng	Department of Civil & Construction Engineering, Taiwan Tech
Prof. Jui-Sheng Chou	Department of Civil & Construction Engineering, Taiwan Tech
Prof. Ting-Yu Hsu	Department of Civil & Construction Engineering, Taiwan Tech
Prof. A.J. Li	Department of Civil & Construction Engineering, Taiwan Tech
Prof. Jun-Yang Shi	Department of Civil and Environmental Engineering, National University of Kaohsiung

International Scientific Committee

Prof. A. H-S. Ang	University of California, Irvine, USA, Chair
Prof. Dan Frangopol	Lehigh University, USA, Co-Chair
Prof. Shi-Shuenn Chen	Taiwan Tech, ex-officio
Prof. Bilal Ayyub	University of Maryland, USA
Prof. Jie Li	Tongji University, China
Prof. Jianbing Chen	Tongji University, China
Prof. Armen Der Kiureghian	University of California, Berkeley, USA
Prof. David De Leon	Mexico State University, Mexico
Prof. Bruce Ellingwood	Colorado State University, USA
Prof. L. Esteva	National University of Mexico
Prof. M. Faber	Aalborg University, Denmark
Prof. H. Fujino	Yokohama University, Japan
Prof. H. Furuta	Kansai University, Japan
Prof. Chul-woo Kim	Kyoto University, Japan
Prof. Paolo Gardoni	University of Illinois at Urbana-Champaign, USA
Prof. Huawei Huang	Tongji University, China
Prof. Sang-Hyo H. Kim	Yonsei University, Korea
Prof. X.L. Liu	Jaio-Tung University, China
Prof. Zhao-Hui Lu	Central South University, China
Prof. R. Melcher	University of Newcastle, Australia
Prof. Phoon Kok Kwang	National University of Singapore, Singapore
Prof. Quek Ser Tong	National University of Singapore, Singapore
Prof. Junho Song	Seoul National University, Republic of Korea
Prof. P.D. Spanos	Rice University, USA
Prof. H. K. Tung	Hong Kong University of Science & Technology, Hong Kong

Prof. C.B. Yun	KAIST, Korea
Prof. Yangang Zhao	Kanagawa University, Japan
Prof. L.Zhang	Hong Kong University of Science & Technology, Hong Kong
Prof. Jianye Ching	National Taiwan University

Local Organizing Committee

Prof. Chien-Kuo Chiu	Chair, Taiwan Tech
Prof. I-Tung Yang	Co-Chair, Taiwan Tech
Prof. Ting-Yu Hsu	Co-Chair, Taiwan Tech
Prof. Chao-Lung Hwang	Taiwan Tech
Prof. Cheng-Cheng Chen	Taiwan Tech
Prof. Rwey-Hua Cherng	Taiwan Tech
Prof. Yu-Chen Ou	National Taiwan University
Prof. Chun-Tao Chen	Taiwan Tech
Prof. Kuo-Hsin Yang	National Taiwan University
Prof. Min-Yuan Cheng	Taiwan Tech
Prof. Jun-Yang Shi	National University of Kaohsiung
Prof. Yin-Nan Huang	National Taiwan University
Prof. Po-Hua Albert Chen	National Taiwan University
Prof. Kuang-Yen Liu	National Cheng Kung University
Prof. Chien-Cheng Chou	National Central University
Prof. Tzu-Kang Lin	National Chiao Tung University
Prof. Rong-Yau Hwang	Taiwan Construction Research Institute
Prof. Cheng- Tao Yang	National Center for Research on Earthquake Engineering

List of Organizers & Sponsors

Organizers

National Taiwan University of Science and Technology (NTUST), Taiwan Tech

Building Technology Center, NTUST, Taiwan Tech

Department of Civil and Construction Engineering, NTUST, Taiwan Tech

Sponsors

Ministry of Education

Ministry of Science and Technology

Architecture and Building Research Institute, MOI (ABRI)

Co-Sponsors

International Association for Structural Safety and Reliability

International Association for Life Cycle Civil Engineering

International Association for Bridge Maintenance and Safety

Ctci Foundation

National Council of Structural Engineers Associations, R.O.C (Taiwan)

Taipei Professional civil Engineers Association

Taipei Structure Engineering Association

Taiwan Professional Geotechnical Engineers Association

Taiwan Professional Geotechnical Engineers Association

Taiwan Shixi Engineering Consulting Co., Ltd.

Sinotech Engineering Consultants, Ltd.

Shiding Engineering Design Co., Ltd.

Keynote Lectures

OPTIMAL RELIABILITY-BASED ASEISMIC DESIGN OF HIGH-RISE BUILDINGS.

Alfredo H-S. Ang

NAE Member, Professor Emeritus of Civil Engineering,

University of Illinois at Urbana Champaign and University of California, Irvine, USA

OPTIMAL RELIABILITY-BASED ASESMIC DESIGN OF HIGH-RISE BUILDINGS

Alfredo H-S. Ang[1], David De Leon[2], Wenliang Fan
[1]*University of California, Irvine, California, USA*
Email: alfred.ang@icloud.com
[2]*Autonomous Metropolitan University, Toluca, Mexico*
email: daviddeleonescobedo@yahoo.com.mx
[3]*Chongqing University, Chongqing, China*
email: davidfwl@126.com

Abstract: The reliability-based design of structural components has been well established based on calibration. However, the reliability-based design of structures as a system remains an issue that has not been addressed adequately. This issue requires the assessment of the system reliability of a complete structure, considering the effects of both the aleatory and epistemic types of uncertainty. This can be addressed effectively using the PDEM (probability density evolution method) for the effects of the aleatory uncertainty, resulting in the PDF of the critical state of a system. The effects of the epistemic uncertainty may be included as the error of the mean-value of the critical state of the system. For illustration, the method is applied to the minimum life-cycle cost aseismic design of a high-rise building in Mexico City

Keywords: Reliability-Based Optimal Design, PDEM Application, High-Rise Buildings

1 Introduction

Thus far, standards for the reliability-based design of structural components, such as beams and columns, are well-known; these were developed largely on the basis of calibration (e.g., Ellingwood and Galambos, 1982). No such standards, however, are available for the design of a complete structure as a system. For that matter, no standard procedure exits thus far; further studies of reliability-based procedures are needed for the system design of complex structures.

Recently, several methods and concepts have been proposed on the topic of reliability-based optimal design, for example the recommendation of best practices to avoid progressive (cascading) failures (e.g. Ellingwood, 2005)

As every system is unique, there cannot be a uniform standard for its design. A systematic procedure is required for the design of a complete system. Proposed here is a probabilistic procedure for the reliability-based optimal design of a structure as a complete system. In other words, the proposed procedure will determine the reliability-based safety index for the optimal design of a complete structure as a system. The consideration of the epistemic uncertainty on some design parameters, allows for an improvement on the decision making process, by enlarging the space for conservative decisions. Additional options are provided for investors and designers, to support the trade-off between cost and safety, by specifying the use of high percentile values, designated here as “high confidence values” for the design of a structural system.

2 On Uncertainty in Structural Designs

In engineering, uncertainties are unavoidable. In fact, the main objective of the reliability approach is to handle uncertainties in a proper and rational basis. The reliability-based design standards for structural components is an appropriate example (Ellingwood and Galambos, 1982).

For practical purposes, engineering uncertainties may be classified into two broad types – namely the *aleatory* and the *epistemic* types.

The aleatory type is the inherent variability or randomness in nature, and may be measured and assessed through statistical observations; whereas the epistemic type is the inaccuracy in the designer's ability (or knowledge) to predict reality. The latter (epistemic type) is seldom measurable in practice, and will often require subjective judgments for its assessment.

These two types of uncertainty have been referred to, respectively, as "data based" and "knowledge based" uncertainties. Being an inherent part of nature, the aleatory type cannot be reduced; whereas, the epistemic type may be reduced with improved knowledge of the true state of nature. In practice, it is seldom practical to reduce the epistemic uncertainty; however, minimizing its effects is practically feasible and important in developing an engineering design.

2.1 Practical Measure of Aleatory Uncertainty

Being the inherent variability of information in nature, the aleatory type of uncertainty can be measured through statistical observations by its probability distribution (probability density function, PDF, or cumulative distribution function, CDF) or approximately with the moments (mean, variance, third moment, and higher moments) estimated on the basis of the observed data.

2.2 Practical Measure of Epistemic Uncertainty

For the epistemic type of uncertainty, it is seldom possible, in practice, to assess the degree of uncertainty in quantitative terms; for the purpose of formulating the design of a structural system, subjective judgment is often invariably necessary. As the mean state of nature is most important, the mean state may be designated within a range of possibilities – as representing the epistemic uncertainty. This range can then be translated into an equivalent c.o.v. (coefficient of variation) and with a prescribed PDF (such as the lognormal) to represent the epistemic uncertainty.

3 On Optimality of Structural System Design

Optimality in the design of structures depends on the field of application. In the field of aerospace engineering, where minimizing the weight of the structure is of paramount importance, optimal design aims to achieve minimum weight.

For land-based or earth-bound structures, cost of the structure is a more mundane and important objective in a particular design, and to achieve the minimum life-cycle cost is most relevant -- that is, minimizing the total cost over the whole life of a structure.

3.1 Expected Life-Cycle Cost, E(LCC), Design of Structures

In minimizing the cost of a structure, it is the expected whole life cost, or expected life-cycle cost, E(*LCC*), that is pertinent. This should include all the cost items over the life (normally >50-100 years) of the structure. Specifically, the total E(*LCC*), C_T, would consist of the following expected cost items.

$$C_T = C_I + C_M + C_S \tag{1}$$

where, C_I = the initial cost, including the design and construction costs;
C_M = the cost of maintenance, including the costs of inspection and repair;
C_S = social cost, including possible loss of lives, injuries, loss of revenues, etc.

For consistency, all cost items must be transformed or expressed in "present value" taking into account the discount rate for the region under consideration.

Graphically, all the expected life-cycle cost items can be displayed as shown in Figure 1. This figure shows the E(*LCC*) versus the mean safety index used in the design of the structure. Observe that the initial cost, C_I, increases monotonically with increasing mean safety index, whereas the maintenance cost plus the social cost, $C_M + C_S$, will decrease monotonically with increasing mean safety index. The sum of these two cost items will give the total expected life-cycle cost, C_T, from which the mean safety index that will yield the minimum E(*LCC*) design can be identified.

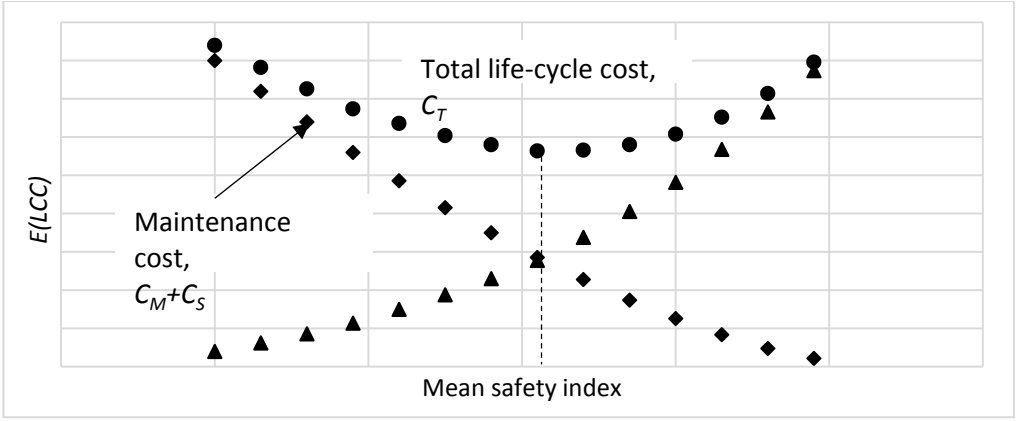

Figure 1. E(*LCC*) versus Mean Safety Index for Respective Cost Items

3.2 Practical Procedure for Determining the Optimal Design

To determine the structural design with the minimum expected life-cycle cost, E(*LCC*), proceed to design the structure with varying design safety indices, β, and estimate the corresponding expected life-cycle cost E(*LCC*). Plot the resulting designs as shown in Fig. 2 showing the various specific designs. From Fig. 2, the optimal design with the minimum E(*LCC*) and corresponding β can be identified.

4 Calculation of Reliability

For the optimal design identified from Fig. 2, its underlying reliability is strictly due to the effects of the aleatory uncertainty or variability of information. For design, the effects of the epistemic uncertainty must also be included which is discussed below in Sect. 4.2.

4.1 System Reliability due to Effects of Aleatory Uncertainty

For a complex system, the PDEM or *probability density evolution method* developed recently by Li and Chen (2009) is highly effective for determining the PDF of the ultimate system performance Z_{max}, i.e., $f_{Z_{\max}}(z)$, from which the mean reliability, *R,* can be assessed through the one-dimensional integration as indicated in Eq. 2.,

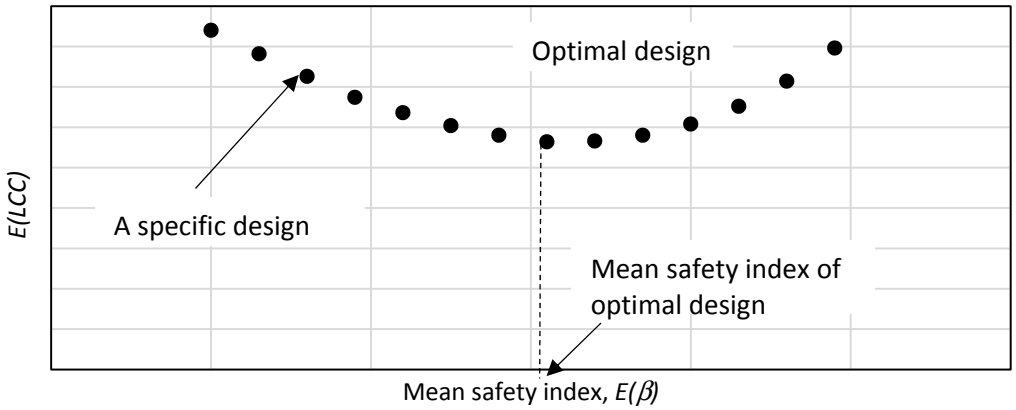

Figure 2. Plot of Various Designs with Varying Mean Safety Indices E( ) and Associated E(LCC)

$$R = \int_{\Omega} f_{Z_{\max}}(z)\,dz \tag{2}$$

where, Ω is the safe domain of the system.

For design, the effects of the epistemic uncertainty must also be included. The question is "how to do this systematically?" in the context of the reliability approach.

For the purpose of resolving the question posed above, the results obtained by the PDEM is useful and significant. In particular, the PDF of Z_{man} provides a rational and practical basis for including the effects of the epistemic uncertainty in the reliability-based design of a complex system.

4.2 System Reliability including Effects of Epistemic Uncertainty

Equation 2 gives the mean reliability (a single value) by the PDEM due to the aleatory uncertainty. To include the effects of the epistemic uncertainty, it is reasonable to limit this uncertainty as the error in the estimation of the mean-value of Z_{max}. That is, the range of possible mean-values of Z_{max} will represent the effects of the epistemic uncertainty.

In other words, the mean-value of Z_{max}, μ_Z, becomes a random variable; its PDF may be assumed (for convenience) to be a lognormal distribution with a mean of 1.0 and a specified c.o.v. (or equivalent range of values). Therefore, with the PDF of $Z_{max,}$ i.e., $f_{Z_{\max}}(z)$

and the PDF of $f_{\mu_Z}(\mu)$,

the convolution integration of these two PDFs would then yield the PDF of the system reliability, i.e.

$$R = \int_{\Omega} f_{Z|\mu}(z) \int_{0}^{\infty} f_{\mu_Z}(\mu)\,dz\,d\mu \tag{3}$$

The overall reliability of a structural system is then given by Eq. 3. Simple Monte Carlo simulation should yield the histogram of the reliability of the system, or its safety index. This histogram contains the effects of both types of uncertainty in the calculated system reliability.

From this histogram, percentile values of the calculated safety index, may be associated with respective levels of statistical "confidence". On this basis, a high confidence level of the safety index would be appropriate and may be specified for the safe design of a complete structural system.

It is well to emphasize also that a high confidence level in design serves to minimize the effects of the epistemic uncertainty.

5 Role of PDEM in Reliability-Based Design

The role of the PDEM is especially significant in the assessment of the reliability of a highly complex system. For such systems, the analysis of its reliability would traditionally rely on Monte Carlo simulations (MCS); however, for dynamic response analysis, because of the large number of degrees-of-freedom needed to accurately model a complex system, requiring very large sample size (of the order of 10^6 for very small failure probabilities) necessary in any MCS for sufficient accuracy, it could be impractical or too expensive to apply the MCS. In contrast, with the PDEM the sample size is around 250-400, irrespective of the size and complexity of a system.

With the PDEM, the reliability of a system can be defined through the complete system failure process defined by Chen and Li (2007). On this latter basis, the reliability of a system becomes

$$R = \text{Prob}\,[Z_{max} > 0] \tag{4}$$

where Z_{max} is the ultimate system performance under the load effects; Z_{max} is a function of the system parameters and of the load effects.

As stated earlier in Sect. 4.1, obtaining the PDF of Z_{man} provides a rational and practical basis for including the effects of the epistemic uncertainty in the reliability-based design of a complex system.

6 Confidence Level Appropriate for Design of High-Rise Building (Example Structural System)

In the reliability approach, particularly with the PDEM, that included the effects of both the aleatory and epistemic uncertainties in design, the underlying safety index, β, would be a random variable.. Clearly, for the design of a structural system, a value of the safety index must be selected at a high percentile value in order to ensure an adequate level of structural safety. For example, the 90% β as illustrated in Figure 8. In other words, for the design of large and complex structural systems, a high "confidence" value (or high percentile value) of the safety index is necessary to ensure an adequate level of safety of the structure as a system.

7 Design of a 15-Story R/C Building in Mexico City – An example of a complex system design, consider the 15-story reinforced concrete building shown in Figure 3; its three dimensional finite element model is shown in Figure 4. This building is located in Mexico City and survived the 1985 Mexico earthquake with minor damage.

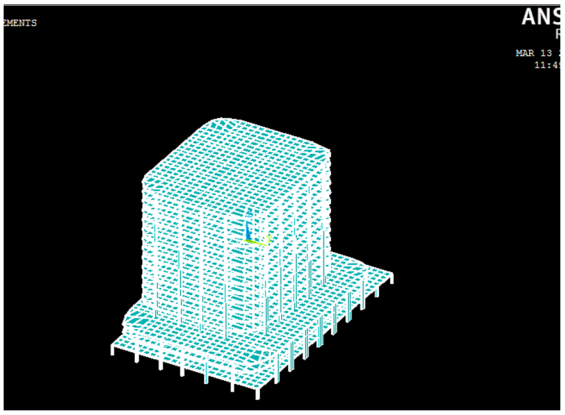

Figure 3. 15-Story R/C Building in Mexico City

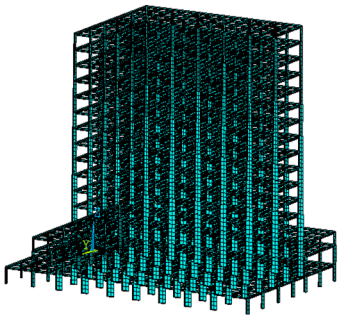

Figure 4. 3D FEM of the 15-Story Building

The two directions of the earthquake ground motions are shown below in Figures 11a and 11b.

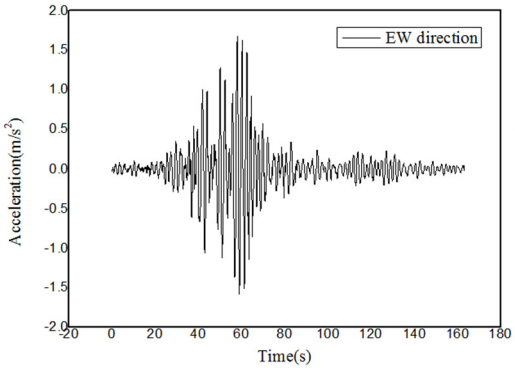

Figure 5a. EW Ground Motions

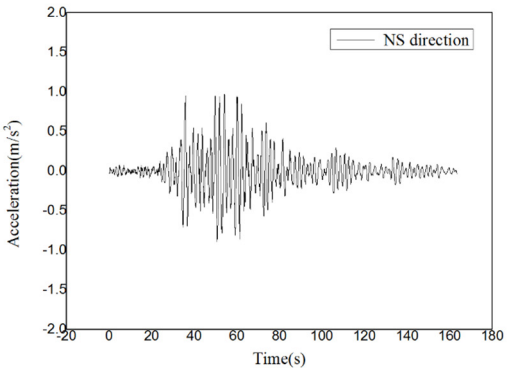

Figure 5b. NS Ground Motions

Therefore, an essential and important remaining question is "*what confidence level is appropriate for the design of a complex structure, as a complete system?*" This is the key question for the design of a complex system. To answer this important question, examine the confidence levels that underlie good professional practice; particularly in the successful design of existing major critical systems. In this regard, and for this purpose, consider the following the high-rise building example illustrated below.

Described below, in Table 1, are the properties of the actual 15 story R/C building as designed and built. The details of the column sizes at the different stories, are shown as indicated in Table 1.

Table 1. Details of Column Sizes and Rebars at Various Story Levels

Level	***Section (cm)***	***Stirrup A***	***Stirrup B***	***Details (below)***	***Rebars A***	***Rebars B***
Basement to level 3	150X60	# 4 @8"	#3 @10"	1 -1	2#10+1#8	1#8
Level 4 to level 6	125X60	#3 @8"	#3 @10"	1-2	2#10	1#8
Level 7 to level 8	100X60	#3 @8"	#3 @10"	1-3	1#10+1#8	1#6

Level 9 to level 10	85X60	#3 @8”	-	2-1	2#8+1#6	-
Level 11 to level 14	60X60	#3 @10”	-	2-2	2#8	-
Level 15	45X45 and 40X40	#3 @10”	-	2-3	1#8+1#6	-

The 2D elevations of the building are shown in Figure 6.

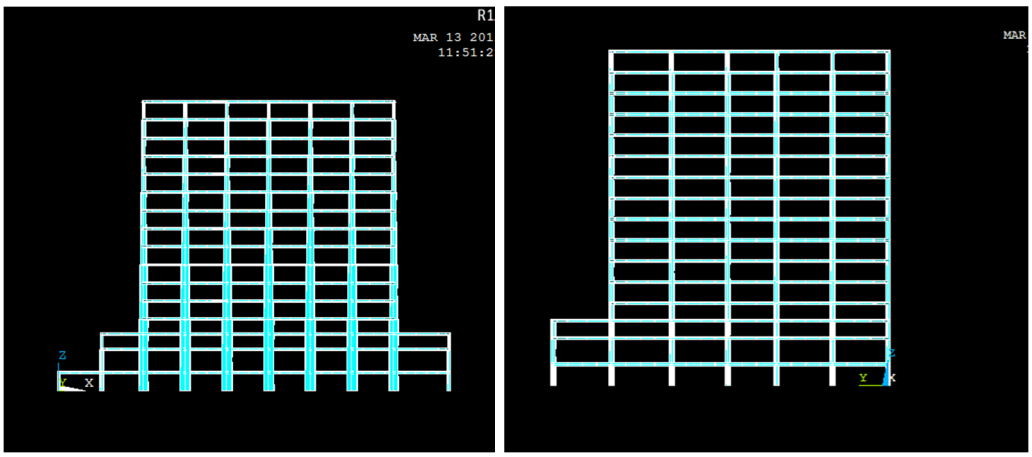

Figure 6. 2D Elevation Sections of the 15-story Building

In this example,. E_1 , E_2 and E_3 are the concrete initial Young’s moduli from the basement to level 7, from level 8 to 9, and from level 10 to 15, respectively, and are random variables with the statistical information listed in Table 2.

Table 2. The concrete initial Young’s modulus (×10^{4}MPa)

Distribution	Normal	Normal	Normal
Mean values	3.250	3.150	3.000
Standard deviations	0.325	0.315	0.300

The reliability of the maximum inter-story drift can be described by:

$$R = \Pr\left\{Z_{max}\left(E_1, E_2, E_3\right) < \phi_B\right\}$$
$$= \Pr\left\{\max_{\tau \in T}\left[\bigcup_{j=1}^{15} X_j\left(E_1, E_2, E_3, \tau\right)/h_j\right] < \phi_B\right\} \quad (5)$$

in which Z_{max} is the performance function and determined by $X_j(.)(j=1,..,15)$, which is the inter-story drift between the (j-1)th story and the jth story at time τ over the time period T. The story height for the jth story is h_j. The ϕ_B is the threshold of the inter-story drift angle, which is set as 0.02.

7.1 Response Analysis and Design of the 15-Story Building -- For this 15-stpry building, the calculations of its response for the 3D model of the building is quite involved. The number of finite elements is over 205,000, and the total number of nodes and dofs are over 140,000

and 800,000, respectively, if the model with shell elements is used. However, the number of finite elements is over 72,000, and the total number of nodes and dofs are over 63,000 and 200,000, respectively, for the model used in the PDEM analysis without the shell elements.

With the PDEM (Li and Chen, 2007), about 135 representative points or samples of deterministic building responses, with their respective probabilities, were necessary to obtain the PDF of the ultimate performance function, Z_{max} of the building as shown in Fig. 7 (with twin modes); and the safety index $\beta = 2.73$. This PDF represents only the effect of the underlying aleatory uncertainty. Introducing the distribution fitting procedure, the same aleatory uncertainty effect can be modeled approximately with the fitted lognormal PDF with a mean value of 0.9 and standard deviation of 0.035 (also shown in Fig. 7 with single mode); the corresponding mean safety index of the fitted lognormal PDF would be $\beta = 2.77$.

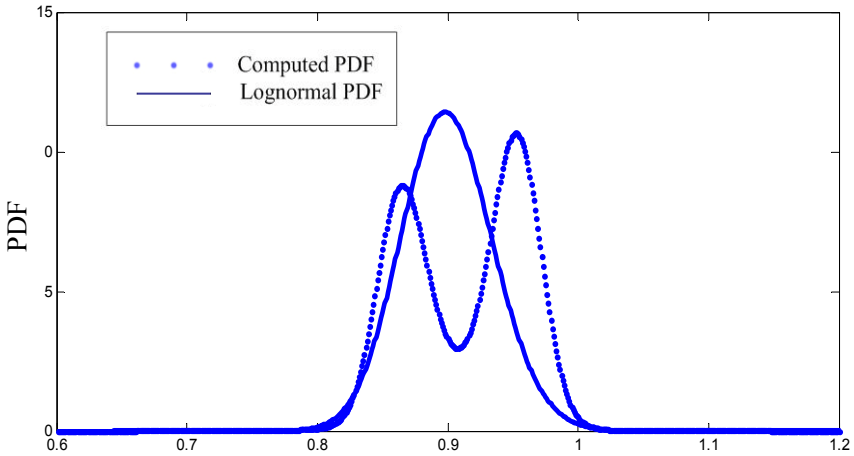

Figure 7. Computed PDF of Zmax of the Building and Corresponding Fitted Lognormal

For this example, assume that the epistemic uncertainty (representing the inaccuracy of the mean-value of Z_{maxx}) can be modeled also with a lognormal PDF with a mean-value of 1.0 and a c.o.v. of 0.10. With Eq. 3, convolution integration of this lognormal PDF and the lognormal PDF of the aleatory uncertainty with a mean of 0.9 and standard deviation of 0.035, would yield the histogram of all possible values of the safety index for the 15-story building.

Similar PDEM calculations were performed for the same building with different percentages of the original building design; namely, 80%, 90%, 95%, and 105%, 110%, 120%, 130% of the original as-built structure. The results of all these cases, together with the corresponding expected life-cycle costs, E(*LCC*), in million U.S. dollars, are summarized below in Table 3.

Table 3. Reliability Index β and E(LCC) for All Cases

Case (% of original)*	80%	90%	95%	100%	105%	110%	120%	130%
Mean β E(*LCC*) **	0.023 876	0.465 576	1.71 82.86	2.72 11.24	2.85 9.59	2.99 8.46	3.31 7.34	3.74 7.21
90% conf. β E(*LCC*)**	0.025 875	0.524 539	1.91 55.14	3.05 7.46	3.23 6.80	3.39 6.59	3.71 6.69	4.22 7.07
95% conf. β E(*LCC*)**	0.026 874	0.545 526	2 45.67	3.18 6.73	3.37 6.36	3.55 6.30	3.87 6.60	4.39 7.05

*in percentage of original as-built structure
**in million U.S. dollars

Plots of the reliability index β (for 90% and 95% confidence) versus the corresponding E(*LCC*), are shown below in Figures 8 and 9, respectively.

Figures8 and 9 clearly show that with 90%-95% confidence the optimal design of the 15-story building would have required a safety index of β = 3.39-3.55 which is 110% of the original as-built design; i.e., to obtain the minimum E(*LCC*) design would require slightly higher, 110%, of the original as-built building. Observe from Table 2, that the original as-built structure was designed with a safety index of β = 3.05-3.18 with the same 90%-95% confidence.

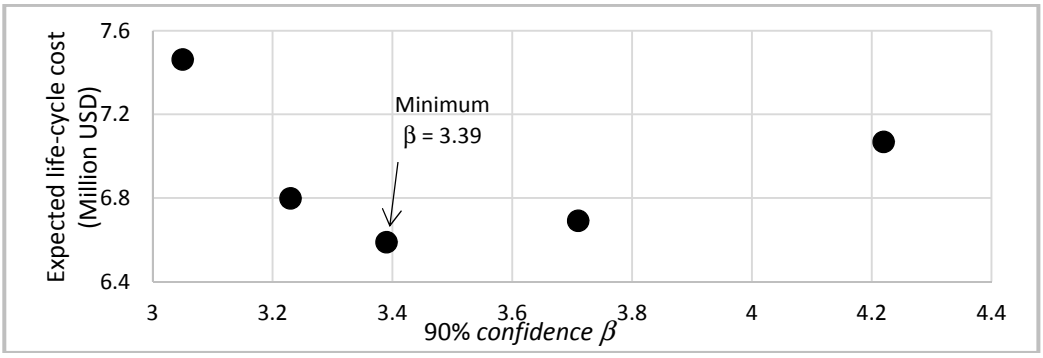

Figure 8. Plots of alternative designs with 90% confidence β versus respective E(*LCC*)

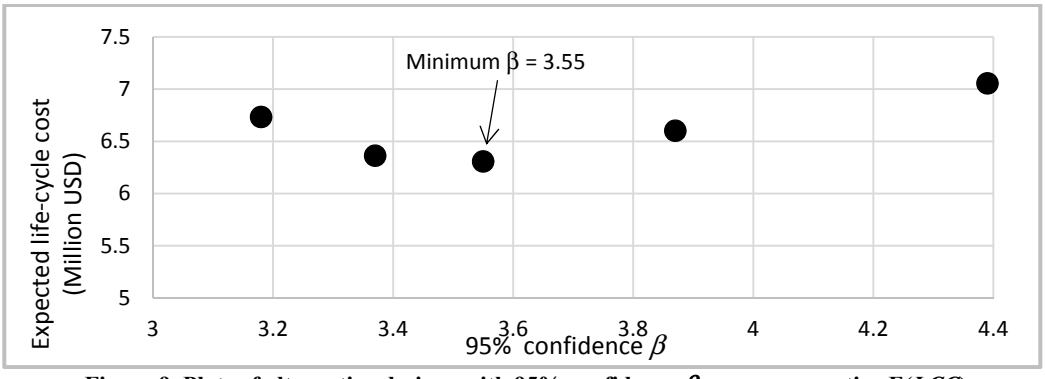

Figure 9. Plots of alternative designs with 95% confidence β versus respective E(*LCC*)

In summary, therefore, on the bases of the results for the high0rise building,, it appears that for the optimal design of critical engineering systems, a safety index within the 90%-95% confidence level would be consistent with good professional practice, and may be considered acceptable to ensure safety for the design of a complete structural system.

8 Conclusions

The main conclusions of this study may be summarized as follows:

1. The required safety in the design of a structural system cannot be prescribed as in the case of a structural component. Each structural system is invariably unique; thus, the required safety for its design must be determined and assessed independently.

2. Procedures for the design of structural systems have been proposed in the past, including recent studies that are based on the reliability approach. However, several issues relating to the optimal design as a complete system require further studies, including the effects of both the aleatory and epistemic uncertainties.

3. A procedure for determining the safety index for the design of a structural system is proposed; the procedure is based on achieving the minimum expected life-cycle cost design of the structure that explicitly includes the effects of the aleatory and epistemic uncertainties.

4. Based on the example of the hugh-rise building illustrated, the proposed procedure shows that a "confidence level" of 90%-95% for the reliability-based design is consistent with existing level of acceptable safety for major structural systems.

5. Moreover, the proposed reliability-based approach, based on achieving the minimum life-cycle cost design, may yield lower life-cycle cost design compared to an existing conventional design. This is illustrated specifically in the case of the 15-story building in Mexico City -- the building could have been designed for earthquake resistance (with the proposed method) with a higher safety level and lower cost.

9 Acknowledgments

This paper is based on background materials that were developed by the authors jointly or independently performed at the University of California, Irvine, USA, at the Chongqing University, Chongqing, China, or at the Autonomous Mexico State University, Toluca, Mexico.

10 References Cited

American Petroleum Institute (API), 1993, "Recommended Practice for Planning, Designing and Constructing Fixed Offshore Platforms – Load and Resistance Factor Design", *API RP 2ª LRFD*, First Edition, July, Washington, D.C.DOI: 10.1155/2019/4291703

Chen JB, Li J., 2007, "Development-process-of-nonlinearity-based reliability evaluation of structures". *Probabilistic Engineering Mechanics*; 22(3): 267-275.

Ellingwood B, Galambos TV. 1982 "Probability-based criteria for structural design", *Structural Safety* 1982;1(1):15–26.

Li Jie & Chen Jian-Bing, 2004, "Probability density evolution method for dynamic response analysis of structures with uncertain parameters", *Computational Mechanics*, 34(5), 400-409.Li

Li Jie and Chen Jian-Bing, 2007, "The Number Theoretical Method in Response Analysis of Nonlinear Stochastic Structures", *Computational Mechanics*, 39(6), 693-708.

Li, J. and Chen, JB. 2009, *Stochastic Dynamics of Structures,* John Wiley & Sons, 103(GT11), 1227-1246.

RISK-INFORMED LIFE-CYCLE MAINTENANCE MANAGEMENT FRAMEWORK FOR CIVIL INFRASTRUCTURE UNDER CLIMATE CHANGE.

Dan M. Frangopol

Professor, Fazlur R. Khan Endowed Chair of Structural Engineering and Architecture

Lehigh University, USA

Mitsuyoshi Akiyama

Professor, Department of Civil and Environmental Engineering, Waseda University, Japan

International Symposium on Emerging Developments and Innovative Applications of Reliability Engineering and Risk Managements (EDIARR2022),30 October-3 November2022, Taipei
Chen, S. S. &Ang, Alfredo. H-S. (Editors)

RISK-INFORMED LIFE-CYCLE MAINTENANCE MANAGEMENT FRAMEWORK FOR CIVIL INFRASTRUCTURE UNDER CLIMATE CHANGE

Dan M. Frangopol[1], and Mitsuyoshi Akiyama[2]
[1]*Department of Civil and Environmental Engineering, Engineering Research Center for Advanced Technology for Large Structural Systems (ATLSS Center), Lehigh University, Bethlehem, PA, USA*
E-mail: dan.frangopol@lehigh.edu
[2]*Department of Civil and Environmental Engineering, Waseda University, Tokyo, Japan*
E-mail: akiyama617@waseda.jp

Abstract: Civil infrastructure systems are subjected to various deterioration processes during their lifetime, including progressive deterioration such as corrosion or sudden deterioration due to natural hazards. However, the future climate change effects are foreseen to exacerbate the deterioration process and increase the failure probability associated with civil infrastructure. Therefore, a risk-based framework for life-cycle maintenance management should be established to improve the communities' disaster preparedness. This paper provides an overview of the risk-based framework for life-cycle assessment associated with civil infrastructure under climate change effects. The progress and future direction of structural design methodology, including reliability-, risk-, and resilience- assessment as essential aspects for life-cycle management, are introduced. The general framework for estimating the life-cycle performance associated with civil infrastructure is presented. Finally, a case study to illustrate the integration of nonstationary climate change effects on tsunami hazards and its potential application in risk-based disaster waste assessment of coastal residential structures is discussed.

***Keywords*:** Life-cycle, reliability, risk, resilience, climate change, maintenance, management, optimization, infrastructure

1 Introduction

Civil infrastructure is essential and should be maintained in a satisfactory performance to ensure economic growth and social development (Frangopol, Dong, and Sabatino 2017; Frangopol and Kim 2019, 2022). In addition, the infrastructure performance under disruptive events plays a crucial role in the real-time emergency decision. Considering the critical role of the civil infrastructure, several intervention actions, such as maintenance or replacement, must be implemented to maintain proper functionality during the infrastructure's lifetime.

Under the risk-based life-cycle management framework, the life-cycle cost-benefit analysis offers the most straightforward manner to quantify the effectiveness of a management plan (Ishibashi, Akiyama, Frangopol, et al. 2021). On the other hand, the probabilistic optimization method based on predetermined objective functions delivers the most representative output. It can be regarded as the core of life-cycle management processes, such as inspection, maintenance, and retrofit under progressive deterioration (Kim and Frangopol 2012) or sudden hazard (Zhu and Frangopol 2013).

However, in the wake of the recent climate change issues, the primary components of the civil infrastructure systems, such as buildings and bridges, are foreseen to become more vulnerable due to the intensification of extreme events (e.g., Alhamid, Akiyama, Ishibashi, et al. 2022; Yang and Frangopol 2018, 2019). Under the limited resources and growing risk, considering climate changes effects on risk-based life-cycle management has become increasingly important to achieve adequate and effective maintenance strategy to improve the disaster preparedness of the possible affected communities. Therefore, this paper aims to provide an overview of the risk-based framework for life-cycle assessment associated with civil infrastructure under climate

change effects to achieve optimum management strategies. The progress and future direction of structural design methodology, including reliability-, risk-, and resilience- assessment as essential aspects for life-cycle management, are introduced. The general framework for estimating the life-cycle performance associated with civil infrastructure is presented. An illustrative example is provided to illustrate the integration of nonstationary climate change on tsunami hazards and discuss its potential application in risk-based disaster waste assessment of coastal residential structures.

2 Overview of life-cycle risk and performance assessment of civil infrastructure

2.1 Progress and future directions of structural design methodology

Figure 1 shows the progress of structural design from the conventional allowable stress design (ASD) to a life-cycle-based design considering multiple hazard exposure (Akiyama, Frangopol, and Ishibashi 2020). The evolution from ASD to load and resistance-factored design (LRFD) indicates the importance of considering uncertainties to balance the structural safety and economic aspects. Following this, the reliability-based method was established to achieve a specific hierarchy of resistance associated with structural components and failure modes to ensure appropriate plastic mechanisms and avoid brittle failure (Akiyama et al. 2012).

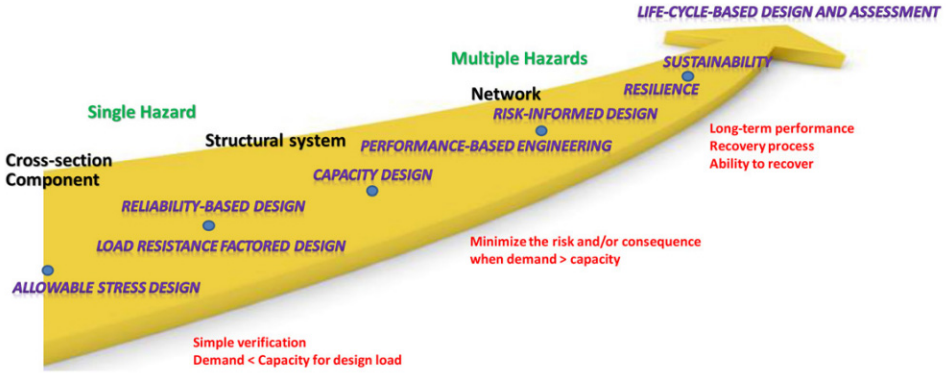

Figure 1. Progress on structural design methodology
(Adapted from Akiyama, Frangopol, and Ishibashi (2020))

A drawback of the reliability-based design is that the failure consequences cannot be explicitly taken into account. This issue needed to pave the way for the widely-implemented performance-based engineering that enable the estimation of the consequences. The probability of a loss exceeding value L (i.e., risk) can be calculated according to the total probability theorem as:

$$P\left[Loss > L\right] = \sum_{LS}\sum_{H} P\left[Loss > L \mid LS\right] \cdot P\left[LS \mid H\right] \cdot P\left[H\right] \tag{1}$$

where $P\left[Loss > L \mid LS\right]$ is the probability of loss exceeding L given the limit state LS, $P\left[H\right]$ is the probability of occurrence of hazard H, $P\left[LS \mid H\right]$ is the conditional probability of the limit state LS given the occurrence of H, and $P\left[LS \mid \mathrm{H}\right]$ is the conditional probability of the limit state LS given the hazard scenario H.

To optimize restoration activities associated with life-cycle management, resilience is defined as the performance indicator after the occurrence of disruptive events. Resilience describes the

ability of a social unit to contain the effects of hazards when they occur and carry out recovery activities in ways that minimize social disruption (Ishibashi, Akiyama, Frangopol, et al. 2021).

Despite the significant progress of life-cycle structural design methodology shown in Figure 1, the effects of climate change have rarely been studied and considered in the design of civil infrastructure. As extreme events become frequent due to climate change, the infrastructure's actual performance could be significantly affected (Dong and Frangopol 2016). Existing studies have been limited to impact analysis of climate change on the life-cycle risk or providing a framework for adaptation strategy under an arbitrary case of climate change projections (Dong and Frangopol 2017). The design methodology considering climate change effects has remained challenging due to the inherent nonstationary characteristics of climate change (Alhamid, Akiyama, Aoki, et al. 2022). Therefore, the structural design methodology should be geared toward the consideration of climate change uncertainties in the future to achieve a more appropriate structural design. The general framework for risk-based life-cycle assessment and management under climate change impacts is overviewed in the following subsection.

2.2 General framework for estimating life-cycle reliability and risk of structure and infrastructure under climate change effects

Figure 2 shows the flowchart for estimating the life-cycle reliability and risk of structure and infrastructure under multiple hazards and climate change effects. In step 1, it is necessary to identify the analyzed civil infrastructure system. This system can include bridges, buildings, seawalls, dams, or other lifeline facilities such as power substations. In addition, each system could be correlated with the others in terms of life-cycle risk.

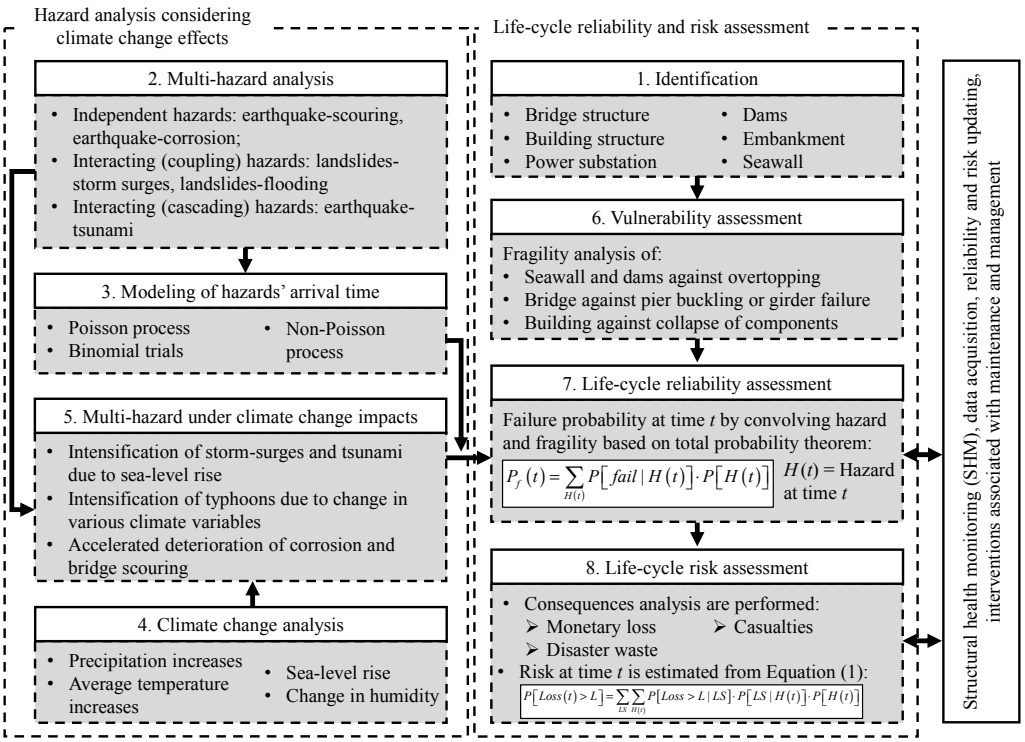

Figure 2. Flowchart for estimating the reliability and risk of structure and infrastructure systems under multi-hazards and climate change impacts

The next step is to identify the potential hazards in the analyzed system. In step 3, the occurrence probability of the identified hazards is modeled according to Poisson or non-Poisson process. On the other hand, climate change analysis, such as temperature increase, humidity changes, and sea-level rise, is performed in step 4. Considering that climate change intensities and associated uncertainties are increasing over time, the nonstationary modeling approach to climate change can be developed (Alhamid, Akiyama, Aoki, et al. 2022). The climate change effects are combined with the multiple identified hazards based on conditional hazard assessment and total probability theorem to obtain a time-variant hazard at time *t*.

After identifying the civil infrastructure system, its vulnerability can be evaluated depending on the corresponding limit-state condition. For instance, seawalls and dams are more prone to tsunami waves overtopping, while bridges and buildings could undergo component failure under extreme events.

The life-cycle reliability of the analyzed system can be estimated by convolving the system's vulnerability with the corresponding time-variant hazards considering climate change effects to obtain the failure probability at time *t* in step 7. For reliability-based design, several interventions associated with life-cycle reliability-based management can be made in this step.

Finally, the life-cycle risk associated with the socioeconomic and environmental consequences and infrastructure performance is evaluated using Equation (1) considering the hazard at time *t*. By applying the framework described in Figure 2, the climate change effects can be adequately incorporated into the life-cycle risk assessment. To comprehend the proposed framework further, a case study illustrating the integration of nonstationary sea-level rise effects on tsunami hazard and its potential application in risk-based disaster waste assessment of coastal residential structures is presented.

3 Case study

3.1 Time-variant tsunami hazard integrated with nonstationary sea-level rise effects

The main challenge in introducing the effects of climate change on the life-cycle risk assessment of structure and infrastructure systems is integrating the associated climate change effects in the hazard assessment. Therefore, as an illustrative example, the integration of nonstationary sea-level rise effects with tsunami hazards is presented herein according to (Alhamid, Akiyama, Aoki, et al. 2022). Their study developed a stochastic renewal process model to deal with the recurring tsunami hazards generated by the anticipated Nankai Trough earthquake. The cumulative distribution function (CDF) associated with the maximum tsunami height H_{max} from the last earthquake occurrence up to an analyzed time t_D can be described as follows:

$$F_{H_{max}}(h;t_D) = \sum_{n=1}^{\infty} \left(F_H(h)\right)^n \cdot \left[\int_0^{t_D} \left\{f_T^{(n)}(t) - f_T^{(n+1)}(t)\right\} dt\right] \tag{2}$$

where $F_{Hmax}(h; t_D)$ denotes the CDF of maximum tsunami height H_{max} with an inundation depth value of h up to time t_D, $F_H(h)$ is the tsunami hazard CDF assuming the earthquake's occurrence, n is the number of earthquake occurrences, and $f_T(t)$ is the probability density function (PDF) of the earthquake's inter-arrival time. For the case of the Poisson process, $f_T(t)$ can be defined as an exponential distribution.

When the effects of sea-level rise are considered, the tsunami hazards H_1, H_2, …, $H_{n=N(t_D)}$ are no longer identically distributed for each event, where $N(t_D)$ denotes the number of earthquake events up to time t_D. Therefore, to introduce the effects of sea-level rise, Equation (2) is extended as follows (Alhamid, Akiyama, Aoki, et al. 2022):

$$\begin{aligned} F_{H_{max}}(h;t_D) &= \sum_{n=1}^{\infty}\int_0^{t_D}\left[\prod_{k=1}^{N(t_D)=n} F_{H(\mathbf{x}_r,t_k)}(h)\right]\cdot\left[f_T^{(n)}(t)-f_T^{(n+1)}(t)\right]dt \\ &= \sum_{n=1}^{\infty}\int_0^{t_D}\left[\prod_{k=1}^{N(t_D)=n}\int_0^{\infty}\left\{F_{H|\Psi}(h\,|\,\psi(\mathbf{x}_r,t))\cdot\left|-\frac{dF_{\Psi}(\psi(\mathbf{x}_r,t))}{d\psi}\right|\right\}d\psi\right]\cdot\left[f_T^{(n)}(t)-f_T^{(n+1)}(t)\right]dt \end{aligned} \tag{3}$$

where $F_{H(\mathbf{x}_r,t_k)}(h)$ is the tsunami CDF considering sea-level rise effects at time t_k, $F_{H|\Psi}(h\,|\,\psi(\mathbf{x}_r, t))$ is the CDF of conditional tsunami probability given that the sea-level rise intensity Ψ over the target earthquake fault location $\mathbf{x}_r$ at time t equals $\psi(\mathbf{x}_r, t)$, and $F_{\Psi}(\psi(\mathbf{x}_r, t))$ is the CDF of the sea-level rise when the sea-level rise intensity Ψ is less than $\psi(\mathbf{x}_r, t)$. According to Equation (3), the sea-level rise hazard is considered in the tsunami hazard through the total probability theorem. The conditional tsunami hazard curve given sea-level rise was obtained from tsunami propagation analyses considering several sea-level rise cases (Alhamid, Akiyama, Ishibashi, et al. 2022).

Figure 3 shows the tsunami inundation map in Susaki city of Japan for 0 m and 0.6 m sea-level rise. Due to the effects of sea-level rise, the tsunami inundation in Susaki city is increased to a greater extent, while the inundation area is hardly affected. Furthermore, Figure 3(c) shows the time-variant tsunami hazard curve in the analyzed site A in 2100 and 2050. In the long-term (i.e., in 2100), the effects of sea-level rise are foreseen to amplify the tsunami hazard substantially compared with 2050. Therefore, climate change effects should be considered during the life-cycle risk assessment to obtain the appropriate maintenance strategy.

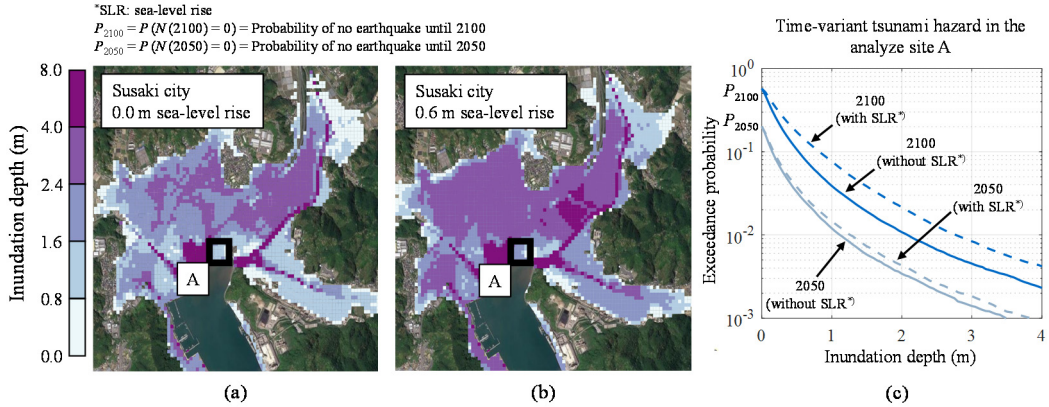

Figure 3. (a) Inundation map in Susaki city for 0 m of sea-level rise, (b) Inundation map in Susaki city for 0.6 m of sea-level rise, and (c) time-variant tsunami hazard evaluated in the analyzed cite A.

3.2 Applicability of the time-variant tsunami hazard assessment

The colossal impact of tsunamis causes not only a significant amount of monetary loss and casualties but also generates a substantial amount of disaster waste. Figure 4 shows the risk-based disaster waste estimation generated in several municipalities of Mie Prefecture of Japan (Ishibashi, Akiyama, Kojima, et al. 2021).

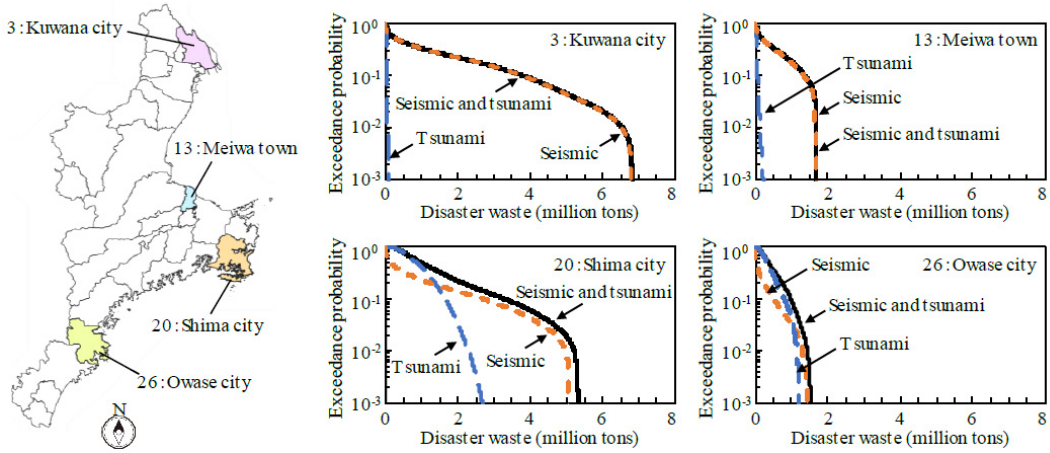

Figure 4. Risk curve associated with disaster waste amount estimated in several municipalities in Mie Prefecture of Japan

Reference: (Ishibashi, Akiyama, Kojima, et al. 2021)

According to the results presented by (Alhamid, Akiyama, Aoki, et al. 2022), sea-level rise could amplify the tsunami hazard by up to 50% in a region sensitive to the sea-level rise hazard. However, it is noteworthy that the time-variant tsunami hazard developed in (Alhamid, Akiyama, Aoki, et al. 2022) is mainly concerned with the maximum tsunami inundation height during the life-cycle period of the infrastructure system. The compound renewal process model should be implemented when the cumulative consequences associated with disaster debris or monetary loss are of interest. Nevertheless, due to the climate change effects, recalculating risk associated with disaster debris should be performed to achieve an accurate risk-informed decision-making process and improve the resilience of coastal communities.

4 Conclusions

The following conclusions are drawn:

1. The framework for risk-based life-cycle maintenance management under climate change effects is presented. The climate change effects are combined with multiple identified hazards based on conditional hazard assessment and total probability theorem before estimating the physical damage state.

2. The uncertainty associated with future climate change (i.e., nonstationary climate change effects) is essential for the structural design methodology. Therefore, the progress of the structural design methodology should shift toward the consideration of climate change uncertainties in the future to achieve a more appropriate structural design methodology.

3. The effects of sea-level rise due to climate change could intensify the tsunami hazard considerably. Therefore, during the risk-based assessment associated with disaster debris, the effects of climate change should be considered to increase the estimation accuracy and improve communities' disaster preparedness.

5 References

Akiyama, Mitsuyoshi, Dan M. Frangopol, and Hiroki Ishibashi. 2020. "Toward Life-Cycle Reliability-, Risk- and Resilience-Based Design and Assessment of Bridges and Bridge Networks under Independent and Interacting Hazards: Emphasis on Earthquake, Tsunami and Corrosion." *Structure and Infrastructure Engineering* 16 (1): 26–50. doi:10.1080/15732479.2019.1604770.

Akiyama, Mitsuyoshi, Hiroshi Matsuzaki, Hai T. Dang, and Motoyuki Suzuki. 2012. "Reliability-Based Capacity Design for Reinforced Concrete Bridge Structures." *Structure and Infrastructure Engineering* 8 (12): 1096–1107. doi:10.1080/15732479.2010.507707.

Alhamid, Abdul Kadir, Mitsuyoshi Akiyama, Koki Aoki, Shunichi Koshimura, and Dan M. Frangopol. 2022. "Stochastic Renewal Process Model of Time-Variant Tsunami Hazard Assessment under Nonstationary Effects of Sea-Level Rise due to Climate Change." *Structural Safety* 99. doi:https://doi.org/10.1016/j.strusafe.2022.102263.

Alhamid, Abdul Kadir, Mitsuyoshi Akiyama, Hiroki Ishibashi, Koki Aoki, Shunichi Koshimura, and Dan M. Frangopol. 2022. "Framework for Probabilistic Tsunami Hazard Assessment Considering the Effects of Sea-Level Rise due to Climate Change." *Structural Safety* 94. doi:10.1016/j.strusafe.2021.102152.

Dong, You, and Dan M. Frangopol. 2016. "Probabilistic Time-Dependent Multihazard Life-Cycle Assessment and Resilience of Bridges Considering Climate Change." *Journal of Performance of Constructed Facilities* 30 (5). doi:10.1061/(ASCE)CF.1943-5509.0000883.

Dong, You and Dan M. Frangopol. 2017. "Adaptation Optimization of Residential Buildings under Hurricane Threat Considering Climate Change in a Life-cycle Context." *Journal of Performance of Constructed Facilities* 31 (6). doi:10.1061/(asce)cf.1943-5509.0001088.

Frangopol, Dan M., You Dong, and Samantha Sabatino. 2017. "Bridge Life-Cycle Performance and Cost: Analysis, Prediction, Optimisation and Decision-Making." *Structure and Infrastructure Engineering* 13 (10): 1239–57. doi:10.1080/15732479.2016.1267772.

Frangopol, Dan M., and Kim, Sunyong. 2019. "Life-Cycle of Structures under Uncertainty: Emphasis on Fatigue-Sensitive Civil and Marine Structures." ISBN-13: 978-0-367-14755-6, CRC Press, Boca Raton, London, New York.

Frangopol, Dan M., and Kim, Sunyong. 2022. "Bridge Safety, Maintenance and Management in a Life-Cycle Context." ISBN: 978-1-032-05281-6, CRC Press, Boca Raton, London, New York.

Ishibashi, Hiroki, Mitsuyoshi Akiyama, Dan M. Frangopol, Shunichi Koshimura, Takayuki Kojima, and Kengo Nanami. 2021. "Framework for Estimating the Risk and Resilience of Road Networks with Bridges and Embankments under Both Seismic and Tsunami Hazards." *Structure and Infrastructure Engineering* 17 (4): 494–514. doi:10.1080/15732479.2020.1843503.

Ishibashi, Hiroki, Mitsuyoshi Akiyama, Takayuki Kojima, Koki Aoki, Shunichi Koshimura, and Dan M. Frangopol. 2021. "Risk Estimation of the Disaster Waste Generated by Both Ground Motion and Tsunami due to the Anticipated Nankai Trough Earthquake." *Earthquake Engineering & Structural Dynamics* 16 (1): 2134–55. doi:10.1002/eqe.3440.

Kim, Sunyong, and Dan M. Frangopol. 2012. "Probabilistic Bicriterion Optimum Inspection/monitoring Planning: Applications to Naval Ships and Bridges under Fatigue." *Structure and Infrastructure Engineering* 8 (10): 912–27. doi:10.1080/15732479.2011.574811.

Yang, David Y., and Frangopol, Dan M. 2018. "Bridging the Gap between Sustainability and Resilience of Civil Infrastructure Using Lifetime Resilience." Chapter 23 in *Routledge Handbook of Sustainable and Resilient Infrastructure*, P. Gardoni, ed., Routledge, 419-442.

Yang, David Y., and Frangopol, Dan M. 2019. "Life-Cycle Management of Deteriorating Civil Infrastructure Considering Resilience to Lifetime Hazards: A General Approach Based on Renewal-Reward Processes." *Reliability Engineering and System Safety*, 183: 197-212. doi: 10.1016/j.ress.2018.11.016

Zhu, Benjin, and Dan M. Frangopol. 2013. "Risk-Based Approach for Optimum Maintenance of Bridges under Traffic and Earthquake Loads." *Journal of Structural Engineering* 139 (3): 422–34. doi:10.1061/(asce)st.1943-541x.0000671.

CHALLENGES AND OPPORTUNITIES IN ANALYSIS OF STRUCTURAL AND SYSTEM RELIABILITY.

Armen Der Kiureghian

President, American University of Armenia, Yerevan
An affiliate of the University of California
Taisei Professor of Civil Engineering Emeritus
Department of Civil & Environmental Engineering
Structural Engineering, Mechanics & Materials Program University of California at Berkeley,USA

International Symposium on Emerging Developments and Innovative Applications of Reliability Engineering and Risk Managements (EDIARR2022),30 October-3 November2022, Taipei
Chen, S. S. &Ang, Alfredo. H-S. (Editors)

CHALLENGES AND OPPORTUNITIES IN ANALYSIS OF STRUCTURAL AND SYSTEM RELIABILITY

Armen Der Kiureghian
Department of Civil and Environmental Engineering, University of California, Berkeley, USA
E-mail: adk@ce.berkeley.edu

Abstract: This paper describes highlights from a recent book by the author on structural and system reliability (Der Kiureghian 2022). The book provides a state-of-the-art description of methods for reliability analysis of structures and systems together with numerous examples and applications. Included are the first- and second-order reliability methods, system characterization and reliability assessment, simulation/sampling methods, methods for time- and space-variant reliability analysis, and Bayesian methods for reliability updating. The last four chapters of the book deal with topics of current research and development interest, including finite-element reliability methods, nonlinear stochastic dynamics, reliability-based optimal design, and Bayesian network for modeling and reliability assessment and updating of infrastructure systems. After a brief review of the main contents of the book on reliability methods, this paper focuses on some of the challenges in structural and system reliability analysis that remain unresolved and, hence, are fruitful areas for further research and development.

***Keywords*:** Bayesian network, sampling, strucrtural reliability, surrogate models, system reliability.

1 Introduction

Computational methods for reliability analysis of structural components and systems have been developing in the past 50 years. These include the first- and second-order reliability methods (FORM and SORM), various simulation or sampling methods, and response-surface or surrogate/meta modeling methods. Additional methods are available for systems, such as bounding or matrix-based methods, which require computation of joint component reliabilities (Der Kiureghian 2022).

In FORM and SORM, the limit-state surfaces delineating the boundary between safe and fail domains of system components are approximated by first or second order surfaces that are tangent to the actual surfaces at the so called "design points." These are points of maximum probability density in the failure domain when the random variables are transformed to the standard normal space. Solution by these methods requires repeated computations of the limit-state function(s) and its gradient(s) with respect to the random variables in order to find the design point(s), and in the case of SORM additional calculations to obtain the curvatures at the design point(s). Naturally, continuous differentiability of the limit-state functions is necessary, and this remains as a limitation of these methods. In most problems 10-100 iterations per design point is necessary. Hence, the number of repeated calculations of the limit-state function and its gradient can be in tens or hundreds, depending on the number of system components. One distinct advantage of FORM is that as a by-product of the analysis, it provides measures of importance of random variables. Furthermore, sensitivities with respect to limit-state or probability distribution parameters are obtained with little additional work. This capability is virtually unique among the various reliability methods.

Simulation or sampling methods are essentially variants of the well-known Monte Carlo Simulation (MCS) method. MCS has no limitations, but it requires a large number of samples particularly for small probability values, i.e., roughly equal to $1/p_f\delta_{\hat{p}_f}^2$, where p_f is the probability to be estimated and $\delta_{\hat{p}_f}$ is the coefficient of variation (c.o.v.) of the probability estimate. Hence, if p_f is of order 10^{-3} and we desire a c.o.v. of the estimate no greater than 25%,

we need a sample of size no less than 16,000, each sample involving computation of the limit-state function(s). Most structural systems have high reliability (small failure probability), and hence the need for more efficient sampling methods is obvious.

Depending on the nature of the problem, more efficient sampling methods include importance sampling, directional sampling with and without importance sampling, orthogonal-plane sampling, and subset simulation. Each of these methods has inherent assumptions or limitations. For example, importance sampling requires knowledge of points within the outcome space of the random variables, the neighborhoods of which contribute significantly to the failure probability. Most often, the design points mentioned above are used, which means they need to be obtained as in FORM. Alternatively, an adaptive method can be used to find these "importance" points by sampling. But this approach naturally requires more samples and has the danger of missing some important regions in the outcome space of the random variables.

Directional sampling is conducted in the standard normal space by searching for the limit-state surface nearest to the origin in randomly sampled directions. While not sensitive to the magnitude of the failure probability, as one can expect the number of directions to be sampled rapidly grows with the dimension (number of random variables) of the problem.

The orthogonal-plane sampling method requires knowledge of the design points (samples are generated in the plane(s) orthogonal to the vector(s) from the origin to the design point(s) in the standard normal space); hence this method can be considered as a correction to the FORM approximation. This method is not sensitive to the magnitude of the failure probability or the dimension of the problem.

Subset simulation breaks down the reliability problem into a series of conditional problems, each having a large probability, roughly of order 0.1. The estimate of the failure probability is obtained as a product of the conditional probabilities. However, since the samples for the conditional problems are statistically dependent, the ordinary MCS is not applicable. For this reason, variants of the Markov-Chain MCS have been used. The total number of simulations in this case can be relatively small (as small as a few hundred), but in the author's experience the resulting coefficient of variation of the probability estimate usually is high because of statistical dependence between the samples.

Details of the above sampling methods are described in Der Kiureghian (2022) and their performances are compared for a number of example applications.

As described above, structural and system reliability methods require repeated computations of the limit-state function(s) and, for some methods, the gradients with respect to the random variables. This does not pose a problem if the limit-state function(s) are given as easily computable analytical functions. However, most real-world problems are a lot more complex and require sophisticated computational tools to evaluate system responses and, thereby, the limit-state function(s). Real-world civil and mechanical problems of interest for reliability analysis are often characterized by high degrees of nonlinearity, fracture, large deformations, dynamic effects, multi-phase flow, etc. In addition, since system failures usually occur well beyond the ordinary range of behavior, consideration of extreme response conditions is essential in assessing safety and reliability of systems. For this to happen, it is necessary that reliability methods are integrated with software for solution of general-purpose structural, mechanical, and flow problems. On the other hand, it is desirable that this integration be non-intrusive so that existing computational software can be used without making major modifications.

With the above in mind, in recent years response surface or surrogate/meta modeling methods have been considered. The idea is to replace the computational (finite element) model with an easily computable mathematical approximation, which can then be used for reliability analysis by use of the methods described above. Most commonly, kriging in conjunction with a Gaussian random field or a polynomial chaos approximation is used together with a learning scheme to find locations within the random variable space where additional runs provide optimal information (Bichon et al. 2008, Schöbi et al. 2017). However, these methods are affected by the dimension of the problem and can be costly for real-world applications. In the current literature, applications of these approaches are limited to relatively simple academic problems.

2 Challenges and opportunities

Even though FORM is an approximate method and has certain limitations, its integration with general-purpose structural and mechanical computational platforms is valuable. This is because FORM analysis provides as a by-product information that is not provided by other reliability methods. Specifically, it provides the most likely failure realization (in the standard normal space), measures of important of random variables, and reliability sensitivities with respect to distribution and limit-state parameters. When mapped into the original space, the most likely failure realization provides insight as to the most likely conditions that will give rise to the failure event. This information can be used to alter the system design and enhance the reliability. The measures of variable importance help us to identify random variables that have greater influence on the reliability. This information can be used to provide more accurate modeling of these random variables, and possibly gathering more information that could reduce the associated uncertainty and thereby improve the system reliability. The sensitivities with respect to the parameters are useful in a variety of ways, including model refinement and reliability-based optimal design.

In order to implement FORM in a general-purpose finite element code, it is necessary to enable the code to compute gradients with respect to the random variables. These variables my define material property constants, load values, or geometric variables, including nodal coordinates. In general, conventional finite-difference methods for computing gradients can be highly costly as well as unreliable for implementation in computational platforms that use iterative methods. For this reason, efficient numerical algorithms for computing gradients that are consistent with the algorithm for computing the response have been developed (Zhang and Der Kiureghian 1993, Conte et al. 2003). These methods have been implemented in a few research-oriented finite element codes, including OpenSees (McKenna et al. 2003); however, few commercial finite element codes possess the capability to compute gradients. This remains a major challenge for use of FORM in conjunction with commercial computational software. It is noted that the availability of gradients in a finite element code is useful for other applications as well, including model refinement, sensitivity analysis, and reliability-based design optimization.

A related challenge in application of FORM in general-purpose computational codes is that one needs to assure continuous differentiability of the limit-state function(s) with respect to the random variables. It has been shown that the response gradients may not be continuously differentiable when the material constitutive law is non-differentiable (Zhang and Der Kiureghian 1993). To overcome this difficulty, rules for “smoothing” constitutive laws have been developed (Haukaas and Der Kiureghian 2005, Barbato and Conte 2005). It is noted that non-smooth constitutive laws (e.g., elasto-plastic) are often idealizations of reality and smoothened laws usually offer more realistic representation of material behavior.

Implementation of FORM in a gradient-enabled, general-purpose finite element code need not be intrusive. One needs to develop a separate code that interprets the random variables for the finite

element code, i.e., allocates them to the right places in the input file, and which repeatedly runs the finite element code for realizations of the random variables selected by the algorithm for finding the design point until convergence is achieved. All calculations, including the FORM approximation and importance and sensitivity measures can be computed with the outside code once the design point(s) are determined.

As mentioned earlier, classical SORM analysis requires computing second derivatives. This is too costly and difficult for general-purpose finite element codes. However, variants of SORM are available that avoid computing the second derivatives (Der Kiureghian 2022). One method fits a piecewise parabolic surface to selected points on the limit-state surface around the design point. This approach only requires repeated computations of the limit-state function to find the fitting points and is practical if the number of random variables is not large. The second approach employs gradient-based computations to iteratively find the principal curvatures of the limit-state surface at the design point in the order of decreasing absolute magnitude. Both methods can use the non-intrusive approach described for FORM.

In recent years, there has been increasing interest in response surface methods, where a surrogate or meta model is fitted to the exact computational (finite element) model and then used for reliability analysis. As mentioned earlier, usually a multidimensional random field is fitted by a kriging method to response values computed by the finite element model at selected realizations of the random variables. The approximating random field has zero variance at the fitted points and growing variance as one moves away from the fitted points. The selection of fitting points is then crucial, and methods have been used to select most informative points through a learning function (see, e.g., Bichon et al. 2008, Schöbi et al. 2017). These methods can be seen as purely data-based in the sense that the connection between the true physical model and the surrogate model is purely the response data computed at the fitting points. The approach is completely non-intrusive as one only needs to compute the actual response at the fitting points. Naturally, the number of needed data points for accuracy increases with the dimension of the problem (the number of random variables) and can grow rather rapidly. Existing applications of this method are for relatively simple, academic problems with small numbers of random variables.

A more promising approach is one that selects a surrogate model that is based on the physics of the problem. The idea for such an approximation was first proposed by Ditlevsen and Arnbjerg-Nielsen (1994) and used in an application dealing with reliability problems involving Gaussian random fields (Franchin et al. 2002). A more comprehensive and modern formulation of the approach is described in (Peherstorfer et al. 2018). The idea is to use a surrogate model that shares some physical features of the real complex model, which is then adjusted to fit the actual model. The surrogate model is easy to compute and is used for reliability analysis by sampling or FORM/SORM. Since the surrogate model is physics based, it is anticipated that it will be less sensitive to the dimension of the problem and more accurate for a given computational effort. Recently, Wang (2022) used this approach to determine the reliability of nonlinear structures subjected to stochastic excitation. The surrogate model used is a linear structure whose properties are adjusted to have maximal correlation between the responses of the linear and nonlinear structures. A limited number of realizations of the nonlinear response are needed to compute the correlation and, hence, the optimal properties of the linear system. Examples show that this approach uses significantly fewer simulations of the nonlinear response to achieve the same level of accuracy as a Monte Carlo simulation approach. On the other hand, the physics-based surrogate modeling approach requires selection of a physical surrogate model specific to each problem. This introduces a certain amount of subjectivity in the approximation, but also an element of creativity in constructing the approximation.

In recent years, a variety of inexpensive sensors have become available to provide measurements in existing buildings and other infrastructure. One can measure in situ strains, deformation, displacements, vibration, temperature, ground motion, etc. This type of information can be used to update the reliability of existing structures. The updating is particularly important when a system is subjected to an extreme environment, such as a severe earthquake, wave, or wind loading. The updated reliability can be used to make decisions regarding continued use of the facility, or actions to be taken to assure safety. Bayesian updating techniques are fundamental to address this problem. In particular, Bayesian network modeling and analysis can be highly effective for post-event risk assessment and decision making of infrastructure systems (Der Kiureghian 2022). As an example, Bensi et al. (2015) present a post-earthquake risk assessment and decision-making framework for a transportation system. The experience has shown, however, that application of these methods to large systems is difficult because of the demand for extremely large computer memory and high computational cost. While some methods have been developed to address the memory and computational demand requirements (Bensi et al. 2013, Tien and Der Kiureghian 2016), applications to large systems, particularly those having multi-state components (e.g., flow networks, such as water distribution or transportation systems), is still not practical. This area offers many challenges and opportunities for further research and development.

3 Conclusions

While reliability analysis methods, such as FORM, SORM and various sampling methods have matured, their applications to real-world complex problems that require large scale computations remains difficult or impractical. These reliability methods need to be integrated with commercial computational (finite element) platforms to facilitate their use in practice. For FORM and SORM, existing computational codes need to be enabled to compute respond gradients with respect to random variables. This requirement is also applicable to several efficient sampling methods, e.g., importance sampling or orthogonal-plane sampling. For problems that require extensive computations to determine the response, sampling methods may become inoperable because of the need for large number of repeated response calculations. Surrogate modeling is an option in such cases, provided an accurate analytical model can be developed with a small number of response calculations. Physics-based models may be preferrable to purely data-based models in order to reduce the number of needed response calculations and enhance accuracy.

For existing infrastructures, sensors may provide information that can be used to update the reliability of the system, particularly after an extreme event. Bayesian network is a highly useful framework for such updating. However, at the present time, the memory and computational demands of this method prohibit the use of this framework for large systems. Efficient formulations are needed to facilitate the modeling and updating of infrastructure systems by Bayesian network.

4 References

Barbato, M., and J.P. Conte (2005). Smooth versus non-smooth material constitutive models in gradient-based optimization for structural reliability analysis. *Proceedings of the 9^h International Conference on Structural Safety and Reliability*, Rome, Italy.

Bensi, M., A. Der Kiureghian and D. Straub (2013). Efficient Bayesian network modeling of systems. *Reliability Engineering & System Safety*, **112**:200-213.

Bensi, M., A. Der Kiureghian and D. Straub (2015). Framework for post-earthquake risk assessment and decision making for infrastructure systems. *ASCE-ASME J. Risk and Uncertainty*

in Engineering Systems, Part A: Civil Engineering, **1** (online).

Bichon, B.J., M.S. Eldred, L.P. Swiler, S. Mahadevan and J.M. McFarland (2008). Efficient global reliability analysis for nonlinear implicit performance function. *AIAA Journal*, **46**:2459-2468.

Conte, J.P., P.K. Vijalapura and M. Meghella (2003). Consistent finite-element response sensitivity analysis. *J. Engineering Mechanics*, ASCE, **129**:1380-1393.

Der Kiureghian, A (2022). *Structural and System Reliability*. Cambridge University Press, Cambridge, UK.

Ditlevsen, O., and T. Arnbjerg-Nielsen (1994). Model-correction-factor method in structural reliability. J. Engineering Mechanics, 120:1-10.

Franchin, P., O. Ditlevsen and A. Der Kiureghian (2002). Model correction factor method for reliability problems involving integrals of non-Gaussian random fields. *Probabilistic Engineering Mechanics*, **17**:109-122.

Haukaas, T., and A. Der Kiureghian (2005). Parameter sensitivity and importance measures in nonlinear finite element reliability analysis. *J. Engineering Mechanics*, ASCE, **131**:1013-1026.

McKenna, F., G.L. Fenves and M.H. Scott (2003). Open system for earthquake engineering simulation. http://opensees.berkeley.edu, Pacific Earthquake Engineering Research Center, Univ. of California, Berkeley, CA.

Peherstorfer, B., K. Willcox and M. Gunzburger (2018). Survey of multifidelity methods in uncertainty propagation, inference, and optimization. *SIAM Review*, 60:550-591.

Schöbi, R., B. Sudret and S. Marelli (2017). Rare event estimation using polynomial-chaos kriging. *ASCE-ASME J. Risk & Uncertainty in Engineering Systems, Part A: Civil Engineering*, **3** (online).

Tien, I., and A. Der Kiureghian (2016). Algorithms for Bayesian network modeling and reliability assessment of infrastructure systems. *Reliability Engineering & System Safety*, **156**:134-147.

Wang, Z. (2022). Optimized equivalent linearization for random vibration. Submitted for publication.

Zhang, Y., and A. Der Kiureghian (1993). Dynamic response sensitivity of inelastic structures. *Computer Methods in Applied Mechanics and Engineering,* **108**:23-36.

BRIDGE RAPID ASSESSMENT CENTER FOR EXTREME EVENTS (BRACE2): AN ARTIFICIAL INTELLIGENCE FRAMEWORK FOR STRUCTURAL HEALTH MONITORING OF INSTRUMENTED BRIDGES.

Khalid M. Mosalam

Taisei Professor of Civil Engineering
Director of the Pacific Earthquake Engineering Research Center (PEER)

University of California, Berkeley, USA

International Symposium on Emerging Developments and Innovative Applications of Reliability Engineering and Risk Managements (EDIARR2022),30 October-3 November2022, Taipei
Chen, S. S. &Ang, Alfredo. H-S. (Editors)

BRIDGE RAPID ASSESSMENT CENTER FOR EXTREME EVENTS (BRACE2): AN ARTIFICIAL INTELLIGENCE FRAMEWORK FOR STRUCTURAL HEALTH MONITORING OF INSTRUMENTED BRIDGES

Khalid M. Mosalam[1]
[1]*Taisei Professor of Civil Engineering, Department of Civil & Environmental Engineering and Director, Pacific Earthquake Engineering Research (PEER) Center, University of California, 723 Davis Hall, Berkeley, CA 94720-1710, USA*
E-mail: mosalam@berkeley.edu

Abstract: Over th elast 30 years, California Department of Transportation (Caltrans) has expanded its efforts to install bridge sensors. The sensor data are used for structural health monitoring of bridges. Advances in computing technologies, and data science, e.g., Computer Vision (CV), allow utilizing the data and images to evaluate bridge conditions. This paper focuses on the "Bridge Rapid Assessment Center for Extreme Events (BRACE2)" by introducing the post-earthquake damage and functionality assessment framework implemented on Route 580/238 separation in Hayward, California, and developed using six other bridges, instrumented with accelerometers or cameras. The developed framework uses the data to estimate the bridge conditions and damage to inform decision-makers about whether to continue normal operation or to close the bridge to traffic for in-depth evaluation including where to expect damage for immediate inspection. Moreover, this framework uses the data to simulate the bridge response for comparison with recordings and observations. At the core of the framework is a decision-making platform that utilizes the data, along with damage states from component models and response from a global bridge model subjected to the recorded ground motions. The paper also describes applications in CV for bridge structures to detect damage from images.

***Keywords*:** BRACE2, Computer vision, Instrumented bridges, Machine learning, Structural health monitoring.

1 Introduction

Structural Health Monitoring (SHM) in the form of rapid and automated damage assessment after natural hazards has become an important focus in structural engineering. SHM is not only important for extreme events, but it is also essential for monitoring the in-service conditions of structures. The tragic collapses of a bridge in Pittsburgh in January 2022 and the Champlain Towers South in Florida in the summer of 2021 highlighted the importance of SHM and the need to increase instrumentation on existing and new structures. A variety of SHM approaches and damage criteria were developed through traditional specimen testing or pattern analysis from data (i.e., data-driven SHM). The boosting of computers and sensing hardware makes the data-driven SHM attract increasing attention from the structural engineering community. Based on the data type and source, data-driven SHM research activities are divided into: (1) vibration-based, and (2) vision-based. The former uses the vibration signals from accelerometers and the latter relies on human visual inspection in the field or from collected data of camera images and videos. The data-driven SHM augments and eventually replaces repetitive human tasks by automated recognition systems using Artificial Intelligence (AI).

Machine Learning (ML) and Deep Learning (DL) are now popular as two realizations of AI, where computers perform labor-intensive repetitive tasks and simultaneously "learn" from performing those tasks. Both ML and DL fall within the scope of empirical models, and data is the most essential component. In SHM, the structural response records and images from post-disaster reconnaissance efforts (e.g., the Structural Extreme Events Reconnaissance (StEER) Network, https://www.steer.network/) or from daily life service conditions, represent the data media. The fundamentals of vibration-based SHM are founded in statistical pattern recognition (Farrar et al.,

1999) to determine location, type, and extent of damage to make decisions (e.g., repair strategy) about the structural health making use of damage feature extraction (feature engineering). Time Series (TS) modeling of vibration signals using Auto-Regressive (AR) models was found to be effective in damage detection and has been used to capture damage features in structures (Lei et al., 2003; Lynch et al., 2003; Mei et al., 2016; Nagi et al., 2011; Nair et al., 2006; Noh et al., 2009; Sohn et al., 2001). Elaborate data preprocessing (e.g., segmenting, de-trending, and de-nosing) and stationarity check are inevitable before such modeling. To address three important issues (requirement of stationary input, intuitive damage feature engineering, and limited data from reduced-scale experiments), it is necessary to develop an end-to-end framework, with TS as inputs and predicted structural Damage States (DS) or patterns as outputs. Moreover, models should be validated by test data or field measurements.

The California State Highway System (CA-SHS) includes a wide variety of assets. According to 2018 data, these include: (1) Pavement for 49,672 lane miles, (2) Bridges & Tunnels for 13,246 structures, (3) Drainage for 212,759 culverts, and (4) Transportation Management System for 20,816 elements. On the other hand, according to the United States Geological Survey (USGS), the probability of exceeding earthquakes of Magnitude 6.7 is higher than 93% in the coming 30 years in California (CA), which can result in loss of billions of dollars for the CA-SHS assets. In the past 20 years, about $25 Million investment in strong motion instrumentation took place for CA-SHS, including 16 toll/major bridges, 66 regular bridges, and 33 geotechnical arrays. There is a need to demonstrate that instrumentation can evaluate the bridge conditions following an earthquake. BRACE2 will assist in the response efforts of the Maintenance & Post Earthquake Investigation Team. Thus, Caltrans instrumentation program currently focuses on upgrading existing instrumentation and telemetry systems, and supporting future research, e.g., BRACE2.

2 BRACE2 Activities

The recent advances in remote sensing, computing technologies, and data science allow utilizing instrumentation to evaluate the conditions of bridge structures in real-time. BRACE2 aims for real-time post-earthquake damage and functionality assessment for decision making. The 580/238 Interchange Bridge in Hayward, CA (Hayward bridge) has real-time data streaming from California Geological Survey (CGS) instruments, and it is the testbed for BRACE2, Figure 1. The core of BRACE2 operation workflow is Python scripts of the Decision-Making Platform (DMP), using data from accelerometers in real-time, along with bridge global model and pre-computed component DS.

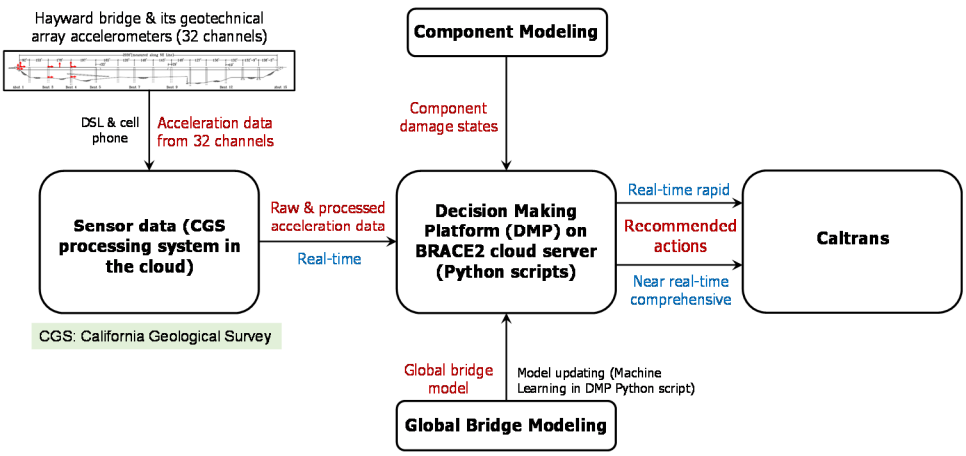

Figure 1. BRACE2 workflow demonstrated using Hayward bridge for vibration-based SHM.

The real-time data streaming capabilities is conducted using a Digital Subscriber Line (DSL) and cell phone service set up by CGS to send the data from the 32 channels (20 sensors on the bridge superstructure and 12 sensors from the eastern geotechnical array) to the CGS real-time data processing center and subsequently to BRACE2. Triggering and de-triggering values of 0.25%g and 0.40%g, where g is the acceleration of gravity, are set to respectively initiate and stop data recording. Upon receiving the data, BRACE2 processes them and assesses the bridge condition to subsequently inform decision makers. From a pilot investigation of data streaming, the streaming duration is about one minute which satisfies the "real timeliness" goal of BRACE2. The received real-time data from March 22, 2021, to April 25, 2022, consist of 51 datasets of small level shaking (peak ground acceleration ranging from 0.011g to 0.072g with corresponding peak structural acceleration ranging from 0.010g to 0.129g). Using data from the moment magnitude Mw 3.9 San Lorenzo earthquake, June 28, 2021, the bridge period in the transverse direction is identified as 1.1 s, matching a previously determined value using the data obtained from Mw 4.4 Berkeley earthquake, Jan. 4, 2018.

The global model of the Hayward bridge is developed in OpenSees (McKenna, 1999). This highway bridge is a cast-in-place prestressed concrete box girder with 14 spans ranging from 92 to 197 feet. The bridge superstructure is supported on single, double, and triple column bents as well as seat-type abutments. The plan shape is curved, and the east end of the bridge main line is split into two lines (NE1 & NR1). The spans of the main line and the NE1 line are supported on double or triple column bents with octagonal column cross-sections and those of the NR1 line are supported on single-column bents with interlocking wide octagonal column cross-sections. The used geometry and material properties of the bridge are consistent with the as-built drawings, Figure 2. Columns are modeled as nonlinear beam-column elements with fiber-discretized cross-sections. Reinforcing steel is modeled with Menegotto-Pinto-Filippou material model (Filippou et al., 1983), unconfined concrete is modeled using Hognestad's curve (Hognestad, 1951) with hysteresis described in (Yassin, 1994), and confined concrete is modeled considering parameters from (Mander et al., 1988). At the top of each column, there is an intermediate node connected by a "rigidLink beam" joint offset to the center of the cap beam. Cap beams and bridge deck are modeled as elastic beam-column elements with cross-section properties determined from the as-built drawings. The bridge abutments are modeled as rigid elements with end boundary conditions defined by zero-length spring elements. The stiffness values of these springs are explicitly calculated in the longitudinal, transverse, and vertical directions based on the "Simplified Abutment Model" in (Kaviani et al., 2012). In-span hinges are modeled as nonlinear elastic springs using zero-length elements. The column-pile interface is currently modeled as a fixed boundary condition.

Component modeling includes the determination of the DS for the main bridge components, Figure 3. It is noted that the shown seven DS are strain-based per Table 1. To develop confidence in the OpenSees component models, comparative study has been conducted with a continuum model in Abaqus (2015). Because the columns are reasonably-confined, the observed failure mode is flexure where OpenSees captures the initial stiffness and base shear response well up to drifts of approximately 3%. Subsequently, Bent 3 column exhibits rapid post-peak strength degradation which leads to some discrepancy in the estimates of the DS between OpenSees and Abaqus as the former does not include shear force-deformation modeling or shear-flexure interaction, as confirmed by Bent 4 column DS (more ductile), with better match between OpenSees and Abaqus.

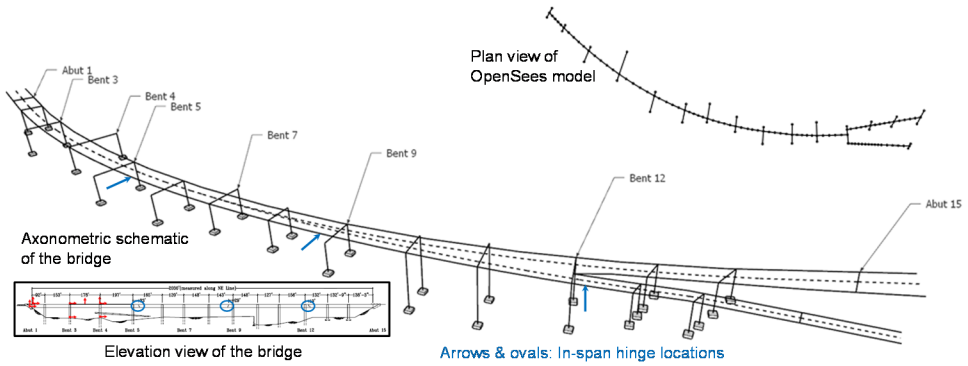

Figure 2. Global modeling of Hayward bridge.

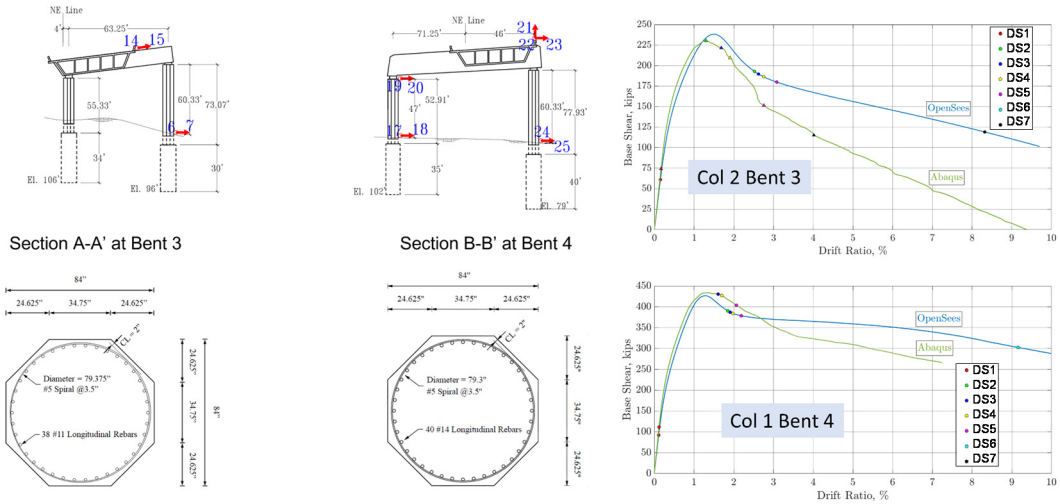

Figure 3. Component modeling of Hayward bridge.

Table 1. Strain-based DS used for BRACE2 component models.

DS	Caltrans-PEER description*	Criteria used to define strain-based damage state	Strain-based damage state			Action***
			Fiber location	Compression or Tension	Strain**	
1	EQ-related **tight cracking** of cover	**Cover cracking**: the cover surface reaches tensile strength	Any outermost cover fiber	Tension	$\varepsilon_t = 1.32 \times 10^{-4}$	**R1**: *Remain open*
2	**Moderate cracking** (mixed orientations) & **minor spalling**/flaking	**Minor spalling**: the cover surface reaches compressive strength		Compression	$\varepsilon_{sp} = 0.005$	**R1**: *Remain open*
3	**Open cracking** or **major spalling** (exterior to confinement)	**Major spalling**: a significant depth of the cover reaches compressive strength	Any cover fiber at ½- ¾ of the cover depth	Compression	$\varepsilon_{sp} = 0.005$	**R2**: *Remain open & inspection needed by SM&I Engineers*
4	**Exposed core** (interior of confinement)	**Exposed core**: the entire depth of the cover reaches compressive strength	Any innermost cover fiber	Compression	$\varepsilon_{sp} = 0.005$	
5	**Visible bar buckling**; confinement loss or **core shedding**	**Core shedding**: the outer surface of the core begins to fail	Any outermost core fiber	Compression	$\varepsilon_{cu} = 0.009$	**R3**: *Close & inspection needed*
6	**Multi-bar rupture or buckling**; large drift; or **core crushing**	**Bar buckling or rupture**: longitudinal bars buckle or reach ultimate tensile strain	Any longitudinal bar	Compression or Tension	Buckling or $\varepsilon_{su} = 0.090$	**R4**: *Close immediately*
7	**Column collapse** (Near-total loss of capacity)	**Significant loss of capacity**: 50% loss in lateral strength	Not Applicable (NA)	NA	NA	**R4**: *Close immediately*

*Caltrans-PEER workshop "Caltrans Column Limit State (CCLS) Uncertainty" **Values for Hayward Bridge column ***Action based on Caltrans First Responder Bridge Assessment Guide

BRACE2 DMP is designed to allow decision makers to seamlessly compose an array of modeling scenarios to rapidly assess the state of a bridge after a given scenario (e.g., an earthquake event), then cycle this output through an updating procedure. The implementation of the DMP consists of a front-end *decision maker's interface* and a back-end *analyst interface*. The former is a web application that is centered around the digital twin of the bridge and represents a high-level overview of this digital twin. The latter is currently being developed as an abstract Python Application Programming Interface (API) which can be used to compose and stage various basic components, or *monads*. The platform views a *digital twin* as a collection of *monads* where several monads are considered currently in the DMP. *Mathematical models* (monad #1) can be categorized as local component models, and global models. Simulation procedures (monad #2) are routines that act upon models, often with additional input from an event, to provide a metric, or an Engineering Demand Parameter (EDP) indicating the state of the structure. *Events* (monad #3) may represent a type of load or intensity measure that the digital twin can be configured to accept as input to a simulation procedure. Finally, monad #4 for *Updating procedure* is used for model updating. To illustrate an important procedure related to the data utilization, Single-Input/Single-Output (SISO) and Multi-Input/Multi-Output (MIMO) System Identification (SI) methods are programmed as part of the BRACE2 digital twin infrastructure to determine modal properties (natural periods, damping ratios, and mode shapes), as detailed in Figure 4 and is applicable to the selected five bridges in CA, currently considered in BRACE2, refer to Figure 5.

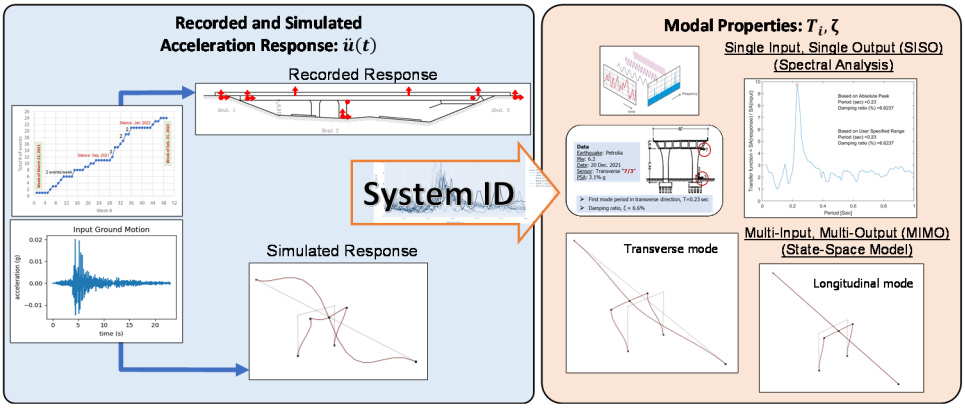

Figure 4. BRACE2 system identification framework.

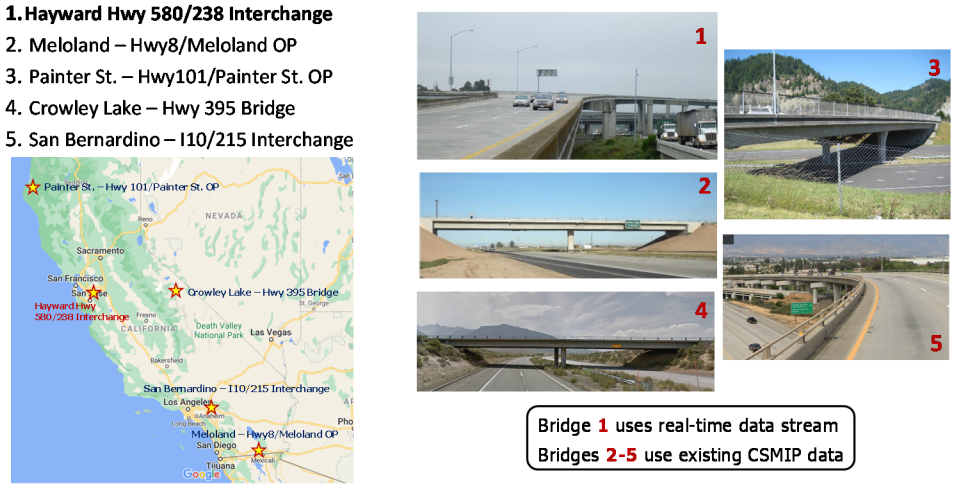

Figure 5. Considered bridges in BRACE2.

The identified natural periods of the Hayward bridge using different SI methods, are plotted in Figure 6 using the data from Mw 3.9 San Lorenzo earthquake, June 28, 2021, and Mw 4.4 Berkeley earthquake, Jan. 4, 2018. Employed methods (Arici & Mosalam, 2006) are: (a) three versions of the common SISO transfer function approach, which use response spectrum, power spectrum, and Fourier amplitude spectrum, and (b) the OKID-ERA-DC (Observer/Kalman filter IDentification and Eigensystem Realization Algorithm with Data Correlations) as a MIMO SI method. It is observed that the identified periods are consistent among the different methods and for the considered two small earthquake events.

The developed DMP is consistent with common practice for "First Responder Bridge Assessment Guide." This guide (refer to the insert in Figure 7) is used by the Structure Maintenance & Investigations (SM&I) of Caltrans on regular basis or following extreme events, e.g., earthquakes. Thus, the column DS in Table 1 are related to the following four bridge operation actions from this guide (last column in Table 1):

1. **R1**: Bridge can remain open.
2. **R2**: Bridge can be open, and SM&I engineering inspection should be requested.
3. **R3**: Bridge should be closed, and SM&I engineering inspection should be requested.
4. **R4**: Bridge should be immediately closed due to collapse or major damage.

This is illustrated for one of the columns of bent 3 of the Hayward bridge in Figure 7.

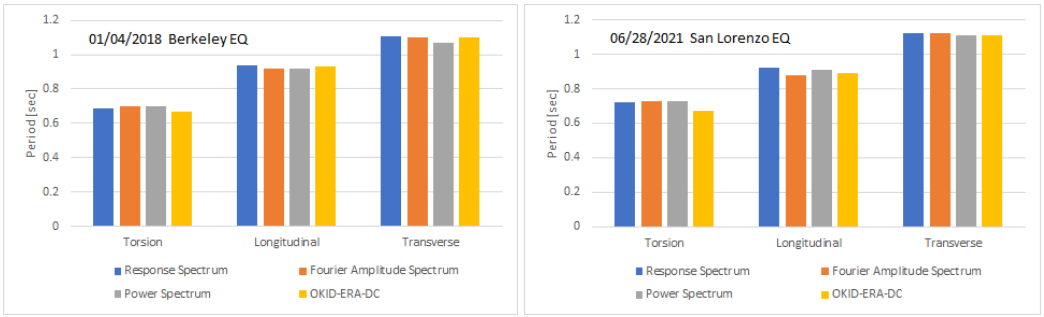

Figure 6. Natural periods of Hayward bridge identified by SI methods for two earthquakes.

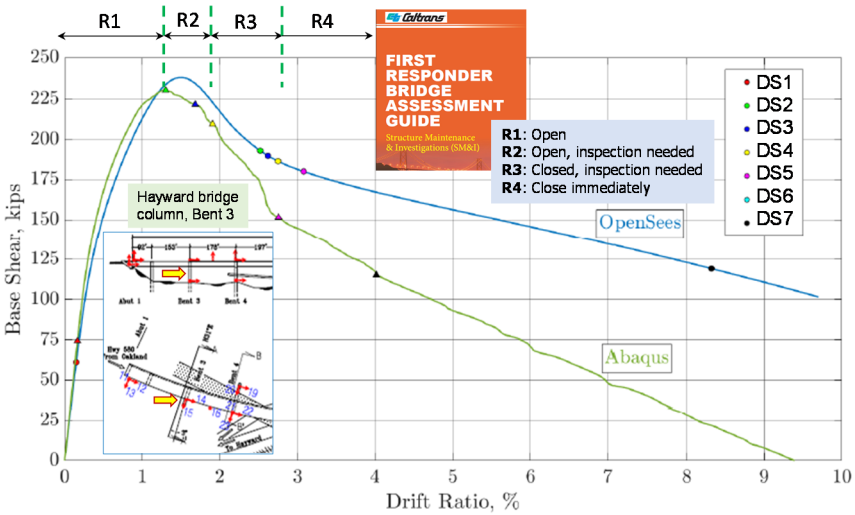

Figure 7. Strain-based component DS vs. ranges of Caltrans SM&I guide for Hayward bridge.

3 Vision-Based SHM

Structural damage recognition using images is an important topic in vision-based SHM and structural reconnaissance. It heavily relies on human visual inspection and experience. Several past studies (Torok et al., 2014; Yeum & Dyke, 2015; Yoon et al., 2016; Feng & Feng, 2017) addressed issues of relatively tedious non-autonomous manual efforts. They developed algorithms and criteria to determine the DS based on human vision (*handcrafted*) features, e.g., crack edges and texture. These features are concise, but they may be limited according to the perspective of the image recognition. In some cases, useful damage features are abstract and exist in high-dimensional spaces. Humans are limited by having only a sense of low-dimensional features, e.g., locations, colors, or edges. Due to the complexity and diverse representations of image data, handcrafted features may work for limited scenarios only. Unlike conventional pipelines of feature engineering and ML, the DL approaches use the concept of representation learning with its abundant number of parameters being proposed to replace the manual feature engineering. In the past decade, great strides have been made by the DL research community, achieving state-of-the-art results in many vision-recognition tasks compared with traditional approaches (Goodfellow et al., 2016). Thus, following the trends of AI and the corresponding improvements of DL in vision-based approaches, it is timely to implement the state-of-the-art DL technologies in structural engineering applications.

Until recently, vision-based SHM applications have not fully benefited from the data-driven DL technologies. Applications to structural engineering have been mainly hamstrung by: (1) the lack of general automated detection principles or frameworks based on domain knowledge, (2) the lack of benchmark datasets with well-labeled large amounts of data, and (3) the lack of interpretation of the trained DL models. To address these three drawbacks, an automated detection framework, Figure 8, along with multiple benchmark detection tasks should be defined and validated using relevant studies and applications. According to the framework and task definition, a large-scale, high-variety, and open-source benchmark dataset should be developed.

In Computer Vision (CV), there exists several large-scale open-source datasets, e.g., ImageNet (Deng et al., 2009), MNIST (LeCun et al., 1998), and CIFAR-10 (Krizhevsky, 2009), with about 15 million, 70,000, and 70,000 images, respectively, and the training of DL models benefit from these large-scale image datasets. However, in structural engineering, especially in vision-based SHM, there is no such large-scale high-variety open-source image dataset until recently. This deficiency is partially attributed to the cost and time in collecting and labelling data requiring domain-specific knowledge, e.g., to understand structural component types, damage patterns, etc. Most past studies related to the image-based SHM using DL conducted validation experiments based on their own custom-labeled small-scale datasets and self-defined tasks. As a result, the numerical results reported in these previous works are incomparable. Moreover, unlike the above-mentioned CV benchmark datasets, image datasets used in SHM usually have highly *imbalanced classes*. Such imbalance originates from the nature of SHM where images with structural damage that occur due to either natural deterioration or extreme events, such as earthquakes, are less frequent cases than the undamaged cases. Moreover, unlike general CV benchmark datasets containing common and natural objects, the labeled images in vision-based SHM are much more different. Two major differences are: (1) complex visual patterns, and (2) abstract semantic meaning of the labels (Wang et al., 2022) to describe the structural attributes, e.g., damage occurrence, damage type, and structural component type. For (1), damage in the form of cracks and concrete spalling do not have fixed shapes and widely vary. For (2), labels in the task to identify damage types, e.g., shear versus flexural damage must engage domain knowledge in structural engineering. For example, flexural damage is attributed to cracks developed horizontally or vertically in the structural component due to the induced bending moments or attributed to excessive cracking and spalling concentrated at the component ends, e.g., column, due to plastic

hinging also induced by bending moments. Both visual patterns are significantly different, but they have the same semantic meaning leading to flexural damage, bringing difficulties in training DL models with limited amount of data.

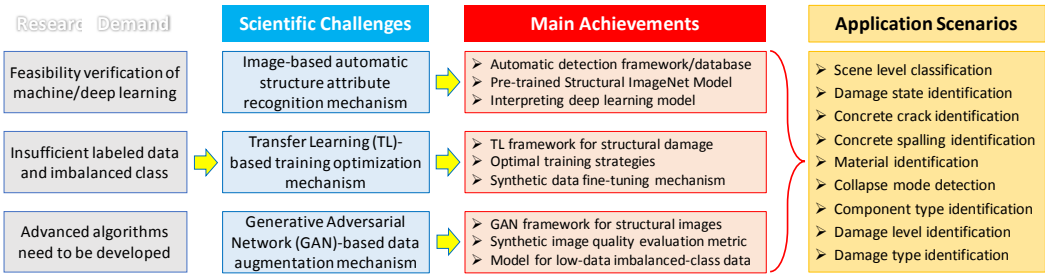

Figure 8. Overview of the conducted research in vision-based SHM.

Inspired by the establishment of the large-scale high-variety dataset of ImageNet, we constructed a Structural ImageNet called PEER Hub ImageNet (ϕ-Net), https://apps.peer.berkeley.edu/phi-net/, which contains images relevant to structural engineering, e.g., buildings and bridges, with both damaged and undamaged status. From past experiences related to earthquake reconnaissance efforts, several structural attributes affecting the structural assessment are considered, i.e., scale of the target object, vision pattern, severity of damage, type of structural component, etc. In the current ϕ-Net, we designed eight classification problems as benchmark tasks based on key attributes: (1) scene level, (2) damage state (presence), (3) spalling condition, (4) material type, (5) collapse mode, (6) component type, (7) damage level, and (8) damage type. The corresponding hierarchy tree is easily expandable as desired. Up till now, 36,413 multi-labeled structural images have been included in the ϕ-Net database and are continuously growing, especially with the availability of Upload Images and Label Images apps, https://apps.peer.berkeley.edu/spo/. The ϕ-Net database not only provides a benchmark for rapid verification for relevant research, but also makes the results of similar research comparable. Moreover, users can add data into their self-made dataset to alleviate the problem of insufficient data and improve the recognition performance. The ϕ-Net is accompanied with a Structural ImageNet Model (SIM) app, http://apps2.peer.berkeley.edu/sim/, that performs the damage detection tasks (Mosalam et al., 2019). Furthermore, the first image-based structural damage recognition competition, namely PHI Challenge, https://apps.peer.berkeley.edu/phichallenge/, was organized. Advantage of automated damage identification from images is that it provides an opportunity to detect damage and identify warning signs in serviceability and extreme event conditions from images that can be uploaded to the sever of the SIM app by any engineer or tenant of a building.

The author presented several applications of ϕ-Net with SIM for rapid assessment of structural images (e.g., Gao & Mosalam, 2020) where images were collected from NISEE library archive, https://nisee.berkeley.edu/elibrary/, or other web resources. The detection procedure is straightforward via feeding the collected images into the trained SIM corresponding to the task of interest, then the model outputs the predicted label and the probabilities of each possible choice. This operation is repeated for multiple tasks, then a comprehensive set of results is obtained for decision-making purposes. From these applications, the SIM achieved desirable performance in rapid assessment even though only benchmarking (not state-of-the-art) models are adopted. Therefore, this application indicates the practical uses and benefits of the ϕ-Net and the well-trained SIM for SHM.

Attention has been given to the applications of AI in practical Bridge Health Monitoring (BHM) projects where crack identification and width measurement are two important metrics to evaluate

the safety conditions of bridges. An application-oriented multistage crack recognition framework called Convolutional Active Learning Identification-Segmentation-Measurement (CAL-ISM) is developed. The performance of the CAL-ISM framework is validated from three practical applications, i.e., a bridge column test specimen, and two BHM field projects. The results from these applications demonstrated the effectiveness of CAL-ISM for BHM (Zheng et al., 2022). CAL-ISM consists of four steps: (1) benchmark classification model pre-training, (2) semi-supervised active learning model re-training, (3) pixel-level crack segmentation, and (4) crack width measurement, as shown in Figure 9.

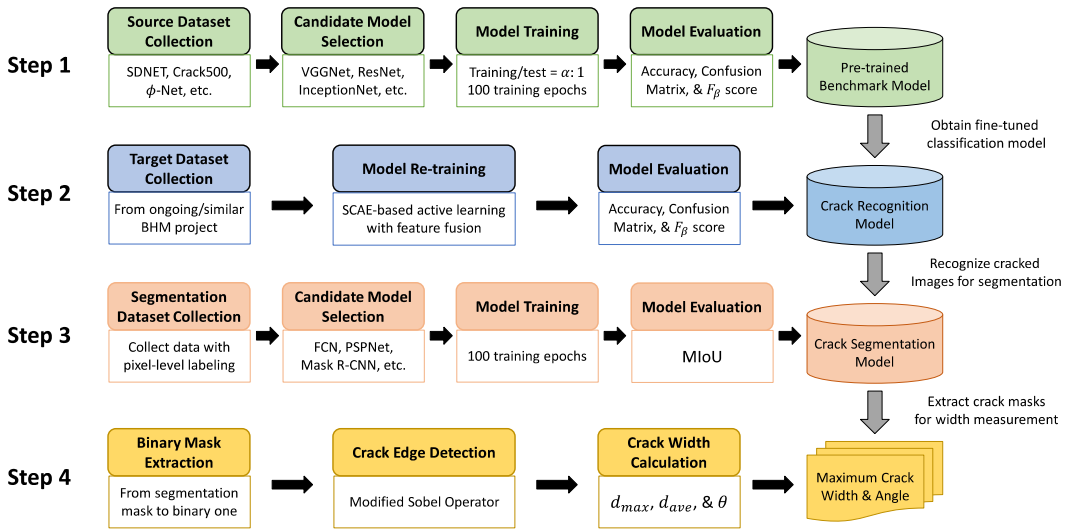

Figure 9. CAL-ISM framework for bridge health monitoring (Zheng et al., 2022).

First, a quasi-statically tested Reinforced Concrete (RC) bridge pier specimen is used to evaluate CAL-ISM framework for crack detection and measurement. The net height of the pier is 1,800 mm measured from the top of the footing to the bottom of the bent cap with a square cross-section of $500 \times 500\ mm^2$. The pier west side (a rectangle area of $500 \times 1{,}300\ mm^2$) is selected for crack identification and measurement and divided into 65 sub-blocks. Each sub-block is photographed by a high-resolution camera of 24 megapixels. These images are somewhat irregular quadrilaterals because the camera could not be perpendicularly mounted to the pier concrete surface during photographing. Thus, a *coordinates transformation algorithm* is employed to convert these quadrilaterals to squares. In this application, detection is conducted for all sub-blocks following the CAL-ISM procedure, and the results for all sub-blocks are assembled into a whole picture using their numbers (1 to 65). For better visualization, non-damage areas, cracks, and spalling zones on the surface of the pier are re-colored in white, black, and purple, respectively. As an example of crack width measurements, one region concatenated from 10 sub-blocks (46 to 55), is shown in Figure 10. Each crack is recognized by CAL-ISM and compared with the actual measured width, Table 2. The obtained results indicate that the identified crack width is always conservatively larger than the measured value. This is attributed to the existence of surface defects, e.g., small pits, on the crack path, making it difficult for the DL model to distinguish these defects. From Table 2, most errors of the recognized crack width are less than 10%, especially for actual crack width less than 0.5 mm (an exception is crack #4). For some wide cracks (#8 & 9), due to the negative effects of surface defects, the identified crack width is over-estimated with larger errors (~28% to 35%). In conclusion, the comparison between the identified and measured crack widths indicates that the proposed CAL-ISM framework is accurate, especially for narrow cracks, and suitable for practical BHM applications and field projects.

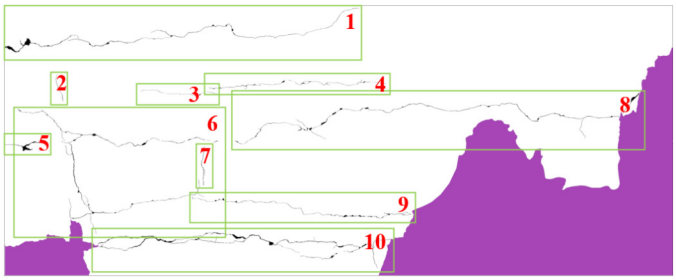

Figure 10. Extracted 10 cracks in sub-blocks 46 to 55 (Zheng et al., 2022).

Table 2. Crack width identification of the pier specimen (Zheng et al., 2022).

Crack #	Max width $D \pm err_\theta$ [mm]	Angle θ [°]	Measured width [mm]	Recognition error (%)
1	0.833±0.012	46.51	0.82	1.6
2	0.178±0.011	31.12	0.17	4.7
3	0.415±0.011	58.05	0.39	6.4
4	0.226±0.008	89.48	0.20	13.0
5	0.864±0.011	28.16	0.81	6.7
6	0.449±0.012	43.60	0.41	9.5
7	0.247±0.008	0.73	0.23	7.4
8	1.313±0.010	69.88	0.97	35.4
9	0.974±0.011	61.61	0.76	28.2
10	1.798±0.011	53.24	1.66	8.3

To demonstrate the proposed vision-based CAL-ISM framework for crack detection and measurement of real BHM projects, the three-span (10, 13, and 10 m) simply supported RC Wutang bridge, Shanghai, China (N31.3745, E121.1454), and the three-span (9 m/span) simply supported RC Xiejinghe bridge, Shanghai, China (N31.36847, E121.12453) are considered. For Wutang bridge, a surface area ($400 \times 500\ mm^2$ located at the bottom of the hollow slab girder near the abutment), having minor cracks, is investigated. This selected area is divided into 20 square sub-blocks ($100 \times 100\ mm^2$) and photographed with 20 images (2,560×2,560 pixels each). The images are processed by a quadrilateral transformation algorithm to convert them to square sub-blocks. Finally, they are spliced together to restore the investigated surface area. On the other hand, for Xiejinghe bridge, a surface area ($300 \times 700\ mm^2$ located at the bottom of the RC girder), is investigated where there are several cracks with different widths. This selected area is divided into 21 square sub-blocks ($100 \times 100\ mm^2$) and photographed with 21 images (2,560×2,560 pixels each). The images are processed by a quadrilateral transformation algorithm to convert them to square sub-blocks. Finally, they are spliced together to restore the investigated surface area.

The trained recognition and segmentation models in CAL-ISM are employed to identify and measure the cracks in the designated region of the surfaces of the above two bridges, and then the recognized cracks are exhibited and numbered in Figure 11. The models accurately identify and segment the cracks. Note that cracks 5, 6, and 7 in Figure 11(a) belong to three parts of the same crack. However, several stains on the surface partly covered the crack leading to identifying it as three discrete segments. The estimated widths of the cracks are listed in Tables 3 and 4 along with the actual width measurements. Note that in Table 2 to 4, the theoretical maximum width error, err_θ, is mainly attributed to the approximation of the pixels in the direction of the crack width, where the projection angle, θ, is defined by the direction of the maximum crack width, D, and the horizontal axis of the image. From the results, the estimated crack widths are conservatively larger than the measured ones. Additionally, the recognition errors are less than 13%, and some of them are even less than 1%. Such estimation accuracy is judged to be acceptable in BHM practice.

Table 3. Crack width identification of Wutang bridge (Zheng et al., 2022).

Crack #	Max width $D \pm err_\theta$ [mm]	Angle θ [°]	Measured width [mm]	Recognition error (%)
1	0.200±0.020	0.00	0.18	11.1
2	0.180±0.027	33.69	0.17	5.9
3	0.825±0.024	14.03	0.80	3.1
4	0.861±0.021	2.73	0.77	12.2
5	0.403±0.022	82.87	0.40	0.8
6	0.762±0.026	23.20	0.72	5.8
7	0.570±0.027	52.13	0.55	3.6

Table 4. Crack width identification of Xiejinghe bridge (Zheng et al., 2022).

Crack #	Max width $D \pm err_\theta$ [mm]	Angle θ [°]	Measured width [mm]	Recognition error (%)
1	0.141±0.027	36.70	0.14	0.7
2	0.100±0.028	44.20	0.10	0.0
3	0.112±0.021	90.00	0.11	1.8
4	0.112±0.026	67.50	0.11	1.8
5	0.123±0.022	86.60	0.12	2.5

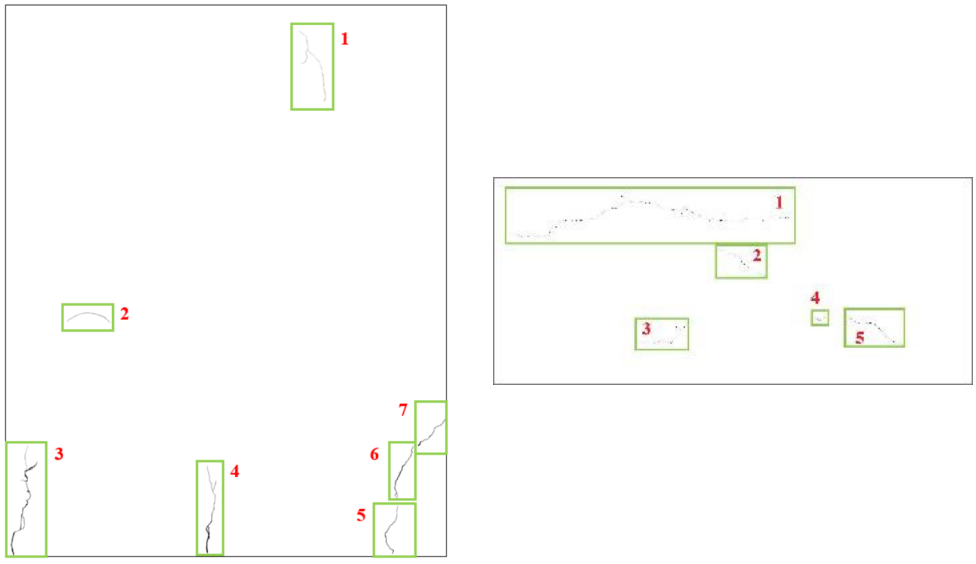

(a)Wutang bridge (b)Xiejinghe bridge

Figure 11. Crack identification of two bridges in China (Zheng et al., 2022).

The detection results of the maximum crack width located in different regions of Wutang and Xiejinghe bridges show respectively that five (#3 to 7) from the 7 cracks and one (#5) from the 5 cracks are larger than 0.2 mm. Consequently, according to most bridge codes (e.g., Ministry of Transport of the People's Republic of China, 2018), the bridges should be repaired by injection to enhance their durability by eliminating deterioration due to water penetration, corrosion, and stress concentration caused by these wide cracks. Although only small surface regions of the bridges are studied as examples for demonstrating the proposed vision-based CAL-ISM framework, the whole surface of the bridge, especially the surfaces of the damage-critical parts in these bridges, e.g., the piers, can be examined using the same framework. The successful application of CAL-ISM framework for crack detection and measurement for bridges under service conditions and following major earthquake events will initiate new directions for effective BHM with powerful impacts on future bridge maintenance and reconnaissance efforts.

4 Conclusions and Future Extensions

The objective of BRACE2 is the post-earthquake real and near real-time damage and functionality assessment of bridges, operated and maintained by Caltrans, with physics-based and data-driven methods using sensor data and numerical simulations. In this paper, the ongoing efforts of implementing this framework on a particular testbed, namely Hayward bridge, is presented. This effort will continue to complete the platform and make it available for effective Structure Maintenance & Investigations (SM&I) by Caltrans engineers.

The developed advances and obtained promising results in AI-enabled SHM studies shed light on the high potential of these state-of-the-art methodologies in practical structural engineering applications. In future pursuits, improved monitoring, learning, maintenance, and ultimately effective decision-making regarding the conditions, replacement, or retrofit of key elements of the built environment can be reliably achieved. Among the AI-enabled SHM studies in literature, there is a lack of studies that focus on critical bridges, e.g., toll and recovery bridges. Future directions towards filling this gap are discussed below.

1. Use of images for evaluation of damage on a structural level: Images collected from bridges during earthquake reconnaissance can be used to develop algorithms for characterizing the damage at the structural level and for maintenance purposes. This can be performed using approaches similar to those in (FEMA-P58, 2018) or (ATC-138, 2022) that relate component damage to structural level damage and recovery states. This can be facilitated by building/bridge information models (BIM) of critical bridges that can provide critical locations of images for identifying component and structural level damage. Such application is not limited to extreme events and can also be used regularly for maintenance and identifying any issues under service conditions. Platforms like ϕ-Net and SIM can be expanded for this purpose and key bridges can be selected as prototypes for development. Such vision-based assessment can complement the vibration-based SHM activities of BRACE2.

2. Hybrid methods that use vibration-based data and vision-based images can be developed. These methods can benefit from (a) sensors at the bridge super-structure and foundation levels and the use of methods, such as ARIMA-ML (Gao et al., 2021) and H-MC (Muin & Mosalam, 2021) to detect presence, severity, and location of damage, and (b) images of different bridge components, and local damage that cannot be identified by sensors, to provide a holistic damage evaluation of these bridges.

3. Early-stage warning applications that uses the results of vision- & vibration-based SHM can be developed to recommend actions of bridge operations and maintenance.

5 Acknowledgments

This research received funding support from Caltrans for the “Bridge Rapid Assessment Center for Extreme Events (BRACE2)” project, Task Order 001 of the PEER–Bridge Program agreement 65A0774 to the PEER Center. Efforts by the CGS team led by Mr. Hamid Haddadi are appreciated. Several collaborators, visiting scholars, postdoctoral researchers, and graduate students from UC-Berkeley and PEER (identified in the different references, listed below) contributed to the presented activities of BRACE2 and AI, including CV, research, refer to https://stairlab.berkeley.edu/.

6 References

Applied Technology Council (ATC). (2018). Seismic performance assessment of buildings volume 1 – Methodology. *Report No. FEMA-P58*, Redwood City, California.

Applied Technology Council (ATC). (2022). Seismic performance assessment of buildings volume 8 – Methodology for assessment of functional recovery time. Preliminary report. *Report No. ATC-138-3*, Redwood City, California.

Arici, Y. & Mosalam, K.M. (2006). Modal identification and health monitoring of bridges using seismic acceleration records. *Technical Report EERC 2006-2*, UC-Berkeley, 261 pages.
Dassault Systems Simulia Corporation, *Abaqus*. (2015). Johnson, RI.

Deng, J., Dong, W., Socher, R., Li, L.J., Li, K. & Fei-Fei, L. (2009). Imagenet: A large-scale hierarchical image database. *Proceedings of the 2009 IEEE Conference on Computer Vision and Pattern Recognition*, 248-255.

Farrar, C.R., Duffey, T.A., Doebling, S.W. & Nix, D.A. (1999). A statistical pattern recognition paradigm for vibration-based structural health monitoring. *Proceedings of the 2nd International Workshop on Structural Health Monitoring*, Stanford, CA, 764-773.

Feng, D. & Feng, M.Q. (2017). Experimental validation of cost-effective vision-based structural health monitoring. *Mechanical Systems and Signal Processing*, 88, 199-211.

Filippou, F.C., Popov, E.P. & Bertero, V.V. (1983). Effects of bond deterioration on hysteretic behavior of reinforced concrete joints. *Technical Report EERC 83-19*, Earthquake Engineering Research Center, University of California, Berkeley.

Gao, Y. & Mosalam, K.M. (2020). PEER Hub ImageNet: A large-scale multiattribute benchmark data set of structural images. *ASCE Journal of Structural Engineering*, 146(10), 04020198.

Gao, Y., Mosalam, K.M., Chen, Y., Wang, W. & Chen, Y. (2021). Auto-regressive integrated moving-average machine learning for damage identification of steel frames. *Applied Sciences*, 11(13), 6084.

Goodfellow, I., Bengio, Y. & Courville, A. (2016). *Deep Learning*. MIT press.

Hognestad, E. (1951). Study of combined bending and axial load in reinforced concrete members. *Technical Report Engineering Experiment Station Bulletin No. 399*, University of Illinois at Urbana Champaign.

Kaviani, P., Zareian, F. & Taciroglu, E. (2012). Seismic behavior of reinforced concrete bridges with skew-angled seat-type abutments. *Eng. Struct.*, 45, 137–150, doi: 10/f4chwq.

Krizhevsky, A. (2009). Learning multiple layers of features from tiny images. http://www.cs.toronto.edu/~kriz/learning-features-2009-TR.pdf.

LeCun, Y., Bottou, L., Bengio, Y. & Haffner, P. (1998). Gradient-based learning applied to document recognition. *Proceedings of the IEEE*, 86(11), 2278-2324.

Lei, Y., Kiremidjian, A., Nair, K.K., Law, K.H., Kenny, T.W., Carryer, E. & Kottapalli, A. (2003). Statistical damage detection using time series analysis on a structural health monitoring benchmark

problem. *Proceedings of the 9th International Conference on Applications of Statistics and Probability in Civil Engineering*. San Francisco, CA.

Lynch, J.P., Sundararajan, A., Law, K.H., Kiremidjian, A.S., Kenny, T. & Carryer, E. (2003). Embedment of structural monitoring algorithms in a wireless sensing unit. *Proceedings of the Structural Engineering and Mechanics*, 15(3), 285-297.

Mander, J.B., Priestley, M.J.N. & Park, R. (1988). Theoretical stress-strain model for confined concrete. *ASCE Journal of Structural Engineering*, 114(8), 1804-1826.

McKenna, F. (1999). Object-oriented finite element programming: Frameworks for analysis, algorithms and parallel computing. *PhD Dissertation*, UC Berkeley.

Mei, L., Mita, A. & Zhou, J. (2016). An improved substructural damage detection approach of shear structure based on ARMAX model residual. *Proceedings of the Structural Control and Health Monitoring*, 23(2), 218-236.

Ministry of Transport of the People's Republic of China (2018). Specifications for design of highway reinforced concrete and prestressed concrete bridges and culverts. *China Communications Press*, Beijing.

Mosalam, K., Muin, S. & Gao, Y. (2019). New directions in structural health monitoring. *NED University Journal of Research*, 2, 77-112.

Muin, S. & Mosalam, K.M. (2021). Human-machine collaboration framework for structural health monitoring and resiliency. *Engineering Structures*, 235, 112084.

Nagi, J., Ducatelle, F., Di Caro, G.A., Cireşan, D., Meier, U., Giusti, A., Nagi, F., Schmidhuber, J. & Gambardella, L.M. (2011). Max-pooling convolutional neural networks for vision-based hand gesture recognition. *Proceedings of the 2011 IEEE International Conference on Signal and Image Processing Applications* (ICSIPA), 342-347.

Nair, K.K., Kiremidjian, A.S. & Law, K.H. (2006). Time series-based damage detection and localization algorithm with application to the ASCE benchmark structure. *Journal of Sound and Vibration*, 291(1-2), 349-368.

Noh, H.Y., Nair, K.K., Kiremidjian, A.S. & Loh, C.-H. (2009). Application of time series based damage detection algorithms to the benchmark experiment at the National Center for Research on Earthquake Engineering (NCREE) in Taipei, Taiwan. *Smart Structures and Systems*, 5(1), 95-117.

Sohn, H., Farrar, C., Hunter, N. & Worden, K. (2001). Applying the LANL statistical pattern recognition paradigm for structural health monitoring to data from a surface-effect fast patrol boat. *Technical Report LA-13761-MS*, Los Alamos National Lab.

Torok, M.M., Golparvar-Fard, M. & Kochersberger, K.B. (2014). Image-based automated 3D crack detection for post-disaster building assessment. *Journal of Computing in Civil Engineering*, 28(5), A4014004.

Wang, Z., Zhang, Y., Mosalam, K.M., Gao, Y. & Huang, S.L. (2022). Deep semantic segmentation for visual understanding on construction sites. *Computer - Aided Civil and Infrastructure Engineering*, 37(2), 145-162.

Yassin, M. (1994). Nonlinear analysis of prestressed concrete structures under monotonic and cycling loads. *PhD Dissertation*, University of California, Berkeley.

Yeum, C.M. & Dyke, S.J. (2015). Vision-based automated crack detection for bridge inspection. *Computer-Aided Civil and Infrastructure Engineering*, 30(10), 759-770.

Yoon, H., Elanwar, H., Choi, H., Golparvar-Fard, M. & Spencer Jr, B.F. (2016). Target-free approach for vision-based structural system identification using consumer-grade cameras. *Structural Control and Health Monitoring*, 23(12), 1405-1416.

Zheng, Y., Gao, Y., Lu, S. & Mosalam, K.M. (2022). Multi-stage semi-supervised active learning framework for crack identification, segmentation and measurement of bridges. *Computer-Aided Civil and Infrastructure Engineering*, Accepted.

Zhou, B., Khosla, A., Lapedriza, A., Oliva, A. & Torralba, A. (2016). Learning deep features for discriminative localization. *Proceedings of the IEEE Conference on Computer Vision and Pattern Recognition*, 2921-2929.

RISK-INFORMED MAINTENANCE STRATEGY FOR THE ARMOUR UNITS OF A BREAKWATER INCLUDING EPISTEMIC UNCERTAINTY

David De-Leon-Escobedo

Professor, School of Engineering

Autonomous University of Mexico State, Mexico

International Symposium on Emerging Developments and Innovative Applications of Reliability Engineering and Risk Managements (EDIARR2022),30 October-3 November2022, Taipei
Chen, S. S. &Ang, Alfredo. H-S. (Editors)

RISK-INFORMED MAINTENANCE STRATEGY FOR THE ARMOUR UNITS OF A BREAKWATER INCLUDING EPISTEMIC UNCERTAINTY

David De-Leon-Escobedo[1], Lourdes Loza-Hernandez[2]
[1]*Professor (Graduate Engineering Program, Autonomous University of Mexico State, Ciudad universitaria, Toluca, Estado de Mexico, Mexico)*
E-mail: daviddeleonescobedo@yahoo.com.mx
[2]*Professor (Graduate Engineering Program, Autonomous University of Mexico State, Ciudad universitaria, Toluca, Estado de Mexico, Mexico)*
E-mail: llozahernandezd@yahoo.com

Abstract: A formulation to select the best maintenance strategy for the armour units of a breakwater is proposed based on risk and reliability techniques. The proposed formulation extends the existent damage assessment of breakwaters, specifically the core elements, to generate practical recommendations to maintain a breakwater on the basis of risk and reliability criteria including epistemic uncertainty on the modeling of the wave hazard. The formulation considers annual and lifetime exceedance probabilities for the wave hazard on the site and develops histograms to make conservative decisions, instead of the traditional use of mean values. The cost of consequences includes potential fatalities and the economic loss of maritime and port activities. Also, acceptable values of reliability are calculated, as a function of the cost of failure consequences, based on minimum expected life-cycle costs. A new curve that relates the required weight of tetrapods (armour units) to fulfill damage level under certain wave heights, is proposed as a practical tool towards the optimal design. Reliability calculations are performed via Monte Carlo Simulations techniques and the optimal maintenance srtategy is selected based on the minimum expected-life-cycle cost. An example illustrates the potential benefits of the proposed formulation.

Keywords: breakwater maintenance strategy, armour units stability, risk and reliability assessments, expected life-cycle costs

1 Introduction

Given that, for any type of infrastructure, risk is unavoidable, the maintenance of large infrastructure systems require that engineers take some provisions (Ang, 1984). In the case of an important port, the breakwaters need to operate within a reasonable reliability level and, as a critical component the core (armour) elements need a careful assessment.

The classical work by Hudson (1959) proposed the first rules for the stability analysis of breakwater core elements. The work by Van de Kreeke and Paape (1964) improved these first proposal. The behaviour of rock slopes was a refinement (Van der Meer, 1988a) and the convenience of probabilistic and deterministic procedures was clarified (Van der Meer, 1988b). The historical progress on the breakwaters design, including practical applications, was studied (D'Angremond & Van Roode, 2004). This paper takes some of their suggestions for optimal maintenance. The time dependent reliability analysis was used to optimize inspection strategies (Nguyen, Van Gelder, Verhagen, & Vrijling, 2010) and the target reliability of caissons-based breakwaters was identified (Cheol-Eung, Seung-Woo, Dong-Heon, & Kyung-Duck, 2012).

Buoys information was used for the analyses of extreme wave heights and several return periods were proposed for some sites in the Gulf of Mexico (Panchang, Kwon, & Demirbilek, 2013); this information is employed in this paper. A tool based on copulas was recently proposed to assess the optimal reliability of breakwaters (Dong, Jingjing, Li, & Wei, 2016). The present study expects to improve the decision-making process for owners, managers or operators willing to implement risk management programs which include a desired degree of protection to their

facilities. In addition, the cost-effectiveness of strategies aimed to reduce the epistemic uncertainty on the wave hazard, enables the optimal allocation of funds for a cost-effective risk management. In the future, decisions on design and safety for this kind of structures may be supported by procedures like the one proposed here, to calibrate the desired degree of protection of the specific risk management plans selected by owners, managers, and operators.

2 Formulation

The following subsections describe the proposed procedure.

2.1 General procedure

The proposed procedure intends to reach the following goals:

- Extreme wave heights on the specific site, Tampico, are characterized including epistemic uncertainty.
- Probability of annual exceedance damage level is calculated for the breakwater armour units.
- Expected damage probabilities and damage costs are assessed for some levels of epistemic uncertainties of significant variables.
- Alternative maintenance strategies are examined for the selection of the optimal plan.

The next sections contain detailed descriptions of all these calculations.

2.2 Wave hazard

The annual cumulative distribution for the wave heights is:

$$F = 1 - e^{-\left(\frac{H_S - 0.97}{1.86}\right)^{2.4}} \tag{1}$$

The mean value and the standard deviation are 2.86 and 1.98 m, respectively.

2.3 Damage assessment of armour units

From Van Der Meer (1998), the damage level S of armour units, for shallow waters, is related to the significant wave height H_s, the relative buoyant density Δ, the nominal diameter of the armour element D_n, the notional permeability factor P, the number of waves N, the breakwater slope and the breaker parameter ξ

$$\frac{H_S}{\Delta D_n} = P^{-0.13}\left(\frac{S}{\sqrt{N}}\right)^{0.2}\sqrt{cot\alpha}\,\xi^{P} \tag{2}$$

the relative buoyant density is:

$$\Delta = \frac{\rho_r}{\rho_w} - 1 \tag{3}$$

where $_r$ and $_w$ are the mass densities of rock and water, and the breaker parameter is:

$$\xi = \frac{1}{(cot\ \alpha)\sqrt{s_{om}}} \tag{4}$$

where s_{om} is the wave steepness. Therefore, the damage level is:

$$S = \left[\frac{H_S}{\Delta D_n}\right]^5 N^{1/2} P^{0.65} (cot\alpha)^{5P-2.5} (s_{om})^{2.5P} \quad (5)$$

2.4 Epistemic uncertainty on the armour damage probability

The epistemic uncertainty, expressed as the variations around the mean value of the significant wave height, means that there is an incomplete knowledge on the mean, or around the conditional wave height for a given value. Numerically, this corresponds to the implementation of a double loop simulation process, the external loop to generate mean values of the wave height, and the internal one to simulate wave heights with the epistemic uncertainty. Other authors (D'Angremond & Van Roode, 2004) operated this uncertainty in a similar way: they considered uncertainties on the parameters of the Weibull distribution intended to model the aleatory uncertainty on the wave heights. The simulated wave heights follow a lognormal distribution where the mean value is the mean wave height, and the coefficient of variation is the level of epistemic uncertainty:

$$LN(E(H_s), CV_e) \quad (6)$$

For example, for CV_e= 0.1, the exceedance distribution of damage for several lifetimes is calculated, see Fig. 1.

Now, the process is repeated for the calculation of the exceedance probabilities, for the epistemic uncertainties of 0.2 and 0.4. The curves move to the right and spread as the epistemic uncertainty becomes large. That means that the damage probability grows, especially for the large lifetime periods. For failure prevention, and maintenance strategies, it is interesting to analyses the failure probability and the influence of the epistemic uncertainty on this probability. If the failure event is the one where S > 9.5 (Vander Meer, 1998), the failure probability for each lifetime *R* and each level of epistemic uncertainty CV_e, are calculated, see Table 1:

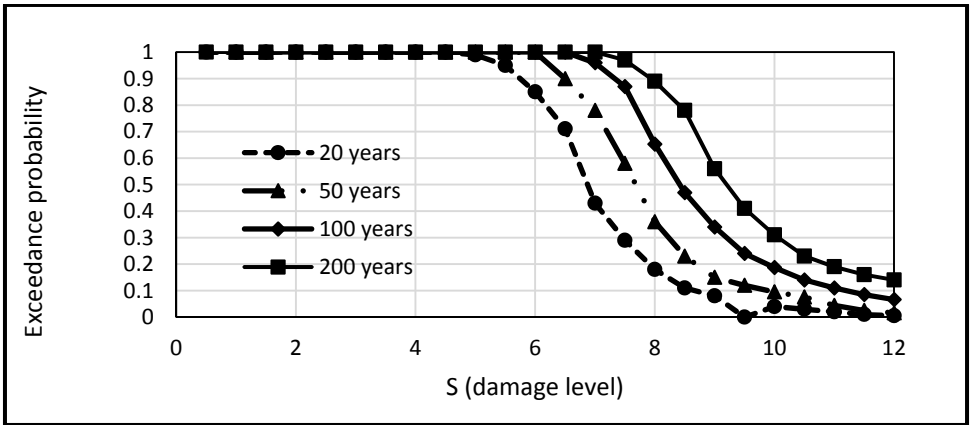

Figure 1. Exceedance damage distribution for lifetime of 20, 50, 100 , 200 years for epistemic uncertainty CV_e =0.1

Table 1. Failure probability per lifetime R and level of epistemic uncertainty *CV*e.

***R* (years)**	**CV_e :**	**0**	**0.1**	**0.2**	**0.4**
200		0.077	0.41	0.8	0.94
100		0.04	0.24	0.51	0.73
50		0.02	0.12	0.25	0.53
20		0.008	0.05	0.16	0.289

In order to prevent failures and adopt a balanced maintenance strategy, the cost of failure needs to be analyzed. The next section will describe the items to detail the failure consequences and after that, in section 3, the specifics for the considered case study are discussed.

2.5 Considered costs

As it is usually done, the expected value of the present worth of the failure or damage cost, *E(FC)* is calculated by:

$$E(FC) = FC * PV * P_f \tag{7}$$

Where *FC* is the cost of failure consequences, i. e. cost of the repairs or reconstruction *rc*, fatalities cost *fc*, loss of properties *lp*, economic loss *ec*, and other costs (like reputation) *oc*. *PVF* is the present value factor expressed in terms of the net annual discount rate , and the projected breakwater design life *L*:

$$PV = [\frac{1-\exp(-\delta L)}{\delta}] \tag{8}$$

P_f is the amour unit failure probability.

3. Illustration for Tampico port in Mexico

3.1 Logistics of the port operation

Tampico is a port located in the southeastern part of the state of Tamaulipas, Mexico and in the north bank of the Pánuco River, about 10 kilometers (6 mi) inland from the Gulf of Mexico, and directly north of the state of Veracruz. Tampico is in latitude 22.28 and longitude -97.87 and the water depth, at the end of the breakwater, is 35 m. Currently, the port is managed through the Administradora Portuaria Integral (API) de Tampico S.A. de C.V., created on June 29th, 1994. It still maintains its economic relevance and it is one of the main seaports of Mexico (API, 2020a). Figures 2 and 3 shows Tampico Port.

Figure 2. Tampico port, Mexico

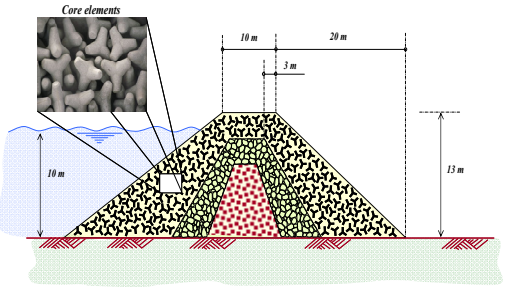

Figure 3. Cross section of the breakwater model

Diagnostic produced within the Development Master Program of Tampico Port 2016-2021, contains the financial analysis for the infrastructure and port equipment investment. Data obtained from the Tampico API for the 2010-2015 period, generated a cash flow from operations for $253.4 million (MX), Federal Government support for $301.8 million (MX), and dredging and maintenance operations of the port infrastructure for $390.8 million (MX). The projections made by the Tampico API consider that the port will generate itself resources for its operations in the period 2016-2021 approximately $301.1 million (MX) (API Tampico, 2020b). Zanela (2019a and 2019b) states that the revenues of Tampico Port, based on data given by the Secretaría de Comunicaciones y Transportes (SCT) for the period of January - September 2019, are $173.4 million (MX).

Besides, the reconstruction cost is 10 million USD, the economic loss is 20 million USD, the loss of properties is 60 million USD and 100 lives lost is the fatality loss. Because of the deceases, the calculation of the fatality loss considers previous works that applied the human capital approach to estimate the loss of contributions to the GNP (Sugiyantoa & Santib, 2017). If the average remaining productive life of the 100 individuals is 40 years and the average per capita annual income is 18000 USD, the fatality loss is:

$$FC = 18000 * 40 * \frac{100}{1000000} = 72 \text{ million USD} \quad (9)$$

Other costs are considered as loss of confidence, the loss of income when, after a failure event, the naval companies take some time to go back to the same port, they do not do it immediately after the reconstruction. In this case, this loss reaches 8 million USD. Therefore, the total potential loss, in case of the breakwater failure, is 170 million USD, approximately; see Table 2.

3.2 Breakwater characteristics

Tampico´s breakwater, built in 1895, has a mile length and a 10 m. width structure with an external layer of core protection elements (tetrapods) at both sides. The purpose of this important infrastructure facility is to provide protection to the ships entering to the Tampico´s port through the Panuco's river by reducing the wave´s energy. Figure 2 shows the cross section of this breakwater.

Reported data from the port of Tampico in Dirección General de Puertos y Marina Mercante (DGPMM), México (DGPMM, 2001), allows for the cost calculations in the next paragraphs. From the recent extension of a similar breakwater, in Tuxpan, Mexico, with a length of 4,300 m and a cost of $1,289,823,856 mxp (Administración Portuaria Integral de Veracruz S. A. de C. V. (API), 2008), it is inferred that the breakwater initial cost is 12,276 USD per linear meter.

3.3 Expected costs of damage/failure consequences including epistemic uncertainty

The weight of wave tetrapods required to withstand several wave heights, for several damage levels, are calculated by solving, trial and error, Equation (6) for the given damage levels (2, 3.45, 9.5) and several wave heights. Figure 4 shows the results.

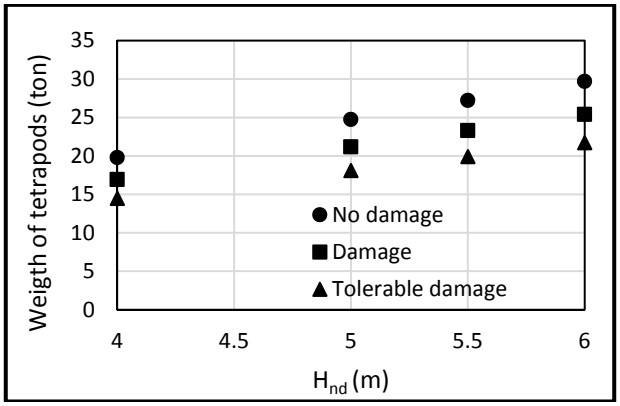

Figure 4. Weight of tetrapods as a function of the wave height for three damage levels

Table 2. Calculation of total losses

Cost component	Cost (in Million USD)
Reconstruction	10
Properties loss	60
Economic loss	20
Fatality loss	72
Other losses	8
Total losses	170

The expected damage cost, the future cost, calculated though the product of the cost of failure consequences, in Table 5, the present value factor, by using L =100 years and $\gamma = 8\%$ in Eq. (24), and the failure probability, from Table 4. The results, in the form of histograms and three percentiles: the median, 75 and 95%, illustrate the effect of the epistemic uncertainty on the future costs of failure consequences.

The MCS used to calculate the failure probabilities and the damage costs, has the following details: the number of trials is 10,000 and the statistical properties and distribution type, for each variable, are according to Table 3.

A sample of the MCS appears in Table 3, where Unif. stands for a uniformly distributed random number between 0 and 1 (for a cumulative distribution) and z is the normal variate for normal and lognormal distributions. The rest of the variables are the parameters of the Equation (6). S is the damage level where, with the definition failure = (S>9.5), allows for the calculation of the failure probability:

$$P_f = {N_f}/{N_T} \tag{10}$$

Where Nf is the number of times the failure condition is fulfilled whereas NT is the total number of trials, 10,000. Table 3 shows the failure probabilities for all epistemic uncertainties.

Table 3. Sample of MCS trials for the failure probability CVe =0

Unif.	z	Dn normal	Unif.	Hs	Unif.	z	Δ normal	Unif.	z	cotα normal
0.63	0.34	1.01	0.22	2.85	0.48	-0.02	1.59	0.87	1.14	3.17
0.11	-1.20	0.96	0.17	2.72	0.11	-1.18	1.54	0.79	0.83	3.12
0.57	0.19	1.00	0.53	2.91	0.07	-1.41	1.52	0.77	0.76	3.11

The histograms and the percentiles show how the costs grow as the epistemic uncertainty grows. See Figure 5 as an example.

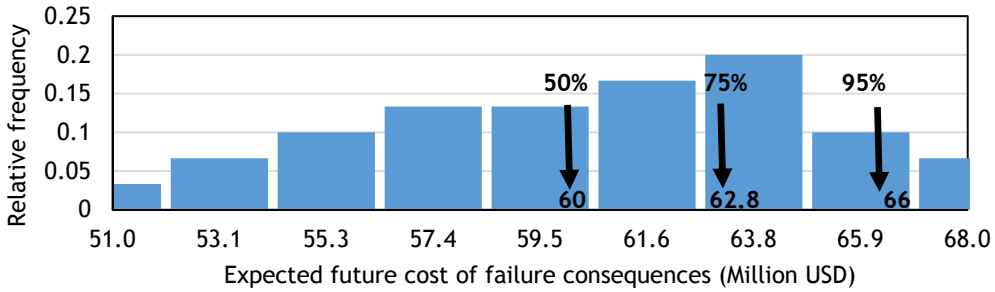

Figure 5: Expected future cost and percentiles for epistemic uncertainty =0.1

3.4 Optimal maintenance

According to a published guide for breakwaters (D'Angremond & Van Roode, 2004), a simplified optimization of maintenance costs is performed, for three alternative strategies: minor repair (or repair of minor damage), repair of serious damage and no repair of minor damage. The following calculations are performed: exceedance probability for wave heights, the wave heights for the onset of damage states (Table 4), the required tetrapod nominal diameter, Dn, and corresponding costs factors of the armour (Table 5), related to the no damage state.

Table 4. Development of damage

Actual Wave height *H*	Damage in % of armour layer
$H < H_{nd}$	0
$H_{nd} < H < 1.17H_{nd}$	4
$1.17H_{nd} < H < 1.37$	8
$H > 1.37\ H_{nd}$	Collapse

Table 5. Cost factors (respect to actual) to avoid damage

H_{nd} (m)	*E(S)*	*F*
4	1.99	1.64
5	1.99	2.05
5.5	1.99	2.255
6	1.99	2.46

If the level S=2 (limit for no damage) in Equation (6), the corresponding significant wave height Hs is 2.44 m whereas the condition for tolerable damage (damage level 4.3) corresponds to Hs =2.85m and the one for collapse (damage level 9.5) corresponds to Hs = 3.33 m. By expressing the damage limits in terms of Hnd, the coefficients 1.17 and 1.37 are calculated; see Table 5 for the onset of the damage levels. Finally, the annual risks and maintenance costs and the annual

capitalised costs, obtained by adding the maintenance to the total (initial + maintenance) costs, drives to the identification of the minimum cost or optimal strategy.

From the total breakwater initial cost of 12,276 USD obtained in section 3.2 and by taking the proportion shown in a guide (D'Angremond & Van Roode, 2004), the cost of the armour layer is 1,630 Hnd USD and the one of the core is 10,646 USD. Several factors F to be applied to the variable E(Dn), the mean value of the nominal tetrapod diameter, are calculated to obtain the costs for several wave heights with no-damage, in terms of the original design. For these original design E(H) = 2.86m; the factors are obtained in this way: Equation (8) is solved for H by trial and error and keeping E(S) = 2 (threshold for no damage). H becomes Hnd in the next Tables. Initial cost, for several tetrapods weights, is calculated for core and for armour layers. The costs of damage/failure, called annual risks, for each damage level are also calculated for the same alternative tetrapods. Then, the average annual risk s = $\Sigma(\Delta p \bullet \Delta w)$ is calculated. The costs for the three alternative maintenance strategies are integrated as follows: a) the cumulative sum of $\Delta p \bullet \Delta w$ for the three columns for 4% damage, b) the sum of $\Delta p \cdot \Delta w$ for the 2nd and 3rd columns for 8%, and c) only $\Delta p \bullet \Delta w$ for the third column (collapse); results are shown in Table 6. For a lifetime of L =100 years, which is a reasonable assumption for a breakwater, a capitalization on an interest rate γ =8% leads to the present value factor PV=12.5he resulting capitalized . The maintenance costs are shown in Table 6 and the total cost, which is I (initial) +S (capitalised maintenance), is shown in Table 7.See in bold the minimum costs.

Table 6. Capitalized maintenance cost for various maintenance options

H_{nd} (m)	*CAPITALISED RISKS*		
	Full repair of partial Damage ($)	**Only repair of serious Damage (>8%)** ($)	**No repair of partial damage** ($)
4	9,411.5	5105	4583
5	2687	1,709	1,301.5
5.5	917.4	469.3	290.1
6	899.1	459.3	292.9

Table 7. Expected total cost

H_{nd} (m)	*CAPITALISED RISKS*		
	Full repair of partial damage ($)	**Only repair of serious damage (>8%)** ($)	**No repair of partial damage** ($)
4	26,870	22,564	5,336
5	**23,511**	**22,533**	1,516
5.5	24,124	23,676	**363**
6	30,188	29,748	365

Δp = pi – pi+1 probability of occurrence of the wave height in the indicated interval
pi = probability of exceedance of the wave height at the lower limit of the interval
pi+1 = probability of exceedance of the wave height at the upper limit of the interval
Δw = cost of repair of the armour layer (2*n*A) and cost of replacement (C) for collapse

4 Analysis of results

As in many published works, like Van Der Meer (1998), and D'Angremond and Van Roode (2004), a Weibull distribution represented the extreme wave heights for the site. In these works, uncertainty on the parameter of this distribution represents the modelling uncertainty. In this work, the mean value of the wave height is a random variable, with a lognormal distribution, and the coefficient of variation contains the level of epistemic uncertainty. The analysis of gradients showed that the wave height is the most significant parameter and, therefore, the introduction of epistemic uncertainty on this parameter is justified.

The band of 90% confidence bounds on the annual wave height distribution, Figure 2, allows for conservative decisions on design or maintenance of breakwaters. These confidence levels may satisfy risk-aversive managers to have informed decisions based on more statistics rather than only the mean values.

As observed in Figure 3, the distribution of damage exceedance for several wave return periods, allows for the design of preventive maintenance strategies However, when epistemic uncertainty is included, the curves move to the right and spread between them as the level of epistemic uncertainty grows. That means, as expected, that the expected damage level is higher as the time projection is larger and that, the failure probabilities, defined as $S>9.5$, become higher as the timetable grows. Table 6 shows how much the difference is and may allow to a risk-aversive manager, to plan adequate preventive maintenance schedules to avoid failures. With these results, operators may perform cost-benefit studies to compare the cost of the wave hazard refinement with the costs of having a high epistemic uncertainty.

As shown in Figure 11, the required weight of tetrapods to withstand several wave heights grows as the prescribed damage level is lower. Breakwater managers may resort on this type of graphs to obtain the damage level expected for the current tetrapods and the weight of the ones that would be required to reduce the damage level, for wave heights between 4 and 6 m. In addition, it is shown that the tetrapods weight increment needed to pass from slight damage to no damage, or from tolerable damage to slight damage, is between 15 and 20%.

As, expected, the cost of failure consequences grows as the epistemic uncertainty grows. For example, from epistemic uncertainty from 0 to 0.4, the median of the cost increases from 22.6 to 60 million USD. Finally, the identification of optimal maintenance strategy shows that the design wave height lies between 5 and 5.5 m for the 3 prescribed maintenance strategies.

In addition, because the cost of the tetrapods is small as compared to the potential losses if the breakwater fails, investments on the breakwater safety are highly recommendable against the potential losses due to the breakwater failure. Besides, as before observed, the cost to reduce damage is cheap and, consequently, the investment on breakwater tetrapods pays off to protect current and future investments on the port. According to the case that practitioners may have, the cost of failure consequences will depend on the level of epistemic uncertainty they have on the wave hazard. Besides, the percentiles provide a wider decision room to managers instead of the practice of using only mean values.

5 Conclusions and recommendations

The paper proposed a formulation to measure the impact of epistemic uncertainty on the breakwaters damage prediction and to select appropriate maintenance strategies. The future cost, in present value, of the breakwater failure consequences included the logistics of the port of Tampico and several histograms show the future cost distribution, for some levels of epistemic

uncertainty. The level of epistemic uncertainty on the wave height has a significant impact on the cost of failure consequences.

It was shown that confidence levels, and percentiles, like 75 or 95, may help owners, operators, or managers to make conservative decisions, as opposite to the practice of relying only on mean values, to enhance the protection of the breakwaters. For the breakwater illustrated, here has currently an adequate safety margin. However, special the probability of breakwater failure for the term of 200 years is high, especially when a high level of epistemic uncertainty is considered.

A curve developed between the weight of the tetrapods and the breakwater damage level for several wave heights, can be used to as a tool to obtain the cost of reducing damage. Future work may derive recommendations for lifetime extension, for older breakwaters approaching the end of their nominal operating life, to establish risk-management strategies to exploit the potential of economic growth of the port considering the risk/benefit balance on the life-cycle perspective.

6 Acknowledgements

The authors acknowledge the breakwater data from Mexican Institutions (Dirección de Puertos, Secretaría de Comunicaciones y Transportes, SCT). (DGPMM, 2001).

This work was partially supported of CONACYT (Consejo Nacional de Ciencia y Tecnología), through a postdoctoral stay granted to Lourdes Loza Hernández in Engineering Faculty of Universidad Autónoma del Estado de México, in Mexico.

7 References

Ang, H-S. A. & Tang, W. H. (1984). Probability concepts in engineering planning and design. Vol. II– Decision, risk, and reliability. John Wiley and Sons. New York.

Administración Portuaria Integral de Veracruz S. A. de C. V. (API, 2008). ANÁLISIS COSTO-BENEFICIO DE LA AMPLIACIÓN NATURAL DEL PUERTO DE VERACRUZ EN LA ZONA NORTE. API Veracruz, Coordinación General de Puertos y Marina Mercante, Secretaria de Comunicaciones y Transportes.

Administración Portuaria Integral, Tampico S.A. de C.V. (API, 2020a). QUIÉNES SOMOS. SECRETARÍA DE COMUNICACIONES Y TRANSPORTES. API Tampico. Coordinación General de Puertos y Marina Mercante. https://puertodetampico.com.mx/quienes-somos/. Accessed January 10, 2020.

Administración Portuaria Integral, Tampico, S.A. de C.V. (API, 2020b). PROGRAMA MAESTRO DE DESARROLLO PORTUARIO DEL PUERTO DE TAMPICO 2016-2021. Secretaría de Comunicaciones y Transportes. API Tampico. Coordinación General de Puertos y Marina Mercante. http://www.puertodetampico.com.mx/Sitio/documents/PMD.pdf. Accessed January 10, 2020. (In Spanish).

Cheol-Eung, L., Seung-Woo, K., Dong-Heon, P., & Kyung-Duck, S. (2012). Target reliability of caisson sliding of vertical breakwater based on safety factors. Coastal Engineering Journal. Vol. 60, pp. 167-173. https://doi.org/10.1016/j.coastaleng.2011.09.005

D'Angremond, K. & Van Roode, F. C. (2004). Breakwaters and Closure Dams. Spon Press, Taylor & Francis.

Dirección General de Puertos y Marina Mercante, México (DGPMM, 2001). MANUAL DE DIMENSIONAMIENTO PORTUARIO, Secretaria de Comunicaciones y Transportes (SCT). Capítulo 3, Condicionantes Físicas.

Dong, S., Jingjing, L., Li, X., & Wei, Y. (2016). Study of vertical breakwater reliability based on copulas. Journal of Ocean University of China. 15. 232-240. DOI: 10.1007/s11802-016-2692-7.

Hudson, R.Y. (1959). Design of quarry-stone cover layers for rubber-mound breakwaters. WES Research Report 2-2. Vicksburg.

Nguyen, D.V., Van Gelder, P.H.A.J.M., Verhagen, H.J., & Vrijling, J.K. (2010). Optimal inspection strategy for rubble-mound breakwaters with time-dependent reliability analysis. Reliability, Risk and Safety – Ale, Papazoglou & Zio (Eds). Taylor & Francis Group, London, ISBN 978-0-415-60427-7.

Panchang, V., Kwon, J. Ch., & Demirbilek, Z. (2013). Analyses of Extreme Wave Heights in the Gulf of Mexico for Offshore Engineering Applications. Journal of Offshore Mechanics and Arctic Engineering. Volume 135, Issue 3. DOI: 10.1115/1.4023205.

Sugiyantoa, G. & Santib, Y. (2017). Road traffic accident cost using human capital method (case study in Purbalingga, Central Java, Indonesia). Jurnal Teknologi. Vol. 79:2 pp. 107–116. www.jurnalteknologi.utm.my. eISSN 2180–3722.

Van de Kreeke, J. & Paape, A. (1964). On optimum breakwater design. In Proceedings of 9th. Conference on Coastal Engineering, Lisbon, Portugal (pp. 532–552). New York, NY: American Society of Civil Engineers.

Van der Meer, J. W. (1988a). Rock slopes and gravel beaches under wave attack. Doctoral thesis, Delft University of Technology. Delft Hydraulics Publication no. 396.

Van der Meer, J. W. (1988b). Deterministic and probabilistic design of breakwater armour layers. Proc. ASCE, Journal of WPC and OE, Vol. 114, No. 1.

Van der Meer, J. W. (1998). Application and stability criteria for rock and artificial units. Chapter 11 from: Dikes and Revetments. Design, Maintenance and Safety Assessment, Edited by Kristian Pilarczyk, 26 Pages.

Zanela, L. A., (2019a). CAEN 11.6% INGRESOS DE LOS PUERTOS AL TERCER TRIMESTRE DE 2019. T21 magazine (Dic. 5th, 2019). Copyright © Grupo Comunicación y Medios, Mexico. http://t21.com.mx/maritimo/2019/12/05/caen-116-ingresos-puertos-tercer-trimestre-2019. Accessed January 10th, 2020.

Zanela, L. A., (2019b). TAMPICO LICITA TERMINAL DE USOS MÚLTIPLES; CHIAPAS DE CONTENEDORES. T21 magazine (Nov. 26th, 2019). Copyright © Grupo Comunicación y Medios, Mexico. http://t21.com.mx/maritimo/2019/11/26/tampico-licita-terminal-usos-multiples-chiapas-contenedores.

VALIDATING THE CURRENT STATE-OF-PRACTICE FOR SEISMIC RISK (AND RESILIENCE) ANALYSIS

Paolo Gardoni

Director, MAE Center

Co-Director, Societal Risk and Hazard Mitigation Program

Professor, Excellence Faculty Scholar in Civil and Environmental Engineering

University of Illinois at Urbana-Champaign, USA

International Symposium on Emerging Developments and Innovative Applications of Reliability Engineering and Risk Managements (EDIARR2022),30 October-3 November2022, Taipei
Chen, S. S. &Ang, Alfredo. H-S. (Editors)

VALIDATING THE CURRENT STATE-OF-PRACTICE FOR SEISMIC RISK (AND RESILIENCE) ANALYSIS

Paolo Gardoni[1], Neetesh Sharma[1], Yun-Chi Yu[1]
[1]*Department of Civil and Environmental Engineering, University of Illinois Urbana-Champaign, Urbana, USA*
E-mail: gardoni@illinois.edu

Abstract: Validating predictive models is critical for decision-making since inaccurate predictions may lead to suboptimal decisions. Seismic risk analysis has an extensive suite of predictive models, including nested models that are part of complex multi-step procedures. However, the validation of seismic risk assessment models has been limited partly due to data scarcity and the difficulties in carrying out such validation. Typical model validation attempts are limited to ground motion prediction equations and a few damage models for buildings and buried infrastructure. Also, most current seismic risk analysis research focuses on add-on formulations for infrastructure functionality, interdependencies, or resilience optimization, while using established resources that form the state of practice, such as HAZUS and MAEViz to predict fundamental quantities. However, it is critical to assess the credibility of such resources. This paper evaluates the current state of practice for the seismic risk analysis of physical infrastructure, including buildings, transportation, power, potable water, and wastewater infrastructure. The predictive models include ground motion prediction equations and damage prediction models. We use the data from the 2016 Kumamoto earthquake in Japan for validation. The comparison shows the predictive ability of available models and directs future research toward essential improvements.

Keywords: Risk, Resilience, Validation, Earthquakes, Infrastructure.

1 Introduction

Communities, utility companies, infrastructure managers, governing, regulatory, and policy bodies, and insurance and re-insurance companies have to make critical decisions concerning natural hazards. Risk (and resilience) analysis supports such decision-making by estimating the probabilities of various hazard scenarios and predicting their consequences. Seismic risk assessment has some of the most extensive suites of predictive models. Examples include seismic predictive models to simulate the earthquake intensity prediction (e.g., ground motion prediction equations, GMPEs) and the hazard impact on buildings and infrastructure (e.g., transportation, electrical power, potable water, wastewater).

Hazard impact models, particularly physical damage prediction models, are often building blocks in subsequent analysis for assessing infrastructure functionality, economic loss, and societal impact. Additionally, hazard impact models are the basis for developing (optimal) mitigation strategies and improving societal resilience. Two widely used resources for hazard impact analysis are HAZUS (FEMA 2014) and MAEViz (MAE Center 2011). They are used either as a whole package or by extracting selected models needed for the analysis of interest. They allow the convenient analysis of the physical structures and infrastructure damage with simple input data. Their conceptual simplicity, extensive coverage of impact metrics, computational efficiency, and significant work done to develop them make HAZUS and MAEViz widely used in seismic risk analysis in academia and practice. However, due to the limited data available for the validation of rare events, the fundamental hazard impact models are often not carefully validated.

A handful of past studies have critically examined seismic impact assessment results. Ellingwood (1988) examined the seismic probabilistic risk assessment methods by comparing the factors (i.e., hazard characteristics and vulnerability) that significantly affect the risk outcomes. Bai et al. (2014) conducted a comparative study for concrete buildings using the fragility curves from the HAZUS

and MAEViz. However, the case study only compared and highlighted the difference between the two predictions (HAZUS vs. MAEViz) but not with real-world data. Recently, Goda et al. (2016) conducted the validation of GMPEs with the recorded data from the 2016 Kumamoto Earthquake. While Crowley et al. (2008, 2020) and Riga et al. (2021) published a comparative analysis for seismic risk assessment considering both the GMPEs and building damage prediction obtained using the European Seismic Risk Model (ESRM20). However, these studies only focused on validating the GMPEs and the damage of a few building types. They did not check the models for other structures and infrastructure damage, and the structural damage for the few building types considered was based on models not widely used. Among the critical infrastructure, buried pipelines' fragilities have also been the subject of a few investigations using laboratory or real-world data (Liu et al. 2017; Bellagamba et al. 2019). However, there remains a consistent scarcity of literature that extensively validates the predictions.

This paper evaluates the current state of practice for seismic risk assessment. In particular, the focus is on the models for predicting hazard intensity measures and damage to buildings, components of the transportation infrastructure (i.e., bridges), components of the electrical power infrastructure (i.e., transmission lines, substations, and power plants), components of the potable water infrastructure (i.e., pipeline and pumping stations), and 6) components of the wastewater infrastructure (i.e., pipeline and wastewater treatment plant).

2 Compiling the validation data from the 2016 Kumamoto Earthquake

We consider the damage from the mainshock of the 2016 Kumamoto earthquake in Japan. We compile and produce the necessary data in Mashiki Town, Kumamoto. A considerable effort in conducting this validation study went into compiling validation data. This section lists the data sources used to generate the validation data from the selected earthquake. We select the study area as Mashiki Town, Kumamoto, Japan, because this region has good data availability. Furthermore, this community was near the epicenter and experienced severe damage to buildings and critical infrastructure.

2.1 Earthquake characteristics and intensity maps

The 2016 Kumamoto earthquake occurred along the Futagawa fault with a magnitude of M_w 7.0 on April 16, 2016. The epicenter was at $32^{\circ}46'N$ and $130^{\circ}43'E$, which is about 4 km northeast of Mashiki Town. Figure 1(a) shows the location of Mashiki Town relative to the epicenter. We obtained the recorded seismic intensity measures for the earthquake from USGS ShakeMap for PGA, PGV, and $S_a(T = 0.3s)$. Figures 1(b) – (d) show the maps of the intensity measures.

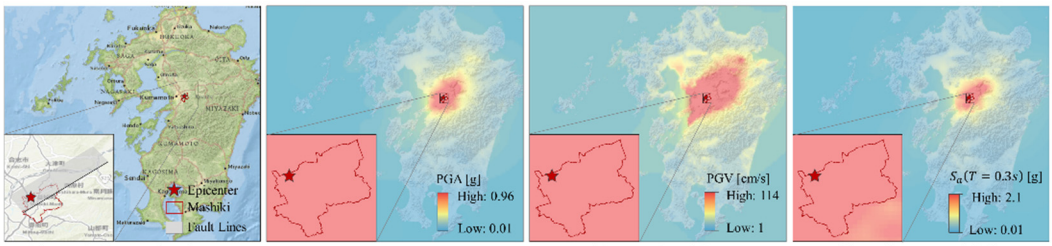

(a) Fault line and epicenter location (b) PGA $[g]$ (c) PGV [cm/s] (d) $S_a(T = 0.3s)[g]$

Figure 1. Region of interest and recorded ground motion intensity measures

2.2 Building Inventory

We collected the field survey and the necessary data on building damage for a subset of ~3,000 buildings (due to data limitation) in and around the main settlement in Mashiki Town (Naito et al. 2020). Figure 2 shows the building inventory, including building years and structural types (Sugino et al. 2016). Structure type symbol C1 represents the Concrete Moment Frame, W1 represents the Wood light frame, and W2 represents Wood Commercial or Industrial. Most of the buildings are wooden structures built before 1982.

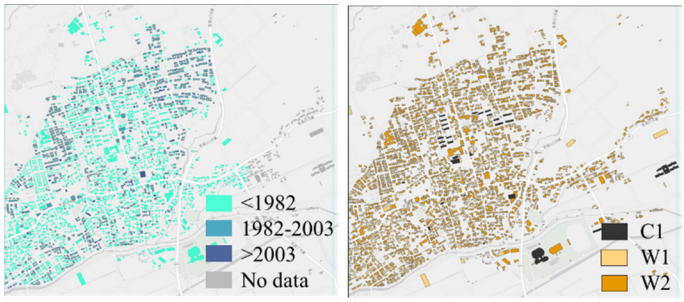

(a) Building construction years (b) Building structural types

Figure 2. Building inventory

2.3 Transportation Infrastructure inventory

We obtained the bridge inventory from the Mashiki Town Bridges Repair Construction Plan (Mashiki Town Government 2013; Mashiki Town Government 2016). A total of 103 bridges are within the region of interest, and 13 bridges were recorded to experience at least slight damage. Figure 3 (a) and (b) show the structural types in HAZUS and MAEViz categories, respectively. These categories differ in design standards, material properties, and geometrical properties (span, lanes, etc.), and detailed descriptions of these categories are available in HAZUS (FEMA 2014) and Choi et al. (2004). In addition, we consider the design standard (i.e., conventional or seismic design) based on the Japanese code update year, which is 1995. Most bridges are conventional concrete bridges, and a few bridges follow the seismic design.

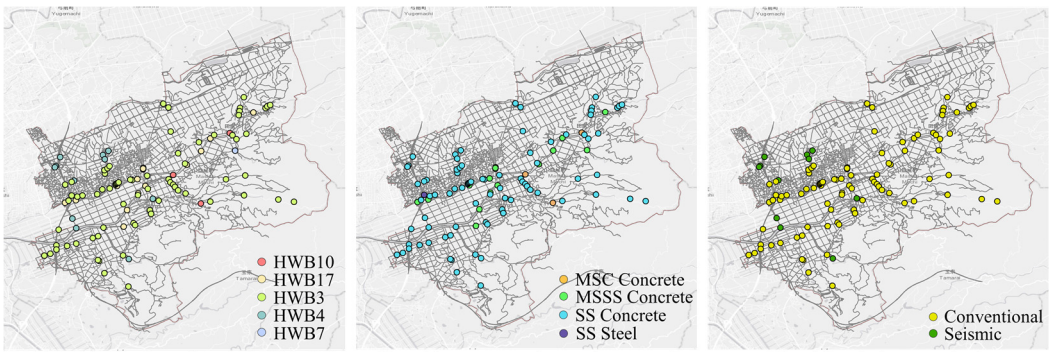

(a) Bridge structural types in HAZUS classification (b) Bridge structural types in MAEViz classification (c) Bridge design standards

Figure 3. Bridge inventory

2.4 Electrical power infrastructure inventory

Since electric grids typically cover vast regions, most significant electrical facilities are far from Mashiki Town. Therefore, we use the entire Kumamoto area for the electrical power network analysis. We collected the topology and damage details for electrical power infrastructure from Tang and Eidiner (2017). Figure 4(a) shows the electrical power inventory. The (blue) lines represent the transmission lines supporting Mashiki Town and nearby regions, while the nodes represent substations and the power plant types (e.g., hydro and thermal).

(a) Electrical power transmission (b) Potable water pipeline (c) Sewage network

Figure 4. The inventory of electrical power transmission, water pipeline, and wastewater network

2.5 Potable water infrastructure network inventory

We collected the potable water network data from the water facilities damage report and the pipeline recovery announcement on the local Government website (Ministry of Health, Labour and Welfare, Japan 2016; Mashiki Town Government 2016). In addition, we obtained the pumping station locations from the Mashiki land use planning map. Figure 4(b) shows the potable water pipeline inventory.

2.6 Wastewater infrastructure inventory

We collected the wastewater infrastructure data from the technical report by the National Institute for Land and Infrastructure Management, Ministry of Land, Infrastructure, Transport and Tourism, Japan (2017). Figure 4(c) shows the wastewater infrastructure inventory.

3 Comparative analysis/validation of the predictive models

This section uses the collected inventory data as inputs for HAZUS and MAEViz to obtain the predictions. We then compare the recorded hazard intensities and damage with the predictions.

3.1 Hazard intensity map: recorded vs predicted

We use the GMPEs developed by Boore et al. (2014) to predict the hazard intensity measures. According to Goda et al. (2016), this GMPE is the most suitable for this case, given the geological site characteristic (Goda et al. 2016). Figure 5 (a) – (c) compares the recorded and predicted values of PGA, PGV, and $S_a(T = 0.3s)$

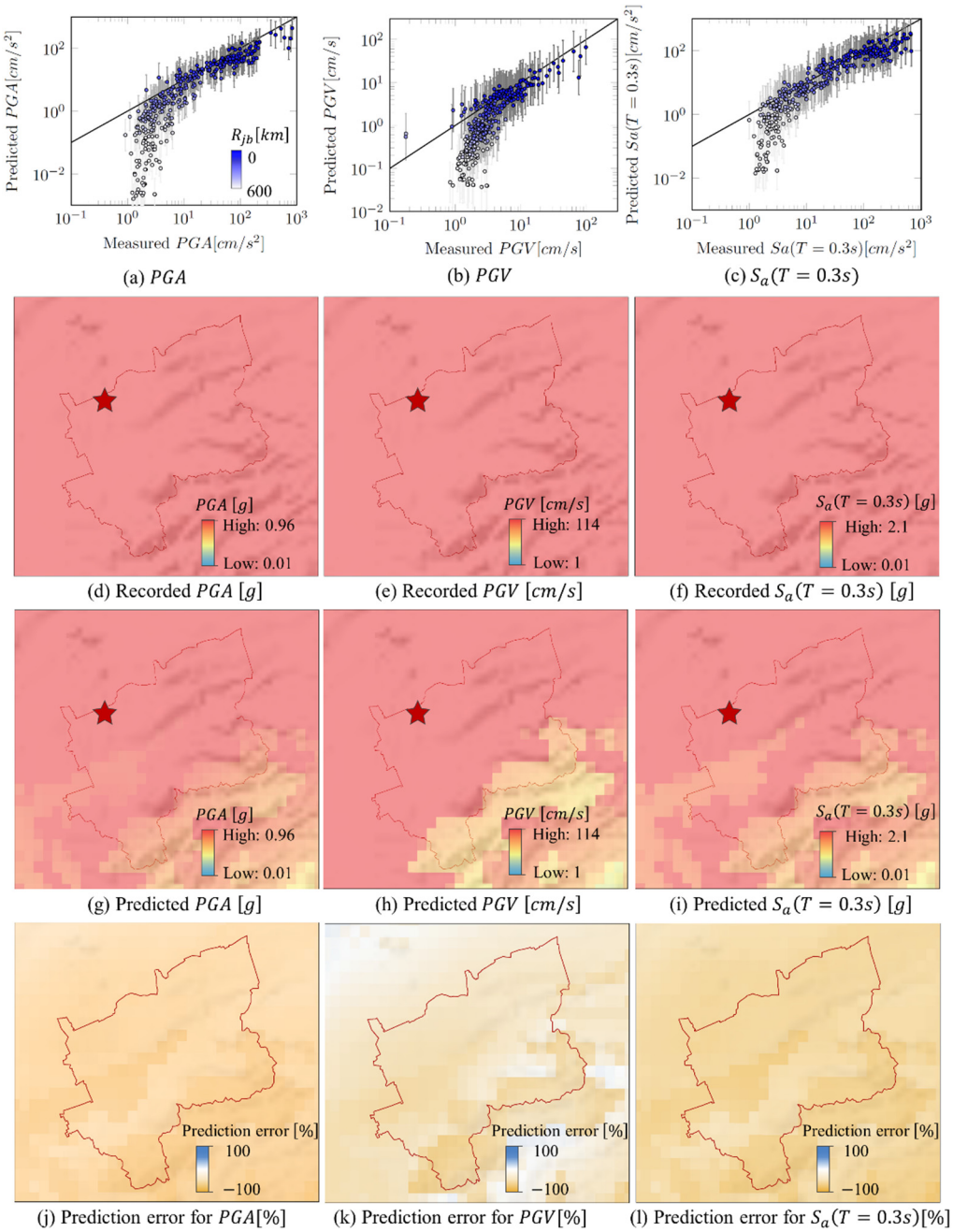

Figure 5. (a) - (c) Comparison between recorded and predicted results, (d) – (f) spatial comparisons for Mashiki Town

We also show the 95% confidence intervals associated with each prediction. The shade of the dots indicates the variation in the distance from the fault plane projection on the ground surface, known as the Joyner Boore distance R_{jb}. As the distance from the fault plane increases, the predicted values go down. However, the accuracy of the prediction also seems to be highly dependent on

R_{jb}. As the distance exceeds 250 km, the points seem to have high bias and depart from the 1:1 line. However, the plots are on the log scale; thus, looking at the confidence intervals, we can see that the prediction has a higher variance for low R_{jb}. Prediction confidence is lowest for the values where the hazard intensity is highest, which is undesirable because those would be locations expecting the most severe damage. We also provide graphical maps of the same analysis for Mashiki Town. Figures (d) – (i) show the recorded and the median of the predicted hazard intensities, while Figures (j) – (l) show the error plots in terms of the percentage difference between the median predicted and the recorded values. We observe that the predicted intensity measures are up to 100% lower than the recorded.

3.2 Building damage: recorded vs predicted

Figure 6 (a) shows the recorded damage state for each building, while Figures 6 (b) and (c) show the most probable damage state predicted by the fragility functions in HAZUS and MAEViz using the predicted hazard intensity measures (PGA for HAZUS and both PGA and Sa for MAEViz). The damage states for the buildings include insignificant, moderate, heavy, and complete; the definitions of these damage states are available in Bai et al. (2014). Figures 6 (d) and (e) show the error associated with the most-likely damage state, which is the number of states between the predicted most likely damage state and the recorded damage state. Overall, HAZUS and MAEViz do not perform well. HAZUS tends to underestimate the complete damage state and sometimes gives completely different predictions (e.g., predict the insignificant damage when the damage is complete). However, HAZUS has a closer prediction than MAEViz for the low- and medium-damage states (e.g., insignificant, moderate, and heavy). Compared with HAZUS, MAEViz gives a more accurate prediction of the higher damage state (i.e., complete). Though MAEViz generally overestimates the damage, it better predicts the variation in the relative damage from building to building, so it would likely be easier to recalibrate the model.

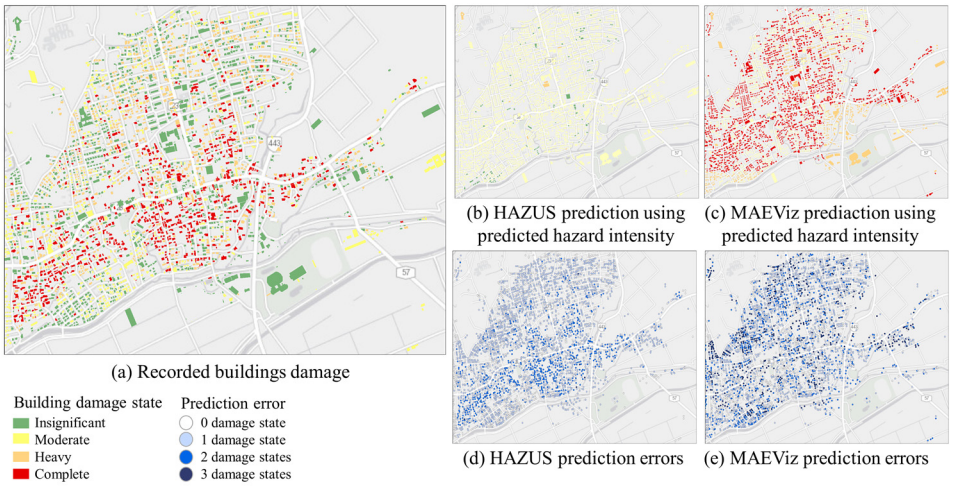

Figure 6. Comparison between recorded and predicted building damage

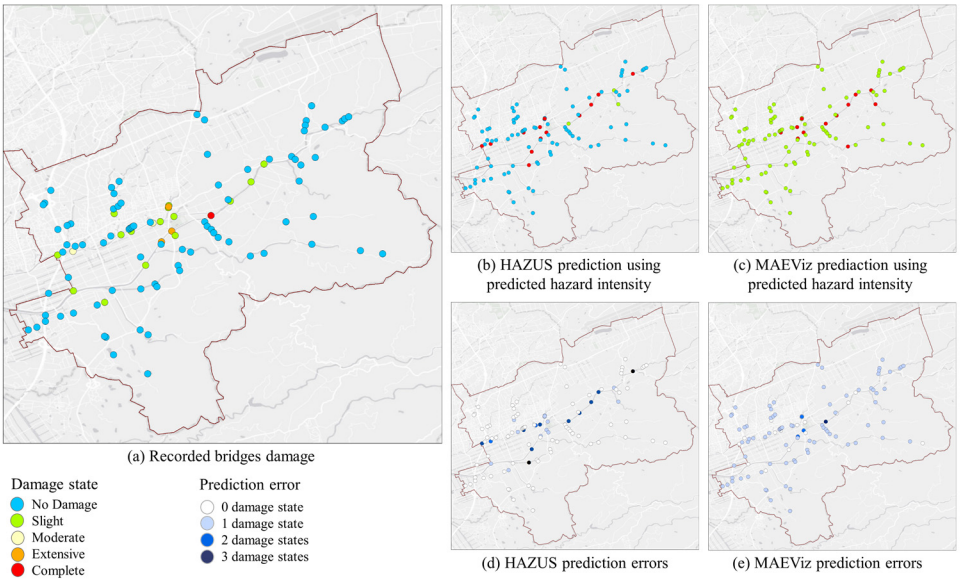

Figure 7. Comparison between recorded and predicted bridge damage

3.3 Transportation damage: recorded vs predicted

Figure 7(a) shows the recorded damage state for each bridge, while Figures 7 (b) and (c) show the most probable damage state predicted by the fragility functions in HAZUS and MAEViz using the predicted hazard intensity measures (PGA and Sa for both HAZUS and MAEViz). The trends from the building results also follow for the predictions of bridge damage. However, HAZUS and MAEViz perform relatively better than when predicting damage to buildings. It is possible partly because the bridge construction is more standardized than the general building stock. Overall, HAZUS predictions are better than MAEViz in the case of no damage. However, it also gives completely wrong predictions for a few bridges (e.g., predicting the undamaged bridges as collapsed). However, MAEViz overestimates the damage, but compared with HAZUS, the predictions are more consistent, and there are no extreme errors.

3.4 Electrical power damage: recorded vs predicted

Figure 8 (a) shows the recorded damage state for the electrical power infrastructure, while Figures 8 (b) and (c) show the most probable damage state predicted by the fragility functions in HAZUS and MAEViz using the predicted hazard intensity measures (PGA for HAZUS and MAEViz). HAZUS and MAEViz predict the damaged state of the electrical substations relatively well. However, they do not have models for predicting damage to transmission lines. Most transmission lines are presumed to be not vulnerable to ground shaking; however, in the current earthquake, a large region in Kumamoto lost access to power because of the damage to transmission towers, mainly due to ground failure, landslides, and dislodging of the conductors from the transmission tower connectors.

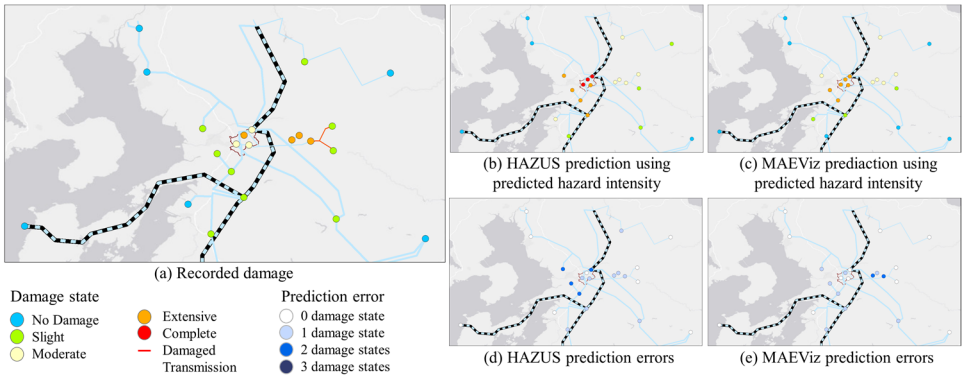

Figure 8. Comparison between recorded and predicted damage in the electrical power infrastructure

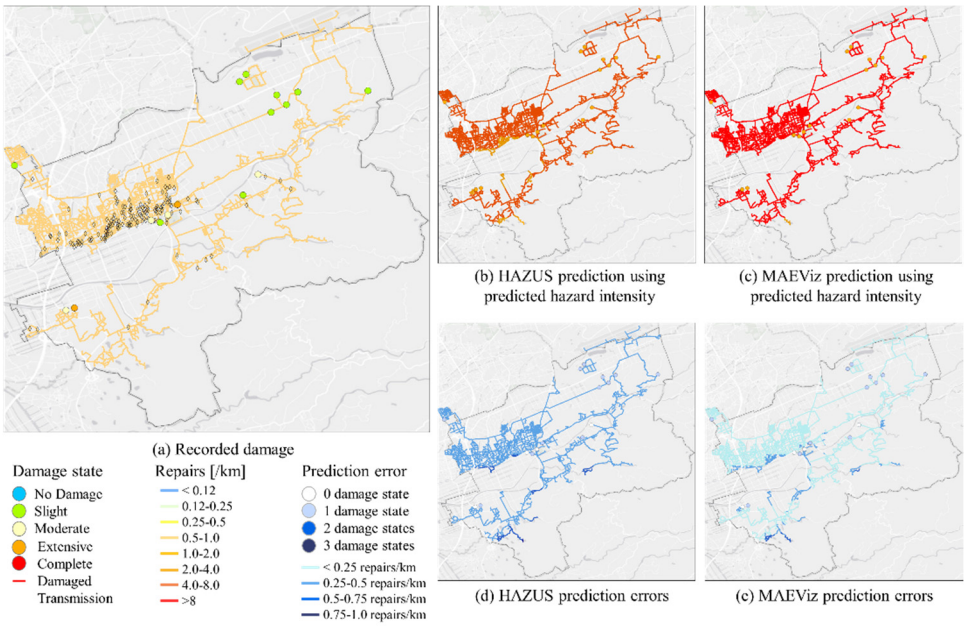

Figure 9. Comparison between recorded and predicted damage in the water infrastructure

3.5 Potable water network damage: recorded vs predicted

Figure 9 (a) shows the recorded damage state for the potable water infrastructure, while Figures 9 (b) and (c) show the most probable damage state predicted by the fragility functions in HAZUS and MAEViz using the predicted hazard intensity measures (PGA (for pumping stations) and PGV (for pipeline) for both HAZUS and MAEViz). The damage to the pumping station was available in the Mashiki Town water pipeline damage report (The Kumamoto Prefecture environmental and living office 2018). We present the damage states for the pumping stations and repair rates for the pipes. The recorded repair rate is ~0.86 repairs per km. Overall, HAZUS and MAEViz tend to overestimate the damage state. HAZUS shows more variation in the predicted result and gives a closer prediction for water facilities; however, MAEviz performs significantly better in predicting the repair rates for pipes.

3.6 Wastewater network damage: recorded vs predicted

Figure 10 (a) shows the recorded damage state for the wastewater infrastructure, while Figures 10 (b) and (c) show the most probable damage state predicted by the fragility functions in HAZUS and MAEViz using the predicted hazard intensity measures (PGA (for treatment plant) and PGV (for pipeline) for both HAZUS and MAEViz). We present the damage states for the wastewater treatment plant and the repair rates for the wastewater pipes. The recorded repair rate for the wastewater pipelines is below 0.5 per km. The repair rate prediction models for wastewater pipelines are identical to the ones for potable water pipelines at the same location because HAZUS and MAEViz do not differentiate between potable water and wastewater pipes. Hence, the trends in the results are similar, with a slight overestimation of damages. We only have one wastewater facility, and both models predict moderate damage, whereas the actual damage state is extensive, which is only one damage stage off.

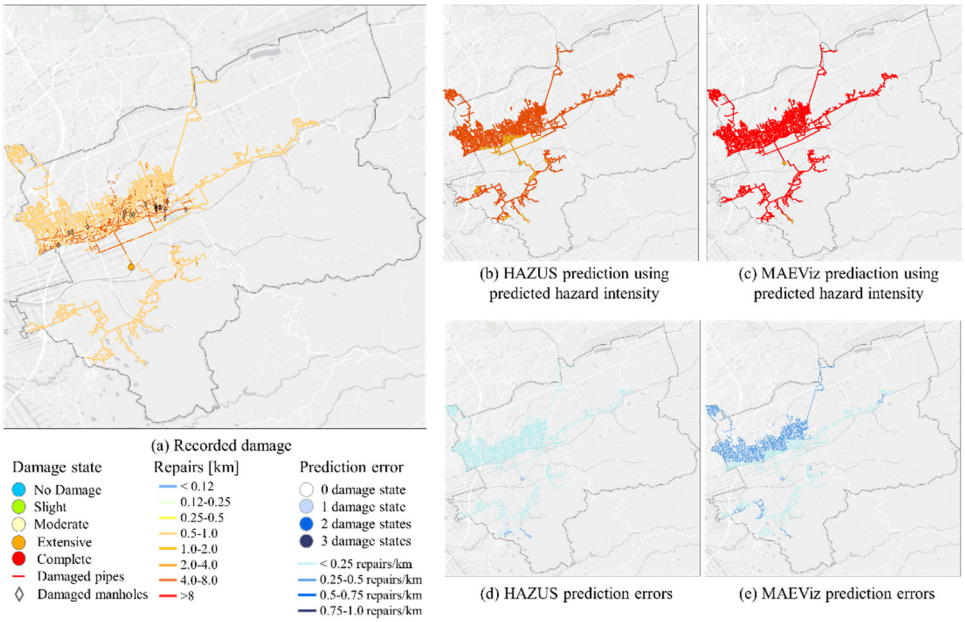

Figure 10. Comparison between recorded and predicted damage in the wastewater infrastructure

4 Conclusions

This paper validated the state of practice for predicting the hazard intensity measures and damage to buildings, components of the transportation infrastructure (i.e., bridges), components of the electrical power infrastructure (i.e., transmission lines, substations, and power plants), components of the potable water infrastructure (i.e., pipeline and pumping stations), and 6) components of the wastewater infrastructure (i.e., pipeline and wastewater treatment plant). The paper compared the recorded values with those predicted by suitable GMPEs, HAZUS, and MAEViz, for Mashiki Town, Kumamoto, Japan, due to the 2016 Kumamoto earthquake. This paper is the first to validate GMPEs and damage models comprehensively. Most analyses show that the predictive models do not accurately predict the recorded values. Instead, the models tend to underestimate the hazard intensity and overestimate the damages. The performance is better for infrastructure components than buildings, which we attribute to higher standardization uniformity in infrastructure components than buildings. The current paper focused on the validation of the damage prediction

models. Ongoing work is extending the validation to the predictive models for building and infrastructure recovery, economic losses, resilience, interdependencies, and network functionality. Beyond the validation, ongoing work is also developing a Bayesian approach for updating the model parameters as data becomes available.

5 Acknowledgments

This work was supported by funding from the Taiwan-UIUC Fellowship, and the Office of Risk Management and Insurance Research (ORMIR) in the Gies College of Business at the University of Illinois at Urbana-Champaign.

6 References

Bai, Jong-Wha, Mary Beth D. Hueste, and Paolo Gardoni. "Case study: Scenario-based seismic loss estimation for concrete buildings in Mid-America." *Earthquake Spectra* 30, no. 4 (2014): 1585-1599.

Bellagamba, Xavier, Brendon A. Bradley, Liam M. Wotherspoon, and Matthew W. Hughes. "Development and validation of fragility functions for buried pipelines based on Canterbury earthquake sequence data." *Earthquake spectra* 35, no. 3 (2019): 1061-1086.

Boore, David M., Jonathan P. Stewart, Emel Seyhan, and Gail M. Atkinson. "NGA-West2 equations for predicting PGA, PGV, and 5% damped PSA for shallow crustal earthquakes." *Earthquake Spectra* 30, no. 3 (2014): 1057-1085.

Choi, Eunsoo, Reginald DesRoches, and Bryant Nielson. "Seismic fragility of typical bridges in moderate seismic zones." *Engineering structures* 26, no. 2 (2004): 187-199.

Crowley, Helen, Peter J. Stafford, and Julian J. Bommer. "Can earthquake loss models be validated using field observations?." *Journal of Earthquake Engineering* 12, no. 7 (2008): 1078-1104.

Crowley, Helen, Vítor Silva, Petros Kalakonas, Luís, Martins, Graeme Weatherill, Kyriazis Pitilakis, Evi Riga , Barbara Borzi, and Marta Faravelli. "Verification of the European seismic risk model (ESRM20)." In *Proceedings of the 17th world conference on earthquake engineering, Sendai, Japan*, vol. 27. 2020.

Ellingwood, Bruce. "Validation studies of seismic PRAs." *Nuclear Engineering and Design* 123, no. 2-3 (1990): 189-196.

Federal Emergency Management Agency (FEMA). "Multi-Hazard Loss Estimation Methodology, Earthquake Model, Hazus-MH 2.1, Technical Manual." (2013).

Geospatial Information Authority of Japan, Accessed July 15, 2022. https://maps.gsi.go.jp/#16/32.782269/130.806055/&base=std&ls=std&disp=1&vs=c1g1j0h0k0l0u0t0z0r0s0m0f1&d=m. (in Japanese)

Goda, Katsuichiro, Grace Campbell, Laura Hulme, Bashar Ismael, Lin Ke, Rebekah Marsh, Peter Sammonds et al. "The 2016 Kumamoto earthquakes: cascading geological hazards and compounding risks." *Frontiers in built environment* 2 (2016): 19.

Liu, Wei, Huiquan Miao, Chuang Wang, and Jie Li. "Experimental validation of a model for seismic simulation and interaction analysis of buried pipe networks." *Soil Dynamics and Earthquake Engineering* 100 (2017): 113-130.

MAE Center. (2011) "Software and Tools." http://mae.cee.illinois.edu/software/.

Mashiki Town Government. "Mashiki Town Bridges Repair Construction Plan." (2013). (in Japanese)

Mashiki Town Government. "Mashiki Town Potable Water Pipeline Recovery Progress". (2016). https://www.town.mashiki.lg.jp/kiji0031475/3_1475_1_up_yjujy41c.pdf.

Mashiki Town Government. "Mashiki Town damage report in the 2016 Kumamoto Earthquake." (2020). https://www.town.mashiki.lg.jp/kiji0033823/3_3823_5427_up_jihuen7n.pdf. (in Japanese)

Mashiki Town Government. "Mashiki Town Bridge recovery after the 2016 Kumamoto Earthquake." (2021). Retrieved from https://www.town.mashiki.lg.jp/kiji0034601/index.html. (in Japanese)

Ministry of Health, Labour and Welfare. "Kumamoto Area Water Facilities Damage Investigation Report in the 2016 Kumamoto earthquake." (2016). https://www.mhlw.go.jp/stf/seisakunitsuite/bunya/0000207309.html (in Japanese)

Naito, Shohei, Hiromitsu Tomozawa, Yuji Mori, Takeshi Nagata, Naokazu Monma, Hiromitsu Nakamura, Hiroyuki Fujiwara, and Gaku Shoji. "Building-damage detection method based on machine learning utilizing aerial photographs of the Kumamoto earthquake." *Earthquake Spectra* 36, no. 3 (2020): 1166-1187. (in Japanese)

National Institute for Land and Infrastructure Management Ministry of Land, Infrastructure, Transport and Tourism, Japan. "Report on a characteristic and countermeasure of the damages to sewer pipes caused by the 2016 Kumamoto Earthquake." (2017). http://www.nilim.go.jp/lab/bcg/siryou/tnn/tnn0997pdf/ks099707.pdf . (in Japanese)

Riga, Evi, Anna Karatzetzou, Stefania Apostolaki, Helen Crowley, and Kyriazis Pitilakis. "Verification of seismic risk models using observed damages from past earthquake events." *Bulletin of Earthquake Engineering* 19, no. 2 (2021): 713-744.

ShakeMap, Accessed July 15, 2022. https://earthquake.usgs.gov/data/shakemap/ .

Sugino, Mina, Ryohei Yamamuro, Sunao Kobayashi, Shiori Murase, Saki Ohmura, and Yasuhiro Hayashi. "Analyses of building damages in Mashiki Town in the 2016 Kumamoto Earthquake." *J Jpn Assoc Earthq Eng* 16, no. 10 (2016): 69-85. (in Japanese)

Tang, Alex K., and John M. Eidiner. "Kumamoto, Kyushu, Japan, Earthquake of Mw 6.0 April 14, 2016, Mw 7.0 April 16, 2016, Lifetime Performance, e Council of Lifeline Earthquake Engineering TCLEE No. 2 and Yokohama National University." *Yokohama, Japan* (2017).

The Kumamoto Prefecture environmental and living office. "Kumamoto water network summary." (2018). https://www.pref.kumamoto.jp/uploaded/attachment/53401.pdf. (in Japanese)

SYSTEM-RELIABILITY-BASED DISASTER RESILIENCE ANALYSIS OF A CABLE BRIDGE UNDER FIRE HAZARD.

Junho Song

Professor, Department of Civil and Environmental Engineering

College of Engineering,
Seoul National University, Republic of Korea

International Symposium on Emerging Developments and Innovative Applications of Reliability Engineering and Risk Managements (EDIARR2022),30 October-3 November2022, Taipei
Chen, S. S. &Ang, Alfredo. H-S. (Editors)

SYSTEM-RELIABILITY-BASED DISASTER RESILIENCE OF A CABLE BRIDGE UNDER FIRE HAZARD

Junho Song[1], Seonghyun Lim[2], Taeyong Kim[3], Sang-ri Yi[4], and Hyun-Joong Kim[5]
1 Department of Civil and Environmental Engineering, Seoul National University, Seoul, South Korea
E-mail: junhosong@snu.ac.kr
2 Department of Civil and Environmental Engineering, Seoul National University, Seoul, South Korea
E-mail: euler1707@snu.ac.kr
3 Department of Civil and Mineral Engineering, University of Toronto, Toronto, Canada
E-mail: tyong.kim@mail.utoronto.ca
4 NHERI SimCenter, University of California, Berkeley, California, USA
E-mail: yisangri@berkeley.edu
5 School of Engineering, Liberty University, Virginia, USA
E-mail: hkim145@liberty.edu

Abstract: As various hazards are threatening complex infrastructure systems, the concept of disaster resilience recently emerged to ensure adequate recovery of the system performance degenerated by potential failures of components. A system-reliability-based disaster resilience framework was recently proposed to promote a holistic understanding of disaster resilience in terms of components, system, and their inter-relationships. In the proposed framework, the disaster resilience of a civil infrastructure system is characterized by three criteria: reliability, redundancy, and recoverability. For a probabilistic evaluation of disaster resilience, the reliability (β) and redundancy (π) indices were defined in terms of component- and system-level reliability, respectively. The reliability-redundancy (β–π) diagram, i.e., the scatter plot of the reliability and redundancy indices computed for each initial disruption scenario, can help a decision-maker check if the system-level risk is socially-acceptable. The diagram also facilitates identifying appropriate decisions to ensure disaster resilience. This paper demonstrates the system-reliability-based disaster resilience framework through its application to a cable-stayed bridge under fire hazards. First, a probabilistic model is developed to describe the hazards of tank truck fires. Next, finite-element reliability analyses are performed to compute the component and system failure probabilities needed in the β–π analysis. To address the computational cost challenge, an active-learning-based reliability method is employed. The example demonstrates that the β–π analysis framework helps us evaluate the disaster resilience of a complex civil infrastructure such as a cable-stayed bridge using detailed finite-element models and advanced reliability methods. The proposed framework also successfully identifies the initial disruptions scenarios, i.e., cable failures against which hazard mitigations or retrofits are needed.

***Keywords*:** disaster resilience, system reliability, reliability, redundancy, cable-stayed bridge, fire hazards

1 Introduction

Civil infrastructure systems should support various activities and functions of ever-growing urban communities worldwide. Accordingly, they become highly complex systems consisting of many interconnected components. As the intensity of extreme loads induced by hazardous events and their uncertainties are significant, it is impossible to keep all civil infrastructure systems perfectly undamaged from external hazards. However, current regulations impose target reliability levels for component failures, which may result in uneconomical or infeasible decisions. Therefore, it is desirable to prioritize components making significant contributions to the system-level failure and pay more attention to the recovery of the system-level functionality.

Recently, *disaster resilience* has been extensively studied to offer such a holistic view. Bruneau et al. (2003) proposed one of the most widely used concepts of disaster resilience, highlighted by functionality curves describing the degradation and recovery of the system functionality. When

disastrous events occur, the functionality curve immediately falls and tends to increase gradually through a recovery process. The total amount of degradation in a restoration curve, determined by the level of degradation and recovery speed, is often used to measure the disaster resilience of a system. However, the utility of the resilience measure is limited in risk evaluations, decision-making, and design optimization because the definition of the functionality is often subjective and ignores significant uncertainty.

Lim et al. (2022) proposed a system-reliability-based framework that characterizes the disaster resilience of a civil infrastructure system through component and system reliability analyses (Byun and Song, 2017; Song et al., 2021) to support disaster resilience evaluation and decision-making. The framework is built on three criteria, i.e., reliability, redundancy, and recoverability, which are defined as follows:

- **Reliability**: the capability of a component to avoid or minimize initial failures or disruptions despite the occurrence of a disastrous event
- **Redundancy**: the capability of a system to avoid or minimize cascading failures and degradation of system-level performance despite component-level disruption(s)
- **Recoverability**: the ability of engineers and society to take proper actions at components to recover the functionality of the system rapidly and completely

Figure 1 illustrates these criteria, inspired by figurative descriptions of metastability in physics. Research needs for the three criteria were identified for each of the three scales of civil infrastructure systems, i.e., individual structure, infrastructure network, and urban community, and presented by the '3×3 resilience matrix' (Lim et al., 2022). In its applications at the individual structure scale, reliability-based indices were proposed for reliability and redundancy criteria. In the 'reliability-redundancy (β–π) analysis,' the reliability and redundancy indices are computed for each initial disruption scenario by component and system reliability analyses, respectively. The pairs of the indices are shown in a 'reliability-redundancy (β–π) diagram' to check if the system's risk is socially acceptable. The β–π analysis method and diagram also facilitate resilience-based decision-making, including design or retrofit optimization.

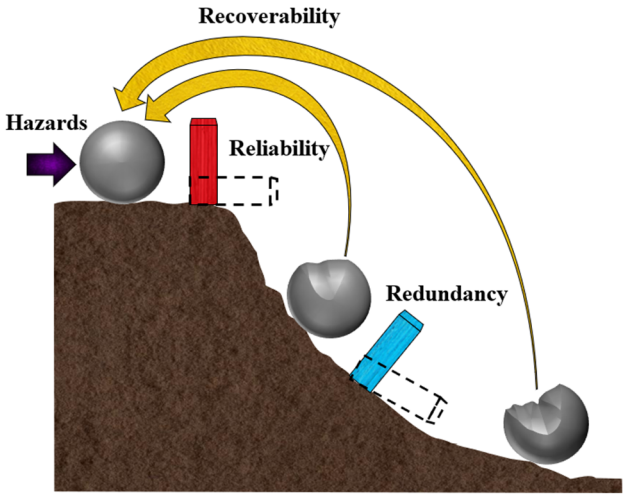

Figure 1. Three criteria of system-reliability-based disaster resilience (Lim et al., 2022)

After a brief review of the reliability-redundancy analysis, this paper presents the example of a cable-stayed bridge in South Korea under fire truck hazards. This paper provides details of the

problem setting, probabilistic modeling of fire truck hazards, and an active learning-based sampling method used for reliability analyses. The example demonstrates the procedure of the reliability-redundancy analysis and how it can support resilience-informed decision-making processes. The paper concludes with a summary and future research topics.

2 Reliability-redundancy analysis

Among the three resilience criteria, probabilistic indices were proposed to quantify the reliability and redundancy of a civil infrastructure system through component and system reliability analyses (Lim et al., 2022). For the i^{th} initial disruption scenario F_i caused by the j^{th} hazard H_j, the reliability and redundancy indices are defined as

$$\beta_{i,j} = -\Phi^{-1}\left(P\left(F_i \middle| H_j\right)\right) \tag{1a}$$

$$\pi_{i,j} = -\Phi^{-1}\left(P\left(F_{sys} \middle| F_i, H_j\right)\right) \tag{1b}$$

where F_{sys} is the system failure event, and $\Phi^{-1}(\cdot)$ is the inverse cumulative distribution function of the standard normal distribution. Higher values of β and π indicate lower likelihoods of the initial disruption F_i under the hazard and the system failure F_{sys} triggered by F_i, respectively.

From the multiplication rule, the conditional probability of the system failure triggered by the i^{th} initial disruption scenario F_i given the j^{th} hazard H_j is derived as

$$P\left(F_{sys,i,j} \middle| H_j\right) = P\left(F_{sys} \middle| F_i, H_j\right) P\left(F_i \middle| H_j\right) = \Phi\left(-\pi_{i,j}\right)\Phi\left(-\beta_{i,j}\right). \tag{2}$$

By multiplying both sides of Eq. (2) by the annual occurrence rate of the j^{th} hazard (λ_{H_j}), one can obtain the annual probability of the system failure triggered by each scenario, $P(F_{sys,i,j})$ to determine if it is socially acceptable by checking

$$P\left(F_{sys,i,j}\right) = \Phi\left(-\pi_{i,j}\right)\Phi\left(-\beta_{i,j}\right)\lambda_{H_j} < P_{dm} \tag{3}$$

where P_{dm} denotes the *de minimis* risk (Pate-Cornell, 1994), for which society does not impose any regulation (Ellingwood, 2006). From Eq. (3), the resilience limit-state surface is identified in terms of the reliability and redundancy indices as

$$P_{dm}/\lambda_{H_j} - \Phi\left(-\pi_{i,j}\right)\Phi\left(-\beta_{i,j}\right) = 0. \tag{4}$$

For the annual hazard occurrence rate λ_{H_j}, the resilience limit-state surface in Eq. (4) can be identified as a contour in the reliability-redundancy (β–π) diagram, as shown in Figure 2. Suppose the marker representing the reliability and redundancy indices computed for an initial disruption scenario is located inside the surface. In that case, the target system is not satisfying Eq. (3) for the initial disruption scenario and thus requires actions to improve the reliability or redundancy. Moreover, one can add the recoverability information to the diagram by the colors or sizes of the markers. The reliability-redundancy (β–π) diagram can facilitate various decision-making processes to manage the disaster resilience of civil infrastructure systems and resilience-based decision optimization.

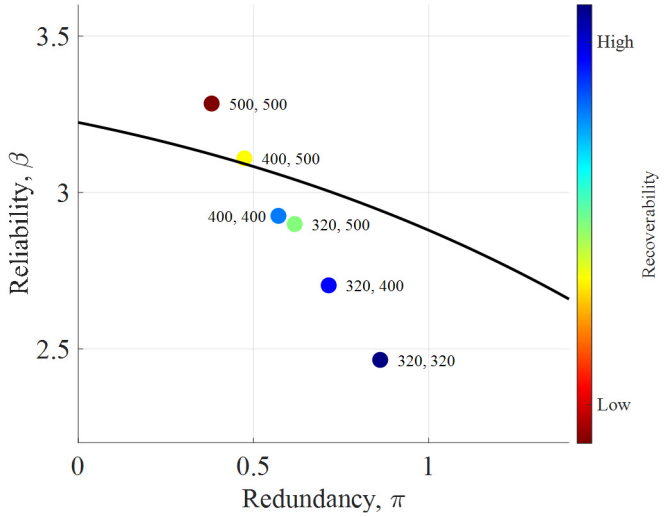

Figure 2. Reliability-redundancy (β–π) diagram with a resilience limit-state surface and recoverability information (Lim et al., 2022)

3 Fire resilience evaluation of cable-stayed bridge

3.1 Problem setting

The applicability of the system-reliability-based disaster resilience framework to the individual structure scale is demonstrated by reliability-redundancy (β–π) analysis of a cable-stayed bridge under fire truck hazards. Figure 3 shows the Seohae Grand Bridge in South Korea, which is critical in satisfying enormous traffic demands along the peninsula's west coast. The ABAQUS® model of the Seohae Grand Bridge in Figure 3 was developed to perform finite element reliability analyses to compute the reliability and redundancy indices for each initial disruption scenario. The hazardous events of interest are fires initiated by tank truck accidents in the shoulder lane adjacent to the cables of the bridge. The failures of cables are considered the initial disruption scenario F_i, while the cascading failure of an adjacent cable is regarded as the system-level F_{sys}.

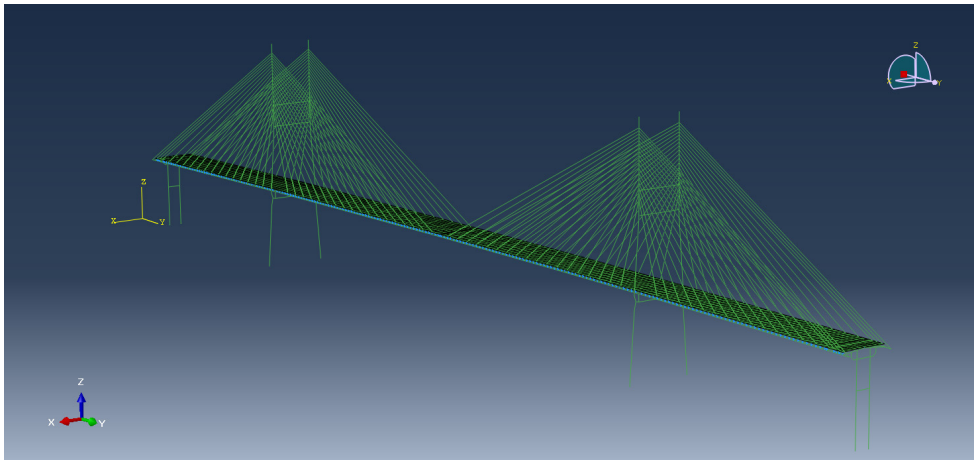

Figure 3. ABAQUS finite element model of the Seohae Grand Bridge

3.2 Probabilistic modeling of fire hazards

In this study, the radiation is assumed to govern the heat effects on the cable-stayed bridge because the tank truck fires occur in an open space. A probabilistic fire hazard model is developed based on the deterministic heat radiation model by Shokri and Beyler (1989). The pool fire is modeled as a cylindrical column whose configuration and relative position from the measuring point work are described by input variables. The effective diameter of the fire area (D), fire location (X), and model uncertainty ($\sigma\epsilon$) are selected as three random variables of the fire hazard model. In short, the heat flux (q'') generated from the pool fire is predicted as:

$$q'' = E \times F_{12} \tag{5}$$

where F_{12} is the configuration factor affected by the effective diameter of the fire area (D) and the fire location (X), and E is the effective emissive power predicted from the regression model $\ln E = 4.0228 - 0.0822 \ln D + \sigma\epsilon$.

For a sample of the random input variables, the model in Eq. (5) computes the heat flux q'', which can be converted as cable temperatures using the MATLAB® partial differential equation toolbox. For each random sample, the cable temperature distribution is simulated by one-meter vertical segments of each cable, as shown in Figure 4. ABAQUS® finite element simulations are performed considering the heat effects on the yield strength degradation and thermal expansion of the cables to determine which cables are failed or safe.

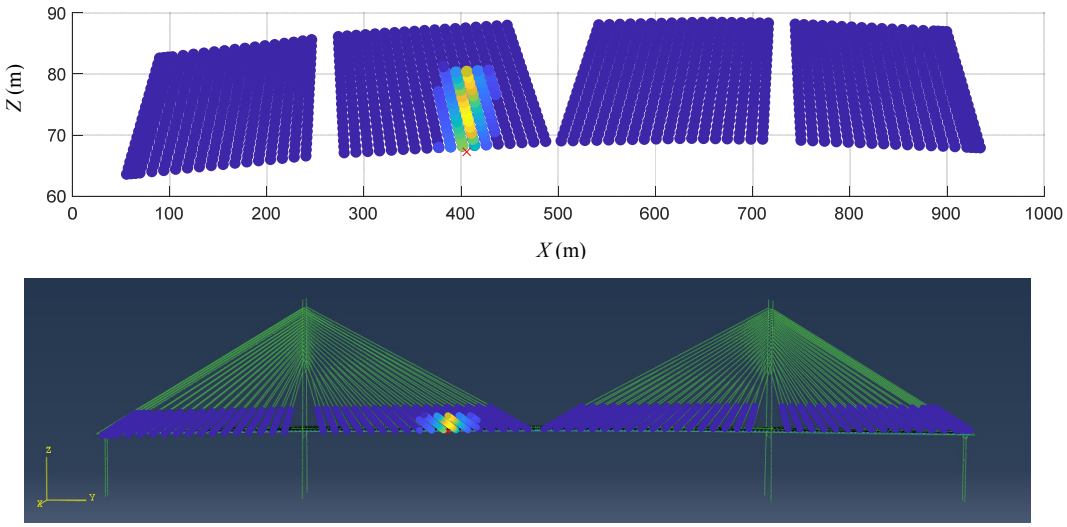

Figure 4. Distribution of cable temperatures (top) and the corresponding heat effects in the Seohae Grand Bridge ABAQUS finite element model (bottom)

3.3 Computing reliability and redundancy indices by AK-MCS

When the limit-state definition of a structural reliability problem includes an implicit function or its gradient is not readily available, sampling-based methods such as Monte Carlo Simulation (MCS) are often employed. However, MCS can be inefficient when the function evaluation is computationally expensive and the likelihood of the failure event is low. To efficiently compute the reliability and redundancy indices for each initial disruption scenario, we adopt an active learning-based sampling method named AK-MCS (Echard et al., 2011). The efficiency of AK-MCS comes from its adaptive construction of the Kriging-based surrogate model and the learning

function, which helps find the next simulation point based on exploitation and exploration. AK-MCS repeats finite element simulations to improve the Kriging surrogate at the simulation points suggested by the learning function until the component or system failure probability converges. Because component and system reliability analyses are performed for each of the 36 initial disruption scenarios, the reliability-redundancy (β–π) analysis of the Seohae Grand Bridge needs 72 AK-MCS-based reliability analyses.

4 Results of reliability-redundancy (β–π) analysis

As a result of β–π analyses, 36 pairs of reliability and redundancy indices are computed, as visualized together with the Seohae Grand Bridge in Figure 5. The top and middle subplots of Figure 5 respectively indicate the reliability and redundancy indices computed for each initial disruption scenario, i.e., the failure of the corresponding cable due to a tank truck fire. The bottom subplot shows $\Phi(-\pi_{i,j})\Phi(-\beta_{i,j}) = P(F_{sys,i,j})/\lambda_{H_j}$, termed "per hazard *de minimis* risk (PHDMR)" (Lim et al., 2022). As shown in Eq. (3), PHDMR is compared with the *de minimis* risk P_{dm} divided by hazard occurrence rate λ_{H_j} to check if the risk is socially acceptable. Therefore, it is found that the initial disruption scenarios whose PHDMR values are higher than P_{dm}/λ_{H_j}, i.e., the failures of cables #5, #6, #7, #32, #33, and #34 failed to meet the resilience limit-state for $\lambda_{H_j} = 10^{-3.8}/yr$.

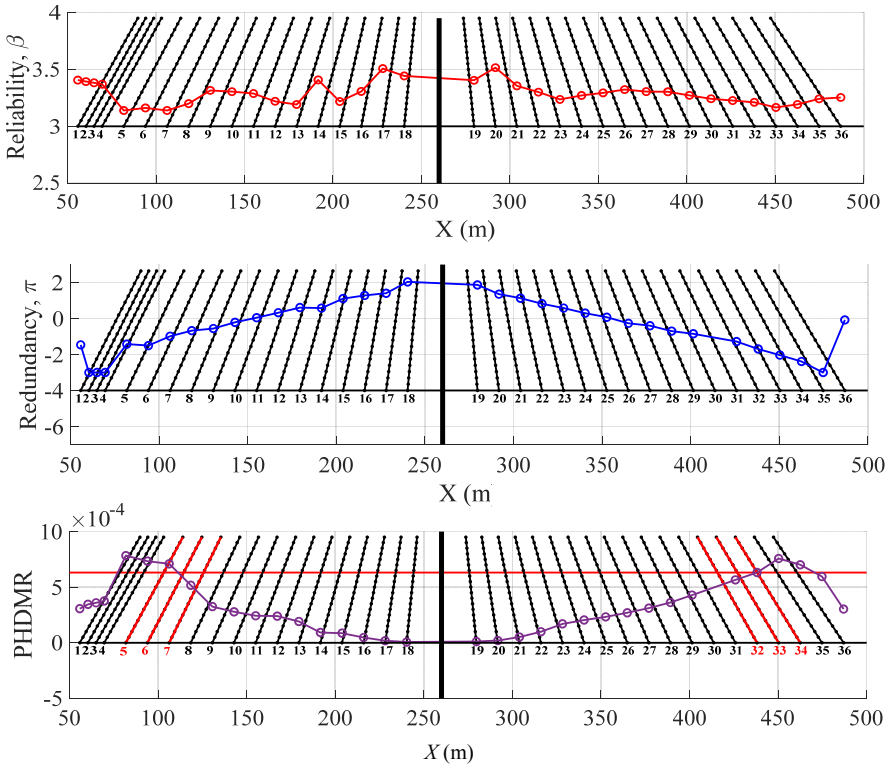

Figure 5. Reliability index (top), redundancy index (middle), and per hazard de minimis risk (bottom) obtained by β–π analysis of the Seohae Grand Bridge under a tank truck fire hazard

Figure 6 shows the analysis results in a β–π diagram. The solid black line is a contour of $\Phi(-\pi_{i,j})\Phi(-\beta_{i,j}) = P_{dm}/\lambda_{H_j}$, i.e., the resilience limit-state surface described in Eq. (4). The reliability and redundancy indices computed for the cable failure scenarios #5, #6, #7, #32, #33, and #34 are located in the domain where the resilience requirement in Eq. (3) is not satisfied. Therefore, decision-makers need to pursue proper actions to move the markers outside the limit-state surface in the β–π diagram.

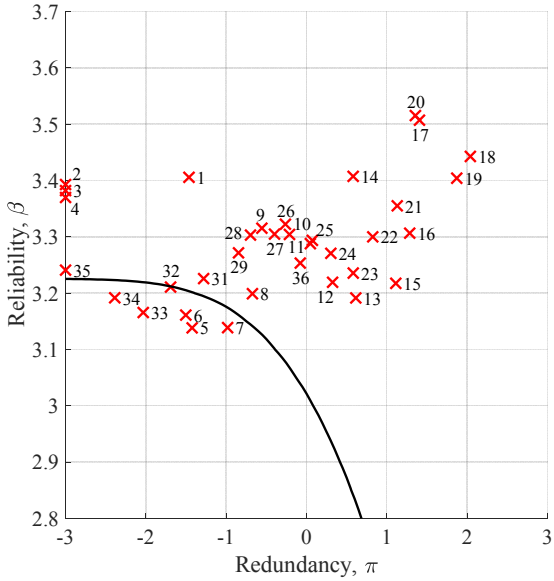

Figure 6. Reliability-Redundancy (β–π) diagram of the Seohae Grand Bridge under tank truck fire hazard

5 Conclusions

This paper presented the system-reliability-based disaster resilience framework (Lim et al., 2022), which characterizes the disaster resilience of a civil infrastructure system in terms of reliability, redundancy, and recoverability. The reliability and redundancy indices were defined for reliability analyses to quantify the components' capabilities to avoid initial disruptions and the system's ability to prevent the initial disruptions from progressing toward system-level failures, respectively. Using the β–π diagram, i.e., the two-dimensional scatter plot of the reliability and redundancy indices computed for each initial disruption scenario, one can check if the risk of the system is socially acceptable. The applicability of the β–π analysis to actual structures was successfully demonstrated by a numerical example of a cable-stayed bridge under tank truck fire hazards. The hazard was first described by a probabilistic model predicting the heat flux from a pool fire. Finite element reliability analyses were performed efficiently by an active learning-based reliability method to compute the reliability and redundancy indices for each initial disruption scenario, i.e., the failure of a cable due to a tank truck fire accident. The cable failure scenarios whose system-level risk exceeds the socially acceptable level were successfully identified to support decision-making processes ensuring disaster resilience from a system reliability perspective.

6 References

Bruneau, M., Chang, S.E., Eguchi, R.T., Lee, G.C., O'Rourke, T.D., Reinhorn, A.M., Shinozuka, M., Tierney, K., Wallace, W.A., and von Winterfeldt, D. 2003. A Framework to quantitatively assess and enhance the seismic resilience of communities. *Earthquake Spectra*. 19 (4): 733-752.

Byun, J., and Song, J. 2017. Structural system reliability, reloaded. Chap. 2-2 in *Risk and reliability analysis: Theory and applications*. edited by P. Gardoni. Berlin. Springer.

Echard, B., Gayton, N., and Lemaire, M. 2011. AK-MCS: An active learning reliability method combining Kriging and Monte Carlo Simulation. *Structural Safety*. 33(2): 145-154.

Ellingwood, B.R. 2006. Mitigating risk from abnormal loads and progressive collapse. *Journal of Performance of Constructed Facilities*. 20(4): 315-323.

Lim, S., Kim, T., and Song, J. 2022. System-reliability-based disaster resilience analysis: Framework and applications to structural systems. *Structural Safety*. 96: 102202.

Pate-Cornell, E. 1994. Quantitative safety goals for risk management of industrial facilities. *Structural Safety*. 13(3): 145–157.

Shokri, M., and Beyler, C.L. 1989. Radiation from Large Pool Fires. *Journal of Fire Protection Engineering*. 1(4): 141-150.

Song, J., Kang, W.-H., Lee, Y.-J., and Chun, J. 2021. Structural system reliability: overview of theories and applications to optimization. *ASCE-ASME Journal of Risk and Uncertainty in Engineering Systems, Part A: Civil Engineering*. 7(2): 03121001.

PROBABILISTIC DESIGN AND CALIBRATION OF PARTIAL FACTORS FOR STRUCTURAL SYSTEMS.

John Dalsgaard Sørensen

Professor, Department of the Built Environment, Division of Civil Engineering and Construction Management
Professor, Risk, Resilience, Safety, and Sustainability of Systems Research Group Danish Center for Risk and Safety Management

Aalborg University, Denmark

International Symposium on Emerging Developments and Innovative Applications of Reliability Engineering and Risk Managements (EDIARR2022),30 October-3 November2022, Taipei
Chen, S. S. &Ang, Alfredo. H-S. (Editors)

PROBABILISTIC DESIGN AND CALIBRATION OF PARTIAL FACTORS FOR STRUCTURAL SYSTEMS

John Dalsgaard Sørensen[1]
[1] *Department of the Built Environment, Aalborg University, Aalborg, Denmark*
Correspondence e-mail address: jdas@build.aau.dk

Abstract: The increased importance on sustainability implies among others a large focus on development of the basis and tools for exploitation of contributions from rational application of reliability-based design and calibration of partial factors for civil engineering and renewable energy structures. Offshore wind turbines are an example as a main contributor to renewable energy in more and more parts of the world. Reliability is a key issue since costs to operation & maintenance may be significant contributors to the Levelized Cost Of Energy and these costs are highly dependent on the reliability of the components implying that it is important to focus on increasing the reliability as much as is economically reasonable. Further, the material costs also depends on the reliability required for the main structural components and systems. The same aspects are important for civil engineering structures composed by structural systems such as offshore structures, buildings and bridges, but with different weights on the cost contributors and further life safety aspects may be important. In addition probabilistic design may use information from proof loading, inspections and monitoring. This paper describes some basic formulations, tools and examples for probabilistic design.

***Keywords*:** Probabilistic design, stochastic modelling, partial factors, wind turbines, target reliability.

1 Introduction

Traditionally codes and standards for design of structural systems such as buildings, bridges, wind turbines and offshore structures are based on the use of the semi-probabilistic design approach for securing an appropriate level of reliability. This implies the use of partial factors for loads and material parameters / resistances. The partial factors may be calibrated to reach a target reliability level over a portfolio of structures for which the partial factors are to be used. A lower bound on the reliability may be included accounting for life safety. Partial factors may also be calibrated for more specific applications as an alternative to direct reliability-based design, especially when detailed data / information is available for the considered failure mode / component.

In probabilistic / reliability-based design a target / minimum reliability level is used as basis for the design modelling failure modes by limit state equations and the uncertainty parameters by stochastic variables. An important step in applying probabilistic design is thus to decide on the required target and/or minimum reliability level which may be evaluated by risk-based methods where in principle probability of failure / adverse events are combined with the consequences of failure. Target reliability levels are often obtained by economic optimization considering the whole design lifetime. The risk-based approach can also be used for design directly. In ISO 2394 (2015) the three design approaches are described and indicative target and minimum reliability levels are described. IEC 61400-1 (2019) opens for probabilistic design of wind turbine components and serves as basis for ongoing development of a IEC TS 61400-9 on 'Probabilistic design measures for wind turbines'.

The objective of this paper is to give an overall presentation of the basis for probabilistic design for civil engineering and renewable energy structures including assessment of the required target / minimum reliability level. Special focus is on wind energy systems. Further, illustrative examples are presented.

2 Target and minimum reliability level

In ISO 2394 (2015) a target and a minimum target reliability level is presented. The target reliability level is based on monetary optimization and the minimum target reliability level is based on life safety considerations by the LQI (Life Quality Index) acceptance criterion. Both target reliability levels depend on the relative cost of safety measure, and the target reliability level also depends on the consequence of failure, see ISO 2394 (2015) and JCSS (2002). The target reliability levels with a one year reference period are shown in Table 1 and 2 for both the annual probability of failure P_F and the corresponding annual reliability index, β^t.

Table 1. Tentative target annual reliability index and probability of failure according to ISO 2394 (2015) and JCSS (2002).

Relative costs of safety measures	Consequences of failure		
	Low	Medium	High
Large	$\beta^t = 3{,}1$, $P_F = 10^{-3}$	$\beta^t = 3{,}3$, $P_F = 5 \cdot 10^{-4}$	$\beta^t = 3{,}7$, $P_F = 10^{-4}$
Medium	$\beta^t = 3{,}7$, $P_F = 10^{-4}$	$\beta^t = 4{,}2$, $P_F = 10^{-5}$	$\beta^t = 4{,}4$, $P_F = 5 \cdot 10^{-6}$
Small	$\beta^t = 4{,}2$, $P_F = 10^{-5}$	$\beta^t = 4{,}4$, $P_F = 5 \cdot 10^{-6}$	$\beta^t = 4{,}7$, $P_F = 10^{-6}$

Table 2. Tentative minimum target reliabilities with a one year reference period according to ISO 2394 (2015).

Relative costs of safety measures	Target reliability
Large	$\beta^t = 3{,}1$, $P_F = 10^{-3}$
Medium	$\beta^t = 3{,}7$, $P_F = 10^{-4}$
Small	$\beta^t = 4{,}2$, $P_F = 10^{-5}$

The target reliability levels in the Eurocodes, EN1990 (2002) for the three consequence classes CC1, CC2 and CC3 are shown in 3.

Table 3. Tentative target reliability index and probability of failure according to EN1990 (2002)

Consequence class / Reliability class	One year reference period	50-year reference period
CC1: Low	$\beta^t = 4{,}2$, $P_F = 10^{-5}$	$\beta^t = 3{,}3$, $P_F = 5 \cdot 10^{-4}$
CC2: Medium	$\beta^t = 4{,}7$, $P_F = 10^{-6}$	$\beta^t = 3{,}8$, $P_F = 10^{-4}$
CC3: High	$\beta^t = 5{,}2$, $P_F = 10^{-7}$	$\beta^t = 4{,}3$, $P_F = 10^{-5}$

It is noted that statistical independence is assumed for the failure events in different years to establish the one year failure probabilities given the 50 year failure probabilities. This assumption is generally not fulfilled due to time-independent uncertainties related to permanent loads, resistances and model uncertainties, see example below.

For wind turbines it is assumed that, see IEC 61400-1 (2019) and Sørensen & Toft (2014):

- A systematic reconstruction policy is used (a new wind turbine is erected in case of failure or expiry of lifetime).
- Consequences of a failure are only economic (no fatalities and no pollution).
- Cost of energy is important which implies that the relative cost of safety measures can be considered large (material cost savings are important).

- Wind turbines are designed to a certain wind turbine class, i.e. not all wind turbines are 'designed to the limit'.

Based on these considerations a target value for the nominal failure probability for structural design for extreme and fatigue failure modes for a reference period of one year is

$$P_F = 5\ 10^{-4} \tag{1}$$

The corresponding target value for the reliability index is $\beta^t = 3{,}3$. The target reliability level is assumed to correspond to normal safety class and to component class 2, i.e. "safe-life" structural components whose failures may lead to failure of a major part of a wind turbine;

The target reliability level in IEC 61400-1 (2019) is in DNVGL-ST-0126 (2018) interpreted as a nominal maximum annual acceptable failure probability is ($5 \cdot 10^{-4}$) and that the target safety level for normal safety class in DNVGL-ST-0126 (2018) is a nominal annual probability of failure of 10^{-4}.

Typically, partial factors used in semi-probabilistic design are calibrated to a target reliability level such that the reliability indices of failure modes / components over a portfolio of structures is as close as possible to the target reliability index. Alternatively, the target probability of failure can be applied. This implies that some components have a larger and others a smaller reliability than the target reliability level. In order to limit the difference between individual component reliabilities and the target it may be required that a coefficient of variation calculated over the portfolio (eventually weighted by importance of the components) has to be smaller than a certain value or that only a certain percentage (e.g. 2%) of component failure probabilities in the portfolio may be larger than e.g. two times the target probability of failure. In addition the minimum target reliability levels in Table 2 must be included if life safety is important.

The target reliability level may be associated to structural component / failure mode level or to structural system level. In semi-probabilistic codes usually the reliability requirements are implicitly associated to requirements to structural components assuming that only one or a few structural components / failure modes are significantly contributing to the system probability of failure, and also that the structural components are statistically dependent due to common load and model uncertainties.

The target reliability level can be specified with different references times. In the Eurocodes one year and 50 years are used, see Table 3. As basis for calibrating partial factors and also to provide a generic stochastic model a simple, representative probabilistic model can be formulated, see Hansen et al. (2015) where the following limit state equation is used:

$$g = z\, X_R R - \left((1-\alpha)G + \alpha\, X_S\, C\, P\right) \tag{2}$$

where

R resistance
X_R model uncertainty for resistance model
z design variable, e.g. cross-sectional area
G permanent load
P maximum annual wind pressure
C shape parameter
X_S model uncertainty site assessment

α models the ratio between variable and permanent loads. α =0 corresponds to no variable load and α = 1 to no permanent load

The representative stochastic model shown in Table 4 is based on the uncertainty modelling applied for calibration of partial factors in Sørensen et al. (2009).

Table 4. Stochastic model.

		Distribution type	COV
Loads			
Permanent load	G	Normal	10 %
Annual maximum wind pressure	P	Gumbel	23 %
Shape factor	C	Gumbel	10-20%
Model uncertainty Site assessment	X_S	Lognormal	5 %
Resistances			
Material parameter	R	Lognormal	Steel: 7 % Concrete: 14 % Timber: 20 %
Model uncertainty	X_R	Lognormal	Steel: 5 % Concrete: 11 % Timber: 5 %

Based on the above generic limit state equation and the stochastic model the annual target reliability index with a one year reference period is of the order β = 4.2-4.5 corresponding to a 50-year target reliability index equal to 3.8 as recommended in EN1990 (2002).

The target reliability level for seismic design of buildings is generally lower than the reliability level required for non-seismic design, e.g. as specified in table 3 and may be explained by

- Relative high cost of safety measures, i.e. it is relatively costly to obtain a higher reliability level for structures exposed to seismic loads compared to 'normal' loads from permanent load, snow load, imposed load, wind actions, …
- The uncertainty of the seismic load expressed e.g. by the coefficient of variation of the annual maximum load is relatively large. This effect has been studied in Streicher & Rackwitz (2006) where a similar difference in reliability levels between 'normal' loads and seismic loads are found.

It is noted that a similar effect could be relevant for loads from typhoons (tropical conditions) where larger uncertainty in annual maximum wind load is observed (coefficient of variation of annual maximum wind pressure larger than 0,5) when compared to wind loads in non-tropical conditions, e.g. in Europe (coefficient of variation of annual maximum wind pressure approximately 0,25).

In the following the target reliability level for seismic sites is considered without including consequence of the human fatalities. Such an investigation is relevant for wind energy structures. The stochastic model and optimization model in the following are for sites where seismic loads may be important and it is assumed that the model in Streicher & Rackwitz (2006) originally developed for civil engineering structures can be used also for wind energy structures.

Earthquakes are assumed to be modelled by a Poisson model with rate λ and magnitude M following a truncated Weibull distribution function:

$$F_M(m) = \frac{exp\left(-\left(\frac{m-m}{w-m_0}\right)^k\right) - exp\left(-\left(\frac{m_u-m_0}{w-m_0}\right)^k\right)}{1-exp\left(-\left(\frac{m_u-m_0}{w-m_0}\right)^k\right)} \qquad m \geq m_0 \tag{3}$$

where k, m_0, w and m_u are parameters. Typical values for a site with high seismic activity are λ = 2.9 / year, k = 8.11, m_0 = 4.7, w = 4.35 and m_u = 4.0, see Streicher & Rackwitz (2006).

The probability density function of the peak ground acceleration A is modelled by

$$f_A(a) = \int_0^{r_{max}} f_A(a,r) \frac{2r}{r_{max}^2} dr \tag{4}$$

where

$$f_A(a,r) = \frac{k\frac{\left(m_0-h^{-1}(a,r)\right)^{k-1}}{(m_0-w)^k} exp\left(-\left(\frac{\left(m_0-h^{-1}(a,r)\right)}{m_0-w}\right)^k\right)\frac{dh^{-1}(a,r)}{da}}{1-exp\left(-\left(\frac{(m_0-m_u)}{m_0-w}\right)^k\right)} \tag{5}$$

with $m_u \leq h^{-1}(a,r) = \frac{1}{b_2}\ln\left(\frac{a}{b(r)}\right) \leq m_0$ and $a = h(m,r) = b_1 \exp(b_2 m)\,(r^2 + 7.3^2)^{-1/2} \exp(-b_3\, r) = \exp(b_2\, m) b(r)$. Further, the following representative constants can be used: r_{max} = 200 km, b_1 = 0.0955g, b_2 = 0.573, b_3 = 0.00587. This implies that the coefficient of variation of the peak ground acceleration becomes V_A = 1.55. The coefficient of variation of the response conditional on peak ground acceleration becomes Lognormal distributed with coefficient of variation V_S = 0.6.

A simplified, generic limit state equation is considered following Streicher & Rackwitz (2006)

$$g(z) = R(z) - S\ A\ E \tag{6}$$

where R is the resistance assumed to be lognormal distributed with coefficient of variation V_R. S is assumed lognormal distributed with coefficient of variation V_S. E is a model uncertainty assumed to be lognormal distributed with coefficient of variation V_E = 0.6. Assuming that the mean values of S and E are equal to 1 and a design parameter z is chosen equal to the mean value of R the conditional probability of failure given a peak ground acceleration a is obtained from the fragility curve:

$$P_f(z|a) = \Phi\left(-\frac{ln\left(\frac{z}{a}\sqrt{\frac{(1+V_S^2)(1+V_E^2)}{(1+V_R^2)}}\right)}{\sqrt{(1+V_R^2)(1+V_S^2)(1+V_E^2)}}\right) \tag{7}$$

where $\Phi(\,)$ is the standard Normal distribution function.

Next, the cost-based objective function excluding consequences of loss of human lives is written, see Streicher & Rackwitz (2006)

$$T(z) = C(z) + E_A\left[\left(C_R(z,a)\left(1 - P_f(z|a)\right)\frac{\lambda}{\gamma}\right) + \left(C(z) + H_0 + H_M(a)\right)\frac{\lambda\, P_f(z|a)}{\gamma}\right] \qquad (8)$$

where γ is the rate of interest, and

- $C(z) = C_0 + C_1 z^{\delta}$ is the material cost
- $C_R(z,a)$ is the repair cost depending on the magnitude a of the earthquake, see Streicher & Rackwitz (2006)
- $H_M(a) = H_{M0}a^{o.4}$ is the direct damage cost depending on the magnitude of the earthquake
- $H_0 = \ell C_0$ is the indirect cost related to e.g. loss of reputation

The following relative values of the constants are assumed to be relevant for wind energy structures:

- C_0 modelling the basic costs,
- C_1 modelling the cost of safety measures,
- δ = 1.1,
- γ = 0.02,
- ℓ = 1.0 modelling indirect costs

The optimal design parameter p^* is found solving $\min_z T(z)$ and the corresponding target annual probability of failure is obtained as $P_f^* = \lambda \int_0^{\infty} P_f(z^*|a)\, f_A(a)\, da$.

For civil engineering structures including cost related to loss of human lives typical resulting values are z^* = 3.5-5.0 and the corresponding annual probability of failure is $P_f^* = 3\,10^{-4} - 9\,10^{-4}$, see Streicher & Rackwitz (2006).

For wind energy structures the results in Table 5 are obtained with different assumptions of the cost model.

Table 5. Optimal design parameters and probability of failure for wind turbines

V_R	C_1/C_0	ℓ	λ	$H_0 + E[H_M(a)]/C_0$	z^*	P_f^*
0.2	0.03	1.0	0.02	1.2	3.0	$13\,10^{-4}$
0.2	0.03	1.0	0.05	1.2	2.7	$17\,10^{-4}$
0.2	0.03	0.5	0.02	0.7	2.9	$16\,10^{-4}$
0.2	0.03	4.0	0.02	4.2	3.8	$7\,10^{-4}$
0.2	0.1	1.0	0.02	1.2	2.1	$32\,10^{-4}$
0.1	0.03	1.0	0.02	1.2	2.9	$13\,10^{-4}$

It is seen that if the assumed models for the seismic events, uncertainties and the relative costs are representative then

- A slightly larger target probability of failure for seismic load cases can be accepted related to seismic load in seismic areas compared to non-seismic areas
- If indirect costs are large a smaller target probability of failure should be chosen
- If the relative cost of safety measure is large then a larger target probability of failure can be accepted. This is in agreement with Table 1.

- The level of uncertainty of the resistance is not important since the uncertainty on the load side dominates
- A larger rate of interest implies a larger target probability of failure may be accepted.

These observations are in line with the target reliability levels in structural codes where a larger target probability of failure is accepted for seismic regions compared to non-seismic areas, and the above results indicate that this also applies to wind turbines but the increase is much smaller for wind energy compared to civil engineering structures such as buildings where the increase can be the order of a factor 100-200.

3 Probabilistic design

For a component where the failure mode can be modelled by a single limit state equation the design can be obtained by the following basic reliability requirement

$$\beta(\mathbf{z}) \geq \beta^t \tag{9}$$

where $\boldsymbol{z}$ is the design parameter(s) and can be geometrical parameters such as wall thickness and cross-sectional area. β^t is the target reliability index corresponding to the target probability of failure $\beta^t = -\Phi^{-1}(P_f^t)$. For component class 2 then $P_f^t = 5 \cdot 10^{-4}$ and β^t = 3.3 as described in section 2. The reliability index is obtained for the limit state equation $g(\boldsymbol{X}, \boldsymbol{z}) = 0$ where $\boldsymbol{X}$ models the basic stochastic variables. The reliability index is obtaoined by FORM/SORM methods or by símulation. In addition sensitivity measures such as the $\boldsymbol{\alpha}$-vector and the elasticity coefficients $e_z = \frac{d\beta(z)}{dz}\frac{z}{\beta}$ are obtained. Iterative solution of the above design requirement with respect to z can efficiently be perfomed using the elasticity coefficients e_z or $\frac{d\beta(z)}{dz}$. It is noted that when Crude Monte Carlo simulation is used then $\frac{d\beta(z)}{dz}$ can also be obtained by simulation (importance sampling).

If many components are considered with common design parameters and stochastic variables the designs are obtained from

$$\begin{aligned} &\beta_1(\mathbf{z}) \geq \beta_1^t \\ &\beta_2(\mathbf{z}) \geq \beta_2^t \\ &\quad ... \\ &\quad ... \\ &\beta_N(\mathbf{z}) \geq \beta_N^t \end{aligned} \tag{10}$$

where the target rekiability indeices $\beta_1^t, \beta_2^t, \ldots, \beta_N^t$ may be different for different components depending on the consequences of failure.

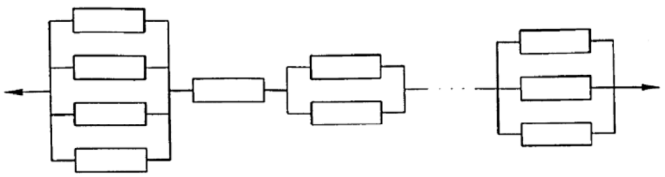

Figure 1. System reliability model

In a system-based design approach relevant failure modes have to be identified. Since the reliability requirement is linked to the consequence of failure, all failure modes having the same consequence of failure may be modelled as parallel systems in a series system, see Figure 1. Each parallel system represents a failure mode which may involve failure of a number of components identified sequentially, and modelled by limit state equations where the first limit state equation is for the most critical component, the second is for the next critical component given failure of the first omponent, etc. It is important to account for the mechanical failure mode (brittle or ductile) when modelling the limit state equations. Such a system modelling may be relevant for jacket type of support structures.

The system probability of failure is obtained from

$$\mathrm{P_f^{system}}(\mathbf{z}) = \mathrm{P}\left(\cup_{\mathrm{i=1}}^{\mathrm{N_S}}\left\{\cap_{\mathrm{j=1}}^{\mathrm{N_{p,i}}}\{\mathrm{g_{i,j}}(\mathbf{X},\mathbf{z}) \le 0\}\right\}\right) \tag{11}$$

Where N_S is the number of failure modes (number of elements in the series system), $N_{P,i}$ is the number of elements in parallel system no i, $g_{i,j}$ is the limit state equation for component j in failure mode i and $\boldsymbol{X}$ models the stochastic variables.

The system probability of failure P_f^{system} and the corresponding system reliability index $\beta^{system} = -\Phi^{-1}\left(P_f^{system}\right)$ can estimated by FORM/SORM or by simulation and should be larger than a corresponding system target reliability index. As mentioned above the basic reliability requirements in IEC 61400-1 are related to components. It is noted that formulation and estimation of the system probability of failure as shown above can be very complex and numerically demanding.

A wind turbine / wind turbine farm system should be designed to have robustness to prevent disproportionate consequences as a result of local failures which could be the consequence of unforeseen adverse events such as failure or collapse of a structural member or part of a wind turbine. E.g. progressive collapse of mooring lines of a floating wind turbine is an example of a damage that is disproportionate to the original cause. Increased robustness may be obtained by a design with increased redundancy and ductility; or be segmentation of major parts of the wind turbine system.

Structural components in wind turbines are designed considering the following design load cases (DLCs) in IEC 61400-1 (2019):

- Failure during normal operation in extreme load or by fatigue (DLC 1)
- Failure under fault conditions (e.g. failure of electrical / mechanical components or loss of grid connection) due to extreme loads or by fatigue (DLC 2)
- Failure during start up, normal shut down or emergency shut down (DLC 3, 4 and 5)
- Failure when the wind turbine is idling / parked and does not produce electricity. Failure can be by extreme loads or by fatigue (DLC 6)
- Failure during transportation and installation (DLC 7)
- Failure during transport, assembly, maintenance and repair (DLC 8)

Generally verification of sufficient reliability of wind turbines systems is performed on a component level, and the components can generally be divided in two groups:

- Structural elements such as tower, main frame, blades and the support structure / foundation with failure modes described by limit state equations, $g_i(\boldsymbol{X},\mathbf{z})$. Failure of the tower can e.g. be buckling or fatigue failure. The variables in the limit state equations $g_i(\boldsymbol{X},\mathbf{z})$ are modelled by n stochastic variables $\boldsymbol{X} = (X_1, X_2, \ldots, X_n)$. $\mathbf{z}$ model the design parameters. The probability of

failure, $P_f = P(g(\boldsymbol{X}, \mathbf{z}) \leq 0)$ and corresponding reliability index $\beta(\mathbf{z})$ can be estimated using Structural Reliability Methods.

- Electrical and control components modelled using classical reliability models described by a failure or hazard rate, λ which are estimated on the basis of time-to-failure data. The failure rate / hazard rate typically follows a bath-tub model describing the time dependent behavior. The reliability is typically modelled using a Weibull model for the time to failure.

In many cases fault of an electrical component or the control system results in increased load effects in the structural components; both for extreme and fatigue failures of the structural components. Examples are design load cases DLC 2.1, 2.2 and 2.3, and DLC 6.2. The annual failure rate for a component can be estimated from, see also Sørensen & Toft (2014):

$$\nu_F(\mathbf{z}) = P(g(\mathbf{X}, \mathbf{z}) \leq 0 | \text{fault}) \cdot \nu_{\text{fault}} \tag{12}$$

where ν_{fault} is the annual failure rate for the considered fault (e.g. grid loss or loss of electrical network connection) which e.g. can be estimated directly based on observed data. $P(g(\boldsymbol{X}, \mathbf{z}) \leq 0 | fault)$ is the conditional probability of failure for the structural component given a fault. $P(g(\boldsymbol{X}, \mathbf{z}) \leq 0 | fault)$ can be estimated by structural reliability methods where the load effects are obtained based on simulation of the fault conditions. The corresponding reliability index $\beta(\mathbf{z}) = -\Phi^{-1}(\nu_F(\mathbf{z}))$ may be used for probabilistic design as described above.

It is noted that a new international technical specification within IEC standardization, IEC-TS-61400-9 on 'Probabilistic design measures for wind turbines' is under development. This TS is expected to provide the background for probabilistic design of wind turbines including assessment of existing wind turbines for eventual life extension and for site suitability assessment of new wind turbine projects. The TS further provides the basis for reliability-based calibration of partial factors specific wind turbine components.

4 Conclusions

The basis for application of reliability-based / probabilistic design is described in this paper for civil engineering and renewable energy structures. This includes considerations on the target reliability level to used for probabilistic design for different applications e.g. wind turbines. An example is shown considering the target reliability level for wind turbines exposed to seismic loads indicating that a slightly lower reliability level can be accepted compared to e.g. extreme load from wind. A general formulation of the basis for probabilistic design is described together with conditions to be included. Generally probabilistic design can be expected to be performed at component / failure mode level following the verification procedures used in semi-probabilistic design codes. System reliability requirements are typically implicitly accounted for together with robustness requirements.

5 Acknowledgements

This research is partly conducted under the project titled 'Data-driven Probabilistic Design of Wind Turbines (ProbWind)' no. 64019-0587 funded by the Danish Energy Technology Development and Demonstration Program (EUDP).

6 References

DNVGL-ST-0126:2018 "Support structures for wind turbines", DNV-GL, 2018.

EN 1990:2002 “Eurocode - Basis of structural design”, European Committee for Standardisation, 2002.

Hansen, S.O., M.L. Pedersen & J.D. Sørensen “Probability based calibration of pressure coefficients”, Proc. ICWE14, 14th Int. Conf. Wind Eng., Brazil, 2015.

IEC 61400-1:2019, International Electrotechnical Commission “Wind Energy Generation Systems – Part. 1: Design requirements”, ed. 4, 2019.

ISO 2394:2015, “General principles on reliability for structures”, International Organization for Standardization.

JCSS:2002 (Joint Committee on Structural Safety), “Probabilistic Model Code”. 2002. https://www.jcss-lc.org/

Streicher, H. & R. Rackwitz “Optimization with a LQI Acceptance Criterion. Background Documents on Risk Assessment in Engineering - Document #5 - Optimization with a LQI Acceptance Criterion”, JCSS Joint Committee of Structural Safety, 2006.

Sørensen, J.D. & H.S. Toft ”Safety Factors – IEC 61400-1 ed. 4 – background document”, 2014, DTU Wind Energy-E Report-0066 (EN).

Sørensen, J.D., J. Munch-Andersen, S.O. Hansen, F.O. Sørensen, H.H. Christensen, P. Lind & A. Poulsen “Background investigations in connection with development of National Annexes to EN1990 and EN1991”. DS/INF 172, Danish Standard, 2009 (in Danish).

HIERARCHICAL BAYESIAN MODEL – A MODEL FOR SITE UNIQUENESS IN GEOTECHNICAL ENGINEERING.

Jianye Ching

Distinguished Professor, Geotechnical Group,
Department of Civil Engineering
National Taiwan University, Taiwan

International Symposium on Emerging Developments and Innovative Applications of Reliability Engineering and Risk Managements (EDIARR2022),30 October-3 November2022, Taipei
Chen, S. S. &Ang, Alfredo. H-S. (Editors)

HIERARCHICAL BAYESIAN MODEL – A MODEL FOR SITE UNIQUENESS IN GEOTECHNICAL ENGINEERING

Jianye Ching
Dept. of Civil Engineering, National Taiwan University, Taipei, Taiwan
E-mail: jyching@gmail.com

Abstract: In geotechnical engineering, data from one site cannot be directly implemented to another site for design purpose due to the uniqueness of each site. Nonetheless, it is possible to transfer the knowledge learned from a geotechnical database to the site-specific design of a new target site. This paper demonstrates how this transfer of knowledge in the context of site uniqueness can be achieved through the hierarchical Bayesian model (HBM). First, some databases are adopted to demonstrate their site-uniqueness structures. Second, the HBM is adopted to learn these data structures, and the learning outcome is transferred to a new target site for site-specific soil property prediction. It is shown that this HBM framework can significantly reduce the transformation uncertainty such that a more effective reliability-based design can be achieved.

***Keywords*:** Geotechnical engineering, site uniqueness, database, data-driven geotechnics, transformation model.

1 Introduction

Site uniqueness is a key feature of geotechnical engineering. The site investigation data for site A cannot be directly implemented to site B. To illustrate site uniqueness, Figure 1a shows the relationships between compression index (C_c) and water content (w) for clays at two different clay sites: an Australia site (Queensland) (Rankine 2007) and a Finnish site (Sipoo) (Di Buò et al. 2019). The background grey dots are from a generic database called CLAY-C_c/6/6203 (Ching et al. 2022). The two sites follow distinct w-C_c trends. Also, both sites have local trends that deviate from the generic trend significantly. Figure 1b shows the relationships between rock mass rating (RMR) and deformation modulus (E_m) for three rock sites situated in sedimentary rock: Khersan II dam site, Iran (Ajalloeian and Mohammadi 2014), Neveda site, USA (Keffeler 2014), and Gotvand dam site, Iran (Nejati et al. 2014). The background grey dots are from a generic database called ROCKMass/9/5876 (Ching et al. 2021a). The RMR-E_m trends are strongly site-specific. There can also be regional trends. For instance, Figure 2 shows the correlation plot between s_u/σ'_v and σ'_v/P_a (P_a = 101.3 kPa = one atmosphere pressure) for SH-CLAY/11/4051 (Zhang et al. 2020). The background grey dots are from CLAY/10/7490 (Ching and Phoon 2014a), a generic database that contains cases worldwide. The data points for Shanghai exhibit less scatters than those for worldwide.

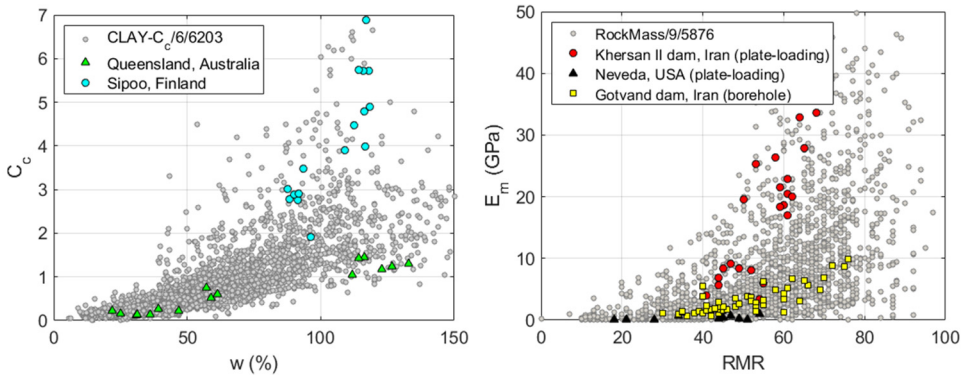

Figure 1. Illustration of local trends: (a) w vs. Cc data for two sites; (b) RMR vs. Em data for three sites.

As such, a site-specific transformation model is more desirable than a generic one. A site-specific transformation model can be constructed if many tests have been conducted at the target site. However, soil design parameters such as C_c require undisturbed samples, and there are typically limited test data for a site (e.g., less than 10 tests). It is infeasible to construct a reliable site-specific transformation model based on such sparse site-specific data – the statistical uncertainty typically overwhelms the desired precision of the prediction. Generic transformation models (Kulhawy and Mayne 1990) are popular for this reason. However, a generic transformation model developed by a generic soil/rock property database is imprecise for a local site.

Nonetheless, this does not imply that a generic database has no value for a site-specific purpose. A generic database usually contains the characteristics of many sites. Each site has its own unique intra-site characteristics, e.g., site-specific mean, variance, correlation between different soil/rock porperties, etc. There are also inter-site variabilities, e.g., different sites have different means, variances, and correlation coefficients. If these intra-site and inter-site variabilities are learned by a certain model, it may be possible to transfer the learning outcome to a new target site. In the current paper, it is shown that the hierarchical Bayesian model (HBM) recently developed by Ching et al. (2021b) can achieve this. This HBM approach consists of two steps. The first step is a learning step that learns the inter-site and intra-site variabilities in a database. The learning outcome can be transferred to a new target site as a prior model for the site. The second step is a Bayesian inference step that updates the prior model into a posterior model by incorporating the target-site data. This posterior model is quasi-site-specific because it is not only constructed from the target-site data but also from relevant information in the database. The main purpose of this paper is to present this HBM and illustrate its usefulness using a real example.

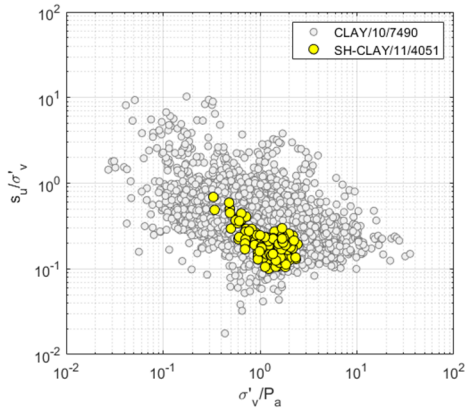

Figure 2. s_u/σ'_v vs. σ'_v/P_a data in SH-CLAY/11/4051.

2 Soil/rock property databases

Soil/rock property datasets are abundant. Since 1990, many generic databases have been compiled. Table 1 shows some databases, labelled as (material type)/(number of parameters of interest)/(number of cases). Some databases are univariate (i.e., only a single parameter is known for each soil/rock case). Many recent databases in Table 1 are multivariate (i.e., multiple parameters are known for each case). For many databases in Table 1, the data points are with "site labels", i.e., the site location for each data point is known. A "site" can be regarded as the footprint below a typical size building or building complex and its peripheral land, occupying a few football fields. Different field and laboratory tests can be conducted at different locations

within a site boundary. The records obtained from these tests conducted at different depths and different locations are grouped into a "site". This site information is important for the hierarchical Bayesian model that is to be introduced later.

3 Generic transformation models

The multivariate soil/rock databases are especially valuable for constructing generic transformation models. For instance, the dark line in Figure 3 shows the generic $(q_t-\sigma_v)/\sigma'_v$ vs. s_u/σ'_v model constructed by CLAY/10/7490, where $(q_t - \sigma_v)/\sigma'_v$ and s_u/σ'_v are denoted by y_1 and y_2, respectively. The dashed lines in the figure indicate the generic 95% confidence interval (CI). Note that the generic 95% CI is wide, because it needs to accommodate generic data with different clay types (e.g., structured vs. non-structured), geology (marine vs. lacustrine), and geographic locations. In the literature, the uncertainty associated with a transformation model is called the transformation uncertainty (Phoon and Kulhawy 1999a), and the 95% CI in Figure 3 reflects the transformation uncertainty. The transformation model in Figure 3 is bivariate (y_1 vs. y_2). It is also possible to construct a multivariate transformation model using multivariate generic data (Ching and Phoon 2012, 2013, 2014b; Ching et al. 2014, 2017b, 2019).

Table 1. Soil/rock parameter databases.

	Database	Reference	Parameters of interest
Univariate	CLAY/16	Phoon and Kulhawy (1999b)	γ, γ_d, w_n, PL, LL, PI, LI, ϕ', s_u, s_u^{FV}, q_c, q_t, SPT-N, DMT (A, B), PMT p_L
	SAND/11	Phoon and Kulhawy (1999b)	ϕ', D_r, q_c, SPT-N, DMT (A, B, I_D, K_D, E_D), PMT (p_L, E_{PMT})
	ROCK/8	Prakoso (2002)	γ (or γ_d), n, R, S_h, σ_{bt}, I_s, σ_c, E
	ROCK/13	Aladejare and Wang (2017)	ρ, G_s, I_{d2}, n, w_c, γ, R_L, S_h, σ_{bt}, I_{s50}, σ_c, E, ν
Multivariate	CLAY/5/345	Ching and Phoon (2012)	LI, s_u, s_u^{re}, σ'_p, σ'_v
	CLAY/7/6310	Ching and Phoon (2013)	s_u from 7 different test procedures
	CLAY/6/535	Ching et al. (2014)	s_u/σ'_v, OCR, q_{tc}, q_{tu}, $(u_2-u_0)/\sigma'_v$, B_q
	CLAY/10/7490	Ching and Phoon (2014a)	LL, PI, LI, σ'_v/P_a, σ'_p/P_a, s_u/σ'_v, S_t, q_{tc}, q_{tu}, B_q
	FI-CLAY/7/216	D'Ignazio et al. (2016)	s_u^{FV}, σ'_v, σ'_p, w_n, LL, PL, S_t
	JS-CLAY/5/124	Liu et al. (2016)	M_r, q_c, f_s, w_n, γ_d
	JS-CLAY/7/372	Zou et al. (2017)	σ_v, σ'_v, q_{tc}, f_s/σ'_v, B_q, V_{s1}, s_u/σ'_v
	SAND/7/2794	Ching et al. (2017a)	D_{50}, C_u, D_r, σ'_v/P_a, ϕ', q_{t1}, $(N_1)_{60}$
	EMI-ROCK/8/26000+	Kim and Hunt (2017)	σ_c, σ_{bt}, ρ, CAI, PPI, cohesion, direction shear, triaxial confining
	FG/5/1000 (FG: fine grain)	Kootahi and Moradi (2017)	e, w_n, LL, PI, C_c
	ROCK/9/4069	Ching et al. (2018)	γ, n, R_L, S_h, σ_{bt}, I_{s50}, V_p, σ_{ci}, E_i
	FG-KSAT/6/1358 (FG: fine grain)	Feng and Vardanega (2019)	e, k, LL, PL, PI, G_s
	SH-CLAY/11/4051	Zhang et al. (2020)	LL, PI, LI, e, K_0, σ'_v/P_a, s_u/σ'_v, S_t, q_c/σ'_v

ROCKMass/ 9/5876	Ching et al. (2021a)	RQD, RMR, Q, GSI, E_m, E_{em}, E_{dm}, E_i, σ_{ci}
CLAY-Cc/6/6203/	Ching et al. (2022)	LL, PI, w_0, e, C_c, C_{ur}

Note: ρ = density; ν = Poisson ratio; γ = unit weight; ϕ' = effective friction angle; σ'_p = preconsolidation stress; σ'_v = vertical effective stress; σ_{bt} = Brazilian tensile strength; σ_{ci} = uniaxial compressive strength of intact rock; γ_d = dry unit weight; $(N_1)_{60} = N_{60}/(\sigma'_v/P_a)^{0.5}$; $(u_2-u_0)/\sigma'_v$ = normalized excess pore pressure; B_q = pore pressure ratio = $(u_2-u_0)/(q_t-\sigma_v)$; CAI = Cerchar abrasivity index; C_c = compression index; C_u = coefficient of uniformity; D_{50} = median grain size; DMT (A, B, I_D, K_D, E_D) = dilatometer A & B readings, material index, horizontal stress index, modulus; D_r = relative density; e = void ratio; E_{dm} = dynamic modulus of rock mass; E_{em} = elasticity modulus of rock mass; E_i = Young's modulus of intact rock; E_m = deformation modulus of rock mass; f_s = sleeve frictional resistance; G_s = specific gravity; GSI = geological strength index; I_{d2} = slake durability index; I_s = point load strength index (I_{s50} = I_s for diameter 50 mm); k = hydraulic conductivity; K_0 = at-rest lateral earth pressure coefficient; LI = liquidity index; LL = liquid limit; M_r = subgrade resilience modulus; n = porosity; N_{60} = corrected SPT-N; OCR = overconsolidation ratio; P_a = atmospheric pressure = 101.3 kPa; PI = plasticity index; PMT (p_L, E_{PMT}) = pressuremeter limit stress, modulus; PPI = punch penetration index; Q = Q-system; q_c = cone tip resistance; q_t = corrected cone tip resistance; $q_{t1} = (q_t/P_a)/(\sigma'_v/P_a)^{0.5}$; $q_{tc} = (q_t-\sigma_v)/\sigma'_v$ = normalized cone tip resistance; $q_{tu} = (q_t-u_2)/\sigma'_v$ = effective cone tip resistance; R = Schmidt hammer hardness (R_L = L-type Schmidt hammer hardness); RMR = rock mass rating; RQD = rock quality designation; S_h = Shore scleroscope hardness; SPT-N = standard penetration test blow count; S_t = sensitivity; s_u = undrained shear strength for clay; s_u^{FV} = field vane s_u; s_u^{re} = remolded s_u; u_0 = hydrostatic pore pressure; V_p = P-wave velocity; V_s = S-wave velocity; $V_{s1} = V_s(P_a/\sigma'_v)^{0.25}$; w_n = water content.

To illustrate the use of a generic multivariate transformation model, consider the site investigation data of a Taipei site (Ou and Liao 1987) in Table 2. Figure 4a shows the CPT data at one sounding at the site. Only three s_u values in Table 2 are treated as known, whereas the other six s_u values (those in the parentheses) are treated as unknown for the purpose of validation. The generic multivariate model for (LL, PI, LI, σ'_v, σ'_p, s_u, q_t) is first constructed by CLAY/10/7490, and the 95% CI of s_u can be estimated by multiple information of (LL, PI, LI, σ'_v, σ'_p, q_t) in Table 2. The dashed line in Figure 4b shows the 95% CI of s_u predicted by the generic multivariate model. The 95% CI is wide, and this wide 95% CI is not very useful in practice.

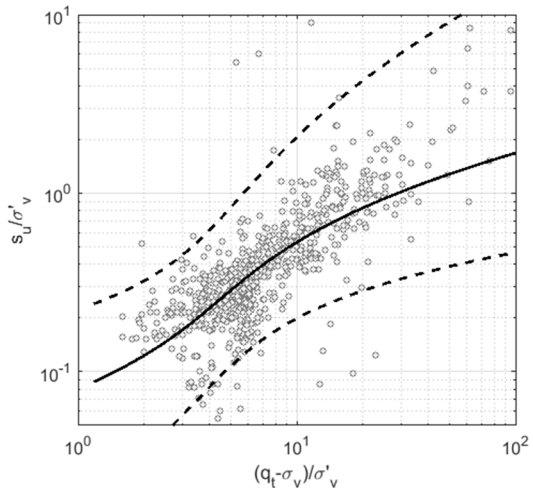

Figure 3. y_1-y_2 transformation model (grey dots are the data points in CLAY/10/7490) (source: Ching et al. 2021b).

Table 2. Site investigation data for a silty clay layer at a Taipei site (source: Ou and Liao 1987)

Depth (m)	LL (%)	PI (%)	LI	σ'_v (kPa)	σ'_p (kPa)	s_u (kPa)	q_t (kPa)
12.8	30.1	9.1	1.20	128.0	172.7	46.9	894.3
14.8	32.8	12.8	1.43	144.9	-	(52.9)	881.2
16.1	36.4	14.5	1.24	155.6	-	(51.7)	933.9
17.8	41.9	18.9	0.90	169.9	181.8	42.8	1009.5
18.3	-	-	-	174.5	-	(59.3)	1252.9
20.2	38.1	17.3	0.70	190.0	-	(60.5)	1228.8
22.7	37.0	16.0	0.58	210.9	-	(64.4)	1417.9
24.0	38.0	16.2	0.75	221.7	221.7	67.5	1573.1
26.6	34.8	13.8	0.80	243.7	-	(82.1)	1779.9

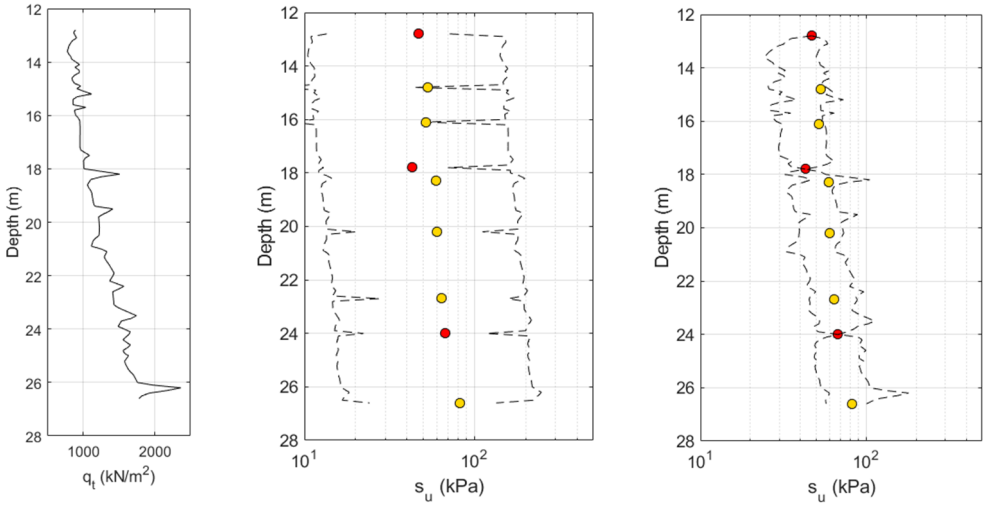

Figure 4. (a) CPT data at the Taipei site; (b) 95% CIs for s_u based on generic model; (c) 95% CIs for s_u based on the quasi-site-specific HBM.

4 Hierarchical Bayesian model

Ching et al. (2021b) proposed a hierarchical Bayesian model (HBM) that can learn the inter-site and intra-site characteristics from a soil/rock property database. Let us consider the CLAY/10/7490 database as an example. The data points in CLAY/10/7490 are from many sites. For instance, Figure 5a re-plots the generic y_1-y_2 data in Figure 2 but now with "site labels". The data points with the same label are from the same site. There are 91 sites with y_1-y_2 data. For the HBM, the data points are first transformed to the standard normal space into x_1-x_2 data. In this standard normal space, data points from the same site are considered to follow a local population (i.e., intra-site variability) modeled by a multivariate normal distribution with mean vector and covariance matrix denoted by $\underline{\mu}_i$ and $\mathbf{C}_i$. The HBM proposed by Ching et al. (2021b) has the model structure in Figure 6. The mean vectors of different sites ($\underline{\mu}_1$, $\underline{\mu}_2$, …, $\underline{\mu}_M$) are distinct (i.e., inter-site variability) but assumed to follow a common multivariate normal distribution governed by ($\underline{\mu}_0$, $\mathbf{C}_0$). Similarly, the covariance matrices of different sites ($\mathbf{C}_1$, $\mathbf{C}_2$, …, $\mathbf{C}_M$) are also assumed to follow a common inverse Wishart distribution governed by (ν_0, $\boldsymbol{\Sigma}_0$). ($\underline{\mu}_0$, $\mathbf{C}_0$, ν_0, $\boldsymbol{\Sigma}_0$)

are called hyper-parameters. The HBM can learn the inter-site and intra-site statistics in CLAY/10/7490 through these hyper-parameters.

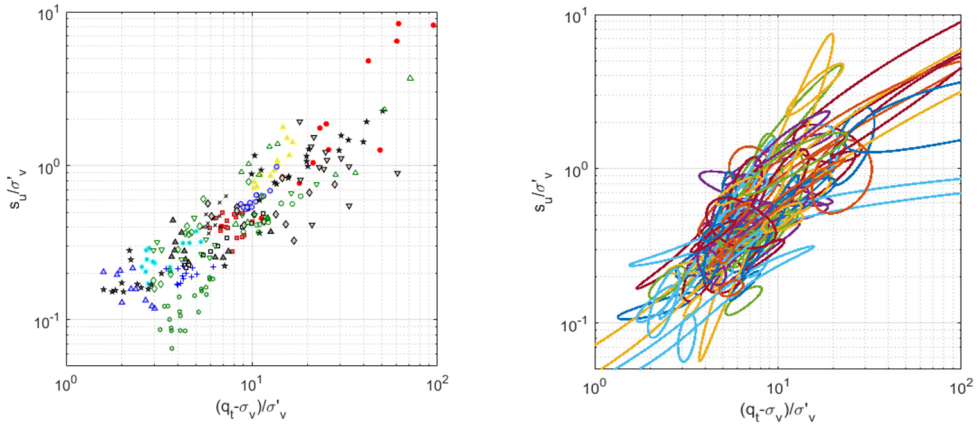

(a) q_t-s_u data with site labels (b) behavior of the trained HBM

Figure 5. Generic q_t-s_u cases and the behavior of the trained HBM (source: Ching 2020).

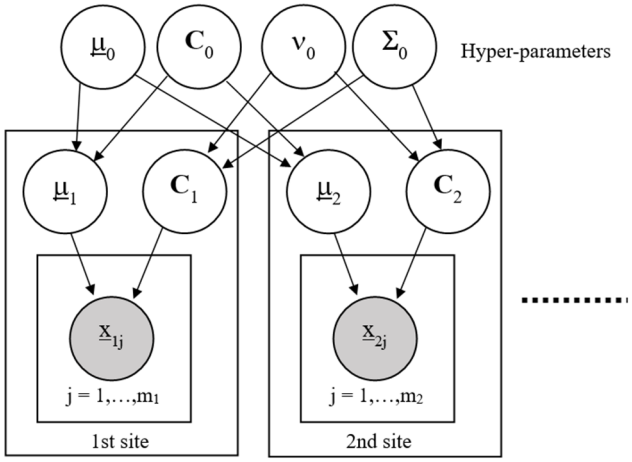

Figure 6. Model structure of the HBM (source: Ching et al. 2021b).

To illustrate the outcome of the learning step, Figure 7 shows the actual site-specific statistics (sample means, sample standard deviations, and sample correlation) for the x_1-x_2 data of the 91 sites (shown as circles and dark histogram). Figure 7 also shows the ($\underline{\mu}_i$, $\mathbf{C}_i$) parameters of a "hypothetical site" simulated by the trained HBM (shown as the cross marks and red histogram). The ($\underline{\mu}_i$, $\mathbf{C}_i$) parameters of the hypothetical site are similar to the actual statistics of the 91 sites. Figure 5b further shows the ($\underline{\mu}_i$, $\mathbf{C}_i$) of the hypothetical site as its 95% confidence ellipse (the ellipse is skewed after transformed back to y_1-y_2 space). The centers and shapes of the ellipses mimic the site-specific mean and correlation behaviors for the 91 sites. There are 7 soil parameters (LL, PI, LI, σ'_v, σ'_p, $(q_t-\sigma'_v)/\sigma'_v$, and s_u/σ'_v) for the Taipei-site data in Table 2. Figure 8 shows the histograms for the actual site-specific statistics (bivariate correlation coefficients) based on all sites in the CLAY/10/7490 database versus those for a hypothetical site simulated by the trained HBM. General consistency is found in Figures 7 and 8, suggesting that the HBM has effectively learned the inter-site and intra-site statistics in CLAY/10/7490.

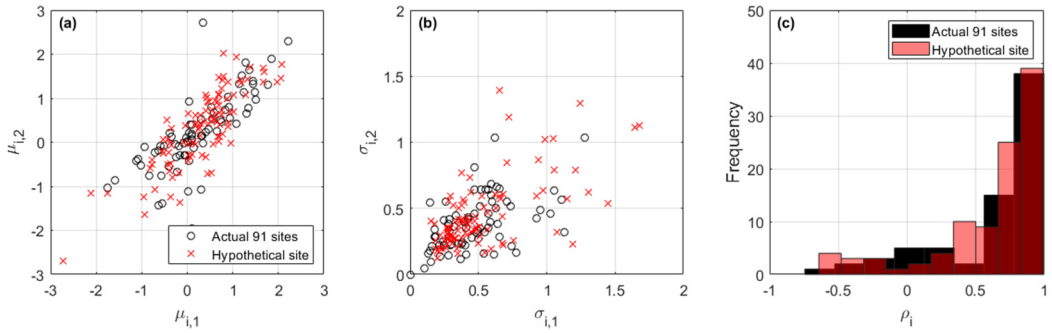

Figure 7. Site-specific statistics for the generic database: (a) $\underline{\mu}_i$; (b) $\sigma_{i,1}$ and $\sigma_{i,2}$; (c) ρ_i (source: Ching et al. 2021b).

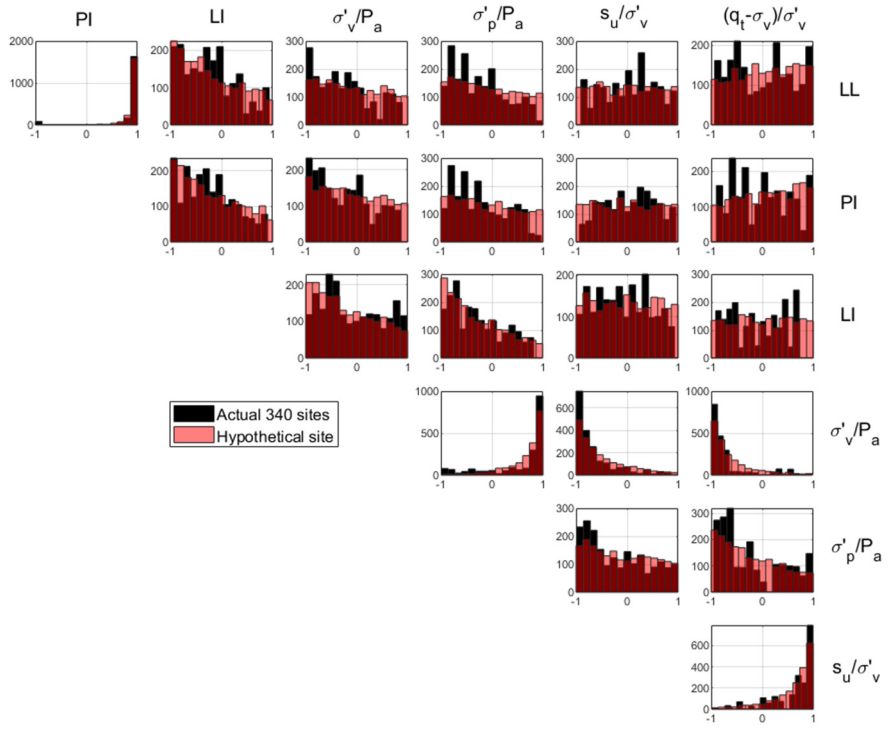

Figure 8. Site-specific bivariate correlation coefficients for the 7 parameters (source: Ching et al. 2021b).

The trained HBM serves as the prior model for the target site. Let us consider the Taipei site in Table 2 as an example. In the inference step, the trained HBM (the prior model) is further updated by the target-site data in Table 2. By conditioning on the target-site data, most (prior) ellipses in Figure 5b are incompatible to the target-site data, and only few ellipses are compatible. Figure 9 shows the incompatible ellipses in grey and compatible ellipses in colors. The red dots in Figure 9 show the three data points in Table 2 with known s_u information. Note that there are many data in Table 2 with q_t information only (s_u is missing), and these data are not shown in Figure 9. The colored (compatible) ellipses illustrate the posterior model after the Bayesian updating. The posterior model is a quasi-site-specific HBM because the prior model is first trained by CLAY/10/7490 and is subsequently updated by the target-site data. The quasi-site-

specific HBM in Figure 9 is bivariate (y_1 vs. y_2). The above learning and inference steps can be conducted to obtained a multivariate quasi-site-specific HBM, and this multivariate quasi-site-specific HBM can be used to predict the missing s_u values. The prediction results by the multivariate quasi-site-specific HBM are shown in Figure 4c, which can be compared with the prediction results by the multivariate generic transformation model in Figure 4b. The general observation is that the multivariate quasi-site-specific HBM has significantly less transformation uncertainty than the multivariate generic transformation model.

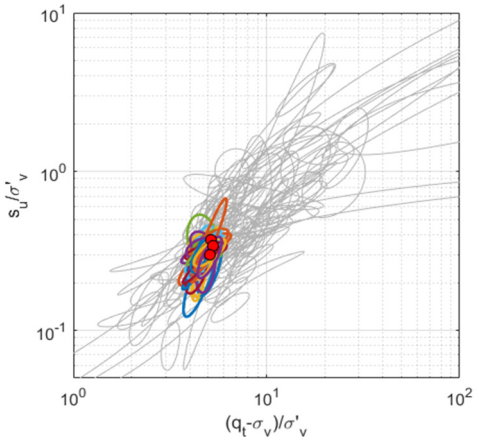

Figure 9. Illustration of the (updated) quasi-site-specific HBM (source: Ching 2020).

5 Conclusions

In this paper, some geotechnical soil/rock property databases are reviewed, and the value of a database in supporting site-specific prediction is demonstrated. It is first shown that a soil/rock property database can be used to construct a generic transformation model, but it usually has large transformation uncertainty. This paper demonstrates that the hierarchical Bayesian model (HBM) can effectively exploit the value in a soil/rock property database to support site-specific prediction. The HBM can effectively learn the intra-site and inter-site variabilities in a soil/rock database. The trained HBM can serve as a prior model for the target site, and this prior model can be further updated into a posterior model by the target-site data. The resulting posterior model is quasi-site-specific. It is shown that the 95% confidence interval (CI) produced by this quasi-site-specific HBM is significantly narrower than that produced by a generic transformation model.

6 References

Ajalloeian, R. and Mohammadi, M. “Estimation of limestone rock mass deformation modulus using empirical equations.” *Bulletin of Engineering Geology and the Environment*, 73(2) (2014): 541-550.

Aladejare, A.E. and Wang, Y. “Evaluation of rock property variability.” *Georisk: Assessment and Management of Risk for Engineered Systems and Geohazards*, 11(1) (2017): 22-41.

Ching, J. and Phoon, K.K. “Modeling parameters of structured clays as a multivariate normal distribution.” *Canadian Geotechnical Journal*, 49(5) (2012): 522-545.

Ching, J. and Phoon, K.K. “Multivariate distribution for undrained shear strengths under various test procedures.” *Canadian Geotechnical Journal*, 50(9) (2013): 907-923.

Ching, J. and Phoon, K.K. "Transformations and correlations among some parameters of clays – the global database." *Canadian Geotechnical Journal*, 51(6) (2014a), 663-685.

Ching, J. and Phoon, K.K. "Correlations among some clay parameters – the multivariate distribution." *Canadian Geotechnical Journal*, 51(6) (2014b): 686-704.

Ching, J., Li, K.H., Phoon, K.K., and Weng, M.C. "Generic transformation models for some intact rock properties." *Canadian Geotechnical Journal*, 55(12) (2018): 1702-1741.

Ching, J., Lin, G.H., Chen, J.R., and Phoon, K.K. "Transformation models for effective friction angle and relative density calibrated based on a multivariate database of coarse-grained soils." *Canadian Geotechnical Journal*, 54(4) (2017a), 481-501.

Ching, J., Lin, G.H., Phoon, K.K., and Chen, J.R. "Correlations among some parameters of coarse-grained soils–the multivariate probability distribution model." *Canadian Geotechnical Journal*, 54(9) (2017b): 1203-1220.

Ching, J., Phoon, K.K., and Chen, C.H. "Modeling CPTU parameters of clays as a multivariate normal distribution." *Canadian Geotechnical Journal*, 51(1) (2014): 77-91.

Ching, J. "Value of geotechnical BIG DATA and its application in site-specific soil property estimation." *Journal of GeoEngineering*, 15(4) (2020): 173-182.

Ching, J., Phoon, K.K., Ho, Y.H., and Weng, M.C. "Quasi-site-specific prediction for deformation modulus of rock mass." *Canadian Geotechnical Journal*, 58 (2021a): 936-951.

Ching, J., Phoon, K.K., Li, K.H., and Weng, M.C. "Multivariate probability distribution for some intact rock properties." *Canadian Geotechnical Journal*, 56(8) (2019): 1080-1097.

Ching, J., Wu, S., and Phoon, K.K. "Constructing quasi-site-specific multivariate probability distribution using hierarchical Bayesian model." *Journal of Engineering Mechanics*, 147(10) (2021b): 04021069.

Ching, J., Phoon, K.K., and Wu, C.T. "Data-centric quasi-site-specific prediction for compressibility of clays." *Canadian Geotechnical Journal* (2022), in press.

Di Buò, B., Tim L., Andrea F., and Mayne, P. "Compressibility of Finnish sensitive clay." *Proceedings of the XVII ECSMGE-2019*, Icelandic Geotechnical Society, 2019.

D'Ignazio, M., Phoon, K.K., Tan, S.A., and Lansivaara, T. "Correlations for undrained shear strength of Finnish soft clays." *Canadian Geotechnical Journal*, 53(10) (2016): 1628-1645.

Feng, S. and Vardanega, P. J. "A database of saturated hydraulic conductivity of fine-grained soils: probability density functions." *Georisk: Assessment and Management of Risk for Engineered Systems and Geohazards*, 13(4) (2019): 255-261.

Keffeler, E.R. "Measurement and prediction of in-situ weak rock mass modulus case studies from Nevada, Puerto Rico, and Iran." (Ph.D. Dissertation, University of Nevada, 2014).

Kim, E. and Hunt, R. "A public website of rock mechanics database from Earth Mechanics Institute (EMI) at Colorado School of Mines (CSM)." *Rock Mechanics and Rock Engineering*, 50(12) (2017): 3245-3252.

Kootahi, K. and Moradi, G. "Evaluation of compression index of marine finegrained soils by the use of index tests." *Marine Georesources and Geotechnology*, 35(4) (2017): 548-570.

Kulhawy, F.H. and Mayne, P.W. *Manual on Estimating Soil Properties for Foundation Design*, Report EL-6800, Electric Power Research Institute, Cornell University, Palo Alto, 1990.

Liu, S., Zou, H., Cai, G., Bheemasetti, B.V., Puppala, A.J., and Lin, J. "Multivariate correlation among resilient modulus and cone penetration test parameters of cohesive subgrade soils." *Engineering Geology*, 209 (2016): 128-142.

Nejati, H.R., Ghazvinian, A., Moosavi, S.A., and Sarfarazi, V. "On the use of the RMR system for estimation of rock mass deformation modulus." *Bulletin of Engineering Geology and the Environment*, 73 (2014): 531-540.

Ou, C.Y., and Liao, J.T. (1987). Geotechnical Engineering Research Report, GT96008, National Taiwan University of Science and Technology, Taipei.

Phoon, K.K. and Kulhawy, F.H. "Evaluation of geotechnical property variability." *Canadian Geotechnical Journal*, 36(4) (1999a): 625-639.

Phoon, K.K. and Kulhawy, F.H.. "Characterization of geotechnical variability." *Canadian Geotechnical Journal*, 36(4) (1999b): 612-624.

Prakoso, W.A. "Reliability-based design of foundations on rock masses for transmission line and similar structures." (Ph.D. Dissertation, Cornell University, 2002).

Rankine, B.R. "Assessment and analysis of Queensland clay behaviour." (PhD. thesis, School of Engineering, James Cook University, 2007).

Zhang, D.M., Zhou, Y., Phoon, K.K., and Huang, H.W. "Multivariate probability distribution of Shanghai clay properties." *Engineering Geology*, 273 (2020): 105675.

Zou, H., Liu, S., Cai, G., Puppala, A.J., and Bheemasetti, T.V. "Multivariate correlation analysis of seismic piezocone penetration (SCPTU) parameters and design properties of Jiangsu quaternary cohesive soils." *Engineering Geology*, 228 (2017): 11-38.

L-MOMENT-BASED NORMAL TRANSFORMATION AND ITS APPLICATION IN STRUCTURAL RELIABILITY ANALYSIS.

Yan-Gang Zhao

Professor, Department of Architecture, faculty of Engineering

Chair, Dept. of Architecture and Building Engineering, Graduate school of Engineering

Kanagawa University, Japan

International Symposium on Emerging Developments and Innovative Applications of Reliability Engineering and Risk Managements (EDIARR2022),30 October-3 November2022, Taipei
Chen, S. S. &Ang, Alfredo. H-S. (Editors)

L-MOMENT-BASED NORMAL TRANSFORMATION AND ITS APPLICATION IN STRUCTURAL RELIABILITY ANALYSIS

Ming-na Tong[1], Yan-Gang Zhao[2,3]

[1] *School of Civil Engineering, ZhengZhou University, 100 Kexuedadao Rd., Zhengzhou 450000, China*

[2] *Department of Architecture, Kanagawa University, 3-27-1 Rokkakubashi, Kanagawa-ku, Yokohama, Japan*

[3] *Key Laboratory of Urban Security and Disaster Engineering of Ministry of Education, Beijing University of Technology, Beijing 100124, China*

Correspondence e-mail address: zhao@kanagaw-u.ac.jp

Abstract: Structural reliability analysis without exclusion of random variables with unknown distributions has attracted increasing attention, and many endeavours have been devoted to this aspect. The statistical moment-based normal transformation is simple and accurate, which can be used for realizing reliability analysis with known statistical moments or statistical data, therefore, it is suitable for reliability calculation of practical engineering. At present, normal transformation can usually be realized by the ordinary central moments (C-moments) of random variables. However, C-moments calculated from the actual data may not be accurate, especially in the case of small samples. Recently, linear moments (L-moments) have been found increasing use for characterizing random variables with unknown distributions, in part since they show less sensitivity to distribution tails and are more stable than C-moments.

In this research, the complete monotone expression of normal transformation based on L-moments is presented, and the application range and monotone region of each expression under different combinations of L-moments are investigated, and the reliability calculation method based on L-moments for independent random variables are developed. Besides, using the first four L-moments of random variables, the monotone calculation formula of equivalent correlation coefficient based on normal transformation is proposed, the application range of L-moment-based normal transformation is explored in the case of considering correlated random variables, and the reliability calculation method based on L-moments for correlated random variables is developed. Several examples are presented to demonstrate the effectiveness of L-moment-based normal transformation in structural reliability analysis.

Keywords: Structural reliability; L-moments; Normal transformation; independent random variables; correlated random variables

1 Introduction

The engineering reliability problem is often formulated in terms of a vector of basic random variables characterizing uncertainties in quantities such as loads, material properties, and structural dimensions. On the basis of probability theory, some various reliability approximation methods have been developed (e.g., Shinozuka1983; Ang and Tang 1984; Cai and Elishakoff 1994; Ditlevsen and Madsen 1996; Zhao and Ono 2001; Melchers and Beck 2018), such as the first-order reliability method (FORM), second-order reliability method (SORM), methods of moment, simulation methods and so on. These methods need to take the system with complete information as object, i.e., PDFs or cumulative distribution functions (CDFs) of the independent random variables and joint PDFs of the correlated random variables. The normal transformation (the *X*-*U* transformation) and its inverse transformation (the *U*-*X* transformation) can be applied using the Rosenblatt transformation (Hohenbichler and Rackwitz 1981) or Nataf transformation (Liu and Der Kiureghian 1986) with known CDFs/PDFs. However, since the probability distributions of the random variables may be unknown in practical engineering problems, it is not easy to realize the *X*-*U* and *U*-*X* transformation by the conventional methods. For this purpose, the *U*-*X* transformation can be realized by assuming that a non-normal random variable can be expressed as a third-order polynomial of the standard normal random variable (Fleishman 1978)

$$X = S_U(U) = a + bU + cU^2 + dU^3 \tag{1}$$

where X is the original non-normal random variable; U is the standard normal random variable; $S_U(U)$ is a third-order polynomial of U; and a, b, c, and d are the polynomial coefficients.
Generally, the polynomial coefficients can be determined by using the first four central moments (C-moments) of X (Fleishman 1978; Chen and Tung 2003; Zhao and Lu 2008), and the complete monotonic X-U transformation corresponding to Eq. (2) has been developed by Zhao et al. (2018a). Therefore, the X-U and U-X transformations can be realized only if the first four C-moments are known, and whether the evaluation of the first four C-moments from samples is accurate or not will have a great effect on the accuracy of the transformations. Studies have shown that the numerical values of sample C-moments, particularly when the sample size is small, may be very different from those of the probability distribution from which the sample was drawn (Hosking 1990). It is in this regard that the linear moments (L-moments) having the advantages over C-moments of being able to characterize a wider range of distributions has been developed (Hosking 1990). In addition, when being estimated from a sample set, L-moments are more robust to the presence of outliers in the data and perform better with smaller sample size than C-moments (Hosking 1990; Sankarasubramanian and Srinivasan 1999; Pandey et al. 2001; MacKenzie and Winterstein 2011).

The transformations discussed in the previous studies are almost focused on the expression of a non-normal random variable by polynomial of a standard normal variable, that is, the U-X transformation. However, in practical reliability analysis, the inverse transformation, i.e., the X-U transformation is also essential, without which, the commonly used reliability methods such as the first/second-order reliability analysis based on L-moments cannot be conducted. Besides, the efficiency and applicable range of the third-order polynomial normal transformation for correlated random variables based on L-moments have not been investigated, furthermore, the complete expression of equivalent correlation coefficients has not been proposed.
The objective of this paper is to propose the complete normal transformation methods based on L-moments for both independent and correlated random variables, and investigate the application scope of the proposed normal transformation based on L-moments.

2 Definition of L-moments of a random variable

When the PDF/CDF of a random variable X is known, the first four L-moments can be expressed as

$$\lambda_1 = EX_{1:1} = \int_0^1 x dF(x) \tag{2}$$

$$\lambda_2 = \frac{1}{2}E(X_{2:2} - X_{1:2}) = \int_0^1 x[2F(x)-1]dF(x) \tag{3}$$

$$\lambda_3 = \frac{1}{3}E(X_{3:3} - 2X_{2:3} + X_{1:3}) = \int_0^1 x[6F^2(x) - 6F(x) + 1]dF(x) \tag{4}$$

$$\lambda_4 = \frac{1}{4}E(X_{4:4} - 3X_{3:4} + 3X_{2:4} - X_{1:4}) = \int_0^1 x[20F^3(x) - 30F^2(x) + 12F(x) - 1]dF(x) \tag{5}$$

In order to describe skewness and kurtosis more conveniently, the L-moment ratios of X is defined to be the quantities (Hosking 1990):

$$\tau_r = \lambda_r / \lambda_2 \ , r = 3, 4, \ldots \tag{6a}$$

in which

$$\lambda_2 \geq 0 \tag{6b}$$

where τ_3 and τ_4 the L-skewness and L-kurtosis, respectively.
In practice, L-moments must usually be estimated from random samples drawn from an unknown distribution. Let $x_1, x_2, \cdots, x_n$ be the samples and $x_{1:n} \leq x_{2:n} \leq \cdots \leq x_{n:n}$, the ordered samples, and the first four sample L-moments, i.e., l_1, l_2, l_3, and l_4, can be given by (e.g., MacKenzie and Winterstein 2011)

$$l_1 = \frac{1}{n}\sum_{j=1}^{n} x_{j:n} \tag{7}$$

$$l_2 = \frac{2}{n}\sum_{j=2}^{n} \frac{(j-1)}{(n-1)} x_{j:n} - \frac{1}{n}\sum_{j=1}^{n} x_{j:n} \tag{8}$$

$$l_3 = \frac{6}{n}\sum_{j=3}^{n} \frac{(j-1)(j-2)}{(n-1)(n-2)} x_{j:n} - \frac{6}{n}\sum_{j=2}^{n} \frac{(j-1)}{(n-1)} x_{j:n} + \frac{1}{n}\sum_{j=1}^{n} x_{j:n} \tag{9}$$

$$l_4 = \frac{20}{n}\sum_{j=4}^{n} \frac{(j-1)(j-2)(j-3)}{(n-1)(n-2)(n-3)} x_{j:n} - \frac{30}{n}\sum_{j=3}^{n} \frac{(j-1)(j-2)}{(n-1)(n-2)} x_{j:n} + \frac{12}{n}\sum_{j=2}^{n} \frac{(j-1)}{(n-1)} x_{j:n} - \frac{1}{n}\sum_{j=1}^{n} x_{j:n} \tag{10}$$

3 Normal transformation based on L-moments for independent random variables

3.1 The U-X transformation based on the first four L-moments

For a random variable, if the first four L-moments are known, explicit and simple expressions for the polynomial coefficients in Eq. (1) have been developed by Tung (1999)

$$a = \lambda_1 - 1.81379937\lambda_3 \tag{11a}$$

$$b = 2.25518617\lambda_2 - 3.93740250\lambda_4 \tag{11b}$$

$$c = 1.81379937\lambda_3 \tag{11c}$$

$$d = -0.19309293\lambda_2 + 1.574961\lambda_4 \tag{11d}$$

It can be observed that the polynomial coefficients based on L-moments are simple explicit functions of the L-moments, they are much simpler and easier than those based on C-moments where the coefficients have to be obtained by nonlinear equations (Zhang et al 2019; Fleshman 1978). This can be seen as one advantage of L-moments method. With the aid of Eq. (1) and Eqs.(11a-11d), the transformation from U to X can be readily realized.

3.2 The Complete Monotonic Expressions of X-U transformation based on the first four L-moments

According to the Cardano formula (Zwillinger 2018) and the property of the first- and second-order derivatives of $S_U(U)$ (Zhao et al. 2018a), the complete expressions of the X-U transformation based on L-moments can be derived and are summarized in Table 1 including six types, i.e., Type 1, 2, 3, 4, 5, and 6 (Zhao et al. 2020).

In Table 1, the parameters of A, h, α, Q_1^*, Q_2^*, Q_0^* and Δ_0 are given by

$$A=\left(-\frac{c^2-3bd}{9d^2}\right)^3+\frac{h^2}{4} \tag{12a}$$

$$h=\frac{2c^3}{27d^3}-\frac{bc}{3d^2}+\frac{a}{d}-\frac{X}{d} \tag{12b}$$

$$\alpha=\arccos\left(-\frac{h}{2\sqrt{\left(\frac{c^2-3bd}{9d^2}\right)^3}}\right) \tag{12c}$$

$$Q_1^*=d\left(-2\left|\frac{\Delta_0}{9d^2}\right|^{3/2}+\frac{2c^3}{27d^3}-\frac{bc}{3d^2}+\frac{a}{d}\right) \tag{12d}$$

$$Q_2^*=d\left(2\left|\frac{\Delta_0}{9d^2}\right|^{3/2}+\frac{2c^3}{27d^3}-\frac{bc}{3d^2}+\frac{a}{d}\right) \tag{12e}$$

$$Q_0^*=a-\frac{b^2}{4c} \tag{12f}$$

$$\Delta_0=\tau_3^2+5.65487\tau_4^2-3.93218\tau_4+0.397092 \tag{12g}$$

Table 1. The complete monotonic expressions of the X-U transformation based on the first four L-moments

L-moment ratios			the X-U expressions	Range of X	Type
$\tau_4\neq 0.1226$	$\tau_3^2\le -5.65487\tau_4^2+3.93218\tau_4-0.397092$		$\sqrt[3]{-h/2-\sqrt{A}}+\sqrt[3]{-h/2+\sqrt{A}}-c/3d$	$(-\infty, +\infty)$	1
$\tau_4>0.1226$	$\tau_3^2>-5.65487\tau_4^2+3.93218\tau_4-0.397092$	$\tau_3\ge 0$	$2\sqrt{\Delta_0/9d^2}\cos(\alpha/3)-c/3d$	$Q_1^*<X<Q_2^*$	2
			$\sqrt[3]{-h/2-\sqrt{A}}+\sqrt[3]{-h/2+\sqrt{A}}-c/3d$	$X\ge Q_2^*$	
		$\tau_3<0$	$\sqrt[3]{-h/2-\sqrt{A}}+\sqrt[3]{-h/2+\sqrt{A}}-c/3d$	$X\le Q_1^*$	3
			$-2\sqrt{\Delta_0/9d^2}\cos[(\alpha-\pi)/3]-c/3d$	$Q_1^*<X<Q_2^*$	
$\tau_4<0.1226$	$\tau_3^2>-5.65487\tau_4^2+3.93218\tau_4-0.397092$		$-2\sqrt{\Delta_0/9d^2}\cos[(\alpha+\pi)/3]-c/3d$	$Q_2^*\le X\le Q_1^*$	4
$\tau_4=0.1226$		$\tau_3>0$	$(\sqrt{b^2-4b(a-X)}-b)/2c$	$X\ge Q_0^*$	5
		$\tau_3<0$	$(\sqrt{b^2-4b(a-X)}-b)/2c$	$X\le Q_0^*$	
		$\tau_3=0$	$(X-a)/b$	$(-\infty, +\infty)$	6

Note: The parameters of A, h, α, Q_1^*, Q_2^*, Q_0^* and Δ_0 are given by Eqs. (12a)-(12g), respectively.

From Table 1, it can be found that the discriminant can be directly expressed by L-skewness τ_3 and L-kurtosis τ_4 rather than the coefficient in Eq. (12). While the discriminant for the complete expressions of the *X-U* transformation based on C-moments cannot be directly expressed by the skewness and kurtosis (Zhao et al. 2018a). This is another advantage of *X-U* transformation based on L-moments over that of C-moments.

4 Normal transformation based on L-moments for correlated random variables

4.1 The proposed formulae of equivalent correlation coefficient

For the *i*th elements of the non-normal correlated random vector **X**, X_i (i=1,…, m), can be expressed as:

$$X_i = S_Z(Z_i) = a_i + b_i Z_i + c_i Z_i^2 + d_i Z_i^3 \tag{13}$$

where Z_i is the *i*th elements of the correlated standard normal random vector **Z**; and a_i, b_i, c_i, and d_i are the polynomial coefficients, which can be determined by Eqs.(11a)-(11d).
According to the definition of the Pearson correlation coefficient, the correlation coefficient between X_i and X_j, ρ_{ij} can be expressed as:

$$\rho_{ij} = \frac{Cov(X_i X_j)}{\sqrt{D(X_i)D(X_j)}} = \frac{E(X_i X_j) - E(X_i)E(X_j)}{\sqrt{D(X_i)D(X_j)}} = \frac{E(X_i X_j) - \mu_i \mu_j}{\sigma_i \sigma_j} \tag{14}$$

in which $Cov(\cdot)$ = covariance; $E(\cdot)$ = expectation; $D(\cdot)$ = variance; μ_i and μ_j are the means of X_i and X_j, respectively; and σ_i and σ_j are the standard deviations of X_i and X_j, respectively.
$E(X_iX_j)$ in Eq. (14) can be expressed as:

$$\begin{aligned} E(X_i X_j) &= E[(a_i, b_i, c_i, d_i)(1, Z_i, Z_i^2, Z_i^3)^T (1, Z_j, Z_j^2, Z_j^3)(a_j, b_j, c_j, d_j)^T] \\ &= (a_i, b_i, c_i, d_i) E[(1, Z_i, Z_i^2, Z_i^3)^T (1, Z_j, Z_j^2, Z_j^3)](a_j, b_j, c_j, d_j)^T \\ &= (a_i, b_i, c_i, d_i)\mathbf{R}(a_j, b_j, c_j, d_j)^T \end{aligned} \tag{15}$$

where **R** can be expressed as follows (Hong and Lind 1996):

$$\mathbf{R} = \begin{bmatrix} 1 & 0 & 1 & 0 \\ 0 & \rho_{0ij} & 0 & 3\rho_{0ij} \\ 1 & 0 & 2\rho_{0ij}^2 + 1 & 0 \\ 0 & 3\rho_{0ij} & 0 & 6\rho_{0ij}^3 + 9\rho_{0ij} \end{bmatrix} \tag{16}$$

where ρ_{0ij} is referred to as the equivalent correlation coefficient between Z_i and Z_j.
Substituting Eq. (16) into Eq. (15) leads to

$$E(X_i X_j) = \mu_i \mu_j + (b_i b_j + 3d_i b_j + 3b_i d_j + 9d_i d_j) \cdot \rho_{0ij} + 2c_i c_j \rho_{0ij}^2 + 6d_i d_j \rho_{0ij}^3 \tag{17}$$

According to Eqs. (17) and (14), the relationship between ρ_{ij} and ρ_{0ij} is given by

$$\rho_{ij} = \frac{(b_i b_j + 3d_i b_j + 3b_i d_j + 9d_i d_j) \cdot \rho_{0ij} + 2c_i c_j \rho_{0ij}^2 + 6d_i d_j \rho_{0ij}^3}{\sigma_i \sigma_j} \tag{18}$$

To fulfill the definition of the correlation coefficient, ρ_{0ij} in Eqs. (17) and (18) should satisfy the following conditions:

$$-1 \le \rho_{0ij} \le 1,\ \rho_{ij} \cdot \rho_{0ij} \ge 0,\ \left|\rho_{0ij}\right| \ge \left|\rho_{ij}\right| \tag{19}$$

With Eqs. (18)–(19) and the applicable range of the L-moment ratios, the expressions of the equivalent correlation coefficient ρ_{0ij} obtained from the Cardano formula (Zwillinger 2018) and the admissible range of the original correlation coefficient ρ_{ij} to ensure the transformation's executability are derived by Tong et al. (2020), in which the upper and lower bounds of the original correlation coefficient ρ_{ij}, i.e., $\rho_{ij-\max}$ and $\rho_{ij-\min}$, are given. The equivalent correlation coefficient ρ_{0ij} can be classified into six types, namely, Types I, II, III, IV, V, and VI.

Similarly, the preceding procedure can be extended to m variables whose first four L-moments, standard deviations, and correlation matrix are known. The equivalent correlation matrix, $\mathbf{C_Z}$, can then be summarized as:

$$\mathbf{C_Z} = \begin{bmatrix} 1 & \rho_{012} & \cdots & \rho_{01m} \\ \rho_{012} & 1 & \cdots & \rho_{02m} \\ \vdots & \vdots & \ddots & \vdots \\ \rho_{0m1} & \rho_{0m2} & \cdots & 1 \end{bmatrix} \tag{20}$$

Theoretically, the equivalent correlation matrix ($\mathbf{C_Z}$) becomes positive semi-definite after the fully correlated variables are excluded. However, small negative eigenvalues of $\mathbf{C_Z}$ might exist because of computational errors during the transformation from correlated non-normal random vectors to correlated normal ones, especially in cases of highly non-normal random variables. To solve this problem, this paper adopts a method which presented by Ji et al. (2018). Under such circumstances, $\mathbf{C_Z}$ may be rewritten as follows:

$$\mathbf{C_Z} = \mathbf{V}\boldsymbol{\Lambda}\mathbf{V}^T \tag{21}$$

where $\mathbf{V}$ is the eigenvector matrix of $\mathbf{C_Z}$; and $\boldsymbol{\Lambda}$ is the diagonal matrix consisting of eigenvalues. The negative eigenvalues in $\boldsymbol{\Lambda}$ can be replaced by positive values which are small enough, e.g., 0.001.

4.2 The inverse normal transformation based on L-moments

The correlated standard normal random vector $\mathbf{Z}$ can be converted to the independent standard normal vector $\mathbf{U}$, which is expressed as

$$\mathbf{Z} = \mathbf{L}_0\mathbf{U} \tag{22}$$

where $\mathbf{L}_0$ is the lower triangular matrix of $\mathbf{C_Z}$ through the Cholesky decomposition, which can be expressed as follows:

$$\mathbf{L}_0 = \begin{bmatrix} l_{11} & 0 & \cdots & 0 \\ l_{21} & l_{22} & \cdots & 0 \\ \vdots & \vdots & \ddots & \vdots \\ l_{m1} & l_{m2} & \cdots & l_{mm} \end{bmatrix} \tag{23}$$

According to Eqs. (22) and (23), Z_i is expressed as follows:

$$Z_i = \sum_{k=1}^{i} l_{ik} U_k \ , i = 1, 2, ..., m \tag{24}$$

With the substitution of Eq. (24) into Eq. (13), the inverse normal transformation based on L-moments can be expressed as follows:

$$X_i = a_i + b_i \sum_{k=1}^{i} l_{ik} U_k + c_i \left(\sum_{k=1}^{i} l_{ik} U_k \right)^2 + d_i \left(\sum_{k=1}^{i} l_{ik} U_k \right)^3 , \ i = 1, 2, ..., m \tag{25}$$

4.3 The normal transformation based on L-moments

For obtaining the normal transformation, the correlated non-normal random vector **X** is first transformed into the correlated standard normal random vector **Z**, which is then transformed into the independent standard normal random vector **U**.
According to Eq. (13), the **X**–**Z** transformation requires finding the suitable roots of the following function:

$$Z_i = S_Z^{-1}(X_i) \ , \ i = 1, 2, ..., m \tag{26}$$

where $S_Z^{-1}(\cdot)$ is the inverse function of $S_Z(\cdot)$. For convenience, the complete monotonic expressions of $S_Z^{-1}(\cdot)$ proposed by Zhao et al. is presented in Table 1.

According to Eq. (14), the independent standard normal vector **U** can be obtained as:

$$\mathbf{U} = \mathbf{L}_0^{-1} \mathbf{Z} \tag{27}$$

where $\mathbf{L}_0^{-1}$ is the inverse matrix of $\mathbf{L}_0$, which can be expressed as follows:

$$\mathbf{L}_0^{-1} = \begin{bmatrix} q_{11} & 0 & \cdots & 0 \\ q_{21} & q_{22} & \cdots & 0 \\ \vdots & \vdots & \ddots & \vdots \\ q_{m1} & q_{m2} & \cdots & q_{mm} \end{bmatrix} \tag{28}$$

According to Eqs. (27) and (28), U_i is expressed as follows:

$$U_i = \sum_{k=1}^{i} q_{ik} Z_k \ , i = 1, 2, ..., m \tag{29}$$

With the substitution of Eq. (29) into Eq. (26), the normal transformation based on L-moments can be expressed as follows:

$$U_i = \sum_{k=1}^{i} q_{ik} S_Z^{-1}(X_k) \ , i = 1, 2, ..., m \tag{30}$$

5 Investigation and Application

In this section, two examples for structural reliability analysis including independent random variables and correlated random variables are provided to demonstrate the proposed normal transformation based on L-moments.

5.1 Example 1: Reliability analysis including independent random variables

The second example considers a simplified bridge model formed by two girders and two continuous spans as shown in Figure 1 (Ghosn and Frangopol 1999). Assuming plastic behavior, one collapse mechanism for this bridge is shown in Figure 2. The collapse mechanism can be represented by a limit state function (LSF), Z_1, which can be written as:

$$Z_1 = 2(M_1 - D_1) + (M_2 - D_2) - \frac{P \times L_1}{2} \tag{31}$$

where M_i is the moment capacity at section i, D_i is the dead load moment at section i, P is the applied maximum lifetime truck load, and L_j is the length of span j. The concentrated load P is used to model the weight of an applied truck. Table 2 gives the properties of the random variables. The applied load is represented as a function of the HS-20 AASHTO design truck.

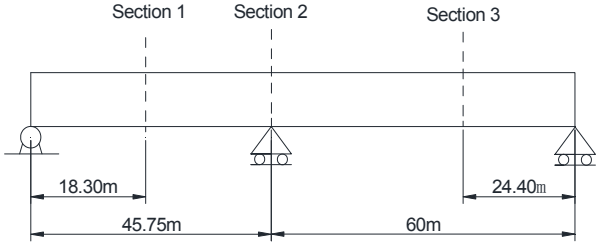

Figure 1. Two-girder continuous bridge configuration

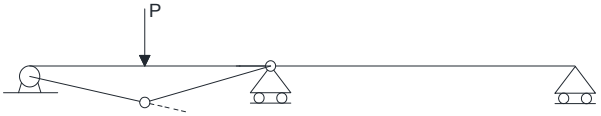

Figure 2. Two span bridge collapse mechanism

Table 2. Random variables for Example 1

Section	Variable	Distribution	Mean	Bias COV(%)
Section1	Moment capacity	Lognormal	8190	1.12 10
	Dead load	Normal	3640	1.05 9
	Live load	Extreme I	HS-20	2.07 19
Section2	Moment capacity	Lognormal	23400	1.12 10
	Dead load	Normal	13755	1.05 9
	Live load	Extreme I	HS-20	2.07 19

Note: COV denotes coefficient of variation

Using the proposed method, the reliability index can be obtained as 3.56. Using the MCS with 4×10^{-6}, the reliability index can be obtained as 3.51. Apparently, the results obtained by the proposed method agree well with the results obtained by MCS.

5.2 Example 2: Reliability analysis including correlated random variables

The second example considers a rock wedge slope problem, and the limit state function for the wedge stability can be expressed as follows (Low 1997):

$$G(X) = (a_1 - \frac{b_1 G_{w1}}{s_\gamma}) \times \tan\phi_1 + (a_2 - \frac{b_2 G_{w2}}{s_\gamma}) \times \tan\phi_2 + 3b_1 \frac{c_1}{\gamma h} + 3b_2 \frac{c_2}{\gamma h} - 1 \tag{32}$$

where c_1 and c_2 are the cohesions of discontinuities 1 and 2, respectively; ϕ_1 and ϕ_2 are the friction angles of discontinuities 1 and 2, respectively; G_{w1} and G_{w2} are the water pressure parameters, $G_{w1} = G_{w2} = G_w$; where γ and γ_w are the unit weight of the rock and water, respectively; $s_\gamma = \gamma / \gamma_w$ is the specific density of the rock; and a_1, a_2, b_1, and b_2 are parameters depending on the geometry of the tetrahedral wedge, which can be obtained by the following:

$$a_1 = \frac{[\sin\delta_2 \cot\delta_1 - \cos\delta_2 \cos(\theta_1 + \theta_2)]}{\sin\psi \sin(\theta_1 + \theta_2)} \tag{33a}$$

$$a_2 = \frac{[\sin\delta_1 \cot\delta_2 - \cos\delta_1 \cos(\theta_1 + \theta_2)]}{\sin\psi \sin(\theta_1 + \theta_2)} \tag{33b}$$

$$b_1 = a_0 \sin\theta_2 \sin\delta_2 \tag{33c}$$

$$b_2 = a_0 \sin\theta_1 \sin\delta_1 \tag{33d}$$

Where

$$\sin\psi = |\sqrt{1 - [\sin\delta_1 \sin\delta_2 \cos(\theta_1 + \theta_2) + \cos\delta_1 \cos\delta_2]^2}\,| \tag{34a}$$

$$a_0 = \frac{\sin\psi}{[\sin(\theta_1 + \theta_2)\sin\delta_1 \sin\delta_2]^2 (\cot\varepsilon - \cot\alpha)} \tag{34b}$$

$$\varepsilon = \arctan[\frac{\sin(\theta_1 + \theta_2)}{\sin\theta_1 \cot\delta_2 + \sin\theta_2 \cot\delta_1}] \tag{34c}$$

Among these equations, h, α , and s_γ are the deterministic parameters (h = 10 m, α=65° , and s_γ = 2.5). The basic random variables in Eq. (32) are c_1, c_2, ϕ_1 , ϕ_2 , δ_1 , δ_2 , G_w , θ_1 , and θ_2 , and the probabilistic information of them are listed in Table 3. c_1 and ϕ_1 , and c_2 and ϕ_2 are treated as correlated random variables, and the correlation coefficient is $\rho = -0.3$. Using Nataf transformation, the equivalent correlation coefficient can then be obtained as -0.3054, and the equivalent correlation coefficient is obtained as -0.3025 using the proposed method. The reliability index $\beta_{L\text{-FORM}}$ can be calculated as 2.8416 by using the normal transformation based on L-moments, and the results obtained by FORM using Nataf transformation is 2.8671. It can be observed that the equivalent correlation coefficient and the reliability index obtained by the proposed method provides a close result to the one compared with those obtained by FORM using Nataf transformation.

Table 3. Probabilistic information of the basic random variables for Example 2

Random Variables	Distribution	Mean	COV	The first four L-moments			
				λ_1	λ_2	λ_3	λ_4
c_1 (kPa)	Lognormal	22	0.1818	22	2.2322	0.1963	0.2872
ϕ_1 (°)	Lognormal	30	0.1667	30	2.7958	0.2258	0.3572
c_2 (kPa)	Lognormal	25	0.16	25	2.2378	0.1736	0.2849
ϕ_2 (°)	Lognormal	32	0.1563	32	2.7983	0.2121	0.3557
G_w	Normal	0.5	0.24	0.5	0.0677	0	0.0083
δ_1 (°)	Uniform	50	0.0346	50	1	0	0
θ_1 (°)	Uniform	62	0.0373	62	1.3333	0	0
δ_2 (°)	Uniform	48	0.0361	48	1	0	0
θ_2 (°)	Uniform	20	0.1155	20	1.3333	0	0

6 Conclusions

This study proposes a monotonic polynomial normal transformation based on the first four L-moments of random variables, which includes six types with different combinations of 3rd and 4th L-moment ratios. Besides, the formula of equivalent correlation coefficients based on L-moments is proposed and the applicable range of the original correlation coefficient to ensure the transformation's executability is also identified. It is found that:

(1) The discriminant of the six types of the transformation can be directly expressed by the 3rd and 4th L-moment ratios rather than the polynomial coefficients, which is clearer and simpler than the discriminant based on C-moments.
(2) The polynomial coefficients determined from the first four L-moments can be explicitly expressed by L-moments. They are much simpler and easier than those based on C-moments where the coefficients have to be obtained by nonlinear equations.
(3) Numerical studies show that the proposed method can give a sufficiently accurate result for both independent and correlated random variables when the first four L-moments, the standard deviations and the correlation matrix of the basic random variables are known.

7 References

Ang A. H.-S., and Tang W. H. *Probability Concepts in Engineering Planning and Design, Vol. II*: *Decision, Risk, and Reliability*. New York: Wiley, 1984.

Cai G.Q., and Elishakoff I. "Refined second-order reliability analysis." *Struct Saf* (1994), 14(4): 267-276.

Chen X. Y., and Tung Y. K. "Investigation of polynomial normal transform." *Struct Saf* (2003), 25(4): 423-445.

Choi M., and Sweetman B. "The Hermite moment model for highly skewed response with application to tension leg platforms." *J Offshore Mech Arctic Eng* (2010), 132(2): 021602.

David H. A. *Order Statistics*, 2nd edn. New York: Wiley, 1981.

Ditlevsen O., and Madsen H. O. *Structural Reliability Methods*. New York: Wiley, 1996.

Fleishman A. I. "A method for simulating non-normal distributions." *Psychometrika* (1978), 43(4): 521-532.

Gao S., Zheng X. Y., and Huang, Y. "Hybrid C- and L-moment–based Hermite transformation models for non-Gaussian processes." *J Eng Mech* (2017), 144(2): 04017179.

Ghosn, M. and Frangopol, D.M. "Bridge safety and reliability." American Society of Civil Engineers: 83–112, 1999.

Hohenbichler M., and Rackwitz R. "Non-normal dependent vectors in structural safety." *J Engrg Mech Div* (1981), 107(6): 1227-1238.

Hong H. P., Lind N. C. "Approximate reliability analysis using normal polynomial and simulation results". *Struct Saf* (1996), 18(4): 329-339.

Hosking J. R. M. "L-moments: analysis and estimation of distributions using linear combinations of order statistics." *J Roy Statist Soc* B (1990), 52(1): 105-124.

Hosking J. R. M., and Wallis J. R. *Regional Frequency Analysis: An Approach Based on L-moments*. Cambridge: Cambridge University Press, 2017.

Ji X. W., Huang G. Q., Zhang X. X, Kopp G. A. "Vulnerability analysis of steel roofing cladding: influence of wind directionality". *Eng Struct* (2018), 156: 587-597.

Liu P. L., and Der Kiureghian A. "Multivariate distribution models with prescribed marginals and covariances." *Probab Eng Mech* (1986), 1(2), 105-112.

Low B. K. "Reliability analysis of rock wedges". *J Geotech Geoenviron Eng* (1997), 123(6): 498-505.

MacKenzie C. A., and Winterstein S. R. "Comparing L-moments and conventional moments to model current speeds in the North Sea." Proceedings of the 2011 Industrial Engineering Research Conference, Inst. Industrial Eng. Annual Meeting, Reno, NV, May 21-25, 2011.

Melchers R. E., and Beck A. T. *Structural Reliability Analysis and Prediction*, Hoboken: Wiley, 2018.

Pandey M. D., Van Gelder P. H. A. J. M., and Vrijling J. K. "The estimation of extreme quantiles of wind velocity using L-moments in the peaks-over-threshold approach." *Struct Saf* (2001), 23(2): 179-192.

Sankarasubramanian A., and Srinivasan K. "Investigation and comparison of sampling properties of L-moments and conventional moments." *J Hydrol* (1999), 218(1-2): 13-34.

Shinozuka M. "Basic analysis of structural safety." *J Struct Eng* (1983), 109(3): 721-740.

Tong M.N., Zhao Y. G., and Lu Z. H. "Normal Transformation for Correlated Random Variables based on L-moments and its Application in Reliability Engineering". *Reliab Eng Syst Saf* (2020), 207:107334.

Tung Y. K. "Polynomial normal transformation in uncertainty analysis." In: Melcher RE, Stewart ME, editors. ICASP 8, Application of probability and statistics. Netherlands: A.A.Balkema Publishersp, 1999.

Winterstein S. R., and Mackenzie, C. A. "Extremes of nonlinear vibration: comparing models based on moments, L-moments, and maximum entropy." *J Offshore Mech Arct* (2013), 135(2): 185-195.

Zhang X.Y., Zhao Y.G., and Lu Z.H. "Unified Hermite polynomial model and its application in estimating non-Gaussian processes." *J Eng Mech*, (2019), 145(3): 04019001.

Zhao Y. G., and Lu Z. H. "Cubic normal distribution and its significance in structural reliability." *Struct Eng Mech* (2008), 28(3): 263-280.

Zhao Y. G., and Ono T. "Moment methods for structural reliability." *Struct Saf* (2001), 23(1): 47-75.

Zhao Y. G., Tong M.N., Lu Z. H., and Xu J. "Monotonic Expression of Polynomial Normal Transformation Based on the First Four L-Moments". *J Eng Mech* (2020), 146(7): 06020003.

Zhao Y. G., Zhang X. Y., and Lu Z. H. "A flexible distribution and its application in reliability engineering". *Reliab Eng Syst Saf* (2018b), 176: 1-12.

Zhao Y. G., Zhang X. Y., and Lu Z. H. "Complete monotonic expression of the fourth-moment normal transformation for structural reliability." *Comput Struct* (2018a), 196(11): 186-199.

Zwillinger D. *CRC Standard Mathematical Tables and Formulae*, 32nd Edition. Boca Raton: CRC Press, 2018.

CORRELATION IN TIME-DEPENDENT SYSTEM RELIABILITY ANALYSIS OF UNDERGROUND PIPE NETWORK.

Chun-Qing Li

Professor, School of Engineering
RMIT University, Australia

International Symposium on Emerging Developments and Innovative Applications of Reliability Engineering and Risk Managements (EDIARR2022),30 October-3 November2022, Taipei
Chen, S. S. &Ang, Alfredo. H-S. (Editors)

CORRELATION IN TIME-DEPENDENT SYSTEM RELIABILITY ANALYSIS OF UNDERGROUND PIPE NETWORK

Wei Yang[1], Weigang Wang[2] and Chun-Qing Li[3,*]

[1] *Lecturer, Faculty of Architecture, Building and Planning, The University of Melbourne, Melbourne, 3010, Australia*

[2] *Research Fellow. School of Engineering, RMIT University, Melbourne, 3001, Australia*

[3] **Professor, School of Engineering, RMIT University, Melbourne, 3001, Australia*

[*] *Corresponding author, email: chunging.li@rmit.edu.au*

Abstract: Due to their long-term service and exposure to aggressive environment, deterioration of and damage to pipelines have resulted in a very high rate of failures. These failures incur considerable costs for their rehabilitation and repair works. The challenge to pipe operators is how to determine the most cost-risk optimised scheme in terms of when, where and what to maintain the pipeline network. In this paper, a methodology for developing such a maintenance strategy for underground pipe networks is presented with focus on the modelling of the stochastic process, in particular, the explicit consideration of the correlations among multiple failure modes and pipe components, and the system failure of pipeline network. Both serviceability and ultimate limits states are sondired. A numerical example is provided to illustrate the application of the developed methodology. It is found in the paper that ignoring the correlation between pipes will overestimate the risk of pipe system failures, which may cause unnecessary maintenance.

***Keywords*:** System reliability, Time-dependent, Correlations, Risk-cost optimization.

1 Introduction

Pipelines are essential infrastructure that play a pivotal role in a nation's economy, prosperity, health, environment, social well-being and quality of life. Due to their long term service, coupled with exposure to aggressive environment (including climate change) and increased demands (including population growth), deterioration of and damage to pipelines have resulted in a very high rate of failures, as characterized by leakage, structural failure and decreased hydraulic capacity. These failures incur pipe operators and asset managers considerable costs for their rehabilitation and repair works. The challenge to pipe operators and asset managers, as a decision-maker, is to determine the most cost-risk optimised scheme in terms of when, where and what to maintain the pipeline network.

There are many methodologies proposed for developing maintenance strategies for structures in general, such as Thoft-Christensen and Sorensen (1987) for general structures, Estes and Frangopol (1999) for bridges, Li et al (2007) for coastal seawalls and Baji et al (2018) for tunnels. There are also various frameworks proposed for inspection, maintenance or decision-making specifically for underground pipe networks. For example, Kleiner et al. (2001) developed a renewal plan for water distribution network. The objective is to minimize the total cost related to repair and rehabilitation for each pipe in the water distribution network. Jayaram and Srinivasan (2008) proposed an optimal design and rehabilitation for a water distribution system. A multi-objective function is established to minimize the life cycle cost and maximize the performance of the pipelines. Zhang and Zhou (2014) developed a method to evaluate the optimal inspection intervals for a gas pipe. The cost related to the number of inspections, excavations, and failures are also estimated. Wang et al (2022) developed a network-based geospatial-temporal solution to predict the risk of pipe failures, considering the spatial dependence and temporal variability of corrosion growth. An algorithm is developed, integrating theories of reliability, corrosion science, random field, stochastic process,

and copula within the framework of Monte Carlo simulation. It is acknowledged that above studies have enhanced the knowledge in formulation of various strategies of pipe network, such as planning, inspection or maintenance in general. There are however two aspects that can further advance the knowledge in this area. One is that the correlation among different modes of failure have not been fully quantified and the other is that system reliability has not been widely employed. This paper intends to add values in these two aspects.

In this paper, a maintenance strategy is developed where the failure of pipe network is determined using systems reliability methods and considering time-variant correlation and temporal variability of pipes. A method is developed for estimating the influence coefficients of variables for a complex pipe system that consists of non-redundant and redundant components. A numerical example is provided to illustrate the application of the developed methodology. It is found that ignoring the correlation between pipes will overestimate the risk of pipe system failures, which may cause unnecessary maintenance. The significance of the developed methodology is that it allows the decision-making of asset managers to shift from reactive to proactive and monitor when, where and what the pipe failure occurs and the overall risk of a pipe system

2 Maintenance strategy for pipe network

The rationale to develop a maintenance strategy for underground pipe network is to eliminate unnecessary inspection and maintenance activities without compromising the safety of the pipe which is paramount. This can be achieved such that the inspection actions take place only when the probability of serviceability failure exceeds the threshold, i.e., the acceptable risk, and the maintenance actions take place only when the probability of ultimate failure reaches the threshold. This is essentially an optimization problem that combines probability of failures at different levels of pipe system and the costs of various events, i.e., failure and maintenance. Mathematically, this optimization problem is formulated as follows (Baji et al 2018)

$$\text{Minimize: } \sum_{i=1}^{N_m}\sum_{j-1}^{N_c}\sum_{k=1}^{N_f}\left\{\left[p_{sys}(t_i)-p_{sys}(t_{i-1})\right]\times\frac{CF_{jk}(t_i)}{(1+i_r)^{t_i}}+\frac{CM_{jk}(t_i)}{(1+i_r)^{t_i}}\right\} \tag{1a}$$

$$\begin{aligned}\text{Subject to: } & p_u(t_i)\le p_{u,a}\\ & p_{sys}(t_i)\le p_{sys,a}\\ & t_i-t_{i-1}\ge\Delta t_{min}\\ & 0<t_i<t_L\\ & p_s(t_i)\ge p_{s,a}\end{aligned} \tag{1b}$$

where t_i is the maintenance time with i refereeing to time sequence, N_m is the number of maintenance actions, N_c is the number of pipe segments in the system, N_f is the total number of failure modes, i_r is the annual discount rate, In Eqs (1), p_{sys} and p_{sys},a are the probability and the acceptable probability of system failure respectively, CF_{jk} is the corresponding cost of failure, CM_{jk} is the cost of maintenance for j^{th} component due to k^{th} failure mode, p_u and $p_{u,a}$ are the probability and the acceptable probability of ultimate failure, and p_s and $p_{s,a}$ are the probability and acceptable probability of serviceability failure. Δt_{min} is the minimum time interval between two consecutive maintenance actions and t_L is the designed or expected lifetime of pipe system.

Details of method and models used to determine probability of failures of individual pipe and pipe system are provided in next sections. With that, an algorithm is developed and coded in Matlab to implement all calculations in Eqs. (1) which also integrates optimization procedure using GA (generic algorithm).

3 Failure modes of pipes

The structural failures underground pipes are either loss of strength or fracture. The limit sate functions is formulated as follows:

$$G_{us}(t) = \sigma_u - \sigma(t) \tag{2a}$$
$$G_{uf}(t) = K_C - K(t) \tag{2b}$$

where the load effects are stress $\sigma(t)$ and stress intensity factor $K(t)$ which can be obtained from structural and fracture mechanics for a given loading conditions, pipe material and geometry. Since almost all pipe are subjected to corrosion, the location or orientation of corrosion also affect the load effects, in particular, stress intensity factor. In Eqs. (2), σ_u is the limit for stress $\sigma(t)$ and K_C is the fracture toughness of the pipe (Kleiner and Rajani 2001, Canadian Standard Association 2007, Raju and Newman 1982).

There are serviceability failures for underground pipes – a widely recognized one is corrosion induced pin-hole, i.e., leakage. The limit state function for this serviceability failure is formulated as follows:

$$G_{sL}(t) = \varepsilon d - a(t) \tag{3}$$

where ε=0.8 is the allowance factor, d is the wall thickness of the pipe and $a(t)$ is the corrosion pit depth (Wang et al 2022). Another serviceability failure is the loss of hydraulic capacity of pipe system, i.e., the residual pressure at given location l below a certain value, known as hydraulic failure (Xu and Goulter 1999). The limit state function for hydraulic failure is formulated as follows:

$$G_{sH}(t) = \omega \cdot P_D - P_l(t) \tag{4}$$

where P_l is the residual pressure after hydraulic deterioration, P_D is the design pressure and ω is a factor (<1) that defines the acceptable level of pressure reduction over distance of l. P_l is determined from Kleiner et al. (2001):

3.1 Modelling of corrosion growth

Corrosion is a core trigger for pipe failures which is not only highly random but also time-variant. In this paper, the corrosion growth, i.e., $a(t)$, is modelled as a gamma process (Zhou et al., 2017) with the corrosion growth increments at a unit area of pipe surface $\delta_{unit}(t) = a_{unit}(t) - a_{unit}(t - \Delta_T)$. Thus its density function can be expressed as follows

$$f\big(\delta_{unit}(t); \alpha(t) - \alpha(t - \Delta_T), \beta(t)\big) = \frac{\delta_{unit}(t)^{[\alpha(t)-\alpha(t-\Delta_T)]-1} e^{-\delta_{unit}(t)/\beta(t)}}{\beta^{\alpha(t)-\alpha(t-\Delta_T)}\Gamma[\alpha(t)-\alpha(t-\Delta_T)]} \tag{5}$$

where α and β are the shape parameter and rate parameter of gamma distribution, respectively. The maximum pit depth in a pipe for certain area of exposure surface is determined from Wang et al. (2022) as follows:

$$a_\Lambda(t) = a_{unit}(t)\Lambda^\psi = \sum \delta_{unit}(t)\Lambda^\psi \tag{6}$$

where Λ is the corrosion exposure area and ψ is the exponent factor which is related to the corrosion environment.

3.2 Modelling of loading process

The loading process applied to pipe system is by and large a nonstationary non-Gaussian process and its simulation remains a serious challenge to researchers. Of various methods available e.g., spectral representation method (Shields and Deodatis 2013) and Karhunen-Loève (K-L) expansion methods (Dai et al 2019), copulas based simulation of a stochastic process is a simple and more efficient method, in which the stochastic process $\boldsymbol{L}(t)$ can be treated as comprising T component random variables $\boldsymbol{L}(t) = [L(t_1), L(t_2), \dots, L(t_T)]$ and for simple presentation, $L(t_j)$ is denoted by L_j. Let $F_{L_j}(l_j) = P[L_j \le l_i]$ be the marginal cumulative distribution function for each component variable. Based on the Sklar's theorem, a joint distribution function $C[\cdot]$ exists such that (Nelsen 2007)

$$F(L_1, L_2, \dots, L_T) = \mathrm{C}[F_{L_1}(l_1), F_{L_2}(l_2), \dots, F_{L_T}(l_T)] \tag{7}$$

where the copula $C[\cdot]$ is expressed as follow

$$C(u_1, u_2 \dots, u_T) = F\left(F_{L_1}^{-1}(u_1), F_{L_2}^{-1}(u_2), \dots, F_{L_T}^{-1}(u_T)\right) \tag{8}$$

where $F_{L_j}^{-1}(\cdot)$ is the inverse function of $F_{L_j}(\cdot)$ and $u_1, u_2 \dots, u_T$ are corresponding uniformly distributed variables. Since Student's *t*-copula exhibits more flexibility in characterizing the correlation structure of the random variables it is adopted In this paper as follows:

$$C(u_1, u_2 \dots, u_T) = \int_{-\infty}^{\mathrm{T}_\upsilon{}^{-1}(u_1)} \dots \int_{-\infty}^{\mathrm{T}_\upsilon{}^{-1}(u_n)} \frac{\Gamma\left(\frac{\upsilon+n}{2}\right)|\mathbf{R}|^{-1/2}}{\Gamma\left(\frac{\upsilon}{2}\right)(\pi\upsilon)^{n/2}} \left(1 + \frac{1}{\upsilon} X^{\mathrm{T}} \mathbf{R}^{-1} X\right)^{\upsilon+T/2} dX \tag{9}$$

where υ is the degree of freedom, T is its dimension and $\boldsymbol{R}$ is the correlation matrix that ensembles the linear correlation coefficients ρ_{ij} between L_i and L_j as follows

$$\rho_{ij} = e^{-\frac{2|t_i - t_j|}{\theta}} \tag{10}$$

where θ is the scale of fluctuation.

4 Probability of pipe failure

A general structural reliability problem can be formulated as follows

$$p_f = P[G(\boldsymbol{X}, t) = R(t) - S(t) \le 0] = P[S(t) \ge (t)R] \tag{11}$$

where $G(\boldsymbol{X})$ is the limit state function, S denotes general load effect and R the general resistance. Eq, (11) represents a typical upcrossing problem for which the advanced time-dependent reliability methods, e.g., first passage probability method, can be readily employed for a solution (e.g., Melchers and Beck 2018). For a pipe network, a system reliability method should be used since a pipeline comprises a number of segments, and each segment can fail in a several modes. Since the failure of one segment can result in the failure of the whole pipe network it can be considered as a series system. Likewise, since some failure modes, e.g., water leakage or hydraulic failure, do not lead to the ultimate failure of the pipe segment, these failure modes are modelled as a parallel system. Since failures of pipe segments are not independent and also the failure modes are not independent, correlation between each segment failure and failure mode needs to be considered in accurately estimation of the probability pipe system failure. As it is known, the failure probability

of pipe system can be estimated buy multi-fold integrals numerically but this is almost impossible when correlation between segments and failure modes are considered. A good approximation is to employ the multi-dimensional standardized normal distribution as proposed in Thoft-Christensen and S∅rensen (1987) as follows

$$p_{sys} = P(\cup_{i=1}^{n} \{G_i(\boldsymbol{X}) \leq 0\}) \approx 1 - \boldsymbol{\Phi}_n(\boldsymbol{\beta}; \boldsymbol{\rho}) \text{ for series system} \quad (12a)$$

$$p_{sys} = P(\cap_{i=1}^{m} \{G_i(\boldsymbol{X}) \leq 0\}) \approx \boldsymbol{\Phi}_m(-\boldsymbol{\beta}; \boldsymbol{\rho}) \text{ for parallel system} \quad (12b)$$

where $\boldsymbol{\beta} = [\beta_1, \beta_2, \ldots, \beta_n]$ is the vector of reliability index for all failures modes and β_i is determined classical reliability methods, e.g., (FORM). In Eqs. (12), $\boldsymbol{\rho}$ is the correlation matrix which accounts for autocorrelation and influence coefficient of each variable. The elements of $\boldsymbol{\rho}$ are determined from Roscoe et al. (2015) as follows

$$\rho_{i,j} = \sum_{k=1}^{\mathrm{K}} \alpha_{ik}\, \alpha_{jk} \rho_{ijk} \quad (13)$$

where K is the number of variables shared by the component i and component j, ρ_{ijk} is the autocorrelation for k^{th} variable between component i and component j, α_{ik} and α_{jk} are the influence coefficients, known as sensitivity index, to be determined at the design point of limit state function as follows (Nowak and Collins 2012)

$$\alpha_i = \frac{-\frac{\partial G}{\partial X_i}\sigma(X_i)}{\sqrt{\sum_{k=1}^{K}\left(\frac{\partial G}{\partial X_k}\sigma(X_k)\right)^2}} \quad (14)$$

Thus the influence coefficient that accounts for the significance of variable i on the parallel system can be obtained as follows:

$$\alpha_i^{eu} = \sqrt{\frac{(\alpha_i^1)^2 + (\alpha_i^2)^2 + \cdots (\alpha_i^M)^2}{M}} = \sqrt{\frac{\sum_{g=1}^{M}(\alpha_i^g)^2}{M}} \quad (15)$$

where α_i^{eu} satisfies $\sum_{i=1}^{K}(\alpha_i^{eu})^2 = 1$, and M is the number of serviceability failure modes. α_i^{eu} is then used to determine the correlation coefficients $\rho_{i,eu}$ and $\rho_{j,eu}$ as inputs to Eq (12a). Likewise, the influence coefficient that accounts for the significance of variable i on the series system can be obtained as follows

$$\alpha_i^{s} = \sqrt{\frac{\sum_{\delta=1}^{N}(\alpha_i^{\delta})^2 + (\alpha_i^{eu})^2}{N+1}} \quad (16)$$

where N is the number of ultimate failure modes in a pipe segment, α_i^{δ}, $\delta = 1,2,\ldots,N$ is the influence coefficient for variable X_i in each ultimate failure mode and α_i^{eu} is given by Equation (15).

5 Worked example

An example of water pipe network is used to illustrate how the proposed methodology can be effectively applied to reliability assessment of pipe system in developing its optimal maintenance strategy when all the correlations between pipe segments and failures modes are considered. This is schematically shown in Figure 1 where the pipe network consists of 7 segments and the supply

pressure P(t) is modelled as a stochastic process. Tow ultimate failures of fracture and burst and three serviceability failures of hydraulic failure and water leakage are considered in the example. More segments of pipes and also more failure modes can be considered when necessary. The general procedure for this example is outlined as follows: 1) simulate the pressure P(t) and corrosion pit a(t) considering temporal variability based on equations presented in Section 2; (2) calculate all the correlations between failure modes and between different pipe segments based on the equations presented in Section 3; (3) calculate the probability of failures for different pipe segments and failure modes individually and the probability of system failure based on equations presented in Section 4; (4) determine the risk-cost optimized maintenance strategy for the given constraints based on equations presented in Section 5.

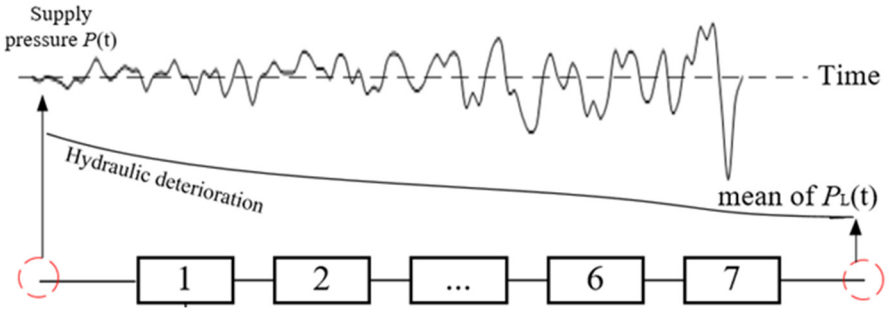

Figure 1. Schematic of example water pipe network

For demonstration, the results of α_i^s in pipe no.1 and no.5 are shown in the Figs. 7(a)-(b), respectively. It can be seen that α_i^s of pressure increases while the others decrease with time. To be more specific, α_i^s of all variables are about 0.5 at year 1 and α_i^s for corrosion depth, wall thickness and pipe diameter gradually decreases to about 0.3 at 100 years. In comparison, α_i^s of pressure increases to over 0.75, which the probability of pipe segment failure becomes more sensitive to the pressure than other variables.

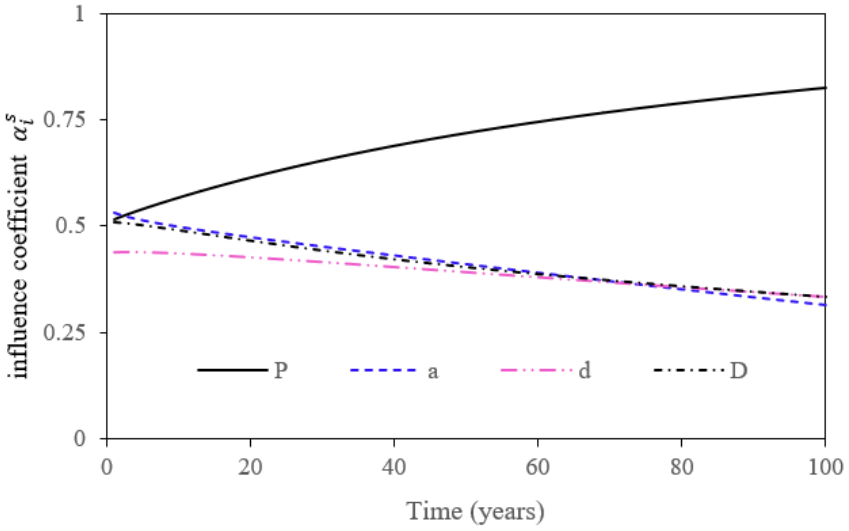

(a)

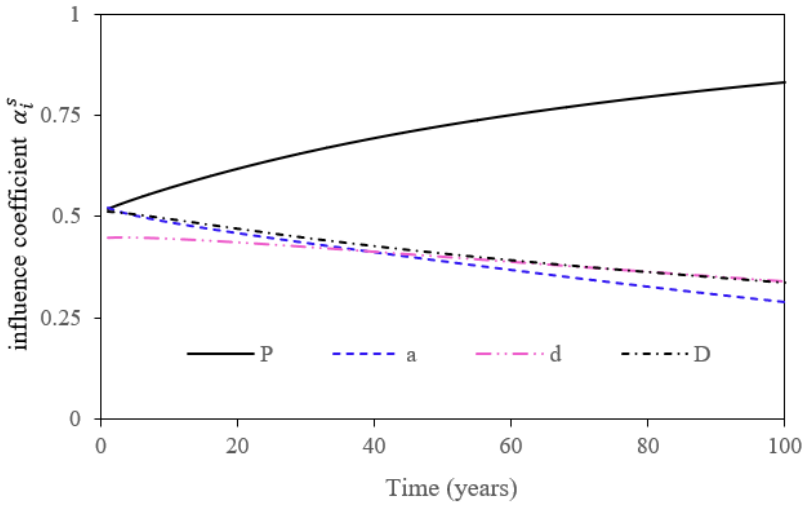

(b)

Figure 2. Influence coefficient α_i^s over time in (a) pipe no.1 (b) pipe no.5

The probability of pipe system failure is shown in Fig. 3 for different auto correlations (i.e., 0.1, 0.5, 0.9). For comparison purpose, the probability of system failure without correlation is also presented. It is clear from the results that correlation makes significant difference in estimating the probability of system failures. From maintenance viewpoint, it is more costly because the neglect of correlation can result in a larger probability of system failure which also increases with time. Larger probability of failure will lead to more inspection or early replacement for deteriorated pipes, which is not justifiable when the budget of water utilities is tight. Results in Fig. 3 also suggest that a larger autocorrelation ρ_{ijk} results in a smaller probability of system failure. It is because when the autocorrelation ρ_{ijk} increases, the overall correlation between pipe segments also increases. The results in Fig. 3 are consistent with basic theory of probability.

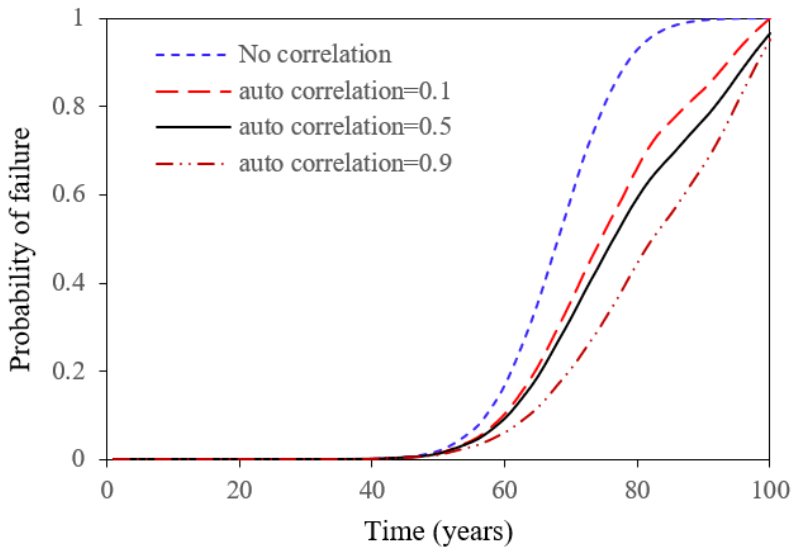

Figure 3. Comparisons of probability of failure for water main with different auto

6 Conclusions

This paper has provided insights into reliability assessment of a practical pipe systems with complex correlations. In developing a risk-cost optimised maintenance strategy for water pipe network, methods for determining time-variant correlations and simulating temporal variability of loading and deterioration processes are integrated. An example is provided to demonstrate the proposed methods. It has been found in the paper that the correlations among failure modes and pipe segments are time-variant, and closely related to the influence coefficients and autocorrelation of basic variables. It has also been found that neglect of correlations in the pipe network may not results in a risk-cost optimised maintenance strategy. The paper can conclude that the presented methodology can help water network operators and asset managers develop an optimal maintenance strategy their pipelines.

7 Acknowledgement

Financial support from the Australian Research Council under LP150100413 and the National Natural Science Foundation of China with Grant No. 51820105014 is gratefully acknowledged.

8 References

ASCE. 2021 INFRASTRUCTURE REPORT CARD. https://infrastructurereportcard.org/wp-content/uploads/2017/01/Drinking-Water-2021.pdf

Baji H, Li CQ (2018) Time-dependent reliability method for service life prediction of reinforced concrete shield metro tunnels. Structure and Infrastructure Engineering 14(8): 1095-1107.

Dai, H., Zheng, Z., and Ma, H. (2019). An explicit method for simulating non-Gaussian and non-stationary stochastic processes by Karhunen-Loève and polynomial chaos expansion. Mechanical Systems and Signal Processing, 115, 1-13.

De Silva, D., Mashford, J., and Burn, S. (2009). Computer aided leak location and sizing in pipe networks. Urban Water Security Research Alliance.

Estes AC, Frangopol DM (1999) Repair optimization of highway bridges using system reliability approach. Journal of Structural Engineering 125(7):766-775.

Jayaram, N., and Srinivasan, K. (2008). Performance-based optimal design and rehabilitation of water distribution networks using life cycle costing. Water resources research, 44(1).

Kleiner, Y., Adams, B. J., and Rogers, J. S. (2001). Water distribution network renewal planning. Journal of Computing in Civil Engineering, 15(1), 15-26.

Li C.Q., Ian Mackie R, Lawanwisut W (2007) A Risk-Cost Optimized Maintenance Strategy for Corrosion-Affected Concrete Structures. Computer-Aided Civil and Infrastructure Engineering 22(5):335-346.

Li, C. Q., and Yang, S. T. (2012). Stress intensity factors for high aspect ratio semi-elliptical internal surface cracks in pipes. International Journal of Pressure Vessels and Piping, 96, 13-23.

National Water Commission Australia. (2021). National performance report 2020–2021: Urban water utilities.

http://www.bom.gov.au/water/npr/docs/2020-21/National_Performance_Report_2019-20_urban_water_utilities.pdf

Nelsen, R. B. (2007). An introduction to copulas. Springer Science & Business Media.
Nowak, A.S. and Collins, K.R., (2012). Reliability of structures. CRC press.

Raju, I.S. and Newman Jr, J.C., 1982. Stress-intensity factors for internal and external surface cracks in cylindrical vessels.

Thoft-Christensen P, Sorensen JD (1987) Optimal strategy for inspection and repair of structural systems. Civil Engineering Systems 4(2):94-100.

Shields, M.D. and Deodatis, G., 2013. Estimation of evolutionary spectra for simulation of nonstationary and non-Gaussian stochastic processes. Computers & Structures, 126, pp.149-163.

Wang, W., Yang, W., Shi, W., and Li, C. Q. (2022). Modeling of Corrosion Pit Growth in Buried Steel Pipes. Journal of Materials in Civil Engineering, 34(1), 04021386.

Xu, C., and Goulter, I. C. (1999). Reliability-based optimal design of water distribution networks. Journal of Water Resources Planning and Management, 125(6), 352-362.

Zhang, S., and Zhou, W. (2014). Cost-based optimal maintenance decisions for corroding natural gas pipelines based on stochastic degradation models. Engineering Structures, 74, 74-85.

Zhou, W., Gong, C., and Hong, H. P. (2017). New perspective on application of first-order reliability method for estimating system reliability. Journal of Engineering Mechanics, 143(9), 04017074.

Zhou, W. (2010). System reliability of corroding pipelines. International Journal of Pressure Vessels and Piping, 87(10), 587-595.

COMBINED PARAMETER AND INPUT IDENTIFICATION OF NONLINEAR SYSTEM USING UNSCENTED KALMAN FILTER

Ser Tong Quek

Professor, Department of Civil and Environmental Engineering, Faculty of Engineering
National University of Singapore, Singapore

International Symposium on Emerging Developments and Innovative Applications of Reliability Engineering and Risk Managements (EDIARR2022),30 October-3 November2022, Taipei
Chen, S. S. &Ang, Alfredo. H-S. (Editors)

COMBINED PARAMETER AND INPUT IDENTIFICATION OF NONLINEAR SYSTEM USING UNSCENTED KALMAN FILTER

Jixing Cao[1], Ser-Tong Quek[1]*, Jianze Wang[2]
[1]*Department of Civil & Environmental Engineering, National University of Singapore, Singapore 117576, Singapore.*
**Corresponding author, e-mail: st_quek@nus.edu.sg.*
[2]*Department of Civil Engineering and Institute for Disaster Management and Reconstruction, Sichuan University, Chengdu 610064, China.*

Abstract: The two major components for structural dynamic analysis and evaluation of operational condition are the structural parameters and time history of external excitations. This work develops a combination of the unscented Kalman filter (UKF) and a moving time window technique to simultaneously estimate the structural parameters and external excitation. Simplified state-space equations are proposed, in which only the variables of parameters and inputs are included in the state equation, and the state vector of the displacement and velocity is implicitly considered in the measurement equation. For unknown input estimation, the whole time history is divided into several windows, and a moving time window technique is employed to overcome the curse of dimensionality in the state vector. The augmented state vector, containing the parameters and time window of excitations, is estimated iteratively using the UKF. To verify the effectiveness and robustness of the proposed method, a two-degrees-of-freedom nonlinear system is employed. Results indicate that the parameters and input time history can be simultaneously estimated with high accuracy.

***Keywords*:** Unscented Kalman filter, nonlinear system, input-parameter estimation, moving time window.

1 Introduction

In structural analysis, design and prediction of behaviour, knowing the structural parameters and the excitation time history highly aid in reliable structural performance assessment and damage diagnosis. These two components are not easy to obtain in practice, whereas structural responses, such as displacement and acceleration, can be measured from deployed sensors. Some researchers have explored ways to infer the parameters and unknown inputs from responses (Zhang et al. 2002, Ding et al. 2015) so as to correctly identify model parameters and/or unknown inputs, with the aim of making the predicted responses consistent with the measured response. To achieve this goal, a robust optimization algorithm is important and necessary. Various types of optimization methods (Reynders 2012), including the least squares method, gradient descent method, and genetic algorithm, have gained wide application in model parameter and input identification. These methods provide accurate and reasonable identification results but the optimization in the high-dimensional parameter space remains a challenge.

There many researches done in relation to system identification and structural condition assessment. Peeters *et al.* (1999) proposed stochastic subspace identification method and Brincker *et al.* (2001) developed the frequency domain decomposition approach to identify the modal parameters of frequency, mode shape and damping ratio from the measured acceleration and displacement. Some efforts also focused on the identification of physical parameters (An et al 2019), such as stiffness and damping coefficients, using the responses. The identified results in the frequency domain and time domain can be used to update the finite element (FE) model and detect structural damage. Although the aforementioned methods give deterministic results, the actual parameters will possess some uncertainty due to model error and measurement noise. Hence, it is necessary to consider the variability of parameters in system identification to enhance the reliability of the identified results.

System identification based on Bayesian concept remains a popular methodology because it facilitates plausible reasoning and quantify the model uncertainty. Kalman filter provides a recursively exact Bayesian solution for the state-space equation of the linear system (Chen 2003). For nonlinear system, Yang *et al.* (2006) and Sen *et al.* (2017) proposed the improved extended Kalmn filter to identify the structural damage. Unlike the extended Kalman filter that linearizes the nonlinear system, both the unscented Kalman filter (UKF) (Wan et al. 2000) and the particle filter (Carpenter 1999) sample a set of representative points to estimate the first two statistical moments of the state vector. Their difference lies in the sampling technique, in which the UKF uses the unscented transform to get deterministic points while the particle filter generates a large number of random samples using Monte Carlo. Compared to the particle filter, the UKF performs better in terms of computational cost and accuracy and hence adopted by researchers to estimate the unknown inputs and model parameters. As the duration of the time history of unknown inputs increases, the dimension of the state vector also increases, which may influence the robustness and efficiency of the results.

This research develops a combination of UKF and moving time window to identify structural parameters and unknown inputs simultaneously. The augmented state vector only contains the variables, such as model parameters and inputs, to be identified whereas the structural responses (e.g., displacement and velocity) are omitted. With this simplification, a complex nonlinear FE model can be incorporated into the state-space equations. To overcome the curse of dimensionality in the state vector, the input time history is broken into several windows and a moving time window technique is proposed to estimate the parameters and inputs iteratively. The proposed method is verified using a two-degree-of-freedom nonlinear system.

2 Combined estimation of inputs and parameters using unscented Kalman filter and moving time window

2.1 Parameter identification using unscented Kalman filter

The dynamic equation of a nonlinear structural system under external excitation can be expressed as

$$\mathbf{M}(\boldsymbol{\theta})\ddot{\mathbf{x}}_{\mathrm{k}}(\boldsymbol{\theta}) + \mathbf{C}(\boldsymbol{\theta})\dot{\mathbf{x}}_{\mathrm{k}}(\boldsymbol{\theta}) + \mathbf{R}_{\mathrm{k}}(\mathbf{x}_{\mathrm{k}}) = \mathbf{f}_{\mathrm{k}}, \tag{1}$$

where $\ddot{\boldsymbol{x}}_k$, $\dot{\boldsymbol{x}}_k$, $\boldsymbol{x}_k$ are the structural responses of acceleration, velocity, and displacement at a time t_k, respectively; $\boldsymbol{\theta}$ denotes model parameters; $\boldsymbol{M}$, $\boldsymbol{C}$, $\boldsymbol{R}_k$, $\boldsymbol{f}_k$ are the mass matrix, damping matrix, restoring force vector and external force vector, respectively.
Equation (1) can be transformed into the state space equation as

$$\mathbf{X}_{\mathrm{k}} = \mathbf{g}_{\mathrm{k}}(\mathbf{X}_{\mathrm{k-1}}, \mathbf{f}_{\mathrm{k}}, \mathbf{w}_{\mathrm{k}}), \tag{2}$$

where $\boldsymbol{X}_k = [\boldsymbol{x}_k, \dot{\boldsymbol{x}}_k]^T$ is the state vector, $\boldsymbol{g}_k$ describes a nonlinear system with parameterization, $\boldsymbol{f}_k$ is the input variable, and $\boldsymbol{w}_k$ represents the system process noise. The measurement equation is written as

$$\mathbf{y}_{\mathrm{k}} = \mathbf{h}_{\mathrm{k}}(\mathbf{X}_{\mathrm{k}}, \mathbf{f}_{\mathrm{k}}, \mathbf{v}_{\mathrm{k}}), \tag{3}$$

where $\boldsymbol{y}_k$ is the measurement data, $\boldsymbol{h}_k$ is a measurement equation and $\boldsymbol{v}_k$ represents the measurement noise.

In modal identification applications, the model parameters are unknown and need to be estimated. For such cases, the strategy is to include the model parameters in an augmented state vector, $\boldsymbol{X}_k =$

$[\boldsymbol{X}_k, \boldsymbol{\theta}_k]^T$, where $\boldsymbol{\theta}_k$ is a vector of model parameters to be identified. The joint state-parameter problem can be estimated using Bayesian filter, which typically is a two-step procedure involving prediction and updating. The prediction process forwards the prior state $(\widehat{\boldsymbol{X}}_{k-1|k-1})$ to the current state $(\widehat{\boldsymbol{X}}_{k|k-1})$, and the updating process corrects the current state prediction $(\widehat{\boldsymbol{X}}_{k|k-1})$ using the measurements $(\boldsymbol{y}_k)$. This is essentially a recursive estimation of the first two statistical moments of the state vector. If the state equation only contains unknown parameters to be estimated $(\boldsymbol{\theta}_k)$, and all the dynamics (e.g., $\ddot{\boldsymbol{x}}_k$, $\dot{\boldsymbol{x}}_k$, $\boldsymbol{x}_k$) are included in the measurement equation, the problem changes to a parameter-only estimation. The new state-space equations for parameter-only estimation problem are formulated as

$$\boldsymbol{\theta}_{\mathrm{k}} = \boldsymbol{\theta}_{\mathrm{k-1}} + \mathbf{w}_{\mathrm{k}}, \tag{4}$$

$$\mathbf{y}_{\mathrm{k}} = \mathbf{h}_{\mathrm{k}}(\boldsymbol{\theta}_{\mathrm{k}}, \mathbf{f}_{\mathrm{k}}) + \mathbf{v}_{\mathrm{k}}, \tag{5}$$

where $\boldsymbol{w}_k$ is a process noise vector accounting for parameter uncertainty, assumed to be Gaussian white noise with zero mean and covariance matrix $\boldsymbol{Q}_k$, i.e., $\boldsymbol{w}_k \in \mathcal{N}(\boldsymbol{0}, \boldsymbol{Q}_k)$; $\boldsymbol{h}_k$ is the nonlinear FE model containing the model parameters $\boldsymbol{\theta}_k$; and $\boldsymbol{v}_k$ is the measurement noise vector, assumed to be Gaussian white noise with zero mean and covariance matrix $\boldsymbol{V}_k$, i.e., $\boldsymbol{v}_k \in \mathcal{N}(\boldsymbol{0}, \boldsymbol{V}_k)$.

The estimation process for Eqs. (4) and (5) is different from that of Eqs. (2) and (3). Eq. (4) predict the parameters driven by process noise, and the displacement and velocity are not explicitly included in the state equation. Eq. (5) updates parameters by comparing the prediction from FE prediction against the measurement data; meanwhile, the displacement and velocity are also implicitly updated. Eqs. (4) and (5) are solved recursively using the unscented transform (UKF), yielding estimates of the mean vector and covariance matrix of parameters. The scaled UKF (Julier 2002) generates a set of sample points $\boldsymbol{\vartheta}^{(i)}$ to represent the random variables, whose mean is $\widehat{\boldsymbol{\theta}}_{k-1|k-1}$ and covariance is $\widehat{\boldsymbol{P}}_{k-1|k-1}$, given by

$$\begin{cases} \boldsymbol{\vartheta}_{\mathrm{k}}^{(\mathrm{i})} = \widehat{\boldsymbol{\theta}}_{\mathrm{k-1|k-1}}, & \mathrm{i} = 0; \\ \boldsymbol{\vartheta}_{\mathrm{k}}^{(\mathrm{i})} = \widehat{\boldsymbol{\theta}}_{\mathrm{k-1|k-1}} + \left[\left(\lambda\sqrt{\widehat{\mathbf{P}}_{\mathrm{k-1|k-1}}}\right)_{\mathrm{i}}\right]^{\mathrm{T}}, & \mathrm{i} = 1, \cdots, \mathrm{n}; \\ \boldsymbol{\vartheta}_{\mathrm{k}}^{(\mathrm{i})} = \widehat{\boldsymbol{\theta}}_{\mathrm{k-1|k-1}} - \left[\left(\lambda\sqrt{\widehat{\mathbf{P}}_{\mathrm{k-1|k-1}}}\right)_{\mathrm{i-n}}\right]^{\mathrm{T}}, & \mathrm{i} = \mathrm{n}+1, \cdots, 2\mathrm{n}. \end{cases} \tag{6}$$

where $\lambda = \sqrt{n+\gamma}$, $\gamma = \alpha^2(n+\kappa) - n$; α and κ are constant values related to spread of the sample points; n is the dimension of parameter vector; $(\cdot)_i$ denotes the row of the matrix inside the parentheses.

The forward parameter prediction $\widehat{\boldsymbol{\theta}}_{k|k-1}$ at time t_k and its covariance is calculated as

$$\widehat{\boldsymbol{\theta}}_{\mathrm{k|k-1}} = \sum_{\mathrm{i=0}}^{\mathrm{2n}} \mathrm{W}_{\mathrm{m}}^{(\mathrm{i})} \boldsymbol{\vartheta}_{\mathrm{k}}^{(\mathrm{i})}, \tag{7}$$

$$\widehat{\mathbf{P}}_{\mathrm{k|k-1}}^{\boldsymbol{\theta\theta}} = \sum_{\mathrm{i=0}}^{\mathrm{2n}} \mathrm{W}_{\mathrm{c}}^{(\mathrm{i})} \left[\boldsymbol{\vartheta}_{\mathrm{k}}^{(\mathrm{i})} - \widehat{\boldsymbol{\theta}}_{\mathrm{k|k-1}}\right]\left[\boldsymbol{\vartheta}_{\mathrm{k}}^{(\mathrm{i})} - \widehat{\boldsymbol{\theta}}_{\mathrm{k|k-1}}\right]^{\mathrm{T}} + \mathbf{Q}_{\mathrm{k}}, \tag{8}$$

where the weights for mean $W_m^{(i)}$ and covariance $W_c^{(i)}$ are given by

$$\begin{cases} \mathrm{W}_{\mathrm{m}}^{(\mathrm{i})} = \Upsilon/(\mathrm{n}+\Upsilon), & \mathrm{i} = 0; \\ \mathrm{W}_{\mathrm{m}}^{(\mathrm{i})} = 1/(2\mathrm{n}+2\Upsilon), & \mathrm{i} = 1, \cdots, 2\mathrm{n}; \end{cases} \tag{9}$$

$$\begin{cases} \mathrm{W}_{\mathrm{c}}^{(\mathrm{i})} = \frac{\Upsilon}{\mathrm{n}+\Upsilon} + (1-\alpha^2+\beta), & \mathrm{i}=0; \\ \mathrm{W}_{\mathrm{c}}^{(\mathrm{i})} = \frac{1}{2\mathrm{n}+2\Upsilon}, & \mathrm{i}=1,\cdots,2\mathrm{n}. \end{cases} \tag{10}$$

in which β is a scaling factor.

Each sample point is input into the nonlinear system $\boldsymbol{y}_k^{(i)} = \boldsymbol{h}_k\left(\boldsymbol{\vartheta}_k^{(i)}, \boldsymbol{f}_k\right)$, and the state prediction $\hat{\boldsymbol{y}}_{k|k-1}$ at time t_k and its covariance are computed by

$$\hat{\mathbf{y}}_{\mathrm{k|k-1}} = \sum_{\mathrm{i=0}}^{\mathrm{2n}} \mathrm{W}_{\mathrm{m}}^{(\mathrm{i})} \boldsymbol{\mathcal{Y}}_{\mathrm{k}}^{(\mathrm{i})}, \tag{11}$$

$$\widehat{\mathbf{P}}_{\mathrm{k|k-1}}^{\mathbf{yy}} = \sum_{\mathrm{i=0}}^{\mathrm{2n}} \mathrm{W}_{\mathrm{c}}^{(\mathrm{i})} \left[\boldsymbol{\mathcal{Y}}_{\mathrm{k}}^{(\mathrm{i})} - \hat{\mathbf{y}}_{\mathrm{k|k-1}}\right] \left[\boldsymbol{\mathcal{Y}}_{\mathrm{k}}^{(\mathrm{i})} - \hat{\mathbf{y}}_{\mathrm{k|k-1}}\right]^{\mathrm{T}} + \mathbf{V}_{\mathrm{k}}, \tag{12}$$

When new measurements $\boldsymbol{y}_k$ are available, the mean $\widehat{\boldsymbol{y}}_{k|k}$ and covariance $\widehat{\boldsymbol{P}}_{k|k}^{\boldsymbol{yy}}$ of parameters can be updated as

$$\widehat{\boldsymbol{\theta}}_{\mathrm{k|k}} = \widehat{\boldsymbol{\theta}}_{\mathrm{k|k-1}} + \mathbf{K}_{\mathrm{k}}\left(\mathbf{y}_{\mathrm{k}} - \hat{\mathbf{y}}_{\mathrm{k|k-1}}\right), \tag{13}$$

$$\widehat{\mathbf{P}}_{\mathrm{k|k}}^{\boldsymbol{\theta\theta}} = \widehat{\mathbf{P}}_{\mathrm{k|k-1}}^{\boldsymbol{\theta\theta}} - \mathbf{K}_{\mathrm{k}} \widehat{\mathbf{P}}_{\mathrm{k|k-1}}^{\mathbf{yy}} \mathbf{K}_{\mathrm{k}}^{\mathrm{T}}, \tag{14}$$

in which the Kalman gain $\boldsymbol{K}_k$ is calculated by

$$\mathbf{K}_{\mathrm{k}} = \widehat{\mathbf{P}}_{\mathrm{k|k-1}}^{\boldsymbol{\theta y}} \left(\widehat{\mathbf{P}}_{\mathrm{k|k-1}}^{\mathbf{yy}}\right)^{-1}, \tag{15}$$

The cross-covariance $\widehat{\boldsymbol{P}}_{k|k-1}^{\boldsymbol{\theta y}}$ is given by

$$\widehat{\mathbf{P}}_{\mathrm{k|k-1}}^{\boldsymbol{\theta y}} = \sum_{\mathrm{i=0}}^{\mathrm{2n}} \mathrm{W}_{\mathrm{c}}^{(\mathrm{i})} \left[\boldsymbol{\vartheta}_{\mathrm{k}}^{(\mathrm{i})} - \widehat{\boldsymbol{\theta}}_{\mathrm{k|k-1}}\right] \left[\boldsymbol{\mathcal{Y}}_{\mathrm{k}}^{(\mathrm{i})} - \hat{\mathbf{y}}_{\mathrm{k|k-1}}\right]^{\mathrm{T}}, \tag{16}$$

The UKF identification process described by Eqs. (6)-(16) is convenient and practical because $(2n+1)$ sample points representing the prior distribution of the parameters are input into the FE model to generate the response prediction, which is then updated through the Kalman gain. The parameters can be estimated on-line if the new measurement becomes available. The procedure has been successfully applied in timber connections (Cao et al 2020).

2.2 Unknown input and parameter joint estimation using unscented Kalman filter

The UKF described above provides an effective tool for parameter estimation. In practice, the input time history is usually unknown or very difficult to estimate. If input excitation can also be estimated or corrected from the structural response, it will increase the reliability of structural health monitoring. Recall in section 2.1 that the parameters are regarded as variables in the state-space equations. If the unknown inputs are also considered as random variables and augmented into the state vector, the state-space is rewritten as

$$\widehat{\mathbf{X}}_{\mathrm{k}} = \widehat{\mathbf{X}}_{\mathrm{k-1}} + \mathbf{w}_{\mathrm{k}}, \tag{17}$$

$$\mathbf{y}_{\mathrm{k}} = \mathbf{h}_{\mathrm{k}}\left(\widehat{\mathbf{X}}_{\mathrm{k}}\right) + \mathbf{v}_{\mathrm{k}}, \tag{18}$$

where $\widehat{\boldsymbol{X}}_k = [\boldsymbol{\theta}_k, \boldsymbol{u}_{0:k}]^T$ is the augmented state, in which $\boldsymbol{u}_{0:k}$ denotes the ground acceleration from time 0 to time k. Note that the dimension of state vector becomes large when the number of time steps k is large. This results in the joint estimation process using a large amount of sample points, where each sample point is passed through the nonlinear system. This makes the solution computationally challenging and costly. To address this issue, a moving time window technique is proposed to reduce the dimension of state vector.

Figure 1 illustrates the concept of moving time window for input estimation. Each time window has a constant length L_s. For example, the j-th time window t_j^A consists of two time series t_j^1 and t_j^2, i.e., $t_j^A = t_j^1 + t_j^2$, where the length of t_j^A equals L_s. The initial guess of time series t_j^1 is obtained from the estimation results of the $(j-1)$-th window estimation t_{j-1}^2, as shown in the top of Figure 1, and the initial guess of time series t_j^2 is set as zero. The entire j-th window time series $t_j^A = t_j^1 + t_j^2$ together with model parameters are estimated using UKF. When the j-th window estimation is completed, the estimated results of t_j^2 is used for the next window estimation as the initial guess of t_{j+1}^1.

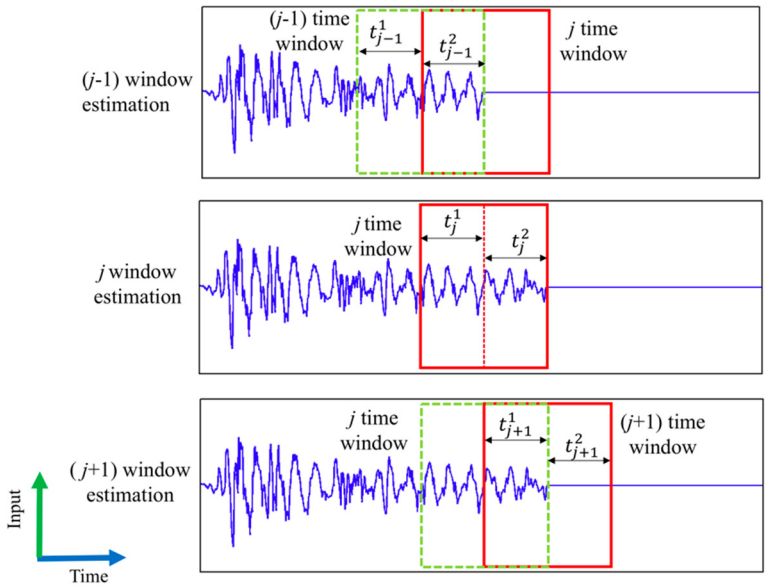

Figure 1. Concept of moving time window

When the moving time window technique is embedded in the UKF, the input time history and parameters can be estimated simultaneously from the structural responses. Figure 2 summarizes the proposed method for the joint input-parameter estimation. The sample point $\boldsymbol{\chi}_j^{(i)}$ is generated by the scaled unscented transform according to Eqs. (6)-(10), where $\widehat{\boldsymbol{\theta}}_{j-1|j-1}$ and $\widehat{\boldsymbol{P}}_{j-1|j-1}$ should be replaced by the augmented state vector $\widehat{\boldsymbol{X}}_{j-1|j-1}$ and the corresponding covariance matrix, in which j denotes the j-th time window.

It is assumed that the predefined length of each time window L_s is smaller than the whole length of time history L_n. In the estimation process of j-th time window, the input time steps $[0: (j-1) * L_s]$ are regarded as known, while the time steps $[(j-1) * L_s + 1: j * L_s]$ are to be estimated. The input time history $\boldsymbol{u}_{(j-1)*L_s+1:j*L_s}$ and model parameters $\boldsymbol{\theta}_j$ are combined together in the

augmented state vector $\boldsymbol{X}_j = [\,\boldsymbol{\theta}_j, \boldsymbol{u}_{(j-1)*L_s+1:j*L_s}\,]$ for estimation. For symbolic simplification, $t_j = (j-1)*L_s+1{:}\,j*L_s$, that is, $\boldsymbol{X}_j = [\boldsymbol{\theta}_j, \boldsymbol{u}_{t_j}\,]$. The prediction and updating process are the same as that introduced in section 2.1.

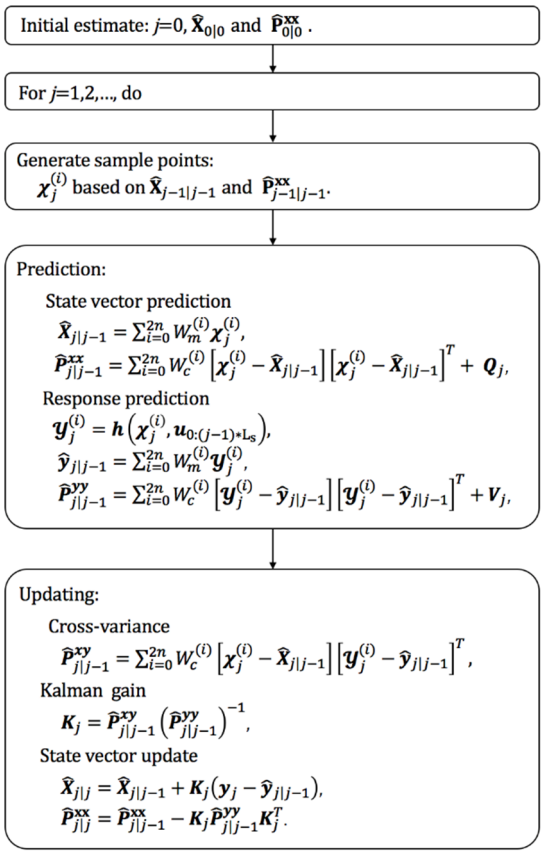

Figure 2. Proposed method of joint parameter-input estimation

3 Case study

3.1 Numerical model information

In this section, a two-story building subjected to earthquake excitation is employed to demonstrate the robustness of the proposed method for joint input-parameter identification. The two-story building is idealized as a two-degrees-of-freedom (2-DOF) system, as shown in Figure 3. The mass and stiffness of the first and second stories is assumed to be $m_1 = m_2 = 33\,kg$, and $k_1 = 560\,N/m$ and $k_2 = 420\,N/m$ respectively. The ground acceleration history recorded from the Kobe 1995 earthquake in Japan (see Figure 3) is used as the input excitation. To simulate the nonlinear behavior, the Bouc-Wen model is employed. The equations are commonly expressed as (Ikhouane and Rodellar 2007)

$$\begin{cases} \mathrm{R(t)} = \alpha \mathrm{Kx(t)} + (1-\alpha)\mathrm{Kz(t)} \\ \dot{\mathrm{z}}(\mathrm{t}) = \mathrm{A}\dot{\mathrm{x}}(\mathrm{t}) - \beta|\dot{\mathrm{x}}(\mathrm{t})||\mathrm{z(t)}|^{\mathrm{n}-1}\mathrm{z(t)} - \gamma\dot{\mathrm{x}}(\mathrm{t})|\mathrm{z(t)}|^{\mathrm{n}} \end{cases}, \tag{19}$$

where $R(t)$ is the restoring force, K is the elastic stiffness, α is the ratio of post-yield stiffness to elastic stiffness, z is the hysteretic displacement, and the four dimensionless parameters A, n, β, γ

control the hysteretic shape. In this example, $\alpha = 0.27$, $A = 1$, $\beta = 1.3$, $\gamma = 1.6$, $n = 0.42$ are set for both stories.

Equation (19) is incorporated into Eq. (1), and the differential equations are integrated using Newmark-beta algorithm. The input ground acceleration time history has 1500 points with time step $\Delta t = 0.02$ s. The length of structural responses employed is 30 s. The calculated acceleration and hysteretic curve are depicted in Figure 3, indicating significant nonlinear behaviour. A 30 dBW white Gaussian noise is superimposed onto the original response to simulate the measurement noise. The simulated accelerations are regarded as measurement data for identification.

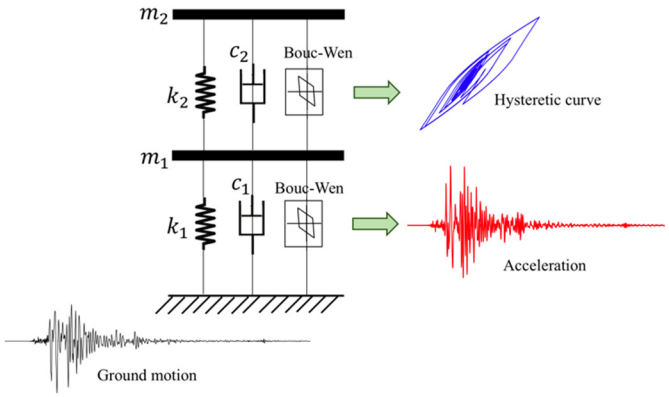

Figure 3. Schematic diagram of 2-DOF nonlinear system considered

3.2 Input and parameter identification results

In the identification process, the parameters k_2 and β, as well as the input ground acceleration are taken as unknowns. They are to be identified using the measured acceleration responses. The unknown augmented state vector is $\boldsymbol{X} = [\boldsymbol{\theta}, (\boldsymbol{u}_{1:1500})^T]$, where $\boldsymbol{\theta} = [k_2, \beta\,]^T$, and $(\boldsymbol{u}_{1:1500})^T$ are the unknown input ground accelerations. As the UKF requires $(2n + 1)$ samples, in which $n = 2 + 1500$, a total of 3005 samples are generated for the FE model calculation at each time step, which poses a huge computational burden. In the proposed moving time window technique, if the length of each time window is $S = 200$, the j-th window for input estimation is $\boldsymbol{U}_j = \boldsymbol{u}_{100*(j-1)+1:\,100*(j-1)+200}$. This significantly reduces the number of samples employed for each time step.

The initial estimate of the unknown augmented state vector is $\widehat{\boldsymbol{X}}_0 = \left[\widehat{\boldsymbol{\theta}}_{0|0}, \widehat{\boldsymbol{u}}_{0|0}\,\right]^T$, where the initial guess of unknown parameters $\widehat{\boldsymbol{\theta}}_{0|0} = [1.16k_2^T, 0.92\beta^T]$ and the initial guess of unknown input $\widehat{\boldsymbol{u}}_{0|0}$ =(1e-6)$*\,\boldsymbol{I}_{200}$, in which $\boldsymbol{I}_{200}$ is an identity matrix of size 200, are considered. The following parameters are predefined during estimation: the covariance matrix of process noise for parameters $\boldsymbol{Q}_k^{\theta\theta}$ and input $\boldsymbol{Q}_k^{uu}$ is assumed to be statistically uncorrelated, i.e., $\boldsymbol{Q}_k = diag\left[\,\boldsymbol{Q}_k^{\theta\theta}, \boldsymbol{Q}_k^{uu}\,\right]^T$, where $\boldsymbol{Q}_k^{\theta\theta}$ =(1e-4)$*\,\boldsymbol{I}_2$; $\boldsymbol{Q}_k^{uu}$ =(1e-6)$*\,\boldsymbol{I}_{200}$; the covariance matrix for measurement noise is $\boldsymbol{V}_k$=(1e-5)$*\,\boldsymbol{I}_2$. The exact model parameters are normalized by their exact values so that the influence of differences in parameter magnitudes can be minimized.

Figure 4 depicts the estimated time history for the two model parameters. The estimated values fluctuate before 7 seconds and then converge to the true values with a relative error (RE) of less than 1%. The identified ground acceleration is presented in Figure 5, showing that it captures the

true acceleration well. To quantify the accuracy of the identified time-history data, the relative root mean square error (RRMSE) is defined as follows:

$$\mathrm{RRMSE}(\%) = \sqrt{\frac{\sum_{k=1}^{N_t}(y_k^E - y_k^T)^2}{N_t}} \Big/ \sqrt{\frac{\sum_{k=1}^{N_t}(y_k^T)^2}{N_t}} \times 100, \tag{20}$$

where $\boldsymbol{y}_k^E$ and $\boldsymbol{y}_k^T$ are estimated and true time series signals, respectively; N_t is the length of time series.

The RRMSE between the true ground acceleration and the estimated results is 7.31%, indicating good agreement. The estimated model parameters and ground acceleration are then used to predict the structural response. The comparison between the true acceleration responses and predicted accelerations is shown in Figure 6, with RRMSE values of less than 6%. The hysteretic curves between the true and predicted results are also compared in Figure 7. The above analysis confirms that the proposed framework for jointly identifying parameters and inputs using output-only responses is efficient and feasible.

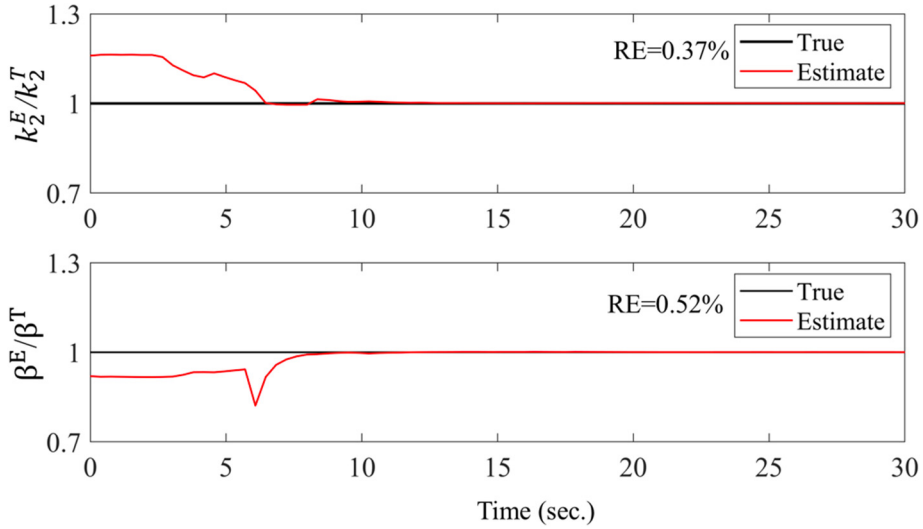

Figure 4. Tracking of normalized estimated parameters

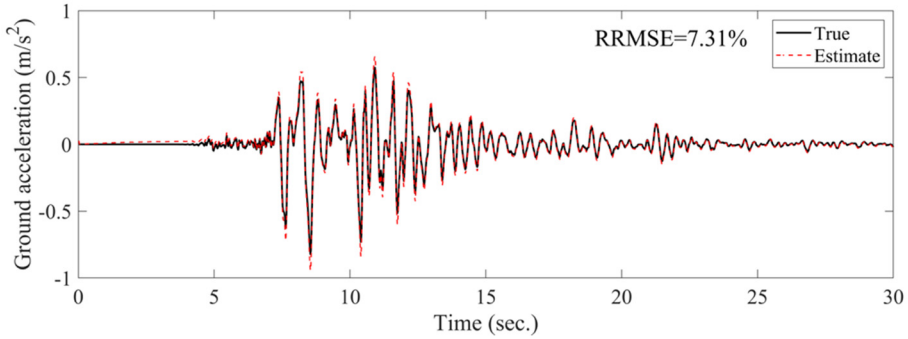

Figure 5. Comparison of ground acceleration between true and estimated results

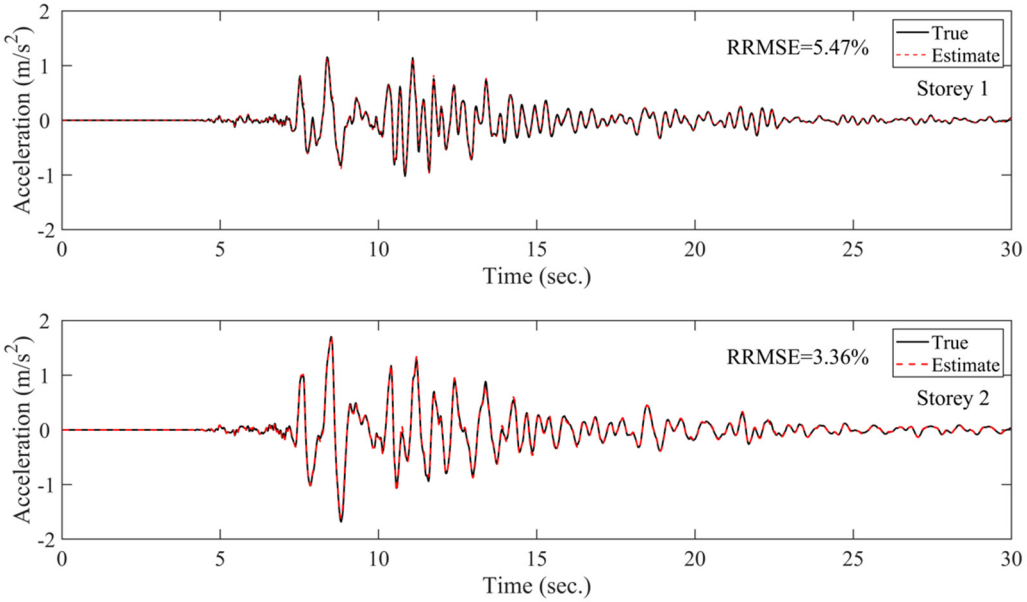

Figure 6. Comparison of true acceleration with predicted results

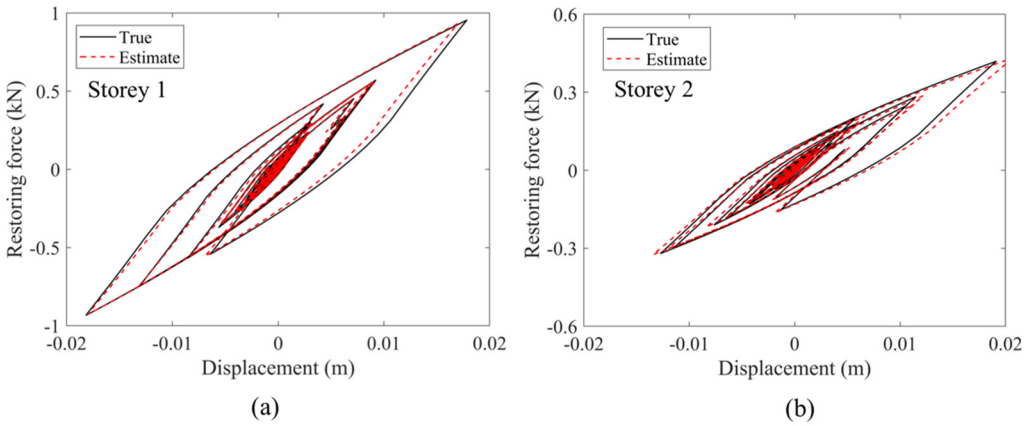

Figure 7. Comparison of hysteretic curves between true and predicted results

4 Concluding remarks

This research proposes the method of joint input-parameter identification from output-only responses using the unscented Kalman filter (UKF). The unknown variables including the model parameters and input excitations are augmented into the state vector, while the state vector of displacement and velocity are to be predicted after the state vector is estimated. This simplification for state-space equations implicitly considers the estimate of displacement and velocity in the measurement equation, allowing incorporating the complex finite element model. To overcome the high-dimensional state vector caused by unknown input variables, a moving time window technique is proposed. It divides the unknown input time history into a set of time windows, each of which has a constant length and is augmented to the state vector. The augmented state vector is then estimated using the UKF. A two-degrees-of-freedom nonlinear system is utilized to demonstrate the effectiveness of the proposed method. Results indicate that the estimate of

parameters and the input time history are in good agreement with actual values. However, the robustness of the proposed method may need to be further verified. For example, different levels of measurement noise and various types of measured responses for identification (e.g., displacement or strain) may affect the identification results. The length of the time window also has a significant influence on the identification results. These factors are currently being investigated.

5 References

An, Y., Chatzi, E., Sim, S. H., Laflamme, S., Blachowski, B., & Ou, J., "Recent progress and future trends on damage identification methods for bridge structures", *Structural Control and Health Monitoring*, 26(10), 2019: e2416.

Brincker R, Zhang L, Andersen P, "Modal identification of output-only systems using frequency domain decomposition", *Smart Materials and Structures*, 10(3), 2001: 441.

Carpenter, J., Clifford, P., & Fearnhead, P., "Improved particle filter for nonlinear problems", *IEE* Proceedings-Radar, Sonar and Navigation, 146(1), 1999: 2-7.

Cao, J., Xiong, H., & Chen, L., "Procedure for parameter identification and mechanical properties assessment of CLT connections". *Engineering Structures*, 203, (2020): 109867.

Chen, Z., "Bayesian filtering: From Kalman filters to particle filters, and beyond", *Statistics*, 182(1), 2003: 1-69.

Ding, Y., Zhao, B. Y., Wu, B., Zhang, X. C., & Guo, L. N., "Simultaneous identification of structural parameter and external excitation with an improved unscented Kalman filter," *Advances in Structural Engineering*, 18(11), 2015: 1981-1998.

Ikhouane, F., & Rodellar, J., Systems with hysteresis: analysis, identification and control using the Bouc-Wen model. John Wiley & Sons, 2007.

Julier S J. The scaled unscented transformation[C]//Proceedings of the 2002 American Control Conference (IEEE Cat. No. CH37301). IEEE, 2002, 6: 4555-4559.

Peeters B, De Roeck G., "Reference-based stochastic subspace identification for output-only modal analysis", *Mechanical Systems and Signal Processing*, 13(6), 1999: 855-878.

Reynders, E., "System identification methods for (operational) modal analysis: review and comparison," *Archives of Computational Methods in Engineering*, 19(1), 2012: 51-124.

Sen S, Bhattacharya B., "Online structural damage identification technique using constrained dual extended Kalman filter", *Structural Control and Health Monitoring*, 24(9), 2017: e1961.

Wan E A, Van Der Merwe R. The unscented Kalman filter for nonlinear estimation[C]//Proceedings of the IEEE 2000 Adaptive Systems for Signal Processing, Communications, and Control Symposium (Cat. No. 00EX373). Ieee, 2000: 153-158.

Yang, J. N., Lin, S., Huang, H., & Zhou, L., "An adaptive extended Kalman filter for structural damage identification", *Structural Control and Health Monitoring*, 13(4), 2006: 849-867.

Zhang, H., Foliente, G. C., Yang, Y., & Ma, F., "Parameter identification of inelastic structures under dynamic loads," *Earthquake Engineering & Structural Dynamics*, 31(5), 2002: 1113-1130.

Organized Sessions

International Symposium on Emerging Developments and Innovative Applications of Reliability Engineering and Risk Managements (EDIARR2022),30 October-3 November2022, Taipei
Chen, S. S. &Ang, Alfredo. H-S. (Editors)

AN INTEGRATED SIMULATION METHOD OF THE TIME-DEPENDENT COMPRESSIVE STRENGTH OF CONCRETE FOR COLUMN MEMBERS BASED ON THE 2D HEAT TRANSFER MODELS

Chiu-Chien Kuo[1], I-Hsiang Liao[1], Hadiyoga Tjitro[1]

[1] *Department of Civil and Construction Engineering, National Taiwan University of Science and Technology, Taipei, R.O.C Taiwan*

E-mail: miloou594@gmail.com (I.-H. Liao)

Abstract: In order to shorten the construction time of a reinforced concrete (RC) building structure, the stripping time of the concrete framework should be determined accurately based on the simulation or measurement of the compressive strength of concrete. Therefore, this work proposes an integrated simulation method for predicting the temperature history and compressive strength development of concrete for an RC column member that incorporates the degree of hydration, thermal properties and heat transfer. Additionally, the time-dependent thermal properties of concrete are obtained from the degree of hydration. For the heat transfer, this work proposes the two-dimensional model for the column specimens instead of the one-dimensional model. Based on the simulated temperature, the compressive strength of concrete for each specimen is calculated using the concept of maturity, which can be expressed as a function of the equivalent age and the temperature. Finally, this work adopts the experimental data to prove that the proposed method can provide the conservative prediction results of the compressive strength of concrete for the column members.

***Keywords*:** Hydration reaction of cement, heat transfer, time-dependent thermal properties, compressive strength.

Introduction

In the cast-in-site concrete construction, how to determine the stripping time of the concrete framework is important. Most of the practical use, the stripping time of the concrete framework is suggested based on the construction guideline (ACI 347, 2015;PN-B-06251,1963;IS 456,2000; BS 8110, 1997) or determined based on the actual testing of the concrete cylinders, which are casted at the same time with the concrete structure. Some construction cases set the thermocouples to measure the temperature of the concrete surfaces of wall members. Moreover, the measured temperature was used to estimate the compressive strength of concrete to determine the stripping time of the concrete framework. However, for a column or beam member, the related research is still needed to build a simulation method of the time-dependent compressive strength of concrete for column members based on the transfer of heat that is generated by the hydration reaction of cement.

Since the cement paste often determines the strength of concrete that forms from it, the mechanical properties of the cement paste, which are closely related to its microstructure, need to be considered to predict the strength and pore structure of concrete. Additionally, the temperature and water content of the cement paste must be considered in the hydration process. Various models of the degree of hydration can be used to simulate the formation of the microstructure of the cement paste. Parrot and Killoh (Parrot et Killoh 1984) proposed a hydration model that consisted of three fundamental processes and described the degree of hydration of each cement clinker. Although the

kinetic aspects of hydration have been considered in the model of Parrot and Killoh (Parrot et Killoh 1984), this model was still considered to be the semi-empirical formula. To simplify the complexity of simulation of this part, the concept of the model of Parrot and Killoh (Parrot et Killoh 1984) is adopted herein. Additionally, the model of Lothenbach et al. (Lothenbach, Matschei, et al. 2008) is also used to consider the temperature effect and model parameters to the fit of experimental data (Lothenbach, Le Saout, et al. 2008).

As mentioned by Maruyama et al. (Maruyama et Igarashi 2015), the temperature history of a concrete member has the large impact on the hydration of its cement and the heat that is produced in the hydration process, resulting in a coupled system in concrete. Therefore, the temperature distribution affects the distribution over the volume of the degree of hydration in concrete. To evaluate the temperature change of concrete due to the cement hydration, a simulation model that includes hydration and the heat transfer is necessary. Therefore, to simulate temperature accurately in the proposed method, the thermal properties of concrete are set as functions of the time-dependent degree of hydration. The temperature history of concrete is thus used to estimate the development of its compressive strength.

For determining the stripping time of the concrete framework accurately, the main purpose of this work is to predict the temperature history and compressive strength development of concrete for a column member. Fig. 1 shows the procedure of the proposed method. The proposed method consists of both a cement hydration model and a heat transfer model, which includes the time-dependent thermal properties of concrete. In this work, since the simulate target is the concrete in the framework after casting, the water vaporization from the concrete is ignored and the relationship between the temperature and cement hydration is built without considering the moisture transfer. Once the degree of hydration of the cement is calculated, its thermal properties are set and its temperature history is determined by numerical analysis. The analyzed temperature history is then brought into the calculation of the degree of hydration, and the process is repeated until the target time is reached. Many models of the relationship between strength development and time have been used to calculate the development of the compressive strength of concrete. This work introduces the concept of maturity to estimate the development of the compressive strength of concrete. Based on the directions of the heat transfer of concrete in the framework for a column member, this work adopts the two- dimensional (2D) model to investigate their temperature histories instead of the one-dimensional (1D) model. Additionally, the specimens that are constructed to simulate column members are used to verify the proposed method.

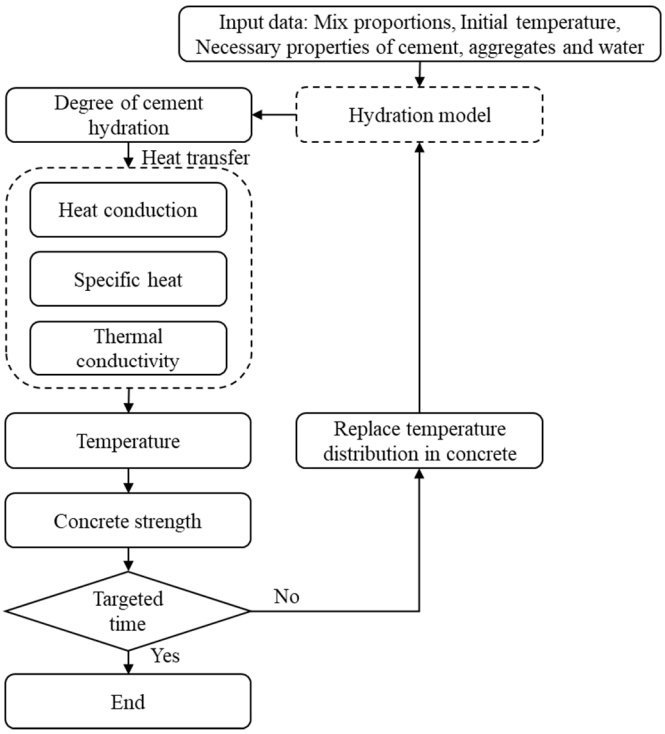

Figure 1. The procedure of the proposed method

Model Formulation

Hydration Model

The model that was proposed by Parrot and Killoh (Parrot et Killoh 1984) includes three fundamental processes, which are nucleation and crystal growth, diffusion, and formation of a hydration shell (Parrot et Killoh 1984). All processes are assumed to occur simultaneously. Since the slowest one dominates the hydration process, their rates must be determined. Parrot and Killoh (Parrot et Killoh 1984) indicated that the slowest process at first is nucleation and crystal growth, and that subsequently is diffusion or formation of a hydration shell.

The initial rate of hydration is determined by a nucleation and growth mechanism. The hydration rate of each compound is assumed to be proportional to the surface area of the cement since this is a reasonable approximation at low degrees of hydration. Additionally, the effect of the surface area on the rate of hydration at later stages (diffusion and formation of a hydration shell) is negligibly small (Parrot et Killoh 1984). Therefore, the surface area of the cement is used only in Eq. (1), which corresponds to nucleation and crystal growth. The rate of diffusion describes the diffusion of the solid reactant through the layers of the previously formed hydrates. In this work, Equation (2) simulates the rate of diffusion. The rate of formation of a hydration shell varies according to a power law. Equation (3) describes the formation of a thick shell around unreacted cement particles, which creates an obstruction that inhibits the transport of dissolved species.

$$R_{NG,t} = \frac{K_1}{N_1}(1-\alpha_t)(-ln(1-\alpha_t))^{(1-N_1)}\left(\frac{rh-0.55}{0.45}\right)^4 \times \left(\frac{surface\ area}{reference\ area}\right) e^{-\frac{E_a}{R}\left(\frac{1}{T}-\frac{1}{T_0}\right)} \quad (1)$$

$$R_{D,t} = \frac{K_2 \times (1-\alpha_t)^{\frac{2}{3}}}{1-(1-\alpha_t)^{\frac{1}{3}}}\left(\frac{rh-0.55}{0.45}\right)^4 e^{-\frac{E_a}{R}\left(\frac{1}{T}-\frac{1}{T_0}\right)} \quad (2)$$

$$R_{FYS,t} = K_3 \times (1-\alpha_t)^{N_3}\left(\frac{rh-0.55}{0.45}\right)^4 e^{-\frac{E_a}{R}\left(\frac{1}{T}-\frac{1}{T_0}\right)} \quad (3)$$

where K_1, N_1, K_2, K_3 and N_3 are the parameters identified by Parrot and Killoh (Parrot et Killoh 1984) and then adjusted the parameters by Lothenbach et al (Lothenbach, Le Saout, et al. 2008); E_a is an activation energy of adsorption (kJ/mol); αt is the degree of hydration of a cement clinker; rh is the relative humidity; R is the gas constant; surface and reference area (Eq. 1) is normalized to the surface area of the cement which adopted 385 m2/kg based on the experiment taken by Daizel and Gutteridge (Dalziel et al. 1986)) are determined based on the blain value (m^2/g); T and T_0 are the temperature and reference temperature (293.15 K), respectively.

Heat Transfer Model

To determine numerically heat transport in concrete, the 1D and 2D models of heat transfer, Equations (4) and (5) respectively, are used. The mechanism of heat transfer involves the specific heat, density, heat of hydration, and thermal conductivity of concrete, which are functions of the degree of hydration (Maruyama et Igarashi 2015).

$$c_{con}\,\rho_{con}\frac{\partial T}{\partial t} = \lambda_{con}\left(\frac{\partial^2 T}{\partial x^2}\right) + \frac{\partial Q_r}{\partial t} \quad (4)$$

$$c_{con}\,\rho_{con}\frac{\partial T}{\partial t} = \lambda_{con}\left(\frac{\partial^2 T}{\partial x^2} + \frac{\partial^2 T}{\partial y^2}\right) + \frac{\partial Q_r}{\partial t} \quad (5)$$

where c_{con} is specific heat of concrete (J/g·K); ρ_{con} is density of concrete (g/cm3); λ_{con} is thermal conductivity of concrete (W/m·K); and Q_r is heat liberation due to hydration (J). All the thermal properties of concrete can be determined based on degree of hydration.

The compressive strength of concrete at a particular age depends on the type and strength of cement from which it was formed, the type and number of admixtures and additions, the water-to-cement ratio and the environmental conditions, such as temperature and humidity. This work introduces the concept of maturity, which is used to predict the development of compressive strength, based on the temperature history (Ministry of Land, Infrastructure, Transport and Tourism Notification No. 503 2016).

Experimental setting

Simulation Target and Design of the Specimens

In this work, two types of specimen (wall and column specimens) with different ratios of water to binder (W/B) are used to verify the 1D and 2D simulations models in the temperature history and compressive strength. The block specimens are used to simulate the transfer of heat from the cement hydration in wall and column members. The sizes of the block specimens are 1000 mm long by 1000 mm wide by and 250 mm thick. To validate the proposed method, the temperature and compressive strength of the block specimens are investigated. Temperatures are measured using thermocouples at four (for the wall specimens) and seven (for the column specimens) locations on the block specimens. The styrofoam with a thickness of 40 mm is placed around the wall specimens to force most of the heat of cement hydration to be transferred in the thickness direction of the specimens. Styrofoam with a thickness of 40 mm is placed on the top and bottom surfaces of the column specimen to force most of the heat of cement hydration to be transferred in the length and width directions of the specimen. The migration of water around a specimen is prevented by covering it with a large tarpaulin. The specimens are constructed outside at a constant temperature of 20 °C. Fig. 2 schematically depicts the wall specimens and Fig. 3 displays the column specimens. Concrete from a single batch is used to cast the cylindrical specimens (10 × 20cm) that are used in the compressive strength test. Table 1 presents the chemical composition of concrete in these specimens. The specimens include three mixing proportions and their W/B ratios are 0.4, 0.5 and 0.6, respectively. Heat is assumed to be generated by the cement hydration. The FDM is used in this work due to the shape of each specimen. Whereas a 1D model was used to simulate wall and column specimens, a 2D model is proposed herein for use in simulating the heat transfer in a column specimen. In each simulation, the targeted analysis time is set to 28 days and the time interval is set to 0.5 hr. In the spatial domain, to compare the temperatures measured on the position of thermocouples with simulation, the spatial intervals of 0.25 cm in the 1D simulation and 1.0 cm in the 2D simulation. These values of intervals are chosen for the numerical convergence.

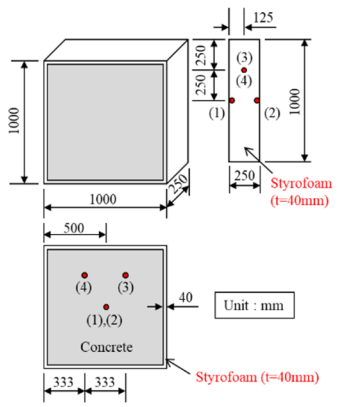

Figure 2. Experimental setup of a wall specimen

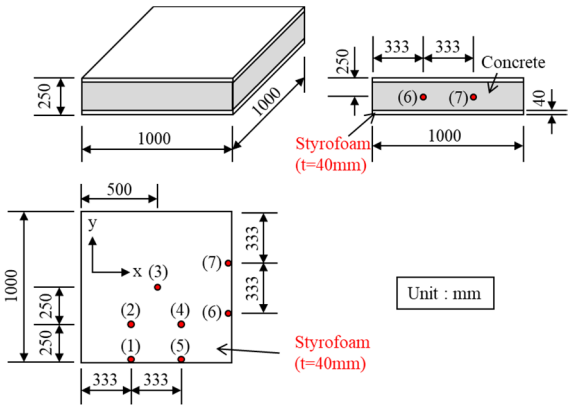

Figure 3. Experimental setup of a wall specimen

Table 1. Coefficients for concrete with different W/B ratios.

W/B	Amount of each material (kg/m^3)								
	Cement (Type I)	Fine aggregates		Coarse aggregate			Water	Slag	Fly ash (Class F)
0.4	197	920		910			158	137.9	59.1
0.5	173	920		910			173	121.1	51.9
0.6	154	920		910			185	107.8	46.2
C_3S	C_2S	C_3A	C_4AF	Free CaO	MgO	SO_3	ρ_{cement} (g/cm^3)		
50%	21%	6%	9%	0.3%	4.3%	2.4%	3.14		

Validation of the proposed method

This section compares the experimental and simulated temperatures and compressive strengths of the wall and column specimens. For the wall specimens, the temperature is simulated based on the 1D model of the heat transfer. Additionally, this work adopts concept of maturity to estimate the compressive strength of concrete and the coefficient s used in calculation (Ministry of Land, Infrastructure, Transport and Tourism Notification No. 503 2016) should be determined by the cement type.

For the column specimens, since the 2D simulation model of the transfer of the heat from the cement hydration is more reasonable than the 1D simulation model, the 2D model is used herein to simulate the development of the compressive strength of concrete. The 2D model considers two directions of heat transfer - x (width direction) and y (depth direction). Fig. 4 shows that the 2D model reduces the difference between the simulated and experimental results from that obtained using the 1D model. To determine the development of the compressive strength of concrete for the column specimens, the experimental results and simulation results obtained using the 1D and 2D models are compared in Fig. 5. The simulation results obtained using the 2D model are much closer to the experimental results than are those obtained using the 1D model. Additionally, the 2D model conservatively predicts the compressive strength of concrete. Therefore, it is more suitable for simulating the development of the compressive strength of a column member.

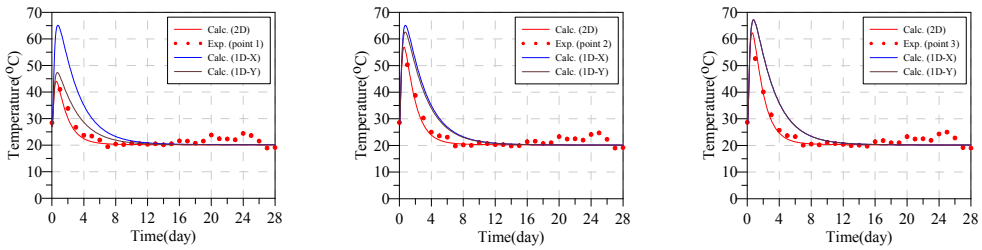

(a) Point 1 (b) Point 2 (c) Point 3

Figure 4. Comparison of the 1D and 2D simulation results of temperature for the column specimens with W/B=0.4

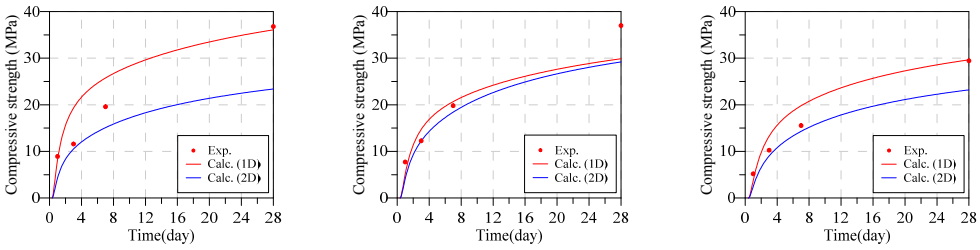

(a) W/C=0.4 (b) W/C=0.5 (c) W/C=0.6

Figure 5. Comparison of the 1D and 2D simulation results of the compressive strength of concrete of the column specimens

Fig. 6 shows comparison results concerning the temperatures of the column specimens, in which the simulation results are obtained using the 2D simulation model. Additionally, Fig. 6 shows that the simulated results for W/B ratios of 0.4 to 0.6 agree closely with the experimental results. However, the simulated temperature still differs from the experimental values and the reasons are speculated as follows: (1) the unconsidered pozzolanic effects on the degree of hydration of cement paste reduces the maximum temperature and the rate of decrease of temperature; (2) the casting time from mixing to the measurement of the starting temperature may also cause some errors in the temperature measurement; (3) the real direction of the heat transfer differs from the assumed direction because the thickness of the styrofoam is insufficient to insulate a specimen completely from the surrounding environment.

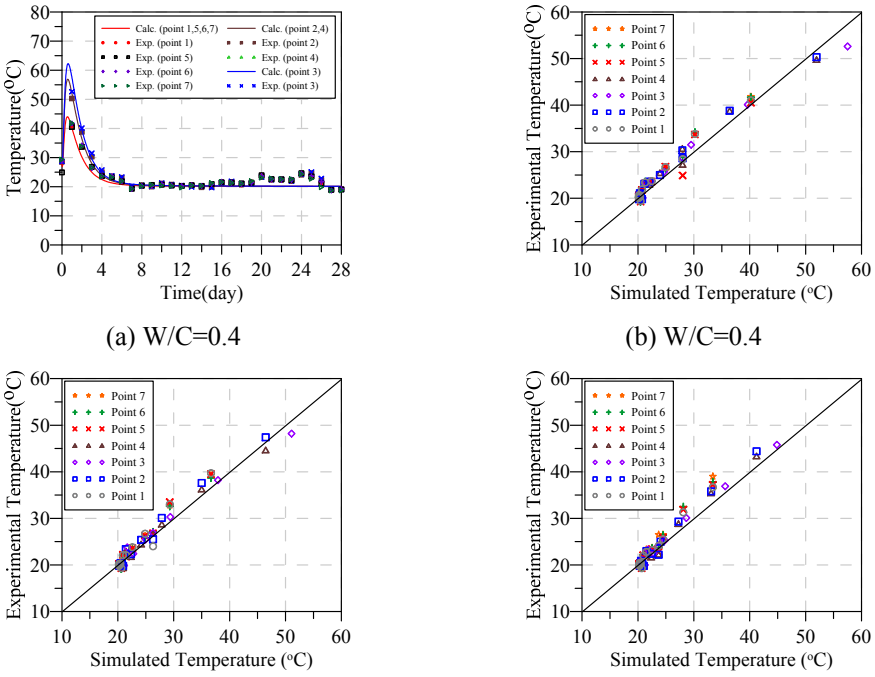

(a) W/C=0.4 (b) W/C=0.4

(c) W/C=0.5 (d) W/C=0.6

Figure 6. Comparison of temperature between the experimental results and the 2D simulation results for the column specimens.

Conclusion

In this work, the proposed method to predict the temperature history and compressive strength of concrete for a column member was built based on the degree of cement hydration and heat transfer in concrete. Additionally, the time-dependent thermal properties that reflect the microstructural properties of concrete were considered in the proposed method based on the previous researches. Based on the verification using the experimental results, it can be said that the proposed method is suitable for the concrete with the OPC and mineral admixtures which include fly ash (replacement ratio of 15 % for cement) and slag (replacement ratio of 35% for cement). Additionally, the proposed method can provide conservative results related to the compressive strength development of the column specimens. Obviously, for the column members, the 2D model was better than the 1D model in the simulation of the heat transfer. In the future, in order to predict temperature history and development of the compressive strength of concrete for various concrete members, the effects of the mineral admixtures on the pozzolanic reaction, hydration and thermal properties should be considered in the proposed method. Furthermore, since water may escape from the concrete surface in the real condition, the moisture transfer in concrete should also be considered in the simulation of the hydration reaction of cement.

References

ACI Committee 228, Report on Methods for Estimating In-Place Concrete Strength (ACI 228.1R-19), Farmington Hills, MI: American Concrete Institute, 2019.

BS 8110, British Standard. Structural use of concrete. Part 1. Code of practice for design and construction. 1997.

IS 456, Indian standard. Plain and reinforced concrete - code of practice. 2000.

Dalziel, J. A., W. A. Gutteridge, Cement, et Association Concrete. 1986. The influence of pulverized-fuel ash upon the hydration characteristics and certain physical properties of a Portland cement paste. Slough: Cement and Concrete Association (C and CA).

Lothenbach, Barbara, Gwenn Le Saout, Emmanuel Gallucci, et Karen Scrivener. 2008. « Influence of limestone on the hydration of Portland cements. » Cement and Concrete Research 38 (6): 848-60. https://doi.org/10.1016/j.cemconres.2008.01.002.

Lothenbach, Barbara, Thomas Matschei, Göril Möschner, et Fred P. Glasser. 2008. « Thermodynamic modelling of the effect of temperature on the hydration and porosity of Portland cement. » Cement and Concrete Research 38 (1): 1-18. https://doi.org/https://doi.org/10.1016/j.cemconres.2007.08.017. https://www.sciencedirect.com/science/article/pii/S0008884607001998.

Maruyama, Ippei, et Go Igarashi. 2015. « Numerical Approach towards Aging Management of Concrete Structures: Material Strength Evaluation in a Massive Concrete Structure under One-Sided Heating. » Journal of Advanced Concrete Technology 13 (11): 500-27. https://doi.org/10.3151/jact.13.500.

Ministry of Land, Infrastructure, Transport and Tourism Notification No. 503. 2016. https://www.mlit.go.jp/notice/noticedata/pdf/201703/00006613.pdf.

Parrot, L. J., et D. C. Killoh. 1984. « Prediction of Cement Hydration. » British Ceramic Proceedings 35: 41-53.

PN-B-06251. 1963. Concrete and reinforced concrete work - Technical specifications (In Polish: Roboty betonowe i żelbetowe -- Wymagania techniczne).

International Symposium on Emerging Developments and Innovative Applications of Reliability Engineering and Risk Managements (EDIARR2022),30 October-3 November2022, Taipei
Chen, S. S. &Ang, Alfredo. H-S. (Editors)

RESILIENCE-CONSIDERED SEISMIC RISK ASSESSMENT AND MITIGATION OF A RETROFITTING METHOD FOR A BRIDGE UNDER MULTIPLE SEISMIC EVENTS

Chiu-Chien Kuo[1], I-Hsiang Liao[1],Santoso Daniel[1] and Eiki Yamaguchi[2]

[1] *Department of Civil and Construction Engineering, National Taiwan University of Science and Technology, Taipei, R.O.C Taiwan*

[2] *Department of Civil Engineering, Kyushu Institute of Technology, Kitakyushu, Japan*

E-mail: miloou594@gmail.com (I.-H. Liao)

Abstract: For determining an appropriate retrofitting method for a bridge structure based on economy, this work proposes an annual-expected resilience index for a bridge to simulate the resilience-considered seismic risk that is caused by multiple seismic events in a given period. Along with the direct costs, the resilience-considered indirect costs are also included in the seismic risk and benefit–cost ratio to determine an appropriate retrofitting strategy for a bridge structure. In this work, a bridge in Taipei is used as an example of the application of the proposed quantification method to determine a retrofitting method with economy based on the resilience-considered benefit–cost ratio.

***Keywords*:** Resilience, seismic risk, benefit-cost ratio, bridge, retrofit.

Introduction

In Taiwan, Taiwan Bridge Management System (TBMS) has been operated over 15 years and has an inventory of over 30,000 bridges. Many bridges must be seismically retrofitted to prevent serious damage and to maintain the functional serviceability of routes for emergency disaster relief after large earthquakes. However, since the seismic performance of a bridge structure is one of its most important characteristics and must be considered in any bridge evaluation with a view to developing an effective retrofitting strategy, this work focuses on the seismic retrofitting of bridge structures. Additionally, because of the limited budget of the maintenance or retrofitting work for bridge structures, not only effectiveness but also the economy should be considered in the determination of the retrofitting strategy. Therefore, the benefit-cost of a retrofitting method for a retrofit-required bridge structure is a common useful index in the maintenance management of aging bridge structures in Taiwan.

In Taiwan Seismic Performance Assessment and Retrofit Manual for Highway Bridges (NCREE, 2009), nonlinear static analysis (pushover analysis) is adopted to assess the seismic performance of a bridge. The specified components/members, which include those of the foundation, the capping beam, the bearing pad, and those of the unseating prevention device of the bridge are inspected to ensure that they have their required capacities under various seismic intensities (effective peak accelerations, EPAs). The method for retrofitting a bridge in Taiwan is currently determined by the seismic performance of its columns and the performance of each specified component/member, which are evaluated by inspection. However, even if each inspection yields satisfactory results, the uncertainty in the capacity of each specified component/member is neglected. Therefore, Chiu et al. (2020) developed a procedure for estimating the seismic reliability of the system for a bridge considering the seismic reliability of each specified component/member. Following the research conducted in Chiu et al. (2020), this work adopts the seismic reliability of

the system for a bridge in the seismic risk assessment and mitigation for a retrofitting method. In practice, a retrofitting method is determined only by the seismic performance requirements and corresponding direct costs in Taiwan. However, in many retrofitting cases, the indirect costs or social impacts of potential retrofitting methods, which probably affect the selected retrofitting strategy, are not quantified or even considered. Therefore, the benefit-cost ratio of a retrofitting method should be calculated considering the direct/indirect costs of the method.

For bridges and bridge networks under single and multiple hazards, Banerjee et al. (2019) presented a systematic and comprehensive review of resilience assessment. Generally, resilience of a bridge under an earthquake can be quantified from the normalized area under the functionality curve between time of occurrence of the seismic event and a time instant. Previous studies (Bocchini et al. (2014), Karamlou (2017) and Frangopol and Dong (2014)) observed that resilience significantly depends on the residual functionality of bridges after an earthquake event and the process of post-event functionality recovery over time. Additionally, they also proposed the corresponding models to quantify the resilience. Based on the research conducted by Bocchini et. al. (2014), a resilience assessment as part of a retrofit strategy for an existing bridge significantly influences the overall benefit that is provided by the retrofit.

Restated, for a bridge under an earthquake, since a retrofitting method would also affect its residual functionality and the recovery time of its functionality, the resilience effect of a retrofitting method for the bridge should be quantified and included in the indirect costs.

According to ACI 364.1R-07 (ACI, 2007), for projects with rehabilitation alternatives that have differing and significant future costs, those rehabilitation alternatives should be evaluated using economic evaluation methods. Recently, life-cycle cost (LCC) has become widely used as a reference index for evaluating the economic effectiveness of an alternative. Generally, LCC is the sum of the specified costs that are incurred during the evaluation period and it is expressed in equivalent terms (often present value) by adjusting future costs using an estimated inflation rate and a selected discount rate that reflects the time-value of money. Vishwanath and Banerjee (2019) proposed a quantitative framework to assess life-cycle resilience of deteriorating reinforced concrete (RC) bridges under seismic ground motion. However, Vishwanath and Banerjee (2019) only simulated the aging or deteriorating effect on the seismic resilience for a bridge under a specified intensity of an earthquake event. Since the main purpose of this work is to develop a seismic risk assessment method for determining an appropriate retrofitting method with economy, the direct/indirect costs that are induced by earthquake in a given period, which are defined as the seismic risk herein, rather than LCC, are the main topic in this work. Additionally, instead of one earthquake event in a specified period, this work adopts the Poisson process to simulate the multiple seismic events for estimating the seismic risk and benefit-cost ratio of a retrofitting method.

For the main purpose stated above, this work proposes an annual expected resilience index for a bridge that can be used to simulate the resilience-considered seismic risk that are caused by multiple seismic events in a given period using the method for determining the relationship between the resilience index and seismic intensity that was proposed by Chiu et al. (2020). Along with the direct costs, the resilience-considered indirect costs are also included in the seismic risk and benefit-cost ratio to develop an appropriate retrofitting strategy with economy for a bridge structure. Additionally, instead of one seismic event, this work simulates multiple seismic events

that would damage the bridge in a specified period based on the seismic hazard curve to do the resilience-considered seismic risk and benefit-cost ratio analyses. In order to consider the uncertainty of the occurring time of a seismic event, the Monte Carlo Simulation (MCS) is adopted to calculated the seismic risk in this work. Finally, a bridge in Taipei is used as an example of the application of the proposed quantification analysis of the resilience-considered benefit-cost ratio to determine an appropriate retrofitting method with economy.

Literature Review

Life-cycle Cost Analysis (LCC analysis)

ACI 365.1R-17: Report on Service-Life Prediction (ACI, 2017) presents detailed economic evaluation and service life models. The report (ACI, 2017) recognized LCC analysis as an important technique for supporting investment decisions related to the selection of the most cost-effective design/rehabilitation option from a set of competing alternatives. The use of LCC to select the optimal option overcomes the limitations of the initial cost-based selection approach. It also allows the consistent inclusion of the cost of monitoring the structure, which can lead to proactive repairs, lowering long-term costs. LCC analysis is based on the concept of the time value of money, which refers to the fact that a dollar spent in the future is worth less than a dollar in present value terms because that dollar can be invested so that its value in the future would be greater in real terms, even after inflation has been accounted for. Converting future expenditures to present value cost by discounting enables the comparison two or more alternative designs with different expenditures at different times in their respective service lives. Based on this simple investment principle, ACI 365.1R-17 (ACI, 2017) presents a function that relates present value cost to its corresponding future value. Considering the effect of inflation and currency interest rate, the net present value method can be applied to correct the cost for each year. according to Eq. (1). ACI 365.1R-17 (ACI, 2017) expresses the LCC as Eq. (2).

$$m(t)=\frac{1}{(1+k)^t} \tag{1}$$

where k is the parameter that considers the rates such as inflation and currency interest rates, and t is the year that is considered in the analysis.

$$LCC=DC+CC+IMC+RRC+UC\pm RV \tag{2}$$

where DC is the design cost, CC is the construction cost, IMC is the inspection and maintenance cost, RRC is the repair and rehabilitation cost, UC is the user cost and RV is the residual or salvage cost.

In this work, various methods for retrofitting bridges are economically compared by focusing the earthquake-induced direct and indirect costs that were originally included in RRC and UC rather than LCC. The following section defines these terms.

Direct and Indirect Costs under an Earthquake

Damage that is caused by various seismic events can be quantified by considering their intensities to obtain their total expected cost including direct and indirect costs. Direct costs are the

sums of losses that occur in various damage states of a bridge system under the influence of seismic forces, and are typically expressed in monetary units. According to Bocchini et al. (2014), direct costs are calculated using Eq. (3).

$$C_{sd}=P_s \cdot C_c \cdot \left(\sum_{i=1}^{5} P_i \cdot D_i\right) \tag{3}$$

where C_{sd} is the expected direct cost under an earthquake event, P_s is the occurrence probability of an earthquake event, C_c is the construction cost of a bridge, i is the damage state of a bridge (1, 2, 3, 4, 5 represent the various damage states from non-damage to complete or total damage), P_i is the occurrence probability under the damage state of i, D_i is the loss ratio of the damage state of i.

Indirect costs refer to losses that are caused by a decline in functionality of a bridge, expressed in terms of vehicle flow capacity. According to the previous research (Hsu, 2014), these costs include accident-related costs, travel delay-related cost, and vehicle operating costs. Additionally, in order to consider the resilience effect on the costs, this work adopts the calculation includes the resilience index based on the research conducted by Liao (2017).

Benefit-cost Ratio

Many decision situations involve multiple hazards and potential failure scenarios. For cases that involve several possible consequent scenarios, the risk associated with each can be evaluated as the product of the corresponding consequence and their probabilities, and the results can be summed to yield the total risk. If the total risk is unacceptable, then mitigating actions should be considered to reduce it. Justification for such actions can be based on a benefit-cost analysis. The costs in such a case are those associated with mitigation actions. The benefits of such associated with mitigation actions can be classified as follows: (1) Reduction in the number of severe accidents, fatalities, and injuries, and reduction in property and environmental losses; (2) Reduction in the numbers of incidents (minor accidents) and consequently injuries, and reduction in property and environmental losses; (3) Reduction in the numbers of incidents and accident precursors, errors and deviations, and equipment failures, and reduction in property and environmental losses, and so on; (4) Secondary and tertiary benefits as a result of intangibles. Benefit assessment sometimes requires the development and use of categories of products and users to obtain meaningful results (Ayyub, 2014). Ayyub (2014) stated that the present value of the incremental costs and benefits of alternative methods of risk mitigation or system design can be compared. Several methods for determining which, if any, option is most worth pursuing. In some cases, no alternative generates a net benefit relative to the base case. Such a finding would be used to argue for the pursuit of the base case scenario. Benefit-cost ratio, which can be computed using Eq. (4), is one of the most widely used methods of comparing present values. Additionally, the ratio >1 is indicated a desirable retrofitting investment. Generally, a larger ratio corresponds to more effective mitigation. Accounting for the time value of money would require defining the benefit-to-cost ratio as the present value of benefits divided by the present value of costs. The benefit-cost ratio ($R_{B/C}$) can then be calculated as in Eq. (5), which can be simplified to yield $m_B(t)$ and $m_C(t)$ by utilizing Eq. (1).

$$R_{B/C}=\frac{B}{C}=\frac{\text{unmitigated risk}-\text{mitigated risk}}{\text{cost of a mitigation action}} \tag{4}$$

$$\frac{B}{C}=\frac{\sum\frac{B}{(1+k)^t}}{\sum\frac{C}{(1+k)^t}}=\frac{\sum(B\times m_B(t))}{\sum(C\times m_C(t))} \tag{5}$$

where B is the benefit value, C is the cost value, $m_B(t)$ is the net present value coefficient of the benefit and $m_C(t)$ is the net present value coefficient of the cost.

Ayyub (2015) performed a benefit-cost analysis to evaluate the benefits of a bridge retrofit. He used risk analysis and risk management to improve the bridge resilience by reducing related direct and indirect costs. He assumed that benefit (B) and cost (C) were normally distributed variables, and calculated the reliability index ($\beta_{B/C}$) and the exceedance probability of a benefit-cost ratio using Eqs. (6) and (7).

$$\beta_{B/C}=\frac{\mu_B-\mu_C}{\sqrt{\sigma_B{}^2+\sigma_C{}^2}} \tag{6}$$

$$P_{f,B/C}=P(C>B)=1-\Phi(\beta_{B/C}) \tag{7}$$

where the mean value and standard deviation of benefit are denoted as μ_B and σ_B respectively; the mean value and standard deviation of cost are denoted as μ_C and σ_C respectively.

Based on the literature review stated above, this work adopts the resilience-considered benefit-cost ratio to determine an appropriate retrofitting method with economy for a bridge under multiple seismic events.

Seismic Reliability and Resilience Index

Seismic Reliability Analysis

According to Chiu et al. (2020), in determining the seismic performance of a bridge, not only the bridge columns but also the components/members of the superstructure and foundation must be considered. Additionally, Table 1 presents the specified members/components of a bridge that should be considered in the system reliability analysis and their methods of damage identification. In the system reliability method that was proposed by Zhao and Lu (2016), a limit state surface is a multi-planar surface that is used to define the boundary of system failure in terms of the system variables. When the limit state functions have been defined, their moment properties can be used to evaluate the reliability of the system. For simple limit state functions, such as a linear summation or the product of independent random variables, a direct estimation method can be used to calculate the moment values. However, for a complicated and implicit limit state function, a point estimation method is more convenient than a direct estimation method for calculating moment values. This work adopt the limit state function and point estimation from Zhao and Lu (2016). For a bridge, the third-moment-based system reliability analysis is used herein to estimate the probability of occurrence of each damage state, which is defined in Table 1, under a specified seismic intensity. Moreover, the curve of the relationship between the probability of occurrence of a specified damage state and seismic intensity can be plotted to estimate the direct cost (Eq. (3)) and resilience index.

Table 1. Damage state definition of bridge for the system reliability analysis (Chiu, Yamaguchi, and Santoso 2020).

No.	Item	No damage	Slight	Moderate	Extensive	Complete
1	Unseating prevention					✓(II)
2	Shear of bearing			✓(II)	✓(III)	
3	Shear of capping beam				✓(II)	✓(III)
4	Moment of capping beam			✓(II)	✓(III)	
5	Column stability					✓(II)
6	Angle of a pile					✓(II)
7	Displacement of a pile					✓(II)
8	Moment of a pile				✓(II)	✓(III)
9	Shear of a pile				✓(II)	✓(III)
10	Pullout force of a pile				✓(II)	✓(III)
11	Axial force of a pile				✓(II)	✓(III)
12	Column					

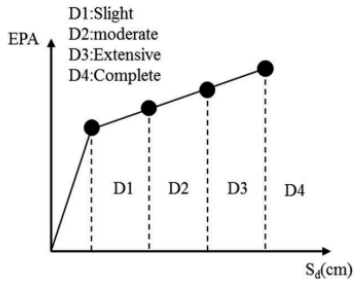

Resilience Analysis and Resilience Index

For a bridge, resilience is an indicator of its ability to recover functionality from a damaged state. Based on the definitions of resilience that were compiled by Karamlou (2017), it can be evaluated from post-disaster residual functionality and the recovery curve or the rate of recovery of that functionality, as plotted in Fig. 1. Equation (8) is used herein to evaluate the resilience index, R, that is realized using various retrofitting strategies; this index influences the indirect cost.

$$R = \frac{\int_{t_0}^{t_r} Q(t)dt}{t_r - t_0} \times 100\% \tag{8}$$

Since the residual functionality of a bridge varies with its damage state, the losses of functionality in all damage states that were identified by Frangopol and Dong (2014) are compiled herein (Table 2). Since the required time to repair each component/member is uncertain, the suggestion of Chiu et al. (2020) is adopted to calculate the expected number of days to repair a bridge in a specified damage state. Additionally, for each damage state of a bridge (Table 3), a work sequence for repair is also considered to determine the number of days required for repair based on the calculation procedure that was suggested by Chiu et al. (2020).

Table 2. Post-disaster residual functionality of bridge (Frangopol and Dong 2014)

Damage condition	Description	Functionality	The functionality of this study
No damage	Immediate access	$>90\%$	100%
Slight	Weight restriction	$90\% - 60\%$	75%
Moderate	Half of lanes open	$60\% - 40\%$	50%
Extensive	Emergency access only	$40\% - 10\%$	25%
Complete	Bridge closed	$\leq 10\%$	0%

Table 3. Components/members included in each damage state of bridge (Chiu,Yamaguchi, and Santoso 2020).

Bridge damage state	Components/members
Slight	Capping beam ∪ Column
Moderate	Capping beam ∪ Column ∪ Bearing
Extensive	Capping beam ∪ Column ∪ Bearing ∪ Pile
Complete	Capping beam ∪ Column ∪ Bearing ∪ Pile

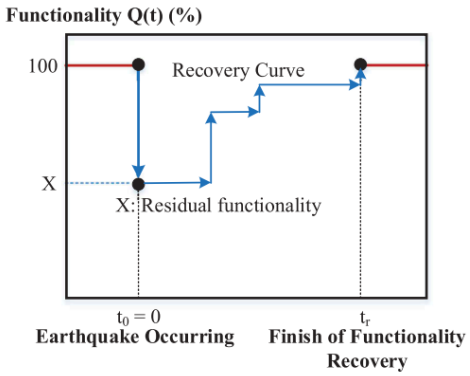

Figure 2. Recovery curve of functionality for a bridge under the repair (Chiu, Yamaguchi, and Santoso 2020)

The recovery curve of the functionality of a damaged bridge can be plotted from the probability of occurrence of each damage state and the number of days required to repair in each state, as recommended by Bocchini et al. (2014) and shown in Fig. 2. To compare retrofitting methods, a recovery curve of the functionality over a year is calculated; this curve can be called an annual recovery curve of the functionality. The deterioration of the bridge structure is neglected so the structure has a functionality of 100 % before a seismic event and after repair. By the above calculation for a retrofitting method, the curve of the relationship between the resilience index, R, and seismic intensity, EPA, can be built. In lifetime cost analysis, the annual seismic hazard curve is used to transform the relationship curve of the EPA and the resilience index (R-EPA curve) into a curve of the relationship between the resilience index and the exceedance probability of EPA, allowing the annual expected indirect cost to be estimated.

Evaluation of Benefit-Cost Ratio for a Retrofitting Method

Annual expected resilience index of a bridge

The indirect costs of work to recover the functionality of a bridge are strongly correlated with its resilience. Restated, if retrofitting work can improve the resilience of a bridge, then the indirect costs that are induced by a seismic event are reduced. According to Chiu et al. (2020), annual expected indirect costs can be calculated from the annual expected resilience index of the bridge. Moreover, the resilience index at each seismic intensity can be estimated from the annual recovery curve of the functionality and is called the annual resilience index of a seismic intensity. The calculation procedure is shown in Chiu et al. (2020). For the cost analysis of a bridge, this work considers only the effect of various seismic events in a given period and neglects the effect of material deterioration of the bridge. Restated, based on Eq. (2), this work considers the direct costs

(DC and CC), indirect costs (US) and retrofitting cost (IMC and PRC) that are associated with the seismic events in the cost analysis of a bridge. Moreover, the specified costs in a given period are transformed to their net present values by applying the discount rate as in Eq. (1).

Monte-Carlo Simulation (MCS) is used to simulate the number of seismic events and the times at which they occur in a specified period. Chiu (2014) noted that some recent models in simulations of events of large magnitudes have assumed a log-normal or Weibull distribution of return periods, whose hazard functions are time-dependent. The number of occurrences in a given period depends on the time of occurrence of the last event. However, in providing statistical evidence of a seismic gap and a typical earthquake hypothesis, engineers commonly have difficulty in using simulation models that correspond to log-normal or Weibull distributions of return periods to estimate the number of earthquake occurrences in a period. For convenience, earthquake occurrences in a specified period are simulated using the Poisson process. Chiu (2014) assumes that earthquakes follow a Poisson process with a mean rate that is appropriate for the region. Only one seismic event is assumed to occur in one year because the indirect and direct costs are estimated using the annual seismic hazard curve. Based on the times of occurrence of the simulated seismic events, the corresponding direct costs and indirect costs can be transformed into net present values and their summation is defined as the seismic risk in this work. Equation (9) provides the benefit of the retrofitting work on the bridge, which is defined as the difference between the seismic risk to the bridge before and after the retrofitting work (LC_N and LC_R). Considering the retrofitting cost, the benefit-cost ratio for a retrofit can be calculated using Eq. (9).

$$R_{B/C} = \frac{LC_N - LC_R}{C_{sr}} \tag{9}$$

where C_{sr} is the retrofit cost; LC_N is the seismic risk of a bridge without any retrofit; LC_R is the seismic risk of a bridge with the retrofitting work.

Case Study

This work selects a bridge in Beitou District of Taipei City, Taiwan, bridge to do the case study. It is in seismic micro-zone Taipei Zone 1 through which no faults pass; the design specifications are from the years 1960 and 1987 (Table 4). According to the TBMS database, the total length of the bridge is 250 m and its daily average traffic flow is 10,000 vehicles (ADT). According to the map, the shortest substitute driving distance is 1.35 km. The superstructure comprises steel I-beams and has a width of 32.5 m; the substructure is a double-column frame-type circular reinforced concrete pier with 86.4 cm φ steel pipe piles. Figure 3 presents the results of a pushover analysis of the bridge without any retrofitting in the direction of (X-direction) and perpendicular to the direction of (Y-direction) vehicular travel.

Table 4. Seismic performance requirements for important bridges (NCREES, 2009).

	Design specification(important bridge = 1.2)		
Seismic level	1995 & 2000 years	1960 &1987 years	<1960 years
Level I (Small or medium earthquake)	PLA	PLA	PLA
Level II (Earthquake with a return period of 475 years)	PLB	PLC	PLC

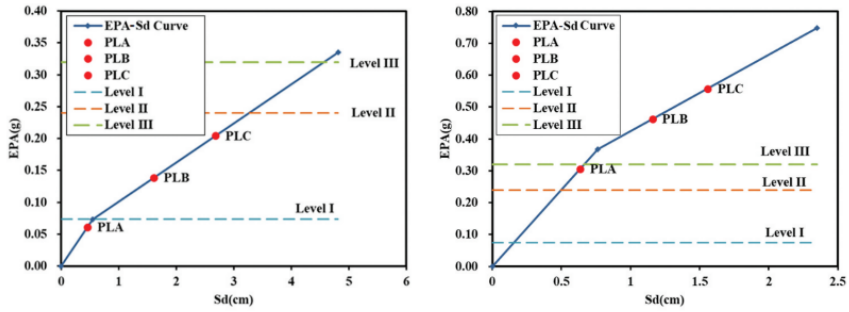

(a) X-direction (b) Y-direction

Figure 3. EPA_s-S_d curves of the targeted bridge without any retrofitting.

Since the bridge does not satisfy the seismic requirements provided in the reference (National Center for Research on Earthquake Engineering 2009), a seismic retrofit is required to ensure its safety and serviceability. Therefore, six retrofitting methods that were proposed by Liao (2017) are used herein to improve column ductility or strength for the bridge (Table 5). Additionally, Liao (2017) also provided the detailed design of each retrofitting method. The method for retrofitting a bridge in Taiwan is currently determined by the seismic performance of its columns and the performance of each specified component/member, which are evaluated by inspection.

Table 5. Retrofitting methods of a bridge (Chiu, Yamaguchi, and Santoso 2020; Liao (2017)).

Retrofitting method	Detail	Description
RCJ1-1 (RC Jacketing)	*LB:D32@30 cm **S:D16@15 cm	Minimum requirements based on JBEC (2005)
RCJ1-2	LB:D32@30 cm S:D22@10 cm	Improve ductility from RCJ1-1
RCJ2-1	LB:D32@15 cm S:D16@15 cm	Improve strength from RCJ1-1
RCJ2-2	LB:D32@15 cm S:D22@10 cm	Both improve strength and ductility from RCJ1-1
SPJ-6 (SP Jacketing)	Plate thickness 6 mm	Minimum requirements based on JBEC (2005)
SPJ-12	Plate thickness 12 mm	Maximum requirements based on JBEC (2005)

*LB: Longitudinal Bar **S: Stirrup

This work follows Liao (2017) in calculating the costs associated with all retrofitting methods. Moreover, Liao (2017) showed that the cost of retrofitting should be calculated with consideration of the costs of material, labor and machine used. However, the labor and machine costs are must less easy to calculate than the material cost. Therefore, as suggested by Liao (2017), the total labor and machine cost is taken to be 60 % of the material cost for each retrofitting method.

Table 6 provides the benefit-cost ratios for each retrofitting method with the discount rates of 0 % and 3 % and an annual mean number of earthquakes of 0.2/year. Even if the variation among the values of the resilience index that are associated with various retrofitting methods is small, it nevertheless significantly influences the annual expected indirect costs and seismic risk. Based on the annual expected resilience index and cost of retrofitting, SPJ-6 is recommended for the targeted bridge. However, if the seismic risk, including the direct and indirect costs, in a specified period is paramount, then RCJ2-2 is preferred. Although the cost of retrofitting using RCJ1-1 is higher than

that using SPJ-6, the former reduces the seismic risk more effectively. Since the benefit-cost evaluation importantly supports investment decisions regarding the selection of the most cost-effective design/rehabilitation option from a set of competing alternatives, RCJ1-1, which has the highest benefit-cost ratio, is the best choice, based on the benefit-cost ratios that are provided in Table 6. Therefore, the proposed procedure for calculating the resilience-relevant benefit-cost ratio is a cost-effective way to determine the best retrofitting method for a bridge.

Table 6. Benefit–cost ratio of each retrofitting method for the targeted bridge ($\lambda = 0.2$/year).

Retrofitting method	k = 0%	k = 3%
RCJ1-1	5.75	2.96
RCJ1-2	5.47	2.81
RCJ2-1	5.41	2.79
RCJ2-2	5.32	2.76
SPJ-6	3.56	1.89
SPJ-12	4.11	2.14

Conclusion

Generally, for a damaged bridge, because of the daily transportation requirement, its corresponding functionality would be recovered gradually during the rehabilitation period. Restated, the timedependent functionality during the rehabilitation period should be considered in the estimation of the indirect costs. For the indirect costs, this work considers the function recovery during the retrofitting/repairing period, which is quantified using the resilience index. Additionally, instead of one earthquake event in a specified period, this work adopts the Poisson process to simulate the multiple seismic events for estimating the seismic risk and benefit–cost ratio of a retrofitting method. Therefore, the novelty of this work is to propose a resilience-considered seismic risk assessment method for determining an appropriate retrofitting method with economy. Additionally, the direct/indirect costs that are induced by earthquake in a given period, which are defined as the seismic risk herein, rather than LCC, are also included in the benefit–cost ratio of a retrofitting method. From the case study, even if the variation among values of the resilience index that are associated with various retrofitting methods is small, it nevertheless significantly influences the annual expected indirect costs and seismic risk. Although the cost of retrofitting method RCJ1-1 is higher than that of SPJ-6, the former reduces the seismic risk more effectively and it yields the highest benefit–cost ratio among all of the considered retrofitting methods. Therefore, the benefit-cost evaluation is important in supporting investment decisions regarding the selection of the most cost-effective design/rehabilitation option from a set of competing alternatives. Although the case study of this work excludes the corrosion effect on the seismic reliability analysis, the proposed method of the seismic risk assessment herein can still be used for a bridge, which may be corroded by the airborne chloride. Additionally, the authors have proposed a model that can be used to estimated seismic reliability analysis for a corroded bridge in the reference (Chiu 2014). Restated, according to the proposed the seismic risk assessment in this work and the model of the reference (Chiu 2014), for a corroded bridge, an appropriate retrofitting method can be determined based on the benefit–cost ratio.

References

ACI Committee 364, (2007), "Guidance for Evaluation of Concrete Structures Before Rehabilitation; ACI 364.1R-07", American Concrete Institute, Farmington Hills, US.

ACI Committee 365, (2017), "Report on Service Life Prediction; ACI 365.1R-17". American Concrete Institute, Farmington Hills, US.

Ayyub, B. M., (2014), "Risk analysis in engineering and economics", 2nd Edition, Chapman & Hall/CRC, Boca Raton, FL.

Ayyub, B. M., (2015), "Practical Resilience Metrics for Planning, Design, and Decision Making," American Society of Civil Engineering, US.

Banerjee, S., B. S. Vishwanath, and D. K. Devendiran, (2019), "Multihazard resilience of highway bridges and bridge networks: a review", Structure and Infrastructure Engineering: Maintenance, Management, Life-Cycle Design and Performance, Vol. 15, Issue 12, pp. 1694-1714.

Bocchini, P., Frangopol, D, Ummenhofer, T., and Zinke, T., (2014), "Resilience and Sustainability of Civil Infrastructure: Toward a Unified Approach", Journal of Infrastructure System, Vol. 20, Issue 2, American Society of Civil Engineers.

Chiu, C. K., (2014), "Reliability-based service life assessment for deteriorating reinforced concrete buildings considering the effect of cumulative damage", Structure and Infrastructure Engineering: Maintenance, Management, Life-Cycle Design and Performance, Vol. 10, Issue 9, pp. 1101-1118.

Chiu, C.K., Yamaguchi, E., Santoso, D. (2020), "Seismic resilience analysis of a retrofit-required bridge considering moment based system reliability", Structure and Infrastructure Engineering: Maintenance, Management, Life-Cycle Design and Performance, DOI: 10.1080/15732479.2020.1767658

Frangopol, D and Dong,Y., (2014), "Risk and resilience assessment of bridges under mainshock and aftershocks incorporating uncertainties", Engineering Structures, Elsevier, Vol. 83, pp. 198-208.

Hsu, Z. L., (2014), "Group Bridges Life Cycle Maintenance Strategy Optimization Model", Master Thesis, Department of Civil and Construction Engineering, National Taiwan University of Science and Technology.

Japan Bridge Engineering Center. (2005). Examples of Seismic Retrofitting Construction Methods for Existing Bridges. Tokyo, Japan: Japan Bridge Engineering Center.

Karamlou, A., (2017), "Multi-Scale Methodologies for Probabilistic Resilience Assessment and Enhancement of Bridges and Transportation Systems", Published doctoral dissertation, Lehigh University, US.

Liao, I. H., (2017)," Benefit-Cost Ratio Analysis of Retrofit Strategies for Bridges Considering the Resilience Effect", Master Thesis, Department of Civil and Construction Engineering, National Taiwan University of Science and Technology.

National Center for Research on Earthquake Engineering, (2009), "Seismic Performance Assessment and Retrofitting Manual for Highway Bridges", National Center for Research on Earthquake Engineering, Taiwan.

Vishwanath, S. B. and Banerjee, S., (2019), "Life-cycle resilience of aging bridges under earthquakes, Journal of Bridge Engineering (ASCE), Vol. 24, Issue 11, 04019106.

Zhao, Y. G., and Lu, Z. H., (2016), "Methods of Moment for Structural Reliability", pp236-238

International Symposium on Emerging Developments and Innovative Applications of Reliability Engineering and Risk Managements (EDIARR2022),30 October-3 November2022, Taipei
Chen, S. S. &Ang, Alfredo. H-S. (Editors)

RELIABILITY-REDUNDANCY-RECOVERABILITY-BASED DECISION OPTIMIZATION (R3-DO) FOR RESILIENT STRUCTURAL SYSTEMS

Seonghyun Lim[1], Jungho Kim[2], and Junho Song[3]

[1] *Department of Civil and Environmental Engineering, Seoul National University, Seoul, South Korea*

E-mail: euler1707@snu.ac.kr

[2] *Department of Civil and Environmental Engineering, Seoul National University, Seoul, South Korea*

E-mail: cong020@snu.ac.kr

[3] *Department of Civil and Environmental Engineering, Seoul National University, Seoul, South Korea*

E-mail: junhosong@snu.ac.kr

Abstract: To achieve a sufficient level of disaster resilience based on a holistic understanding of the system-level risk, the concept of system-reliability-based disaster resilience was recently proposed. The proposed framework characterizes the disaster resilience of a civil infrastructure system by evaluating the capabilities of the components, system, and society by the three criteria: reliability, redundancy, and recoverability. The risk of structural system failure caused by each initial disruption scenario can be evaluated systematically by the reliability-redundancy diagram. This study proposes reliability-redundancy-recoverability-based decision optimization (R3-DO) to facilitate decision-making using the system-reliability-based disaster resilience framework. R3-DO aims to optimize the cost function representing recoverability while satisfying the probabilistic constraints defined by the reliability-redundancy analysis. The matrix-based systems reliability method (MSR) is employed to derive the design parameter sensitivities of the resilience criteria. Using R3-DO, one can maximize recoverability while managing the system-level risk at a socially acceptable level. A numerical example of a ten-member-truss system is introduced to test the applicability of the proposed R3-DO method.

***Keywords*:** system reliability, disaster resilience, decision optimization, reliability, redundancy, recoverability.

Introduction

The concept of disaster resilience has recently emerged with increasing interest for a comprehensive understanding of the risk civil infrastructure systems face under various hazards. In the structural engineering field, disaster resilience is usually characterized by the functionality curve proposed by Bruneau et al. (2003), which degrades as a disaster occurs and gradually recovers from the damage. The resilience is often quantified by the amount of functionality degradation, a decreasing slope of functionality right after the disaster, and recovery time to the original state. However, there is a lack of discussion regarding system reliability, which is a critical aspect to consider for a comprehensive understanding of the resilience of structural systems consisting of many interconnected components.

Recently, Lim et al. (2022) proposed a system-reliability-based disaster resilience framework for three scales of civil infrastructure systems, i.e., individual structures, infrastructure networks, and urban communities. The framework evaluates the resilience of components, systems, and society in terms of three criteria, i.e., reliability, redundancy, and recoverability, to ensure a socially acceptable level of resilience. The proposed reliability (β) and redundancy (π) indices and their

corresponding resilience assessment method, i.e., β–π analysis, enable us to check if the system-level risks caused by initial disruption scenarios are socially acceptable. This paper extends the applicability of the proposed disaster resilience framework to optimization problems to support the risk-informed decision-making process regarding the design or retrofits of structural systems.

This paper first presents the concepts of the system-reliability-based disaster resilience framework with three disaster resilience criteria. Next, reliability-redundancy-recoverability-based decision optimization (R3-DO) will be introduced to facilitate applications to the decision-making process. Then, details of the proposed R3-DO will be explained in terms of the cost function, probabilistic constraints defined by the reliability-redundancy analysis, and design parameter sensitivities of the corresponding indices obtained by the matrix-based system reliability (MSR) method. A numerical example of a truss system will be provided to demonstrate the applicability and performance of the proposed R3-DO framework. The paper concludes with a summary.

System-Reliability-Based Disaster Resilience Framework

A system-reliability-based disaster resilience framework was proposed to characterize the disaster resilience of a civil infrastructure system in terms of three criteria, i.e., reliability, redundancy, and recoverability (Lim et al., 2022). The three criteria represent the capabilities of the components, system, and society to ensure a proper level of disaster resilience. Figure 1 illustrates the three criteria using a ball near a cliff representing a civil infrastructure system that could fall to the cliff due to external hazards. The reliability (red wall) is the ability of the components to avoid initial disruptions during disastrous events. The redundancy (blue wall) is the capability of the system to prevent further system-level failure despite the given initial disruption. Finally, recoverability (yellow arrows) is the ability to restore the system from damage to its original state. In the proposed R3-DO method, "local recovery" refers to the recovery from a component-level-failure state (shorter arrow). In comparison, "global recovery" is the restoration from a system-level-failure state (longer arrow).

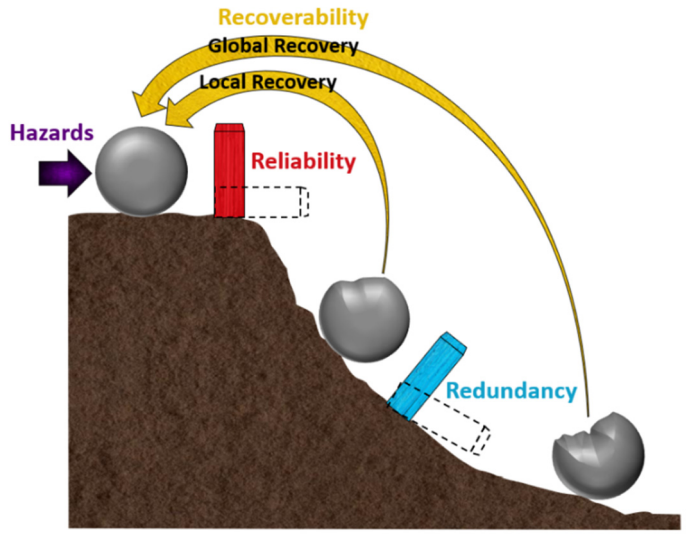

Figure 1. Three criteria of system-reliability-based disaster resilience framework (modified from Lim et al. (2022))

Among the three criteria, the reliability (β) and redundancy (π) indices are defined as

$$\beta_{i,j} = -\Phi^{-1}\left(P\left(F_i \middle| H_j\right)\right) \tag{1a}$$

$$\pi_{i,j} = -\Phi^{-1}\left(P\left(F_{sys} \middle| F_i, H_j\right)\right) \tag{1b}$$

where $\Phi^{-1}(\cdot)$ denotes the inverse cumulative distribution function of the standard normal distribution, F_i is the i-th initial disruption scenario, H_j is the j-th hazard, and F_{sys} is the system failure event. According to Eq. (1), β and π can be calculated by component and system reliability methods, respectively, for each initial disruption scenario. By multiplying the two conditional probabilities $P\left(F_i \middle| H_j\right)$ and $P\left(F_{sys} \middle| F_i, H_j\right)$, the annual system failure probability induced by i-th disruption scenario and j-th hazard, $P\left(F_{sys,i,j}\right)$ is derived in terms of β and π as

$$P\left(F_{sys,i,j}\right) = P\left(F_{sys,i,j} | H_j\right)\lambda_{H_j} = P\left(F_{sys} \middle| F_i, H_j\right)P\left(F_i \middle| H_j\right)\lambda_{H_j} = \Phi\left(-\pi_{i,j}\right)\Phi\left(-\beta_{i,j}\right)\lambda_{H_j} \tag{2}$$

where λ_{H_j} denotes the occurrence rate of the j-th hazard. One can determine if the annual system failure probability is at a socially acceptable level by checking

$$\Phi\left(-\pi_{i,j}\right)\Phi\left(-\beta_{i,j}\right)\lambda_{H_j} < P_{dm} \tag{3}$$

where P_{dm} denotes *de minimis risk* (Pate-Cornell, 1994), i.e., the level of risk for which society does not impose regulations, which is often employed in various risk assessment frameworks (Ellingwood, 2006). In the system-reliability-based disaster resilience framework by Lim et al. (2022), the reliability and redundancy indices of each initial disruption scenario are visualized by a scatter plot, termed a reliability-redundancy (β–π) diagram to check if the resilience constraint in Eq. (3) is satisfied. For the initial disruption scenarios which cannot satisfy the constraint, decision-makers need to pursue proper actions such as design changes, hazard mitigation, and retrofits to ensure a proper level of disaster resilience.

Reliability-Redundancy-Recoverability-based Decision Optimization

Problem formulation

To optimize a decision on a structural system while considering system-reliability-based disaster resilience, the reliability-redundancy-recoverability-based decision optimization (R3-DO) aims to minimize a cost function related to the recoverability while satisfying the constraints of the reliability-redundancy analysis, i.e., Eq. (3). Accordingly, an R3-DO problem can be described as

$$\begin{aligned} &\text{minimize} \quad f_{cost}(\boldsymbol{\theta}) \\ &\text{subject to} \quad \Phi\left(-\pi_i(\boldsymbol{\theta})\right)\Phi\left(-\beta_i(\boldsymbol{\theta})\right) \le P_{dm}/\lambda_H, \quad i = 1, \dots, n_{sc} \end{aligned} \tag{4}$$

where $\boldsymbol{\theta}$ denotes the vector of design parameters, which often includes the means of the random variables in $\mathbf{X}$; $f_{cost}(\boldsymbol{\theta})$ is the cost function introduced to describe the recoverability of the system; and n_{sc} is the number of the probabilistic constraints, i.e., initial disruption scenarios. Details about the cost function, the probabilistic constraints, and the corresponding design parameter sensitivities are explained as follows:

Cost functions of R3-DO

The cost function is defined as the cost or time required for the recovery process to maximize the recoverability of the system. As illustrated by the yellow arrows in Figure 1, two types of recoveries, i.e., the local and global recoveries, are considered. Local recovery should be achieved when only component-level failures occur. Thus its likelihood is described by the reliability index β. On the other hand, global recovery is defined as the recovery after a system-level failure F_{sys}. As a result, the following cost function including the initial, local recovery, and global recovery costs is introduced for R3-DO:

$$f_{cost}(\boldsymbol{\theta}) = IC(\boldsymbol{\theta}) + ELRC(\boldsymbol{\theta}) + EGRC(\boldsymbol{\theta}) \tag{5}$$

where $\mathrm{IC}(\boldsymbol{\theta})$ refers to the initial cost, $\mathrm{ELRC}(\boldsymbol{\theta})$ denotes the expected total cost for the local recovery, and $\mathrm{EGRC}(\boldsymbol{\theta})$ is the expected total cost for the global recovery. Therefore, R3-DO reflects the trade-off between the initial investments to make the system more resilient and the recovery costs of society.

To demonstrate R3-DO, in the example of this paper, we assign a design parameter θ_i to each structural member, and the initial disruption scenario is defined as the failure of a single structural member. Then, the cost functions in Eq. (5) are defined as

$$IC(\boldsymbol{\theta}) = \sum_{i=1}^{n_{sc}} \theta_i \tag{6a}$$

$$ELRC(\boldsymbol{\theta}) = \sum_{i=1}^{n_{sc}} LRC_i(\theta_i)\Phi\big(-\beta_i(\boldsymbol{\theta})\big) \tag{6b}$$

$$EGRC(\boldsymbol{\theta}) = GRC(\boldsymbol{\theta}) \sum_{i=1}^{n_{sc}} \Phi\big(-\pi_i(\boldsymbol{\theta})\big)\Phi\big(-\beta_i(\boldsymbol{\theta})\big) \tag{6c}$$

where θ_i is the i-th element of the design parameter vector $\boldsymbol{\theta}$; $LRC_i(\theta_i)$ denotes the cost assessed for the local recovery caused by the i-th initial disruption scenario; and $GRC(\boldsymbol{\theta})$ is the cost of the global recovery from the system failure F_{sys}. $ELRC(\boldsymbol{\theta})$ and $EGRC(\boldsymbol{\theta})$ are the expectations of the local and global recovery costs computed by use of their occurrence probabilities, i.e., $\Phi\big(-\beta_i(\boldsymbol{\theta})\big)$ and $\Phi\big(-\pi_i(\boldsymbol{\theta})\big)$. The design parameters, initial disruption scenarios, and the cost functions in R3-DO can be defined differently for a given problem.

Constraints of R3-DO

As shown in Eq. (4), R3-DO performs β–π analyses at each iteration to check the resilience-based constraints that manage the risk of system failure caused by each initial failure scenario under the *de minimis* risk P_{dm}. Thus, the optimal solution from R3-DO represents the decision which maximizes the recoverability while keeping a proper level of system-level risk. The number of R3-DO constraints is the same as the number of initial disruption scenarios, n_{sc}. If the complexity of the structural system increases, the number of constraints becomes large, which can be prohibitive in terms of computational cost. However, this challenge can be addressed by focusing on significant scenarios identified by a preliminary β–π analysis rather than covering all scenarios.

Design parameter sensitivities for optimization

If a gradient-based optimizer is adopted for R3-DO, the design parameter sensitivities of β and π should also be computed by component and system reliability methods (Der Kiureghian,

2005; Song et al., 2021). In summary, R3-DO needs evaluations of reliability and redundancy indices and their design parameter sensitivities, i.e., β, π, $\partial\beta/\partial\theta$, and $\partial\pi/\partial\theta$. To evaluate the sensitivities of β, we employed a first-order reliability method (FORM) based approach (Bjerager and Krenk, 1989). The redundancy index π and its parameter sensitivities $\partial\pi/\partial\theta$ are computed by the matrix-based system reliability method (MSR; Song and Kang, 2009).

Numerical example

Figure 2 shows the example truss system with ten members with a yield stress of 276 Mpa. The cross-sectional areas are modeled as normal random variables whose mean values are selected as the design parameters for R3-DO. Using the symmetric configuration, the design parameters of components #1 and #3, #4 and #6, #7 and #8, and #9 and #10 are identical to each other and modeled as θ_A, θ_C, θ_E, and θ_F, respectively. Additionally, the design parameters for the components #2 and #5 are denoted by θ_B and θ_D, respectively. P_1 and P_2 in Figure 2 denote the external forces assumed to follow normal distributions with means of 140 kN and 120 kN, respectively. Each force's coefficient of variation (c.o.v.) is assumed as 0.3.

Figure 3 shows the convergence histories of the cost function and the design parameters during R3-DO for the 10-member-truss system. The plots show that the recovery cost and all design parameters converged to the optimal solutions around 40 iterations of R3-DO. As a result, the optimal design parameters are identified as $\boldsymbol{\theta}^{\text{optimal}} = [1.3 \quad 1.0 \quad 0.9 \quad 0.8 \quad 0.9 \quad 0.2]^{\text{T}} \times 10^{-3}$ m^2. The successful optimization can be also confirmed in the β–π diagram in Figure 4, in which yellow markers represent the pairs of β and π at the current R3-DO iteration. As R3-DO optimization progresses, β–π points gradually approach the resilience limit-state surface $\Phi(-\pi_{i,j})\Phi(-\beta_{i,j})\lambda_{H_j} = P_{dm}$ to achieve the optimal trade-off between the initial investment and recoverability.

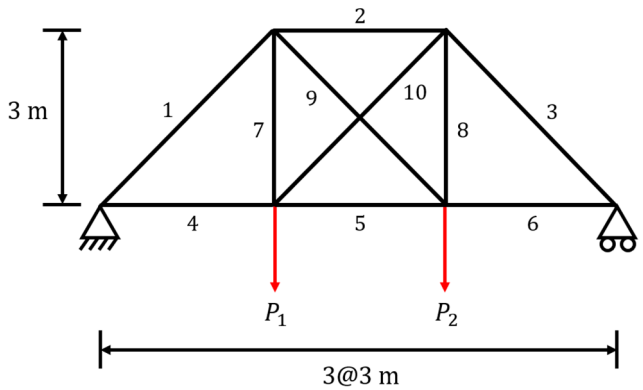

Figure 2. Configuration of truss system consisting of ten members

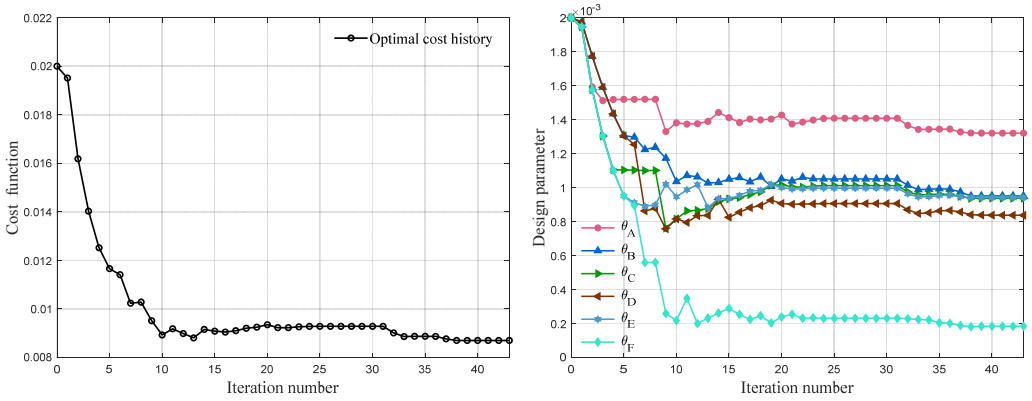

Figure 3. Convergence histories of cost function (left) and design parameters (right) for R3-DO of ten-member-truss system

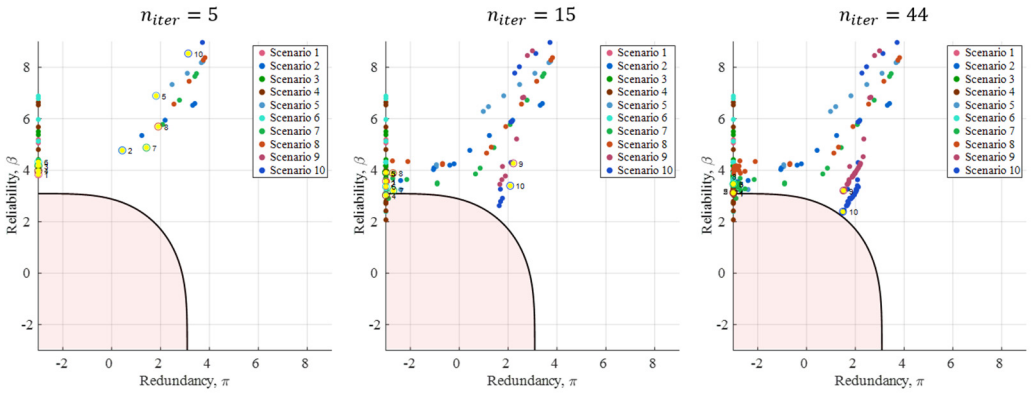

Figure 4. R3-DO process in β–π diagram for iteration numbers 5, 15, and 44

Conclusions

This paper proposed a reliability-redundancy-recoverability-based decision optimization (R3-DO) framework to facilitate decision-making processes to ensure maximum recoverability while managing the system-level risk at a socially acceptable level. The cost function of R3-DO is defined as the recovery cost, while the constraint on the system-level failure is introduced for each initial disruption scenario. In the example, component and system reliabilities and their parameter sensitivities are computed by a FORM-based approach and the matrix-based system reliability method. The R3-DO of an example truss structure demonstrated that the proposed method could help identify decisions that lead to maximum recoverability while managing the system-level risk at a socially acceptable level. The ongoing research further develops the R3-DO framework to improve its applicability to more complex structures by using a system reliability analysis method that can handle many components in computing the redundancy index and its parameter sensitivities.

References

Bjerager, P., and Krenk, S. 1989. Parametric sensitivity in first-order reliability theory. *Journal of Engineering Mechanics, ASCE*. 115(7): 1577-1582.

Bruneau, M., Chang, S.E., Eguchi, R.T., Lee, G.C., O'Rourke, T.D., Reinhorn, A.M., Shinozuka, M., Tierney, K., Wallace, W.A., and von Winterfeldt, D. 2003. A Framework to quantitatively assess and enhance the seismic resilience of communities. *Earthquake Spectra*. 19 (4): 733-752.

Der Kiureghian, A. 2005. First- and second-order reliability methods. Chap. 14 in *Engineering design reliability handbook*. E. Nikolaidis et al., eds. Boca Raton. CRC Press.

Ellingwood, B.R. 2006. Mitigating risk from abnormal loads and progressive collapse. *Journal of Performance of Constructed Facilities*. 20(4): 315-323.

Lim, S., Kim, T., and Song, J. 2022. System-reliability-based disaster resilience analysis: Framework and applications to structural systems. *Structural Safety*. 96: 102202.

Pate-Cornell, E. 1994. Quantitative safety goals for risk management of industrial facilities. *Structural Safety*. 13(3): 145–157.

Song, J., and Kang, W.-H. 2009. System reliability and sensitivity under statistical dependence by matrix-based system reliability method. *Structural Safety*, 31(2), 148-156.

Song, J., Kang, W.-H., Lee, Y.-J., and Chun, J. 2021. Structural system reliability: overview of theories and applications to optimization. *ASCE-ASME Journal of Risk and Uncertainty in Engineering Systems, Part A: Civil Engineering*. 7(2): 03121001.

International Symposium on Emerging Developments and Innovative Applications of Reliability Engineering and Risk Managements (EDIARR2022),30 October-3 November2022, Taipei
Chen, S. S. &Ang, Alfredo. H-S. (Editors)

DECISION-SUPPORT MEASURES FOR DISASTER RESILIENCE OF INFRASTRUCTURE NETWORKS

Youngjun Kwon[1], and Junho Song[2]

[1]*Civil and Environmental Engineering, Seoul National University, Seoul, South Korea*

E-mail: yjkweon@snu.ac.kr

[2]*Civil and Environmental Engineering, Seoul National University, Seoul, South Korea*

E-mail: junhosong@snu.ac.kr

***Abstract*:** As civil infrastructure systems increase in size and complexity, they become more vulnerable to disasters. From this concern, the concept of disaster resilience, i.e., the overall ability of a system to respond to and prepare for disasters, is taking the center stage. For reasonable evaluation of disaster resilience, the uncertainty of the state of the components constituting the system in the pre- and post-disaster must be considered probabilistically. In this paper, the recently proposed system-reliability-based disaster resilience analysis framework is applied to infrastructure networks to analyze their resilience characteristics. The framework evaluates the system's disaster resilience based on two criteria: component-level reliability index (β) and final system-level redundancy index (π) initiated by potential disruption scenarios. We also propose a method to quantify the relative importance of components using the causal model that can simulate the impact of the scenarios. The numerical examples demonstrate that the proposed method can be applied to various types of infrastructure networks. The proposed measure adaptively evaluates the component importance according to the resilience level which is set in advance by the system administrators. Therefore, the measure facilitates establishing proper decision-making strategies in terms of disaster resilience.

***Keywords*:** Resilience, System reliability, Importance measure, Causality, Infrastructure network

Introduction

To respond to the socio-economic demands caused by the rapidly growing population, modern society is increasing the size and complexity of major infrastructure networks such as water and sewage system, power grids, and transportation networks. Under these circumstances, rapid climate change is further exacerbating the vulnerability of the system. For these reasons, accordingly, the concept of *Disaster Resilience*, which is defined as the holistic ability of infrastructure to cope with external risks, is being developed (Bruneau et al., 2003). Since the system-level performance is differently defined depending on the scale and type of infrastructure facility, disaster resilience characteristics of the infrastructures need to be approached accordingly. Also, appropriate disaster resilience assessment aims to integrate the relationship between the states of components and the system to provide a basis for decision-making to secure the target resilience considering the uncertainty in the state of the components.

A practical decision-making process is usually carried out component-wise to manage the disaster resilience of infrastructure (Lin et al., 2022). Therefore, it is crucial to prioritize and identify the impact of individual components on the system-level performance. Various importance measures (IMs), i.e., measures quantifying the contribution of a component to system performance, have been developed based on different viewpoints as useful decision-supporting measures. However,

the existing IMs are defined with simple mathematical expressions based on the correlation between the states of components, which can consider nonrelevant components as important ones in terms of the system reliability perspective.

This paper applies the recently proposed system-reliability-based disaster resilience analysis framework (Lim et al., 2022) to infrastructure networks to demonstrate the effectiveness of the framework. In addition, we propose a new decision-support measure based on the framework considering the connectivity between major components as the target system-level performance. The measure involves the causal influence of the external hazards on the component state, and that of the component state on the system-level state. Numerical application examples illustrate the validity of the proposed measure.

Background Knowledge

System-reliability-based Disaster Resilience Analysis Framework

Lim et al. (2022) recently proposed to characterize disaster resilience by three criteria at three scales of the infrastructure system, which led to a '3x3 resilience matrix.' Table 1 shows a part of the matrix for the infrastructure network scale. Infrastructure networks are usually described with nodes and interconnecting links. Since these node- and link-type components are distributed over a large area, *reliability* should be evaluated with appropriate consideration of the spatial correlation between the component states and variability. According to Table 1, to evaluate *redundancy* of the system, the eventual system-level degradation due to sequential failures triggered by initial component disruption should be considered.

Table 1. Three resilience criteria of infrastructure network scale in the '3x3 resilience matrix'

Criteria / **Scale**	***Reliability***	***Redundancy***	***Recoverability***
Infrastructure network	Avoiding initial disruption of network components	Preventing cascading failures causing degradation of network performance	Executing proper actions for loss of network functionality

The system-reliability-based disaster resilience analysis (S-DRA) framework considers the *reliability* and *redundancy* criteria in the generalized indices form. For the *i*th initial disruption scenario F_i, the pair of redundancy index π_i and reliability index β_i is defined as

$$(\pi_i, \beta_i) = \left(-\Phi^{-1}\left[P\left(F_{sys}\middle|F_i, H\right)\right], -\Phi^{-1}[P(F_i|H)]\right) \quad (1)$$

where $\Phi^{-1}[\cdot]$ stands for the inverse of the standard normal cumulative distribution function (CDF), and H and F_{sys} denotes external hazard and system-level failure, respectively.

To assess the impact of the disruption scenarios on the system level, the final system failure probability is set as a standard. The probability of the system failure caused by F_i, $F_{sys,i}$ can be computed using the conditional probabilities in Eq. (1) and should be managed below "*de minimis* risk," the threshold probability of the risks that society can or decides to neglect, i.e.,

$$P(F_{sys,i}) = P(F_{sys}|F_i, H)P(F_i|H)\lambda_H < P_{dm} \tag{2}$$

where λ_H denotes the mean occurrence rate of H. P_{dm} in this paper is set as $10^{-7}/yr$ (Paté-Cornell, 1994). Dividing Eq. (2) by λ_H, the disaster resilience constraint $\mathcal{D}_H$ can be expressed as

$$\mathcal{D}_H: \Phi[-\pi_i]\Phi[-\beta_i] < \frac{P_{dm}}{\lambda_H} = H_{dm} \tag{3}$$

The scatter plot of the pair in Eq. (1) along with the disaster resilience constraint in Eq. (3) is called the β-π diagram (Lim et al., 2022). This graphical representation helps identify critical disruption scenarios and the effect of decision-making strategy at both component- and system-level resilience.

Importance Measures of Components

Importance measures (IMs) quantify the relative contribution of component *e* to the system-level failure $\boldsymbol{F_{sys}}$. Table 2 summarizes the definitions of six IMs (Song and Der Kiureghian, 2005): Conditional-probability-based importance measure (CP), the inverse of CP (ICP), Fussell-Vesely (FV), risk achievement worth (RAW), risk reduction worth (RRW), and bound probability (BP).

Table 2. Mathematical definitions of importance measures: CP, ICP, FV, RAW, RRW, and BP

$CP_e = P(E_e\|F_{sys}) = \frac{P(E_eF_{sys})}{P(F_{sys})}$	$ICP_e = P(F_{sys}\|E_e) = \frac{P(E_eF_{sys})}{P(E_e)}$	$FV_e = \frac{P(\bigcup_{l:C_l \supset E_e} C_l)}{P(F_{sys})}$
$RAW_e = \frac{P\left(F_{sys}^{(e)}\right)}{P(F_{sys})}$	$RRW_e = \frac{P(F_{sys})}{P\left(F_{sys}^{(\overline{e})}\right)}$	$BP_e = P\left(F_{sys}^{(e)}\right) - P\left(F_{sys}^{(\overline{e})}\right)$

In Table 2, $\boldsymbol{E_e}$ denotes the failure of component *e*, $\boldsymbol{C_l}$ is the *l*th cutset, and $\boldsymbol{F_{sys}^{(e)}}$ and $\boldsymbol{F_{sys}^{(\overline{e})}}$ respectively denote the system failure event with component *e* is guaranteed to fail and survive unconditionally. By the definitions, RAW and RRW always have a value greater than or equal to 1, while the other IMs are greater than or equal to 0 and less than or equal to 1.

Causality-based Decision-support Measure

To evaluate the effect of multiple component failures on the final system failure, the resilience index pair (π_i^k, β_i^k) for the *i*th initial disruption scenario involving failures of *k* components, F_i^k is defined similarly to Eq. (1) as

$$(\pi_i^k, \beta_i^k) = \left(-\Phi^{-1}\left[P(F_{sys}|F_i^k, H)\right], -\Phi^{-1}\left[P(F_i^k|H)\right]\right) \tag{4}$$

Introducing the *do*-operation (Pearl, 2009) to component *e* in F_i^k, which is discriminated from conditional operation in that it does not update the likelihood of other variables, $F_{i,e}^k$, the causal effect of component *e* on the system failure is defined as the change rate of the system failure probability due to a change in the state of component *e* as

$$\partial_e P\left(F_{sys}\middle|F_i^k,H\right)=\begin{cases}0 & \text{if } P\left(F_{sys}\middle|do(E_e),F_{i,e}^k,H\right)=0\\ 1-\frac{P\left(F_{sys}\middle|do(\bar{E}_e),F_{i,e}^k,H\right)}{P\left(F_{sys}\middle|do(E_e),F_{i,e}^k,H\right)} & \text{otherwise}\end{cases} \tag{5}$$

$\mathcal{F}_{i,e}^k$ is also defined as a set with the elements of the mutually exclusive and collectively exhaustive (MECE) event space constituting $F_{i,e}^k$. Then, the merged contribution (MC) of component e for F_i^k, $MC_{i,e}^k$ is defined as the summation of the products of the causal effect and the occurrence probability for all elements in $\mathcal{F}_{i,e}^k$, i.e.,

$$MC_{i,e}^k=\sum_{F\in\mathcal{F}_{i,e}^k}\partial_e P\left(F_{sys}|F,H\right)P(F|H) \tag{6}$$

Finally, for the critical scenarios that do not satisfy the resilience constraint, i.e., inducing a higher probability of the final system failure than the target resilience level, the causality-based importance measure (CIM) and normalized CIM (NCIM) for component e are proposed as Eq. (7) and (8), respectively.

$$CIM_e^k=\sum_{i:\,(\pi_i^k,\beta_i^k)\notin\mathcal{D}_H}\Phi\left[-\pi_i^k\right]\Phi\left[-\beta_i^k\right]\times MC_{i,e}^k \tag{7}$$

$$\mathbf{NCIM}^k=\mathbf{CIM}^k/\max(\mathbf{CIM}^k) \tag{8}$$

where $\mathbf{CIM}^k=[CIM_1^k,CIM_2^k,\cdots,CIM_n^k]^{\mathrm{T}}$ denotes the CIM vector for all n components. In other words, a new CIM describes the weighted average of the contour values in the β-π diagram for the critical scenarios using merged contributions as weights.

Numerical Examples

The proposed causality-based IM based on the β-π analysis is applied to two numerical examples: hypothetical bridge network and plant system. For the applications, a seismic hazard is represented by the ground-motion prediction equation (GMPE) describing the attenuation of seismic intensity. A generalized form of GMPE (Goda and Hong, 2008) is

$$\ln Y_e=gm(M,R_e)+\eta+\varepsilon_e \tag{9}$$

where Y_e is the seismic response of component e, $gm(\cdot)$ is the ground-motion model (GMM) which is a function of the earthquake magnitude M and the distance R_e between the source and component e, and η and ε_e are inter- and intra-event residuals, respectively. The residuals are assumed to follow the zero-mean standard normal distribution and be statistically independent of each other. For the variance of residuals, σ_η^2 and σ_ε^2, the total variance of the logarithmic response, σ_T^2 is derived as $\sigma_\eta^2+\sigma_\varepsilon^2$. The correlation coefficient of the logarithm of responses between components m and n separated by distance Δ, $\rho_{\ln PGA_m\ln PGA_n}(\Delta)$ is derived as

$$\rho_{\ln Y_m\ln Y_n}(\Delta)=\frac{\sigma_\eta^2}{\sigma_T^2}+\rho_{\varepsilon_m\varepsilon_n}(\Delta)\frac{\sigma_\varepsilon^2}{\sigma_T^2} \tag{10}$$

where $\rho_{\varepsilon_m\varepsilon_n}(\Delta)$ is the spatial correlation between components m and n.

Then, for node-type component *e*, the safety factor β_e^1 is derived as follows based on the fragility analysis:

$$\beta_e^1 = -\Phi^{-1}[P(E_e|H)] = \frac{\ln \alpha_{DS}^e - gm(M,R_e)}{\sqrt{(\beta_{DS}^e)^2 + \sigma_T^2}} \tag{11}$$

where α_{DS}^e and β_{DS}^e are the median and the standard deviation of response in the fragility curve, respectively. The correlation coefficient between the safety factors for different components *m* and *n* (Lee and Song, 2021) is expressed as

$$\rho_{mn} = \frac{\sigma_\eta^2 + \rho_{\varepsilon_m\varepsilon_n}(\Delta)\sigma_\varepsilon^2}{\sqrt{\left\{(\beta_{DS}^m)^2 + \sigma_T^2\right\}\left\{(\beta_{DS}^n)^2 + \sigma_T^2\right\}}} \tag{12}$$

Hypothetical Bridge Network

Figure 1 shows a hypothetical bridge network with a potential earthquake scenario with a magnitude of 7.5. The system-level performance is the connectivity between the virtual nodes *S* and *T*. Since every node-type component is located in the middle of the link, the failure of the bridge leads to the disconnection of the corresponding road. The GMPE and the variances of residuals for peak ground acceleration (PGA) in Boore and Atkinson (2008) are adopted for probabilistic analysis, and the fragility parameters α_{DS} and β_{DS} are assumed as 1.50 and 0.60 respectively for all bridge components. The spatial correlation model is set as $\rho_{\varepsilon_m\varepsilon_n}(\Delta) = \exp(-0.27\Delta^{0.40})$.

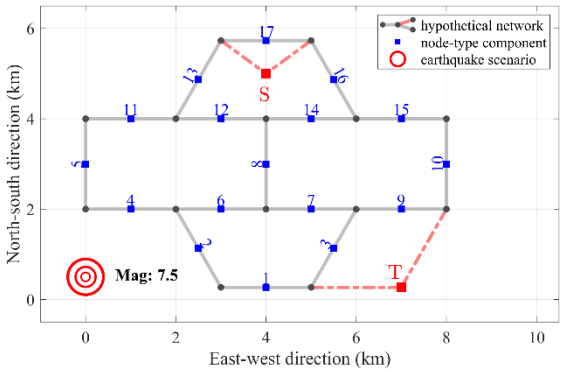

Figure 1. Hypothetical bridge network with an earthquake scenario

Figure 2 shows six IMs (presented in Table 2), in which the probability of the intersection for multiple component failure events can be calculated in a closed form with the multivariate standard normal CDF using Eqs. (11) and (12). All six IMs commonly indicate that component 16 has the highest importance. In particular, it was noted that RAW, RRW, and BP captured relatively high importance for components 8, 10, 13, and 15, which are not close to the seismic source. While individual reliability for those components against the earthquake is low, the impact that will lead to the final system-level failure from the failures of the components is high in terms of system reliability.

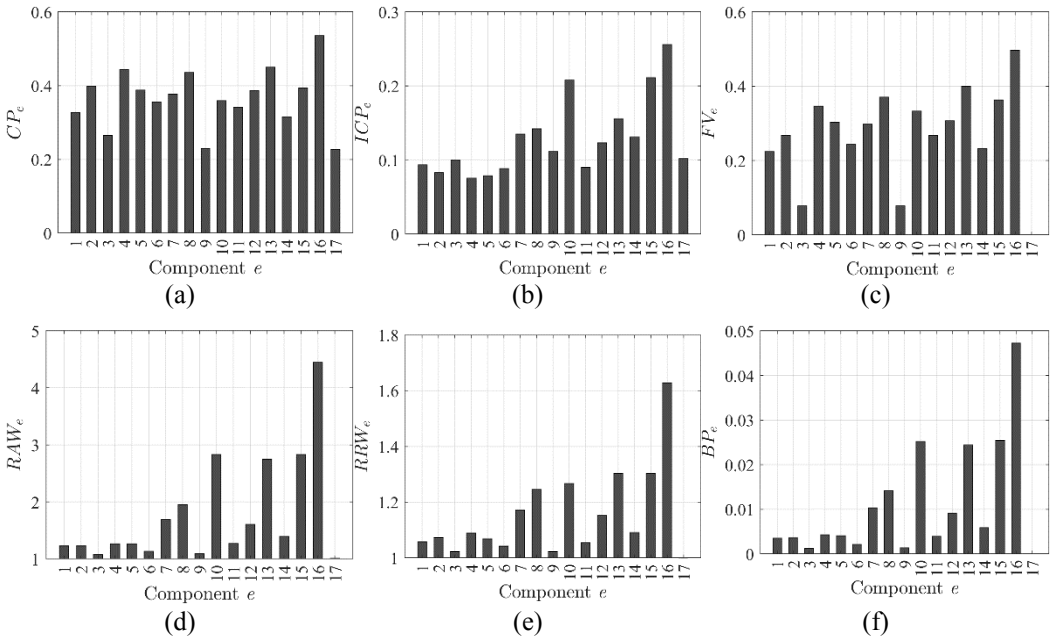

Figure 2. IMs of hypothetical bridge network: (a) CP, (b) ICP, (c) FV, (d) RAW, (e) RRW, and (f) BP

The disaster resilience characteristics can be further analyzed through the β-π diagram. Figures 3(a) and 3(c) respectively show the diagram with and without dependency between component states. Figures 3(b) and 3(d) show the calculated NCIM for the mean occurrence rate $10^{-4}/yr$ and $10^{-2}/yr$, respectively using Eqs. (8) and (9). The points of the β-π diagram in Figure 3(a) are more scattered in terms of the redundancy index than the reliability index. This phenomenon implies that the component importance in this system tends to be more sensitive to the topological location rather than the failure probability, i.e., the distance from the source.

Since most of the scenarios in which one or two components are initially disrupted are included in the target resilience constraint dissatisfaction region, NCIM is calculated with a constant priority regardless of the dependency. On the other hand, $\mathbf{NCIM}^3$ differs adaptively by the introduction of the correlation due to the different trends of disruption scenarios included in the region.

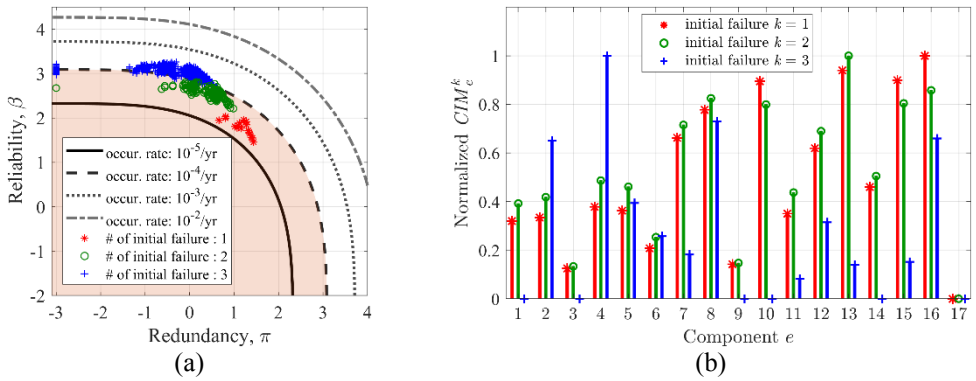

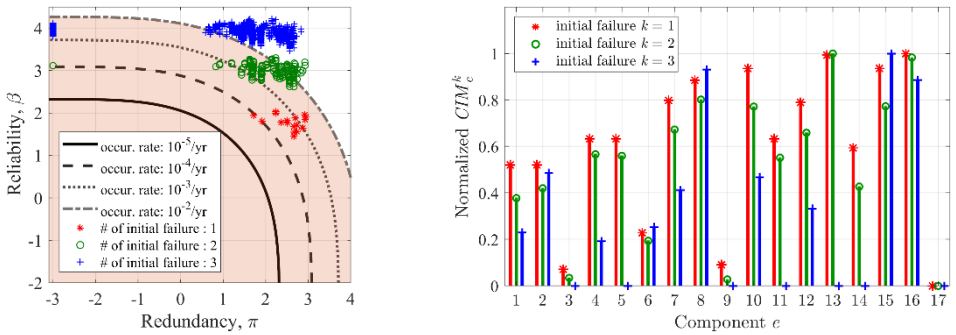

(c) (d)

Figure 3. (a) β-π diagram with dependency, (b) following NCIM for $10^{-4}/yr$ occurence rate; (c) β-π diagram with independency, and (d) following NCIM for $10^{-2}/yr$ occurence rate of hypothetical bridge network

Plant System: Limerick Generation Station

Next, we evaluate the disaster resilience of Limerick Generation Station (LGS), a plant system consisting of a Boiling Water Reactor (BWR) in Philadelphia, USA, using the S-DRA framework. Figure 4(a) shows the fault tree in which a core meltdown accident occurs at the system level. The system can be analyzed using the network in Figure 4(b) in which the connectivity between the core melting nodes is the system performance. The fragility parameters of the seismic components $(S_1, S_4, \cdots, S_{17})$, and the average failure rate of the non-seismic components (DG_R, W_R, C_R, SL_R) are adopted from Ellingwood (1990). The earthquake with a PGA of $0.2g$ is set as a potential hazard.

Figure 5(a) is the β-π diagram of LGS when the correlation coefficient between the failure events $S_{11}, S_{12}, S_{13}, S_{14}$ and S_{15}, S_{16} located in the same buildings are 0.7. Figures 5(b) and 5(c) are the proposed NCIM for the dependent components and perfectly independent components, respectively considering the 10-year return period earthquake. From the diagram, the redundancy index is clustered around some values, while the reliability index is evenly distributed. This phenomenon implies that there exist a couple of highly important components in terms of network topology. The implication is also consistent in the calculated NCIMs in Figures 5(b) and 5(c), in that component 1 occupies the overall component importance. In addition, for the same target resilience level, a higher correlation assumption makes initial disruption points move to the lower left of the diagram, resulting in increases in the importance of the corresponding components.

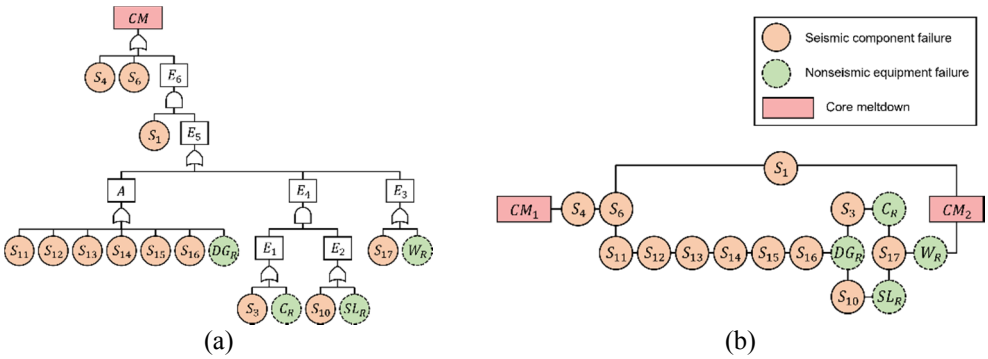

(a) (b)

Figure 4. Accident sequence of core meltdown in LGS: (a) Fault tree structure, and (b) Network structure

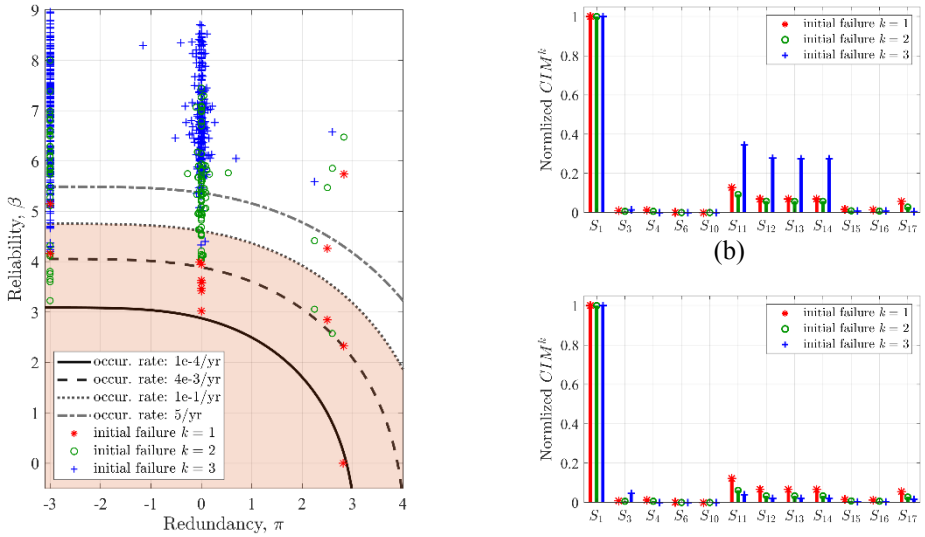

Figure 5. (a) β-π diagram, (b) NCIM, and (c) NCIM (independent case) for a core meltdown in LGS

Conclusions

In this paper, we applied the system-reliability-based disaster resilience analysis framework to infrastructure networks considering the uncertainties of the response induced by a hazard. It was confirmed that the framework facilitates identifying the component criticality of the system-level performance by a comprehensive perspective combining reliability and redundancy. Based on the results of the β-π analysis we also proposed a new importance measure that can adaptively calculate the component importance according to the target resilience level, and balance between the topological placement and the individual reliability. The measure is constructed component-wise based on the causality of the system-level performance degradation. Two numerical examples of the virtual bridge network and the plant system verified the applicability of the measure to general types of networks represented by the nodes and the interconnecting links. It is expected that the proposed measure can support decision-making processes to ensure disaster resilience of infrastructure networks.

References

Boore, D.M., & Atkinson, G.M. (2008). Ground-motion prediction equations for the average horizontal component of PGA, PGV, and 5%-damped PSA at spectral periods between 0.01s and 10.0s. *Earthquake spectra,* 24(1), 99-138.

Bruneau, M., Chang, S.E., Eguchi, R.T., Lee, G.C., O'Rourke, T.D., Reinhorn, A.M., Shinozuka, M., Tierney, K., Wallace, W.A., and von Winterfeldt, D. (2003). A framework to quantitatively assess and enhance the seismic resilience of communities. *Earthquake spectra,* 19(4), 733-752.

Ellingwood, B. (1990). Validation studies of seismic PRAs. *Nuclear Engineering and Design*, 123(2-3), 189-196.

Goda, K., & Hong, H. P. (2008). Spatial correlation of peak ground motions and response spectra. *Bulletin of the Seismological Society of America,* 98(1), 354-365.

Lee, D., & Song, J. (2021). Multi-scale seismic reliability assessment of networks by centrality-based selective recursive decomposition algorithm. *Earthquake Engineering & Structural Dynamics,* 50(8), 2174-2194.

Lim, S., Kim, T., & Song, J. (2022). System-reliability-based disaster resilience analysis: Framework and applications to structural systems. *Structural Safety,* 96, 102202.

Lin, C., Song, J., & Pozzi, M. (2022). Optimal inspection of binary systems via Value of Information analysis. *Reliability Engineering & System Safety,* 217, 107944.

Paté-Cornell, M. E. (1994). Quantitative safety goals for risk management of industrial facilities. *Structural Safety,* 13*(*3), 145-157.

Pearl, J. (2009). *Causality: Models, Reasoning and Inference, 2nd ed.* Cambridge university press, Cambridge, UK.

Song, J., & Der Kiureghian, A. (2005). Component importance measures by linear programming bounds on system reliability. In *Proceedings of the 9th International Conference on Structural Safety and Reliability (ICOSSAR9)*, Rome, Italy.

International Symposium on Emerging Developments and Innovative Applications of Reliability Engineering and Risk Managements (EDIARR2022),30 October-3 November2022, Taipei
Chen, S. S. &Ang, Alfredo. H-S. (Editors)

THE STRIKE AND DIP JOIT SPACING UNCERTAINTY ON THE LANDSLIDE DEBRIS RUN-OUT FEATURES

Yu-Han Cheng[1] and Wen-Chao Huang[2]

[1] *Graduate student, Department of Civil Engineering, National Central University, Taiwan*

[2] *Professor, Department of Civil Engineering, National Central University, Taiwan*

Correspondence e-mail address: wenchaoh@g.ncu.edu.tw

Abstract: In this study, we focused on the effect of geological model uncertainty, expressed as the strike and dip joint spacing uncertainty, on the debris run-out features of a dip slope sliding case in Taiwan. 3D discrete element models were established by incorporating LiDAR DEM (digital elevation model) and the joint set spacing information from the literature. Then, debris run-out analyses were performed based on Point Estimate Method. In the current study, the debris run-out features include the run-out distances and the debris coverage area. Analysis results indicate that the debris run-out distance variability is more sensitive to the variability of dip joint spacing. However, it was found that the coverage area uncertainty of the sliding mass is more sensitive to the variability of strike joint spacing. Therefore, if the debris run-out risk could threaten the nearby residents or facilities, it is crucial to consider the joint spacing uncertainty and other possible geological model uncertainties in the corresponding analyses.

***Keywords*:** Joint Spacing Uncertainty, Numerical Modeling, Point Estimate Method, Landslide Debris Run-Out Features

Introduction

The geotechnical, ground, and geological model uncertainties are often considered crucial in a geotechnical design (Keaton, 2013). It is relatively easier for geotechnical engineers or researchers to consider the effect of geotechnical and ground model uncertainties in the geotechnical analysis. However, geotechnical engineers often treat the geological model given to them by geologists as a constant model; hence, the effect of geological model uncertainty on a geotechnical design was seldom considered in the past. Yeh et al. (2021) have demonstrated the importance of geological model uncertainty expressed as the dip angle of the sliding plane on the sliding probability of an actual dip slope sliding event. Based on Yeh et al. (2021) research results, it was concluded that the variability of the dip angle on the sliding plane is highly related to the probability of failure of the dip slope. In this study, the same dip slope sliding case was chosen as the studied case. The effect of geological model uncertainty is explored through the joint spacing of the sliding block, and its effect on the debris run-out distance and debris coverage area on the highway was studied by numerical modeling.

Figure 1 The National Highway No. 3 landslide Aerial Photo (TGS, 2011)

In this study, we used an actual dip slope sliding case, as shown in Figure 1. The sliding event occurred on April 25, 2010, at a sedimentary dip slope site. There was no record of rainfall or earthquake several days before the landslide, and a detailed investigation was conducted to explore the possible reasons for the failure. We would like to investigate the effect of strike and dip joint spacing on the debris run-out features, expressed as the run-out distance and debris coverage area. 3DEC was employed in this study to conduct the numerical analysis because the given joint sets could be configured in the sliding mass. Therefore, the blocks separated by the given joint sets could move under the effect of gravity.

Methodology

The debris run-out responses expressed as the debris run-out distance and the debris coverage area are explored through numerical analysis and Point Estimate Method. Numerical analysis was conducted using 3DEC by Itasca Inc. 3DEC is a numerical approach that adopted the distinct element modeling method. The LiDAR DEM was incorporated into 3DEC; hence, the terrain information was loaded to obtain the numerical model. Afterward, the joint distribution and attitudes were obtained from Lo et al. (2011), as shown in Figure 2. The two major joint sets were identified as strike and dip joints. Eight strike joints are perpendicular to the true dip of the landslide, and five dip joints are parallel to the true dip direction. The dip angle for the strike joints is mostly around 45 degrees, while the dip angle for the dip joints is around 55 degrees. Finally, the dip angle of the bedding plane is around 15 degrees. In the numerical models, the above-mentioned numbers for strike and dip joints and the attitudes of the strike and dip joints were integrated into the 3DEC model as the base model.

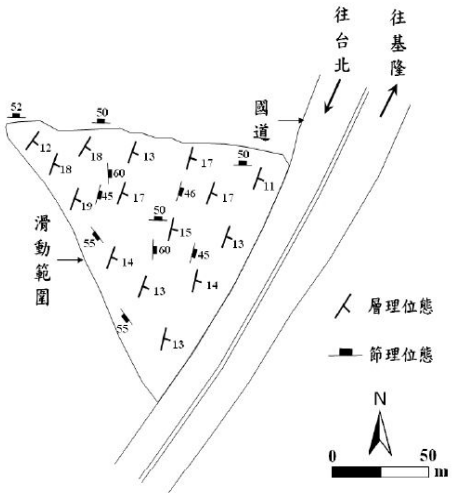

Figure 2 Investigation results for the strike and dip joint distribution (Lo et al., 2011)

Once the base model was established, the uncertainty of the strike and dip joint spacing was explored by various numbers of the strike and dip joints. Due to the lack of in-situ information regarding the spacing of the joints, we assumed that the standard deviation of the strike and dip joints is one joint. Therefore, the effect of uncertainty for dip joints was investigated by analyzing two cases with eight strike joints and four/six dip joints. Similarly, the effect of uncertainty for strike joints was studied by analyzing two cases with five dip joints and seven/nine strike joints. Finally, the debris run-out features expressed as run-out distance and coverage area on the highway were selected to investigate the effect of joint uncertainty. As shown in Figure 3, the debris run-out distance was the distance the farthest block can travel from the resting point to the toe of the slope. (Please note that under a 3D analysis, any 2D cross-section may intersect some blocks, and some blocks may seem floating, but the blocks are in contact with the ground at other locations). Figure 3 also shows the definition of the coverage area on the highway. After the debris movement stabilized, the area that covered the highway was identified, and the corresponding area was analyzed.

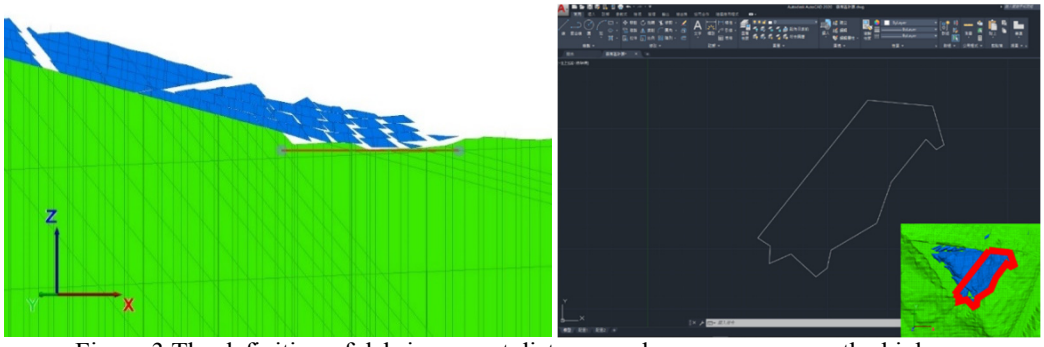

Figure 3 The definition of debris run-out distance and coverage area on the highway

Once the debris run-out distances and coverage area were analyzed under various strike and dip joint numbers combinations, the Point Estimate Method (PEM) was employed to calculate the average and standard deviations of the debris run-out distance and coverage area.

Research Results and Discussions

Before the numerical model can regarded as valid to perform the following parametric studies, the numerical model must be verified by comparing to the actual data. In this study, we have obtained the debris run-out distance and coverage area of 50 m and 10200 m^2, respectively, based on the investigation report. In the numerical analysis, the base model gives 50 m and 10000 m^2 run-out distance and coverage area on the highway. Therefore, the given numerical parameters and the established numerical model can correctly simulate the debris run-out responses.

Based on the results of the 3DEC analysis and PEM, the following discussions are presented individually for the effect of uncertainty on debris run-out distances and coverage area:

- Debris run-out distance:

  (1) Considering that the dip joint number is uncertain (two cases with eight strike joints and four/six dip joints), the average debris run-out distance is around 57m, and the standard deviation is 3.6m, resulting in a coefficient of variation of 6%.

  (2) Considering that the strike joint number is uncertain (two cases with five dip joints and seven/nine strike joints), the average debris run-out distance is around 55m, and the standard deviation is 1.6m, resulting in a coefficient of variation of 3%.

  Looking at the debris run-out distance of the base model, one can see that when considering the uncertainty of the strike or dip joint numbers, the debris run-out distance increases slightly. However, the values are close when comparing the average debris run-out distances for both cases. The result is because a local high terrain can be found on the other side of the sliding site. Because of the barrier across the sliding site, the strike or dip joints' uncertainty may not affect the debris run-out distance much. However, by analyzing the coefficient of variation to identify the sensitivity of strike or dip joint numbers, we can see that the uncertainty of dip joint numbers can result in a higher variability in the debris run-out distance.

- Debris coverage area on the highway:

  (1) Considering that the dip joint number is uncertain (two cases with eight strike joints and four/six dip joints), the average debris coverage area is around 10126 m^2, and the standard deviation is 33.5 m^2, resulting in a coefficient of variation of 0.33%.

  (2) Considering that the strike joint number is uncertain (two cases with five dip joints and seven/nine strike joints), the average debris coverage area is around 10238 m^2, and the standard deviation is 270 m^2, resulting in a coefficient of variation of 2.6%.

  Although the volume of the sliding block is fixed in this study (the depth of the sliding plane is constant), the debris sliding and accumulation behavior could be highly influenced by the uncertainty of the joint numbers. Based on the above analysis results, when considering the uncertainty of the dip or strike joint numbers, one can see that the results by considering the dip joint number, the average coverage area is smaller than that of the base model. On the other hand, considering the uncertainty of the strike joint number, the average area is larger than that of the base model. Therefore, the results indicate that the uncertainty of the dip joint

number may result in a small coverage area. Similarly, the standard deviation considering the uncertainty of the dip joint is also small, leading to a coefficient of variation of 0.3%, meaning that the uncertainty of the dip joint number may not influence the coverage area and its variability too much. However, when considering the strike joint uncertainty, one can see that the debris coverage area's average and standard deviation increase significantly, leading to a much larger COV (2.6%) than the other case. Hence, the uncertainty of the debris coverage area may be more sensitive to the uncertainty of the strike joint numbers.

Conclusions

In this study, we explored the effect of geological model uncertainty, expressed as the strike and dip joint spacing, on the debris run-out distance and debris coverage area on the highway. The analyses were based on an actual landslide case. The distinct element modeling technique was combined with Point Estimate Method to explore the relationship between the joint number and the debris run-out response uncertainties. Based on the analysis results, it was found that the debris run-out variability is more affected by the dip joint numbers. A local high terrain across the landslide site may also affect the result. The debris coverage area is more affected by the uncertainty of the strike joint numbers. The average value and the standard deviation of the debris coverage area are increased significantly compared to the other case (considering only the dip joint uncertainty), resulting in a higher COV. The analysis results indicate that when a facility is nearby a potential landslide site, it is crucial to perform a similar analysis to understand the possible threats that the debris could cause.

References

Keaton, J. R. (2013). Engineering Geology: Fundamental Input or Random Variable? Foundation Engineering in the Face of Uncertainty: 232-253.

Lo, Chia-Ming, Cheng, Tien-Yao, Lin, Yen-Hsiang, Hsiao, Cheng-Yang, Wei, Lun-Wei, Huang, Chuen-Ming, Chi, Shu-Yuon, Lin, Hsi-Hung and Lin, Ming-Lang (2011). "A Kinematic Model of the Translational Slide at the Cidu Section of Formosan Freeway", Journal of Chinese Soil and Water Conservation, 42 (3):175-183. (in Chinese)

TGS (2011). "The investigation report of the landslide at Taiwan highway No. 3: Ministry of Transportation and Communications investigation report." Taiwan Geotechnical Society, Taipei (in Chinese).

Yeh, C.-H., Dong, J.-J., Khoshnevisan, S., Juang, C. H., Huang, W.-C. and Lu, Y.-C. (2021). "The role of the geologic uncertainty in a geotechnical design – A retrospective view of Freeway No. 3 Landslide in Northern Taiwan." Engineering Geology 291: 106233.

International Symposium on Emerging Developments and Innovative Applications of Reliability Engineering and Risk Managements (EDIARR2022),30 October-3 November2022, Taipei
Chen, S. S. &Ang, Alfredo. H-S. (Editors)

APPLICATION OF ARTIFICIAL INTELLIGENCE FOR PROBABILITY OF FAILURE PREDICTION IN ROCK SLOPES

A.J. Li1, Abdoulie Fatty[1], Li-Hsuan Chen[1], Yun-Rong Li[1], Zhao-Yang Liu [1], Fu-Kuo Huang[2]

[1]*Department of Civil and Construction Engineering, National Taiwan University of Science and Technology, Taipei City, Taiwan*

E-mail: laj871@mail.ntust.edu.tw

[2]*Department of Water Resources and Environmental Engineering, Tamkang University, New Taipei City, Taiwan*

Abstract: The construction of infrastructure on slopes makes them vulnerable to damages triggered by slope failures. Slope instability leads to colossal financial losses, human causalities, and immense maintenance costs. Therefore, engineers must have a good understanding of the processes that trigger slope failure as well as access to tools that can predict the vulnerability of slopes for proper slope hazard mitigation. Various attempts have been made to assess the stability of slopes using techniques such as the limit equilibrium method, finite element method, and statistical methods. In recent years, Artificial intelligence (AI) techniques have demonstrated great convenience for slope stability assessment while maintaining good accuracy. This study uses Monte Carlo simulation to establish the probability distribution for earthquakes and the probability relationship of various rock slope strength parameters in order to obtain the probability of failure (P_f) for thousands of rock slope cases. Results from the Monte Carlo simulation are then used to train a predictive Random Forest (RF) model for P_f prediction. The prediction performances of the RF model are evaluated in terms of the coefficient of determination (R^2) and the root mean square error (RMSE). The proposed RF model could be used to efficiently predict the P_f of rock slopes.

***Keywords*:**Artificial intelligence, Random Forest ,Slope stability, Monte Carlo method, Probability of failure

Introduction

Geotechnical engineers usually deploy analytical and empirical techniques for the safety evaluation of slopes based on design parameters and engineering properties of rock or soil material. It is a complicated task to develop efficient and accurate models to simulate site-specific engineering geological conditions. Slope stability analysis is a standard process used in geotechnical engineering to estimate the stability of natural and man-made slopes. The stability of slopes is influenced by key parameters that define the geometry of slopes (height and slope angle) and the material properties (internal friction angle, cohesion, pore water pressure). In addition, many sources of loading such as soil properties and loading also trigger slope instability (Koopialipoor et al. 2019, Fatty, Li, and Chen 2022). Slope stability assessment is usually performed using analytical methods such as the limit equilibrium method (LEM) and finite element methods (FEM).

The difficulty associated with further development of slope stability analysis techniques is to devise accurate and comprehensive design tools to conduct precise slope stability assessment. In the past before the advent of computers, engineers use semi-graphical solutions, manual calculations, or stability charts to perform stability analysis (Hoek and Bray 1981). With the advent of computers, engineers have developed various computational tools for efficient stability assessment of slopes. Geotechnical software developed based on analytical methods such as the

limit equilibrium method (LEM) are often used for slope stability analysis. However, this method has proven to be insufficient when dealing with complex slope conditions that require more sophisticated designs, prompting the need for more advanced tools like the finite element method (Göktepe and Keskin 2018).

In recent years, artificial intelligence (AI) algorithms have been successfully implemented to solve stability problems (Hoang and Pham 2016, Li et al. 2018, Lu and Rosenbaum 2003). Algorithms such as Artificial neural network (ANN) have been implemented as benchmark models by several studies (Lu and Rosenbaum 2003, Sakellariou and Ferentinou 2005) for slope stability prediction. Comparisons between the prediction results of the AI models in these studies and analytical results were found to concur. In another study, (Li, Lim, and Fatty 2020) proposed an extreme learning neural network model for the stability evaluation of three-layered soil slopes. The proposed model was able to efficiently and accurately predict the stability of three layered soil slopes. In another study, (Fatty, Li, and Chen 2022) developed RNN-based iOS mobile applications for stability assessment of slopes. The RNN-based mobile applications are able to predict the stability number of slopes under earthquake and rainfall effects with great accuracy and convenience. Based on a review of published works, AI models have demonstrated outstanding potential in slope stability assessment.

Even though AI techniques have achieved promising results for solving prediction problems, the predictive performance of such models significantly relies on the quality of the input data. As a result, reliability sensitivity analysis is often conducted to enhance the performance of AI models. The application of reliability methods in slope stability assessment was first initiated in 1970 (Wu and Kraft Jr 1970, Catalan and Cornell 1976). These methods enable the consideration of the uncertainties of material properties, strength parameters, slope geometries and potential damages and thereby proposing more rational and effective designs. (Tobutt 1982) used the Monte Carlo method as a sensitivity testing tool for slope stability and also as an approach to determine the probability of failure (P_f) for a given earth slope. Probabilistic risk assessments are being increasingly seen as the most appropriate framework for engineers to systematically base decisions on hazard mitigation issues (Li et al. 2012). As indicated by (Nilsen 2000), the probabilistic method for stability assessment of slopes has obvious advantages as the uncertainty and variability of the input parameters can be taken into consideration.

This study proposes a prediction system for the probability of failure prediction of rock slopes based on Random forest. Based on our review, there is a limited number of studies that are aimed at stability prediction of slopes that consider earthquake effect on slope stability. In this study, the horizontal seismic coefficient (k_h) is included in the input parameters to include the earthquake effect on rock slope stability. This study uses Monte Carlo simulation, rock mass strength parameters, horizontal seismic coefficient, and the Hoek-Brown failure criterion to evaluate the P_f for thousands of rock slope cases. The predictive Random forest based model is built using results obtained from Monte Carlo analysis.

Material and Methods

Hoek-Brown failure criterion

Generally, most geotechnical software are predominantly based on the Mohr-Coulomb soil parameters as input, thereby ignoring the non-linear nature of rock mass failure envelope. The

nonlinearity of rock masses is more pronounced at low confining stresses that are operational in slope stability problems. Figure 1 shows an illustration of the Hoek-Brown criterion and the equivalent Mohr-Coulomb envelope. The Hoek-Brown failure criterion is one of the few non-linear criteria often used by practicing engineers to estimate rock mass strength. This study adopted the Hoek-Brown yield criterion as the failure envelope for the rock masse of the slopes.

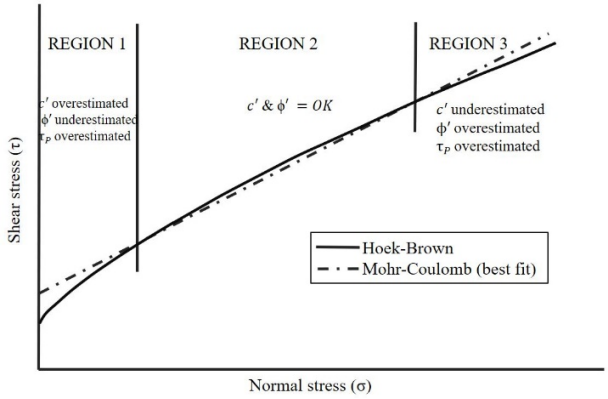

Figure 1. Hoek-Brown and the equivalent Mohr-Coulomb envelope

The latest version of the Hoek-Brown yield criterion (Hoek, Carranza-Torres, and Corkum 2002) is expressed as:

$$\sigma_1' = \sigma_3' + \sigma_{ci}\left(m_b \frac{\sigma_3'}{\sigma_{ci}} + s\right)^{\alpha} \tag{1}$$

where

$$m_b = m_i \exp\left(\frac{GSI-100}{28-14D}\right) \tag{2}$$

$$s = \exp\left(\frac{GSI-100}{9-3D}\right) \tag{3}$$

$$\alpha = \frac{1}{2} + \frac{1}{6}\left(e^{-GSI/15} - e^{-20/3}\right) \tag{4}$$

the magnitudes of m_b, s, and α depends on the geological strength index (GSI). The parameter D is a factor that is dependent upon the degree of disturbance and it ranges from 0 to 1.

Random forest (RF)

Random forest (RF) also referred to random decision forest is an ensemble modelling method for grouping, regression, and various other tasks. The final output of RF regression is the average of the outputs of all the individual decision trees. The trees in RF grow at training time depending on the complexity of the training data used for training. RF uses a technique called bagging to combine all the decision trees generated during training. The implementation of bagging in RF significantly enhances the diversity of the trees, this help in obtaining better model stability, thereby making random forest robust and effective when dealing with problems.

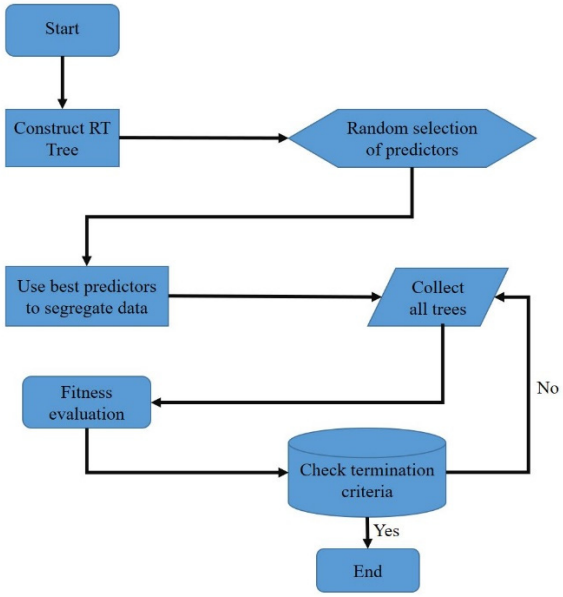

Figure 2. Methodology flowchart for RF modelling

Proposed methodology

Data preparation

In this study, in order to develop a comprehensive database for $\boldsymbol{P_f}$ prediction of rock slopes under earthquake conditions, a series of cases were constructed using Monte Carlo simulation to calculate the $\boldsymbol{P_f}$. Random forest algorithm was used as the base model to develop the predictive model. Rock slope strength parameters, slope geometry parameters, and horizontal seismic coefficient ($\boldsymbol{k_h}$) were chosen as input parameters with the $\boldsymbol{P_f}$ values obtained for Monte Carlo simulation as the target (output) value. In this study, a large number of rock variables such as unconfined compressive strength ($\boldsymbol{\sigma_{ci}}$), unit weight ($\boldsymbol{\gamma}$), geological strength index ($\boldsymbol{GSI}$), and intact rock constant ($\boldsymbol{m_i}$), as well as the external factor horizontal seismic coefficient ($\boldsymbol{k_h}$) were all be sampled from their known probability distribution. To achieve this, the coefficient of variation ($\boldsymbol{COV}$) or standard deviation (Std) was specified for each of the above-mentioned rock parameters and the horizontal seismic coefficient. Once the type of distribution for each of the parameters is specified, the corresponding factor of safety can be estimated. The safety of factor values is plotted on a probability distribution paper to obtain the distribution of the factor of safety. The probability distribution of the factor of safety is then used to calculate the probability of failure ($\boldsymbol{P_f}$). The $\boldsymbol{P_f}$ values obtained in our study were based on comparisons between the $\boldsymbol{k_h}$ distribution of Taipei and the suggestion by Hoek.

Table 1. Input and output variables for $\boldsymbol{P_f}$ prediction

Variable	Category	Min	Max	Std
COV $\boldsymbol{\sigma_{ci}}$	Input	0.125001	0.374930	0.071446
COV $\boldsymbol{\gamma_t}$	Input	0.100012	0.199979	0.029046
Std ***GSI***	Input	1.250110	3.749757	0.720656
COV $\boldsymbol{m_i}$	Input	0.062500	0.187472	0.036377
COV $\boldsymbol{k_h}$	Input	0.006311	0.999741	0.151162
$\boldsymbol{\beta^o}$	Input	13.470445	79.631925	8.986732
H(m)	Input	2.357085	150.770226	19.795228
$\boldsymbol{P_f}$	Output	0.000000	100.000000	33.262996

Performance evaluation

In this study, various performance measures are used to evaluate the performance of the proposed RF model for the prediction of rock slope P_f. The two indicators used for performance evaluation are the coefficient of determination (R^2) and root mean square error (RMSE). The evaluation indicators used are shown in Equations (5) and (6).

$$R^2 = 1 - \frac{\sum_{i=1}^{n}(y_i - y_i^*)^2}{\sum_{i=1}^{n}(y_i - y_i^m)^2} \tag{5}$$

$$RMSE = \sqrt{\left(\frac{1}{n}\right)\sum_{i=1}^{n}(y_i - y_i^m)^2} \tag{6}$$

Implementation of RF based P_f predictive model

The implementation of the proposed predictive RF based $\boldsymbol{P_f}$ prediction model consists of three major steps. Firstly, the dataset is randomly divided into two sets of training and testing sets. 80% of the data was chosen as the training set and the remaining 20% as the testing set. Secondly, different tree numbers and the minimum limit of split subsets are experimented so as to obtain the most effective RF model with optimal values. Thirdly, the performance of the RF model is evaluated using two commonly used performance indicators, namely $\boldsymbol{R^2}$ and RMSE. The optimal values of the RF model are reported in Table 2.

Table 2. The optimal parameters for the RF model

RF Parameter	Value
Number of trees	100
Minimum samples for split	2

Results and discussion

The results obtained from the RF based model for the prediction of rock slope $\boldsymbol{P_f}$ were subjected to various performance indicators: namely, $\boldsymbol{R^2}$ and $\boldsymbol{RMSE}$ to determine the efficiency of the proposed model for slope stability probability of failure prediction. Table 3 shows the performance of the RF model on both the training and the testing sets. Evidently, the model demonstrated high accuracy in predicting the $\boldsymbol{P_f}$ for rock slopes. The high performance of the model on the training set shows that the learning process of the predictive model was satisfactory. Whereas, the high performance on the testing set shows that the model has attained a satisfactory high generalization performance.

Table 3. Predictive RF model performance

	Performance measures	
Set	$\boldsymbol{R^2}$	RSME
Training	0.9998	0.4389
Testing	0.9987	1.1941

Conclusion

This study presented an RF based algorithm to predict the probability of failure for rock slope cases, under the seismic influence of 1 PGA, the slope cases were analyzed using Monte Carlo simulation. The variables COV σ_{ci}, COV γ_t, Std *GSI*, COV m_i, COV k_h, β, and H were set as model inputs with P_f as the output. To measure the performance of the RF model R^2 and $RMSE$ were used as performance indicators for both the training and testing sets. The values of the performance indicators confirmed the successful use of RF model for the prediction of rock slope probability of failure.

References

Catalan, J Morla, and C Allin Cornell. 1976. "Earth slope reliability by a level-crossing method." *Journal of the Geotechnical Engineering Division* 102 (6):591-604.

Fatty, Abdoulie, An Jui Li, and Li-Hsuan Chen. 2022. "Recurrent Neural Network Based IOS Mobile Applications for Slope Safety Assessment." *IEEE Consumer Electronics Magazine*.

Göktepe, Fatih, and Inan Keskin. 2018. "A comparison study between traditional and finite element methods for slope stability evaluations." *Journal of the Geological Society of India* 91 (3):373-379.

Hoang, Nhat-Duc, and Anh-Duc Pham. 2016. "Hybrid artificial intelligence approach based on metaheuristic and machine learning for slope stability assessment: A multinational data analysis." *Expert Systems with Applications* 46:60-68.

Hoek, Evert, and Jonathan D Bray. 1981. *Rock slope engineering*: CRC Press.

Hoek, Evert, Carlos Carranza-Torres, and Brent Corkum. 2002. "Hoek-Brown failure criterion-2002 edition." *Proceedings of NARMS-Tac* 1 (1):267-273.

Koopialipoor, Mohammadreza, Danial Jahed Armaghani, Ahmadreza Hedayat, Aminaton Marto, and Behrouz Gordan. 2019. "Applying various hybrid intelligent systems to evaluate

and predict slope stability under static and dynamic conditions." *Soft Computing* 23 (14):5913-5929.

Li, AJ, MJ Cassidy, Y Wang, RS Merifield, and AV Lyamin. 2012. "Parametric Monte Carlo studies of rock slopes based on the Hoek–Brown failure criterion." *Computers and Geotechnics* 45:11-18.

Li, An-Jui, Kelvin Lim, Chien-Kuo Chiu, and Benson Hsiung. 2018. "Application of artificial neural network in assessing fill slope stability." *World Academy of Science, Engineering and Technology, International Journal of Geotechnical and Geological Engineering* 5 (2).

Li, An Jui, Kelvin Lim, and Abdoulie Fatty. 2020. "Stability evaluations of three-layered soil slopes based on extreme learning neural network." *Journal of the Chinese Institute of Engineers* 43 (7):628-637.

Lu, P, and MS Rosenbaum. 2003. "Artificial neural networks and grey systems for the prediction of slope stability." *Natural Hazards* 30 (3):383-398.

Nilsen, B. 2000. "New trends in rock slope stability analyses." *Bulletin of Engineering Geology and the Environment* 58 (3):173-178.

Sakellariou, M. G., and M. D. Ferentinou. 2005. "A study of slope stability prediction using neural networks." *Geotechnical & Geological Engineering* 23 (4):419. doi: 10.1007/s10706-004-8680-5.

Tobutt, DC. 1982. "Monte Carlo simulation methods for slope stability." *Computers & Geosciences* 8 (2):199-208.

Wu, Tien H, and Leland M Kraft Jr. 1970. "Safety analysis of slopes." *Journal of the Soil Mechanics and Foundations Division* 96 (2):609-630.

International Symposium on Emerging Developments and Innovative Applications of Reliability Engineering and Risk Managements (EDIARR2022),30 October-3 November2022, Taipei
Chen, S. S. &Ang, Alfredo. H-S. (Editors)

REAL-TIME HYBRID SIMULATION FOR A BRIDGE RC PIER SUBJECTED TO HORIZONTAL AND VETICAL GROUND MOTIONS

Jamin Park[1], Minseok Park[2], Yunbyeong Chae[3], and Chul-Young Kim[4]

[1]*Department of Civil and Environmental Engineering, Seoul National University, 1 Gwanak-ro, Gwanak-gu, Seoul, Korea*

E-mail: jaminpark86@gmail.com

[2]*Hybrid Structural Testing Center, Myongji University, 116 Myongi-ro, Cheoin-gu, Yongin, Gyeonggi-do, Korea*

E-mail: itfeels@nate.com

[3]*Department of Civil and Environmental Engineering, Seoul National University, 1 Gwanak-ro, Gwanak-gu, Seoul, Korea*

E-mail: ybchae@snu.ac.kr

[4]*Department of Civil and Environmental Engineering, Myongji University, 116 Myongi-ro, Cheoin-gu, Yongin, Gyeonggi-do, Korea*

E-mail: cykim@mju.ac.kr

Abstract: Recent advance in real-time force control enables real-time dynamic testing that was quite difficult to be implemented in the past. In this study, real-time hybrid simulation (RTHS) for a two-span bridge subjected to both horizontal and vertical ground motions is introduced. A reinforced concrete (RC) pier at the center of the bridge is experimentally tested in the lab, while the remaining parts are numerically modeled. The time varying axial force of the RC pier due to the presence of vertical ground motion was simulated by using a newly developed real-time force control method along with the use of a flexible loading beam (FLB). The RTHS was repeated by adjusting the ratio of the peak vertical ground acceleration to the peak horizontal acceleration (V/H ratio) and the weight of the bridge superstructure to investigate the influence of the vertical ground motion on the lateral response of the bridge. It was found that the gravity load (constant axial force) on the RC pier can significantly affect on its post-yield behavior. However, the time varying axial force due to the given vertical ground motion did not change the lateral response substantially. More details of test results are presented and discussed.

***Keywords*:** Real-time hybrid simulation, RC pier, Vertical ground motion, Seismic performance evaluation.

Research background

It had been assumed that the influence of the vertical component of ground motions on a structure's behavior during a seismic event is less significant in comparison with that of the horizontal component. Since Newmark et al. (1973), the V/H ratio, the ratio of the vertical peak acceleration to the horizontal peak acceleration, had been assumed to be 2/3, which implies the smaller influence of the vertical component than its horizontal counterpart. However, it was reported by Bozorgnia and Campbell (2004) that the V/H ratio of 2/3 is not realistic, and its value depends on site-to-source distance and period. It was also reported by Kim et al. (2011) that the V/H ratio for a relatively large earthquake of which source distance is less than 50 km can be up to 2.0.

For investigating the influence of vertical ground motion on the behavior of reinforced concrete (RC) piers and columns, several experimental studies have been conducted. Kim and Elnashai (2008) conducted cyclic pushover tests for RC columns under constant axial compressive or tensile force, showing that the strength of the specimens subjected to constant axial tension increased marginally, while that of specimens subjected to axial compression showed significant strength degradation. Kim et al. (2011) conducted pseudo-dynamic hybrid simulations for a bridge with an RC pier subjected to both horizontal and vertical ground motions and showed that the vertical ground motion leads to large fluctuation in axial force, leading to axial tension at times. It was also shown in the study that the large axial force variation due to the vertical component leads to the fluctuation in lateral stiffness, more severe cracking and damage, and a change in the column's failure mode from flexure to shear. Though the aforementioned studies shed a light on the behavior and performance of RC columns subjected to both horizontal and vertical ground motions, those studies were conducted in a quasi-static fashion where the loading speed is smaller than that the RC columns experience during an actual seismic event.

On the other hand, it is broadly accepted that both steel and concrete are rate-dependent materials, and their material properties vary depending on the rate of loading to which the material is subjected. The loading rate is often referred to as a strain rate. Though there is still disagreement between researchers on the influence of strain rate on the concrete's properties (Saatci et al. 2009a, Meng et al. 2011), it is typically accepted that reinforced concrete exhibits a significant increase in strength when loaded at a high strain rate (Mander et al. 1988, Fu et al. 1991). Otani et al. (2003) conducted a series of dynamic cyclic pushover tests of RC columns under the loading speed of 200 mm/s and showed that the flexural strength of RC columns increases about 15 to 20 % in comparison with that under static loading of 0.1 mm/s.

Therefore, it is necessary to conduct testing in real-time to accurately evaluate the seismic performance of RC columns subjected to both horizontal and vertical ground motions, considering the reinforced concrete's non-negligible rate-dependent properties. However, the real-time testing or RTHS for RC columns has been scarcely conducted, mainly due to the difficulties in accurate control of multiple actuators in real-time, which is essential for considering the influence of both horizontal and vertical ground motions. Nevertheless, due to the recent advances in controlling actuators for real-time testing and hybrid simulation (Chae, Kazemibidokhti, and Ricles 2013; Fermandois and Spencer 2017; Chae et al. 2018 and 2019, Najafi, Fermandois, and Spencer 2020), accurate multi-axial control of a RC column in real-time, especially for axial displacement and force acted upon the specimen, becomes available.

In this study, a series of RTHS with 4 RC pier specimens subjected to both horizontal and vertical ground motions were conducted such that the seismic performance of the RC piers under more realistic loading conditions induced by a given seismic event can be investigated. The tests were conducted for various V/H ratios in the range of 0.0 to 1.97 and the constant axial force corresponding to the self-weight of the bridge superstructure acted upon the pier's cross-section. Details of the RTHS, test results, and conclusions drawn from the results are presented in the following sections.

Experimental program

Target structure

Figure 1(a) shows the target structure of the RTHS, a two-span bridge with an RC pier at the center. The superstructure is mounted on hinge supports at the top of the RC pier and roller supports on both abutments. It is assumed that the bridge is subjected to both horizontal and vertical ground motions, i.e., $\ddot{x}_g^h(t)$ and $\ddot{x}_g^v(t)$. The mass of the superstructure was assumed to be 80 tons. The flexural stiffness of the superstructure was determined such that the fundamental natural frequency is 2.68 Hz. In the RTHS, the RC pier was physically tested in the lab, while the remaining part of the bridge was numerically modeled.

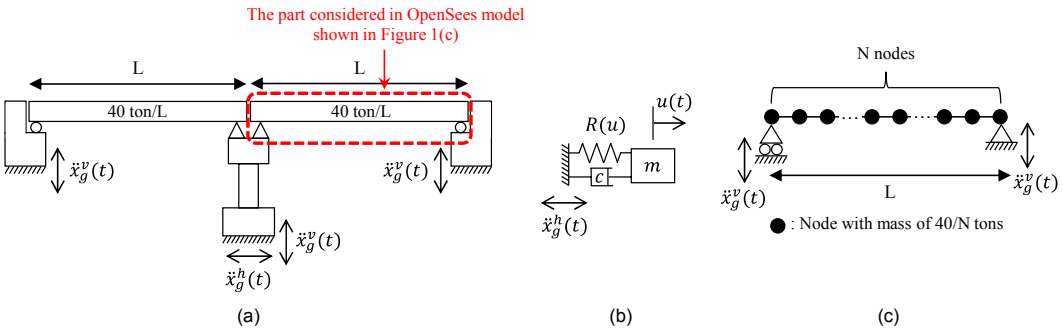

Figure 1. Target structure for RTHS (a); SDOF model used for calculating the horizontal displacement of the bridge (b); OpenSees model for calculating the axial force boundary condition of the RC pier (c)

Figure 2 shows the dimensions and reinforcing details of the RC pier specimens. The specimens were designed to be failed in flexure. The top and bottom stubs were strongly reinforced such that no deformation or premature failure occurred in the stubs during the tests. The material properties of concrete used for fabricating the specimens were obtained through standard compression tests with 12 concrete cylinders according to ASTM C469 (2014) and ASTM C39 (2021). The average concrete compressive strength and elastic modulus were 34.3 MPa and 21.0 GPa, respectively. The yield strength of the reinforcements was 400 MPa.

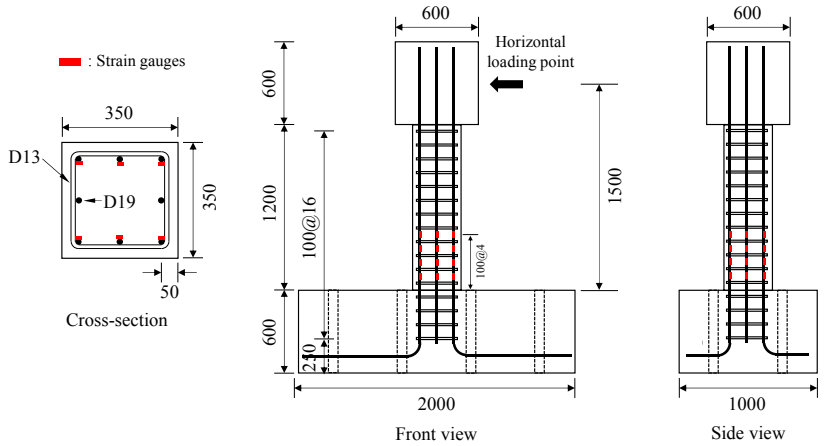

Figure 2. Test specimen (unit: mm)

Test setup and implementation

Figure 3 shows the test setup used for the RTHS. A total of three actuators were used for imposing the boundary conditions on the control point located at the center of the head block. The boundary conditions consist of a displacement boundary condition in the horizontal direction and a force boundary condition in the axial direction. A specially designed load transfer element, called Flexural Loading Beam (FLB), was mounted on top of the specimen. The FLB was employed to accurately control the force boundary condition through the displacement control of the two vertical actuators. Details on the FLB can be found in Chae et al. (2019).

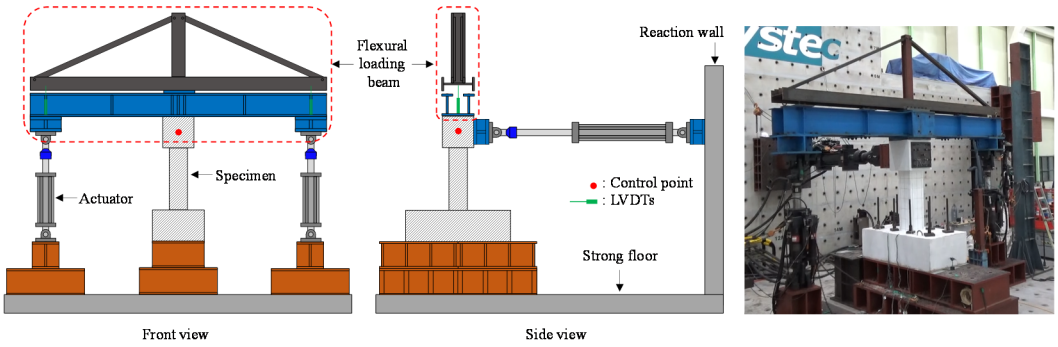

Figure 3. Test setup for the RTHS

Configuration of RTHS

The displacement and force boundary conditions imposed on the specimen were calculated in different ways. For the displacement boundary condition, it was assumed that the axial stiffness of the superstructure is rigid such that the horizontal behavior of the RC pier can be modeled as a single-degree-of-freedom (SDOF) model as shown in Figure 1(b). The equation of motion for the SDOF model can be written as follows:

$$m_a\ddot{u}_h(t) + c\dot{u}_h(t) + R\big(u_h(t)\big) = -m\ddot{u}_g^h(t) \tag{1}$$

where, m denotes the total mass of the superstructure, i.e., 80 tons, c denotes a damping coefficient, $u_h(t)$ denotes the horizontal displacement at the top of the RC pier, and $R(u)$ denotes the restoring force from the RC pier at the horizontal displacement u.

During the RTHS, the restoring force $R(u)$ was experimentally obtained from the test specimen. At the *i*-th step of the RTHS, the restoring force can be calculated from the measured forces of the three actuators as follows:

$$R\big(u_h(t_i)\big) = F_h + (F_{v1} + F_{v2}) \times (u_h(t_i)/L_e) \tag{2}$$

where, F_h, F_{v1}, and F_{v2} denote the measured forces from the horizontal and two vertical actuators, respectively. L_e denotes the distance between the top and bottom swivel joints of the vertical actuator, which is 1,800 mm. In Equation (2), the second term on the right-hand side is the horizontal contribution of the two vertical actuator forces which needs to be subtracted from the horizontal actuator force for obtaining the actual resistance of the column. The calculated restoring

force is used for calculating the displacement boundary condition for the (i+1)-th step, i.e., $u_h(t_{i+1})$, by solving Equation (1) numerically using the CR integration algorithm (Chen and Ricles 2010). The time step length of 1/1024 s was used. The damping coefficient c was determined to be 3% of the critical damping. The force calculated by Equation (2) contains an inertia force associated with the test setup, i.e., the FLB and actuators, as well as the restoring force from the specimen. Thus, the mass m_a was determined to be $m - m_e$, where m_e denotes the mass of the test setup.

For the force boundary condition, the characteristic that the horizontal behavior of the superstructure does not significantly influence the axial forces acted upon the RC pier when the axial stiffness of the RC pier is much larger than the flexural stiffness of the superstructure was used (Chae et al. 2018). Thus, the whole time history of the axial force resulting from the vertical ground motion was calculated before implementing the RTHS and imposed on the specimen as a pre-defined target force boundary condition during the RTHS. Figure 1(c) shows an OpenSees (2006) model for calculating the force boundary condition, which models half of the superstructure and the top of the RC pier (see the part inside the dotted rectangle in Figure 1(a)). In the model, the superstructure was modeled using *N* equally spaced nodes with a mass of $40/N$ tons each. The *N* larger than 30 provides almost the same result. With the model, dynamic analysis was conducted by assuming that the beam is subjected to the vertical component of the input ground motion $\ddot{x}_g^v(t)$. The force boundary condition was calculated by summing the reactions from both supports.

Figure 4 illustrates the configuration of the RTHS. The configuration was implemented in MATLAB's Simulink environment, which integrates the SDOF model, integration algorithm, actuator control algorithms, and other functions used for exchanging data with the actuator controller and the data acquisition (DAQ) device. In Simulink, the target boundary conditions are determined through numerical integration with the SDOF model. The boundary conditions are transferred to the ATS (Chae et al. 2013) compensator and the D-ATS controller (Chae et al. 2018) where the command strokes for the three actuators corresponding to the displacement and force boundary conditions are determined. The command strokes are transferred to the actuator controller MTS FlexTest. From LVDTs and load cells of the actuators, displacements and reactional forces are measured and fed back to the Simulink via DAQ devices. The measured displacements and forces are then used for the numerical integration and a delay compensator for calculating the command strokes of the actuators for the next time step during RTHS.

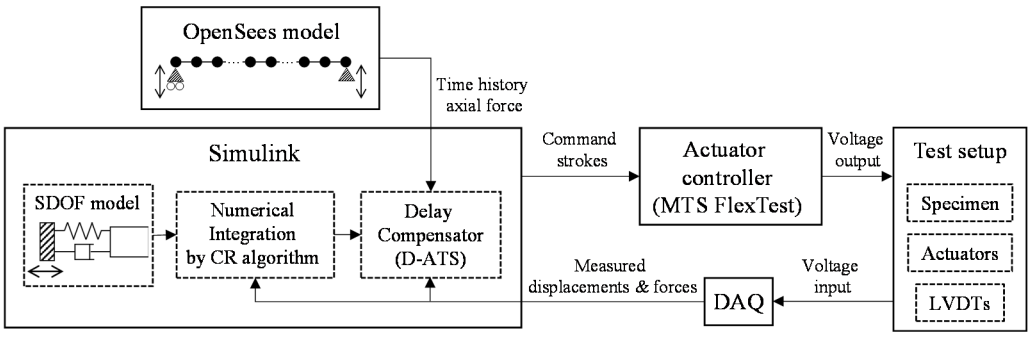

Figure 4. Test configuration for the RTHS

Input ground motion and test cases

Figure 5 shows the input ground motion used for the RTHS, the horizontal (142) and vertical components of the 1994 Northridge earthquake measured at the Sylmar-Converter station. The peak ground accelerations are 0.923 g and 0.605 g for the horizontal and vertical components, respectively.

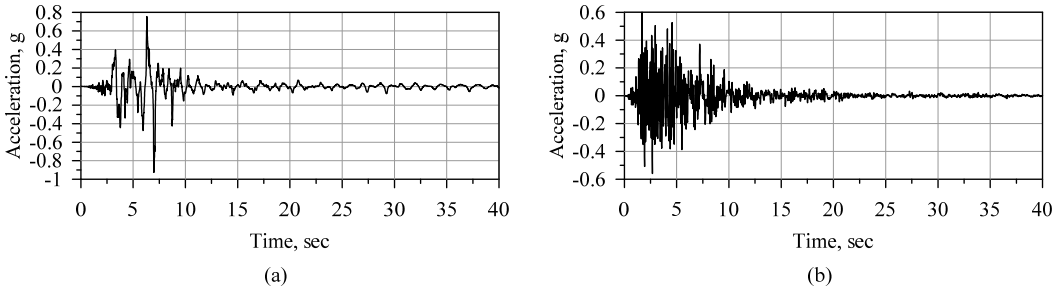

Figure 5. Input ground motions: (a) horizontal component; (b) vertical component

Table 1 shows the text matrix. The main test parameters were 1) V/H ratio and 2) presence of gravity load corresponding to the self-weight of the superstructure. For all cases, the horizontal component of the input ground motion was scaled by multiplying a scale factor of 0.3, while the vertical component was scaled by multiplying a scale factor in the range from 0.3 to 1.0. Subscripts are used to distinguish each case, where the number in the subscripts denotes the V/H ratio and the letters 'S' or 'NS' denote whether the gravity load was considered or not, respectively. Except for the case VH_{0NS}, the constant axial compressive force of 392 kN corresponding to the half of the superstructure's self-weight, i.e., 40 tons, was imposed throughout the RTHS.

Table 1. Test matrix

Tag	Scale factor		V/H ratio	Gravity load
	Horizontal (H)	Vertical (V)		
VH_{0NS}	0.3	0.0	0.0	X
VH_{0S}				O
$VH_{0.66S}$		0.3	0.66	
$VH_{1.97S}$		1.0	1.97	

Results and discussion

Influence of the gravity load

Figure 6 compares the test results for the cases VH_{0NS} and VH_{0S}. The constant axial force of 392 kN was imposed on the specimen for the case VH_{0S} only. It is shown in Figures 6(a) and 6(b) that the constant axial force led to a smaller maximum displacement, larger initial stiffness, and larger maximum force. The maximum horizontal force for the case VH_{0S} was 140 kN, which is 18 % greater than 118 kN for the case VH_{0NS}. It can be noted that the case VH_{OS} shows clear strength degradation, i.e., a decrease of the restoring force after reaching the maximum, while no such degradation was observed for the case VH_{0NS}. The increase in the initial stiffness is also evidenced

in Figure 6(c) which shows the frequency response of the horizontal displacement obtained by fast Fourier transform (FFT). The figure shows that the responses in the higher frequency domain are greater for the case VH_{0S}, indicating the increase in the specimen's stiffness.

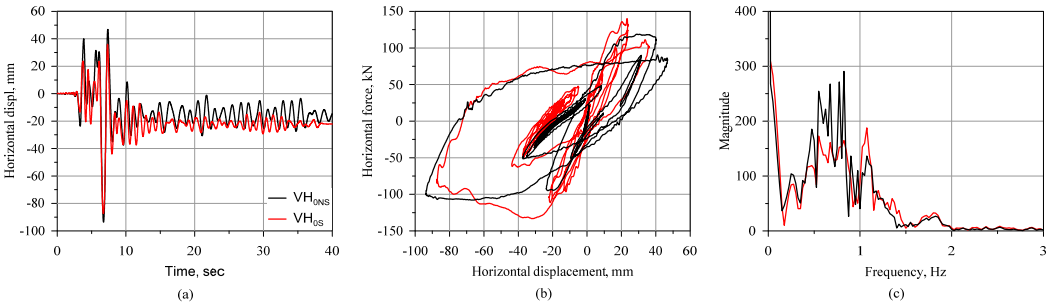

Figure 6. Comparison of test results for the cases VH0NS and VH0S: (a) Time history of the horizontal displacement, (b) Horizontal force-displacement relation, (c) Frequency response of the horizontal displacement

Influence of the V/H ratio

Figure 7 compares the test results for the cases VH_{0S}, $VH_{0.66S}$, and $VH_{1.97S}$. The same constant axial force of 392 kN was imposed on the specimen for all cases, while the V/H ratio ranged from 0.0 to 1.97 in each case. Figure 7(a) shows large fluctuations in the axial force for the case $VH_{0.66S}$ and $VH_{1.97S}$. The magnitude of the force fluctuation increased in proportion to the V/H ratio. Note in Figures 7(b), 7(c), and 7(d) that the large force fluctuation did not much affect the behavior of the RC pier in the horizontal direction, as the force-displacement relation and the displacement in the frequency domain show the minor difference between the three cases.

Overall, the influence of the V/H ratio was limited in comparison with that of the gravity load. This was partly due to the difference in time to reach the peak axial force and the time to reach the peak horizontal displacement was reached. As shown in Figures 7(a) and 7(b), the peak axial force was reached at 7.33 s while the peak horizontal displacement was reached at 6.71 s. For the case $VH_{1.97S}$, the horizontal displacement at 7.33 s was 30.2 mm, far smaller than the maximum displacement of 89.7 mm. Similarly, the axial force at 6.71 s was 200 kN, far smaller than the peak axial force of 663 kN. Figure 7(a) also shows that the frequency of the force fluctuations is much higher than that of the horizontal displacement shown in Figure 7(b), which attributes to the high-frequency content of the vertical ground motion shown in Figure 5(b). The high frequency oscillation of the axial force resulted in a limited influence on the V/H ratio, as it makes it difficult for the horizontal displacement and axial force to be large at the same time.

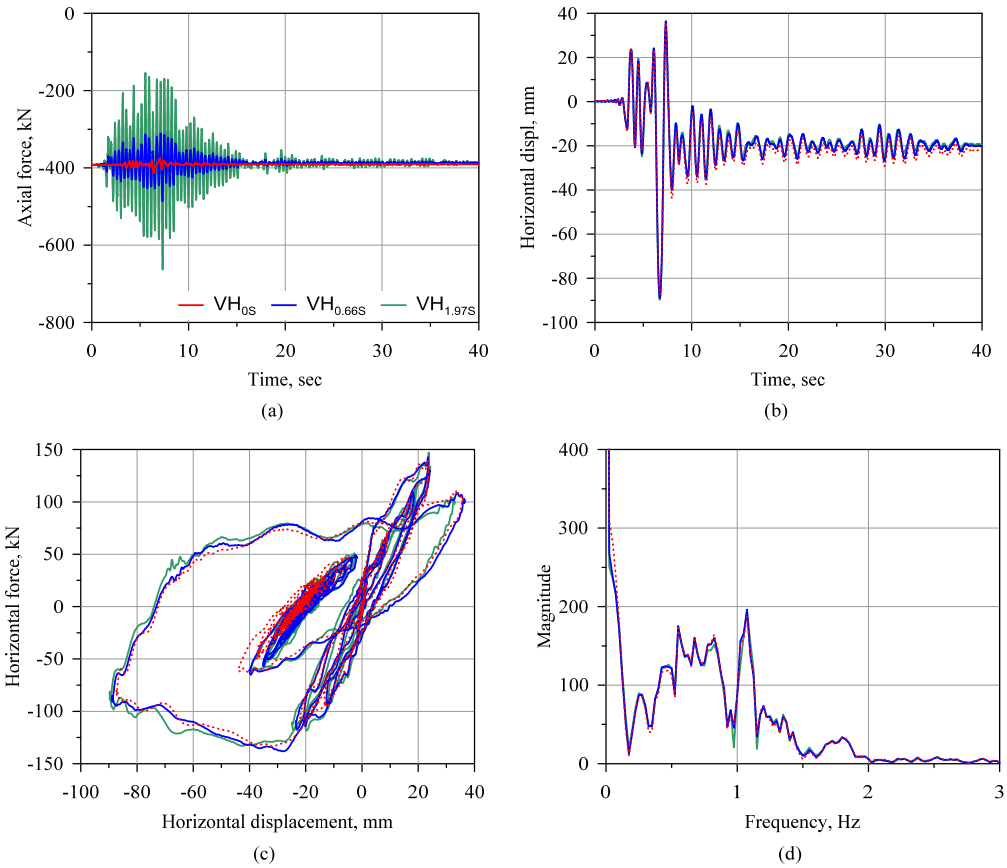

Figure 7. Comparison of test results for the cases VH_{0S}, $VH_{0.66S}$, and $VH_{1.97S}$: (a) time history of the axial force; (b) time history of the horizontal displacement; (c) the horizontal force-displacement relation; (d) frequency response of the horizontal displacement

Conclusions

In this study, by applying one of the recently developed real-time actuator control methods, the D-ATS compensator, a series of RTHS for a two-span bridge with an RC pier in the middle were successfully carried out. In the RTHS, the RC pier was experimentally considered while the other structural components were numerically considered. The RTHS was conducted for various V/H ratios of the input ground motion and the gravity load associated with the self-weight of the bridge superstructure.

The RTHS results show that the gravity load can greatly affect the behavior of RC piers, leading to an increase in the initial stiffness and maximum force as well as more strength degradation associated with the reduced displacement capacity. In comparison with the gravity load, the influence of the V/H ratio was not significant in this study. Though a large fluctuation in the axial force was observed in the cases with a high V/H ratio, the influence of the force fluctuation on the behavior of RC piers in the horizontal direction was almost negligible. This is partly due to the difference in time to reach the peak axial force and the time to reach the peak horizontal displacement as well as the high frequency of the force fluctuation compared to that of the

horizontal displacement. Consequently, it is clearly shown in the RTHS results that the gravity load, not the force fluctuation resulting from the vertical ground motion, has a greater effect on the behavior and performance of the RC pier.

It is worth mentioning that the conclusions drawn from the RTHS of this study is only relevant for the specific types of RC pier specimen and the selected earthquake ground motion used in this study. All specimens were failed in flexure, and the change of failure mode from flexure to shear due to the fluctuation in the axial force, reported by Papazoglou and Elnashai (1996) and Kim et al. (2011), was not observed in this study. Further experimental studies need to be conducted with higher V/H ratios, various earthquake ground motions, and RC piers with various dimensions and reinforcing details, in order to fully understand the behavior and performance of RC piers subjected to both horizontal and vertical ground motions.

Acknowledgement

This work was supported by the New Faculty Startup Fund from Seoul National University.

References

American Society for Testing and Material. 2021. *ASTM C39: Standard Test Method for Compressive Strength of Cylindrical Concrete Specimens*. West Conshohocken, PA: American Society for Testing and Materials.

American Society for Testing and Materials. 2014. *ASTM C469: Standard Test Method for Static Modulus of Elasticity and Poisson's Ratio of Concrete in Compression*. https://doi.org/10.1520/C0469-02E01.2.

Bozorgnia, Yousef, and Kenneth W. Campbell. 2004. "The Vertical-to-Horizontal Response Spectral Ratio and Tentative Procedures for Developing Simplified V/H and Vertical Design Spectra." *Journal of Earthquake Engineering* 8 (2): 175–207. https://doi.org/10.1080/13632460409350486.

Chae, Yunbyeong, Karim Kazemibidokhti, and James M. Ricles. 2013. "Adaptive Time Series Compensator for Delay Compensation of Servo-Hydraulic Actuator Systems for Real-Time Hybrid Simulation." *Earthquake Engineering and Structural Dynamics* 42: 1697–1715.

Chae, Yunbyeong, Jinhaeng Lee, Minseok Park, and Chul Young Kim. 2019. "Fast and Slow Cyclic Tests for Reinforced Concrete Columns with an Improved Axial Force Control." *Journal of Structural Engineering (United States)* 145 (6): 1–12. https://doi.org/10.1061/(ASCE)ST.1943-541X.0002334.

Chae, Yunbyeong, Ramin Rabiee, Abdullah Dursun, and Chul Young Kim. 2018. "Real-Time Force Control for Servo-Hydraulic Actuator Systems Using Adaptive Time Series Compensator and Compliance Springs." *Earthquake Engineering and Structural Dynamics* 47 (4): 854–71. https://doi.org/10.1002/eqe.2994.

Chen, Cheng, and James M. Ricles. 2010. "An Unconditionally Stable Explicit Integration Algorithm with Controllable Numerical Damping for Real-Time Testing." *Structures Congress 2010*, 3387–96. https://doi.org/10.1061/41130(369)306.

Fermandois, Gaston A, and Billie F Spencer. 2017. "Model-Based Framework for Multi-Axial Real-Time Hybrid Simulation Testing." *Earthquake Engineering and Structural Dynamics* 16 (4): 671–91.

Kim, S J, C J Holub, and Amr S. Elnashai. 2011. "Experimental Investigation of the Behavior of RC Bridge Piers Subjected to Horizontal and Vertical Earthquake Motion." *Engineering Structures2* 33 (7): 2221–35.

Kim, Sung Jig, and Amr S Elnashai. 2008. "Seismic Assessment of RC Structures Considering Vertical Ground Motion." *Mid-America Earthquake Center*.

Kim, Sung Jig, Curtis J. Holub, and Amr S. Elnashai. 2011. "Analytical Assessment of the Effect of Vertical Earthquake Motion on RC Bridge Piers." *Journal of Structural Engineering* 137 (2): 252–60. https://doi.org/10.1061/(asce)st.1943-541x.0000306.

Mazzoni, Silvia, Frank McKenna, Michael H. Scott, and Gregory L. Fenves. 2006. "Open System for Earthquake Engineering Simulation (OpenSEES) User Command-Language Manual." *Pacific Earthquake Engineering Research Center*, 465.

Najafi, Amirali, Gaston A Fermandois, and Billie F Spencer. 2020. "Decoupled Model-Based Real-Time Hybrid Simulation with Multi-Axial Load and Boundary Condition Boxes." *Engineering Structures* 219.

Newmark, Nathan M., John A. Blume, and Kanwar K. Kapur. 1973. "Seismic Design Spectra for Nuclear Power Plants." *ASCE Journal of the Power Division* 99 (2): 287–303.

Otani, Shunsuke, Takashi Kaneko, and Hitoshi Shiohara. 2003. "Strain Rate Effect on Performance of Reinforced Concrete Members." In *Proceedings of the Fib 2003 Symposium*, 226–29. Athens, Greece.

Papazoglou, A. J., and A. S. Elnashai. 1996. "Analytical and Field Evidence of the Damaging Effect of Vertical Earthquake Ground Motion." *Earthquake Engineering and Structural Dynamics* 25 (10): 1109–37. https://doi.org/10.1002/(SICI)1096-9845(199610)25:10<1109::AID-EQE604>3.0.CO;2-0.

International Symposium on Emerging Developments and Innovative Applications of Reliability Engineering and Risk Managements (EDIARR2022),30 October-3 November2022, Taipei
Chen, S. S. &Ang, Alfredo. H-S. (Editors)

DEVELOPMENT AND VERIFICATION OF SIMPLIFIED GEOMETRY-BASED STRUCTURAL MODELS FOR URBAN EARTHQUAKE SIMULATION

Narutoshi Nakata[1], Masaki Takenaka[2] and Shota Saito[3]

[1,2,3]*Department of Civil and Environmental Engineering, Tokushima University, Tokushima, Japan*

E-mail: nnakata@tokushima-u.ac.jp

Abstract: This paper presents development of simplified geometry-based structural models for urban earthquake simulation. The simplified geometry-based structural models are constructed using GIS building information. Because the simplified models do not require structural drawings that are not available for most of the residential houses and private buildings, they have definitive advantages for urban earthquake simulation. The proposed structural models herein are simple but are able to incorporate structural material as well as structural type such as frame, wall, and combination of those. With those simplicity and flexibility in the proposed simplified geometry-based structural models, majority of buildings in many cities in Japan can be modeled for urban earthquake simulation. Selected types of the simplified structural models are verified through comparison in the fundamental dynamic characteristics with those obtained from system identification of real buildings. The details, dynamic characteristics, and the verification results of the simplified models are presented. Furthermore, the paper introduces an information system for urban earthquake simulation as well as an ongoing city-wide implementation project of the urban earthquake simulation.

***Keywords*:** Urban earthquake simulation, GIS, finite element model, system identification.

Background

Urban earthquake simulation is a regional-scale earthquake simulation in which great majority of structures within the area of interest are modeled individually and their responses to earthquakes are computed independently (Fujita et al. 2014). It makes it possible to conduct simulation-based earthquake risk assessment in the urban and reginal scales. Furthermore, it would even enable evaluation of disaster prevention measures and emergency response plans, accounting for the states of built environment and characteristics of earthquakes. Because of these features, urban earthquake simulation can be considered as a major element in the digital twin for the earthquake disaster management. In order to improve accuracy, applicability and scalability of the urban earthquake simulation, much more research efforts and advances are indispensable.

One of the challenges in the urban earthquake simulation is structural analysis modeling. Because of the facts that modeling has to be applied to structures with different types and that available levels of information for each structure are different, none of the existing structural models are suited as they are. For example, a simple single-degree-of-freedom model may seem attractive from the viewpoint of simplicity and computational time. However, it is not straightforward to accurately estimate natural frequencies of structures from limited information of structures. Furthermore, because of its simplicity, the single-degree-of-freedom model is not able to capture an eccentricity that is attributed from the geometry of the structure. Therefore, the single-degree-of-freedom model may not be sufficient as a primary model for the urban earthquake simulation that requires accurate modeling of vibration responses and consequential damages.

On the other hand, finite element model, one of the most widely-used structural models, is capable of capturing structural details including element-wise stress-strain relations, and thus, it is considered attractive for the model in the urban earthquake simulation. However, it requires not only detail levels of structural information such as structural drawings but also time, efforts and experience in creating a complete model. Therefore, the finite element model is not certainly easy, while not impossible, to apply to many numbers of structures that are required in the urban earthquake simulation. In recent years, quite a few efforts have been made towards conversions of building information models to finite element models. Thus, simplification of the finite element modeling process is becoming available in a seamless manner. While such advancing techniques are promising, the building information model is applied to limited structures, and their data are not generally available in public.

This study presents a simplified geometry-based structural modeling procedure for urban earthquake simulation. The proposed model is a finite element model that consists of columns, beams and walls. For an efficient and seamless definition of nodal coordinates and element connectivity, building information in GIS is adopted. To facilitate the map-based model creation and evaluation of simulation results, the proposed simplified geometry-based structural model is integrated into a GIS system. The proposed model is applied to the Minami-Josanjima district in Tokushima city. To refine and verify the dynamics of the proposed analytical models for those buildings in the area, system identification using ambient vibration are conducted. This paper presents a formulation procedure of the simplified geometry-based structural model and research efforts for the verification of this model.

Geometry-Based Structural Models

This section starts with a brief discussion of building information in the GIS. Then, the formulation procedure as well as required addition information are presented to facility the creation of the urban earthquake simulation model.

Building information in GIS

Building information in GIS is handled in several formats depending on objectives, usages, and providers. Esri's shapefile stores building geometries in ground level as a polygon containing latitude and longitude of sequential edges. Height of building is included as an independent attribute in each building object. The other details such as roof shapes and number of floors are not included in the shapefile. GeoJson and GML are similar to the shapefile in terms of types of stored building information. While in theory they could be expanded to include complex three-dimensional shapes and building details, building information in their formats that are publically available are nothing different from those in shapefile.

CityGML developed by the Open Geospatial Consortium (OGC) is an open standardized data format that helps creation of virtual 3d city models. It provides ways to define common 3d features and objects found in city, such as buildings, roads, rivers and so on. For the representation of buildings, it accepts different standard levels of details (LoDs). LoD0 defines a perimeter of building, and LoD1 adds height to it. While the basic information in LoD1 are same in those in the aforementioned formats, buildings are represented by a boundary representation method (Brep); all of the building surfaces that form box models are defined in each building model in LoD1. In

addition to the features in LoD1, LoD2 adds roof shapes in the model. Further advanced LoD3 and LoD4 have features to model building exteriors and interiors, respectively.

The CityGML facilitates the integration of urban geodata for a variety of applications for smart cities, and it has been used for simulation and visualization of 3d digital cities. In Japan, the Ministry of Land, Infrastructure, Transport and Tourism launched in 2020 an open-data project to promote the use of CityGML for digital twin and Society 5.0. Until now, 3d models of 56 cities have been made public from the project website in the CityGML format, and more and more cities will be made available for the advanced use of 3d city models.

As reviewed above, various types of building information are stored in the GIS data formats. However, judging from the viewpoint of structural analysis models, useful pieces of information that are stored in most of the GIS data formats might be building geometry and height. While the CityGML's higher LoDs provide building details, they may not be suitable for forming structural analysis models. In the future, much more relevant information such as building types and construction year are expected to be included in the GIS building information. Based on the above reviews, this study utilizes building geometry and height to form simplified finite element models for the application to urban earthquake simulation.

Formulation procedure of the simplified FEM from GIS building information

Finite element models require definition of nodes, elements, materials, sections, boundary conditions, and constraints. As mentioned earlier, defining the nodes require geometric information of the building, and in this process, the GIS building information is used. Following is a proposed procedure to form a simplified finite element model for each of the building in urban earthquake simulation. Figure 1 shows views of the GIS and structural models seen in the proposed process.

(1) Coordinate transformation: First, latitude and longitude in the building polygon are extracted from the GIS data. They are converted to the plane Cartesian coordinate system, and then area and centroid of the building are calculated. By subtracting the centroid in the plane Cartesian coordinate system, relative coordinates of the building polygon are obtained with respect to its centroid. See Figure 1 (i).

(2) Nodes at the ground level: In many cases, GIS contains redundant points that are not the edges of the building. By judging the angle at each point in the relative coordinates from the process (1), redundant points can be identified and removed from the building polygon. The resulting building polygon in the relative coordinate have only representative edges of the building. These edges are defined as nodes at the ground level.

(3) Nodes at upper levels: If the building polygon at the ground level is extruded with the height, it becomes BOX model (see Figure 1(b)). From the building height in GIS and general floor heights, number of floors is found for each building. Then, nodes at the upper levels are created by shifting the nodes at the ground level by each story height.

(4) Elements and connectivity: Nodes in the same vertical line are connected to form column elements. By going every edge of the building polygon from the ground level to the top floor, all the building columns are generated. For every floor, each node is connected to the next one in the building polygon to define floor edge beam element. Then, nodes at the same floor are

grouped together to form floor elements. With these processes, a basic structural model seen in Figure 1(c) is created.

(5) Additional columns and walls: In the basic structural model, columns are defined only at the edges of the building polygon. However, buildings in general have multiple columns in each side. Therefore, the model has a feature to insert columns between existing ones. Furthermore, many structures have load-bearing walls that provide stiffness to the direction parallel to it. The model can add such structural walls by specifying wall segments. The walls are modeled as 2D in-plane stress elements. Figure 1(iv) shows a 3d view of modified structural model with additional column and wall elements.

(6) Materials and sections: Material and sectional properties have to be assigned to all of the structural members in FEM. Structural material for each building can be found in GIS or identified from appearance survey. On the other hand, sectional properties such as column and wall widths are not obtained for most of the structures. In this proposed model, general values in sectional properties categorized by structural material are used by default.

(7) Boundary conditions and constraints: The last items required for the formulation of structural analysis model are boundary conditions and constraints. All the nodes at the ground levels are fixed as the boundary conditions. And then, the simplified structural analysis model here adopts following constraints. The first constraint is an internal constraint in which an element axial degree-of-freedom is ignored. The second constraint is an external constraint where external moment inputs are assumed zero so that rotational degrees-of-freedoms are statically condensed. These internal and external constraints reduce the model size and improve stability and computational efficiency that is necessary for urban earthquake simulation.

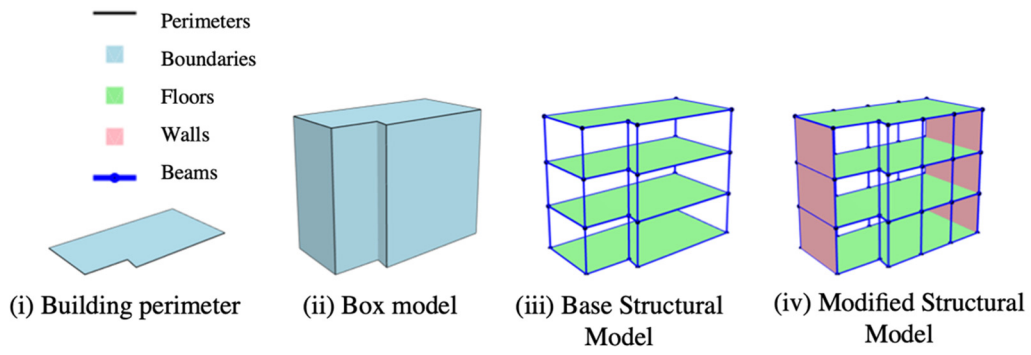

Figure 1. GIS and structural models in the formulation process.

Application of the Geometry-Based Structural Models

Structural analysis software defines structural models in their local coordinates, and it does not store location information such as latitude and longitude. Therefore, it is not possible to manage model properties and visualize simulation results on a map in the linked manner. It requires another system to link the structural models and maps to improve data management including visualization and evaluation of simulation results. One the other hand, GIS allows for addition of attributes to existing building data. Because of these reasons, rather than structural analysis software, this project adopts GIS as the primary platform for urban earthquake simulation by integrating structural analysis models and tools into GIS.

The developed system in this project is built on a Linux operating system with MySQL database, Django web framework, and Leaflet Java script library for GIS API. Structural models and analysis tools are developed in a programming language, Python, and are integrated as the module to the GIS. Building information in this project is downloaded from the Geospatial Information Authority of Japan in the GML format. The imported mesh grid ID is 513404 that includes Tokushima city. This mesh file contains information of 189,124 buildings.

Case study: Tokushima University Josanjima Campus

The Mimami-Josanjima district in Tokushima city is selected as the target area. There are 129 buildings in this district including those in Tokushima University Josanjima Campus. Structural models for thirty buildings on the campus are created for the evaluation of the proposed simplified geometry-based models. Figure 2 shows a 3D view of this district. In this figure, box models represent structures with only GIS building information whereas those with floors, walls and columns represent buildings of which structural models are constructed. Information needed for the creation of the models such as structural type, number of columns and location of walls are collected from drawings of each building.

Table 1 shows a list of buildings of which structural models are constructed. In this case study, structural types are frame or wall-type frame with reinforced concrete (RC) or steel reinforced concrete (SRC). Number of floors of the buildings ranges from one to eight.

Table 1. Tokushima University Campus buildings of which structural models are created.

No.	Story	Type	Material	Year Built	No.	Story	Type	Material	Year Built
1	8	Frame	SRC	1991	16	3	Frame	RC	1965
2	8	Frame	SRC	1998	17	3	Frame	RC	1973
3	7	Frame	SRC	2002	18	3	Frame	RC	1966
4	6	Wall-type Frame	SRC	2000	19	3	Frame	RC	1988
5	6	Frame	RC	1962	20	2	Wall-type Frame	RC	1976
6	6	Frame	RC	2015	21	2	Frame	RC	1977
7	5	Wall-type Frame	RC	1970	22	2	Wall-type Frame	RC	1973
8	5	Frame	RC	1997	23	2	Frame	RC	1976
9	5	Frame	RC	1975	24	2	Wall-type Frame	RC	1960
10	4	Frame	RC	1997	25	2	Wall-type Frame	S	1993
11	4	Frame	RC	1970	26	2	Frame	S	2002
12	4	Wall-type Frame	RC	1977	27	2	Frame	RC	1996
13	4	Wall-type Frame	RC	1971	28	2	Frame	S	2014
14	3	Frame	RC	1964	29	1	Frame	S	1966
15	3	Frame	RC	1966	30	1	Frame	S	1984

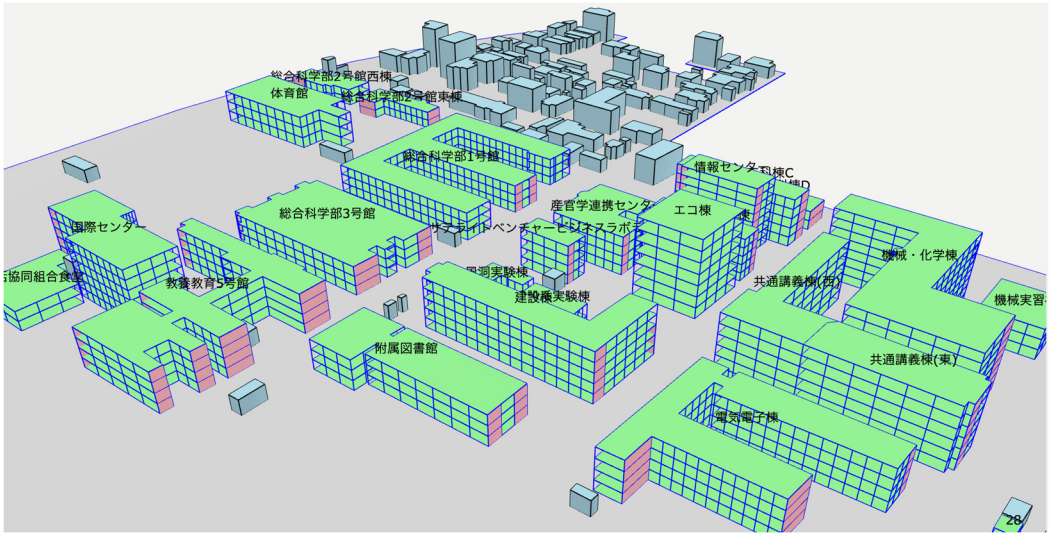

Figure 2. Schematic of the Minami-Josanjima district with structural models.

Parameter Refinement with Measured Dynamic Properties

With estimates of required parameters such as column width, each model becomes complete and then, urban earthquake simulation can be performed with a group of structures. However, these models are not likely to reproduce comparable earthquake responses due to a lack of model fidelity. In this study, dynamic characteristics of the simplified geometry-based structural model applied to the real structures are evaluated. To obtain the dynamic characteristics of the structures, system identification of the buildings on the Tokushima University Josanjima Campus is conducted through ambient vibration measurements. In this section, a detailed evaluation process for a selected building is discussed.

Ambient vibration measurement and system identification

Figure 3 (a) shows one of the SRC frame buildings on the Tokushima University Josanjima campus in which ambient vibration measurement is conducted. Figure 3 (b) shows the simplified geometry-based structural model for this building. Vertical and lateral motion seismographs called RS3D are used for the measurement of the building vibration. Figure 3 (c) shows the RS3D. The RS3D is an advanced high-quality velocity sensor that consists of three geophones, a sensor board, and a raspberry-pi computer.

Two RS3Ds are attached to the target building, one at the 1st-floor and the other at the 7th-floor. Ambient vibrations are measured for an hour at the sampling rate of 100Hz. Figure 4 shows three-minutes of velocity responses in two horizontal directions. While it's not obvious, a certain level of correlation is seen between the 1st floor and the 7th floor responses.

The ambient vibration responses are then transformed into impulse responses using the Random Decrement (RD) method[ref]. The RD method is a time domain procedure that averages response segments that meet triggering conditions in the random responses. With the assumption that

stationary responses are cancelled out by averaging while free vibration responses remain, the averaged response is expected to converge to the impulse response. Impulse responses obtained from the RD method are shown in Figure 5. In this case study, the number of averaged segments for the 1st floor NS direction, 7th floor NS direction, 1st floor EW direction, 7th floor EW direction are 1303, 418, 943, and 1107, respectively. It can be seen from the figure that the impulse responses at the 7th floor are larger than those at the 1st floor in both directions.

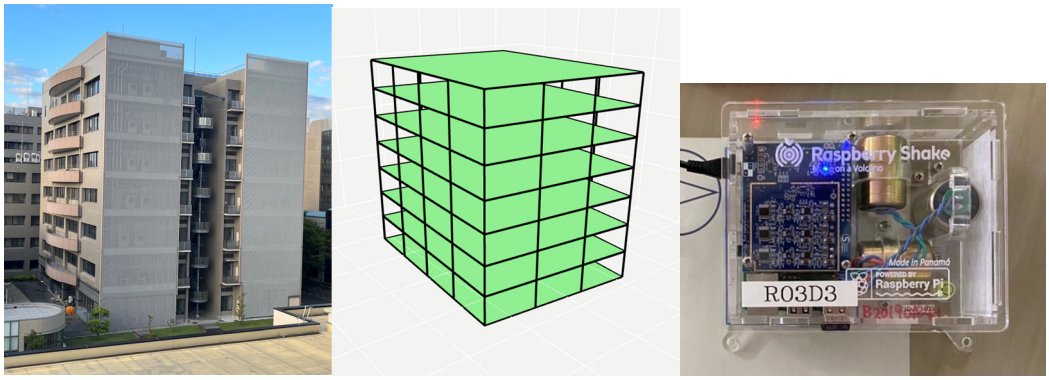

(a) (b) (c)

Figure 3. a 7-story SRC building: (a) photo of the building, (b) structural model, and (c) measurement device.

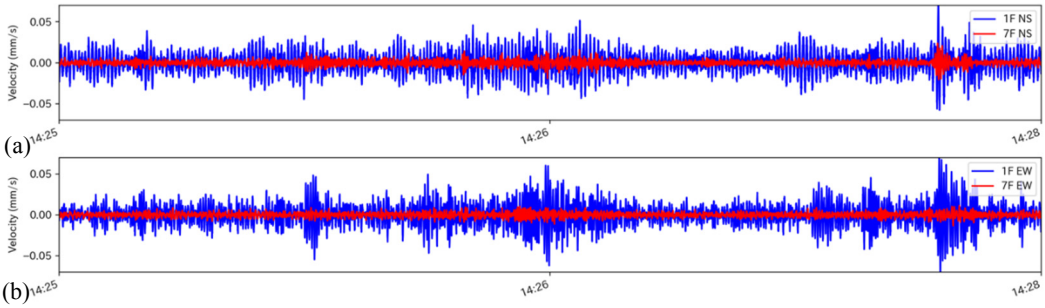

Figure 4. Ambient vibration responses of the 7-story SRC building: (a) NS direction and (b) EW direction.

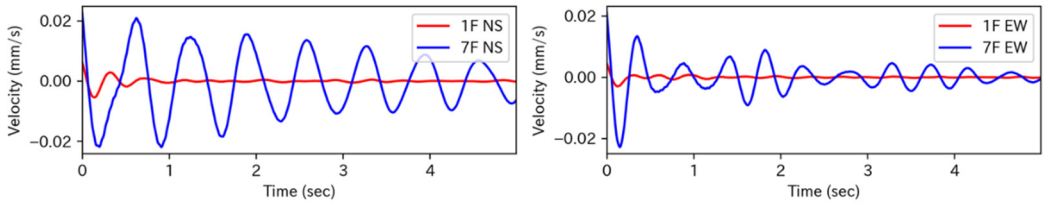

(a) (b)

Figure 5. Ambient vibration responses of the 7-story SRC building: (a) NS direction and (b) EW direction.

For the next process in the system identification, the eigensystem realization algorithm (ERA) is adopted. The obtained impulse responses are processed to form a Hankel matrix of the Markov parameters. Then, singular value decomposition is performed to decompose the Hankel matrix into a singular value matrix, an observability matrix, and a controllability matrix. From these matrices, a discrete state space model is constructed for the 7-story SRC building. For more information about RD method, refer to Ibrahim (1977).

Because inputs to the building are not measured, it is not possible to correlate directions of the responses to the directions of inputs. In this case study, it is assumed that inputs exist in the three orthogonal directions and that responses are excited by unmeasured input in the same direction.

With such assumptions, the ERA method is applied to a Hankel matrix that is obtained from the impulse responses by the RD method. The ERA is one of the popular time-domain system identification techniques for modal analysis of structures using ambient vibration. Identified system matrices are based on the singular value decomposition of the Hankel matrix. For more details about the ERA, please refer to Juang and Pappa(1985).

Table 2. Comparison of natural frequencies between system identification and structural analysis.

	System Identification		Structural Analysis	
Mode	Frequency (Hz)	Direction	Frequency (Hz)	Direction
1	1.493	NS	1.510	NS
2	2.110	EW	1.926	EW
3	2.457	NS	2.116	Twisting
4	2.667	NS,EW	4.794	EW

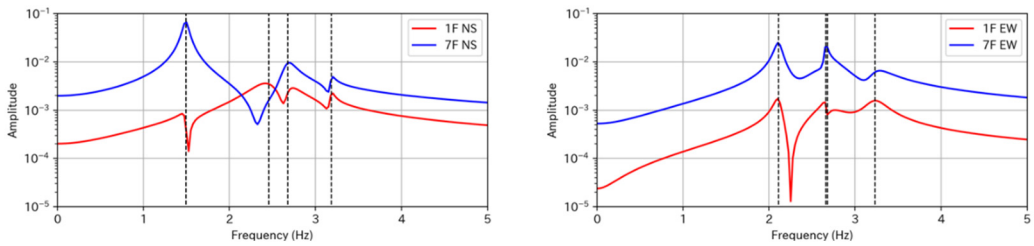

(a) (b)

Figure 6. Transfer functions for the 1st and the 7th floors at the 7-story SRC building identified from ambient vibration responses: (a) NS direction and (b) EW direction.

Table 2 lists four natural frequencies and their primary directions identified from the system identification. Figure 6 shows transfer functions for the 1st and the 7th floors in the two horizontal directions. These transfer functions are obtained from the identified state space model by the ERA method. It can be seen that four vibration modes in the NS direction and three vibration modes in the EW direction are identified from the ambient velocity responses.

Based on these identified dynamic properties of the building, dynamic characteristics of the structural analytical model is evaluated. Natural frequencies and primary directions from the simplified geometry-based structural model are also listed in Table 2 for a comparative purpose. The structural parameters such as effective column with and mass per unit area in the analytical model are refined to match the first natural frequency from the system identification.

Although the first two vibration modes are similar, the third and fourth vibration frequency and primary directions are different in the system identification and structural model. These discrepancies may imply that the simplified geometry-based structural model is not capable of capturing fundamental dynamic characteristics of the buildings. However, it was found from thorough investigation that any conclusive remarks cannot be made from the preliminary comparison in this study because of the following two reasons.

(1) The boundary conditions of the structural analysis model here are fixed base at the ground level. On the other hand, the real buildings are on soil foundation that affects the dynamics of structure. The identified building dynamics from the ambient vibration include influence of the soil foundation. In order to properly evaluate the fidelity of the proposed simplified geometry-based structural model, either influence of the soil foundation is removed from the system identification, or the soil foundation has to be included int the analytical model of the structure.

(2) Because of unmeasured inputs in the ambient vibration, correlation between response direction and input direction cannot evaluated. Therefore, coupling of responses in the orthogonal directions was not identified in the system identification in this study. Figure 7 shows the first three vibration modes in the structural model. As shown in Figure 7 (c), the third mode is torsional mode. This mode of vibration was also not seen from the measurement in this study. It is because two sensors were placed in the centroid of floors in this study. A refined measurement plan with multiple sensors at the same floor is needed to capture couple and torsional mode of vibration in the system identification.

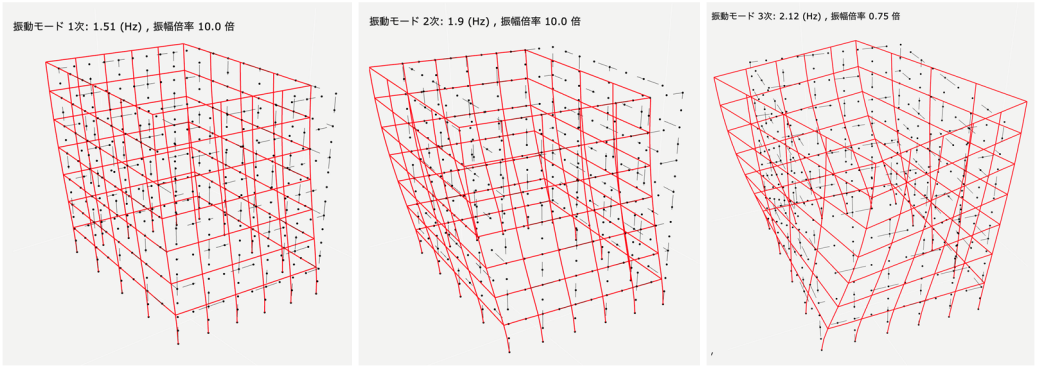

(a) (b) (c)

Figure 7. Fundamental mode shapes of the 7-story SRC building: (a) 1st mode, (b) 2nd mode, and (c) 3rd mode.

Summary

This paper presented development of simplified geometry-based structural models for urban earthquake simulation. The simplified geometry-based structural models are formulated using GIS building information. The proposed models are applied to a district that includes Tokushima Unviersity Mimani-Josanjima campus. System identification of selected buildings are conducted to refine and verify the simplified geometry-bases structural models. The attempt was made to refine the proposed models based on the system identification using ambient vibration. It was found that it is necessary to isolate the effect of the soil conditions from the identified vibration modes to evaluate the dynamics of the structural models. The project team continues to make efforts on the structural models for urban earthquake simulation.

References

Fujita, K., Ichimura,T., Hori, M., Wijerathne, M.L.L., and Tanaka,S. "A Quick Earthquake Disaster Estimation System with Fast Urban Earthquake Simulation and Interactive Visualization", Procedia Computer Science, 29: 866-876 (2014).

Ibrahim, S.R. "Random Decrement Technique for Modal Identification of Structures". Journal of Spacecraft and Rockets 14(11):696(1977). DOI:10.2514/3.57251

Juang, J.-N., Pappa, R. S. "An Eigensystem Realization Algorithm for Modal Parameter Identification and Model Reduction". Journal of Guidance, Control, and Dynamics. 8 (5): 620–627 (1985). doi:10.2514/3.20031.

International Symposium on Emerging Developments and Innovative Applications of Reliability Engineering and Risk Managements (EDIARR2022),30 October-3 November2022, Taipei
Chen, S. S. &Ang, Alfredo. H-S. (Editors)

HYBRID SIMULATION OF A STEEL FRAME USING MIXED CONTROL MODES INCORPORATING EXPERIMENTALLY MEASURED DISPLACEMENT TO CONSIDER COLUMN SHORTENING DUE TO LOCAL BUCKLING

Kung-Juin Wang[1], Chung-Che Chou[2], Cheng-Wei Huang[2], Hou-Kuan Shen[2], Man-Hong Tam[2], Claudio Sepulveda[3], Gilberto Mosqueda[3], Chia-Ming Uang[3]

[1]*National Center for Research on Earthquake Engineering, 200 Sec. 3, Xinhai Rd., Taipei, Taiwan*

E-mail: kjwang@narlabs.org.tw

[2]*Department of Civil Engineering, National Taiwan University, No. 1, Sec. 4, Roosevelt Rd., Taipei, Taiwan*

E-mail: cechou@ntu.edu.tw, andy1002011@gmail.com, manhong9707@gmail.com, r08521262@ntu.edu.tw

[3]*Department of Structural Engineering, University of California San Diego, La Jolla, USA.*

E-mail: csepulve@eng.ucsd.edu, gmosqueda@eng.ucsd.edu, cmu@ucsd.edu

Abstract: This paper presents an implementation of a series of hybrid simulation (HS), with the considered structure a two-dimensional seven-story two-bay steel frame subjected to near-fault ground motions. The specimen is a full-scale cruciform beam-column connection subassembly and is controlled by the actuation system that provides four degree-of-freedom (DOF) control. The structural analysis program "Platform of Inelastic Structural Analysis for 3D Systems" (PISA3D) is used as the analysis kernel for the HS. Preliminary PISA3D and Abaqus FEA (ABAQUS) simulations were conducted to confirm the adequacy of the control method and the test assumptions. By applying a set of time-varying fictitious force in the HS, this work incorporated the experimentally obtained column shortening due to local buckling into the PISA3D analysis in the HS. In addition, the shortening of the two other first-story columns was also considered by incorporating preliminary ABAQUS simulation results. Test results confirmed that the proposed modeling and control methods could successfully integrate the information available only in the laboratory or ABAQUS simulation into the PISA3D analysis, and provide more realistic structural responses otherwise cannot be obtained by traditional numerical simulation or testing methods.

***Keywords*:** hybrid simulation, local buckling, force control, displacement compatibility

Introduction

In Asia, box columns are widely used in constructing high-rise buildings since they are easy to build and provide desirable seismic resistance capacity for both horizontal directions. However, under large frame drift and high column axial load, local buckling can occur at the column base, which can result to significant column shortening [Nakashima and Liu 2005; Fadden and McCormick 2011; Wang et al. 2014; Onogia et al. 2019; Chou and Wu 2019; Chou and Chen 2020]. Moreover, in seismic events different amount of shortenings can occur in different columns because of the overturning effects of the swaying frame. Different amount of column shortening can cause redistribution of the internal force of the other members in the frame. Such phenomena have not been experimentally studied in the past and therefore this work aims to investigate this effects via hybrid simulation (HS). A specimen of full-scale steel cruciform beam-column subassembly was fabricated and tested in National Center for Research on Earthquake Engineering (NCREE). The specimen includes the first-story interior column and is a part of a two-dimensional

seven-story two-bay steel frame. The structural analysis program "Platform of Inelastic Analysis for 3D Systems" (PISA3D) [Lin et al. 2009] was adopted as the analysis kernel in the HS.

PISA3D Model and Experimental Setup

Fig. 1 (a) shows the PISA3D inelastic model of the prototype frame, which is a dual system consisting of a special moment frame (SMF) and a buckling-restrained braced frame (BRBF) at the left and the right bay, respectively. The columns are fabricated by SM570 steel, while the beams and the buckling-restrained braces (BRBs) are made of SN490 steel. The left column (C1) is a wide-flange column while the interior and the right columns (C2 and C3) are built-up box shaped. The gravitational second-order effect was not considered. Rayleigh damping was specified based on the assumption of 3% damping ratios for the first and the second mode. The TCU052 (1999 Taiwan Chi-Chi earthquake) EW component was selected as the input ground motion. It was scaled to two levels, maximum considered earthquake (MCE) and 1.5 times the MCE (1.5MCE), to be used in two HS tests, respectively.

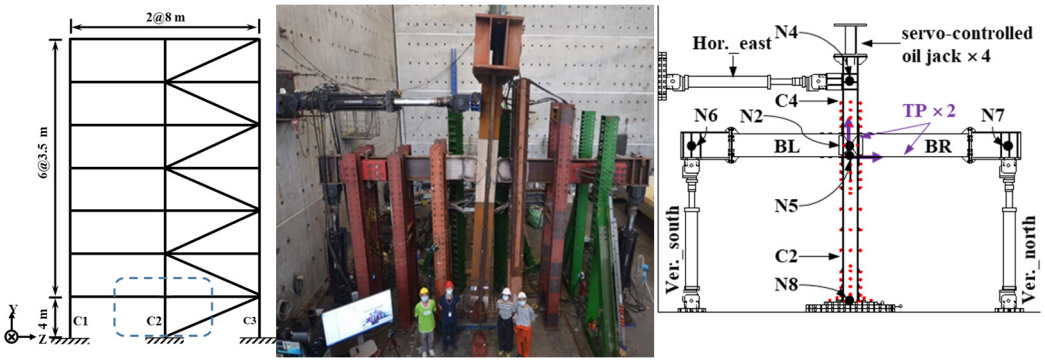

(a) Prototype frame (b) Specimen (c) Test setup

Figure 1. The prototype frame, the PISA3D model, the specimen, and the test setup

Fig. 1 (b) shows the specimen which includes the first-story column, two half-span of the second-story beams, and the lower-half of the second-story column. It is the part enclosed by the dash-line box in Fig. 1 (a). Fig. 1 (c) shows the test setup. Two horizontal and two servo-controllable actuators were used to impose the displacement on the specimen. Four servo-controllable oil jacks were used to impose time-varying force on the column. Two digital displacement transducers (TPs) were mounted on top of the first-story column such that the achieved horizontal and vertical displacements of node N5 can be calculated on a real-time basis (1024 Hz). Miscellaneous sensors including strain gauges, PI gauges, 3D optical displacement trackers, and other traditional displacement sensors were used to monitor the responses of the specimen during the tests.

Hybrid Simulation Method

Physical Substructure and Control Targets

Instead of using the complete specimen as the physical substructure (PS), only the first-story column was chosen as the PS and the rest part in the specimen was considered the fixture for the PS. This results to only one node (N5) that interfaces with the numerical substructure (NS) such

that only three DOFs are required to be considered. In addition, this selection of PS equipped the PS with the actual boundary condition (BC) which enhances the simulation fidelity. The achieved horizontal displacement at node N5 ($u_{z,5}$) can be calculated jointly by the measurement of two TPs, and can be controlled mainly by the two horizontal actuators. The vertical DOF at the node N5 was chosen to be force-controlled, because bad control results can be expected if it is displacement-controlled due to the high-stiffness associated with this DOF. To this end, in each integration time step, after the axial resisting force of the PZ was recovered, it was conveyed out and used as the command of the axial force for the PS. Then the four servo-controlled oil jacks were used to impose this time-varying force command on the first-story column. Regarding the rotational DOF, it was also difficult to accurately control $\theta_{x,5}$ due to the long distance between the point of actuation and the point to be controlled. Fortunately, since the PS was equipped with a realistic BC in this experimental setup, $\theta_{x,5}$ might automatically achieve the desired displacement level if $u_{z,5}$, $u_{y,6}$, and $u_{y,7}$ are reasonably imposed. The effect of not explicitly controlling $\theta_{x,5}$ is numerically investigated by performing a PISA3D displacement-control analysis on a beam-to-column subassembly model that represented the specimen. The simulation results verified that $\theta_{x,5}$ can be achieved accurately enough without being explicitly controlled [Wang *et al.* 2022].

Enforcing Displacement Compatibility in PISA3D

Since the vertical DOF is force-controlled, the corresponding displacement $u_{y,5}$ which includes significant component of column buckling would not be the same as that predicted by PISA3D which supports only elastic modeling of column axial behavior. Redistribution of the restoring force of other members in the system can be caused by different magnitudes of the shortening of the three first-story columns. Unfortunately, such phenomenon were usually neglected in the past experimental studies. In this study an innovative method [Sepulveda *et al*. 2022] was implemented to address this issue. The concept is to add a set of fictitious force in the system to shorten the first-story columns to the desired shortening magnitudes. In each integration time step of the time-history response analysis (THRA), the following three tasks are added to consider the column shortening in the analysis: (1) The magnitudes of the shortening due to buckling were experimentally measured (for C2) or estimated (by ABAQUS for C1 and C3), and are assembled into a displacement vector $\{u_y^{bcl}\}$. (2) A fictitious force vector $\{F_{eq}\}$ was calculated by multiplying a condensed elastic stiffness matrix associated with the three vertical DOFs with $\{u_y^{bcl}\}$. (3) The vector $\{F_{eq}\}$ is added as an additional term of the external force into the system equations in the next integration time step.

Test Results

Two HS tests were conducted with MCE and 1.5MCE magnitude levels, respectively. Fig. 2(a) – (d) show the observation at the column base and the beam ends. Local buckling did not occur at the column base in the MCE test while minor buckling was observed in the RBS of the beams. In the 1.5MCE test, significant local buckling was observed at the column base and the permanent column shortening was about −10 mm at the end of the test.

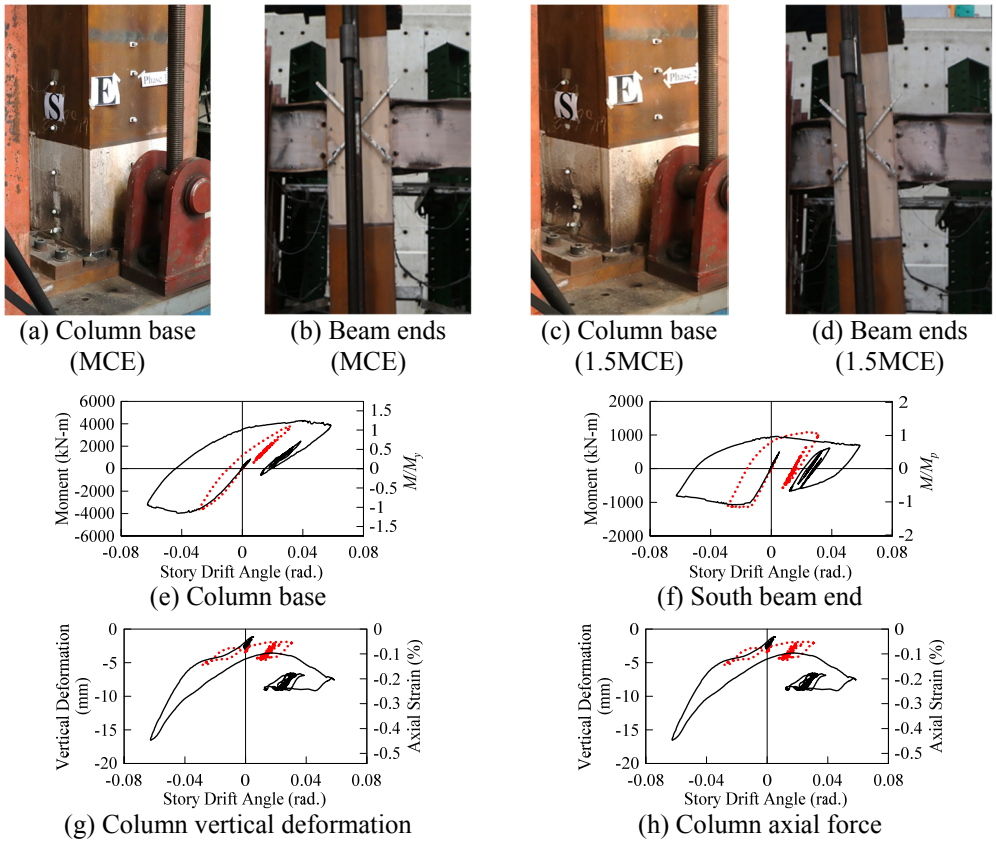

Figure 2 Test observation and specimen responses

Fig. 3 shows the vertical displacements of the top nodes of the three first-story columns. "PisaRef" and "PisaHS" refer to the PISA3D analyses performed on the "Reference model" and "Hybrid simulation model", respectively. It is clear that the vertical displacements obtained from PisaHS agreed well with the measured displacement (for C2) and that estimated by the offline ABAQUS analyses (for C1 and C3). It is also evident that they were significantly larger than the corresponding values obtained from PisaRef which did not consider the experimentally measured or ABAQUS predicted column shortenings due to local buckling. This verified the effectiveness of the proposed method to address the issues of displacement compatibility when the associated DOF is force-controlled.

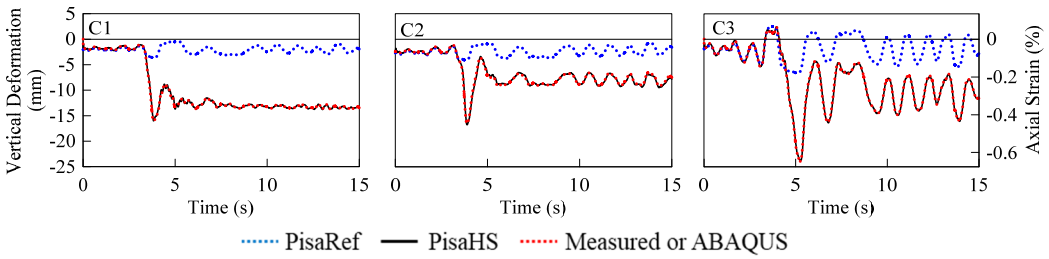

Figure 3 Column top vertical displacement in different analyses (1.5MCE)

Conclusions

The seismic responses of a seven-story steel frame subjected to near-fault ground motion via HS. The specimen was a full-scale beam-to-column subassembly but only the first-story column was treated as the PS. Both displacement- and force-control modes were used in the HS. The vertical deformation of the three first-story columns were measured experimetnally or estimated by offline ABAQUS analyses, and were used to calculate an set of fictitious equivalent force to enforce the displacement compatibility in the THRA. Test results verified the proposed method, which augmented the capacity of HS to provide more realistic structural responses otherwise cannot be obtained by traditional numerical simulation or testing methods.

Acknowledgements

This work is funded by the Ministry of Science and Technology under the project number MOST 109-2625-M-002-005, Taiwan. Additional support from the National Institute of Standards and Technology under Award 70NANB171TZ91, USA to UC San Diego for the international cooperation is also appreciated. Sincerest gratitude also goes to NCREE staff for the exceptional laboratory support.

References

Nakashima, M., & Liu, D. (2005). "Instability and complete failure of steel columns subjected to cyclic loading," *Journal of Engineering Mechanics*, 131(6), ASCE, 559-567.

Fadden, M., McCormick, J. (2011). "Cyclic quasi-static testing of hollow structural section beam members," *J. Structural Engineering*, ASCE, 138(5), 561-570.

Wang, Y. B., Li, G. Q., Cui, W., & Chen, S. W. (2014). "Seismic behavior of high strength steel welded beam-column members," *J. Constructional Steel Research*, 102, 245-255.

Onogia, T. Sato, A., and Yoshioka, Y. (2019). "Experimental study on square steel tubular columns under compressive axial force with cyclic biaxial bending moment," XII Conference on Steel and Composite Construction, Coimbra, Portugal.

Chou, C. C., Wu, S. C. (2019). "Cyclic lateral load test and finite element analysis of high-strength concrete-filled steel box columns under high axial compression," *Engineering Structures*, 189, 89-99.

Chou, C. C, and Chen, G. W. (2020). "Lateral cyclic loading testing and backbone curve development of high-strength steel built-up box columns under axial compression," *Engineering Structures* 223 (2020) 111147.

Lin, B.Z., Chuang, M.C. and Tsai, K.C. (2009). "Object-oriented Development and Application of a Nonlinear Structural Analysis Framework," *Advances in Engineering Software*, 40, pp. 66-82.

Wang, K. J., Chou, C. C., Huang, C. W., Shen, H. K., Sepulveda, C., Mosqueda, G., and Uang, C. M. (2022). "Hybrid simulation of a steel BRBF with a first-story beam-to-column subassemblage using a mixed control mode for considering column shortening," *Earthquake Engineering and Structural Dynamics*, (in preparation).

Sepulveda, C., Mosqueda, G., Uang, C. M., Chou, C. C., Wang, K. J. (2022). "Hybrid simulation using mixed displacement and equivalent-force control to capture column shortening in frame structures," Proceedings of the 12th National Conference in Earthquake Engineering, Earthquake Engineering Research Institute, Salt Lake City, UT.

International Symposium on Emerging Developments and Innovative Applications of Reliability Engineering and Risk Managements (EDIARR2022),30 October-3 November2022, Taipei
Chen, S. S. &Ang, Alfredo. H-S. (Editors)

IMAGE-BASED DISPLACEMENT FEEDBACK CONTROL OF ACTUATORS FOR EXPERIMENTAL EARTHQUAKE ENGINEERING

Pei-Ching Chen[1], Po-Hsuan Kung [2]

[1] *Department of Civil and Construction Engineering, National Taiwan University of Science and Technology, No.43, Keelung Rd., Sec.4, Da'an Dist., Taipei City 106335, Taiwan.*

E-mail:peichingchen@mail.ntust.edu.tw

[2] *Department of Civil and Construction Engineering, National Taiwan University of Science and Technology, No.43, Keelung Rd., Sec.4, Da'an Dist., Taipei City 106335, Taiwan.*

E-mail: m10905316@ mail.ntust.edu.tw

Abstract: Conventional external displacement control of servo-hydraulic actuators has been applied to structural testing to ensure that the specimen deformation meets the predefined profile accurately. However, external displacement transducers could be detached from the specimen with severe damage which may cause safety issues during the test. In this study, image-based analysis is applied to real-time displacement feedback control of servo-hydraulic actuators. Low-discrepancy sampling matching method with edge detection is used for reducing computational time of image analysis. In addition, subpixel algorithm is applied to alleviate the repeatability problem of image analysis. Moreover, the computational rate of image analysis is increased by ten times through introducing the proposed middleware which generates implicit displacement feedback between each two displacement measurements. The technology is completely verified in the small-scale structural laboratory of NCREE. Experimental results demonstrate that stable and accurate displacement tracking of actuators can be achieved both for quasi-static cyclic loading tests and dynamic-loading tests.

***Keywords*:** Image analysis, displacement feedback control, servo-hydraulic actuator, low-discrepancy sampling, subpixel algorithm, middleware

Introduction

Experimental earthquake engineering focuses on investigation of structural behavior subjected to loading or deformation. In Taiwan, the most common testing methods contain cyclic testing, dynamic loading testing, shake table testing, hybrid simulation, and real-time hybrid simulation [1-3]. These testing methods utilize servo-hydraulic actuators for applying predefined or calculated loading or deformation to specimens. Control of an actuator requires a servo digital controller, sensors for feedback, a servo-valve, and a hydraulic cylinder which can be illustrated in Figure 1 where the parameter A is the piston area of the actuator. Normally, a proportional-integral-derivative (PID) controller is used to generate the control command based on the desired deformation and the measured deformation of specimen, which is fixed on a strong floor by using prestressing rods. For large and complex testing, fixtures, transfer beams, and plates are required to configure the geometric boundary conditions of the test specimens. In this manner, the actuators may not be able to connect to the specimen directly. Therefore, there could be inconsistency between the deformation of specimen and the actuator displacement due to the gap that cannot be neglected among the experimental setup. Accordingly, external displacement control (EDC) becomes essential.

An additional displacement transducer is used for actuator feedback control in EDC. It is connected to the specimen at one end and the other hand is fixed to a reference frame. EDC provides accurate deformation control of the specimen; however, the external displacement transducer must be installed in a reliable manner because it is involved in the control loop of servo-hydraulic actuator. Sometimes, the displacement transducer could lose contact with the specimen due to concrete spalling or steel buckling. Thus, wrong feedback signal causes loss of actuator control which could damage the specimen and equipment. As a result, non-contact measurement technology may become an alternative for EDC. From the former study, the image-based measurement technology has been developed and used to obtain the specimen deformation during testing in order to perform EDC of actuators [4]. In this study, pattern matching with low-discrepancy sampling method is used to increase the computational rate of image analysis. In addition, a simple subpixel algorithm is applied to improve the resolution of image-based displacement measurement. Moreover, the computational rate of image analysis is further increased by ten times through introducing the proposed middleware which is not documented in this extended summary due to page limitation. Experimental results demonstrate that the proposed image-based displacement feedback control of actuator can be applied to both quasi-static testing and dynamic testing successfully and stably.

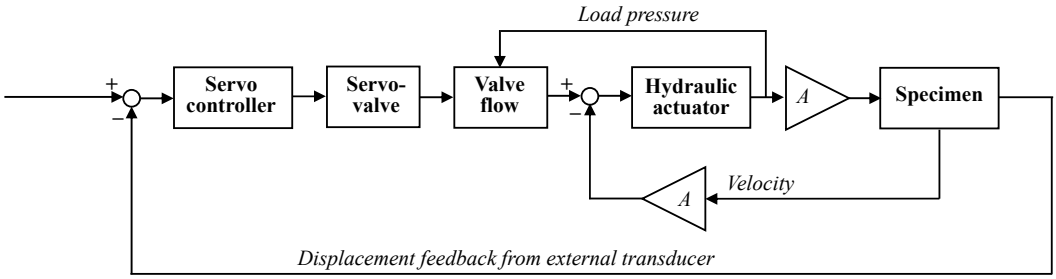

Figure 1. Block diagram of a structural test in EDC.

Image Analysis Methods

Pattern Matching

Pattern matching method finds the position which leads to the maximum of correlation between the pattern and the image of the specimen. For a trial position (i, j), which presumes the pattern is at i pixels from the left and j pixels from the top of the image taken during the experiment, the correlation $R(i, j)$ is defined by:

$$R(i,j) = \frac{\sum_{x=0}^{L-1}\sum_{y=0}^{K-1}(w(x,y)-\bar{w})(f(x+i,y+j)-\bar{f}(i,j))}{\left[\sum_{x=0}^{L-1}\sum_{y=0}^{K-1}(w(x,y)-\bar{w})^2\right]^{\frac{1}{2}}\left[\sum_{x=0}^{L-1}\sum_{y=0}^{K-1}(f(x+i,y+j)-\bar{f}(i,j))^2\right]^{\frac{1}{2}}} \quad (1)$$

where $w(x, y)$ is the gray-scale intensity at the position x pixels from the left and y pixels from the top of the pre-defined pattern; $\bar{w}$ is the average of the w over the pattern; $f(x+i, y+j)$ is the gray-scale intensity at the position $(x+i, y+j)$ of the experimental image; $\bar{f}$ is the average of the f in the region coincident with the presumed location of the pattern; L and K are the width and height of

the pattern in unit of pixels. Finding the position that results in the maximum correlation is to find the most likely position of the pattern in the experimental image.

Low-discrepancy Sampling

Most images contain unexpected noise; therefore, using all the information in the image for pattern matching takes much time that could be further reduced. Low-discrepancy sampling (LDS) uses a non-uniform sampling technique to filter images during the learning phase. It removes redundant information and retains the pixels related to the template area for performing grayscale pattern matching. The edge in an image is a group of continuous pixels that exist on the boundary between two areas with discontinuous gray levels. By detecting the edge of the object in a picture, the elapsed time of conducting pattern matching can be reduced which increases the update rate of displacement feedback for actuator control.

Subpixel Algorithm

After the edge position is specified, multiple virtual pixels are inserted between two adjacent pixels to improve the measurement accuracy, which is called subpixel accuracy. In this study, parabolic interpolation algorithm is applied to obtain the subpixels. The left and right adjacent pixels are simultaneously used to calculate the coefficients in a parabolic equation. The position of the maximum value of the parabolic equation is determined as the subpixel edge. After the subpixel edge position of the template is determined, the template center position expressed in subpixel precision can be obtained.

Experimental Setup

The proposed image-based displacement feedback control method for EDC of servo-hydraulic actuators was developed and validated in the small-scale structural laboratory (SSL) in the National Center for Research on Earthquake Engineering (NCREE), Taiwan [5]. The experimental setup for the proposed image-based displacement feedback control of servo-hydraulic actuators is illustrated in Figure 2. In this study, the NI PXI Express system was adopted for image analysis because it was able to feature specialized synchronization for tests and measurement applications. A Camera Link image acquisition device was installed in the PXI system. Designed. In addition, a Shared Common Random Access Memory Network (SCRAMNet) GT200 was also installed in the PXI system for communication with the actuator controller (MTS FT-100). Furthermore, a Basler acA2000-340km camera was adopted which was able to achieve 340 frames per second at 2 MP resolution. The NI LabVIEW and Vision Development Module (VDM) were installed on a host compute for achieving the functions of inspecting objects, searching for features, identifying objects, and achieving measurement. The layout of hardware and software is illustrated in Figure 3.

The specimen was composed of a transfer column made by H100×100×6×8 cross section and a pin-support underneath the transfer column. It was mounted on the strong floor at the bottom of the pin-support. A horizontal actuator was installed between the reaction wall and the specimen to apply the horizontal displacement at the top of the transfer column. Meanwhile, an external displacement transducer was attached to the specimen for comparison purposes.

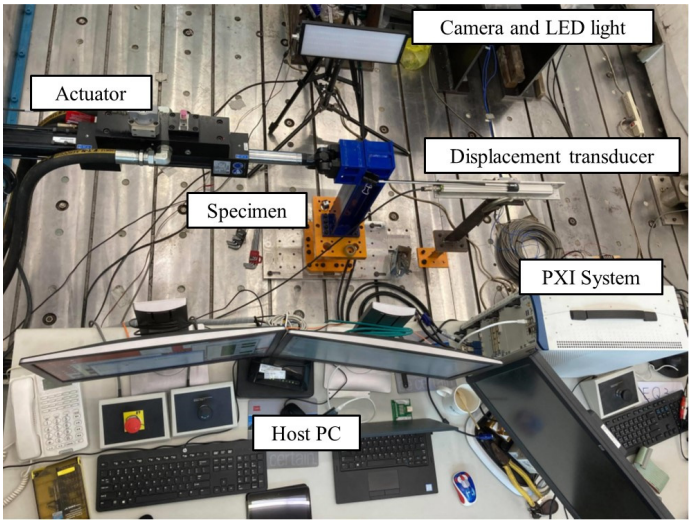

Figure 2. Experimental setup.

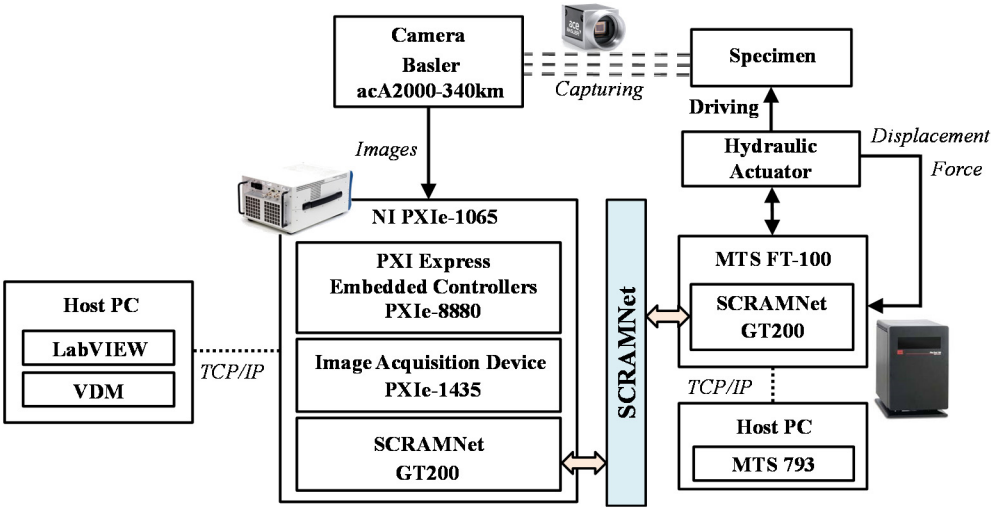

Figure 3. Layout of hardware and software.

Experimental Results

For the ramp-and-hold tests, it was found that a small amount of displacement jitter was reduced after applying the LDS and subpixel algorithm as shown in Figure 4. For the dynamic loading tests, Figures 5 show the displacement time histories of the 1995 Kobe earthquake under the image-based displacement feedback control. The maximum loading rate achieved in the Kobe dynamic loading test was 323.6 mm/s, which was considered significantly larger than conventional quasi-static loading tests.

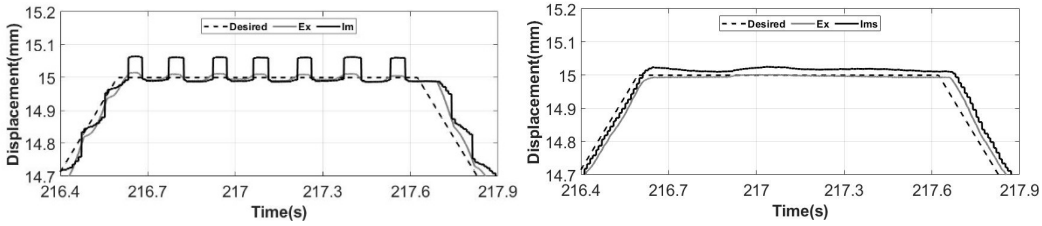

(a) (b)

Figure 4. Ramp-and-hold test results (a) without LDS and subpixel (b) with LDS and subpixel.

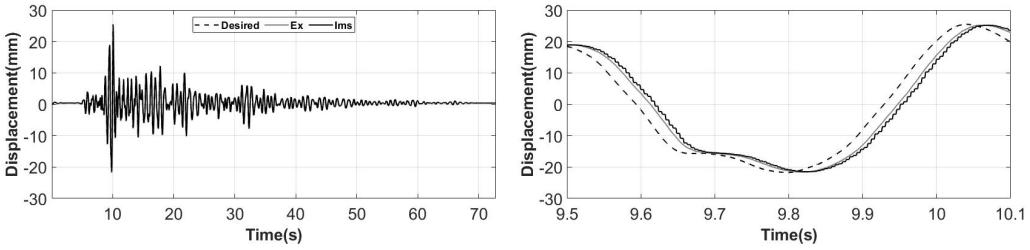

(a) (b)

Figure 5. Dynamic loading test results (a) time history response (b) enlarged part.

The dynamic displacement tracking performance of the conventional displacement control and the proposed image-based displacement feedback control can be evaluated by calculating the root-mean-square error (RMSE) between the desired and measured displacements, which can be expressed as:

$$\mathrm{RMSE}(\%) = \sqrt{\frac{\sum_{k=1}^{N}\left(x_d[k]-x_m[k]\right)^2}{\sum_{k=1}^{N}x_d[k]^2}}\times 100\% \tag{2}$$

where $x_d[k]$ and $x_m[k]$ are the desired and the measured displacements at the k-th step, respectively. The number of data points in each test is N. Note that better displacement tracking performance leads to a smaller RMSE. The RMSEs of the dynamic loading tests are shown in Table 1. Although EDC with image analysis feedback has larger RMSE than EDC with external displacement transducer does, exceptional tracking performance can still be achieved since the RMSEs are mostly smaller than 3%.

Table 1. Displacement tracking performance of dynamic loading tests.

Earthquake	RMSE (%)	
	EDC with external displacement transducer	EDC with image analysis
Capemendocino	1.221	2.555
Chi-Chi (TCU052)	1.160	1.692
Darfield	1.225	2.257
El Centro	1.420	4.007
El Mayor	1.298	2.956
Kobe	1.611	3.463
Kumamoto	1.878	2.249
Meinong	1.312	2.701
Northridge	1.320	3.286
Parlfield	0.979	2.028

Conclusions

The image-based displacement feedback control for servo-hydraulic actuators has been further improved by applying low-discrepancy sampling (LDS) method and subpixel algorithm. It has been validated by conducting both ramp-and-hold tests and dynamic loading tests. Experimental results demonstrate that slight jitter which occasionally occurred before has been significantly reduced due to LDS and subpixel information. For dynamic loading tests, ten earthquake displacement time histories were taken as the desired displacement for actuator tracking. Experimental results demonstrate the image-based displacement feedback control achieves satisfactory dynamic displacement tracking performance with a root-mean-square error less than 3% in average. Further studies will be focused on two-dimensional actuator EDC with image analysis feedback.

References

Tsai, K. C., Hsu, C. H., Li, C. H., and Chin, P. Y. (2018), "Experimental and analytical investigations of steel panel dampers for seismic applications in steel moment frames." *Earthquake Engineering and Structural Dynamics*, 47(6), 1416-1439.

Wang, K. J., Chuang, M. C., Tsai, K. C., Li, C. H., Chin, P. Y., and Chueh, S.Y. (2019). "Hybrid testing with model updating on steel panel damper substructures using a multi-axial testing system." *Earthquake Engineering and Structural Dynamics*, 48(3), 347-365.

Chen, P. C., Hsu, S. C., Zhong, Y. J., and Wang, S. J. (2019), "Real-time hybrid simulation of smart base-isolated raised floor systems for high-tech industry." *Smart Structures and Systems*, 23(1), 91-106.

Chen, P. C., Yang, Y. S., and Cheng, Y. C. (2022), "Displacement feedback control of actuators for structural testing using image processing and analysis." *Earthquake Engineering and Structural Dynamics*, 51(3),630-647.

Chen, P. C., Ting, G. C., and Li, C. H. (2020), "A versatile small-scale structural laboratory for development of novel earthquake engineering testing techniques." *Earthquakes and Structures*,18(3), 337-348.

International Symposium on Emerging Developments and Innovative Applications of Reliability Engineering and Risk Managements (EDIARR2022),30 October-3 November2022, Taipei
Chen, S. S. &Ang, Alfredo. H-S. (Editors)

NUMERICAL AND EXPERIMENTAL INVESTIGATION OF TRACK NONLINEAR ENERGY SINK WITH ROTATIONAL MASS FOR SEISMIC MITIGATION OF BUILDINGS

Tzu-Lun Kao[1], Chia-Ming Chang[2]

[1]*Department of Civil Engineering, National Taiwan University, No. 1, Sec. 4, Roosevelt Rd., Taipei 10617, Taiwan*

E-mail: r09521240@ntu.edu.tw

[2] *Department of Civil Engineering, National Taiwan University, No. 1, Sec. 4, Roosevelt Rd., Taipei 10617, Taiwan*

E-mail: changcm@ntu.edu.tw

Abstract: Mass dampers are a commonly used control device for buildings against strong winds and earthquakes. When these dampers are optimally tuned to the dynamics of buildings, building responses (i.e., floor accelerations and inter-story drifts) can be effectively reduced. Still, this effective control performance relies on large damper displacements and sufficient damper mass. Therefore, this study investigates a new type of mass damper for buildings against earthquakes. This mass damper consists of rotational mass by a flywheel, which moves on a nonlinear trajectory formed by a polynomial function known as a track nonlinear energy sink. The rotational mass can amplify the effect of inertia force without introducing additional translational mass, while the polynomial trajectory of the nonlinear energy sink tends to lower damper displacements when subjected to a considerable input. In this study, the equation of motion for a building with the proposed mass damper is derived. A design method based on the frequency-domain input-output relationship is established. To further verify the damper performance, a prototype track nonlinear energy sink with a mass moment of inertia is fabricated and experimentally evaluated by real-time hybrid simulation. As seen in the experimental results, the proposed mass damper outperforms the conventional track nonlinear energy sink. Moreover, only adequately effective mass, i.e., sufficient momentum to maintain kinetic friction, is feasible to generate control performance against input ground motion.

***Keywords*:** track nonlinear energy sink with a mass moment of inertia, building control, nonlinear frequency-domain input-output relationship, harmonic integration method, real-time hybrid simulation

Introduction

For tall buildings, tuned mass dampers are a widely accepted choice to increase the seismic performance of structures. However, excessive damper displacements are always a concern during severe hazard events, e.g., strong earthquake inputs. To resolve this issue, Karayannis et al. developed a tuned mass damper (TMD) with a displacement restraint [1]. In addition, the detuning effect also degrades the TMD control performance due to the allowable tuning frequency band. Wang et al. developed a new device, namely the track nonlinear energy sink (Track NES), which can address the excessive damper displacements due to the hardening-like restoring mechanism [2]. To further limit allowable damper displacement, Wang et al. developed a new type of Track NES by adding a displacement limiter, namely the single-sided vibro-impact track nonlinear energy sink (SSVI track NES). In addition, Marian and Giaralis[4] also combined the TMD with the inerter. Because the inerter can amplify the effective mass, which makes the device need more momentum to drive, its displacement reduces correspondingly. To sum up, effective limitations of excessive displacements are of importance for the development of mass dampers.

In this study, a track nonlinear energy sink with rotational mass (Track NES-RM) is developed and experimentally investigated for seismic protection of building structures. The equation of motion for a building with the proposed mass damper is derived. A design method based on the frequency-domain input-output relationship is established. A prototype track nonlinear energy sink with a mass moment of inertia is fabricated and experimentally evaluated by the real-time hybrid simulation to verify the damper performance. The experimental results show that the proposed mass damper outperforms the conventional track nonlinear energy sink, resulting in lower damper displacements and reduced structural responses.

Modeling of Building with Track NES-RM

Assume that the NES mass remains in contact with the track while the rotational mass rotates continuously. Then, the equation of motion for the Track NES-RM alone can be derived from Newton's law and written by

$$m_{\mathrm{N}}\ddot{u}_{\mathrm{N}} + F_{\mathrm{N}}(u_{\mathrm{N}}, \dot{u}_{\mathrm{N}}, \ddot{u}_{\mathrm{N}}) = -m_{\mathrm{N}}\ddot{x}_{\mathrm{g}} \tag{1}$$

Where

$$F_N(u_N, \dot{u}_N, \ddot{u}_N) = m_N\{\ddot{u}_N h'^2(1+H) + \ddot{u}_N H + \dot{u}_N^2 h' h''(1+H) + h' g\} \tag{2}$$

u_{N} is the displacement of the Track NES-RM; m_{N} is the translational mass of the Track NES-RM; $\ddot{x}_{\mathrm{g}}$ is the ground acceleration input at the base of this Track NES-RM; h represents the track shape, which is a fourth-order polynomial function, such as $h(u_{\mathrm{N}}) = a u_{\mathrm{N}}^4$; a is the coefficient of track shape; H is the ratio of the effective rational mass to the total mass; the Track NES-RM inertia force is F_{N}. If $H = 0$, the conventional track NES is presented. In addition, the Track NES-RM does not have a linear spring and only relies on nonlinear restoring force to move back to the equilibrium position.

Consider a Track NES-RM attached to the top of a two-story building, as shown in Figure 1. The equation of motion can be written by

$$m_1\ddot{x}_1 + c_1\dot{x}_1 + c_2(\dot{x}_1 - \dot{x}_2) + k_1 x_1 + k_2(x_1 - x_2) = -m_1\ddot{x}_g \tag{3}$$

$$m_2\ddot{x}_1 + c_2(\dot{x}_2 - \dot{x}_1) + k_2(x_2 - x_1) - c_N\dot{u}_N - F_N(u_N, \dot{u}_N, \ddot{u}_N) = -m_2\ddot{x}_g \tag{4}$$

$$m_{\mathrm{N}}\ddot{u}_{\mathrm{N}} + c_{\mathrm{N}}\dot{u}_{\mathrm{N}} + F_{\mathrm{N}}(u_{\mathrm{N}}, \dot{u}_{\mathrm{N}}, \ddot{u}_{\mathrm{N}}) = -m_N(\ddot{x}_2 + \ddot{x}_g) \tag{5}$$

where the mass, damping coefficient, and stiffness of the structure are m_1, c_1, and k_1 and m_2, c_2, and k_2 for the first and second floors, respectively. The damping coefficient of the NES, c_{N}, is assumed to represent all types of damping in the Track NES-RM system (e.g., track friction and inherent damping). The displacement of the first and second floors relative to the ground are x_1 and x_2, while u_{N} represents the relative displacement from the Track NES-RM to the roof (i.e., $u_{\mathrm{N}} = x_3 - x_2$).

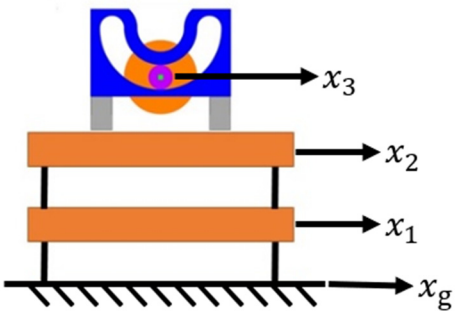

Figure 1. A two-story building with a Track NES-RM on top.

In Figure 1, the difference between the conventional and proposed NES is the amplification factor of rotational mass, such as *H* in Eq. (1). This amplification factor can be defined by

$$H = \frac{1}{2}\left(\frac{r_{\text{disk}}}{r_{\text{wheel}}}\right)^2 \tag{6}$$

where r_{disk} and r_{wheel} are the radiuses of the flywheel and drive wheel. As seen in this equation, a flywheel with a sufficiently large radius can provide a more effective inertia force from the rotational mass. Note that if the flywheel is too heavy to allow the wheel rotating, then the flywheel will no longer turn and maintain a sliding motion.

Frequency-Domain Input-Output Relationship

The input-output relationship in the frequency domain is first derived. In Eq. (1), the output and input of the system are assumed to be presented by $u_{\text{N}} = A\cos\omega t$, and $-\ddot{x}_{\text{g}} = B\cos(\omega t + \alpha)$ into Eq. (1), where *A*, *B,* ω and α represent the output amplitude, input amplitude, input frequency, and phase, respectively. Then, by integrating over 0 to 2π, the input-output relationship in the frequency domain, namely the frequency response, is obtained.

With the frequency response of the Track NES-RM, the overall input-output relationship from the ground motion to structural responses can be derived by an iterative approach, as shown in Figure 2. Because the primary structure is a linear system, the top floor acceleration can be obtained by the transfer function after inputting $\ddot{x}_{\text{g}}$, which is a constant in the frequency domain and also represents the impulse function in the time domain. Moreover, the magnitude of the constant is defined by the input PGA. Subsequently, the top floor acceleration is treated as the input to the frequency response of the NES. At the same time, the restoring force is calculated and sent back to the structure (e.g., similar to the feedback control). Repeating the same procedure would lower the errors of the calculated roof acceleration in the frequency domain. This iterative approach helps to design the proposed Track NES-RM.

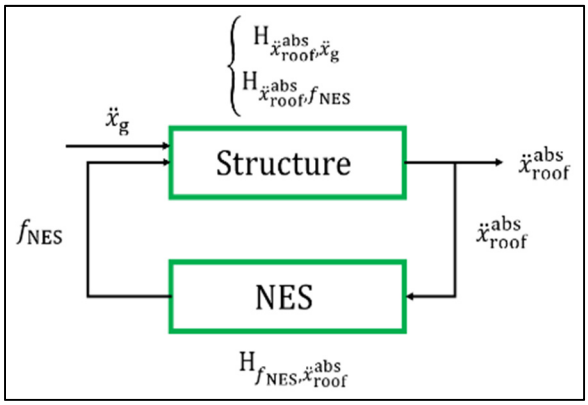

Figure 2. Framework of iterative approach in the frequency domain.

Experimental Investigation

The proposed Track NES-RM is then experimentally verified by real-time hybrid simulation, as shown in Figure 3. This hybrid simulation combines the dSPACE, controller for the numerical substructure, with a physical specimen of the track NES-RM. A 2-story building is formed by a discrete-time state-space model and simulated in dSPACE. Meanwhile, the track NES-RM is physically evaluated by a shake table. The input to the shake table is the roof absolute displacement of the building. Then, the measured acceleration from the Track NES-RM allows calculating the inertial force that inputs to the roof of the building. By closing the loop, the real-time hybrid simulation is realized to examine a 2-story building with the proposed Track NES-RM.

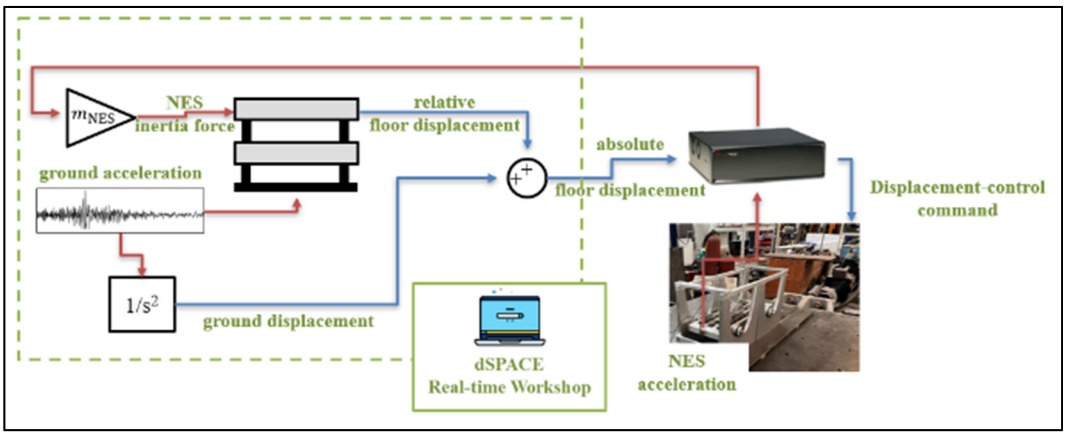

Figure 3. Real-time hybrid simulation for investigation of Track NES-RM.

Figure 4 shows the results obtained from real-time hybrid simulation and compares the ones obtained from numerical simulation. As seen, both results have a good agreement. In Figure 5, the proposed Track NES-RM (H=1) is compared to the conventional track NES (H=0). The test results demonstrate that the Track NES-RM outperforms the conventional one. Moreover, the displacement in the NES-RM can be better reduced.

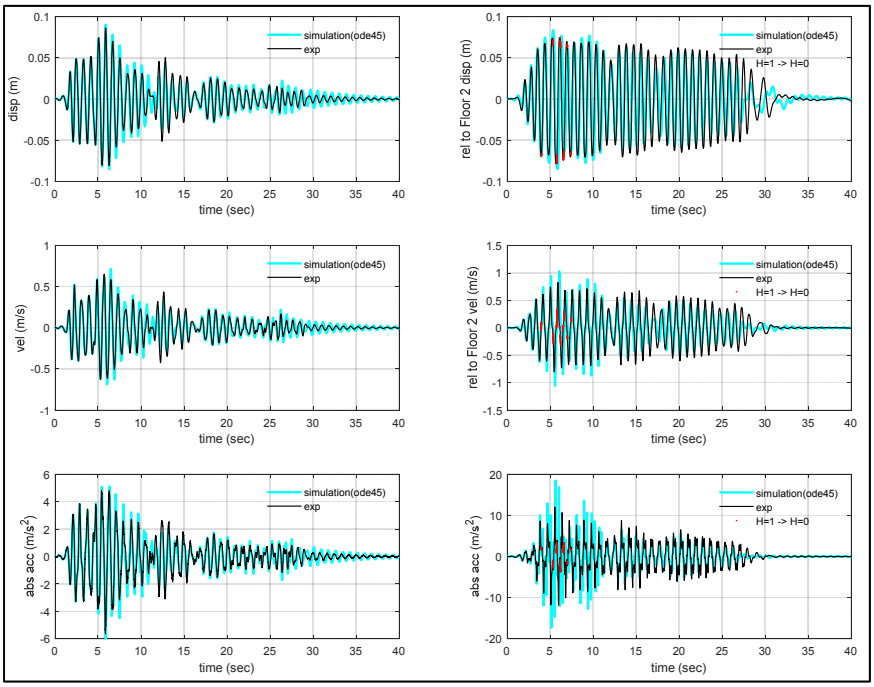

Figure 3. Comparison of responses of roof and Track NES-RM between simulation and experimental results.

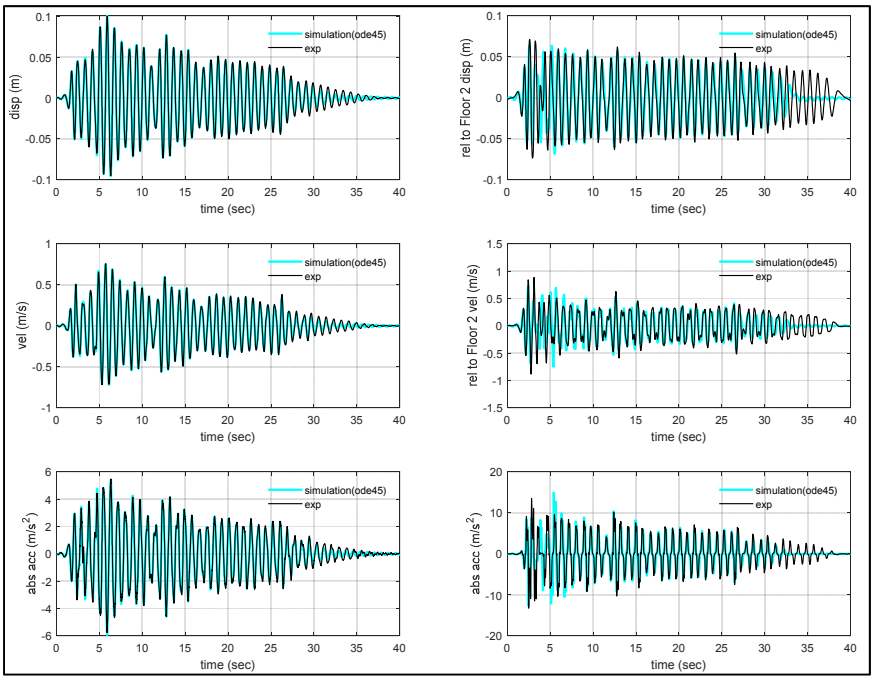

Figure 4. Performance comparison between the conventional (H=0) and proposed NES, where the left column presents the roof responses, and the right column shows the responses of Track NES-RM.

Conclusions

The track nonlinear energy sink with rotational mass (Track NES-RM) was developed and experimentally verified for buildings against earthquakes. The equation of motion for this Track NES-RM was derived, and the rotatable mass was converted into the translational mass with a magnifying factor. By considering harmonic excitation, the input-output relationship of the Track NES-RM was derived, and this relationship allowed calculating the frequency responses of a building with this control device by the proposed iterative approach. Moreover, this iterative approach can be employed to design the Track NES-RM, i.e., the effective mass ratio for a specific track shape. To evaluate the control performance, real-time hybrid simulation was carried out where the Track NES-RM fabricated in-house was physically tested by a shake table. Meanwhile, a two-degree-of-freedom building was numerically simulated. As seen in the results, the proposed track NES-RM generated better control performance than the conventional track NES.

References

Karayannis, I., Vakakis, A., and Georgiades, F. (2008). "Vibro-impact attachments as shock absorbers." Proceedings of the Institution of Mechanical Engineers, Part C: Journal of Mechanical Engineering Science, 222(10), 1899-1908.

Wang, J., Wierschem, N. E., Spencer Jr, B. F., and Lu, X. (2014). "Track nonlinear energy sink for rapid response reduction in building structures." ASCE Journal of Engineering Mechanics, 141(1), 04014104.

Wang, J., Wierschem, N., Spencer Jr, B. F., and Lu, X. (2016). "Numerical and experimental study of the performance of a single-sided vibro-impact track nonlinear energy sink." Earthquake Engineering & Structural Dynamics, 45(4), 635-652.

Marian, L., and Giaralis, A. (2014). "Optimal design of a novel tuned mass-damper–inerter (TMDI) passive vibration control configuration for stochastically support-excited structural systems." Probabilistic Engineering Mechanics, 38, 156-164.

International Symposium on Emerging Developments and Innovative Applications of Reliability Engineering and Risk Managements (EDIARR2022),30 October-3 November2022, Taipei
Chen, S. S. &Ang, Alfredo. H-S. (Editors)

A SIMPLE THIRD-MOMENT RELIABILITY INDEX

Jiayi Cai[1], Yan-Gang Zhao[1] , Zhanyi Peng[2]

[1] *Faculty of Architecture and Building Engineering, Kanagawa University, Yokohama, Japan*

E-mail: r202270187cz@jindai.jp

E-mail: zhao@kanagawa-u.ac.jp

[2] *School of Civil Engineering, Guangzhou University, Guangzhou, China*

E-mail: 2111716202@e.gzhu.edu.cn

Abstract: The third-moment (3M) method is widely used in calculating the reliability index due to its simplicity and accuracy. However, the current 3M method raised the issues of existing logarithm term and a square root term. Thus, there are some limitations in the calculation of 3M method. To overcome these limitations, a simple empirical formula was proposed to estimate the reliability index in this paper. Though the example, the proposed method has a closer calculation result than the existing method. Therefore, the proposed 3M reliability index has the expectation to replace the current index and put into the practical application.

***Keywords*:** third-moment method, second-order reliability index, skewness, MC.

Introduction

When analyzing the structure reliability, the most important step is to calculate the failure probability, the calculation method is (Wang, L. et al., 2014):

$$P_F = P[Z = G(X) \le 0] = \int_{G(X)\le 0} f_X(x)dx \tag{1}$$

Where PF is the failure probability of the structure; X is the N dimension vectors of random variables (such as load and material properties); G(X) is the fuctions of X; fX(x) is the probability density function (PDF) of G(X). When G (X)⩽0, the structure is in the failure state.

Based on Eq. (1), the PF is given by the integral of multi probabilities. Difficulty in computing this reliability index has led to the development of various approximation methods, among which the first-order reliability method (FORM) (Rosenblatt, 1952), the second-order reliability method (SORM) (Der Kiureghian et al., 1987) are now used worldwide in practical engineering. Although the accuracy of these methods is high enough, they also require the calculation of the design point and the curvature of failure of the limit state curve at the design point. However, when the distribution information of the basic random variables is unknown, neither FORM nor SORM is applicable. For such cases, sampling simulation methods are known to be sufficiently accurate; However, when high reliability is required, such methods are time-consuming.

Because the 3M method requires neither iteration nor computation of derivatives(Ugata, T. et al., 1996) and has no shortcomings associated with the design point(Xu, L et al.,2003), it has been

applied to various aspects of structural analysis, including corrosion probability of RC structures, seismic reliability of structures, etc((Zhao & Ono, 2007).

However, existing 3rd Moment methods do have some limitations(Pearson K,1895). By focusing on the problems in the mathematical formulae of existing 3rd Moment methods, namely, the inclusion of the square root, the unknown value of the denominator, and the logarithmic term in the approximation formula, existing 3rd Moment methods can neither be used to calculate the reliability index nor get an accurate result(Zhao & Ono, 2001,2006).

Through solving the existing mathematic problem of the current 3M method, a simple 3M reliability index was proposed in this paper. The examples revealed that the proposed method has higher accuracy and applicability. Hence, the reliability index proposed in this paper is expected to replace the existing reliability index and be put into practical design.

Review of existing 3M reliability indexes

Principle of 3M method

Normally, the function can be standardized with mean and standard deviation:

$$Zs = \frac{G(x) - \mu_G}{\sigma_G} \tag{2}$$

Where μ_G and σ_G are the mean value and standard deviation of $G(x)$ respectively; Zs is the standardized variable of $G(x)$. Then the failure probability can be defined as follow:

$$\begin{aligned} &P_F = Prob[G(x) \le 0] = Prob[Zs \le -\frac{\mu_G}{\sigma_G}] = Prob[Zs \le -\beta_{2M}] \\ &= F_{Zs}(-\beta_{2M}) = \int_{-\infty}^{-\beta} f_{Zs}(Zs) d_{Zs} \end{aligned} \tag{3}$$

Where β_{2M} is the second-moment (2M) reliability index.
Based on the theory of normal transformation, the CDF of Zs should be equal to the CDF of standardized normal variable U:

$$F_{Zs}(Zs) = \Phi(U) \tag{4}$$

According to Eq. (4), the relationship Zs between and U can be expressed by the correlation function with the third moment:

$$Zs = S(u, \alpha_{3G}) \tag{5}$$

Where is α3G the skewness of $G(x)$.
According to the theorem of inverse function, the expression of U and skewness could be obtained as follow:

$$U = S^{-1}(Zs, \ \alpha_{3G}) \tag{6}$$

Substitute Eq. (4) and Eq. (5) into Eq. (6), a simple failure probability could be derived as:

$$\mathrm{P}_F = P[U \le S^{-1}(-\beta_{2M})] = \Phi[S^{-1}(-\beta_{2M}, \alpha_{3G})] \tag{7}$$

Based on the equations above, the structure reliability could be furtherly expressed in a third-moment form:

$$\beta_{3\mathrm{M}} = -\Phi^{-1}(P_F) = -S^{-1}(-\beta_{2M}, \alpha_{3G}) \tag{8}$$

Where $\beta_{3\mathrm{M}}$ is the third-moment (3M) reliability index.

3M reliability index based on lognormal distribution

When U follows the three-parameters lognormal distribution, the correlation between U and $\alpha_{3\mathrm{G}}$ could be expressed as follow:

$$U = \frac{Sign(\alpha_{3G})}{\sqrt{\ln(A)}} \ln[\sqrt{A}(1 - \frac{Zs}{u_b})] \tag{9}$$

Where u_b represents the standardized boundary of lognormal distribution; A is the correlation function that depends on the value of skewness. The expression of u_b and A are as follow:

$$\mathrm{A} = 1 + \frac{1}{{u_b}^2} \tag{10}$$

$$u_b = (a+b)^{\frac{1}{3}} + (a-b)^{\frac{1}{3}} - \frac{1}{\alpha_{3G}} \tag{11}$$

$$a = -\frac{1}{\alpha_{3G}}(\frac{1}{{\alpha_{3G}}^2} + \frac{1}{2}) \quad , \quad b = \frac{1}{2{\alpha_{3G}}^2}\sqrt{{\alpha_{3G}}^2 + 4} \tag{12}$$

$$\alpha_{3X} = -(3 + \frac{1}{{u_b}^2})\frac{1}{u_b} \tag{13}$$

Based on Eq. (8), the third-moment reliability index of lognormal distribution could be obtained as:

$$\beta_{3\mathrm{M}\text{-}1} = -\frac{sign(\alpha_{3G})}{\sqrt{\ln(A)}} \ln[\sqrt{A}(1 + \frac{\beta_{2\mathrm{M}}}{u_b})] \tag{14}$$

3M reliability index based on square normal distribution

When Zs follows the square normal distribution, the standardized normal variable U could be expressed as:

$$U = \frac{1}{2\lambda}(\sqrt{1+2\lambda^2+4\lambda Xs}) - \sqrt{1-2\lambda^2} \tag{15}$$

Where λ is calculated as follow:

$$\lambda = sign(\alpha_{3G})\sqrt{2}cos[\frac{\pi+|\theta|}{3}] \tag{16}$$

$$\theta = \arctan(\frac{\sqrt{8-\alpha_{3G}{}^2}}{\alpha_{3G}}) \tag{17}$$

Based on the theory above, the third-moment reliability index of square normal distribution could be calculated as follow:

$$\beta_{3\text{M-2}} = \frac{1}{2\lambda}(\sqrt{1-2\lambda^2} - \sqrt{1+2\lambda^2-4\lambda\beta_{2\text{M}}}) \tag{18}$$

Empirical applicable range of third-moment method

After a considerable training, the application range of proposed third-moment method is as follow:

$$\frac{-120r}{\beta_{2M}} \le \alpha_{3G} \le \frac{40r}{\beta_{2M}} \tag{19}$$

Where r is the allowed relative difference. It was notable that r is the reference error of third-moment reliability instead of third-moment reliability index. When r meets the range of Eq. (19), the $\beta_{3M\text{-}1}$ and $\beta_{3M\text{-}2}$ could be used. Therefore, the third-moment reliability index could be employed only if the skewness is in the allowed range.

Proposed 3M method

Proposed formula

To overcome the deficiency in mathematics and accuracy of the current 3M reliability, a comprehensive study into the relationship between the 3M reliability index and the 2M reliability index was carried out. Though considerable training on the mean value of current third-moment, a novel third-moment reliability index was proposed:

$$\beta_{3M-3} = \frac{\beta_{2M}}{3}\left[2+e^{\frac{1}{2}\alpha(\beta-\frac{\alpha}{4})}\right] - \frac{\alpha_{3G}}{6} \tag{20}$$

Where $\beta_{3M\text{-}3}$, $\beta_{3M\text{-}1,}$ and $\beta_{3M\text{-}2}$ are the fitting equation of mean value.

Compared with β_{3M-1} and β_{3M-2}, the proposed equation has no limitation in mathematics. When calculation error was in an acceptable range, Eq. (20) could calculate the third-moment reliability index under any circumstance in theory.

Applicability of proposed method

Fig.1 to Fig. 3 presented the comparison between β_{3M-3} and the current 3M reliability index under different β_{2M} and α_{3G}.

As it can be seen from Fig. 1, under the same, the error between β_{3M-3} and existing β_{3M} became obvious. However, when skewness was in the range of (-1.0， 1.0) and β_{2M} in the range of (1.0， 4.0), the proposed method has higher applicability than the existing method.

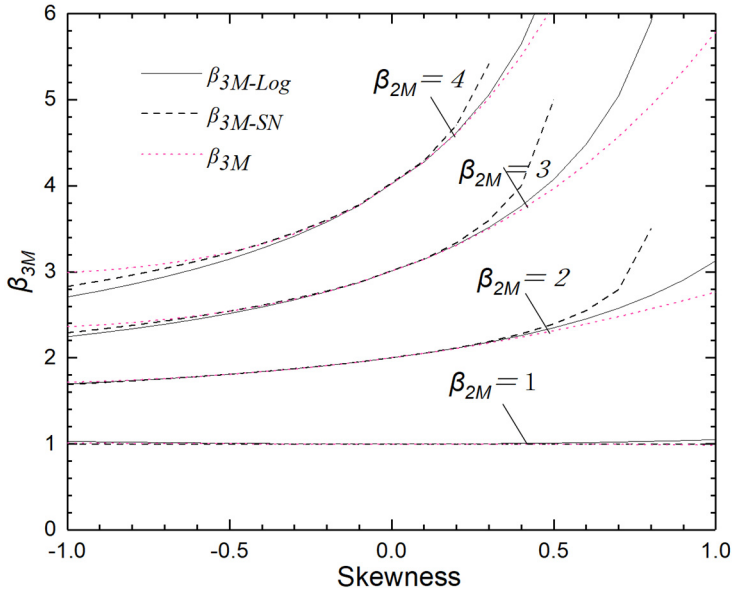

Fig. 1 Comparison of β_{3M} under different skewness

Fig.2 and Fig. 3 presented the variation of β_{3M-3} and current 3M reliability index under different skewness. Fig. 2 indicated that, when skewness was small enough, the difference between three reliability indexes was minor. Whereas β_{3M-1} gives a higher prediction and β_{3M-2} was not accurate. It was inaccurate to estimate β_{3M-3} only based on the comparison of β_{3M-1} and β_{3M-2}. To this end, the mean value of β_{3M-1} and β_{3M-2}, and the error of β_{3M-3} were derived and compared. The results were shown in Table 1 and Table 2.

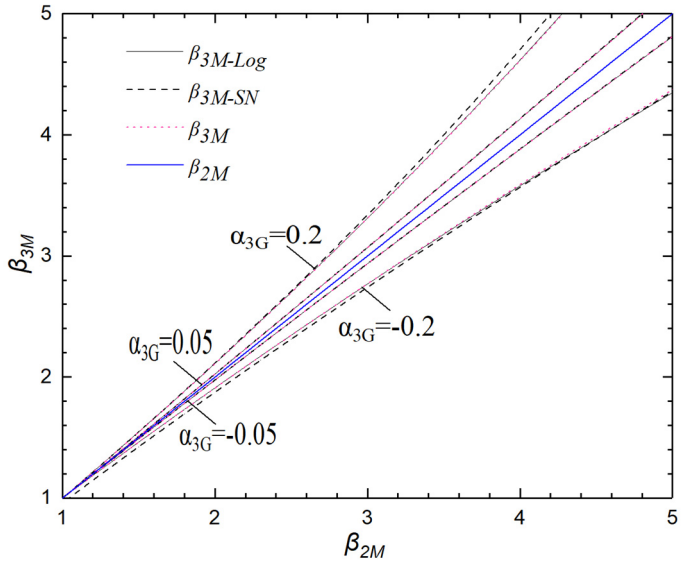

Fig. 2 Comparison of β_{3M} under small skewness

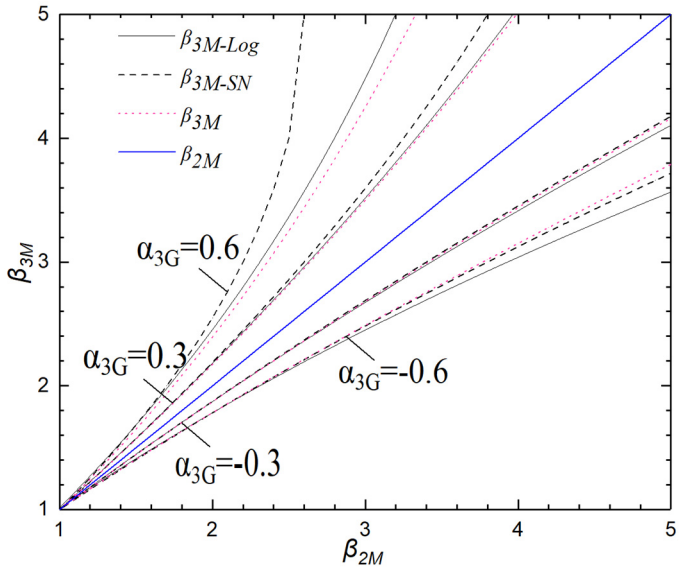

Fig. 3 Comparison of β_{3M} under large skewness

The results in Table 1 and Table 2 showed that, under the same β_{2M}, r raised as the absolute value of α_{3G} increase. Meaning a better fitting of $\beta_{3M\text{-}3}$ could be achieved in the small skewness range. When r was given, the absolute value of α_{3G} decreased gradually as the β_{2M} increase. When $2<\beta_{2M}<4$ and $0.82<\alpha_{3G}<0.31$, the relative error was smaller than 5% and the fitting was more accurate. As the larger α_{3G} and β_{2M} was adept, $\beta_{3M\text{-}1}$ and $\beta_{3M\text{-}2}$ was no longer applicable while $\beta_{3M\text{-}3}$ maintained the applicability. Therefore, the $\beta_{3M\text{-}3}$ have a better applicability than existing method.

Table 1. The Relative Difference between $\beta 3M$-1, $\beta 3M$-2, and $\beta 3M$-3 ($\alpha 3G > 0$)

β_{2M}		2.0			3.0			4.0	
$a_{3G}>0$	0.47	0.62	0.74	0.32	0.42	0.48	0.24	0.31	0.36
r	2%	5%	10%	2%	5%	10%	2%	5%	10%

Table 2. The Relative Difference between $\beta 3M$-1, $\beta 3M$-2, and $\beta 3M$-3 ($\alpha 3G < 0$)

β_{2M}		2.0			3.0			4.0	
$a_{3G}<0$	-1.14	-1.56	-2.10	-0.77	-1.08	-1.48	-0.58	-0.82	-1.14
r	2%	5%	10%	2%	5%	10%	2%	5%	10%

Conclusions

Based on the concept of the existing 3M reliability index, a simple 3M method was proposed in this paper. The main conclusions could be drawn as follow:

(1) The proposed method overcame the limitations in the calculation. It has a wider application range and could be used in any condition in theory.

(2) Compared with the existing 3M method, the proposed method has a smaller error. The fitting was better in the case of negative α_{3G}. Therefore, the proposed 3M reliability index was superior than the existing method.

References

Wang, L., Luo, Z., Gong, W., Khoshnevisan, S. and Juang, C. Moment methods for assessing the probability of serviceability failure in braced excavations. *Geo-Congress 2014 Technical*, pp.3293-3302, (2014).

ROSENBLATT, M. Remarks on a multivariate transformation. *The annals of mathematical statistics*, 470-472, (1952).

Der Kiureghian, A., Lin, H.Z. and Hwang, S.J. Secondorder reliability approximations. *J Engrg Mech*, 113 (8), 1208-1225, (1987).

Zhao, Y. G. and Ono, T. An investigation on the third- and fourth-moment methods for structural reliability. *J. Struct. Constr.*, 530, 21-28, (2000).

Pearson K. Contributions to the mathematical theory of evolution, II: skew variation in homogeneous material. *Philos Trans R Soc Lond (A)*, 186, 343-414, (1895).

Y.G.Zhao,T.Ono,H.Idota,T.Hirano. A Three-Parameter Distribution Used for Structural Reliability Evaluation. *J.Structural and construction engineering*, 546, 31-38, (2001).

Ugata, T. and Moriyama, K. Simple method of evaluating the failure probability of structure considering the skewness of distribution. *Nucl. Eng. Des.*, 160, 307-319, (1996).

Xu, L. and Cheng, G.D. Discussion on: moment methods for structural reliability. *Struct. Saf.* 25, 193–199, (2003).

Zhao, Y.G. and Lu, Z.H. The first three moments for some commonly used performance function. *J. Struct. Constr. Eng*., 613, 31–37, (2007).

Zhao, Y.G., Lu, Z.H. and Ono, T. A simple third-moment method for structural reliability. *Journal of Asian Architecture and Building Engineering,* 5, 129-136, (2006).

International Symposium on Emerging Developments and Innovative Applications of Reliability Engineering and Risk Managements (EDIARR2022),30 October-3 November2022, Taipei
Chen, S. S. &Ang, Alfredo. H-S. (Editors)

Compression Performance of Circular CFDST Short Columns with Eccentric Inner Steel Tube

Wei Fu[1], Yan-Gang Zhao[2]

[1] *Faculty of Architecture and Building Engineering, Kanagawa University, Yokohama, Japan*

E-mail: r202170098fn@jindai.jp

[2]*E-mail: zhao@kanagawa-u.ac.jp*

Abstract: This paper presents short columns tests on concrete-filled double-skin steel tubus (CFDST) with eccentric inner steel tube construct. Aims to experimentally and numerically investigate the compressive behavior of circular concrete-filled double-skin steel tubular (CFDST) with eccentric inner steel tube short columns, with eccentric inner steel tube under entire-section loading. In total, the outer and inner skin is made of different diameters STK400 circular hollow sections tube 16 CFDST columns were loaded axially, and their axial load-shortening curves, ultimate strength and performance of steel and concrete were briefly discussed. The results show that the eccentricity of the inner steel tube has no obvious effect on the ultimate strength and malleability, but the stiffness decreases with the increase of the eccentricity，the steel and concrete properties of the CFDST column are well exerted, and the eccentricity of the inner steel tube has no obvious influence on the performance of the steel and concrete.

***Keywords*:** CFDST, Compressive strength, Short colum.

1. Introduction

Concrete-filled steel tubes (CFT) are widely employed in various modern building structures, especially in high-rise buildings, owing to their excellent structural performance, which includes large energy-absorption capacity, high ductility and stiffness. However, with the development of high-rise building, long span and heavy load structures, columns with larger cross-sections are required, thus resulting in the frame structures to be too heavy and the foundation to bear excessive load, which is not conducive to seismic resistant design. To address this issue, concrete-filled double-skin steel tubes (CFDST) were proposed. This type of columns is an innovative composite member filled concrete between the two skins and their center hollow portion offers an accessible dry space for installation. At the same time, outer and inner steel tubes can be used as formwork to facilitate the pouring of concrete. CFDST columns will be more conducive to seismic resistant design than conventional CFST counter-parts owing to lower self-weight and convenient construction as well as higher ductility and energy absorption. Also, previous studies found that the axial load-carrying capacity of such composite stub columns was 10%-30% higher in comparisons with the combined strengths of individual components. Three components can work well together to undertake axial loads. The outer steel tube confined the sandwiched concrete well and an outward buckling occurred at the crushed location of concrete. Although the inner steel tube afforded insignificant confinement effect to the sandwiched con-crete, it played a key role in compression, bending and shear resistance. Of interest here are circular CFDST columns (both inside and outside skins are circular steel tubes), which are deemed to achieve a better confinement effect and ductility than CFDST columns with other cross-section combinations.

However, with the increasing use of CFDST in practical projects, it cannot be guaranteed that the inner steel tube must be in the center, so it is necessary to consider the eccentricity of the inner steel tube. but, there are few CFDST studies on the eccentricity of the inner steel tube at present. Therefore, this paper mainly takes the eccentricity of the inner steel tube as the parameter, aims to axial load test by CFDST with different eccentricity of inner steel tube (shown in Figure 1) and numerically investigate the compressive behavior of circular concrete-filled double-skin steel tubular (CFDST) with eccentric inner steel tube short columns under entire-section loading.

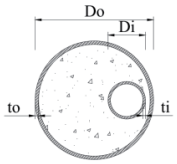

Figure 1. CFDST section of eccentric inner steel tube eccentric

2. Experimental investigation

2.1. Test specimens

In total, 16 test experiments were performed to investigate the structural performance of concrete axially compressed circular CFDST short columns with eccentric of inner steel tubes. The three typical cross- sectional diagrams of CFDST columns were depicted in Fig. 2. According to JIS G 3444-2015 , in this study, The STK400 steel tubes with the dimensions of 190.7 × 5.3 mm (diameter × thickness). The inner skins were STK400 steel tubes with the dimensions of 60.5 × 3.8 mm. The tested specimens were poured using concrete with a nominal cylinder strength of 24 MPa, 36 MPa and 48 MPa. The ratio (L/Do) of the nominal short column length-to-outside diameter of outer steel tube was maintained at a constant value of 3 to avoid overall buckling, and the nominal length of all specimens is taken as 570 mm. Tested circular CFDST short column specimens in table 1.

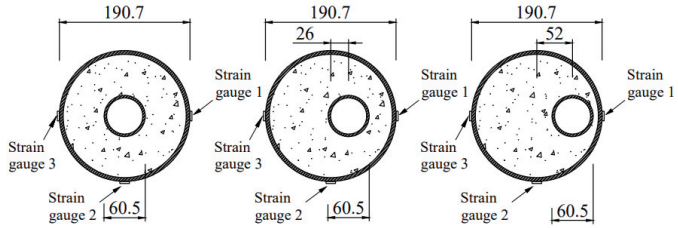

Figure 2. Typical cross-sections of specimens

Table 1. Tested circular CFDST short column specimens

Series	Tag	Do	To	Di	Ti	Do/to	χ	Di/ti	Fsyo	Fsyi	fc	Nu
Series1	C4-48-0 ①	190.7	5.3	60.5	3.8	36	/	15.9	346.9	/	50.9	2336.7
	C4-48-0 ②	190.7	5.3	60.5	3.8	36	/	15.9	346.9	/	50.9	2434
	C4-48-0.34-e0 ①	190.7	5.3	60.5	3.8	36	0.34	15.9	346.9	342.1	50.9	2660.1
	C4-48-0.34-e0 ②	190.7	5.3	60.5	3.8	36	0.34	15.9	346.9	342.1	50.9	2634.8
	C4-48-0.34-e26 ①	190.7	5.3	60.5	3.8	36	0.34	15.9	346.9	342.1	50.9	2662
	C4-48-0.34-e26 ②	190.7	5.3	60.5	3.8	36	0.34	15.9	346.9	342.1	50.9	2675.5
	C4-48-0.34-e52 ①	190.7	5.3	60.5	3.8	36	0.34	15.9	346.9	342.1	50.9	2581.4
	C4-48-0.34-e52 ②	190.7	5.3	60.5	3.8	36	0.34	15.9	346.9	342.1	50.9	2676
Series2	C4-60-0 ①	190.7	5.3	60.5	3.8	36	/	15.9	346.9	/	62.8	2900.8
	C4-60-0 ②	190.7	5.3	60.5	3.8	36	/	15.9	346.9	/	62.8	2730.5
	C4-60-0.34-e0 ①	190.7	5.3	60.5	3.8	36	0.34	15.9	346.9	342.1	62.8	2972.1
	C4-60-0.34-e0 ②	190.7	5.3	60.5	3.8	36	0.34	15.9	346.9	342.1	62.8	2821.1
	C4-60-0.34-e26 ①	190.7	5.3	60.5	3.8	36	0.34	15.9	346.9	342.1	62.8	2936.3
	C4-60-0.34-e26 ②	190.7	5.3	60.5	3.8	36	0.34	15.9	346.9	342.1	62.8	2921.2
	C4-60-0.34-e52 ①	190.7	5.3	60.5	3.8	36	0.34	15.9	346.9	342.1	62.8	2887
	C4-60-0.34-e52 ②	190.7	5.3	60.5	3.8	36	0.34	15.9	346.9	342.1	62.8	2913.6

2.2. Specimen labelling

For simplicity, the tested CFDST columns were generally labelled as: section shape of columns, material grade of outer steel tube, nominal strength of concrete, hollow ratio, number of specimens and load con-dition. For instance, the label “C4-48-0.34-e26 ①” defines the following specimen: The first letter “C” means the circular section; number “4” refers to STK400 ; number “48” after he first en dash indicates the nominal compressive strength of concrete, 48 MPa; number “0.34” after the second en dash denotes the hollow ratio of column and is computed by Di/(Do-2to); “e26”after the third en dash denotes eccentricity of inner steel tube (the distance between the center of the outer steel tube and the center of the inner steel tube); the last“①” symbolizes the first test body in the identical set of specimens.

"Do" is the outer steel tube diameter (mm), "To" is the outer steel tube thickness (mm), "Di" is the inner steel tube diameter (mm), "Ti" is the inner steel tube thickness (mm), and "Do/to" is The outer steel tube diameter-thickness ratio, "χ" is the hollow ratio, "Di/ti" is the inner steel tube diameter-thickness ratio, "Fsyo" is the outer

steel tube yield strength (Mpa), "Fsyi" is the inner steel tube yield strength (Mpa)," fc" is the actual strength of concrete (Mpa), "Nu" is the experimental ultimate load (KN).

2.3. Material properties

The tensile coupon tests on external and internal tube skins were carried out to determine their material properties. The tensile coupons were longitudinally cut from the curved face of the circular hollow steel tubes (CHS) with the same parent material as the test specimens. The material properties of external and internal tube skins are listed in Table 2. In this table, fsy represents the yield strength of CHS tubes, and it is a general term, which is the same as the yield stress fsyo of the external tube skin and the yield stress fsyi of the internal tube skin; fsu denotes the ultimate tensile strength; Es stands for the Young's modulus.

Table 2. Material properties of external and internal skins

Type of steel	Location	Nominal sectional size (mm)	fsy (Mpa)	fsu (Mpa)	Es (Mpa)
STK400	Internal skin	60.5 × 3.8	342.1	406.4	199.6
	External skin	190.7 × 5.3	346.9	413.2	200.4

The material properties of the concrete used were determined by performing the standard concrete cylinder tests. According to the American Standard, the dimensions of concrete cylinder are 150 mm × 300 mm (diameter × height). The mix design of concrete used, which was achieved from commercially available materials, measured strength of concrete cylinders was listed in Table 3.

Table 3. Measured strength of concrete cylinders

Nominal concrete strength (MPa)	Average concrete strength at 28 days (MPa)	Number of cylinder tests	Average concrete strength at test day (MPa)	Number of cylinder tests
C48	52.1	2	50.9	2
C60	61.7	2	62.8	2

3. Test findings and analysis

3.1 The relationship between the eccentricity inner steel tube and the compressive performance of the CFDST short column

Figure 3. is the relationship between ultimate strength and eccentricity. We can know that the average ultimate loads of the three kinds of eccentricity inner steel tube e0, e26, and e52 of concrete C48 are 2647.45KN, 2668.75KN, and 2628.7KN, respectively, the standard deviation is 16.36 and the coefficient of variation is 0.62%. The average ultimate loads of the three eccentricity inner steel tube e0, e26, and e52 of concrete C60 are 2896.6KN, 2928.75KN, and 2900.3KN, respectively, the standard deviation is 14.36 and the coefficient of variation is 0.49%. It can be found that the eccentricity of the inner steel tube has no obvious effect on the ultimate compressive strength of the CFDST short column.

Figure 4. is relationship between eccentricity inner steel tube and compressionstiffness. In order to avoid the error caused by the incomplete fitting of the test body and the pressure plate at the initial stage of compression, as well as the influence after yielding, the range of 500KN-2000KN in the elastic phase is used to calculate the stiffness of the CFDST short column with eccentric inner steel tube. The results are shown in Figure 4. It can be found that the compressionstiffness of the CFDST short column decreases with the increase of the eccentricity of the inner steel tube.

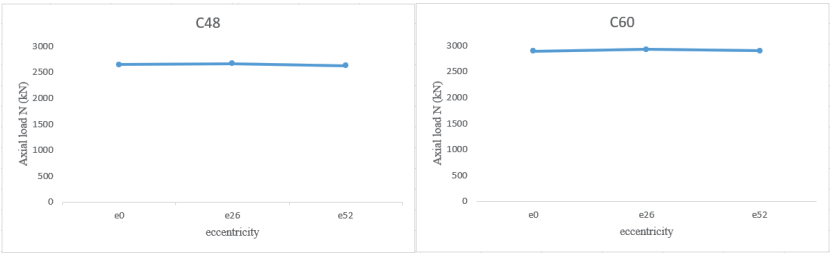

Figure 3. relationship between ultimate strength and eccentricity

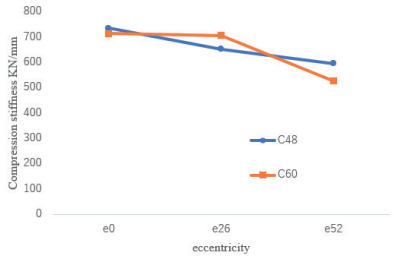

Figure 4. Relationship between eccentricity inner steel tube and compressionstiffness

3.2 Performance of steel and concrete materials

Figure 5. is Load- equivalent strain relationship, the vertical line ε=1700 represents the yield strain of the steel. The Mises stress is converted to Mises strain (equivalent strain) by generalized Hooke's law, and then the equivalent strain is calculated from the axial strain and hoop strain. Therefore, the equivalent strain is compared with the yield strain of the steel. It can be seen from Figure 5 that the yield strain of the steel is basically located at the yield point of the CFDST column, and it can be inferred that the steel and the column basically yield at the same time, no premature buckling. If the yield strain line of the steel is to the left or right, buckling may have occurred in advance, so that the performance of the steel has not been fully exerted. The experimental data shows that the eccentricity of the inner steel tube does not have much influence on the performance of steel and concrete.

Mises stress:

$$\sigma_e = \sqrt{\sigma_z^2 - \sigma_z\sigma_\theta + \sigma_\theta^2}$$

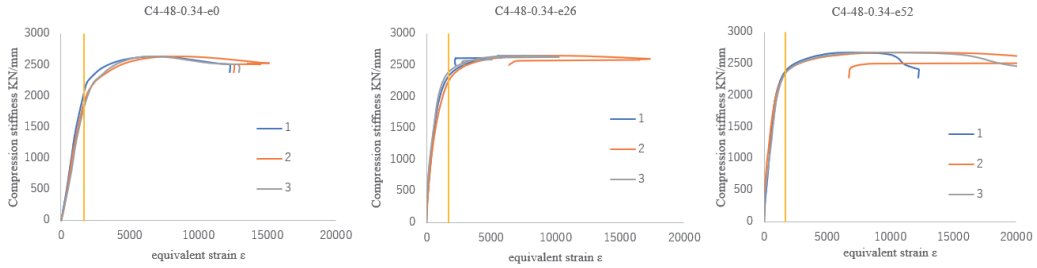

Figure 5. Load- equivalent strain relationship

4. Conclusion

A comprehensive experimental and numerical studies on the behavior of the circular CFDST short columns with Eccentric Inner Steel Tube was conducted in the present paper. The following conclusions can be drawn within the scope of this study:

- The eccentricity of the inner steel tube has no obvious effect on the ultimate compressive strength of the CFDST short column. But,the compressionstiffness of the CFDST short column decreases with the increase of the eccentricity of the inner steel tube.
- The eccentricity of the inner steel tube does not have much influence on the performance of steel and concrete.

References

D. Lam, L. Gardner. Structural design of stainless steel concrete filled columns, *J.Constr. Steel Res.* 64 (11) (2008) 1275–1282.

L.H. Han, W. Li, R. Bjorhovde. Developments and advanced applications of concrete-filled steel tubular (CFST) structures. *Members. J. Constr. Steel Res.* 100 (2014)211–228.

V.I. Patel, B. Uy, K.A. Prajwal, F. Aslani. Confined concrete model of circular, elliptical and octagonal CFST short columns. *Steel Compo. Struct.* 22 (2016) 497–520.

X.F. Yan, Y.G. Zhao. Experimental and numerical studies of circular sandwiched concrete axially loaded CFDST short columns. *Eng. Struct.* 230 (2021) 111617.

X.F. Yan, Y.G. Zhao. Compressive strength of axially loaded circular concrete-filled double-skin steel tubular short columns. *J. Constr. Steel Res.* 170 (2020) 106114

Y.G. Zhao, X.F. Yan, S.Q. Lin. Compressive strength of axially loaded circular hollow centrifugal concrete-filled steel tubular short columns. *Eng. Struct.* 201 (2019)109828.

International Symposium on Emerging Developments and Innovative Applications of Reliability Engineering and Risk Managements (EDIARR2022),30 October-3 November2022, Taipei
Chen, S. S. &Ang, Alfredo. H-S. (Editors)

EFFECT OF EARTHQUAKE SCENARİOS ON RESPONSE SPECTRAL RATİO

Haizhong Zhang[1], Yan-Gang Zhao[1]

[1]*Department of architecture, Kanagawa University, Yokohama, Japan*

E-mail: zhang@kanagawa-u.ac.jp

E-mail: zhao@kanagawa-u.ac.jp

Abstract: The response spectral ratio (RSR) used to construct a design spectrum that incorporates site effects is conventionally assumed to be independent of an earthquake scenario in linear analysis. However, recent studies have found that the RSR varies significantly with an earthquake scenario, even in linear analysis. In this study, the mechanism behind the effect of earthquake scenarios, i.e., the variation in the RSR with an earthquake scenario, is systematically investigated by comparisons with the scenario-independent Fourier spectral ratio based on random vibration theory.

***Keywords*:** site effects, effect of earthquake scenarios, design spectrum, Fourier spectral ratio.

1. Introduction

The ratio of the response spectrum on a ground surface to that on a reference bedrock plays an important role in the construction of a design spectrum (International Building Code (IBC) 2012; European Committee for Standardization CEN 2004; Japanese Seismic Design Code 2000). The response spectral ratio (RSR) reflects the site amplification effects on the response spectrum; by multiplying the RSR with the spectrum specified on the bedrock, a design spectrum incorporating site effects can be obtained. Many RSR models have been developed to construct a design spectrum (Borcherdt 1994; Dobry et al. 2000; Lam et al. 2001; Tsang et al. 2006, 2017; Zhang and Zhao 2018, 2019; Japanese Seismic Design Code 2000). The basic principle to develop RSR models is generally based on the Fourier spectral ratio (FSR), which categorizes the RSR into linear and nonlinear components. The nonlinear component reflects the modification of soil properties resulting from the nonlinear hysteretic behavior of the soil when exposed to strong levels of excitation. The linear component is from the site and independent of the earthquake scenario.

However, recent studies have found that even in linear analysis, the RSR is affected not only by the properties of soil profiles but also by those of earthquake scenarios (Zhao et al. 2009; Zhao and Zhang 2010). Bora et al. (2016) and Stafford et al. (2017) presented a theoretical explanation for this phenomenon and further pointed out that the effect of the earthquake scenario is particularly significant in very short periods. Zhang and Zhao (2021) investigated the variation in the RSR with earthquake scenarios by comparing the RSR and FSR based on statistical analyses of seismic records.

When the RSRs used for seismic design are derived based on statistical analyses of seismic records from one region and applied to this or another region with similar seismological properties (including various factors affecting characteristics of the earthquake scenario, e.g., tectonic context, source mechanisms, and attenuation), ignoring the effect of earthquake scenarios on the RSR may not have significant impacts on the design spectrum. This is because to a certain extent, the effect of earthquake scenarios in this region has been included in the statistical analysis. However, when the RSRs from a region are applied to other regions with completely different seismological properties (such applications often occur in regions with a lack of seismic records for the statistical analysis (Tsang et al. 2006)), ignoring the effect of the earthquake scenario on the RSR can lead to certain unrealistic behaviors of the design spectrum. This is because, as mentioned previously, different characteristics of the earthquake motion may lead to completely different values of the RSR. In this study, the mechanism behind the effect of earthquake scenarios, i.e., the variation in the RSR with an earthquake scenario, is systematically investigated.

2. Expression for the RSR

Stafford *et al*. (2017) presented an approach for the analysis of the RSR based on RVT, which is efficient for solving this problem. According to the RVT, the response spectrum $R(\bar{\omega}, h_0)$ can be obtained from the zeroth

moment of the Fourier amplitude spectrum (FAS) of the response of a single-degree-of-freedom (SDOF) oscillator (Boore 1983, 2003), which is expressed as

$$R(\bar{\omega}, h_0) = \frac{pf_r}{\sqrt{D_r}}\sqrt{m_{0,r}} \tag{1}$$

where $\bar{\omega}$ and h_0 are the circular frequency and damping ratio of the SDOF oscillator (hereafter referred to as the oscillator), respectively; pf_r and D_r are the peak factor and duration of the oscillator response, respectively; and $m_{0,r}$ is the zeroth moment of the FAS of the oscillator response.

Thus, the RSR can be obtained by dividing the ground-surface response spectrum by the bedrock response spectrum, which is expressed as

$$RSR(\bar{\omega}, h_0) = \sqrt{\frac{m_{0,sr}}{m_{0,br}}} \times \frac{pf_{rs}/\sqrt{D_{rs}}}{pf_{rb}/\sqrt{D_{rb}}} \tag{2}$$

where, pf_{rs} and pf_{rb} are the peak factors of the oscillator responses for the ground surface and reference bedrock motions, respectively; D_{rs} and D_{rb} are the durations of the oscillator responses for the ground surface and bedrock motions, respectively; $m_{0,sr}$ and $m_{0,br}$ denote the zeroth spectral moments of the oscillator responses for the ground surface and bedrock motions, respectively. Here, the reference bedrock motion is assumed to represent the incident motion beneath the soil profile corresponding to the ground-surface motion.

The zeroth spectral moment of the bedrock motion's oscillator response $m_{0,br}$ can be obtained from the FAS of the bedrock motion's oscillator response by

$$m_{0,br} = \frac{1}{\pi}\int_0^{\infty} |A_B(\omega)\,|H_0(\omega, \bar{\omega}, h_0)||^2 d\omega \tag{3}$$

where ω is the circular frequency, $A_B(\omega)$ is the FAS of the bedrock motion, and $H_0(\omega, \bar{\omega}, h_0)$ is the SDOF transfer function, expressed as

$$|H_0(\omega, \bar{\omega}, h_0)| = \frac{\bar{\omega}^2}{\sqrt{(2h_o\omega\bar{\omega})^2 + (\omega^2 - \bar{\omega}^2)^2}} \tag{4}$$

Similarly, the zeroth spectral moment of the ground-surface motion's oscillator response $m_{0,sr}$ can be obtained from the FAS of the ground-surface motion's oscillator response by

$$m_{0,sr} = \frac{1}{\pi}\int_0^{\infty} |A_S(\omega)\,|H_0(\omega, \bar{\omega}, h_0)||^2 d\omega \tag{5}$$

Here, $A_S(\omega)$ is the FAS of the ground-surface motion, which can be obtained from the bedrock-motion FAS via

$$A_S(\omega) = A_B(\omega)|T(\omega)| \tag{6}$$

where $T(\omega)$ is the site transfer function and $|T(\omega)|$ represents the Fourier spectral ratio (FSR) between the seismic motion on the ground surface and that on the reference bedrock. As the paper focuses on the response spectrum of acceleration, throughout the paper, the response spectra, Fourier spectra, and transfer functions are all for acceleration.

For convenience in the following analysis, equation (2) is rearranged as

$$RSR(\bar{\omega}, h_0) = \sqrt{\frac{\int_0^{\infty} W(\omega, \bar{\omega})|T(\omega)|^2 d\omega}{\int_0^{\infty} W(\omega, \bar{\omega}) d\omega}} \times \frac{pf_{rs}/\sqrt{D_{rs}}}{pf_{rb}/\sqrt{D_{rb}}} \tag{7}$$

where $W(\omega, \bar{\omega})$ is the square of the FAS of the bedrock motion's oscillator response, expressed as

$$W(\omega, \bar{\omega}) = A_B^2(\omega)|H_0(\omega, \bar{\omega}, h_0)|^2 \tag{8}$$

3. Investigating the effect of earthquake scenarios

This section explores the effect of earthquake scenarios on the RSR using equation (7). Equation (7) is the product of two terms: the first term is determined by $|T(\omega)|^2$ and $W(\omega, \bar{\omega})$, and the second term is determined by the durations and peak factors. The characteristics of these two terms are investigated in the following two sections. Then, the effect of earthquake scenarios on the RSR is discussed according to the characteristics. Because the RSR and FSR are often used to characterize site effects, and the FSR is independent of the earthquake scenario for linear analysis, the effect of earthquake scenarios on the RSR is explored by comparing the two spectral ratios. Although the FSR, $T(\omega)$, and RSR are functions of circular frequency, the two frequencies are physically different: the FSR one ω is the circular frequency of the seismic motion's FAS, whereas the RSR one $\bar{\omega}$ is the oscillator circular frequency.

3.1 Characteristics of the first term

To demonstrate the characteristics of the first term, simple cases of a soil layer with a constant velocity underlain by a rock half-space are considered. The thickness H of the soil layer and shear-wave velocity of the rock half-space V_B are varied, as summarized in Table 1. The shear-wave velocity of the soil layer V_S was set as 300 m/s, and the damping ratio h was set as 0.1 for the soil layer and 0 for the bedrock. Ten soil profiles were created and named as sites 1–10, as listed in Table 1. The impedance ratio a of soil layer to rock layer is 0.5 for sites 1–5 and 0.2 for sites 6 –10. The undamped fundamental period T_1 of the sites ranges from 0.1 s for the shallowest site to 2 s for the deepest site. In addition, five levels of input bedrock motions with $M = 3$, $R = 10$ km, $M = 5$, $R = 10$ km, $M = 7$, $R = 10$ km, $M = 5$, $R = 100$ km, and $M = 5$, $R = 200$ km were considered. The first term of each soil profile is estimated for all considered FASs of the input bedrock motion. Then, the calculated results for the first term are compared with those for the FSR at the same frequency values. Comparisons of the results using site 8 as a representative are shown in Figure 1.

Table 1 Characteristics of the created sites

Name	Site 1	Site 2	Site 3	Site 4	Site 5	Site 6	Site 7	Site 8	Site 9	Site 10
H (m)	7.5	15	37.5	75	150	7.5	15	37.5	75	150
V_s (m/s)	300									
V_B (m/s)	600					1500				

Comparisons of the first term and FSR for all sites indicate that the maximum value of the first term is consistently smaller than that of the FSR, and the value of the first term differs from that of the FSR in the short-period band, the first term is similar to the FSR at long oscillator periods. Further, the overall shapes of the first term and FSR are similar, and they reach their maximum values at the same period, as shown in Figure 1. In addition, the value of the first term gradually approaches that of the FSR with increasing magnitude and distance at long oscillator periods, and the difference in values of the first term and FSR at very short oscillator periods tends to increase with increasing magnitude and distance, as shown in Figure 1. Moreover, it is noted that the first term varies more significantly with magnitude than distance.

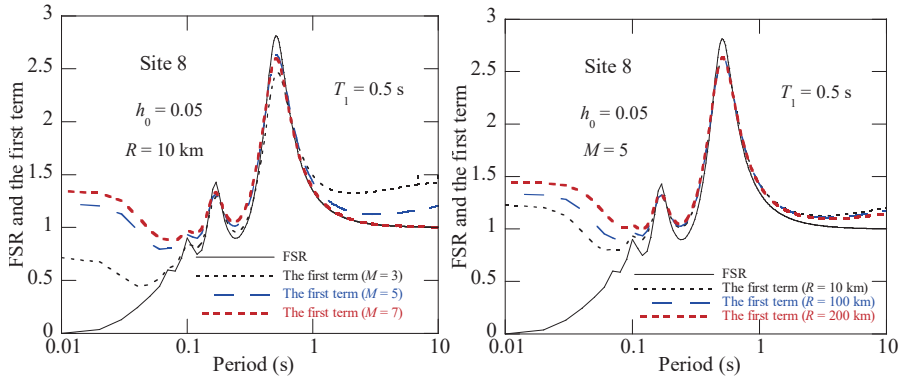

Fig. 1 Variation in the first term with (a) magnitude and (b) distance of the earthquake scenario for site 8

3.2 Characteristics of the second term

To investigate the characteristics of the second term, the second term in equation (7) is analyzed. The second term can be considered as the product of pf_{rs}/pf_{rb} and $\sqrt{D_{rb}/D_{rs}}$, which represent the rates of change of the peak factor and duration of the oscillator response generated by the site response, respectively. Generally, the peak factor varies little with the affected parameters. Therefore, the second term is dominated by the duration part, $\sqrt{D_{rb}/D_{rs}}$. The duration ratio D_{rs}/D_{rb} was calculated for a range of site conditions and input motions in previous studies (Kottke and Rathje 2013; Wang and Rathje 2016). Because the second term is inversely proportional to D_{rs}/D_{rb}, using the characteristics of the duration ratio D_{rs}/D_{rb} derived in the previous studies, the characteristics of the second term can be understood. Previous studies found that the shape of D_{rs}/D_{rb} is very similar to that of the FSR, and their peaks occur at the same site's natural periods (Kottke and Rathje 2013). This implies that the minimum valley value of the second term and maximum value of the FSR occur at the same period. In addition, it was found that the duration of the oscillator response at the fundamental period is generally extended by site response (Wang and Rathje 2016); the peak value of D_{rs}/D_{rb} at the fundamental period are always greater than unity. This implies that the minimum valley value of the second term is consistently smaller than unity. Moreover, the peak value of D_{rs}/D_{rb} at the fundamental period was found to decrease to unity with increasing magnitude (Wang and Rathje 2016). This implies that the minimum valley value increases to unity with increasing magnitude.

To demonstrate the characteristics of the second term, further analyses were conducted for the series of site conditions and input motions considered above. To accurately obtain the values of the second term, the second term is estimated using time-history analysis by the program Strata (Kottke and Rathje 2008), which has been widely used as a reference to calibrate the RVT-based analyses. The input time histories for the time-history analysis are generated from the FAS by the program SMSIM (Boore 2005) using stochastic simulation (Boore 1983). According to Atkinson and Silva (2000), the duration D_{gm} of the time history is determined using $D_{gm}=1/f_0+0.05R$, where f_0 is the corner frequency representing the frequency below which the FAS decays. For each FSA, a suite of 100 time histories is generated, and the simulated time histories match the FAS on average.

Then, the surface response spectral accelerations of each soil profile for all the generated time histories were calculated. For each magnitude, the 100 corresponding bedrock response spectra and surface response spectra of each soil profile were averaged. The RSR is obtained as the ratio of the average surface response spectrum to the average bedrock response spectrum. Subsequently, using equation (7), the values of the second term are obtained as the quotient of the RSR to the first term obtained above. Representative results and their corresponding FSRs for the second term of site 8 are shown in Figure 2. All comparisons of the second term and FSR support that the minimum valley value of the second term is consistently smaller than unity and increases to unity with increasing magnitude. In addition, it was found that the shapes of the second term are much flatter when compared with those of the FSR, all values of the second term approach unity, and the shape of the second term tends to flatten with increasing magnitude and distance.

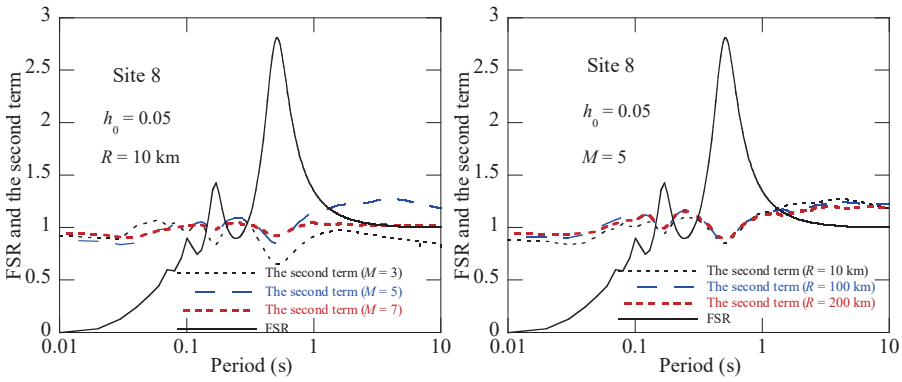

(a) (b)

Fig. 2 Variation in the second term with (a) magnitude and (b) distance of the earthquake scenario for site 8

3.3 Characteristics of the effect of earthquake scenarios on the RSR

Based on the characteristics of the first and second terms established in the previous two sections, the characteristics of the effect of earthquake scenarios on the RSR are discussed in this section.

According to the characteristics: (1) at long periods, the values of the first term gradually approach those of the FSR with increasing magnitude and distance, and (2) the values of the second term approach unity, and the shape of the second term tends to flatten with increasing magnitude and distance. It can be inferred that the values of the RSR at long periods gradually approach those of the FSR with increasing magnitude and distance. The values of the RSR obtained above are compared with those of the FSR, and representative comparisons for site 8 are presented in Figure 3, all results support this inference.

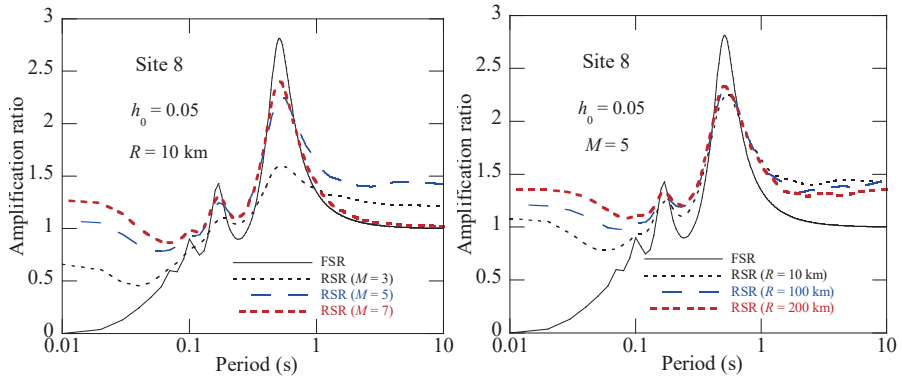

Fig. 3 Variation in the RSR with (a) magnitude and (b) distance of the earthquake scenario for site 8

According to the characteristics: (1) the maximum values of the first term and FSR occur at the same period, and the maximum value of the first term is consistently smaller than that of the FSR, and (2) the minimum valley value of the second term and maximum value of the FSR occur at the same period while the minimum valley value of the second term is consistently less than unity. It can be inferred that the maximum value of the RSR should be consistently smaller than that of the FSR. This is reported in Figure 3 and previous statistical analyses (Rosenblueth and Arciniega 1992, Zhang and Zhao 2021).

According to the characteristics: (1) the overall shape of the first term is similar to that of the FSR and the maximum values of the first term and FSR occur at the same period, and (2) the shape of the second term is much flatter when compared with that of the FSR, and all values of the second term are approximately unity. Hence, it can be inferred that the overall shape of the RSR should be similar to that of the FSR, and the maximum values of the RSR and FSR should occur at the same period, as shown in Figure 3. This conclusion is consistent with that based on statistical analysis (Dobry 1991, Zhang and Zhao 2021).

According to the characteristics: (1) the values of the first term and FSR in the short-period band are very different, and the difference tends to increase with increasing magnitude and distance, and (2) all the values of the second term approach unity with increasing magnitude and distance. It can be inferred that the values of the RSR and FSR in the short-period band are different, and the difference tends to increase with increasing magnitude and distance, as shown in Figure 3.

Moreover, according to the characteristics: (1) the effect of earthquake scenarios on the first term is governed by the ground-motion frequency content, and (2) the effect of earthquake scenarios on the second term is much smaller than that on the first term (at 0.03 and 3 s, the average rates of change of the first term with magnitude are 18% and 7.6%, respectively, while the average rates of change of the second term with magnitude are only 0.22% and 2.3%, respectively). It can be inferred that the effect of earthquake scenarios on the RSR is governed by the ground-motion frequency content.

4. Conclusions

This clarified the mechanism of the effect of earthquake scenarios, i.e., the variation in the RSR with the earthquake scenario by comparing it with the scenario-independent FSR based on random vibration theory. The main conclusions of this study can be summarized as follows:

1. The overall shape of the RSR is similar to that of the FSR, their maximum values occur at the same period, and the maximum value of the FSR consistently exceeds that of the RSR.

2. The values of the RSR and FSR are similar at long periods, and the RSR values at long periods gradually approach those of the FSR with increasing magnitude and distance.

3. The values of the RSR and FSR at very short periods are very different, and the difference increases with increasing magnitude and distance.

References

Atkinson GM, and Silva W (2000). Stochastic modeling of California ground motions, Bull Seism Soc Am 90: 255–274.
Boore DM (1983). Stochastic simulation of high-frequency ground motions based on seismological models of the radiated spectra, Bull Seism Soc Am 73: 1865–1894.
Boore DM (2003). Simulation of ground motion using the stochastic method, Pure Appl Geophys 160: 635–676.
Boore DM (2005). SMSIM—Fortran programs for simulating ground motions from earthquakes: version 2.3, U.S. Geol. Surv. Open-File Rept. 2005 OFR 96-80-A, Menlo Park, California.
Bora SS, Scherbaum F, Kuehn N, and Stafford PJ (2016). On the relationship between Fourier and response spectra: Implications for the adjustment of empirical ground-motion prediction equations (GMPEs), Bull Seis Soc Am 106: 1235–1253.
Borcherdt RD (1994). Estimates of site-dependent response spectra for design (Methodology and Justification), Earthq. Spectra 10: 617–653.
Dobry R (1991). Soil properties and earthquake response, 1171-1187, IV, Proceeding of X European Conference of Soil Mechanics and Foundation Engineering;26–30 May, 1991, Florence, Italy.
Dobry R, Borcherdt RD, Crouse CB, Idriss IM, Joyner WB, Martin GR, Power MS, Rinne EE, and Seed RB (2000). New site coefficients and site classification system used in recent building seismic code provisions, Earthq Spectra 16: 41–67.
European Committee for Standardization CEN (2004). Eurocode 8: design of structures for earthquake resistance—part 1: general rules, seismic actions and rules for buildings, European Standard EN 1998-1.
International Building Code (IBC) (2012). Country Club Hill, Illinois, USA: International Code Council.
Japanese Seismic Design Code (2000). Technical Standard for Structural Calculation of Response and Limit Strength of Buildings. Notification No.1457–2000, Ministry of Land, Infrastructure and Transport. (In Japanese)
Kottke AR, and Rathje EM (2013). Comparison of time series and random-vibration theory site-response methods, Bull Seism Soc Am 103: 2111–2127.
Kottke AR, and Rathje EM (2008). Technical Manual for Strata, University of California, Berkeley.
Lam NTK, Wilson JL, and Chandler AM (2001). Seismic displacement response spectrum estimated from the analogy soil amplification model, Eng Struct 23: 1437–1452.
Stafford PJ, Rodriguez-Marek A, Edwards B, Kruiver P, and Bommer JJ (2017). Scenario dependence of linear site effect factors for short-period response spectral ordinates, Bull Seism Soc Am 107: 2859–2872.

Tsang HH, Adrian MC, and Lam NTK (2006). Estimating non-linear site response by single period approximation, Earthq Eng Struct Dyn 35: 1053–1076.
Tsang HH, Wilson JL, Lam NTK, and Su RKL (2017). A design spectrum model for flexible soil sites in regions of low-to-moderate seismicity, Soil Dyn Earthq Eng 92: 36–45.
Wang X, and Rathje EM (2016). Influence of peak factors on site amplification from random vibration theory based site-response analysis, Bull Seism Soc Am 106: 1–14.
Zhang HZ, and Zhao YG (2018). A simple approach for estimating the first resonance peak of layered soil profiles, J Earthq Tsunami 12: 185005.
Zhang HZ, and Zhao Y (2019). A simple approach for estimating the fundamental mode shape of layered soil profiles, J Earthq Tsunami 13: 1950003.
Zhang HZ, and Zhao Y (2021). Investigation of Relationship Between the Response and Fourier Spectral Ratios Based on Statistical Analyses of Strong Motion Records, J Earthq Tsunami: 2150008.
Zhao JX, Zhang J, and Kojiro I (2009). Side effect of using response spectral amplification ratios for soil sites-variability and earthquake-magnitude and source-distance dependent amplification ratios for soil sites, Soil Dyn Earthq Eng 29: 1262–1273.
Zhao JX, and Zhang J (2010). Side-effect of using response spectral amplification ratios for soft soil sites—Earthquake source-type dependent amplification ratios, Soil Dyn Earthq Eng 30: 258–269.

International Symposium on Emerging Developments and Innovative Applications of Reliability Engineering and Risk Managements (EDIARR2022),30 October-3 November2022, Taipei
Chen, S. S. &Ang, Alfredo. H-S. (Editors)

STRUCTURAL RELIABILITY ANALYSIS USING INFORMATION EXCHANGE PARTICLE SWARM OPTIMİZATION ALGORITHM

Lixiang Cheng[1], Yan-Gang Zhao[1]

[1] *Faculty of Architecture and Building Engineering, Kanagawa University, Yokohama, Japan E-mail: chenglixiang1994@gmail.com*

E-mail: zhao@kanagawa-u.ac.jp

Abstract: The first-order reliability method (FORM) is one of the most reliable calculation methods for structural reliability analysis, where the reliability index is interpreted as the minimum distance from the origin to the limit state surface when normalized. Mathematical algorithms are generally one of the ways to solve such optimization problems. The normal space (u-space) and the most probable failure points (design points) are searched using mathematical algorithm methods. Among the existing search design point algorithms, particle swarm optimization (PSO) algorithm is widely used in engineering optimization because of its good optimization ability and fast convergence speed. However, with the increasingly complex engineering problems, the PSO algorithm also has some shortcomings, such as: it is easy to fall into local optimum when solving multi-extremum, and the low convergence of complex optimization problems. To avoid these shortcomings, this paper proposes an information exchange particle swarm (IEPSO) algorithm. Finally, the combination of IEPSO and FORM method is used to solve the structural reliability index. The results demonstrate the efficiency and quasi-accuracy of IEPSO in structural reliability assessment.

Keywords: Structural reliability, reliability index, FORM, information exchange, particle swarm optimization algorithm.

Introduction

Structural reliability analysis is one of the main contents of structural safety research (Zhao & Ono, 1999), and the basic problem of structural reliability analysis is to solve the Eq. (1)

$$P_F = \int_{G(X)<0} f(X)d(X) \tag{1}$$

where X is the random variable vector of the structural system uncertainty described; $f(X)$ is the joint probability density function of X; G(X) is the functional function of the structure; $G(X)<0$ indicates structural failure and G(X)=0 indicates that it is in the limit state surface. The search of accurate and fast near-analytic methods is an urgent need for that the integral in Eq. (1) is difficult to be solved directly in most of the actual structural reliability analysis.

First order reliability method (FORM) (Rosenblatt, 1952) is one of the most reliable calculation methods for structural reliability. FORM is an analytical approximation in which the reliability index is interpreted as the minimum distance from the origin to the limit state surface in normalization. Mathematical algorithm is generally one of the methods to solve such optimization problems. Use mathematical algorithm methods to search for normal space (u space) and the most likely point of failure (design point). In the existing search design point algorithm, the Particle

swarm optimization algorithm is widely used to obtain design points, which however, have several shortcomings, e.g.: tending to fall into local optimum when solving multi-extremal, and low convergence for complex optimization problem. To avoid such shortcomings, an information exchange particle swarm optimization (IEPSO) algorithm is proposed in this paper. Several examples are used to assess the performance of IEPSO. Results demonstrate the efficiency and accuracy of the IEPSO in structural reliability assessment, in which Monte-Carlo simulation is used for comparison.

This paper is organized as follows: In section 2, how to solve the structural failure probability with optimization algorithm based on FORM was introduced. In section 3, the PSO and IEPSO framework and their operating rules were presented. Section 4, some limit states functions reported in the literature was studied. Section 5 the main conclusions and perspectives were provided.

Form-based meta-heuristic algorithm for solving failure probability

In the FORM method, the solution of the failure probability P_F is approximately equal to $P_F \approx \phi(-\beta_{\mathrm{HL}})$, where β_{HL} is the reliability index, indicating the shortest distance from the origin to the restricted surface in the standard normal space. The purpose of this paper is to calculate β_{HL} in the standard normal space using IPSO. To achieve this, we need to solve a constrained optimization problem given in Eq. (2). This paper uses the penalty function (Fiacco and McCormick, 1968; Ashgar, 1999) to solve this constrained optimization problem and convert the above formula to Eq. (3).

$$\begin{cases} \mathrm{Minimize} \ \|\mu\| \\ Subject\ to\ G(\mu)=0 \end{cases} \tag{2}$$

$$\mathrm{Minimize} \ \|\mu\| + \xi|G(\mu)| \tag{3}$$

where ξ is function of the absolute value of the equality constraint.

The principle of PSO and IEPSO

The principle of PSO algorithm and IEPSO algorithm is described in this section.

Particle swarm algorithm

Particle swarm optimization algorithm (Kennedy and Eberhart, 1995) is a solution algorithm that simulates the foraging of birds. A bird is regarded as a particle, a particle is a solution, and the food position is the optimal solution. The birds find their nearest position to the food through individual birds, and share the position with other birds, to determine the nearest position to the food in the birds, move the position and exchange information repeatedly until they find the food, which is abstracted as the process in the solution space, A group of particles are randomly generated to form a population. Each particle searches the solution space at a certain speed and uses the fitness function to evaluate the position of the particle. For each search, each particle will determine the optimal position searched by itself as the individual optimal position, and

determine the optimal position searched by the whole population as the global optimal position. Through continuous search, the current search speed, current front the individual optimal position and the global optimal position are continuously updated until the optimal solution is obtained. The particle velocity update formula is as follows:

$$V_i(t+1) = wV_i(t) + c_1 r_1 (P_{bl} - X_i(t)) + c_2 r_2 (P_g - X_i(t)) \quad (4)$$

The particle position update formula is as follows:

$$X_i(t+1) = X_i(t) + V_i(t+1) \quad (5)$$

where $X_i(t)$ is the current position of particle i in iteration t; $V_i(t)$ is the current search speed of iteration t of particle

i. w is inertial factor; c_1 and c_2 are self-learning factor and social learning factor respectively; r_1 and r_2 are randomly generated constraint factors and are random numbers in the interval of (0,1). P_g is the global optimal position; P_{bi} is the individual optimal position of particle i.

Step1: Population initialization, randomly generate the positions and velocities of m particles, evaluate the initial positions of particles using fitness function, take the pre-initial positions of each particle as the individual optimal position P_{bi}, and take the most fitness position in the population as the global optimal position P_g.

Step2: Use equations (4) and (5) to update the velocity and position of each particle respectively.

Step3: Use fitness function to evaluate the current position of each particle. If the fitness of the current position of each particle is better than the fitness of the individual optimal position, the individual optimal position is updated. The maximum fitness of the individual optimal position of each particle is compared with the self-fitness of the global optimal position. If the fitness of the current population optimal position is better, the global optimal position is updated.

Step4: Determine whether the termination conditions are met. If so, the global optimal position P_g, namely the optimal solution, is output. If not, Step2 is carried out.

The flow chart of particle swarm algorithm is shown in Figure 1.

Information Exchange Particle swarm algorithm

IEPSO is based on the robustness of the basic particle swarm algorithm and makes full use of the information of the optimal particle and historical optimum to guide the particle swarm to find the optimal solution. The specific improvement is divided into 3 steps.

First for simple multidimensional optimization problems, the standard particle swarm optimization algorithm can quickly converge to the global optimum (Liu et al., 2007). However, when faced with some complex multi- extremum problems, it often falls into local search and the convergence rate is slow. Therefore, this paper proposes an information exchange particle swarm optimization algorithm to improve the global optimization performance of particle swarm optimization algorithm. To enhance the diversity of particles in the population, adaptive Cauchy variation was carried out for the optimal particles in the population. At the same time, the fitness values of the new particle and the worst particle after Cauchy mutation are compared, and the optimal value between them is selected to enter the next iteration of the cycle.

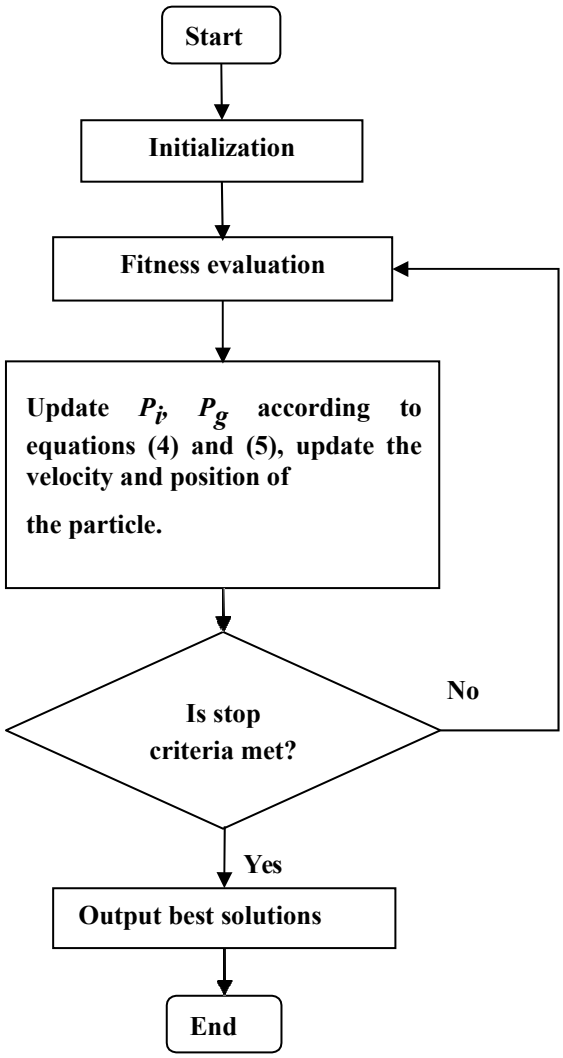

Figure 1. Flowchart of Particle Swarm Optimization

Since the intelligent optimization algorithm is easy to fall into local optimum, Cauchy variation (Wang et al., 2007) can be used to increase the diversity of the population and improve the global searching ability of the algorithm. Cauchy variation is the operation of adding random

perturbation terms subject to Cauchy distribution to individuals. The probability density function of Cauchy distribution is given by Equation (6), and the waveform is shown in Fig. 2.

$$f(x) = \frac{1}{\pi(x^2+1)}, -\infty < x < +\infty \tag{6}$$

It can be seen from Figure 2 that the Cauchy distribution graph has very narrow two wings, that is, the probability of generating a large random number is very high. Therefore, at the beginning of the iteration of the intelligent algorithm, adding a random disturbance conforming to the Cauchy distribution can reduce the possibility of the search falling into the local optimum. However, when the individual information is close to the global optimal in the iterative process, the large variation step size of Cauchy variation is not conducive to the accurate search in a small range.

Second, Optimal particle and historical optimum are the main optimization factors that guide the particle swarm to keep close to the optimal value. Compare the optimal particle value with the historical optimum. If the historical optimum value is better, use historical optimum instead of the optimal particle to guide the movement of the later particle swarm. To take advantage of these two global optimization factors. Each of the optimal particle and a portion of the historical optimum are crossed to produce a new particle. If the new particle is better than the best particle, replace it.

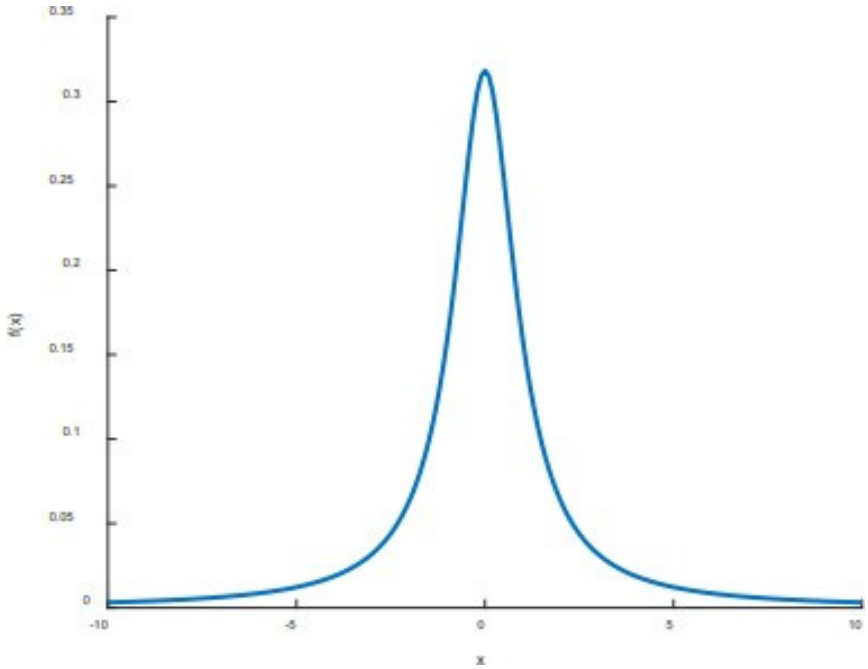

Figure 2. Cauchy distribution of probability density function waveform

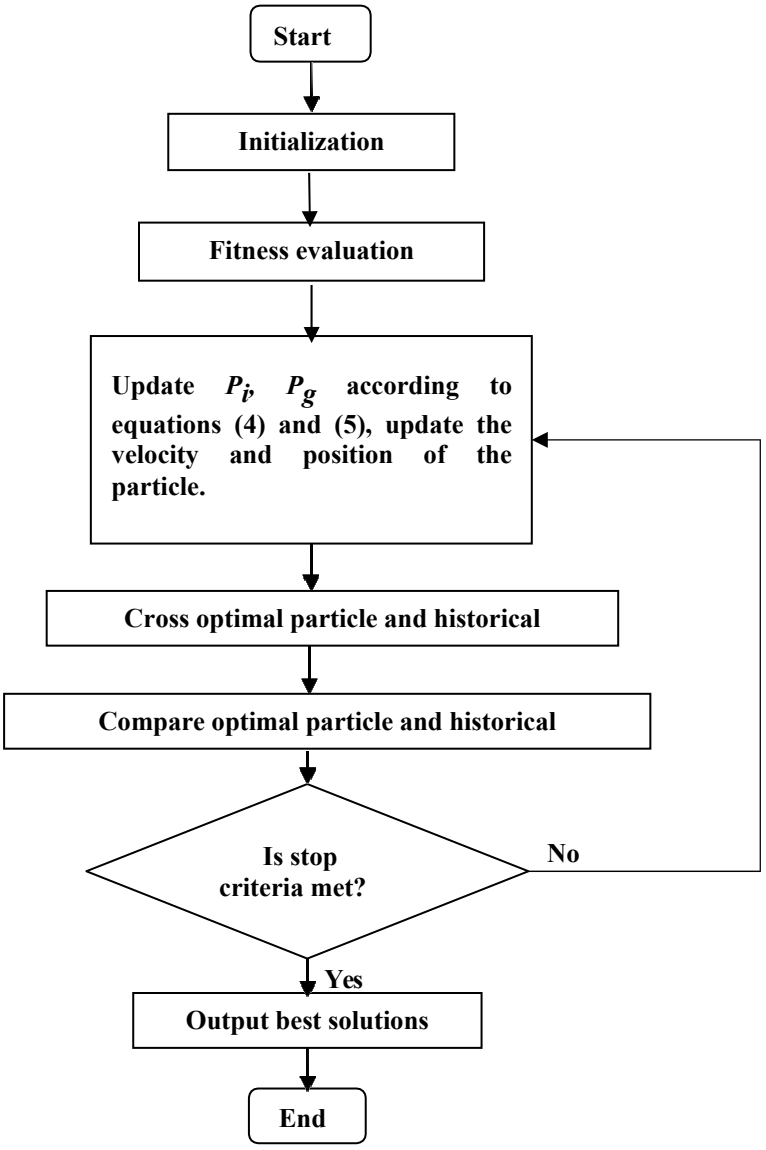

Figure 3. Flowchart of information exchange particle swarm optimization

The basic framework of IEPSO algorithm is shown in figure 3. IEPSO pseudocode are shown in Table 1.

Table 1. IEPSO algorithm pseudocode

IEPSO algorithm

Begin

Step 1:**Initialization**. Input parameters,initialize the population P of NP particle individuals randomly and each particle corresponds to a potential solution to the given problem; set the inertia weight. Initialize velocity V_i and position X_i for particle *i.* Evaluate particle *i* and set pbest*i* = X_i

Step 2: Calculate the value of each particle fitness

Step 3:Enter the main loop

While not stop

for i = 1 to N

Update the velocity and position of particle i

Cauchy variation of particles

The optimal particle and the historical extreme value are crossed to generate a new candidate solution

Evaluate particle i

if fit(X_i) < fit($pbest_i$)

$Pbest_i = X_i$;

if fit(*pbesti*) < fit(*gbest*)

gbest = *pbesti*;

end for end while

Print gbest

End loop;

Post-processing the results and visualizations;

End

IEPSO for structural reliability problems

Three examples to verify the efficiency of the IEPSO algorithm to solve the reliability index.

Example 1

This example considers a cantilever beam with a rectangular cross section and is subjected to a uniformly distributed load, which has been studied by (Gayton et al., 2003) The limit state function is formulated as:

$$G(X) = 18.46154 - 7.476923 \times 10^{10} \frac{X_1}{X_2} \tag{7}$$

where X_1 and X_2 are two independent normal random variables defined as (see Table 2).

Table 2. Distribution of two independent variables

Variables	Mean	Standard deviation	COV (%)
$X1$	0.001	0.0002	20.0
$X2$	250	37.5	15.0

The results obtained by IEPSO compared with CQ2RS and RYFES/COMREL (Kim and Na, 1997) are shown in the Table 3.

Table 3. Structural reliability calculation result

Method	Design point X	β	Pf
CQ2RS	X=(0.0011,165.88)	2.318	0.010
RYFES/	X=(0.0011,165.43)	2.331	0.0098
COMREL IEPSO	X=(0.0012,166.06)	2.345	0.0095

Example 2

The limit state function of this example is as follows (Hohenbichler and Rackwitz, 1982-1983).

$$G(X_1, X_2) = e^{(0.4(X_1+2)} - e^{(0.3X_2+5.0)} - 200 \tag{8}$$

where $X1$ and $X2$ are two independent standard normal random variables. The results obtained by IEPSO compared with Kim & Na and MC (Hohenbichler and Rackwitz, 1982-1983) are shown in the Table 4.

Table 4. Structural reliability calculation result

Method	Design point X	β	Pf
Kim and Na	Not available	2.668	0.00382
MC	Not available	2.685	0.00363
IEPSO	X=(-2.57,0.86)	2.721	0.00335

Example 3

In actual engineering, depending on the structure and nature of the fault, the fault mechanism can be considered as a parallel or series system. Therefore, the limit state function may also be a system of equations. Systems that are composed of components connected in series (series systems) are such that the failure of any one or more of these components constitutes the failure of the system. Such systems, therefore, have no redundancy and are also known as "weakest link" systems. In other words, the reliability or safety of the system requires that none of the components fail (Borri and Speranzini, 1997).

In this paper, two sets of limit state functions are considered, which are serial systems. These functions are highly nonlinear systems with multiple points of failure.

For all these limit state functions (Grooteman, 2008; Au and Beck, 1999), the variables follow the standard normal distribution.

The serial systems are:

$$\begin{cases} G_1(X) = 2 - X_2 + \exp(-0.1X_1^2) + (0.2X_1)^4 \\ G_2(X) = 4.5 - X_1X_2 \\ G_{s1}(X) = \min(G_1, G_2) \end{cases} \tag{9}$$

$$\begin{cases} G_1(X) = 0.1(X_1 - X_2)^2 - ((X_1 + X_2)/\sqrt{2}) + 3 \\ G_2(X) = 0.1(X_1 - X_2)^2 + ((X_1 + X_2)/\sqrt{2}) + 3 \\ G_3(X) = X_1 - X_2 + 3.5\sqrt{2} \\ G_4(X) = -X_1 + X_2 + 3.5\sqrt{2} \\ G_{s2}(X) = \min(G_1, G_2, G_3, G_4) \end{cases} \tag{10}$$

The structural reliability indicators gs1 and gs2 finally obtained by using the IEPSO algorithm are 3.00.

Conclusion

This paper proposes IEPSO, which is used to balance the exploration and exploitation of PSO. The particle swarm is artificially divided into large particle swarm and small particle swarm. The

large particle is mainly responsible for exploration. Its effect is the same as PSO particle, which retains the original strong exploration ability of PSO. Small particle is mainly exploited in the better areas where large particle has been explored, looking for better solutions and making up for the shortage of PSO exploitation. At the same time, the best large particle and historical extremum are crossed to produce a better solution and speed up convergence. The proposed algorithm, combine with FORM method, is used to the analysis of structural reliability. Results show it is successful to use the IEPSO to determine the reliability index and the failure point, then comparison with the response surface method and Monte Carlo simulation is quasi-accurate. In addition to the good quality of the IEPSO results, this method is easy to implement because it is a zero-order method, which means no need to calculate the derivative. Since the solution reliability index has constraints, the limit state function is combined with the penalty equation to construct the objective function, which improves the efficiency and reliability of the algorithm to converge on the reliability index.

References

Ashgar B. Nonlinear constrained optimization using penalty function. In: *Mathematica developer Conference proceedings*, (1999).

Au, S. & Beck, J. L. A new adaptive importance sampling scheme for reliability calculations. *Structural Safety*, 21, 135-158, (1999).

Borri, A. & Speranzini, E. Structural reliability analysis using a standard deterministic finite element code.

Structural Safety, 19, 361-382, (1997).

Fiacco AV, McCormick GP. Non linear programming: sequential unconstrained minimization techniques. New York: Wiley (1968).

Gayton, N., Bourinet, J. & Lemaire, M. CQ2RS: a new statistical approach to the response surface method for reliability analysis. *Structural Safety*, 25, 99-121, (2003).

Grooteman, F. Adaptive radial-based importance sampling method for structural reliability. *Structural Safety*, 30, 533-542, (2008).

Hohenbichler.M and R. Rackwitz. First-order concepts in system reliability, *Struct. Safety*, 1(3): 177-188, (1982-1983).

Kennedy J, Eberhart R. Particle swarm optimization，*Proceedings of ICNN'95-international conference on neural networks.* IEEE, 4: 1942-1948, (1995).

Kim S-H, Na S-W. Response surface method using vector projected sampling point. *Struct Safety*; 19(1): 3–19, (1997).

Liu Y, Qin Z, Shi Z, et al. Center particle swarm optimization. *Neurocomputing*, 70(4-6): 672-679, (2007).

ROSENBLATT,M .Remarks on a multivariate transformation. *The annals of mathematical statistics*, 470- 472. (1952).

Wang H, Li H, Liu Y, et al. Opposition-based particle swarm algorithm with Cauchy mutation. *congress on evolutionary computation*. IEEE: 4750-4756, (2007).

Y.G. Zhao and T. Ono, A general procedure for first/second-order reliability method (FORM/SORM), *Struct. Saf.*,21(2), 95-112 (1999).

International Symposium on Emerging Developments and Innovative Applications of Reliability Engineering and Risk Managements (EDIARR2022),30 October-3 November2022, Taipei
Chen, S. S. &Ang, Alfredo. H-S. (Editors)

ENERGY METHOD OF CONFINED CONCRETE IN AXIALLY COMPRESSED CIRCULAR CONCRETE-FILLED STEEL TUBE COLUMNS

Di Yang[1], Yan-Gang Zhao[1]

[1] *Faculty of Architecture and Building Engineering, Kanagawa University, Yokohama, Japan*

E-mail: yangdi202170197@gmail.com

E-mail: zhao@kanagawa-u.ac.jp

Abstract: Compressive capacity of concrete-filled steel tube (CFT) columns is an important concern in structure design and many studies in this field have focused on understanding the confinement mechanism of the steel tube to the concrete. In this paper, the interaction mechanism between the concrete and steel tube of CFT columns is investigated for the first time from an energy transfer point of view, since the process of restraining from the steel tube due to the expansion of the concrete is essentially a work process of concrete driven by energy. For this object, the energy method is proposed as an investigation approach of the interaction mechanism between the components of CFT columns. Two indices, namely the concrete domination index and concrete comprehensive contribution index, are proposed to characterize the energy method and evaluate the effect of the energy method on the compressive capacity of CFT columns.

***Keywords*:** Energy method, Concrete-filled steel tube, Concrete domination index, Concrete comprehensive contribution index, Interaction mechanism

Introduction

Concrete-filled steel tube (CFT) columns have been widely used in civil engineering, such as in high-rise buildings, factories, and subway projects[1, 2]. The CFT columns take full advantage of the tensile properties of the external steel tube and the compressive properties of the infill concrete. Compared with the reinforced concrete columns, the external steel tube not only bears the vertical load but also provides confinement to the concrete. The interaction between the concrete and steel tube enables CFT columns to exhibit excellent properties of high strength, good ductility, lightweight, and so on[3-5]。

The compressive capacity and load-deformation curves of CFT columns have always been an important concern in practical engineering and structural design. Researches[6-12] on this field have been conducted over the last several decades. It is well know that the transmission and transformation of energy are the fundamental reasons for the deformation and failure of materials[13, 15]. The process of restraining from the steel tube due to the expansion of the concrete is essentially a process of energy transfer. Therefore, the energy method based on thermodynamic theory is an effective way to reveal the strength increase phenomenon of CFT columns. In this paper, the interaction mechanism between the components of CFT columns is investigated for the first time from an energy transfer point of view.

Determination of energy method

In order to explain the interaction mechanism between the concrete and steel tube of CFT columns from an energy transfer point of view, it is necessary to investigate the energy absorption relationship between the concrete and steel tube, and the ratio of the two is used to express this

relationship. The relationship between the energy absorption ratio of the concrete column to steel tube and the normalized compressive stress of the concrete with respect to the unconfined concrete strength is defined as the energy method. The determination of the energy method from the test results is described below.

The lateral stress of the concrete can be calculated based on the force equilibrium condition of the column section:

$$\sigma_r = \frac{2t}{D-2t}\sigma_\theta \tag{1}$$

Where D is the diameter of the column; t is the thickness of the steel tube; σ_r and σ_θ are the lateral stress of the concrete and vertical stress of the steel tube, respectively.

The compressive stress of the concrete can be calculated as below.

$$f_{cz} = \frac{N-\sigma_z A_s}{A_c} \tag{2}$$

where f_{cz} is the compressive stress of the concrete; N is the axial load of the column obtained from the testing machine; A_s and A_c are the section areas of the steel tube and the concrete, respectively; σ_z is the axial stress of the steel tube. The determinations of the axial and vertical stresses of the steel tube are summarized below.

The von Mises stress σ_e is utilized to describe the steel tube's stress state:

$$\sigma_e = \sqrt{\sigma_z^2 - \sigma_z\sigma_\theta + \sigma_\theta^2} \tag{3}$$

where σ_z and σ_θ signify the axial and lateral stress of the steel tube, respectively.

During the elastomeric phase , the stress of the steel tube is evaluated by the generalized Hooke law:

$$\begin{Bmatrix} d\sigma_z \\ d\sigma_\theta \end{Bmatrix} = \frac{E_s}{1-\upsilon^2}\begin{bmatrix} 1 & \upsilon \\ \upsilon & 1 \end{bmatrix}\begin{Bmatrix} d\varepsilon_z \\ d\varepsilon_\theta \end{Bmatrix} \tag{4}$$

Where $d\varepsilon_z$ and $d\varepsilon_\theta$ signify the incremental axial strain and rim strain, respectively; υ is the Poisson ratio and E_s is the tangent modulus[20].

During the plastic phase, the stress of the steel tube is evaluated by the Prandtl-Reuss flow criterion:

$$\begin{Bmatrix} d\sigma_z \\ d\sigma_\theta \end{Bmatrix} = \frac{E_s}{1-\upsilon^2}\begin{bmatrix} 1 & \upsilon \\ \upsilon & 1 \end{bmatrix}\begin{Bmatrix} d\varepsilon_z \\ d\varepsilon_\theta \end{Bmatrix} - \frac{Ed\gamma}{3(1-\upsilon^2)}\begin{bmatrix} 2-\upsilon & 2\upsilon-1 \\ 2\upsilon-1 & 2-\upsilon \end{bmatrix}\begin{Bmatrix} \sigma_z \\ \sigma_\theta \end{Bmatrix} \tag{5}$$

The scalar $d\gamma$ is given by:

$$d\gamma = \frac{9G(s_z de_z + s_r de_r + s_\theta de_\theta)}{2\sigma_e^2 (H + 3G)} \tag{6}$$

$$G = \frac{E}{2(1+\upsilon)} \tag{7}$$

where e_i and s_i signify the deviatoric strain and stress, respectively; H signifies the gradient of the equivalent stress-equivalent plastic strain curve, which is regarded as the gradient of the plastic stress-strain curve of the steel from tensile testing; G and E signify the shear modulus and the elastic modulus of steel, respectively.

Based on the recorded axial and vertical strain at each loading step, the axial and vertical stress may be computed using Eqs. (3)-(7). The lateral stress and the compressive stress of the concrete might be calculated by replacing Eq. (1) and (2) with the axial stress and vertical stress of the steel tube at each loading step. The energy absorbed by a steel tube and concrete respectively at each loading step can be obtained based on thermodynamic theory.

$$Q_c = A_c H U_c = A_c H \left(\int_0^{\varepsilon_c} f_c d\varepsilon_c + 2 \int_0^{\varepsilon_r} \sigma_r d\varepsilon_c \right) \tag{8}$$

$$Q_s = A_s H U_s = A_s H \left(\int_0^{\varepsilon_z} \sigma_z d\varepsilon_z + \int_0^{\varepsilon_\theta} \sigma_\theta d\varepsilon_\theta \right) \tag{9}$$

where Q_c and Q_s signify energy absorbed by the concrete column and steel tube at each loading step, respectively; A_s and A_c signify the sectional area of the concrete specimen and steel tube, respectively; H signifies the height of the concrete specimen; U_c and U_s signify the energy density of the concrete column and steel tube, respectively; f_c signifies the stress of concrete; ε_c and ε_r signify the vertical strain and radial strain of concrete, respectively.

The compressive stress at each loading step was normalized with the unconfined concrete strength. The energy method was then expressed as a relationship between the energy absorption ratio of the concrete column to steel tube and the normalized compressive stress of the concrete with respect to the unconfined concrete strength.

Investigation of energy method and energy method effect

Analysis of the interaction mechanism between concrete and steel tube

One typical energy method of confined concretes in the whole-section-loaded CFT columns is shown in Fig. 1. The energy method can be divided into four stages to analyze the energy variation of the CFT column during the loading process.

In the OA stage, under the whole-section-loaded condition, the steel tube and the core-concrete are jointly subjected to external loads during the initial phase. The distribution of steel tubes and core concrete under external loads was determined by the specimen conditions, such as the flatness of the specimen ends or the bonding of the concrete to the steel tubes. This causes the OA phase energy method to exhibit large fluctuations. When the compressive stress exceeds point A, the

energy method scarcely increases and then decreases. This shows that the concrete and the steel tube are no longer in the same state of stress as at the initial stage of loading, and interaction between the concrete and the steel tube begins to occur. In this stage, microcracks develop rapidly in the concrete, and the lateral expansion of the concrete becomes larger than that of the steel tube, causing the lateral stress to develop smoothly.

A sharp decrease in the energy ratio at point B (about $0.75f_c$) indicates that a large amount of external energy is absorbed by the steel tube through direct or indirect transfer, which is macroscopically manifested by the lateral expansion of the concrete and the steel tube entering the yielding phase. During this stage, the compressive stress nearly gains no increase.
At the BC stage, the energy ratio curve starts to raise gradually and this means the energy absorbed by the steel tube starts to decline compared to the energy absorbed by the concrete. This is due to the vertical and vertical stresses in the steel tube grow less in the yielding stage, while the compressive strength of concrete increases further due to external constraints, and This results in an upward tendency of the energy ratio curve. The steel tube enters the strengthening stage at point C.

After that, the energy ratio picks up slightly until reaching the ultimate state at point D. The core-concrete dissipates some of the energy due to plastic deformation, and less energy is transferred to the steel tube through lateral expansion.

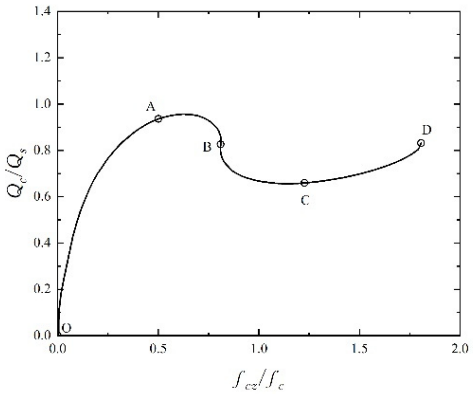

Figure 1. Typic energy method of confined concrete in a whole-section-loaded CFT column

Evaluation tools of the energy method

Two evaluation indexes are defined in this section to characterize the energy method of confined concrete in a certain condition. To express the changing relationship of the energy ratio during the whole loading process, a concrete dominate index, is defined by eliminating the influence of different compressive strengths as:

$$K = \frac{\int_0^{f_{cz}} Q_c df_c}{\int_0^{f_{cz}} Q_s df_c} \tag{10}$$

To reflect the contribution of concrete to the load bearing capacity provided in a CFT column, a concrete comprehensive contribution index, is defined as,

$$\Omega = \frac{\int_0^{f_{cc}} Q_c df_c}{\int_0^{f_{cc}} Q_s df + \int_0^{f_{cc}} Q_c df_c} \tag{11}$$

Obviously, the concrete dominate index K is related to the concrete comprehensive contribution index Ω as in Eqs. (12). From the definition, it can be seen that the larger the value of Ω, the concrete plays more important role in providing load bearing capacity. In addition, considering the limiting case, when Ω equals 0, it represents hollow steel tube, and when Ω equals 1, it represents unconfined concrete.

$$\Omega = \frac{K}{K+1} \tag{12}$$

In Eq. (10), a higher value of K denotes the concrete absorbs more energy and compressive stress in the energy method plays a more dominant role in the confined concrete.

Effect factors on energy method

The effect factors affecting the energy method obtained through experimental tests are strength ratio f_c/f_y and the D/t ratio. The specific effect relationships are shown in Figure 2 and 3,respectively.

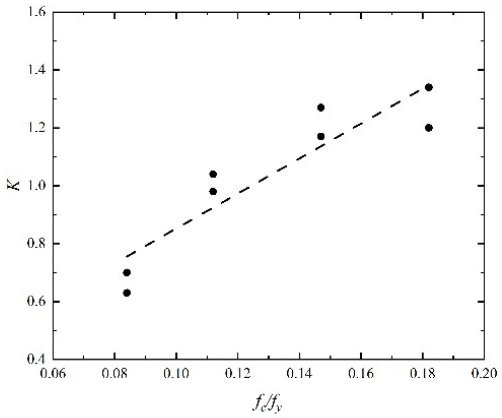

Figure 2. Relation between concrete dominate index K and f_c/f_y ratio

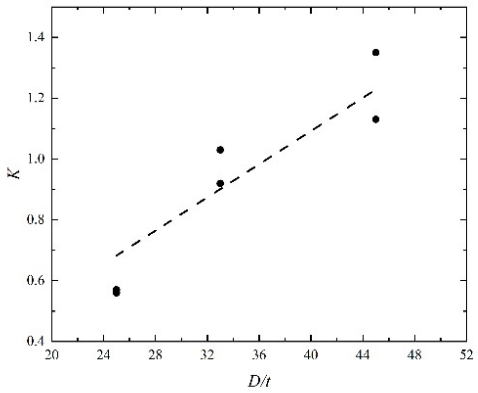

Figure 3. Relation between concrete dominate index K and D/t ratio

Based on the investigation before, it is known that the energy method is influenced by column parameters, which suggests the concrete dominate index K could be determined by these parameters. A confinement coefficient η including all the parameters is defined as:

$$\eta = \frac{D-2t}{2t}\frac{f_c}{f_y} \tag{13}$$

The relationship between the concrete dominate index and the confinement coefficient is given in Fig. 4. It seems that the concrete dominate index increases linearly with the confinement coefficient. Therefore, a simple model for the concrete dominate index is proposed as:

$$K = 0.55\eta \tag{14}$$

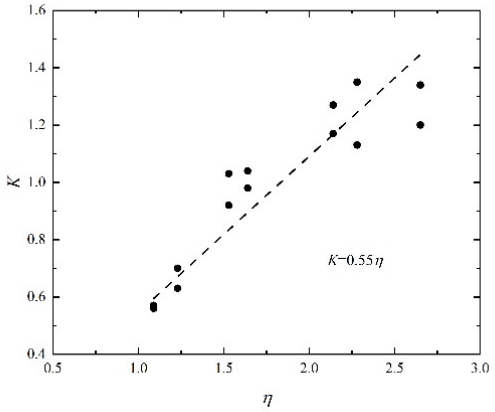

Figure 4. Relation between concrete dominate index K and η

The energy ratio represents the relative relationship between the energy absorbed by the concrete and the steel tube, while the concrete dominate index *K* expresses the certainty of this relationship for a given structural composition. From the initial energy accumulation to the energy release, there was inevitably an absorption energy maximum in the whole loading process, which means the energy accumulated at a peak point which was named the energy storage limit. The relationship between the energy storage limit and the concrete dominate index *K* for concrete and steel tubes under the peak stress state still needs further study.

Conclusion

Based on the experimental tests, the energy method, and the interaction mechanism between the concrete and steel tube of the whole-section-loaded CFT columns were studied in this paper. The energy method based on thermodynamic theory is an effective way to reveal the strength increase phenomenon of CFT columns. The energy method was proposed by calculating the energy absorbed by the concrete column and the steel tube to analyze the interaction mechanism between the concrete and steel tube of CFT columns. Energy method of confined concrete in a CFT column is affected by the parameters of the column, namely steel strength f_s, unconfined concrete strength f_c and D/t ratio. Energy methods under different test conditions are indicated by the concrete dominate index. The results show that the concrete dominate index increases with the strength ratio f_c/f_y and the D/t ratio, which may suggest that the concrete plays a more dominant role in the energy method with a higher strength ratio f_c/f_y and a bigger D/t ratio.

References

Siqi Lin, Yan-Gang Zhao,Liusheng He. Stress methods of confined concrete in axially loaded circular concrete-filled steel tube stub columns, Engineering Structures 2018; 173: 1019-1028.

J. C. Ho, J. Y. Lam,A. K. Kwan. Effectiveness of adding confinement for ductility improvement of high-strength concrete columns, ENGINEERING STRUCTURES 2010;

Shosuke Morino,Jun Kawaguchi. Research on and Construction of the Concrete-filled Steel Tube Column System in Japan, International Journal of STEEL STRUCTURES 2005; 5: 277-298.

B. Uy. Strength of short concrete filled high strength steel box columns, Journal of Constructional Steel Research 2001; 57: 113-134.

M. C. Sundarraja,G. G. Prabhu. Experimental investigation on strengthening of CFST columns using CFRP composites, International Journal of Earth Sciences and Engineering 2013; 6: 15-20.

L. Han,S. Zhong. Study on the Working Mechanism and Behavior of Concrete Filled Steel Tubular(CFST) Members Subjected to Compression, Bending and Torsion, JOURNAL OF BUILDING STRUCTURES 1995; 16:

Schneider,P. Stephen. Axially Loaded Concrete-Filled Steel Tubes, Journal of Structural Engineering 1999; 124: 1125-1138.

J. Xiao,C. Zhang. Seismic behavior of RC columns with circular, square and diamond sections, Construction & Building Materials 2008; 22: 801-810.

Takamasa Yamamoto, Jun Kawaguchi,Shosuke Morino. Experimental Study of Scale Effects on the Compressive Behavior of Short Concrete-Filled Steel Tube Columns, ASCE 2002;

Chee-Loong Chin, Chau-Khun Ma, Abdullah Zawawi Awang, Jia-Yang Tan, Chin-Boon Ong,Wahid Omar. Confining stress method dependent stress-strain model for pre-tensioned steel-confined concrete, Engineering Structures 2019; 201:

Hai-bei Xiong, Ben-ben Li,Jia-fei Jiang. Load method dependence of strain and stress for confined concrete, Magazine of Concrete Research 2016; 68: 604-618.

Xiaoyong Zhang, Yu Chen, Xiaosheng Shen,Yao Zhu. Behavior of Circular CFST Columns Subjected to Different Lateral Impact Energy, Applied Sciences 2019; 9:

Liangliang Zhang, Hua Cheng, Xiaojian Wang, Jimin Liu,Longhui Guo. Statistical Damage Constitutive Model for High-Strength Concrete Based on Dissipation Energy Density, Crystals 2021; 11:

T. Nishiyama, Y. Chen, H. Kusuda, T. Ito, K. Kaneko, H. Kita,T. Sato. The examination of fracturing process subjected to triaxial compression test in Inada granite, 2002;

M. J. Mcsaveney,T. R. Davies. Surface energy is not one of the energy losses in rock comminution, Engineering Geology 2009; 109: 109-113.

International Symposium on Emerging Developments and Innovative Applications of Reliability Engineering and Risk Managements (EDIARR2022),30 October-3 November2022, Taipei
Chen, S. S. &Ang, Alfredo. H-S. (Editors)

RELIABILITY ANALYSIS OF RAIL IRREGULARITY FOR CRTS II SLAB BALLASTLESS TRACK BASED ON SPARSE POLYNOMIAL CHAOS EXPANSION

Teng Lıu[1], Ye-Yao Weng[1], Yan-Gang Zhao[1,2]

[1]*Affiliation (Key Laboratory of Urban Security and Disaster Engineering of Ministry of Education, Beijing University of Technology, Beijing, China)*

E-mail: 1191373506@qq.com

[2]*Affiliation (Department of Architecture, Kanagawa University, Yokohama, Japan)*

Abstract: The state control of rail irregularity is one of the core issues to ensure the safety of high-speed railways. The reliability analysis of rail irregularity has significant engineering practice value for line maintenance and management operations. To assess the reliability of rail irregularity of CRTS II slab ballastless track under the uncertainty of wheel loads, temperature loads and material parameters, a reliability analysis method based on sparse polynomial chaos expansion (SPCE) has been used. According to the actual working conditions, wheel loads, temperature loads, and several material parameters are treated as input random variables of the ballastless track structure. The initial experimental design points are generated by the cubature collocation, and the responses of the rail irregularity are obtained by finite element analysis. Then, a SPCE model is constructed by identifying the effect of each polynomial term in the target variance, thereby predicting the response of the rail irregularity. Finally, the SPCE model is combined with Monte Carlo simulation to estimate the reliability of rail irregularity under different working conditions. The results show that: when considering the interaction of wheel loads and temperature loads, the reliability of rail irregularity under negative temperature gradient is higher than that under positive temperature gradient. The reliability index of rail irregularity decreases with increasing values of positive or negative temperature gradients, while the reliability index decreases with increasing coefficient of variation of positive or negative temperature gradients.

***Keywords*:** rail irregularity, ballastless track, sparse polynomial chaos expansion, reliability, Monte Carlo method

Introduction

Rail irregularity is an important control index of ballastless track structure of high-speed railways [a]. Its state is directly related to the service performance of the track structure, which has a direct impact on the safety and comfort of train operation. The railway administration achieves effective management of rail irregularity by controlling the geometric displacement amplitude and the rail irregularity spectrum. In recent years, with the increase in the service time and running speed of trains, higher requirements have been put forward for track smoothness and reliability.

Reliability indices have been useful for evaluating structural reliability [b]. However, in structural reliability analysis, the limit state function that measures the performance of the track structure is often implicit and requires the invocation of time-consuming finite element analysis. The computational time consumed by invoking finite element analysis accounts for the main computational cost of reliability analysis, and its high computational cost even makes reliability analysis impossible. At present, the surrogate model is one of the effective methods to solve the above problems [c-e]. It only uses a small amount of structural response analysis to construct the

mapping relationship between input and output random variables. The model replaces the original limit state function to predict the structural response. Response surface method has been used to analyze the influence of rail irregularity on traffic safety and reliability [f]. However, on the one hand, the number of design points in response surface method increases sharply with the increase of the dimension of the input random vector. On the other hand, response surface method cannot consider the common action and higher-order influence of input random variables.

For reliability analysis of rail irregularity, the uncertainty factors causing rail irregularity are complex and diverse. Among them, the wheel loads and temperature loads are the main factors. Based on this, the purpose of this study was to analyze the reliability of CRTS Ⅱ slab ballastless track structure irregularity reliability under the consideration of random factors such as wheel loads, temperature loads and structural material parameters. In this paper, the finite element model of slab ballastless track structure was established to realize the effective simulation of rail irregularity. The sparse polynomial chaos expansion method was used to construct the explicit limit state function of rail irregularity. Finally, the reliability evaluation of CRTS Ⅱ slab ballastless rail irregularity was realized by Monte Carlo simulation.

Method and anslysis

Finite element model

The analysis model of CRTS Ⅱ slab ballastless track on subgrade was established by using finite element software ANSYS. In order to eliminate the influence caused by boundary effect, three slab ballastless track elements were connected.The rail was simulated by BEAM188; The fastener and the subgrade were regarded as springs, which were simulated by COMBIN14. The track slab, cement asphalt (CA) mortar and foundation plate were simulated by SOLID65. The reinforcement was simulated by LINK180. The rail is CHN60, its elastic modulus is 2.1×10^5 MPa, Poisson's ratio is 0.3. The fastener is WJ-8 with a spacing of 0.65 m; The length of the track slab is 6.45 m, the width is 2.55 m, the thickness is 0.2 m. It is made of C55 concrete and Poisson's ratio is 0.2; The length and width of CA mortar are the same as the track slab, the thickness is 0.03m, the elastic modulus is 10000MPa, Poisson's ratio is 0.34. The length of the foundation plate is 6.61 m, the upper and lower widths are 2.95m and 3.25 m, respectively, and the thickness is 0.3 m. It is made of C30 concrete and Poisson's ratio is 0.2. The foundation coefficient is 75 MPa/m.

Construct sparse polynomial chaos expansion model of CRTS II slab ballastless rail irregularity

Train wheel loads, temperature gradient, axial temperature, track slab elastic modulus, foundation plate elastic modulus, fastener stiffness as basic random variables. According to the cubature collocation, 57 cubature points can be generated [g]. The cubature point distributions in the ξ_1–ξ_2, ξ_3–ξ_4 and ξ_5–ξ_6 planes are shown in Fig.1.

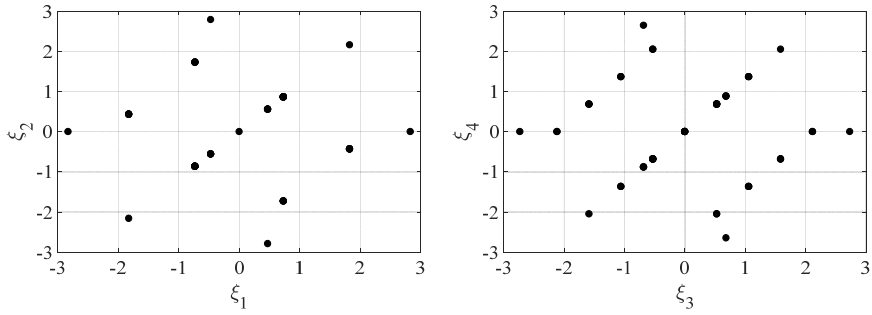

(a)ξ_1–ξ_2 plane (b)ξ_3–ξ_4 plane

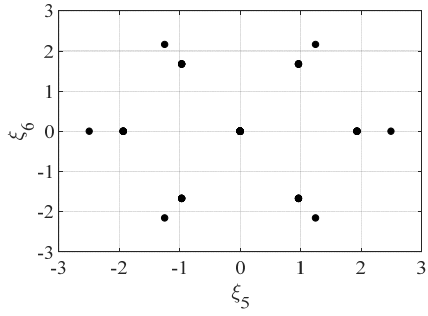

(c)ξ_5–ξ_6 plane

Fig 1. Distribution of cubature points

And then,cubature points in ξ space are transformed with equal probability to obtain the experimental design points in the original space, which are used as the input parameters of the finite element model. The displacement response samples of 57 rails under positive and negative temperature gradients can be obtained by finite element analysis.

The threshold of rail irregularity index is set as 1.25 mm, and the order of polynomial chaos expansion is 4. The SPCE model is obtained by eliminating the polynomial basis functions that contribute less to the model and retaining the polynomial basis functions that contribute more to the model [h]. The undetermined coefficients can be obtained by least square regression at the design points. Finally, the constructed SPCE model will replace the original time-consuming limit state function for structural reliability analysis.

Reliability analysis of sparse polynomial chaos expansion model

Monte Carlo simulation method is used to estimate the failure probability and standard deviation of SPCE model. The influence of positive temperature gradient, negative temperature gradient and their variation of coefficient on the reliability index were studied. The mean positive temperature gradients are 40 ℃/m, 50 ℃/m, 60 ℃/m, 70 ℃/m, 80 ℃/m, and the mean negative positive temperature gradients are -10 ℃/m, -15 ℃/m, -20 ℃/m, -25 ℃/m, -30 ℃/m. The changes of reliability index with mean values of positive and negative temperature gradients are shown in Fig.2 and 3, respectively.

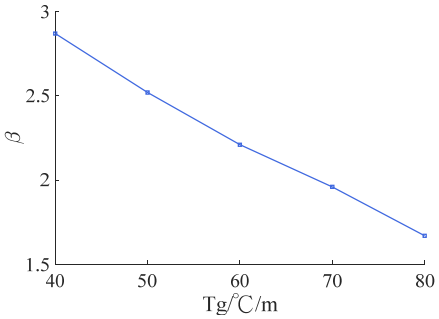

Fig 2. Relationship between the mean value of positive temperature gradient and reliability index

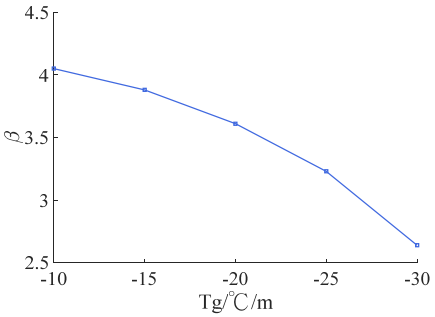

Fig 3. Relationship between the mean value of negative temperature gradient and reliability index

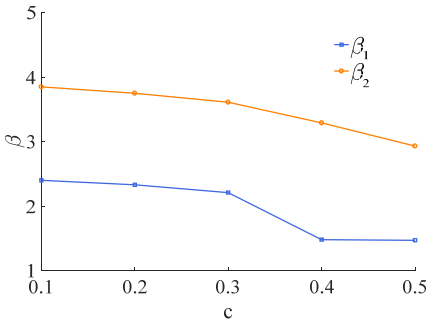

Fig 4. Relationship between the coefficient of variation of temperature gradient and reliability indices

The influence of the coefficient of variation of the temperature gradient on the rail irregularity reliability index was investigated when the mean positive temperature gradient was 60 ℃/m and the mean negative temperature gradient is -20 ℃/m. Their coefficients of variation were 0.1, 0.2, 0.3, 0.4 and 0.5, respectively. The change of reliability index β_1 under positive temperature gradient and β_2 under negative temperature gradient with coefficient of variation is shown in Fig.4.

Conclusion

(1) Based on the principle of sparse polynomial chaos expansion, an explicit surrogate model of the limit state function of CRTS II slab ballastless track rail irregularity under the action of random factors such as wheel loads, temperature gradient and material parameters is constructed, and the efficient and accurate evaluation of rail irregularity reliability is realized by combining Monte Carlo simulation.

(2) When the mean value of the positive temperature gradient is 60 ℃/m, the rail irregularity reliability index is 2.21; When the mean value of the negative temperature gradient is -20 ℃/m, the rail irregularity reliability index is 3.61. The reliability of rail irregularity is relatively low under positive temperature gradient.

(3) With the increase of the mean values of positive and negative temperature gradients, the reliability indices of rail irregularity gradually decrease. When the mean positive temperature gradient increases from 40 ℃/m to 80 ℃/m, the reliability index decreases from 2.87 to 1.67. When the mean negative temperature gradient decreases from -10 ℃/m to -30 ℃/m, the reliability index decreases from 4.05 to 2.64. In addition, the reliability index gradually decreases with the increase of the coefficient of variation of the positive and negative temperature gradients.

References

M.H. Harun, W.M. Zailimi, Hishamuddin Jamaluddin, et al, "Dynamic response of commuter rail vehicle under lateral track irregularity" *Applied Mechanics & Materials*, no.548-549 (April 2014): 948–952.

Yan-Gang Zhao, Alfredo H-S Ang, "System Reliability Assessment by Method of Moments" *Journal of Structural Engineering*, no.10 (October 2003):1341–1349.

Y. Zheng, P.K. Das, "Improved response surface method and its application to stiffened plate reliability analysis", *Engineering Structures*, no.5 (May 2000):544–551.

Irfan Kaymaz, "Application of Kriging method to structural reliability problems", *Structural Safety*, no.2 (April 2005):133–151.

Dongbin Xiu, George Em Karniadakis, "Modeling uncertainty in flow simulations via generalized polynomial chaos", *Journal of computational physics*, no.1 (May 2003):137–167.

Z.W. Li, X.Y. Lei, L. Gao, "Reliability analysis of import of ballastless track irregularity on train operation safety", *Journal of the China Railway*, no.10 (2020):101–105.

I.P.Mysovskikh, "The approximation of multiple integrals by using interpolatory cubature formulae", *Quant Approx*, (1980):217–243.

Jun Xu, Fan Kong, "A cubature collocation based sparse polynomial chaos expansion for efficient structural reliability analysis", *Structural Safety*, (September 2018):24–31.

International Symposium on Emerging Developments and Innovative Applications of Reliability Engineering and Risk Managements (EDIARR2022),30 October-3 November2022, Taipei
Chen, S. S. &Ang, Alfredo. H-S. (Editors)

CASE STUDY RESEARCH: AN EFFICIENT PGA EVALUTION METHOD OF PROBABILISITIC PREDICTION OF GROUND MOTION USING FOURIER AMPLITUDE SPECTRA

Rui Zhang[1], Haizhong Zhang[2,a], Yan-Gang Zhao[1,2],

[1] *Key Laboratory of Urban Security and Disaster Engineering of Ministry of Education, Beijing University of Technology, Beijing 100124, China*

[1]*zhangrui-zr@qq.com*

[2] *Department of Architecture, Kanagawa University, 3-27-1 Rokkakubashi, Kanagawa-ku, Yokohama 211-8686, Japan*

[a]*zhang@kanagawa-u.ac.jp*

Abstract: In recent years, probabilistic prediction of ground motion using Fourier amplitude spectra (FAS) has gained much attention benefit that FAS is consistent with linear system theory. Typically, the probabilistic prediction of ground motion using FAS is calculated by Monte Carlo simulation (MCS). However, the computational cost of MCS is too high. This study aims to propose an efficient evaluation method of probabilistic prediction of ground motion from FAS. For this purpose, the random vibration theory is adopted to evaluate the ground motion intensity such as peak ground acceleration (PGA) from FAS. Then a probabilistic analysis method, namely the moment method, is introduced to improve computational efficiency. In this study, the first three moments of PGA are used to obtain its probability distribution, and furthermore obtain its exceedance probability. The first three moments of PGA are obtained by a point-estimation method based on dimension-reduction integration, and then, the exceedance probability of PGA can be obtained simply and accurately. Numerical studies show that the efficiency of the proposed method was well above that of MCS without loss of accuracy.

Keyword: Probabilistic Prediction; Peak Ground Acceleration; Fourier Amplitude Spectrum; Moment Method; Point-estimation; Dimension-reduction integration.

Extended summary

Probabilistic prediction of ground motion was the core of seismic hazard analysis[1] used to determine the seismic effect in seismic design[2-4]. The execution of probabilistic prediction of ground motion usually needs a ground motion prediction equation (GMPE) of ground motion intensity to assess the ground motion at an interesting site, and the most commonly used ground motion intensity measure is peak ground acceleration (PGA)[5]. The general processes of establishing GMPE are as follows, select a mass of earthquake data at first, then select the predictive variables (such as magnitude, source-to-site distance, etc.) and equation form, and finally, perform regression analysis on ground motion intensity[6]. This process is available only for seismically active regions with a mass of earthquake data, such as the Western United States, China Taiwan, and Japan. However, there are many seismically active regions lacking sufficient earthquake data, such as India and Central Europe, so it is difficult to establish a reasonable GMPE using the above process.

To solve this problem, several approaches have been suggested, such as direct “important” and “host-to-target” adjustments of GMPE from data-rich regions [7–11]. However, the scaling of ground motion response from the source to the site is not consistent with the linear system theory, such that the import and adjustment do not purely reflect the differences between the host (data-rich) and target (data-poor) regions [12]. To avoid the above problems, recently, a PSHA method based on Fourier amplitude spectra (FAS) model was proposed by Zhao et al.. Since FAS conforms to linear system theory and the determination of the FAS model does not need too many ground motion records, the method should be convenient for PSHA for regions lacking strong ground-motion records. In that method, a FAS model is used to express the seismic transmission process from source to site, and PGA is obtained from FAS using random vibration theory. In addition, the exceedance probability of PGA is calculated by Monte Carlo simulation (MCS). However, for this approach, MCS is too time-consuming, especially for small exceedance probability, the computation cost is almost unacceptable.

To improve the computational efficiency, an efficient PGA evaluation method of PSHA from the FAS model is proposed in this study. Firstly, PGA is obtained from FAS based on random vibration theory (RVT). Secondly, a probability analysis method named the "moment method" is introduced to improve computational efficiency. Herein, considering the uncertain seismological parameters, the proposed method uses the point-estimation method based on dimension-reduction integration to obtain the first three moments of PGA [13–15]. Then the probability distribution of PGA is obtained by the first three moments approximately. Finally, the exceedance probability of PGA is obtained, which is the seismic hazard curve.

The technical flow chart of this paper is shown in Figure.1.

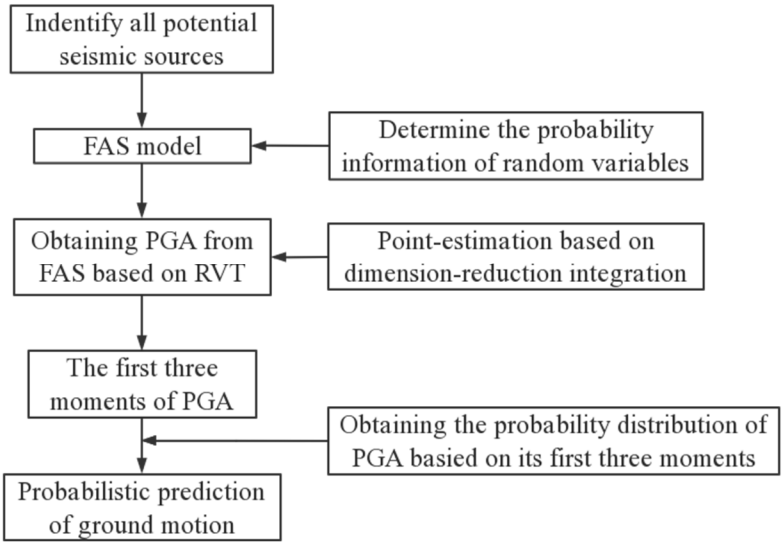

Fig.1 Flow chart of the proposed method

This study presents an efficient evaluation method of probabilistic seismic hazard analysis using Fourier amplitude spectral. Different from Monte Carlo simulation, the moment method is introduced to simply calculate the exceedance probability of peak ground acceleration in the proposed method. Firstly, random vibration theory is used to obtain peak ground acceleration from the Fourier amplitude spectrum. Secondly, the first three moments of peak ground acceleration are obtained using the point-estimate method based on dimension reduction. And then, the exceedance probability of peak ground acceleration can be estimated simply and accurately by using a three-parameter probability distribution, in which the three parameters in the probability distribution are directly defined in terms of their first three moments.

References

C.A. Cornell, Engineering seismic risk analysis, B SEISMOL SOC AM, (1968) 1583-1606.

Seismic Ground Motion Parameters Zonation Map of China, China Standards Publishing House, Beijing, China (in Chinese), 2015.

Eurocode 8: Design of structures for earthquake resistance.

S. Australia, Structural Design Actions, Part 4: Earthquake Actions in Australia(Standards Australia AS 1170.4 – 2007 (R2018)/Amdt 2-2018), Sydney, NSW, 2018.

S.S. Bora, F. Scherbaum, N. Kuehn, P. Stafford, On the Relationship between Fourier and Response Spectra: Implications for the Adjustment of Empirical Ground‐Motion Prediction Equations (GMPEs), B SEISMOL SOC AM, (2016) 1235-1253.

J. Douglas, Ground motion predition equations 1964-2021, 2021.

D.M.B. A, Simulation of Ground Motion Using the Stochastic Method, PURE APPL GEOPHYS, (2003) 635-676.

X. Wang, E.M. Rathje, Influence of Peak Factors on Site Amplification from Random Vibration Theory Based Site‐Response Analysis, B SEISMOL SOC AM, (2016) ssabull;0120150328v1.

E.M. Rathje, M.C. Ozbey, Site-Specific Validation of Random Vibration Theory-Based Seismic Site Response Analysis, Journal of Geotechnical & Geoenvironmental Engineering, 132 (2015) 911-922.

A.R. Kottke, E.M. Rathje, Comparison of Time Series and Random-Vibration Theory Site-Response Methods, B SEISMOL SOC AM, 103 (2013) 2111-2127.

D.E. Cartwright, M.S. Longuet-Higgins, The Statistical Distribution of the Maxima of a Random Function, Proceedings of the Royal Society of London. Series A, Mathematical and Physical Sciences, (1956) 212-232.

S.S. Bora, F. Scherbaum, N. Kuehn, P. Stafford, Fourier spectral- and duration models for the generation of response spectra adjustable to different source-, propagation-, and site conditions, B EARTHQ ENG, (2014) 467-493.

Y. Zhao, T. Ono, H. Idota, A Three-Parameter Distribution Used For Structural Reliability Evaluation, 日本建築学会構造系論文集, (2001).

Y. Zhao, T. Ono, Third-Moment Standardization for Structural Reliability Analysis, J STRUCT ENG, (2000) 724-732.

Y.O.T. Zhao, New point estimates for probability moments, J ENG MECH, (2000) 433-436.

International Symposium on Emerging Developments and Innovative Applications of Reliability Engineering and Risk Managements (EDIARR2022),30 October-3 November2022, Taipei
Chen, S. S. &Ang, Alfredo. H-S. (Editors)

A PRATICAL THREE PARAMETER DISTRIBUTION AND ITS APPLICATION TO ARCHITECTURE SYSTEM

YuTao Lu[1], Yan-Gang Zhao[1]

[1] *Faculty of Architecture and Building Engineering, Kanagawa University, Yokohama, Japan*

E-mail:lyt07015940128@gmail.com

E-mail: zhao@kanagawa-u.ac.jp

Abstract: In practical engineering application, statistical data for most structural parameters are greater than zero, and the existing commonly used distributions to describe the characteristics of the data are two-parameter distributions. However, these two-parameter distributions cannot well reflect the flexibility of the data when the skewness of the data has a greater impact on the data. The three-parameter distribution which is determined by the first three moments of the statistical data can achieve better fitting results than the two-parameter distribution, but the widely used three-parameter distributions based on statistical data do not have a domain of definition greater than 0. Therefore, a three-parameter distribution with a domain restriction greater than zero needs to be proposed. In this study, a three-parameter distribution, which takes into account skewness and starts its point from zero. This distribution uses the relationship between the raw moments and the first three central moments to derive its distribution parameters. It is found that the GLD can approximate many well-known distributions, and can be used to fit actual inspection data collected from practical engineering.Therefore, this three-parameter distribution int in this study has rich flexibility in shape and can be applied to fit the actual distributions accrued in the architecture system.

***Keywords*:** Moments, GLD, Three-parameter distribution, PDF

Introduction

In structure reliability, the material properties, loads, environmental factors and other uncertainties[1], as well as the probability distribution characteristics of these factors, should have a full understanding. For concrete structures, there has seldom been research on the probability distribution characteristics of concrete strength. In past researches, it is generally believed that the concrete strength conforms to the normal distribution. Based on the central extreme value theorem, the concrete strength of the building should approximately obey the normal distribution. However, some studies have pointed out that it is not accurate enough describe the distribution of actual concrete strength data by using the normal distribution.

On the other hand, from the view of mathematical statistics, the range of normal distribution is from negative infinity to positive infinity. But for concrete strength and other statistics in architecture are mostly positive. That is in the physical sense, the normal distribution does not reflect this material characteristic. In addition, as a two-parameter distribution, the normal distribution cannot reflect the skewness of the data since the skewness is very important for the distribution. When fitting the actual data and other aspects, the three-parameter distribution[2-3] is considered to show better results due to the skewness is considered. Therefore, in this paper, the concrete stength data was used as an example and a three-parameter GLD distribution with the domain of definition greater than 0 is discussed. This distribution is determined by the average value, standard deviation and skewness of the actual data. In most cases, it can have the same or better effect as the commonly used two-parameter distribution and three-parameter distribution. The GLD and other three-parameter distributions were used to fit the actual data and compared.

The Existing Three-parameter Distributions

Three Parameter Lognormal Distribution

For a standardized variable

$$Xs = (X - \mu_x) / \sigma_x \tag{1}$$

The random variable X obeys the 3P lognormal distribution which The probability density function (PDF) can be defined as

$$f(x) = \frac{1}{\sqrt{2\pi \ln(A)}\left|\frac{x-\mu_x}{\sigma_x} - u_b\right|} \exp\left\{-\frac{1}{2\ln(A)}[\ln\left|\frac{x-\mu_x}{\sigma_x} - u_b\right| - \ln\frac{|u_b|}{\sqrt{A}}]^2\right\} \tag{2}$$

Where the parameters $A$and u_b are given by Zhao and Ono[4]

$$\mathrm{A} = 1 + \frac{1}{u_b^{\,2}} \tag{3}$$

$$u_b = (a+b)^{\frac{1}{3}} + (a-b)^{\frac{1}{3}} - \frac{1}{\alpha_{3G}} \tag{4}$$

$$a = -\frac{1}{\alpha_{3X}}\left(\frac{1}{\alpha_{3X}^{\,2}} + \frac{1}{2}\right), \quad b = \frac{1}{2\alpha_{3X}^{\,2}}\sqrt{\alpha_{3X}^{\,2} + 4} \tag{5}$$

The random variable x is defined in the following ranges

$$Xs \neq u_b \tag{6}$$

The third central moments are given as

$$E[X] = \mu_X \tag{7}$$

$$E\left[(X - \mu_X)^2\right] = \sigma_X^2 \tag{8}$$

$$E\left[\left(\frac{X - \mu_X}{\sigma_X}\right)^3\right] = -(3 + \frac{1}{u_b^{\,2}})\frac{1}{u_b} \tag{9}$$

Based on Eq.6, when Xs equals ub , the PDF of Lognormal distribution does not apply.

Three Parameter Square Normal Distribution

For a standardized variable

$$Xs = (X - \mu_x) / \sigma_x \tag{10}$$

The random variable X obeys the square normal distribution[5] when Xs can be expressed by

$$Xs = -\lambda + \sqrt{1 - 2\lambda^2}U + \lambda U^2 \tag{11}$$

In which λ is the three parameters of the distribution.

The random variable x is defined in the following ranges

$$-\infty \le Xs \le -\frac{1}{4\lambda} - \frac{1}{2}\lambda \quad \text{for } \lambda > 0 \tag{12}$$

$$-\frac{1}{4\lambda} - \frac{1}{2}\lambda \le Xs \le +\infty \quad \text{for } \lambda < 0 \tag{13}$$

The PDF is defined by Zhao[5]

$$f(x) = \frac{\phi[\frac{1}{2\lambda}\sqrt{1 + 2\lambda^2 + 4\lambda Xs} - \sqrt{1 - 2\lambda^2})]}{\sigma\sqrt{1 + 2\lambda^2 + 4\lambda Xs}} \tag{14}$$

The third central moments are given as

$$E[X] = \mu_X \tag{15}$$

$$E\left[(X - \mu_X)^2\right] = \sigma_X^2 \tag{16}$$

$$E\left[\left(\frac{X - \mu_X}{\sigma_X}\right)^3\right] = 6\lambda - 4\lambda^3 \tag{17}$$

In the case of Square Normal, the pdf depends on the value of λ, and when λ is fixed and exceeds the range of the Eq.12 and Eq.13, the PDF loses its applicability.

The Generalized Lognormal Distributions

3.1 Definition of the Distribution and Moments

Y.M.Low[6] proposed a four-parameter shifted generalized lognormal distribution (SGLD), by the

usual location and scale transformation

$$Y=(X-b)/\theta \tag{18}$$

then X can be represented by the following PDF

$$f(x)=\frac{\alpha}{x-b}\exp(-\frac{1}{r\sigma^r}\left|\frac{(\ln x-b)}{\theta}\right|^r),b<x<\infty \tag{19}$$

The distribution has four parameters: r and σ are for shape, while b and $\theta$are for location and scale. In order to achieve the goal that the boundary starts from zero, let the location parameter b be equal to 0, then a new generalized lognormal distribution[7-8] can be shown as

$$f(x)=\frac{\alpha}{x}\exp(-\frac{1}{r\sigma^r}\left|\frac{\ln x}{\theta}\right|^r),0<x<\infty \tag{20}$$

The raw moments of GLD can be shown as

$$E\left[Y^k\right]=\frac{1}{\Gamma(1/r)}\sum_{n=0}^{\infty}\frac{(k\sigma)^{2n}}{(2n)!}r^{2n/r}\Gamma(\frac{2n+1}{r}) \tag{21}$$

Through the relationship between raw moments and central moments, the first three moments can be easily shown as

$$E\left[X\right]=\theta E\left[Y^1\right] \tag{22}$$

$$E\left[\left(X-\mu_X\right)^2\right]=\theta\sqrt{\left\{E\left[Y^2\right]-E\left[Y^1\right]^2\right\}} \tag{23}$$

$$E\left[\left(\frac{X-\mu_X}{\sigma_X}\right)^3\right]=\frac{E\left[Y^3\right]-3E\left[Y^1\right]E\left[Y^2\right]+2E\left[Y^1\right]^3}{\theta\sqrt{\left\{E\left[Y^2\right]-E\left[Y^1\right]^2\right\}}^3} \tag{24}$$

Comparisons with other Three-Parameter Distributions

Figures (1) ~ (4) describe the 3P-LogNormal distribution, 3P-Square Normal distribution, and the GLD distribution when $\alpha_{3x}=0.4/0.6/0.8/1.0$, respectively.

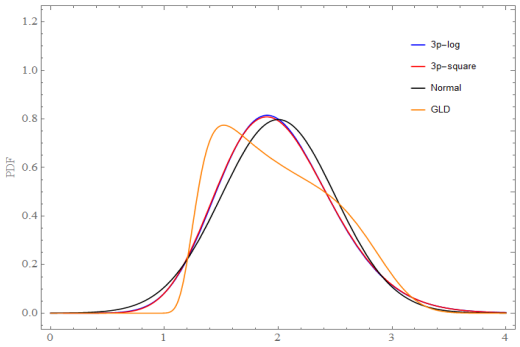

Fig 1. Comparisons of 3P-Distributions (α_{3x}=0.4)

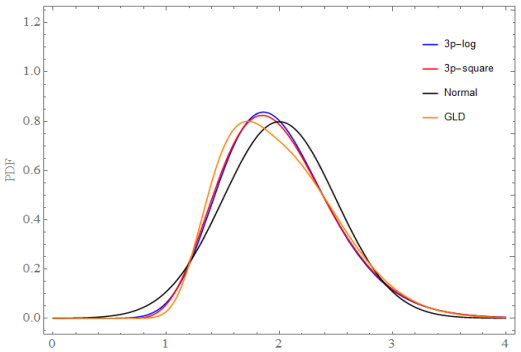

Fig 2. Comparisons of 3P-Distributions(α_{3x}=0.6)

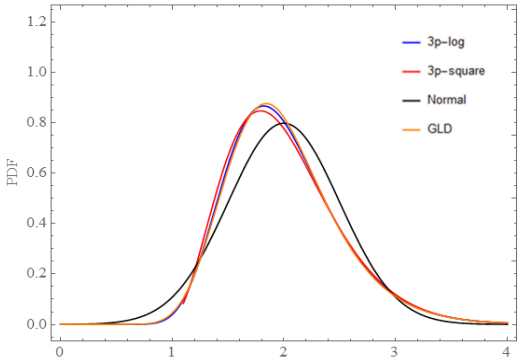

Fig 3. Comparisions of 3P-Distributions(α_{3x}=0.8)

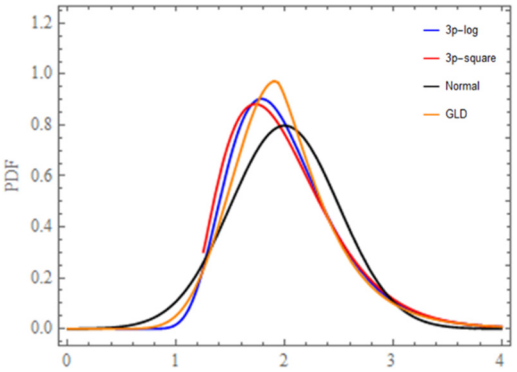

Fig 4. Comparisions of 3P-Distributions(α_{3x}=1.0)

As can be seen from Fig.3 and Fig.4, when α_{3x} = 0.6 and 0.8, there is no significant difference between the three parameter distributions.

Application to Data Analysis

In order to investigate the effect of the GLD in fitting the actual statistical data of random variables, two groups of concrete strength data were selected. The fitting effect of concrete strength's data histogram is shown in Fig. 5. The quantity of first group of data is 801, the first three moments are: 22.981 for mean value, 7.423 standard deviation, 0.643 for skewness. The quantity of second group of data is 550, the first three moments are: 21.879, 8.776 and 0.786 for mean value, standard deviation, and skewness, respectively.

In Figure (5), the PDFs of these distributions have the same mean value, standard deviation and skewness from the data, which are added to the fitting work with the actual data. The fitting effect of the concrete strength is shown in Figure (5). When the mean value is 22.981, the standard deviation is 7.423, and the skewness is 0.643, the 3P-LogNormal distribution and the 3p-Square Normal distribution show a very similar fitting effect, while the PDF of the GLD on both sides of the histogram obviously shows better fitting effect than the other three distributions.

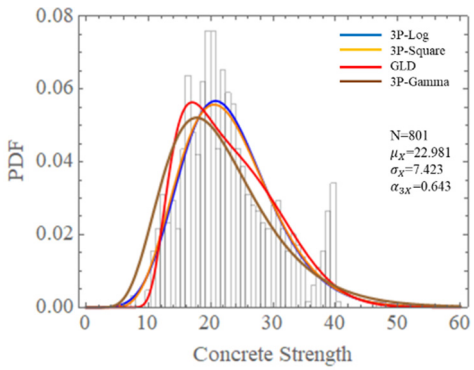

Fig 5. Data Fitting for Concrete Strength (1)

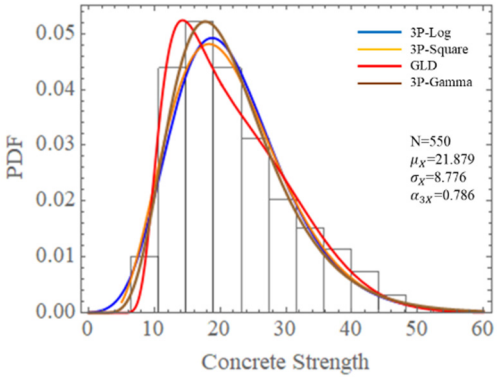

Fig 6. Data Fitting for Concrete Strength (2)

Similarly, in the second group, although slightly inferior to the 3P-Gamma distribution in the middle region, the GLD performed significantly better than the other three distributions on both sides of the histogram, especially in the right region.

The chi-square test values of these four distributions are shown in Table (1), where the calculation of goodness of fit is obtained using the following formula

$$T = \sum_{i=1}^{k} (Oi - Ei)^2 / Ei \tag{25}$$

where Oi and Ei are the observed frequency and the expected frequency respectively, $k$is the number of histogram groups divided and $T$is the calculated value of goodness of fit. From Table 1, it can be seen that the GLD shows a better fitting effect than the other three distributions in both cases. In group (1), the chi-square test value of the GLD is 175.252. In group (2), the chi-square test value of the GLD is 7.774.

Table 1. Results of test

Distribution / Number	3P-Log	3P-Square	3P-GLD	3P-Gamma
1	189.797	180.985	175.252	180.985
2	23.990	20.3216	7.774	20.317

It can be clearly seen from the above examples that since the first three moments of the GLD are equal to the statistical data, it is more consistent with the histogram than the 3p-Gamma distribution, 3p-LogNormal distribution and 3P-Square Normal distribution. That is to say, GLD is more suitable for fitting statistical data like concrete strength.

Conclusion

It is recommended to use the generalized lognormal distribution, which has the characteristics of generality and flexibility and can be applied to various situations of actual statistical data. According to the investigation:

(1) The GLD can be used as a candidate distribution for statistical data fitting of basic random variables. Since this distribution effectively reflects the skewness of random variables, it is usually more suitable for the histogram of basic random variables than the two-parameter distribution.

(2) For most statistical data in architecture, the definition domain of the GLD can satisfy the characteristics of statistical data from the aspect of mathematical statistics.

References

L.P. Yang, K.R. Gurley, D.O. Prevatt, Probabilistic modelling of wind pressure on low-rise buildi ngs, *Journal of Wind Engineering and Industrial Aerodynamics,* Vol114, pp.18-26, (2013).

Y.G. Zhao, Z.H. Lu, T. Ono, 4P-Lambda Distribution and its Application to Structural Reliability Assessment, *J. Structural and construction engineering, AIJ*, no.604, pp.47-54(200 6).

Y.G. Zhao, Alredo. H-S.ANG, Three-Parameter Gamma Distribution and Its Significance in Stru ctural Reliability, *Computational Structural Engineering, AIJ*, Vol.2, No.1, pp.1-1 0, (2002).

Y.G. Zhao, T. Ono, H. Idota, T. Hirano, A Three-Parameter Distribution Used for Structural Reli ability Evaluation, *J. Structural and construction engineering, AIJ*, No.546, pp.31-38, (2001).

Y.G. Zhao, Z.H. Lu, STRUCTURAL RELIABLITY APPROACHES FROM PERSPECTIVES O F STATISTICAL MOMENTS, Appendix B.3, pp.568, (2021).

Y.M. Low, A new distribution for fitting four moments and its applications to reliability analysis, *Structural Safety*, Vol.42, pp.12-25,(2013).

Kleiber. C, The Generalized Lognormal Distribution and the Stieltjes Moment Problem. *J Theor Probab* 27, 1167–1177 (2014).

G. Chen, Generalized log-normal distributions with reliability application, *Computational Statisti cs & Data Analysis*,Volume19, Issue3, pp.309-319, (1995).

International Symposium on Emerging Developments and Innovative Applications of Reliability Engineering and Risk Managements (EDIARR2022),30 October-3 November2022, Taipei
Chen, S. S. &Ang, Alfredo. H-S. (Editors)

FUNDAMENTAL NATURAL FREQUENCY ESTIMATION OF BUILDINGS DURING EARTHQUAKES USING CROWD'S SMARTPHONES

Ting Y. Hsu[1], Yi-Wen, Ke2, Yo M. Hsieh[3], and Chi T. Weng[4]

[1]*Department of Civil and Construction Engineering, National Taiwan University of Science and Technology, Taipei 10607, Taiwan*

E-mail：tyhsu@ ntust.edu.tw

[2]*Department of Civil and Construction Engineering, National Taiwan University of Science and Technology, Taipei 10607, Taiwan*

E-mail：yiwenke12@gmail.com

[3]*Department of Civil and Construction Engineering, National Taiwan University of Science and Technology, Taipei 10607, Taiwan*

E-mail：ymhsieh@ntust.edu.tw

[4]*Department of Civil and Construction Engineering, National Taiwan University of Science and Technology, Taipei 10607, Taiwan*

E-mail：m10305502@gapps.ntust.edu.tw

Abstract: After an earthquake strike, the information of potential damage to buildings close to the epicenter is very important for the first stage of emergency response. This study proposes to employ crowds' smartphones in buildings to perform system identification of building structures using the measured acceleration response during earthquake excitations. The principal advantage of using crowds' smartphones is the potential to capture the healthy condition of millions of buildings without hardware costs, installation labor, and long-term maintenance. This study's goal is to understand the feasibility to identify the lowest fundamental natural frequency of buildings without knowing the orientations and precise locations of the crowds' smartphones in advance. Both input-output and output-only identification methods are used to identify the lowest fundamental natural frequencies of numerical finite element models of a real building structure. The effects of time synchronization and the orientation alignment between nearby smartphones on the identification results are discussed.

Keywords: crowdsourcing; smartphones; post-earthquake building safety; orientation alignment; fundamental natural frequency

Introduction

In this study, we propose to employ smartphone-based crowdsourcing approaches to estimate the lowest fundamental natural frequency of the buildings during earthquakes without the help of Bluetooth-beacon-equipped products for precise locations of the smartphones. Thus, the lowest fundamental natural frequency of large number of buildings could be collected for prompt earthquake emergency response without deploying a costly structural health monitoring system in buildings. The methodology with which crowds' smartphones are used to estimate buildings' lowest fundamental natural frequency is explained in the next section. Next, the numerical study performed to verify the algorithm proposed is described.

Methodology

In order to explain the procedures employed in using crowds' smartphones to identify the lowest fundamental natural frequency of buildings during earthquakes, a flow chart of the procedures is shown in Figure 1. The first two procedures have already been developed and utilized in earthquake early warning systems (Hsu and Nieh 2020), while the third and fourth procedures have already been developed and utilized in previous works (Hsu et al. 2022); hence, only a brief introduction of these procedures is provided here. In this study, we investigated whether crowds' smartphones in a stable state could be harnessed for estimating the lowest fundamental natural frequency without knowing the precise locations and orientations of smartphones using the smartphone application developed in this study. Note that only the smartphone lying horizontally will be treated as in a stable state.

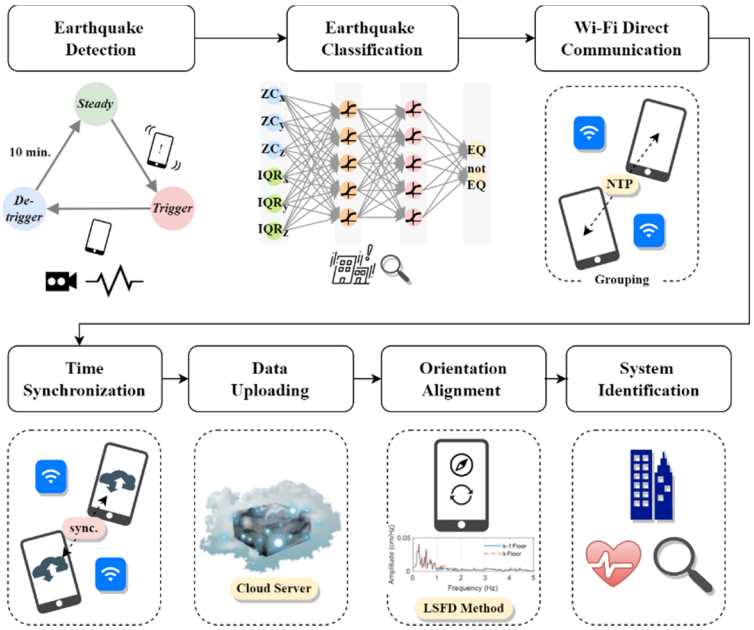

Fig. 1 The flow chart of the procedures using crowds' smartphones to identify fundamental natural frequency of buildings during earthquakes.

The first procedure consists of detecting the occurrence of an earthquake event. To that end, the smartphones are triggered and de-triggered based on the short-term average/long-term average (STA/LTA) algorithm. When the smartphones remain de-triggered for more than 10 minutes, the state of the smartphones is defined as "Steady". Relatedly, only when the smartphones are triggered after having been in the "Steady" state will the triggering be viewed as indicative of a potential earthquake event, at which time the acceleration signals between the triggering and de-triggering of the event will be recorded. Hence, the mere vibrations of the smartphones carried by people will not be recorded.

The second procedure consists of distinguishing whether the recorded acceleration signals are due to an earthquake event or not. To that end, the artificial neural network (ANN) approach is employed to construct the earthquake classifiers. The input features we used are the interquartile

range (IQR) between the 25th and 75th percentile of the acceleration vector sum of the three-component acceleration and the zero-crossing (ZC) rate from the component with the highest value.

If an event is classified as an earthquake event, the third procedure employed consists of establishing a wireless connection between nearby smartphones using Wi-Fi Direct technology. This allows the phones to identify nearby peer devices and establish a direct wireless link without an intermediate Wi-Fi access point.

The fourth procedure consists of synchronizing the smartphones. Although each smartphone has a built-in clock, the time on the clock may not be sufficiently accurate because of drift if the smartphone does not update its clock from the Internet time servers regularly. Even with the regular and standard time synchronization mechanism referred to as NTP, smartphones may have hundreds and tens of milliseconds of error through early (Miškinis et al. 2011) and 5G (Borenius et al. 2019) mobile networks, respectively. We employed the NTP mechanism through Wi-Fi Direct link to synchronize the time of the acceleration signals recorded.

The fifth procedure consists of performing orientation alignment of the smartphones. Although most smartphones are equipped with a magnetometer, the orientation determined with it is not sufficiently accurate to calculate interstory drifts, particularly during the excitation of earthquakes. Hsu et al. (2022) proposed the least Fourier spectrum difference (LFSD) method to address orientation alignment in the frequency domain. When the orientations of two smartphones are identical, the difference between their Fourier spectra in both horizontal components, defined as Equation (1), should be very small:

$$\begin{aligned}\Delta U_k^x(\omega_j,\theta) &= \left|U_k^x(\omega_j,\theta) - U_r^x(\omega_j)\right| \\ \Delta U_k^y(\omega_j,\theta) &= \left|U_k^y(\omega_j,\theta) - U_r^y(\omega_j)\right|\end{aligned} \tag{1}$$

in which U_k^x represents the Fourier spectrum of the k-th's smartphone's local x-direction, and ω_j represents the jth discrete frequency. U_r^x represents the Fourier spectrum of the reference smartphone, which can be selected randomly from the available smartphones. The smartphone's orientation of the k-th's smartphone, θ, begins from the orientation of the smartphone. It will rotate at an interval of Δθ, and the rotated Fourier spectra of the k-th's smartphone are calculated as:

$$\begin{aligned}U_k^x(\omega_j,\theta) &= U_k^x(\omega_j)\cos\theta + U_k^y(\omega_j)\sin\theta \\ U_k^y(\omega_j,\theta) &= -U_k^x(\omega_j)\sin\theta + U_k^y(\omega_j)\cos\theta\end{aligned} \tag{2}$$

The summation of the Fourier spectra difference $\Delta U_k(\theta)$ is calculated as:

$$\Delta U_k(\theta) = \sum_{j=1}^{M}\left(\Delta U_k^x(\omega_j,\theta) + \Delta U_k^y(\omega_j,\theta)\right) \tag{3}$$

in which M represents the total number of discrete frequencies considered. The orientation with the smallest value of $\Delta U_k(\theta)$ was selected as the best estimation of the orientation, denoted as θ_B.

The last procedure consists of performing system identification of the building using the acceleration data uploaded by the smartphones to estimate the lowest fundamental natural frequency of the building. We assume the smartphones are widely speeded and sufficient in a building, hence all the acceleration response of each floor including the lowest floor were measured. The algorithm of the combined deterministic and stochastic system identification (CSI; e.g. Reynders and De Roeck, 2008) is employed in this study.

Numerical Study

A finite element model of an eight-story reinforced concrete (RC) building with one-story basement was constructed, as shown in Fig. 2. The story height was 3.65 m, except the one of the basement was 3.95 m, results in a total height of 33.2 m. The dimensions of each story were 35.4 m (X) × 59.6 m (Y). The fundamental natural frequency of the X-direction, Y-direction, and Z-rotation was 1.771 Hz, 1.494 Hz, and 2.558 Hz.

The linear elastic earthquake response of the buildings with a 5% damping ratio excited during 17 earthquakes simulated using the ETABS commercial software was studied. The acceleration response of five locations on each floor, i.e. Center, Corner A, Corner B, Corner C, and Corner D, was assumed to be measured during seismic excitations, as shown in Fig. 3.

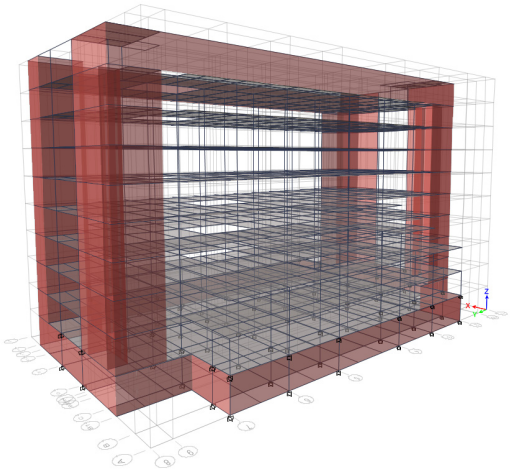

Fig. 2 The numerical model of the eight-story RC building.

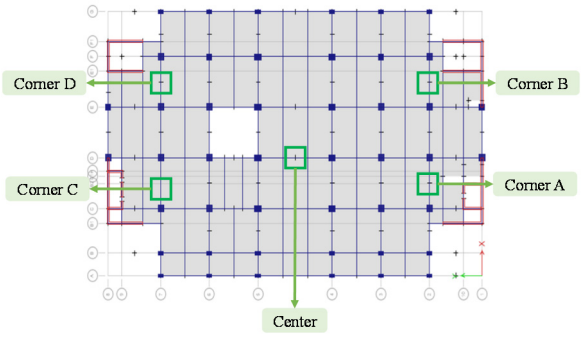

Fig. 3 Plan view of the numerical model and the locations of the smartphones.

The smartphones are assumed to be placed horizontally on the floors or rigid furniture, hence only the structural response and ground excitation are measured without slipping of the smartphones during excitations. The target natural frequency to be identified is the lowest fundamental natural frequency. It is assumed that the natural frequency will become lower due to damage and the maximum frequency variation due to environmental and operational condition changing is approximately 10% (Wu et al. 2017). Hence only the frequency range between 0.1 Hz and the 1.1 times of the lowest fundamental natural frequency, i.e. 1.1×1.494=1.643Hz, will be considered in the analysis.

We consider the noise floor and resolution of the acceleration signals of smartphones. Also, it is possible that time synchronization could be impossible if Wi-Fi Direct is failed, hence the time of different smartphones could be different. The original acceleration records were artificially contaminated with noise of noise floor of 1.0 cm/s2 and then the resolution was changed to 0.5 cm/s2 to simulate the possible situation when application.

Because the noise was added randomly, the time window between trigger and de-trigger of each acceleration time history was different. If time has been synchronized, the intersection of all the acceleration time histories of different floors will be truncated and used. As for the acceleration time histories without time synchronization, i.e. time asynchronization, the trigger time of different floors was aligned and then the time histories of shorter length were zero-padding to the same length of the longest one.

The effect of time synchronization and orientation alignment on the performance using the CSI methods to estimate the lowest fundamental natural frequency is discussed. The boxplot of the relative error of the identified frequency at five different locations of all the datasets using the CSI algorithm is shown in Fig. 4. The error when time is synchronized using the CSI algorithm is always smaller than approximately 3%, either with or without the orientation alignment. However, if time is not synchronized, the maximum relative error could reach approximately 17%.

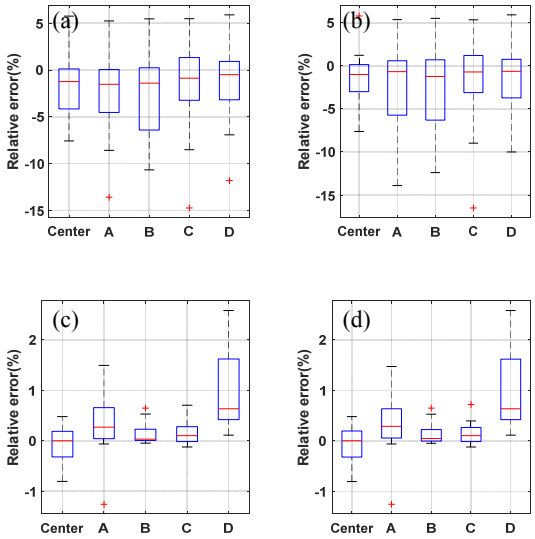

Fig. 4 The boxplot of the relative error of the identified frequency at five different locations using the CSI algorithm: (a) asynchronized and without orientation alignment, (b) asynchronized and with orientation alignment, (c) synchronized and with orientation alignment, (b) synchronized and with orientation alignment.

Conclusions and Discussions

This study proposed to use crowds' smartphones distributed in a building to estimate the building's lowest fundamental natural frequency during earthquake excitation. It is also found the CSI algorithm is sensitive to time synchronization but not sensitive to orientation alignment, hence if Wi-Fi Direct communication between adjacent smartphones is available, i.e. time is synchronized, CSI is suggested to estimate the lowest fundamental natural frequency because of its high accuracy.

Although the potential of using crowds' smartphones to estimate the lowest fundamental natural frequency of buildings during earthquakes has been illustrated based on the results of the numerical studies, it is actually based on some assumptions. The input excitation is assumed to be measured, otherwise the input-output system identification algorithms can not be employed. In order to elevate the applicability in practice, one fixed smartphone is recommended to be deployed on the ground floor of the building. It is also possible to use the acceleration measured by nearby seismic stations on the basement of a nearby building or in the nearby free field as the input, but more study is required to understand the feasibility. In addition, it is assumed that all the acceleration response of each floor were measured. It is also worse to be studied when the acceleration measured on only some of floors is available in the future.

References

Borenius, S., Costa-Requena, J., Lehtonen, M., Kantola, R. (2019), "Providing Network Time Protocol Based Timing for Smart Grid Measurement and Control Devices in 5G Networks", 2019 IEEE – International Conference on Communications, Control, and Computing Technologies for Smart Grids (SmartGridComm), Beijing, China, pp. 1-6.

Hsu, T.Y., Nieh, C.P. (2020), On-site Earthquake Early Warning Using Smartphones", Sensors, 20, 2928.

Hsu, T.Y., Liu, C.Y., Hsieh, Y.M., Weng, C.T. (2022), "Post-earthquake fast building safety assessment using smartphone-based interstory drifts measurement", Smart Structures and Systems, 29(2), 287-299.

Miškinis, R., Smirnov, D., Urba, E., Dzindzelėta, B. (2011), "Timing and synchronization in mobile telecommunication networks. Frequency Control and the European Frequency and Time Forum (FCS)", 2011 Joint Conference of the IEEE International, San Francisco, CA, 2-5 May 2011, pp. 665-669.

Reynders, E., De Roeck, G. (2008), "Reference-based combined deterministic-stochastic subspace identification for experimental and operational modal analysis", Mech Syst Signal Process, 22(3), 617–637.

Wu, W.H, Wang, S.W., Chen, C.C., Lai, G. (2017), "Assessment of environmental and nondestructive earthquake effects on modal parameters of an office building based on long-term vibration measurements", Smart Mater. Struct., 26, 055034.

International Symposium on Emerging Developments and Innovative Applications of Reliability Engineering and Risk Managements (EDIARR2022),30 October-3 November2022, Taipei
Chen, S. S. &Ang, Alfredo. H-S. (Editors)

BAYESIAN MODEL UPDATING OF A SIMPLY-SUPPORTED TRUSS BRIDGE BASED ON DYNAMIC RESPONSES

Xin Zhou[1], Chul-Woo Kim[1], Feng-Liang Zhang[2], Kai-Chun Chang[1], Yoshinao Goi[1]

[1]*Department of Civil and Earth Resources Engineering, Kyoto University, Kyoto 615-8540, Japan.*

[2]*School of Civil and Environmental Engineering, Harbin Institute of Technology, Shenzhen 518055, China.*

Correspondence e-mail address: kim.chulwoo.5u@kyoto-u.ac.jp

Abstract: This study aims to investigate applicability of a vibration-based model updating method to damage detection of a simply-supported truss bridge. The model updating process is expected to obtain a FE model that can fit better with experimental data for improving the accuracy of structural prediction and damage detection. Natural frequencies and mode shapes were adopted as objective variables in the objective function for the model updating. Vibration and damage experiments were carried out on the target bridge. A fast Bayesian FFT method is employed to identify the modal properties from collected raw data, and the Transitional Markov Chain Monte Carlo (TMCMC) algorithm is taken as a sampler. A cluster model updating scheme based on the sensor deployment is proposed to improve the engineering significance of the updated model parameters. Observations showed that the discrepancy between the FE model and experimental data would decrease after updated, and the model parameters were affected by damages. The possible damage indicated by the changes in model parameters showed the similar trend from the damage experiment. In other words, feasibility of the model updating and damage detection of simply-supported truss bridge was observed.

Keywords: Bayesian model updating, Damage detection, Field vibration test, Simply-supported truss bridge, Transitional Markov Chain Monte Carlo.

Introduction

In structural engineering, finite element (FE) models are widely used for structural analysis. Comparing to field experiments, FE analysis can save time and costs. However, due to the limited available information and simplification in modeling, uncertainties, such as material properties, geometric properties, boundary conditions, and load conditions, invariably exist in the system. Model updating methods would calibrate these uncertain parameters in the FE model based on the measurement data, so called a data-driven model calibration.

The Bayesian model updating which is based on Bayes' theorem (Jaynes, and Edwin 2003; Patelli et al. 2017, 905-25) is one of the most popular probabilistic-based approaches. Uncertain parameters are assumed to follow a certain probability distribution based on experimentally obtained data. Beck and Katafygiotis (Beck, and Katafygiotis 1998, 455-61) and Katafygiotis and Beck (Katafygiotis, and Beck 1998, 463-7) comprehensively improved the framework of Bayesian model updating, including model classes for structures and probability models for system errors. The model classes and probability models in the Bayesian model updating are furtherly investigated in many studies (Beck, and Yuen 2004, 192-203; Muto, and Beck 2008, 7-34; Goller, and Schueller 2011, 6122-33; Goller, Beck, and Schueller 2012, 430-40). The Bayesian model updating approaches have been conducted for reliability analysis and damage detection on many linear or nonlinear structures in laboratory and actual conditions (Lam, Hu, and Yang 2017, 314-36; Lam, Yang, and Au 2018; Jang, and Smyth 2017; Song et al 2018, 1129-50; Moravej et al. 2019, 3487-502; Ramancha et al. 2020, 389-97).

Most existing studies have verified the validity of model updating methods using numerical simulations [e.g., Ching, and Chen 2007, 816-32; Rocchetta et al. 2012. 174-95] or laboratory experiments [e.g., Goller, and Schueller 2011, 6122-33; Lam, Yang, and Au 2018]. However, the numerical simulations or laboratory experiments often refer to well-controlled measurement noise and a simple FE model with fewer modeling errors and fewer uncertain parameters, thereby showing a marked difference from actual structural conditions. Few studies have verified methods using field experiments for actual bridge structures. Even fewer studies have investigated the feasibility of applying a damage detection-aimed model update to actual bridge structures. The experimentally obtained data are often collected from a few sensors despite the higher degrees of freedom (DOF) of actual bridges. The wholly insufficient data cannot support the identification of many parameters. Moreover, sampling in an extremely high-dimensional solution space is a computationally expensive task. Therefore, it is impractical to conduct member-level or element-level model updating of an actual structure. An available approach to reduce the number of parameters is the grouping of multiple members into a block and assuming that values of uncertain parameters of the members in the same block are equal. A bridge structure with a complex model might have many available model classes with different grouping schemes. With these model classes, the updated results might also vary. To acknowledge these challenges, one must investigate the performance of the vibration-based FE model update method for actual bridge structures.

This study investigates feasibility of damage detection of an actual steel truss bridge considering different damage scenarios using the Bayesian FE model updating. Vibration and damage experiments were conducted on a steel truss bridge (Kim et al. 2021). A fast Bayesian FFT (Au 2011, 214-26; Au, Zhang, and Ni 2013, 3-14) method is adopted as an operational modal analysis method. The transitional Markov chain Monte Carlo (TMCMC) (Ching, and Chen 2007, 816-32) method is taken as the sampling method to generate a sample sequence from the posterior distribution. Based on sensitivity analysis, a cluster model class was examined in the FE model updates for bridge damage detection.

Bayesian Model Updating and Sampling

Bayesian model updating method

The formulation of the posterior PDF of uncertain parameter vector θ ($\theta \in \mathbf{R}^{N_\theta}$), under the condition system response *D,* is given as follows.

$$P(\theta|D,M) = \frac{P(D|\theta,M)P(\theta|M)}{P(D|M)} \tag{1}$$

where M is the assumed probabilistic model class for the structure; $P(D|M)$ is the evidence of model class M, and $P(D|M) = \int P(D|\theta,M)P(\theta|M)d\theta$; $P(\theta|M)$ is the prior PDF; $P(D|\theta,M)$ is the likelihood function, which donates the conditional probability of D given θ; N_θ is the number of uncertain parameters.

Even if the experimental data available is insufficient to constraint all updated parameters, the Bayesian model updating methods also can provide a posterior distribution of the uncertain parameters. Assuming the variances is same for each natural frequencies and mode shapes, the likelihood function becomes:

$$P(D|\theta,M) = c_l\, e^{-J(\theta)/2\sigma^2} \tag{2}$$

where $J(\theta) = \sum_{i=1}^{N_m}\left((1-\langle\varphi_i(\theta),\hat{\varphi}_i\rangle^2) + \left(1-f_i(\theta)/\hat{f}_i\right)^2\right)$; $f_i(\theta)$ and $\varphi_i(\theta)$ are the ith natural frequency and normalized mode shape vector under the given uncertain parameter vector θ obtained from the FE model while $\hat{f}_i$ and $\hat{\varphi}_i$ are the measured values from the experiments; N_m is the total number of modes; c_l is the normalized constant.

Transitional Markov chain Monte Carlo

Although the Bayesian model updating method can provide a posterior distribution, the complexity of its PDF makes it difficult to generate samples directly from the posterior distribution. Therefore, an efficient sampler is necessary. In this study, Transitional Markov chain Monte Carlo (TMCMC) (Ching, and Chen 2007, 816-32) is used to generate samples efficiently. The essence of TMCMC is to use a series of asymptotic intermediate distributions, $(P(\theta|D)^{(j)}(j = 1,2,3\ldots))$, to approach the final distribution. The importance sampling method is used to transfer between the intermediate distributions, $(P_j(\theta|D), j = 0,1\ldots m,\ \theta \in \mathbf{R}^{N_\theta})$. With the value of j increasing, the $P(\theta|D)^{(j)}$ becomes more closed to the target distribution $P(\theta|D)$.

For the asymptotic intermediate distribution $P_j(\theta|D,M)$, the values of their variances $(\sigma_j, j = 1\ldots m)$ are different, and $P_j(\theta|D,M)$ is shown as:

$$P_j(\theta|D,M) = c_j e^{-J(\theta)/2\sigma_j^2} \qquad j = 1,2\ldots m \tag{3}$$

Especially, assuming $P_0(\theta|D,M) = c_0$ follows a uniform distribution. The adjacent intermediate distributions are connected by importance sampling, and the weighting $w_j(\theta)$ is shown as:

$$w_j(\theta) = \frac{P_{j+1}(\theta|D)}{P_j(\theta|D)} = \frac{c_{j+1}}{c_j} e^{-\frac{J(\theta)}{2}\left(\frac{1}{\sigma_{j+1}^2}-\frac{1}{\sigma_j^2}\right)} \tag{4}$$

Because some unknown parameters exist, it is impractical to use $w_j(\theta)$ directly in the resampling process. Therefore, the normalized weighting $w_{j,k}^n$ is proposed as

$$w_{j,k}^n = \frac{w_j(\theta_{j,k})}{\sum_{l=1}^{N_j} w_l(\theta_{j,k})} = \frac{e^{-\frac{J\left(\theta_{j,k}\right)}{2}\left(\frac{1}{\sigma_{j+1}^2}-\frac{1}{\sigma_j^2}\right)}}{\sum_{l=1}^{N_j} e^{-\frac{J\left(\theta_{j,l}\right)}{2}\left(\frac{1}{\sigma_{j+1}^2}-\frac{1}{\sigma_j^2}\right)}} \tag{5}$$

Then, with the normalized weighting $w_{j,k}^n$, the sample sequence of $\theta_{j+1,l}$, which follows the distribution of $P_{j+1}(\theta|D,M)$, is generated from $\theta_{j,k}$.

$$\theta_{j+1,l} = \theta_{j,k} \quad with\ the\ probability \quad w_{j,k}^n \tag{6}$$

Case Study: Steel Truss BRIDGE

Field Vibration and Damage Experiments

This section would briefly introduce the target bridge, field tests, and modal identification. More details can be found in reference (Chang, and Kim 2016, 156-73; Kim et al. 2021; Zhang, Kim, and Goi 2021).

The target bridge shown in Figure 1 is a simply supported steel truss bridge built in 1959 and removed in 2012. The main components consist of concrete slabs, main girders, and truss members. The length and width of the main span were 59.2 m and 3.6 m respectively. Ambient and vehicle-induced vibration experiments were arranged before removal. Eight uniaxial accelerometers were installed on the bridge deck, as shown in Figure 2(a), to measure the vertical bridge acceleration responses. Five scenarios (INT, DMG1, DMG2, RCV, and DMG3) were considered consecutively for the bridge, as shown in Figure 2(b). Damage in the DMG1, DMG2, and RCV states was imposed mid-span, whereas the damage in the DMG3 state was imposed in the 5/8 span. The form of damage appears as severance of the tension members. A full cut and half cut represent different degrees of damage. A 21 kN vehicle was used to excite the bridge with an average speed of about 20 km/h under each damage scenario.

Accurate identification of modal properties is necessary for model updating. The data from vehicle-induced vibration test described above is used for modal identification. Five stable modes were identified by means of a fast Bayesian FFT method (Au 2011, 214-26; Au, Zhang, and Ni 2013, 3-14), given as Table 1. The frequencies were approximately 3 Hz, 5 Hz, 7 Hz, 9.5 Hz, and 10.5 Hz for the first bending mode, the first torsional mode, the second bending mode, the third bending mode, and the fourth bending mode respectively. Figure 3 presents the corresponding mode shapes.

Figure 1. Target bridge.

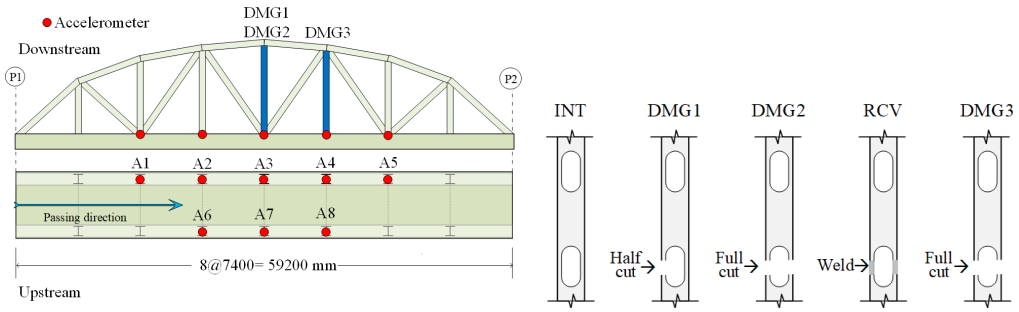

(a) Sensor deployment (b) Sketch of damage scenarios

Figure 2. Sensor layout and damage scenario (Kim et al. 2021).

Table 1. Identified frequencies for the respective damage scenarios considered in the field experiment

Scenario	1st bending mode		1st torsional mode		2nd bending mode		3rd bending mode		4th bending mode	
	Freq. (Hz)	COV (%)	Freq. (Hz)	COV (%)	Freq. (Hz)	COV (%)	Freq. (Hz)	COV (%)	Freq. (Hz)	COV (%)
INT	2.98	0.0932	5.21	0.3181	6.87	0.1188	9.61	0.1087	10.57	0.2472
DMG2	2.88	0.0259	4.99	0.2232	6.87	0.1308	9.67	0.0195	10.59	0.1623
DMG3	2.92	0.0555	5.10	0.1870	6.46	0.1800	8.66	0.32	10.07	0.1686

Freq., denotes frequency for each mode; COV, coefficient of variation of the identified frequency

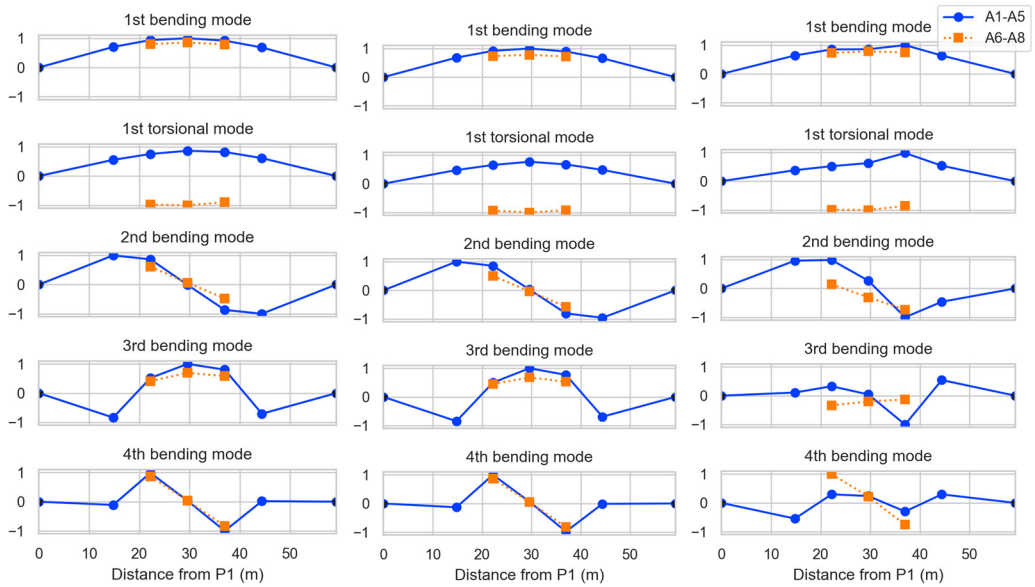

(a) INT state (b) DMG2 state (c) DMG3 state

Figure 3. Identified mode shapes

FE Model and Model Class

The ABAQUS, a finite element analysis software suite, was used for analyses. In the FE model, concrete slabs were modeled by shell elements, main girders by beam elements, and truss members by truss elements, as shown in Figure 4(a). It is always an issue to trade off computational efficiency against accuracy in finite element modelling and updating. A too simple model may fail to reflect the properties of the real bridge, causing accuracy problems, while a too complicated model may take a huge amount of computation time and resources, causing efficiency problems. Thus, the following simplifications were introduced to reduce the computational burden without losing generality: using truss elements rather than beam elements to model top chords, vertical and diagonal truss members; and using shell elements rather than solid elements to model the concrete slabs. The FE model comprises more than one hundred members and three thousand elements. Table 2 shows the design values of truss-bridge model parameters.

Table 3 presents the frequencies and mode shapes from eigenvalue analysis using FEA considering the design values in Table 2. MAC values are compared with those from experiments conducted under INT and DMG2 states. The greatest discrepancy of natural frequencies between FEA and modal properties identification from measured accelerations was observed in the first bending mode: approximately 8% under INT state and 10% under DMG2 states. For the largest discrepancy of mode shapes, approximately 6% difference of MAC values was observed in the third and fourth bending modes.

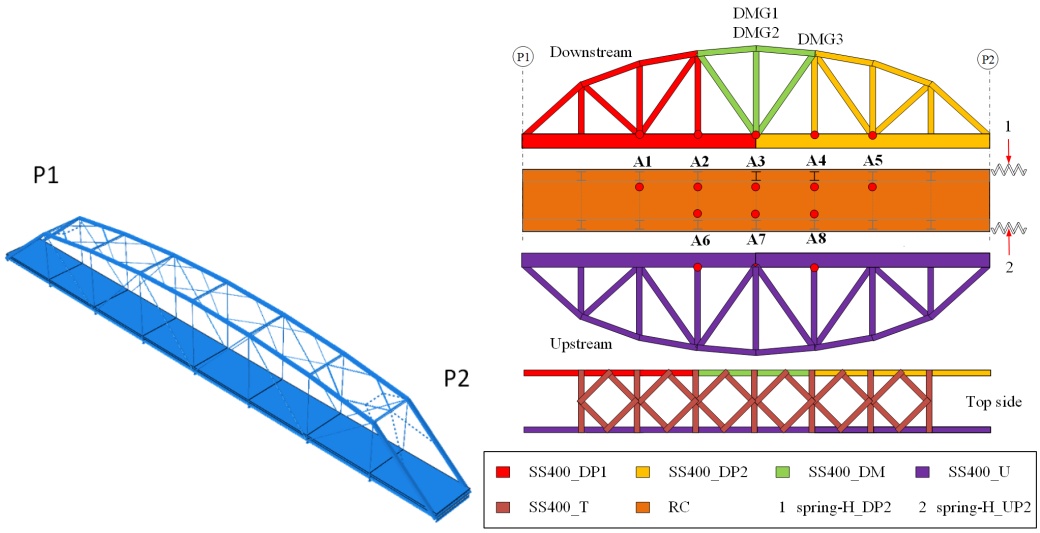

(a)FE model (b)Model class

Figure 4. FE model and Model class

Table 2. Design values of parameters

Parameter	Young's modulus of steel	Young's modulus of RC	horizontal spring constant	vertical spring constant	rotation spring constant
Value	200 GPa	21 GPa	10^9 kN·m^{-1}	∞ N·m^{-1}	0 kN ·m^{-1} ·rad^{-1}

Table 3. Frequencies and MAC values of eigenvalues analysis using design values of parameters

		1st bending mode	1st torsional mode	2nd bending mode	3rd bending mode	4th bending mode
INT	Freq. (Hz) (experiment)	2.98	5.21	6.87	9.61	10.57
	Freq. (Hz) (FE update)	3.20	4.96	6.78	9.97	10.71
	Difference of Freq. (%)	7.49	-4.77	-1.25	3.68	1.37
	MAC	0.9948	0.9906	0.9703	0.9389	0.9464

DMG2	Freq. (Hz) (experiment)	2.88	4.99	6.87	9.67	10.59
	Freq. (Hz) (FE update)	3.20	4.96	6.78	9.97	10.71
	Difference of Freq. (%)	10.88	-0.57	-1.35	3.13	1.19
	MAC	0.9885	0.9715	0.9752	0.9431	0.9414

As a result of the limited experimental information, it was not possible to update the model, regardless of whether it is at member or element level. In order to reduce the number of updating parameters, a model class shown in Figure 4(b) was proposed, in which multiple members are grouped into a block and assumed that values of uncertain parameters of the members in the same block are equal.

Three types of model parameters, such as spring constants, steel stiffnesses, and concrete stiffnesses, are considered in the proposed model class. Only the springs in the longitudinal direction at P1 are considered in this study. Considering the asymmetry of the sensor layout, the model incorporates the assumption of a single model parameter for the upstream side of the bridge and the horizontal spring at P2. The parameters starting with 'SS400' represent the elastic modulus of steel members. 'RC' denotes the elastic modulus of the reinforced concrete. Also 'spring-H' stands for the horizontal springs. The 'D' and 'U' respectively signify the downstream and upstream sides; the 'P1', 'M', and 'P2' respectively denote the P1 end, mid-span, and P2 end. Characters 'B' and 'T' respectively represent members at the bottom and top of the bridge.

Modal parameter-based model updating

Figure 5 presents selected histograms of the updated model parameters. From the obtained posterior probability distribution, the global maximum could be identified and the model parameter values that give this global maximum were termed most probable value (MPV). The MPVs of the updated model parameters and the corresponding updated natural frequencies and MAC values are presented in Table 4 and Table 5.

Two peaks in the marginal distributions of the updated model parameter of the DMG2 state are observed as shown in Figure 6: each peak is denoted as DMG2(1) and DMG2(2). The first and third bending modes of DMG2(1) are closer to experimentally obtained data, whereas the first torsional mode, second bending mode, and fourth bending modes of DMG2(2) are closer to experimental data, as shown in Table 5.

Because of the artificial damage at mid-span on the downstream side, it is expected that the SS400_DM stiffness will decrease, whereas stiffness of other model parameters will be nearly unchanged. Based on the prior information from visual inspections, the possible damage type of this bridge should be local. Therefore, the DMG2(2) histogram is more like the expectation. From Table 4, the MPV of SS400_DM of DMG2(2) decreased about 16.2 GPa, whereas tiny changes in SS400_U, SS400_DP1, and SS400_DP2 were observed. Observations demonstrated that the possible damage was located in the block of SS400_DM. The distribution of spring-H_UP2 was almost unchanged, although a clear decrease of spring-H_DP2 was observed.

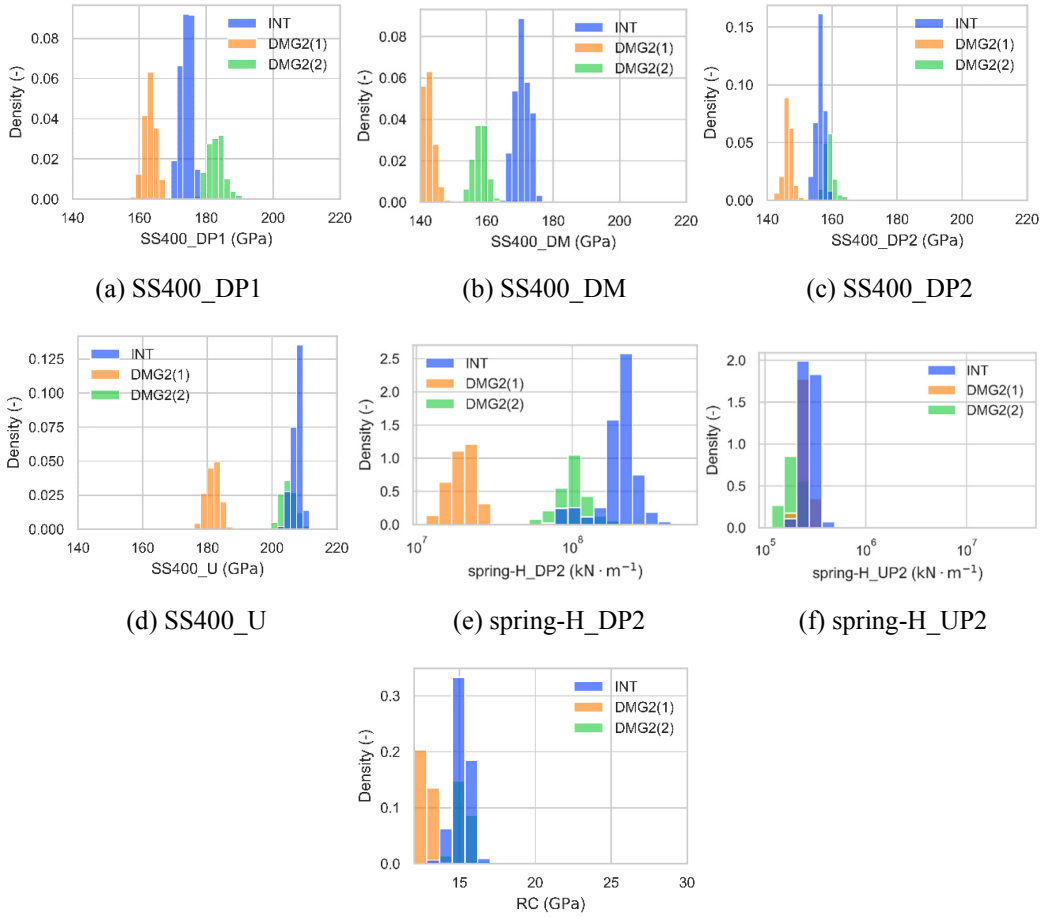

(a) SS400_DP1 (b) SS400_DM (c) SS400_DP2

(d) SS400_U (e) spring-H_DP2 (f) spring-H_UP2

(g) RC

Figure 5. Marginal distribution of elastic modulus in the Case 3 model

Table 4. MPV of the updated parameters under INT and DMG2 states

Model parameter	SS400_DP1 (GPa)	SS400_DM (GPa)	SS400_DP2 (GPa)	SS400_U (GPa)	spring-H_DP2 ($kN \cdot m^{-1}$)	spring-H_UP2 ($kN \cdot m^{-1}$)
INT	172.6	168.8	154.9	205.0	1.9×10^{8}	2.8×10^{5}
DMG2(1)	165.2	143.3	147.3	185.0	2.0×10^{7}	2.1×10^{5}
DMG2(2)	179.7	152.6	156.1	199.8	6.6×10^{7}	1.7×10^{5}

Table 5. MPV of the updated frequencies and MAC under INT and DMG2 states

		1st bending mode	1st torsional mode	2nd bending mode	3rd bending mode	4th bending mode
INT	Freq. (Hz) (experiment)	2.98	5.21	6.87	9.61	10.57
	Freq. (Hz) (FE update)	3.18	4.92	6.78	10.10	10.60
	Difference of Freq. (%)	7.01	-5.59	-1.32	5.05	0.29
	MAC	0.9991	0.9974	0.9819	0.9904	0.9766
DMG2(1)	Freq. (Hz) (experiment)	2.88	4.99	6.87	9.67	10.59
	Freq. (Hz) (FE update)	3.04	4.69	6.47	9.69	10.14
	Difference of Freq. (%)	5.37	-6.10	-5.89	0.20	-4.21
	MAC	0.9991	0.9824	0.9961	0.9909	0.9726
DMG2(2)	Freq. (Hz) (experiment)	2.88	4.99	6.87	9.67	10.59
	Freq. (Hz) (FE update)	3.14	4.82	6.64	9.90	10.29
	Difference of Freq. (%)	8.80	-3.38	-3.48	2.44	-2.76
	MAC	0.9992	0.9818	0.9957	0.9901	0.9732

Conclusions

This study investigates applicability of the model updating method on the actual bridges. Similar to the numerical simulations or laboratory experiments, the performance of the updated natural frequencies and mode shapes on actual bridges were also significantly improved as a decrease in prediction error of modal parameters. The updated FE model can be used to predict the dynamic properties of structures, which are significant for design support and maintenance.

By modeling boundary condition with spring constants, the performance of FEA was improved, and the horizontal spring was the most significant. When the model class, which has considered the difference in sensor number on the upstream and downstream sides, was considered, the damaged block was successfully identified. The model class of truss bridge, whose design is based on the engineering experiences, such as the possible type and location of the structural damage, can fit the experimental prediction.

The feasibility of damage detection by the modal parameter-based FE model updating is verified. Correctly detecting structural damage is also significant for improving the accuracy of FEA. In actual bridges, structural damage, like crack or corrosion, inevitably exists in the system. Even in the initial state where no artificial damage was applied, the structural damage existing has a significant impact on the model updating process. With a suitable model class, the damaged block can be identified correctly. Using prior information about damage type can effectively improve the performance of FE model update and damage detection. Moreover, prior information, including geometric characteristics, sensor deployment, and damage information, can provide a powerful supplement for the design of the model class.

References

Au, S.K. 2011. "Fast Bayesian FFT method for ambient modal identification with separated modes" *Journal of Engineering Mechanics* 137(3), 214–26. https://doi.org/10.1061/(ASCE)EM.1943-7889.0000213.

Au, S.K., Zhang, F.L. and Ni, Y.C. 2013. "Bayesian operational modal analysis: theory, computation, practice" *Computers and Structures* 126, 3–14. https://doi.org/10.1016/j.compstruc.2012.12.015.

Beck, J.L. and Katafygiotis, L.S. 1998. "Updating models and their uncertainties. i: Bayesian statistical framework" *Journal of Engineering Mechanics* 124(4), 455–61. https://doi.org/10.1061/(ASCE)0733-9399(1998)124:4(455).

Beck, J.L. and Yuen, K.V. 2004. "Model selection using response measurements: Bayesian probabilistic approach" *Journal of Engineering Mechanics* 130(2), 192–203. https://doi.org/10.1061/(ASCE)0733-9399(2004)130:2(192).

Chang, K. C. and Kim, C. W. 2016. "Modal-parameter identification and vibration-based damage detection of a damaged steel truss bridge." *Engineering Structures* 122, 156-73. https://doi.org/10.1016/j.engstruct.2016.04.057.

Ching, J. and Chen, Y.C. 2007. "Transitional Markov chain Monte Carlo method for Bayesian model updating, model class selection, and model averaging" *Journal of Engineering Mechanics* 133(7), 816–32. https://doi.org/10.1061/(ASCE)0733-9399(2007)133:7(816).

Goller, B., Beck, J.L. and Schueller, G.I. 2012. "Evidence-based identification of weighting factors in Bayesian model updating using modal data" *Journal of Engineering Mechanics* 138(5), 430–40. https://doi.org/10.1061/(ASCE)EM.1943-7889.0000351.

Goller, B. and Schueller, G.I. 2011. "Investigation of model uncertainties in Bayesian structural model updating" *Journal of Sound and Vibration* 330(25), 6122–36. https://doi.org/10.1016/j.jsv.2011.07.036.

Jang J. and Smyth A. 2017. "Bayesian model updating of a full‐scale finite element model with sensitivity‐based clustering" *Structural Control and Health Monitoring* 24(11), e2004. https://doi.org/10.1002/stc. 2004.

Jaynes, Edwin T. 2003. "Probability theory: The logic of science." Cambridge university press.

Katafygiotis, L.S. and Beck, J.L. 1998. "Updating models and their uncertainties. ii: model identifiability" *Journal of Engineering Mechanics* 124(4), 463–7. https://doi.org/10.1061/(ASCE)0733-9399(1998)124:4(463).

Kim, C. W., Zhang, F. L., Chang, K. C., McGetrick, P. J. and Goi, Y. 2021. "Ambient and vehicle-induced vibration data of a steel truss bridge subject to artificial damage." *Journal of Bridge Engineering* 26(7), 04721002. https://doi.org/10.1061/(ASCE)BE.1943-5592.0001730.

Lam, H. F., Hu, J. and Yang, J. H. 2017. "Bayesian operational modal analysis and Markov chain Monte Carlo-based model updating of a factory building." *Engineering Structures* 132, 314-36. https://doi.org/10.1016/j.engstruct.2016.11.048.

Lam, H.F., Yang, J.H. and Au, S.K. (2018), "Markov chain Monte Carlo-based Bayesian method for structural model updating and damage detection" *Structural Control and Health Monitoring* 25(4), e2140. https://doi.org/10.1002/stc.2140.

Moravej, H., Chan, T. H., Nguyen, K. D. and Jesus, A. 2019. "Vibration-based Bayesian model updating of civil engineering structures applying Gaussian process metamodel." *Advances in Structural Engineering* 22(16), 3487-502. https://doi.org/10.1177/1369433219858723.

Muto, M. and Beck, J.L. 2008. "Bayesian updating and model class selection for hysteretic structural models using stochastic simulation" *Journal of Vibration and Control* 14(1-2), 7–34. https://doi.org/10.1177/1077546307079400.

Patelli, E., Govers, Y., Broggi, M., Gomes, H. M., Link, M. and Mottershead, J. E. 2017. "Sensitivity or Bayesian model updating: a comparison of techniques using the DLR AIRMOD test data" *Archive of Applied Mechanics* 87(5):905-25. https://doi.org/10.1007/s00419-017-1233-1.

Ramancha M.K., Astroza R., Conte J.P., Restrepo J.I. and Todd M.D. 2020. "Bayesian nonlinear finite element model updating of a full-scale bridge-column using sequential Monte Carlo" *Model Validation and Uncertainty Quantification* Volume 3. Springer, Cham.

Rosenblatt, M. 1956. "Remarks on some nonparametric estimates of a density function." *Annals of Mathematical Statistics* 27(3):832–7.

Song, M., Yousefianmoghadam, S., Mohammadi, M.E., Moaveni, B., Stavridis, A. and Wood, R.L. 2018. "An application of finite element model updating for damage assessment of a two-story reinforced concrete building and comparison with lidar." *Structural Health Monitoring* 17(5), 1129–50. https://doi.org/10.1177/1475921717737970.

Zhang, F. L., Kim, C. W. and Goi, Y. 2021. "Efficient Bayesian FFT method for damage detection using ambient vibration data with consideration of uncertainty." *Structural Control and Health Monitoring* 28(2), e2659. https://doi.org/10.1002/stc.2659.

International Symposium on Emerging Developments and Innovative Applications of Reliability Engineering and Risk Managements (EDIARR2022),30 October-3 November2022, Taipei
Chen, S. S. &Ang, Alfredo. H-S. (Editors)

APPLICATIONS OF DEEP LEARNING MODELS TO FREQUENCY-DOMAIN PHASE RESPONSES FOR DAMAGE DETECTION OF BUILDING STRUCTURES

Jau-Yu Chou [1], Chia-Ming Chang [2]

[1]*Department of Civil Engineering, National Taiwan University, No 1, Sec 4, Roosevelt Rd, Taipei 10617, Taiwan*

E-mail: d06521008@ntu.edu.tw

[2] *Department of Civil Engineering, National Taiwan University, No 1, Sec 4, Roosevelt Rd, Taipei 10617, Taiwan*

E-mail: changcm@ntu.edu.tw

Abstract: Lower stories of building structures are much more vulnerable due to the supported dead load from the structure above. Extreme loadings such as earthquakes can also result in the service life shortening of a building by means of structural degradation. Researchers usually developed damage indices to quantify structural damage. However, these indicators are usually not directly related to structural performance and therefore difficult to be adopted as a reference for decision making. In this study, a neural network damage detection method based on frequency response phase angle differences is proposed. The vibrational responses are first used to generate a simplified structural model through the optimized least-squared stiffness method. Then, multiple damage scenarios are applied to this model, and a large amount of datasets via frequency response phase angle difference between the original and current states are derived for training the deep learning model. Finally, the trained model can be used to estimate the structural condition and to predict remaining stiffness percentage. In this study, a five-story shear building is numerically developed to investigate effectiveness of the proposed method, i.e., deep learning model architectures, frequency bands, number of selected inputs, noise robustness, and estimated stiffness errors. In addition, a scaled six-story steel-frame building structure is experimentally tested using shake table testing to evaluate the proposed method. As seen in the results, the proposed method realizes four stages of damage detection, i.e., the damage occurrence, damage locations, damage levels, and remaining performance. Moreover, the results also demonstrate accurate stiffness estimation from structural responses with measurement noise by the proposed method.

Keywords**:** Damage Deetection, Deep Neural Network, Phase Angle Difference, Remaining Stiffness Estimation, Frequency Response Function

Introduction

Quantifying the remaining performance of structures is still a challenging task in the field of structural health monitoring. Moreover, lower stories in a building structure are often planned to be an open space for commercial use, resulting in relatively vulnerable stories [1]. In the field of damage detection, frequency response functions (FRF) are shown to better represent the dynamic behavior and inform structural damage as compared to input-output time-domain methods [2]. However, constructing the relationship between the phase angle variations and remaining stiffness parameters is a highly nonlinear and challenging problem. Alternatively, machine learning methods offer an opportunity to establish a prediction model from the input and output information of a complex system [3-4] Therefore, this study develops a deep neural network model that employs the phase differences of frequency response functions between an intact and damaged building as inputs to estimate the remaining performance of the building.

Deep Learning Model for Damage Detection Using Phase Differences

In Figure 1, the input-output responses are first utilized for initial story stiffness estimation using the least square stiffness method with nonlinear least square optimization. Multiple objective functions are adopted to the simplified numerical model to minimize the natural frequencies error and the root mean square error (RMSE) of the mode shapes. This simplified model will share similar dynamic behavior with the true structure because of tuned modal properties. Thus, multiple damage states with stiffness limited between 0 % and 100 % can be artificially generated from the simplified model and the frequency phase angle difference between the intact and damage structure are exploited to the deep neural network. Finally, the pre-trained deep neural network is capable of estimating the remaining stiffness percentage of a structure.

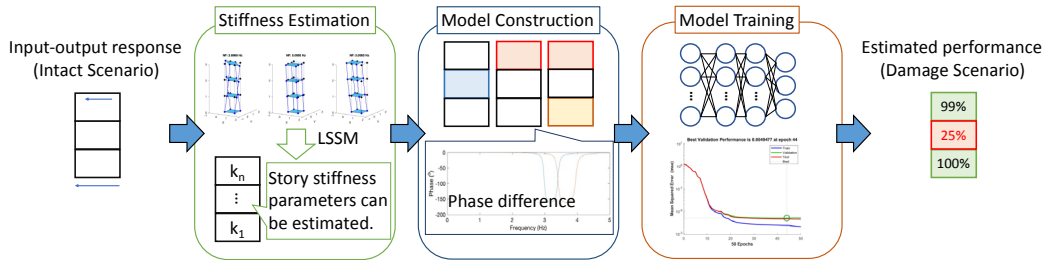

Figure 1. Flowchart of proposed deep learning inspired damage detection method.

Numerical Example of Damage Detection on Five-Story Shear Building

To better establish this deep learning model, a number of parameters are numerically investigated. In this study, different number of hidden layers with different number of neurons (nodes) are selected to investigate the performance via R^2, as shown in Fig. 2(a). When the R^2 is close to one, the regression model achieves better performance. In contrast, when R^2 approaches zero, the model can be viewed to fail for estimation. From Fig. 2(a), the best performance can be observed at 4 hidden layers with each containing 35 neurons, which has a R^2 of 0.9936. In addition, different number of input story response and the selected frequency range are compared in Fig. 2(b). The results indicate that the when using the phase difference of the first three stories with 0-10 Hz will achieve optimal performance. On the contrary, using only the first story response with 0-3 Hz will result in inefficient model because of the lack of damage information.

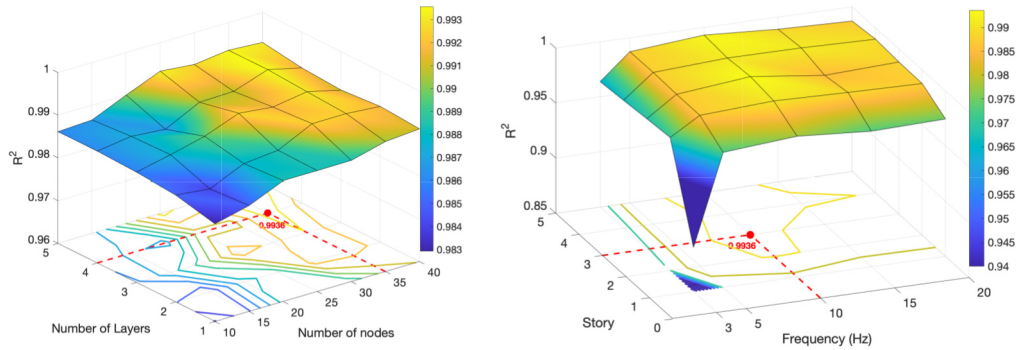

(a) (b)

Figure 2. (a) Performance of different number of layers and different number of nodes and (b) Performance of different number of input story and different frequency range.

When training a neural network, one important factor that affects the prediction accuracy is the sampling size. In this study, different Training data samples are generated by dividing the stiffness reduction factor into different numbers. The sample sizes are 1860, 5130, 10920, 19950, 32940, 50610, and 73680. After training, the deep neural network is evaluated using a test dataset with 119985 samples. The performance in terms of mean absolute percentage error (MAPE, [5]) is shown in Fig. 3(a), where the smallest error is achieved when using 19950 samples for training. By using the optimal parameters, including the number of hidden layers, number of neurons, number of input story response, frequency range, and training sample size, the optimal deep neural network is established. Fig. 3(b) represents the noise robustness of the optimal neural network. As shown in this figure, the RMSE reduces as the signal to noise ratio (SNR) increases. After the SNR is larger than 70 dB, the error becomes stable and have similar RMSE with noiseless inputs, indicating that the neural network is robust to a wide range of signal noise.

In addition, although stiffness estimation methods from modal properties (i.e., natural frequency and mode shapes) can determine story stiffness parameters, still difference between the exact stiffness and the estimated ones can be observed. Here, the stiffness errors in the 1st to 3rd story range from -15% to +15%. As shown in this Fig. 4, the color distribution indicates the accuracy in terms of mean absolute error (MAE, [5]). From the figure, the error significantly increases only when 3-story stiffness parameters are detuned in the same direction. As a result, the proposed method is capable of estimating the stiffness reductions with high accuracy when the intact stiffness parameters are well determined. Moreover, the proposed method can offer decent accuracy even when the intact story stiffness parameters are slightly detuned.

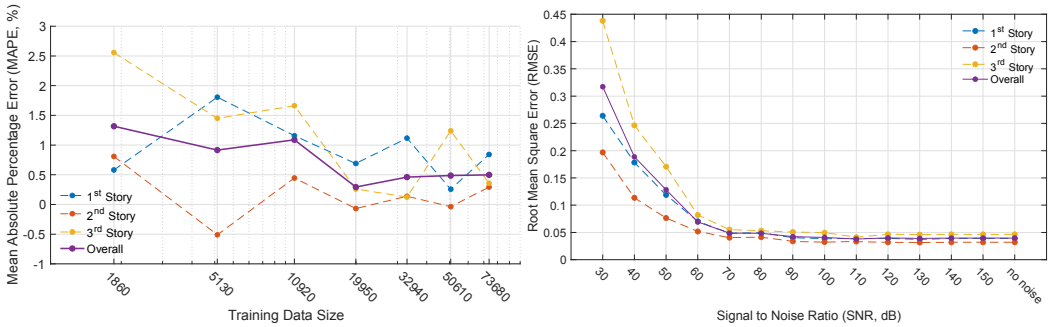

(a) (b)

Figure 3. (a) Performance of different number of layers and different number of nodes and (b) Performance of different number of input story and different frequency range.

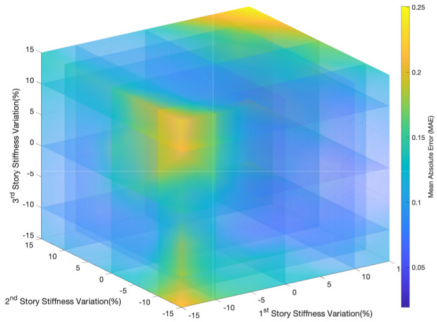

Figure 4. Model performance with simplified model uncertainty.

Experimental Verification on Five-Story, Steel-Frame Building

This damage detection strategy is experimentally applied to and implemented in a six-story, steel-frame scaled building [6], in which the damaged stories are manipulated by connection plates with lower stiffness. Besides the intact structure (Case 1), four damage scenarios (Case 2 to Case 4) are studied and focused only on the first three stories. As seen in the results in Fig. 5(b), the stiffness reductions in lower stories of this building can be estimated with decent accuracy as compared to a conventional method. As a result, the proposed method realizes four stages of damage detection, i.e., the damage occurrence, damage locations, damage levels, and remaining performance. Moreover, the results also demonstrate accurate stiffness estimation from structural responses with measurement noise by the proposed method.

Conclusions

A neural network damage detection method using frequency response phase angle differences was proposed in this study. In this proposed method, a simplified model that described the structural dynamic behavior was first developed by the optimized least-squared stiffness method. The synthetic data (i.e., intact and damaged cases) were established by changing story stiffness parameters. Meanwhile, the damping variances were also artificially added for the damaged cases. Then, a neural network model was constructed by the frequency response phase angle differences as the input and the remaining stiffness levels as the output. In this study, a five-story shear building was employed to numerical evaluate the proposed method, including the size of the neural network model, frequency bands, number of selected inputs, noise robustness, and estimated stiffness errors. Moreover, the proposed method was experimentally verified on a scaled six-story steel-frame building structure. As seen in the results, the proposed method enabled the detection of damage occurrence, damage locations, and damage levels and remaining performance estimation.

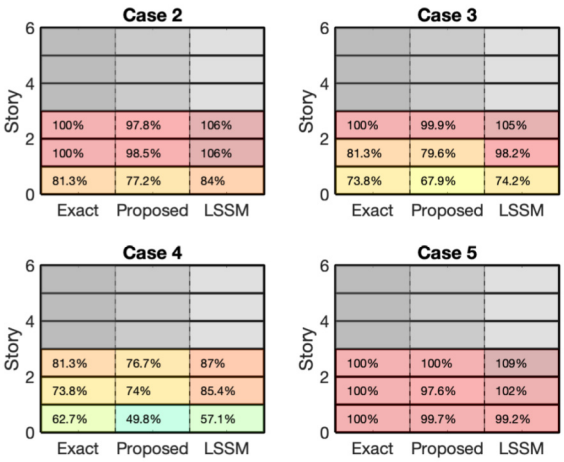

(a) (b)

Figure 5. (a) Photo of tested structure and (b) test results.

References

Hejazil F, Jilani S, Noorzaei J, Chieng CY, Jaafar MS, and Abang Ali AA. Effect of soft story on structural response of high rise buildings. *IOP Conference Series: Materials Science and Engineering* 2011; 17, 012034.

Padil KH, Bakhary N, Abdulkareem M, Li J and Hao H. Non-probabilistic method to consider uncertainties in frequency response function for vibration-based damage detection using artificial neural network. *J Sound Vib* 2020; 467,115069.

Mousavi Z, Ettefagh MM, Sadeghi MH, and Razavi SN. Developing deep neural network for damage detection of beam-like structures using dynamic response based on FE model and real healthy state. *Appl Acoust* 2020; 168, 107402.

Kiranyaz S, Avci O, Abdelijaber O, Ince T, Gabbouj M, and Inman DJ. 1D convolutional neural networks and applications: A survey. *Mech Syst Signal Process* 2021; 151, 107398.

Botchkarev A. Performance metrics (error measures) in machine learning regression, forecasting and prognostics: properties and typology. *ArXiv* 2018; 1809.03006.

Hsu TY, Loh, CH. A frequency response function change method for damage localization and quantification in a shear building under ground excitation. *Earthq Eng Struct Dyn* 2013; 42:653-668.

International Symposium on Emerging Developments and Innovative Applications of Reliability Engineering and Risk Managements (EDIARR2022),30 October-3 November2022, Taipei
Chen, S. S. &Ang, Alfredo. H-S. (Editors)

SENSOR PLACEMENT OPTIMIZATION AND RESPONSE RECONSTRUCTION FOR STRUCTURAL HEALTH MONITORING WITH LONG-GAUGE FBG STRAIN SENSORS

Zhenwei Zhou[1, 2], Chunfeng Wan[3], Chul-Woo Kim[2]

[1] *School of Civil Engineering &Architecture, East China Jiao Tong University, Nanchang 330013, People's Republic of China*

E-mail: zhouzwseu@gmail.com

[2] *Department of Civil and Earth Resources Engineering, Kyoto University, Kyoto 615-8540, Japan*

Correspondence E-mail address: kim.chuiwoo.5u@kyoto-u.ac.jp

[3] *Southeast University, Key Laboratory of Concrete and Pre-stressed Concrete Structure of Ministry of Education, Nanjing 210096, People's Republic of China*

E-mail address: wan_seu@163.com

***Abstract*:** Long-gauge fiber Bragg grating (FBG) strain sensor has been widely implemented on large-scale structures to provide real-time measurement of structural responses for evaluating their serviceability, safety, and sustainability. As a limited number of FBG sensors are installed in a large-scale structure, the safety evaluation of the whole structure is hard to assess. A new framework is presented in this study that enables the optimal placement of long-gauge FBG strain sensors on one hand and therefore reconstructs structural macro strain responses at unmeasured locations using the information from the optimally located sensors on the other hand. The procedure of sensor placement optimization, the principle for the quantity of sensor determination, and macro strain response reconstruction are briefly described. Numerical and experimental investigations of a cantilever steel beam are performed to verify the feasibility and effectiveness of the proposed method. The results show that the reconstructed macro strain response at desired locations is agreed well with those of real or measured using a limited number of FBG sensors. The proposed method has proved effective in the application of real structure and has a good potential in structural health monitoring of civil engineering.

Keywords: Optimal sensor placement, macro strain reconstruction, long-gauge FBG sensor, structural health monitoring.

Introduction

Structural health monitoring (SHM) has become an important means to evaluate performance and avoid sudden destruction of structures. A larger number of SHM systems which measure various quantities such as acceleration, velocity, displacement, and strain thus has been proposed (Barke and Chiu 2005, Ou and Li 2010). However, due to the cost of sensor deployment and also the corresponding difficulties in handling massive data, sensors are often installed only on few locations, and the number of sensors are much less than the total degrees of freedom for a large structure (Ostachowicz *et al* 2019). Therefore, a keen issue in SHM of large structures is to determine the optimal locations for monitoring so called optimal sensor placement (OSP), as well as exploiting the response reconstruction methods to accurately reconstruct the dynamic response at the unmeasured locations using the limited number of sensors.

OSP has received much attention for the main advantage of reducing the cost of the SHM system without big loss of monitoring quality. Kammer (1991) proposed a significant approach named as effective independence (EFI) that focused on the OSP for modal identification of space structures. A drawback of the EFI method is that sensor locations might be choose with less energy content leads to loss of information. To eliminate this problem, various modified EFI-based approaches are therefore presented such as the driving point residue (EFI-DPR) method (Papadopoulos and Garcia 1998) and kinetic energy-based (EFI-KE) method (Heo 1997) by means of multiplying DPR coefficient and KE weight factor, respectively. With the development of computer science and technology, intelligent algorithm-based methods have also received much attention in OSP for large-scale structures, such as the artificial bee colony algorithm (Sun and Büyüköztürk 2015), hybrid particle swarm optimization approach (Rao and Anandakumar 2007), genetic algorithms (Yi *et al* 2011, Liu *et al* 2008), and monkey algorithms (Yi *et al* 2015, Yi *et al* 2012). However, most of the existing sensor optimization methods are oriented to point sensors, such as accelerometers, displacement transducers, and conventional point strain gauges, but few to long-gauge strain sensors exist. Long-gauge fiber Bragg grating (FBG) strain sensors have the advantages of excellent accuracy, high data acquisition speed, and multiplexing performance and thus have been received attentions in structural health monitoring, damage detection, dynamic analysis of engineering structures in recent years (Zhou *et al* 2020). Therefore, developing an effective optimization method for long-gauge FBG sensor placement is urgently needed in civil engineering.

Reconstructing dynamic response from the limited number of sensors to obtain detailed information of the structural system as much as possible also has drawn wide attention. A number of approaches considering transmissibility matrix (Wang *et al* 2014), Kalman filter (Zhang and Xu 2016), Bayesian multi-task learning (Wan and Ni 2019) have been developed to reconstructing force excitation, displacement, and acceleration. As for strain response reconstruction, several reconstruction algorithms have been developed. Zhang and Wu (2019) proposed a moving-window Kalman filter for dual-type responses reconstruction, and verified validity of the proposed reconstruction method for both the strain and displacement reconstructed. Gill *et al.* (2004) presented a genetic algorithm (GA)-based method to reconstruct the Bragg grating sensor strain profiles. He *et al.* (2016) put forward an EMD-based method with intermittency criteria for strain and stress reconstruction, and the accuracy of reconstruction results has been proved through numerical and experimental studies. However, there are still some limitations and needs to be further improvement. As already mentioned, the EMD-based method for strain reconstruction is not suitable for problems with equal and closely spaced modes, while the GA-based method requires optimal parameters through trials to avoid the local best solutions. Also, the moving-window Kalman filter method relies on mode shapes of a finite element model, the unavoidable modeling error between the real structure and the numerical model will affect the reconstruction results. Therefore, developing the fast and effective structural response reconstruction method is still necessary in dynamic and static tests.

This study aims to present an effective method for sensor placement and response reconstruction based on long-gauge FBG strain sensing network to address above gap of long-gauge FBG strain sensor in structural health monitoring applications. A modified approach is proposed to determine the optimal long-gauge strain sensor layout on a structure based on the EFI algorithm, which ensures modal observability and adequate macro-strain response at the measurement location. Based on the long-gauge FBG strain sensor placement optimization, a macro-strain reconstruction method based on the interpolation of measured responses through a shape function is proposed to reconstruct unmeasured responses. Numerical investigation and experimental

verification are conducted to examine the feasibility and effectiveness of the proposed method for sensor placement and macro-strain reconstruction.

Methodology and framework

Modified EFI method

The EFI method is one of the most influential and commonly used methods for sensor placement, which ranks sensor locations to their independence of the target modal matrix (Ostachowicz *et al* 2019). The objective is to select measurement positions that make the mode shapes of interest as linearly independent as possible while containing sufficient information about the target modal responses in the measurements. Here, the modal macro-strain (MMS) is set as the target mode for long-gauge strain sensor placement optimization, and the effective independence coefficients E_{mD} of the candidate sensor can be computed as the diagonal of the following matrix:

$$E_{mD} = diag(\Phi_m[\Phi_m{}^T\Phi_m]^{-1}\Phi_m{}^T) \tag{1}$$

where Φ_m is the target MMS matrix, the subscript m represents macro-strain.

As mentioned earlier, the classical EFI may select the low signal-to-noise ratio of the locations, making subsequent analysis of the measured response difficult. To ensure the modal observability of the measurement locations, and retain the significant strain response simultaneously, the long-gauge FBG strain sensor placement method is proposed based on the FEI, which focuses on the optimal sensor placement and response reconstruction of long-gauge FBG strain sensor. Considering a linear type structure with N+1 nodes and N elements, the modal expansion of multiple-input multiple-output macro strain frequency response function (FRF) can be expressed as

$$[H_m(\omega)] = \sum_{r=1}^{N} \frac{\boldsymbol{\varphi}_{mr}\boldsymbol{\varphi}_{dr}^T}{M_r(\omega_r^2 - \omega^2 + j2\xi_r\omega_r\omega)} \tag{2}$$

in which, the subscript d represents displacement, $\boldsymbol{\varphi}_{mr}$, $\boldsymbol{\varphi}_{dr}$, ξ_r, M_r, and ω_r denote the r-th modal macro-strain, displacement mode, modal damping ratio, modal mass, and modal frequency, respectively. The above expression of FRF is the superposition of all modes, and the complete mode set is used for calculation. However, it is unrealistic to calculate or identify all modes for the actual structure. Considering the high-order mode has little effect on the low-frequency response, the first several modes are useful for estimating the FRF, which is given as

$$[H_m(\omega)] = \sum_{r=1}^{p} \frac{\boldsymbol{\varphi}_{mr}\boldsymbol{\varphi}_{dr}^T}{M_r(\omega_r^2 - \omega^2 + j2\xi_r\omega_r\omega)} \tag{3}$$

where p is the selected total number of modes.

The structural flexibility matrix is the reciprocal of the stiffness matrix. Similar to stiffness matrix, macro-strain flexibility matrix $[F^{\varepsilon}]$ is composed by strain flexibility coefficient of all nodes of the whole structure to all elements. Also, the macro-strain flexibility matrix has similar properties to the displacement FRF matrix, and the value of the matrix of macro-strain FRF at zero frequency is the macro-strain flexibility matrix of the structure (Guo 2018). Then, the

macro-strain flexibility matrix is computed from the following equation:

$$[F^{\varepsilon}]=\sum_{r=1}^{p}\frac{\varphi_{mr}\varphi_{dr}^{T}}{M_r\omega_r^2} \tag{4}$$

As the structural mass matrix is given, the *r*-th modal mass can be calculated:

$$M_r=\varphi_{dr}^{T}[M]\varphi_{dr} \tag{5}$$

The normalized displacement mode can be computed from the following:

$$\overline{\varphi}_{dr}=\frac{\varphi_{dr}}{\sqrt{M_r}} \tag{6}$$

Because the relationship between nodal displacement mode and modal macro-strain of element is an explicit linear distribution, and the modal macro-strain vector also can be divided by the same coefficient $\sqrt{M_r}$, i.e.,

$$\overline{\varphi}_{mr}=\frac{\varphi_{mr}}{\sqrt{M_r}} \tag{7}$$

Hence, the macro-strain flexibility matrix can also be written as

$$[F^{\varepsilon}]=\sum_{r=1}^{p}\frac{\overline{\varphi}_{mr}\overline{\varphi}_{dr}^{T}}{\omega_r^2} \tag{8}$$

Also, the macro-strain response of a structure under environmental excitation is directly proportional to the following formula:

$$\varepsilon\propto\sum_{r=1}^{p}\frac{\overline{\varphi}_{mr}\overline{\varphi}_{dr}^{T}}{\omega_r^2} \tag{9}$$

Thus, a modified EFI method by multiplying the weight factor of macro-strain flexibility matrix coefficient to concentrates the selected sensor locations in the high macro-strain energy content is presented, and it can be expressed as

$$EI_{mD}=diag(\Phi_m(\Phi_m^{T}\Phi_m)^{-1}\Phi_m{}^{T})\cdot diag(\Phi_m\Phi_d^{T}) \tag{10}$$

Comparing equation (10) with equation (1), we can see that the operation of the modified EFI method is the same as the classical EFI method. The main difference is that the average macro-strain amplitude of each degree of freedom is used for weighted correction when choosing the least degree of freedom (DOF) for the rank contribution of the truncated modal matrix, and the goal is to eliminate the DOF with the lowest macro-strain response. Also, it should be noted that the average macro-strain amplitude of each DOF of the structure will not change due to cyclic operation.

Evaluation criteria for determination of the number of sensors

Modal assurance criterion (MAC) is a mathematical method to evaluate the intersection angle of modal vectors, and it can be used to distinguish the linear independence of the measured modal vectors of the structure. Since modal macro-strain vectors are orthogonal, similar to MAC, strain modal assurance criteria (SMAC) can also be written as

$$SMAC_{i,j} = \frac{(\boldsymbol{\Phi}_{m,i}^T \boldsymbol{\Phi}_{m,j})^2}{(\boldsymbol{\Phi}_{m,i}^T \boldsymbol{\Phi}_{m,i})(\boldsymbol{\Phi}_{m,j}^T \boldsymbol{\Phi}_{m,j})} \tag{11}$$

where i, j denote the i-th and j-th columns of $\boldsymbol{\Phi}_m$, indicating the orders of selected modes. The off-diagonal value of the SMAC is between 0 and 1. If two modal macro-strain vectors are orthogonal, the corresponding off-diagonal element value is tending to zero, and it means there are easy to distinguish. Therefore, it is possible to minimizing the off-diagonal elements of the SMAC matrix to get the number of long-gauge FBG strain sensors in OSP.

Sensor placement aims to minimize the average value of off-diagonal elements to determine what is the number of sensors to be installed. The target is designed as

$$f = \sum_{i=1}^{s}\sum_{j=1}^{s} SMAC_{i,j} \Big/ \left[s(s-1)\right] \qquad (i \neq j) \tag{12}$$

where s is the number of rows in SMAC matrix. $SMAC_{i,j}$ denotes the value in SMAC matrix of the element at the i-th row and the j-th column. If the off-diagonal values of SMAC matrix approach to zero, the orthogonality of the modal macro-strain vectors of measured locations will be good. Thus, the smaller f is, the better effect of OSP will be.

Macro-strain response reconstruction

For a cantilever beam, the curvature at a location i can be described as Equation (13) using a second-degree polynomial, defined as

$$\kappa_i = c_2 x_i^2 + c_1 x_i + c_0 \tag{13}$$

where c_0, c_1 and c_2 are the coefficients of the curvature function that are obtained by the curvature measurements, and x denotes curvilinear abscissa of the beam. Also, the relationship between the curvature (κ), rotation (θ) and vertical displacement (w) can be written as,

$$\kappa = \frac{d\theta}{dx} = \frac{d^2 w}{dx^2} \tag{14}$$

Based on the Equation (14), the rotation can be integrated with respective to x as

$$\theta = \int \kappa dx \tag{15}$$

Combining with Equation (13), the rotation along the beam can be calculated by

$$\theta_i = \frac{c_2 x_i^3}{3} + \frac{c_1 x_i^2}{2} + c_0 x_i + \beta \tag{16}$$

where β is an integration constant, and it can be determined using the boundary condition. For the cantilever beam, θ_0=0 at the fixed-end, and then β=0 .

Assuming the beam has n elements and n+1 nodes, its macro-strain, the average strain within the m element with the length of L_m is given as (Zhou *et al* 2019)

$$\varepsilon_m = \frac{h}{L_m}(\theta_q - \theta_o) \tag{17}$$

where h is the distance between the sensor and the beam's neutral axis, θ_0 and θ_q are the rotations of nodes o and q. Thus, it can be concluded from the above derivation that the shape function of the macro strain along the beam is a cubic function with the location x, and can be defined as

$$\varepsilon_m(x) = ax^3 + bx^2 + cx + d \tag{18}$$

Thus, a macro-strain reconstruction method is proposed based on the interpolation of available macro-strain responses using a cubic spline shape function. The measurement elements are seen as the interpolation points along the x axis. At any time t, consider the measured macro-strain responses of four locations $x_{i\text{-}1}$, x_{i+1}, x_{i+2} and x_{i+3} are $\varepsilon_{test}(t, x_{i-1})$, $\varepsilon_{test}(t, x_{i+1})$, $\varepsilon_{test}(t, x_{i+2})$ and $\varepsilon_{test}(t, x_{i+3})$, respectively, and are described as

$$\begin{aligned}
\varepsilon_{test}(t, x_{i-1}) &= \frac{a(t)x_{i-1}^3}{3} + \frac{b(t)x_{i-1}^2}{2} + c(t)x_{i-1} + d \\
\varepsilon_{test}(t, x_{i+1}) &= \frac{a(t)x_{i+1}^3}{3} + \frac{b(t)x_{i+1}^2}{2} + c(t)x_{i+1} + d \\
\varepsilon_{test}(t, x_{i+2}) &= \frac{a(t)x_{i+2}^3}{3} + \frac{b(t)x_{i+2}^2}{2} + c(t)x_{i+2} + d \\
\varepsilon_{test}(t, x_{i+3}) &= \frac{a(t)x_{i+3}^3}{3} + \frac{b(t)x_{i+3}^2}{2} + c(t)x_{i+3} + d
\end{aligned} \tag{19}$$

In case of four equations with four unknowns, the polynomial can be solved. Thus, if the number of measured elements is greater than the number of unknown parameters, the unique cubic spline at time t can be estimated, as well as the macro-strain response at location x_i can be reconstructed. The further information on cubic spline–based interpolation is referred to McKinley and Levine (1998).

Numerical study

A cantilever beam is used to validated the proposed method. Fig. 1 shows the cantilever beam is divided into 9 consistent elements and 10 nodes, and mechanical properties are presented in Table 1. Each element has a stiffness matrix with 4×4 DOFs, that is, two rotations and two

displacements. The first three modes were selected as the target modes for sensor placement optimization, and nine elements were considered as the candidate locations to placement.

Table 1. Mechanical properties of the cantilever beam.

Beam length	Cross-sectional area	Young's modulus	Density	Poisson's ratio
1.8 m	0.08×0.005 m^2	210 GPa	7850 kg/m^3	0.3

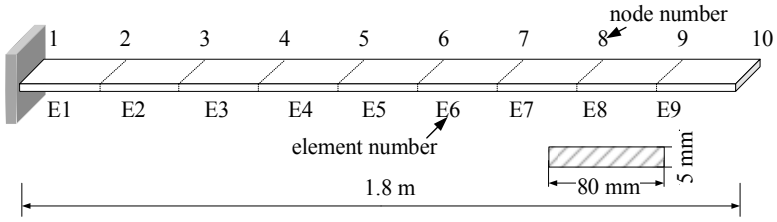

Figure 1. The diagram of the cantilever steel beam.

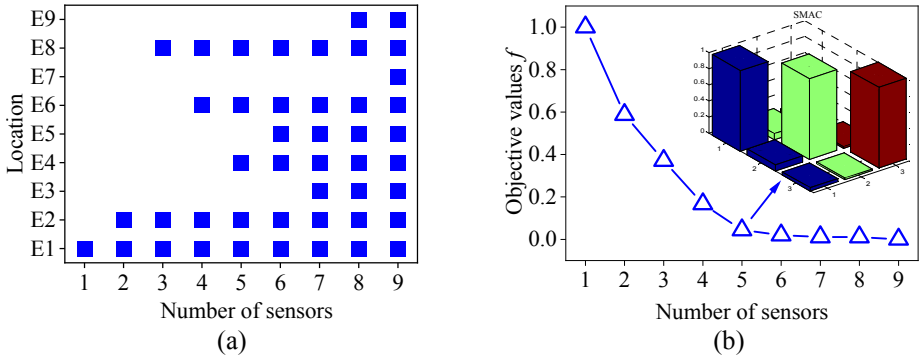

Figure 2. Optimal long-gauge FBG strain sensor placement: (a) optimal from one-to-nine long-gauge sensor locations of 9-element cantilever beam, (b) number of sensors based on the Equation (12).

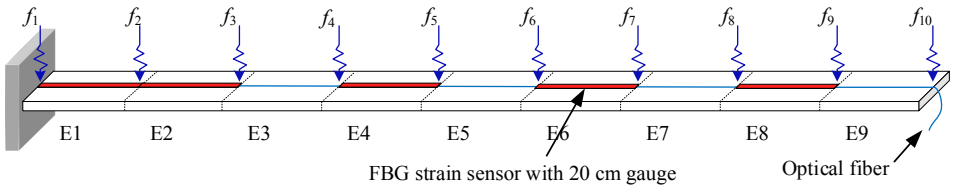

Figure 3. Sensor placement for structural macro strain monitoring under ambient excitation.

Long-gauge FBG strain sensor placement optimization

The operational parameters include the candidate locations for the long-gauge strain sensor placement and the available number of sensors. It is expected to ensure the modal observability of the structure while minimizing the number of sensors simultaneously. The optimal placement of one-to-nine long-gauge sensors is solved by the proposed OSP method, and the results are presented in Fig. 2(a). Subsequently, the corresponding objective results of the OSP method are given, as shown in Fig. 2(b). It can be seen that the value of the objective function decreases with the increase of the number of sensors increases, and the objective value *f* shows little change after the number of sensors reaches five. The SMAC with five sensors of the OSP method is also plotted in Fig. 2(b). It is clear that all the off-diagonal values are minimal. Thus, the performance of the OSP method for the cantilever beam is examined by considering five sensors.

The proposed OSP method to place the optimal number of long-gauge FBG strain sensors in the proper locations to monitor the cantilever beam under the random excitation is illustrated in Fig. 3, and a set of random load time histories with a time interval of 0.01s is vertically applied to ten nodes of the FE model. Macro-strains computed from five long-gauge strain sensors are taken as "measured", E3, E5, E7, and E9 elements were left for macro-strain response reconstruction.

Macro-strain reconstruction

The macro-strain responses of the beam were calculated and regarded as the actual responses. Besides, macro strain responses of the selected five long-gauge sensors were applied to reconstruct the macro-strain at the elements without long-gauge sensor deployment. Fig. 4(a) shows the reconstructed and real macro-strain responses at elements E3, E5, E7, and E9, respectively. It can be clearly seen that the reconstructed macro-strain follows the same trend as the real value. Furthermore, the relative error is introduced to describe the error between the reconstructed and measured response, as plotted in Fig. 4(b). The results show that the reconstructed macro-strain responses match quite well with the actual responses, as the maximum relative error was less than 0.5 με. However, this is the macro-strain response reconstruction under ideal conditions, and environmental noise is inevitable in real applications. The validity of the proposed method needs further investigation.

Experimental verification

Experiment outline

A laboratory experiment was performed to assess the practicability and effectiveness of the proposed OSP method for long-gauge FBG strain sensor optimal placement and structural response reconstruction using a cantilever steel beam. The sizes and material characteristics of the experimental cantilever beam are the same as those of the numerical example; that is, the number and optimal placements of FBG sensors in the experiment are also the same as those of the numerical study.

Fig. 5(a) shows a package FBG strain sensor with a 20 cm gauge length, and long-gauge sensors in series on a single fiber to realize a quasi-distributed sensing system for monitoring the macro-strains of each element. Fig. 5(b) shows the overview of the experimental setup, in which, the blower fan generated the stochastic wind loads to simulate the random vibration applied to

the cantilever steel beam. The optical sensing interrogator SM230 (in Fig. 5(c)), which provides simultaneous, static, and dynamic interrogation of hundreds of fiber optic sensors, were employed to synchronous collect the macro-strain from the long-gauge FBG sensors.

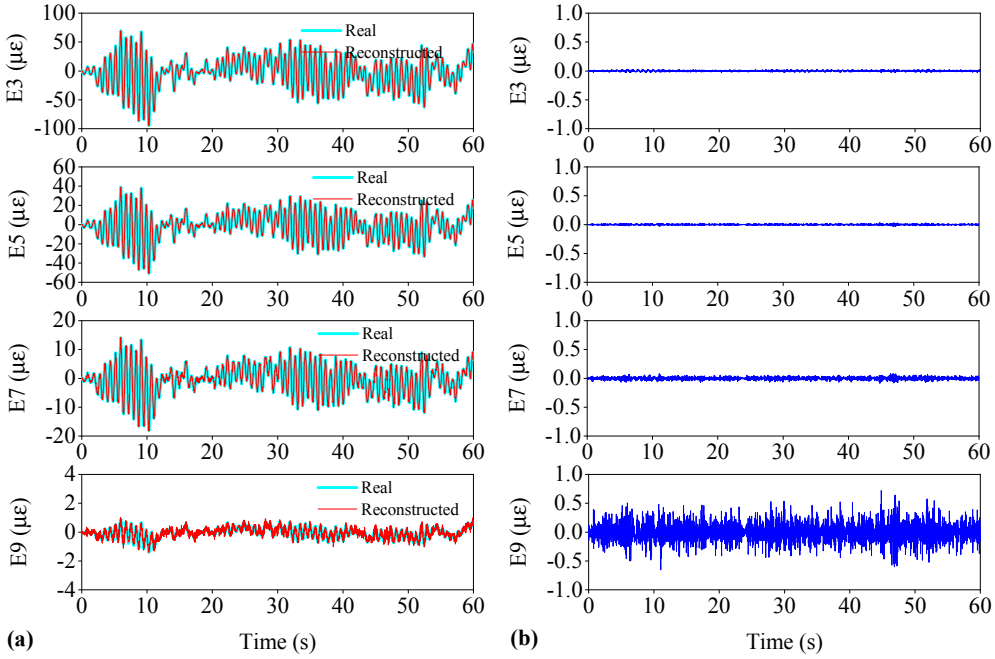

Figure 4. Comparison of real and constructed macro strain response time-histories: (a) macro-strain at element E3, E5, E7, and E9; (b) corresponding relative errors of macro-strain at element E3, E5, E7, and E9.

Figure 5. Components of the dynamic experiment under ambient excitations: (a) a single FBG strain sensor with 20 cm gauge; (b) overview of the experiment; (c) data acquisition devices.

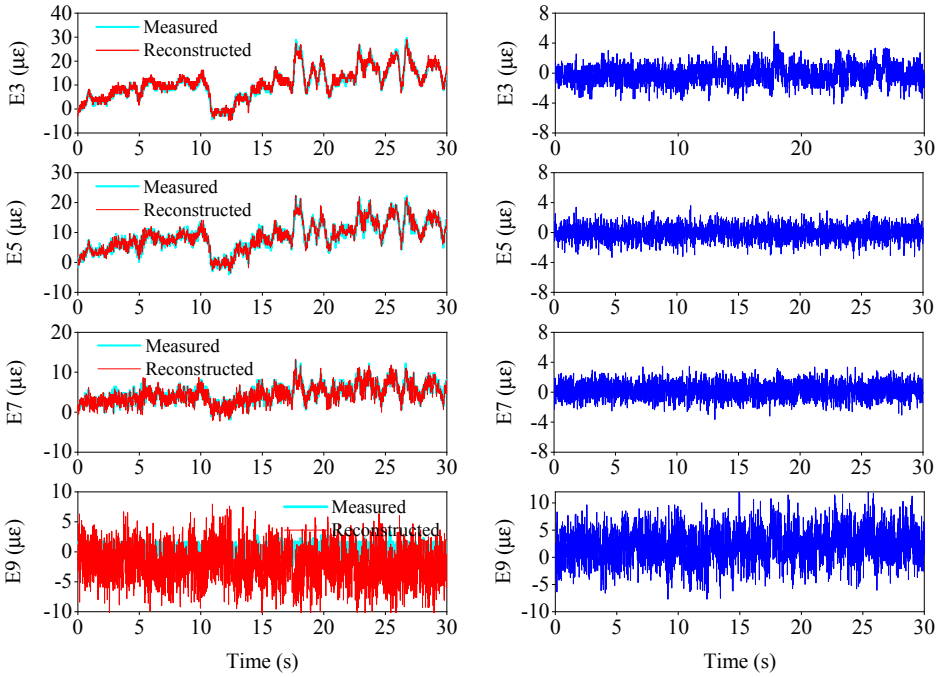

Figure 6. Comparison of measured and reconstructed macro-strain response from dynamic experiment: (a) macro-strain at element E3, E5, E7, and E9, respectively; (b) the corresponding relative errors of macro-strain at element E3, E5, E7, and E9, respectively.

Results and discussions

Fig. 6(a) compares the measured and reconstructed macro-strain response, and the relative errors are shown in Fig. 6(b). It can be seen that the reconstructed and measured response from the dynamic test exhibits good agreement at elements E3, E5, and E7. Despite the relative errors of E3 being close to 4 με at some points, the tendency of reconstructed macro-strain is consistent with the measured value, and their peak values are also close. The macro-strain reconstruction is a high-precision interpolation method that does not eliminate the influence of environmental noise on the reconstruction, and this is one of the factors affecting the accuracy of the reconstruction in the real application. Moreover, it should be noted that the reconstructed macro-strain at element E9 significantly deviated from the corresponding measured macro-strains. These results can be attributed to two main reasons: one is the macro-strain of E9 submerged in environmental noise; the other is FBG sensor measurement error is ±1 με, which is hard to measure such a low strain response accurately. Overall, it can be observed that the proposed method does not require a network of closely-spaced long-gauge FBG sensors for the whole structural measurement, and a limited number of sensors become sufficient for the whole structural macro-strain monitoring.

Conclusions

An effective approach for sensor placement and multi-type response reconstruction based on long-gauge FBG strain sensor is presented and validated. A modified sensor placement method has been adopted to determine the optimal sensor layout on a structure based on the EFI

algorithm, which provides adequate dynamic macro-strain information of the structure with a limited number of sensors. The macro-strain response reconstruction method depends only on the measured response and can rapidly reconstruct dynamic macro strains without any mathematical models. Numerical studies and experimental investigations with a cantilever steel beam were conducted to examine the effectiveness and feasibility of the proposed method for long-gauge FBG strain sensor placement and multi-type response reconstruction. For an actual application, the proposed approach's reliability needs to be studied by a more complex and large-scale structure in future work.

Acknowledgments

This paper is supported by Natural Science Foundation of Jiangxi Province (Grant No. 20212BAB204010), which is greatly appreciated.

References

Barke D and Chiu WK. Structural health monitoring in the railway industry: a review. *Struct Health Monit* 2005; 4: 81-93.

Gill A, Peters K and Studer M. Genetic algorithm for the reconstruction of Bragg grating sensor strain profiles. *Meas Sci Technol* 2004; 15: 1877-1884.

Guo S. Structural flexibility identification through impact testing. Master thesis, Southeast University, Nanjing.

Heo G, Wang ML and Satpathi D. Optimal transducer placement for health monitoring of long span bridge. *Soil Dyn Earthq Eng* 1997; 16: 495-502.

Kammer DC. Sensor placement for on-orbit modal identification and correlation of large space structures. *J Guid Control Dynam* 1991; 14: 251-259.

Liu W, Gao WC, Sun Y, et al. Optimal sensor placement for spatial lattice structure based on genetic algorithms. *J Sound Vib* 2008; 317: 175-189.

McKinley S and Levine M. Cubic spline interpolation. *College of the Redwoods* 1998; 45:1049-1060.

Ostachowicz W, Soman R and Malinowski P. Optimization of sensor placement for structural health monitoring: A review. *Struct Health Monit* 2019; 18: 963-988.

Ou JP and Li H. Structural health monitoring in mainland China: review and future trends. *Struct Health Monit* 2010; 9: 219-231.

Papadopoulos M and Garcia E. Sensor placement methodologies for dynamic testing. *AIAA J* 1998; 36: 256-263.

Rao ARM and Anandakumar G. Optimal placement of sensors for structural system identification and health monitoring using a hybrid swarm intelligence technique. *Smart Mater Struct* 2007; 16: 2658-2672.

Sun H and Büyüköztürk O. Optimal sensor placement in structural health monitoring using discrete optimization. *Smart Mater Struct* 2015; 24: 125034.

Wang J, Law SS and Yang QS. Sensor placement method for dynamic response reconstruction. *J Sound Vib* 2014; 333: 2469-2482.

Wan HP and Ni YQ. Bayesian multi-task learning methodology for reconstruction of structural health monitoring data. *Struct Health Monit* 2019; 18: 1282-1309.

Yi TH, Li HN and Gu M. Optimal sensor placement for structural health monitoring based on multiple optimization strategies. *Struct Des Tall Spec* 2011; 20: 881-900.

Yi TH, Li HN and Zhang XD. Health monitoring sensor placement optimization for Canton Tower using immune monkey algorithm. *Struct Control Hlth* 2015; 22: 123-138.

Yi TH, Li HN and Zhang XD. Sensor placement on Canton Tower for health monitoring using

asynchronous-climb monkey algorithm. *Smart Mater Struct* 2012; 21: 125023.

Zhang CD and Xu YL. Optimal multi-type sensor placement for response and excitation reconstruction. *J Sound Vib* 2016; 360: 112-128.

Zhang XH and Wu ZB. Dual-Type Structural Response Reconstruction Based on Moving-Window Kalman Filter with Unknown Measurement Noise. *J Aerospace Eng* 2019; 32: 04019029.

Zhou ZW, Wan CF, Fang D, et al. Quasi-static macrostrain-based structural damage detection with distributed long-gauge fiber Bragg grating sensing. *J Intel Mat Syst Str* 2020; 31: 2137-2151.

Zhou ZW, Wan CF, Wen B, et al. Structural damage detection with distributed long-gauge FBG sensors under multi-point excitations. *Smart Mater Struct* 2019, 28: 095023.

International Symposium on Emerging Developments and Innovative Applications of Reliability Engineering and Risk Managements (EDIARR2022),30 October-3 November2022, Taipei
Chen, S. S. &Ang, Alfredo. H-S. (Editors)

NUMERICAL STUDY OF DAMAGE DETECTION OF A TRUSS BRIDGE USING PSEUDO LOCAL FLEXIBILITY METHOD

T.Y. Hsu [1], M.C. Lu [1],S.Y. Shiao [2], C.W. Kim [3], K.C. Chang [3]

[1] *Department of Civil and Construction Engineering, National Taiwan University of Science and Technology, Taipei, Taiwan*

E-mail:tyhsu@ntust.edu.tw

[2] *National Center for Research on Earthquake Engineering, Taipei, Taiwan*

[3] *Department of Civil and Earth Resources Engineering, Graduate School of Engineering, Kyoto University, Kyoto, Japan*

***Abstract*:** The virtual forces of the original local flexibility method are restricted to inducing stress on the local parts of a structure. To circumvent this restriction, we developed pseudo local flexibility (PLFM) method that can successfully detect damage to hyperstatic beam structures using fewer modes. In this study, the feasibility to detect damage of a truss bridge using PLFM using a numerical bridge model is discussed. A numerical model of a real truss bridge is constructed with 5 different damage cases. This preliminary case study is the first step to employ PLFM to a real bridge. A promising results of damage localization using the first three modes of the bridge are obtained in this study.

Keywords: pseudo local flexible method, virtual strain energy, bridge structure, damage detected

Introduction

Bridge structures are widely used as important structures, hence structural condition assessments of in-service bridge structures play a critical role, especially for old bridges. In recent years, the research community has paid particular attention to vibration-based structural damage detection techniques that can be used to perform damage diagnosis based on modal parameters.

Reynders & De Roeck (2010) recently developed the local flexibility method (LFM) to determine not only the damage location but also the severity of damage sustained. The general procedure of the LFM involves using flexibility matrices and designated virtual forces that generate locally restricted stress fields in the structure to localize and quantify damage. The structural modal parameters identified from the ambient vibration signals both before and after damage can be used to construct the flexibility matrices, and are key data for the LFM. Thus, the LFM does not require a finite element model of the structure. The general theory of the LFM has been applied to beam structures for damage detection, and few modes are typically necessary.

Especially for simple cases such as those involving a simply supported beam, there are conditions where the first mode alone suffices. However, for a hyperstatic beam or other, more complex structures, the number of modes required for damage estimation can increase significantly. This reduces the feasibility of the LFM because, in practice, only the first few modes can be identified accurately using ambient vibration signals. Moreover, application of the LFM to other structures has not been achieved, mainly because of the difficulty in identifying virtual forces guaranteed to limit the existence of the induced stress to the local region of another structure.

Hsu et al. (2014) developed the pseudo local flexibility method (PLFM), which successfully detects damage to hyperstatic beam structures using fewer modes. The PLFM eliminates the limitation of virtual forces inducing stress only to the local part of a structure, as is the case with the LFM. In this manner, the non-local virtual forces that generate concentrated stresses in a local part, and relatively small stresses in other parts of a structure, can be employed. Most importantly, removing this limitation enables the identification of suitable virtual forces for bridge structures.

In this study, we study the feasibility to detect damage of a truss bridge using PLFM using a numerical bridge model. A numerical model of a real truss bridge is constructed with different damage cases. This preliminary case study is the first step to employ PLFM to a real bridge.

Numerical Study

The target bridge

The target bridge constructed in 1959 was already studied by Chang & Kim (2016). It is a simply-supported through-type steel Warren truss bridge. The span length, maximum height, and width of the bridge is 59.2 m, 8.2 m, and 3.6 m, respectively.

Bridge model

Because this paper is merely a preliminary study, we focus on the change of modal properties, which will be used for the PLFM. Hence, only a simplified bridge model with main components but without secondary components is constructed using SAP2000 software. As a result, without loss of generality, the feasibility of employing PLFM to detect damage of the Warren truss bridge can be studied even though the modal properties are not identical to the measured ones.
The bridge model and the measurement points are shown in Figure 1. It is assumed only the vertical responses of these points are measured as was done in the filed tests. We consider five damage cases. The cross section of the vertical component at A3 is reduced to 0.1%, 0.5%, and 1% for the first three damage cases, as shown in Figure 2, to understand the effects of damage extent. The cross section of the vertical component at A7 is reduced to 0.1% for the fourth damage case, as shown in Figure 3; while the one at A4 is reduced to 0.1% for the fifth damage case, as shown in Figure 4. The modal shapes of the first three bending modes when the bridge is intact and damaged are shown in Figure 5 to 7. The natural frequencies of these modes of the intact and damaged bridge models are listed in Table 1. Damage detection will be conducted using these modal parameters.

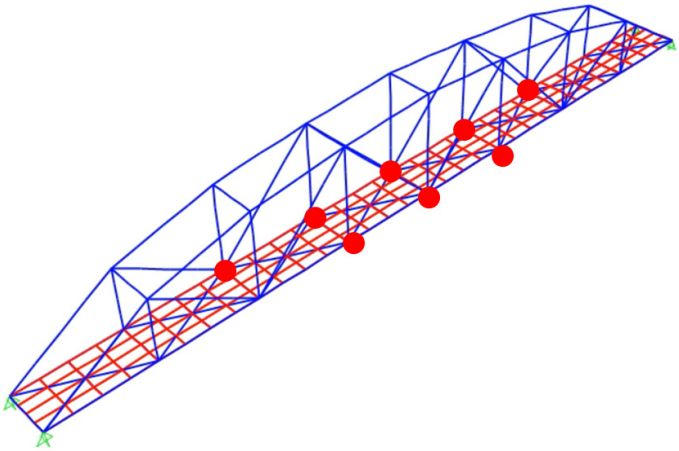

Figure 1. The FE model of the target bridge and layout of measurement points (in red points).

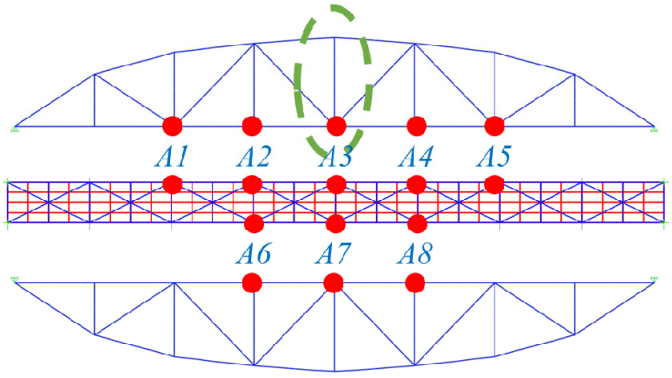

Figure 2. Damage location of the first three damage cases.

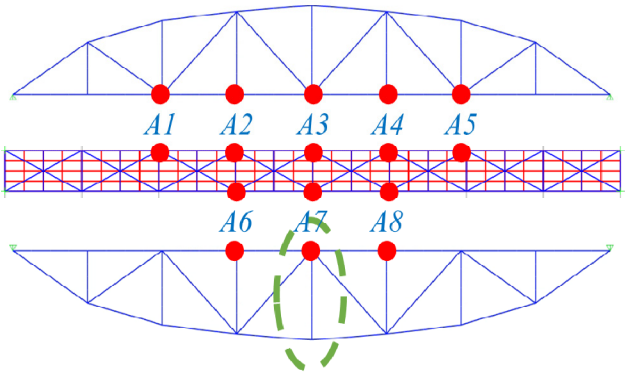

Figure 3. Damage location of the fourth damage case.

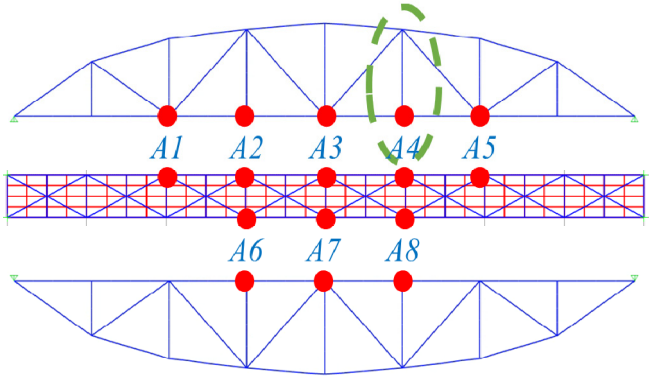

Figure 4. Damage location of the fifth damage case.

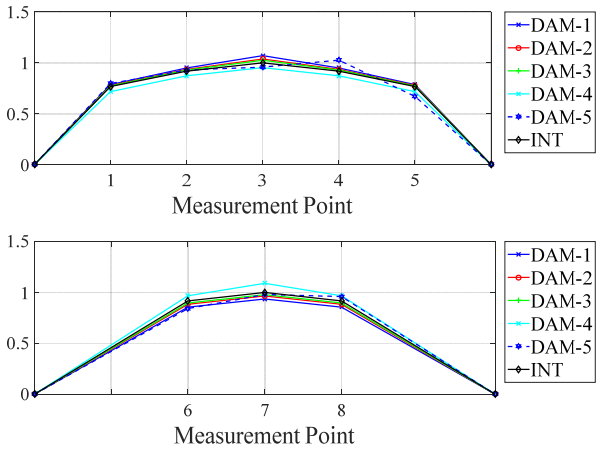

Figure 5. The first bending mode shape.

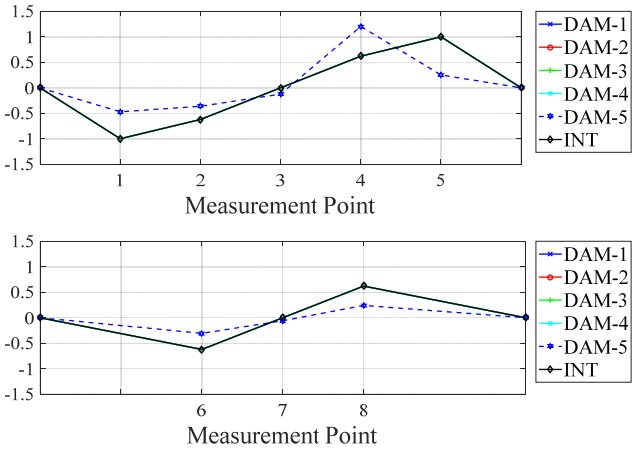

Figure 6. The second bending mode shape.

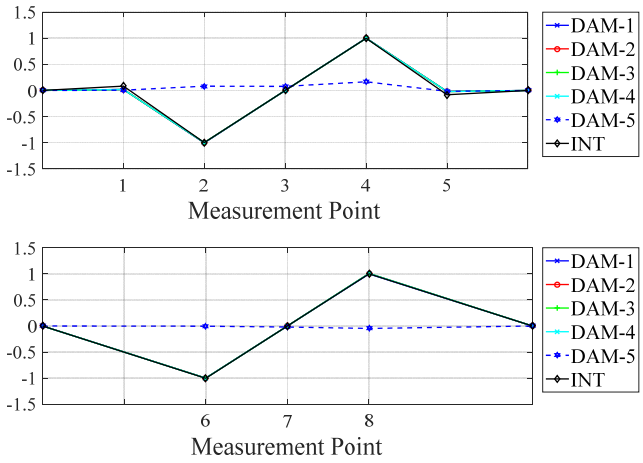

Figure 7. The third bending mode shape.

Table 1. Natural frequencies.

Case	*Damage Location*	*Cross-Section Area (%)*	*Modal Frequency (Hz)*		
			1	*2*	*3*
INT	-	100.00	4.44	10.28	14.47
DAM-1	A3	0.10	4.37	10.22	13.75
DAM-2	A3	0.50	4.42	10.22	13.75
DAM-3	A3	1.00	4.45	10.22	13.75
DAM-4	A7	0.10	4.37	10.22	13.75
DAM-5	A4	0.10	4.45	9.58	13.76

Plfm

The PLFM considers a structure with volume $\boldsymbol{\Omega}$ and boundary $\boldsymbol{\Gamma}$ that is subjected to the Dirichlet boundary conditions along part of the boundary. A first load configuration $\boldsymbol{f}^1$ is applied at a limited number of *r* DOFs where the response can be measured. The first load configuration for the PLFM is chosen such that the induced stress field $\boldsymbol{\sigma}^1$ consists of concentrated stresses in the local volume $\boldsymbol{\Omega}_p$ and also a small stress outside $\boldsymbol{\Omega}_p$. Note that $\boldsymbol{f}^1$ is assumed to only cause non-zero stress within $\boldsymbol{\Omega}_p$ for the LFM. Based on the virtual work principle with the body force neglected:

$$\int_\Gamma \mathbf{t}^T \delta\mathbf{x} d\Gamma = \int_\Omega \boldsymbol{\sigma}^T \delta\boldsymbol{\varepsilon} d\Omega \tag{1}$$

where $\boldsymbol{t}$ is the vector with applied tractions, $\boldsymbol{\sigma}$ is the corresponding stress vector, $\boldsymbol{\delta x}$ is a virtual displacement field that obeys the Dirichlet boundary conditions, and $\boldsymbol{\delta\varepsilon}$ is the corresponding virtual strain vector. Based on the assumption that the stresses due to both the first load configuration $\boldsymbol{f}^1$ and the second load configuration $\boldsymbol{f}^2$ are concentrated within the local volume $\boldsymbol{\Omega}_p$, and the stresses outside the local volume are small, Eq. (1) can be derived to obtain a general

equation of the PLFM to estimate the stiffness ratio within the local volume, denoted as R: (Hsu et al., 2014)

$$\frac{\sum_{j=1}^{r} f_j^2 x_j^1}{\sum_{j=1}^{r} f_j^2 x_{jd}^1} \cong \frac{K_p + \Delta K_p}{K_p} \equiv R \tag{2}$$

where subscript j represents the *j-th* DOF, superscript 1 and 2 represent the number of load configuration. For instance, x^1_j is the displacement at DOF j corresponding to the first load configuration; K_p and ΔK_p represents the stiffness and change of stiffness in the local volume $\boldsymbol{\Omega}_p$, respectively; and the subscript d indicates that the stucture is in damage state. The virtual displacement vector $\boldsymbol{x^1}$ under the first load configuration $\boldsymbol{f^1}$ can be obtained using the following equation:

$$\mathbf{x}^1 = \mathbf{H}\mathbf{f}^1 \tag{3}$$

where $\boldsymbol{H}$ is the flexibility matrix. With the assumption of lumped and approximately equally distributed mass, the flexibility matrix can also be estimated using the identified unscaled modal parameters as (Reynders & De Roeck, 2010)

$$\mathbf{H} \cong \mathbf{H}^n = -\boldsymbol{\Phi}\boldsymbol{\Lambda}_c^{-1}(\boldsymbol{\Lambda}_c^{H}\boldsymbol{\Phi}^{H}\boldsymbol{\Phi}\boldsymbol{\Lambda}_c + \boldsymbol{\Phi}^{H}\boldsymbol{\Phi})^{-1}\boldsymbol{\Lambda}_c^{H}\boldsymbol{\Phi}^{H} \tag{4}$$

where $\boldsymbol{\Phi}$ is the matrix of mode shapes, $\boldsymbol{\Lambda}_c$ is the diagonal matrix of system poles, and the superscript H is the Hermitian transpose. If only the first n modes are available, then the flexibility matrix is truncated, and denoted as $\boldsymbol{H^n}$. The typical virtual load configuration for location A7 is shown in Figure 8 (left). The stress caused by this virtual load configuration mainly concentrates within the structural elements between measurement point 6 and 8 as shown in Figure 8 (right). Similar virtual load configurations will be applied at different measurement points to detect the change of stiffness of the elements around the measurement points.

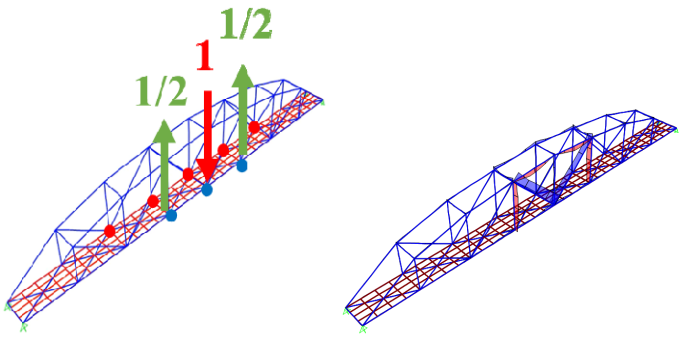

Figure 8. The typical virtual load configuration for location A7 (left) and the distribution of resulting stress (right).

Results

The stiffness ratios of different locations obtained using the three modes of five different damage cases are shown in Figure 9 to 13. The stiffness ratios "R" calculated using Eq. (2) represent the

average stiffness ratio within the region of stress due to the virtual load configuration applied at different locations. For the first three damage cases, using the first mode (PLFM-NM-1 curve in corresponding figures) is enough to detect the location of the damage at A3 as it shows a stiffness ratio *R* smaller than 1. But in order to have less error of the other locations, it is required to use the first three modes together, as indicated by PLFM-NF-3 curve that *R* values are close to 1 for measurement points at non-damaged members (A1, A2, A4 and A5). Similarly, for the fourth damage case, using the first mode is enough to detect the location of the damage at A7. But in order to have less error of the other locations, it is required to use the first three modes together. It seems that the change of the stiffness ratios due to the fifth damage case is much larger than the one due to the other damage cases. However, if only the first mode is used, large error of stiffness ratios is obtained. At least two modes are required to obtain the stiffness ratio with acceptable error.

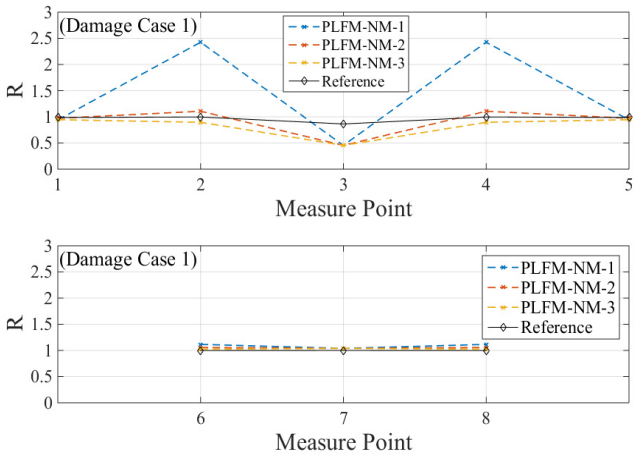

Figure 9. Stiffness ratio of the first damage case.

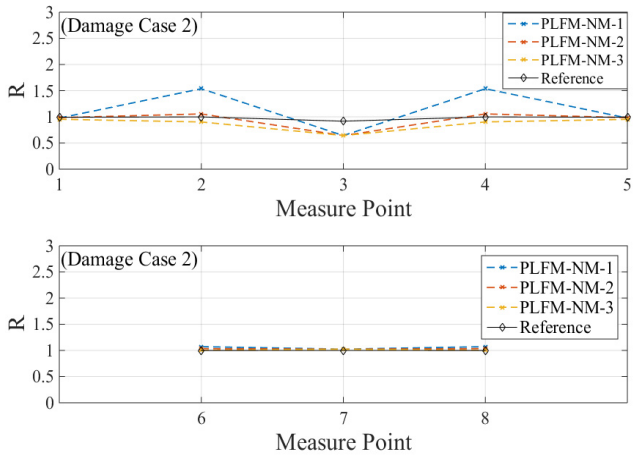

Figure 10. Stiffness ratio of the second damage case.

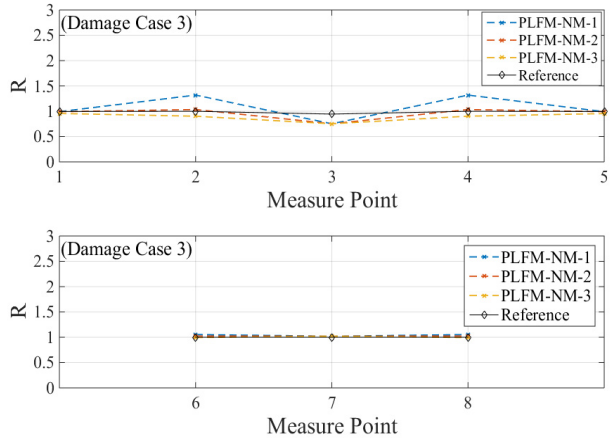

Figure 11. Stiffness ratio of the third damage case.

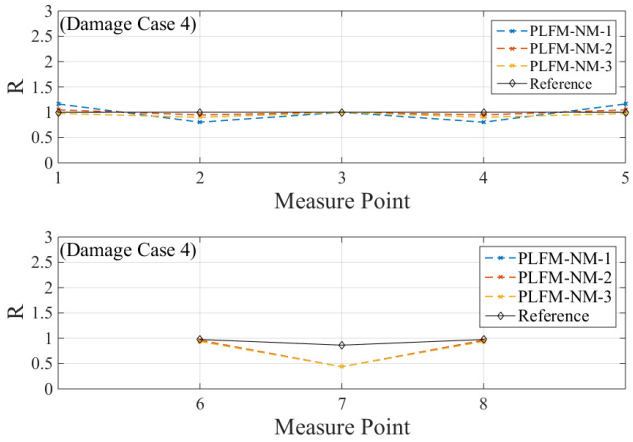

Figure 12. Stiffness ratio of the fourth damage case.

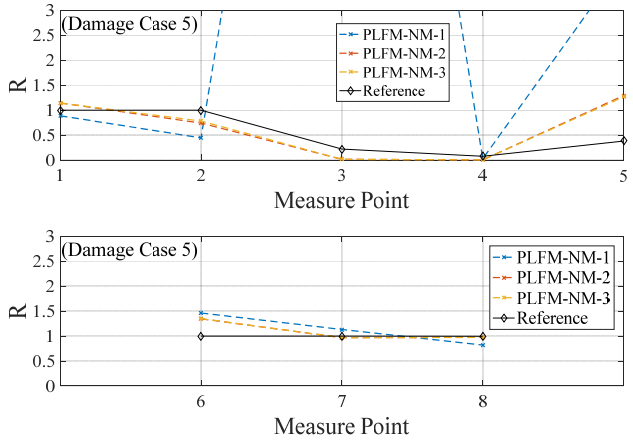

Figure 13. Stiffness ratio of the fifth damage case.

Conclusion

In this study, the feasibility of using PLFM to detect damage of a truss bridge is studied. Based on the results of the numerical study, the damage locations could be identified using the first three modes. Note that perfect modal parameters without noise and measurement error are used in this study. Further study is required to understand the feasibility of employing PLFM to detect damage of a real truss bridge.

Reference

Reynders E, De Roeck G. A Local Flexibility Method for Vibration-based Damage Localization and Quantification. *Journal of Sound and Vibration* 2010; 329(12): 2367-2383.

Hsu TY, Shiao SY, Liao WI. (2015), "A pseudo local flexibility algorithm for vibration-based damage detection of hyperstatic beams", *Journal of Structural Control & Health Monitoring*, 22:682–693.

Chang KC and Kim CW. Modal-parameter identification and vibration-based damage detection of a damaged steel truss bridge. *Eng Struct* 2016; 122: 156–173

International Symposium on Emerging Developments and Innovative Applications of Reliability Engineering and Risk Managements (EDIARR2022),30 October-3 November2022, Taipei
Chen, S. S. &Ang, Alfredo. H-S. (Editors)

RESEARCH AND DEVELOPMENT OF SLOPE ROLLING-TYPE SEISMIC ISOLATORS COMBINED WITH INERTER

Ting-Yu Hsu[1],Cheng-Teng Lee[2]

[1]*Department of Civil and Construction Engineering, National Taiwan University of Science and Technology, No. 43, Sec. 4, Keelung Rd., Taipei 106335, Taiwan*

[2]*Department of Civil and Construction Engineering, National Taiwan University of Science and Technology, No. 43, Sec. 4, Keelung Rd., Taipei 106335, Taiwan*

Abstract: The sloping rolling-type isolators (SRI) can make the extreme value of the uploaded acceleration value not increase with the earthquake intensity, and has no natural vibration frequency, so it is not easy to have a resonance reaction with the input disturbance. However, previous studies have found that the design displacement may be exceeded when the peak ground velocity (PGV) is large. In order to reduce the displacement response of SRI in earthquakes with large PGV, this study uses the inerter force related to relative acceleration to reduce the relative displacement. In order to be able to combine the best combination of inerter force and damping force, compare its performance index with SRI to obtain a better combination. From the simulation results, it can be seen that under the same number of earthquakes exceeding the displacement response limit, the acceleration response ratio (R) of 86.95 is better than that of the SRI under the earthquake with a smaller PGV.

***Keywords*:** slope rolling-type seismic isolators; passive control; inerter;PGV; Performance Testing;

Introduce

Up to now, the principle of earthquake-resistant design, in addition to considering the safety of users' living and life, must also consider the economic considerations of the cost of repair and operation of the important instruments and equipment in the building after the earthquake, and derived from its concept. Design for performance. The more effective and economical method is to use seismic isolation bearings on important equipment, while SRI is a metal rolling bearing often used on equipment, and its characteristic is that the upload acceleration can maintain a constant value, which can easily meet the performance design. However, when the SRI is subjected to earthquakes with different characteristics, the variability of its maximum isolation displacement is quite high, and when the isolation system is subjected to an earthquake with a larger PGV, a larger isolation displacement response will occur. In order to suppress the maximum displacement response, the most of them will add additional friction damping, and this study designs an inerter mechanism and applies inerter force [1] related to relative acceleration on SRI and compares the response difference of traditional SRI.

The establishment of inerter combined with SRI

The rack, gearbox and flywheel are used to establish the inertial mass device as shown in Figure 1. The four harmonic equations found based on the geometric motion are shown in Figure 2 [2]. The inertial device is connected to the ground surface and the upper plate of the SRI. When the ground is disturbed, the upper plate will drive the rack and drive the inerter mechanism to generate inerter force that inhibits the upper plate. The whole set of seismic isolation system is referred to as iSRI for short. Since its inerter force is applied to the upper plate, it is necessary to change the horizontal

dynamic equation of the formula of SRI in the derivation equation, as shown in Equation (1), ,where F_D is the friction damping force、N_1 is the contact force between the upper plate and the roller in the normal direction、f1 is the contact force between the upper plate and the tangential direction of the roller、M is the total mass of the upper plate、 θ_1 and θ_2 is the angle of the upper and lower slopes、 $\ddot{x}_g$ is the horizontal disturbance、b is the inerter coefficient (Inertance)、 $\ddot{x}_1$ is the relative acceleration.

$$\sum F_x = -F_D \cos\theta_1 \operatorname{sgn}(\dot{x}_1) - N_1 \sin\theta_1 \operatorname{sgn}(x_1) - f_1 \cos\theta_1 \operatorname{sgn}(\dot{x}_1) = M(\ddot{x}_1 + \ddot{x}_g) + b\ddot{x}_1 \qquad (1)$$

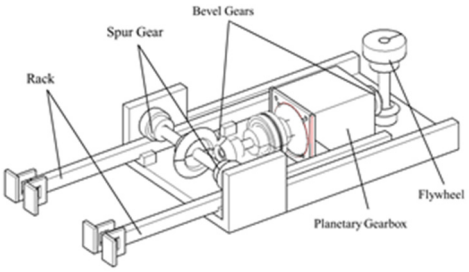

Figure 1. Inerter mechanism

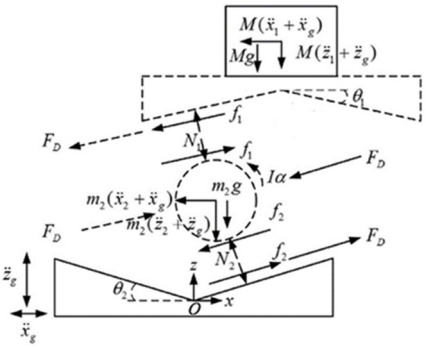

Figure 2. Simplified Analysis Model Schematic of SRI

The absolute acceleration of iSRI is mainly related to friction damping, upper and lower plate angle and external force excitation, while friction damping and upper and lower plate slope angle are fixed values, as shown in Eq. (2). But because the external force excitation is not a constant value, the absolute acceleration of iSRI is not a constant value. When the inertance is larger, the influence of the external force excitation on the absolute acceleration is larger.

$$\ddot{x}_1 + \ddot{x}_g = \frac{-(\cos\theta_1 + \cos\theta_2)}{4(M+b)}[2F_D \operatorname{sgn}(\dot{x}_1) + Mg(\sin\theta_1 + \sin\theta_2)\operatorname{sgn}(x_1)] + \frac{b}{(M+b)}\ddot{x}_g \qquad (2)$$

In this study, two dimensionless parameters are used as design parameters, the first is the damping factor (C), which is the ratio of the damping force (F_D) to the total weight (W), and the other is the inerter ratio (μ_b) is the ratio of the inertance (b) to the mass (M), and its formula is as follows.

$$C = \frac{F_D}{W} \qquad (3)$$

$$\mu_b = \frac{b}{M} \qquad (4)$$

Seismic data

The seismic data of TSMIP magnitude 5 (80gal) or above from 1992 to 2017 is used, referred to as T-80data, with a total of 3181 records, and the PGA is between 1113 and 80gal and the PGV is between 285.9 and 0.6cm /sec. The minimum damping factor range discussed in this study is 0.01,

and in order to ensure that the group that does not exceed the design displacement can be classified, the minimum damping factor of 0.01 is applied by SRI as the condition, and Figure 3 is the maximum displacement of PGV and SRI. The relationship diagram, the red dotted line above is the earthquake that exceeds the design displacement by 20cm, the blue dotted line is the earthquake that exceeds the design displacement, and the earthquake with the smallest PGV is taken as the threshold value (20.7cm/sec). Earthquakes with PGV greater than the threshold are classified into Group-1, with a total of 402 earthquakes.

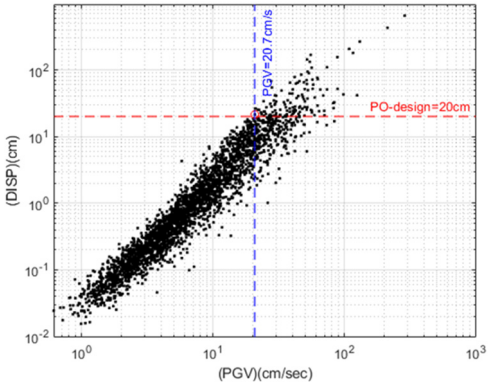

Figure 3. PGV and SRI maximum displacement relationship

Simulation analysis

In order to investigate the seismic response of iSRI under different μ_b and C, this study used the number of earthquakes with a maximum displacement response exceeding 20 cm (Pounding occurred, referred to as PO) as an important parameter to investigate the displacement response of iSRI and SRI. In order to compare the acceleration performance of iSRI and SRI, it is necessary to have the same displacement condition as the threshold, so the same number of POs is used as the comparison standard, and the performance index results of iSRI and SRI under Group-1 and Group-2 will be discussed later. In order to compare the acceleration response of iSRI with the same allowable PO number as SRI but with different combinations, the performance indicators acceleration response ratio R and effective isolation ratio P are used this time, and their definitions are as follows:

$$R_i = \frac{(\ddot{x}_{1,i} + \ddot{x}_{g,i})_{iSRI}}{(\ddot{x}_{1,i} + \ddot{x}_{g,i})_{SRI}} \tag{5}$$

$$R = \frac{\sum_{i=1}^{n} R_i}{n} \times 100\% \tag{6}$$

$$P(R_i \le 1) = \frac{m}{n} \times 100\% \tag{7}$$

where n is the total number of T-80data, i is the ith earthquake, and m is the number of $R_i \le 1$ earthquakes

Figure 4 shows the change of PO under different combinations of μ_b and C. In order to select a reasonable PO as the reference value of the design displacement, this time, the PO of the SRI under different C is used as the standard as shown in Figure 5. It can be seen from the figure that when the C is 0.11, continue to increase the damping factor PO drop range Therefore, in this study, PO=7 was used as the threshold for comparing displacement of iSRI and SRI.

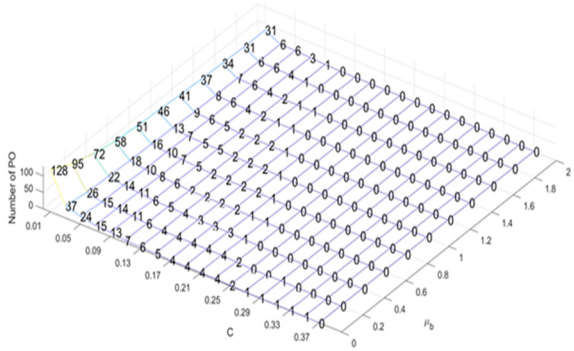

Figure 4. The relationship between μ_b and C with PO

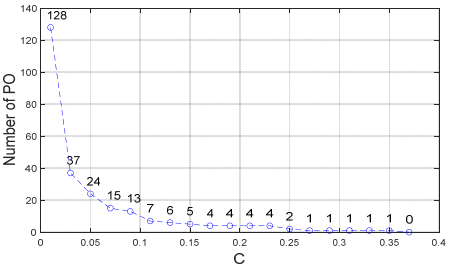

Figure 5. The number of PO under different C

From Figure 4, when PO=7, iSRI has three groups of the same PO combination, the damping factors are 0.03, 0.05, 0.07, and the corresponding μ_b are 1.5, 1.0, 0.8, respectively. Table 1 shows the SRI and iSRI results of P and R values under different μ_b and C. C_{SRI} is the damping factor of the comparative SRI, μ_b and C_{iSRI} is the iSRI's μ_b and C combination , and Group represents an earthquake group. In Table 1, under the combination of C= 0.03 and μ_b =1.5, Group-2 has the best R value of 86.23%. Under the combination of C= 0.05 and μ_b =1.0 has the best P value under Group-1 is 84.06%, and the best R and P values under Group-1 are 102.23% and 69.65%, respectively. Since the difference between the R values of the above two combinations under Group-1 is very small about 0.72%. In the case of PO=7, iSRI takes the combination of C=0.05 and μ_b =1.0 as the best parameters for analysis.

Table1. The seismic isolation effect of iSRI of T-80data in the case of PO=7

PO	Group	R(%)	P(%)	C_{iSRI}	μ_b	C_{SRI}
7	Group-1	108.53	63.43	0.03	1.5	0.11
	Group-2	**86.23**	82.26			
	Group-1	**102.23**	**69.65**	0.05	1.0	
	Group-2	86.95	**84.06**			
	Group-1	104.17	68.41	0.07	0.8	
	Group-2	93.61	80.32			

In order to explore the situation of R value under different earthquake characteristics, the acceleration response ratio distribution diagram is used, as shown in Figure 6, and the critical damping force causes the roller to roll (M) or no roll (NM) to separate different CASE. For

discussion, and Table 2 shows the symbol interpretation and the number of earthquakes in different CASE under T-80data.

From Table 2 and Figure 6, it can be seen that PO=7 acceleration response ratio distribution diagram, iSRI due to the small damping force applied, its design friction force for earthquakes above 80gal, the situation that the roller does not roll (CASE3). CASE1 accounts for the most earthquakes (43.1%), and the distribution range of the seismic PGA is mainly below 180gal and more than 100gal. When the seismic PGV range is within Group-1, the upper limit of the distribution range will be increased to more than 250gal; In the case of CASE2, there are nearly 40% earthquakes, and the SRI does not move relative to the critical damping force, and the main distribution range of its PGA is within 100 gal. The occurrence of CASE4 accounted for 17.8% of the total. Due to the large seismic disturbance acceleration, the inerter will produce large force on the iSRI, which will amplify the maximum acceleration of the iSRI, and the main distribution range of the seismic PGA is more than 180gal. Knowing that when the earthquake is within 180gal, iSRI can have lower acceleration response than SRI.

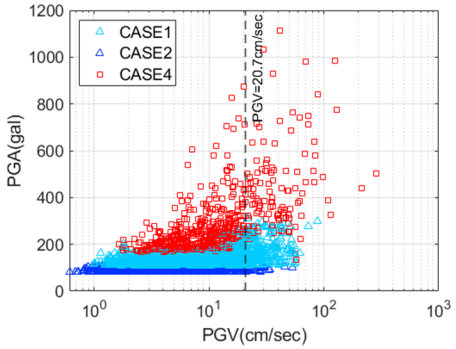

Figure 6. Acceleration response when PO=7

Table 2 The meanings of symbols in Figure 6

	R<1		R=1	R>1
	CASE1	CASE2	CASE3	CASE4
iSRI	M	M	NM	M
SRI	M	NM	NM	M
Symbol	△	△	○	□
Number	1372	1244	0	565

Conclusion

The iSRI has three combinations of damping factor and inerter ratio for the same displacement condition when PO=7. After comparison, the combination of inerter ratio μ_b =1 and damping factor C=0.05 has a smaller iSRI acceleration response. Therefore, this combination of parameters was selected for comparison with SRI. It is found that the R value of Group-2 is 86.95%, and the acceleration is better than that of SRI.

In Group-2, for earthquakes below 180 gal, the acceleration response of iSRI is better than that of SRI, while in Group-1, for earthquakes below 250 gal, the acceleration response of iSRI is better than that of SRI.

References

M. C. J. I. T. o. a. c. Smith, "Synthesis of mechanical networks: the inerter," vol. 47, no. 10, pp. 1648-1662, 2002.

S.-J. Wang, C.-H. Yu, W.-C. Lin, J.-S. Hwang, and K.-C. Chang, "A generalized analytical model for sloped rolling-type seismic isolators," *Engineering Structures,* vol. 138, pp. 434-446, 2017/05/01/ 2017.

International Symposium on Emerging Developments and Innovative Applications of Reliability Engineering and Risk Managements (EDIARR2022),30 October-3 November2022, Taipei
Chen, S. S. &Ang, Alfredo. H-S. (Editors)

AK-MCB-IS: AN ADAPTIVE KRIGING WITH MULTI CONCENTRIC BALL-BASED IMPORTANCE SAMPLING

Handy Prayogo[1], I-Tung Yang[2]

[1] *PhD Student, Department of Civil and Construction Engineering, National Taiwan University of Science and Technology, Taipei, Taiwan.*

E-mail: D10905818@mail.ntust.edu.tw.

[2] *Professor, Department of Civil and Construction Engineering, National Taiwan University of Science and Technology, Taipei, Taiwan.*

E-mail: ityang@mail.ntust.edu.tw.

Abstract: The complexity of today's engineering systems makes computational simulation more challenging and time-consuming. This time-consuming operation is performed repeatedly to compute the probability of failure, therefore minimizing the number of such operations will be the key of attaining efficiency. By employing suitable learning functions, Kriging-based adaptive structural reliability analysis techniques can replace such structural performance function and perform reliability analysis accurately and efficiently. In order to fulfill this aim, a novel adaptive reliability analysis, namely, Adaptive Kriging with Multi Concentric Ball-based Importance Sampling (AK-MCB-IS) to calculate the probability of failure. The method uses uniformly-distributed samples from multiple non-intersecting concentric balls in a standard normal space to enrich the Kriging model. The method starts with a small ball region that is expanded continuously until the samples produced sufficiently represent the failure regions of the problem. A novel sample filtering system and a more robust convergence criterion for the active learning phase is also introduced to further improve the consistency and efficiency of the method. The numerical results demonstrated the efficiency, consistency, and accuracy of the proposed method outperforming existing relevant methods.

***Keywords*:** Active Learning, Reliability Analysis, Failure Probability, Importance Sampling

Introduction

In a structural reliability analysis with an n-dimensional random variable $\mathbf{X}$, the failure probability P_f can be calculated by a high dimensional integral:

$$P_f = \int_{G(\boldsymbol{x})\leq 0} f_X(\boldsymbol{x})\, d\boldsymbol{x} \tag{1}$$

where $f_X(\boldsymbol{x})$ is the joint probability density function (PDF) of $\mathbf{X}$, and $G(\boldsymbol{x})$ refer to the limit-state function (LSF) negative sign of which indicates a failure event. Computing the high dimensional integral over the failure region is difficult and inapplicable for engineering problems. Thus, various reliability analysis methods have been developed in order to assess the reliability efficiently and accurately.

A popular method for reliability analysis is to use the first- and second-order reliability method (FORM & SORM). The methods estimate the failure probability based on the Taylor expansion approximation of most probable failure point (MPP). However, the accuracy of these methods may suffer when the performance function shows high level of non-linearity, or has multiple design points (T. Kim and Song 2018).

The brute-force Monte-Carlo simulation (MCS) approach is an alternative method which has attracted much interest in this area due to its simplicity and accuracy given a sufficiently enough number of samples. However, the computational effort of MCS is very demanding when faced with rare failure event with time-consuming LSF evaluation, i.e. $P_f \leq 10^{-4}$ (Bichon et al. 2008). Various variance reducing techniques have been used to improve the efficiency of MCS such as: importance sampling (IS) (Melchers 1989), directional sampling (DS) (Bjerager 1988), and subset simulation (SS) (Au and Beck 2001).

Despite the advancement of variance reducing techniques, the reliability analysis still requires a large number of computationally intensive evaluations. The use of meta-modeling techniques is one strategy that has shown a lot of promise in reducing the computation demand of reliability analysis. The meta-model or surrogate model can replace the time-consuming function with only a fraction of the cost. Various meta-models have been employed for this purpose (Pan and Dias 2017; Xiang et al. 2020; Hawchar, El Soueidy, and Schoefs 2017). Among which, the Kriging model or Gaussian process regression (GPR) has been growing in popularity due to its desirable characteristics and accuracy. In particular, the Kriging model provides an approximation value of the point of interest and the estimated variance of the prediction. This stochastic property encourages the development of adaptive strategies for constructing an accurate model.

The adaptive or active-learning strategy is a method of iteratively adding the most informative samples in order to efficiently improve the prediction accuracy with the fewest number of function evaluations. A widely known adaptive Kriging approach is the active-learning method combining Kriging and Monte Carlo simulation (AK-MCS) (Echard, Gayton, and Lemaire 2011). When compared to MCS, AK-MCS dramatically reduces the number of function evaluations. However, the method must nonetheless generate a large number of candidate samples when faced with a low failure probability problem. The method's efficiency may be affected due to the cost of accessing and computing samples alone. Other researchers have implemented variance reducing techniques into the AK-MCS framework such as: AK-IS (Echard et al. 2013), AK-LS (Lv, Lu, and Wang 2015), AK-SS (Huang, Chen, and Zhu 2016), AK-MSS (Xu et al. 2020), and AK-DS (Xiaobo Zhang, Zhenzhou, and Cheng 2021).

One approach to overcome the drawback of AK-MCS is to employ a more efficient sampling region. Wen et al. (2016) proposed truncated sampling region which adapts to the failure probability calculated in the last iteration. Xufang Zhang, Wang, and Sørensen (2019) combines the adaptive sampling region with low-discrepancy samples and importance sampling approach to improve the efficiency of the reliability analysis. Xufang Zhang, Wang, and Sørensen (2020) proposed a multiple small sampling subregion centered on the MPPs to deal with multiple failure modes. J. Kim and Song (2020) uses a sampling region based on n-dimensional ball which is used to calculate the failure probability. Song et al. (2021) adopts a Six Sigma ($\mu \pm 6\sigma$) low-discrepancy uniform sampling region. These methods all employ a more efficient sampling region as their candidate pool to enrich the Kriging model. However, when confronted with a high-dimensional problem, the efficacy of these methods decreases dramatically, which will be explained in a later section.

In order to overcome the shortcomings of the previous methods, a novel Adaptive Kriging with Multi Concentric Ball-based Importance Sampling (AK-MCB-IS) is proposed. AK-MCB-IS uses multiple concentric hyperball as its sampling region, which is not affected by the dimensionality

of the problem. In addition, a new method to efficiently filters the candidate samples and an improved stopping condition which is less susceptible to undesired convergence. The rest of this paper is organized as follows: Section 2 discusses in detail about the proposed methods; Section 3 presents a comparative discussion to validate the proposed method; Finally, the main conclusions of the work is summarized in Section 4.

Adaptive Kriging with Multi Concentric Ball-based Importance Sampling

Sampling domain

The proposed AK-MCB-IS uses multiple concentric balls in the standard normal space as its sampling region. Sampling uniformly within the hyperball allow the easy generation of low probability samples and removing the clustering of redundant candidate samples in higher density area. Most adaptive sampling region used by the other methods such as PAK-B^n (J. Kim and Song 2020) generates their candidate samples by sampling within a certain interval e.g. ($\mu \pm 6\sigma$) and filtering out the samples lower than the specified joint probability density. This sample generation strategy is also known as rejection sampling or accept-reject algorithm. Although the procedure is straightforward, as the dimension of the problem increases, the acceptance ratio becomes excessively small. The acceptance rate continues to decrease such that in a 10-dimension problem the only 0.25% of the generated samples are accepted. In this study, Muller's algorithm (Muller 1959) is adopted to generate uniformly distributed samples inside the ball sampling region without the curse of dimensionality. The algorithm is stated as follows:

$$\boldsymbol{x} = (U)^{1/d} \frac{\boldsymbol{Z}}{\|\boldsymbol{Z}\|_2} \tag{2}$$

where U is a uniformly distributed random number between [$R_{in}{}^d$, $R_{out}{}^d$], R_{in} is the inner radius of the hyperball, R_{out} is the outer radius of the hyperball, $\boldsymbol{Z}$ is a d-dimension standard normal random vector, and $\|\cdot\|_2$ denotes the Euclidean norm.

Domain expansion

The radius of the sampling region in AK-MCB-IS dictates the precision of the reliability analysis; a larger radius covers smaller density however may incur unnecessary calculation. As a result, the balance can be achieved by expanding the sampling region by a small amount. The present study proposes the domain to be expanded in small radius increment until one of two criteria is met: (1) the number of expansion limit is achieved; or (2) the failure probability is converged. The expansion limit is introduced to ensure the domain does not expand endlessly. The second criteria, on the other hand, guarantees that the domain expand only to the required precision. The convergence criterion based on the reliability index $\hat{\beta} = -\Phi^{-1}(\hat{P}_f)$, is formulated as

$$\frac{|\hat{\beta}_i - \hat{\beta}_{i-1}|}{\hat{\beta}_i} \leq \epsilon_{thres} \tag{3}$$

where $\hat{\beta}_i$ denotes the reliability index for the i-th expansion and ϵ_{thres} is the specified threshold value. According to the results of preliminary experiments, ϵ_{thres} of 10^{-3} to 10^{-4} is sufficient to establish a reliable probability of failure. The samples that meet the aforementioned criteria will be added to the candidate pool to enrich the Kriging model.

Failure probability calculation

Importance sampling is used to calculate the failure probability in AK-MCB-IS. The failure probability is computed by:

$$P_f = \int I_F(\boldsymbol{x}) \frac{f(\boldsymbol{x})}{h(\boldsymbol{x})} h(\boldsymbol{x}) dx = \frac{1}{n} \sum_i^n I_F(\boldsymbol{x}) \frac{f(\boldsymbol{x})}{h(\boldsymbol{x})} \tag{4}$$

where $I_F(\boldsymbol{x})$ is the indicator function for failure ($G(\boldsymbol{x}) < 0$), $f(\boldsymbol{x})$ is the original joint probability density, which is standard normal in this instance, and $h(\boldsymbol{x})$ is the joint probability density from the chosen distribution. The joint probability density of the sampling regions with multiple different layer densities is calculated by solving the equations below:

$$V(R_{in}, R_{out}) = \frac{\pi^{\frac{d}{2}}}{\Gamma\left(\frac{d}{2}+1\right)} \left({R_{out}}^d - {R_{in}}^d\right) \tag{5}$$

$$\int h(\boldsymbol{x})\, d\boldsymbol{x} = \sum_i^m V_{l_i} h_i = 1 \tag{6}$$

$$\frac{V_{l_1}}{n_{l_1}} h_1 - \frac{V_{l_i}}{n_{l_i}} h_i = 0, \text{for } i = 2, \dots, m \tag{7}$$

where V_{l_i} is the volume of hyperball for layer *i*, h_i is the joint PDF for layer *i*, and n_{l_i} is the number of samples located in layer *i*. Equation (6) impose the characteristic of a PDF function, while Equation (7) defines the ratio between the densities is according to the number of samples and the volume of each layer. The equations can be simplified as a matrix form as:

$$\begin{bmatrix} V_{l_1} & V_{l_2} & \cdots & V_{l_m} \\ \frac{V_{l_1}}{n_{l_1}} & -\frac{V_{l_2}}{n_{l_2}} & \dots & 0 \\ \vdots & \vdots & \ddots & \vdots \\ \frac{V_{l_1}}{n_{l_1}} & 0 & \dots & -\frac{V_{l_m}}{n_{l_m}} \end{bmatrix} \begin{bmatrix} h_1 \\ h_2 \\ \vdots \\ h_m \end{bmatrix} = \begin{bmatrix} 1 \\ 0 \\ \vdots \\ 0 \end{bmatrix} \tag{8}$$

Stopping condition for active learning phase

AK-MCB-IS has two types of stopping condition for the active learning phase. The first stopping condition is based on the sample filtering process. Each iteration, the samples with a learning function value that fulfill the threshold is temporarily deactivated. The active learning phase terminated once no candidate samples after the sample filtering process. The second stopping condition is based on a convergence of failure probability. Since the failure probability fluctuates easily during the active learning phase, the convergence is dictated by the relative change in the current reliability index $\hat{\beta}_i$ and the average reliability index over the past (n_{conv}) iterations $\bar{\beta}$. The relative change is formulated as:

$$\Delta_i = \frac{|\hat{\beta}_i - \bar{\beta}|}{\hat{\beta}_i} \tag{9}$$

In order to ensure a more robust stopping condition, AK-MCB-IS adopts the method proposed by Basudhar and Missoum (2008). An exponential curve is used to fit Δ_i as:

$$\hat{\Delta}_i = Ae^{Bi} \tag{10}$$

where $\hat{\Delta}_i$ is the fitted value of Δ_i; A and B are the parameters of the exponential curve. As a result, the active-learning process is terminated based on convergence when the following equation is fulfilled:

$$\begin{cases} \Delta_i \leq \epsilon_{thres} \\ \quad and \\ \hat{\Delta}_i \leq \epsilon_{thres} \end{cases} \tag{11}$$

Algorithm Framework

Figure 1 depicts the flowchart of the proposed AK-MCB-IS. The proposed method consists of two phases: active-learning phase and the hyperball expansion phase. The detailed steps are summarized as follows:

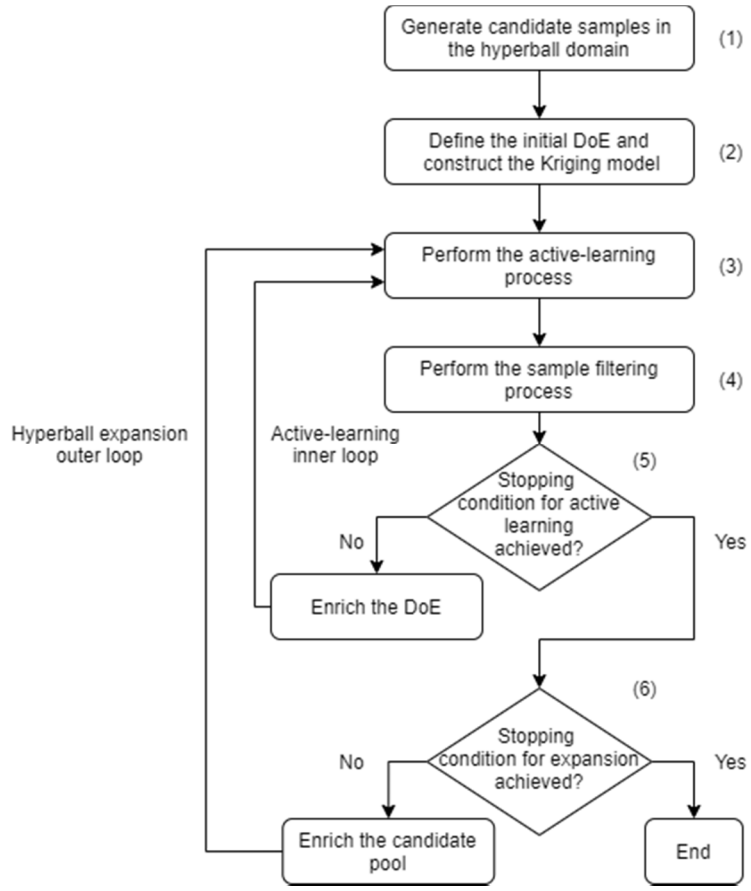

Figure 1. The flowchart of the AK-MCB-IS method.

1. **Generate the candidate sample in the hyperball domain.** The initial stage in AK-MCB-IS is to generate N_{IS} uniformly distributed candidate samples in a hyperball using Equation (1). The samples represent the possible samples that will be evaluated to improve the Kriging model.

The reference value of the initial N_{IS} suggested by this paper is 10^4 to 10^5 samples.

2. **Define the initial design of experiment and construct the Kriging model**. The active learning process uses a design of experiment to construct the initial Kriging model. The DoE is made up of N_I number of samples with a low-discrepancy characteristic. Latin hypercube sampling (LHS) is utilized here to generate the samples in the standard normal space. The LHS is generated with a boundary of four sigma, which is equal to the interval [-4, 4] in standard normal space. For the Kriging model, an ordinary Kriging with a Gaussian correlation function is chosen.
3. **Perform the active-learning process to refine the model.** The learning function is computed for every active candidate sample in the hyperball. The learning function is used to find the best sample to refine the model further. The present study adopts the REIF2 learning function (Xufang Zhang, Wang, and Sørensen 2019). The sample with the highest REIF2 value is added into the DoE and deactivated indefinitely to avoid duplicated samples in the DoE.
4. **Perform the sample filtering process.** The samples that have fulfilled the learning function threshold are temporarily deactivated. For REIF2, the samples with the REIF2 value less than zero are deactivated.
5. **Check the stopping condition for the active-learning phase.** In AK-MCB-IS, there are two stopping conditions for the active learning loop. The first stopping condition is met when no samples remain due to the sample filtering process. The second stopping condition is concerned with the convergence of probability of failure. If any stopping condition is fulfilled, the model refinement phase is terminated, and the hyperball will be expanded. On the other hand, if none of the conditions is met, the sample chosen in Step 3 is evaluated and added into the Kriging model. The method continues and returns to Step 3.
6. **Check the stopping condition for the hyperball expansion phase.** Once the model refinement phase is completed, the hyperball will undergo expansion until one of two stopping conditions, the limit on expansion or the convergence of probability of failure, is satisfied. The newly generated samples from the expansion are then added into the candidate pool along with the samples that were deactivated during the sample filtering process. The method then returns to the model refinement phase in Step 3.
7. **End of the AK-MCB-IS method.** If no additional layers are formed during the hyperball expansion due to the convergence of probability of failure, the hyperball is considered to be large and therefore precise enough to estimate the probability of failure.

Case Study

In order to validate the proposed method, the performance of AK-MCB-IS is compared to the previous methods: AK-MCS and PAK-B^n. The relative error compared with MCS estimation represents estimation accuracy. The number of samples and total computation time shows computational efficiency. The relative error is calculated using the reliability index β which is calculated by:

$$err = \frac{|\hat{\beta} - \beta_{MCS}|}{\beta_{MCS}} \times 100\% \tag{12}$$

As the random samples may influence the result, all the methods are performed ten times to compare the general performance. Therefore, the relative error (*err*) and the number of samples in the DoE (*Ns*) are the averages across the ten runs. All methods in this study set the number of initial DoE (N_I) to be 7*d,* which scales with the dimension of the problem (*d*). The parameters for AK-

MCB-IS is set as follows: the initial radius (R_{out}) is set to 3; the small increment of the radius (ΔR) is set to 0.2; the limit of expansion (n_{exp}) is set to 5; the number of iterations considered for the convergence (n_{conv}) is set to 5; the threshold for convergence (ϵ_{thres}) is set to 10^{-4}; the number of initial candidate samples (N_{IS}) is set to 1×10^4; the number of samples for the layer expansion (ΔN_{IS}) is set to 2×10^3.

The case study deals with a series system with four branches (Wen et al. 2016). The limit state function for this problem is formulated by:

$$G(x_1, x_2) = \min \begin{Bmatrix} 3 + \frac{(x_1 - x_2)^2}{10} - \frac{(x_1 + x_2)}{\sqrt{2}} \\ 3 + \frac{(x_1 - x_2)^2}{10} + \frac{(x_1 + x_2)}{\sqrt{2}} \\ x_1 - x_2 + 7/\sqrt{2} \\ x_2 - x_1 + 7/\sqrt{2} \end{Bmatrix} \tag{13}$$

where x_1 and x_2 are independent standard normal random variables.

The development of the Kriging model by AK-MHIS is shown in Figure 2 (a) to (d). From Figure 2 (a) to Figure 2 (c) the sampling region is expanded until the required precision for the failure probability is achieved. In the final result displayed in Figure 2 (d), the model refinement process is terminated even though there are still inaccurate predictions of the limit state function near the edge of the hyperball; this is because the predictions at the edge carry less impact to the failure probability and can be disregarded. This enables AK-MCB-IS to use less function evaluation than the other methods.

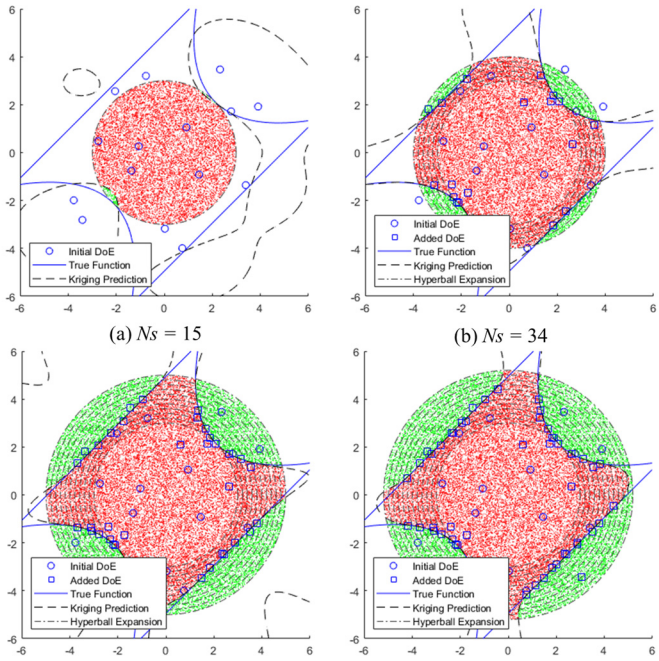

(a) *Ns* = 15 (b) *Ns* = 34

(c) *Ns* = 52 (d) *Ns* = 70

Figure 2. Development of AK-MCB-IS model for the case study.

The comparison of the reliability results obtained from various active-learning algorithms is presented in Table 1. The proposed AK-MCB-IS and PAK-B^n managed to consistently obtain a satisfactory failure probability, with AK-MCB-IS obtaining superior average and standard deviation in the number of samples needed. On the other hand, the AK-MCS in 7 out of 10 runs fails to identify the limit state function; this is due to the random samples chosen as the DoE does not contain enough information to improve the model. This issue can be easily solved by utilizing a low discrepancy sampling technique such as LHS as the initial DoE.

Table 1. Comparison of the reliability results.

Method	Avg *Ns*	std *Ns*	Avg P_f	Avg β	Avg *err (%)*
MCS	2.00E+05	-	2.21E-03	2.847	-
AK-MCB-IS	**64**	**7.211**	**2.21E-03**	**2.847**	**0.000**
AK-MCS	35.4	32.911	6.88E-04	3.200	12.412
PAK-B^n	67.7	14.445	2.19E-03	2.849	0.086

Conclusion

In this paper, a novel adaptive kriging method called AK-MCB-IS is introduced. The method uses a sampling region based on multiple concentric balls to reduce the computational and memory demand of calculating the failure probability. A more efficient generation of samples in the sampling region is proposed to avoid the curse of dimensionality that the rejection sampling introduced. Sample filtering system is also implemented to increase the efficiency by temporarily ignoring candidate samples that are in well-defined regions. A more robust stopping condition is also provided to avoid the chance of premature convergence. The performance of the proposed method is validated trough the case study. The result shows that the proposed AK-MCB-IS able to consistently produce accurate estimation of failure probability with a low average number of limit-state function evaluation compared to the previous Kriging-based methods.

References

Au, Siu-Kui, and James L. Beck. 2001. "Estimation of small failure probabilities in high dimensions by subset simulation." *Probabilistic Engineering Mechanics* 16 (4): 263-277. https://doi.org/10.1016/S0266-8920(01)00019-4. https://www.sciencedirect.com/science/article/pii/S0266892001000194.

Basudhar, Anirban, and Samy Missoum. 2008. "Adaptive explicit decision functions for probabilistic design and optimization using support vector machines." *Computers & Structures* 86 (19): 1904-1917. https://doi.org/https://doi.org/10.1016/j.compstruc.2008.02.008. https://www.sciencedirect.com/science/article/pii/S0045794908000515.

Bichon, B. J., M. S. Eldred, L. P. Swiler, S. Mahadevan, and J. M. McFarland. 2008. "Efficient Global Reliability Analysis for Nonlinear Implicit Performance Functions." *AIAA Journal* 46 (10): 2459-2468. https://doi.org/10.2514/1.34321. https://arc.aiaa.org/doi/abs/10.2514/1.34321.

Bjerager, Peter. 1988. "Probability Integration by Directional Simulation." *Journal of Engineering Mechanics* 114 (8): 1285-1302.

https://doi.org/10.1061/(ASCE)0733-9399(1988)114:8(1285). https://ascelibrary.org/doi/abs/10.1061/%28ASCE%290733-9399%281988%29114%3A8%281285%29.

Echard, B., N. Gayton, and M. Lemaire. 2011. "AK-MCS: An active learning reliability method combining Kriging and Monte Carlo Simulation." *Structural Safety* 33 (2): 145-154. https://doi.org/10.1016/j.strusafe.2011.01.002. https://www.sciencedirect.com/science/article/pii/S0167473011000038.

Echard, B., N. Gayton, M. Lemaire, and N. Relun. 2013. "A combined Importance Sampling and Kriging reliability method for small failure probabilities with time-demanding numerical models." *Reliability Engineering & System Safety* 111: 232-240. https://doi.org/10.1016/j.ress.2012.10.008. https://www.sciencedirect.com/science/article/pii/S0951832012002086.

Hawchar, Lara, Charbel-Pierre El Soueidy, and Franck Schoefs. 2017. "Principal component analysis and polynomial chaos expansion for time-variant reliability problems." *Reliability Engineering & System Safety* 167: 406-416. https://doi.org/10.1016/j.ress.2017.06.024. https://www.sciencedirect.com/science/article/pii/S0951832016302587.

Huang, Xiaoxu, Jianqiao Chen, and Hongping Zhu. 2016. "Assessing small failure probabilities by AK–SS: An active learning method combining Kriging and Subset Simulation." *Structural Safety* 59: 86-95. https://doi.org/10.1016/j.strusafe.2015.12.003. https://www.sciencedirect.com/science/article/pii/S0167473016000035.

Kim, Jungho, and Junho Song. 2020. "Probability-Adaptive Kriging in n-Ball (PAK-Bn) for reliability analysis." *Structural Safety* 85: 101924. https://doi.org/10.1016/j.strusafe.2020.101924. https://www.sciencedirect.com/science/article/pii/S0167473020300035.

Kim, Taeyong, and Junho Song. 2018. "Generalized Reliability Importance Measure (GRIM) using Gaussian mixture." *Reliability Engineering & System Safety* 173: 105-115. https://doi.org/https://doi.org/10.1016/j.ress.2018.01.005. https://www.sciencedirect.com/science/article/pii/S0951832017308384.

Lv, Zhaoyan, Zhenzhou Lu, and Pan Wang. 2015. "A new learning function for Kriging and its applications to solve reliability problems in engineering." *Computers & Mathematics with Applications* 70 (5): 1182-1197. https://doi.org/10.1016/j.camwa.2015.07.004. https://www.sciencedirect.com/science/article/pii/S0898122115003399.

Melchers, R. E. 1989. "Importance sampling in structural systems." *Structural Safety* 6 (1): 3-10. https://doi.org/10.1016/0167-4730(89)90003-9. https://www.sciencedirect.com/science/article/pii/0167473089900039.

Muller, Mervin E. 1959. "A note on a method for generating points uniformly on n-dimensional spheres." *Commun. ACM* 2 (4): 19–20. https://doi.org/10.1145/377939.377946. https://doi.org/10.1145/377939.377946.

Pan, Qiujing, and Daniel Dias. 2017. "An efficient reliability method combining adaptive Support Vector Machine and Monte Carlo Simulation." *Structural Safety* 67: 85-95. https://doi.org/10.1016/j.strusafe.2017.04.006. https://www.sciencedirect.com/science/article/pii/S0167473016300819.

Song, Kunling, Yugang Zhang, Xinchen Zhuang, Xinshui Yu, and Bifeng Song. 2021. "An adaptive failure boundary approximation method for reliability analysis and its applications." Engineering with Computers 37 (3): 2457-2472. https://doi.org/10.1007/s00366-020-01011-0. https://dx.doi.org/10.1007/s00366-020-01011-0.

Wen, Zhixun, Haiqing Pei, Hai Liu, and Zhufeng Yue. 2016. "A Sequential Kriging reliability analysis method with characteristics of adaptive sampling regions and parallelizability." *Reliability Engineering & System Safety* 153: 170-179.

https://doi.org/10.1016/j.ress.2016.05.002.
https://dx.doi.org/10.1016/j.ress.2016.05.002.

Xiang, Zhengliang, Jiahui Chen, Yuequan Bao, and Hui Li. 2020. "An active learning method combining deep neural network and weighted sampling for structural reliability analysis." *Mechanical Systems and Signal Processing* 140: 106684. https://doi.org/https://doi.org/10.1016/j.ymssp.2020.106684. https://www.sciencedirect.com/science/article/pii/S0888327020300704.

Xu, Chunlong, Weidong Chen, Jingxin Ma, Yaqin Shi, and Shengzhuo Lu. 2020. "AK-MSS: An adaptation of the AK-MCS method for small failure probabilities." *Structural Safety* 86: 101971. https://doi.org/10.1016/j.strusafe.2020.101971.

Zhang, Xiaobo, Lu Zhenzhou, and Kai Cheng. 2021. "AK-DS: An adaptive Kriging-based directional sampling method for reliability analysis." *Mechanical Systems and Signal Processing* 156: 107610. https://doi.org/10.1016/j.ymssp.2021.107610.

Zhang, Xufang, Lei Wang, and John Dalsgaard Sørensen. 2019. "REIF: A novel active-learning function toward adaptive Kriging surrogate models for structural reliability analysis." Reliability Engineering & System Safety 185: 440-454. https://doi.org/10.1016/j.ress.2019.01.014. https://dx.doi.org/10.1016/j.ress.2019.01.014.

International Symposium on Emerging Developments and Innovative Applications of Reliability Engineering and Risk Managements (EDIARR2022),30 October-3 November2022, Taipei
Chen, S. S. &Ang, Alfredo. H-S. (Editors)

A NONLINEAR MULTI-CLASS CLASSIFIER OF VIBRATIONAL SIGNALS OF A HIGH-PRESSURE CHEMICAL REACTOR

Po Ting Lin[1], Shih-Jie Pan[2], Cheng-Liang Chen[2,*]

[1]*Department of Mechanical Engineering, National Taiwan University of Science and Technology, Taipei 10607, Taiwan*

[2]*Department of Chemical Engineering, National Taiwan University, Taipei 10617, Taiwan*

Corresponding author's email: ccl@ntu.edu.tw

Recently, Industry 4.0 technologies have drawn great attention in the monitoring and reliability analysis of chemical factories. In this paper, the vibrational responses of a high-pressure chemical reactor during its operation were investigated. The vibrational signal in every five days was converted to the frequency domain using Fourier Transform. It was found that vibration occurred mostly in a low-frequency region. Principal Component Analysis (PCA) was then utilized to acquire the first three major characteristics from the low-frequency region. Four sensors were used in this paper. For the i-th time period, three PCA responses were acquired from each sensor. In total, twelve PCA responses were labeled based on the event class of the time period. Three classes were considered: (1) normal, (2) warning, and (3) failure. A Kriging regression was used to estimate the class function with respect to the twelve PCA responses. Finally, ten-fold cross validation was used to verify that the accuracy of the Kriging-based multi-class classifier was 94%.

International Symposium on Emerging Developments and Innovative Applications of Reliability Engineering and Risk Managements (EDIARR2022),30 October-3 November2022, Taipei
Chen, S. S. &Ang, Alfredo. H-S. (Editors)

RELIABILITY BASED OPTIMIZATION OF CONTROLLED STRUCTURE CONSIDERING STRUCTURAL STIFFNESS.

John Thedy[1], Kuo-Wei Liao[1]

[1] *Department of Bioenvironmental Systems Engineering, National Taiwan University, Taiwan*

Correspondence e-mail address: thedy.john@yahoo.com

Abstract: In structural control design, most design put structure and control parameter design separately. Commonly a fix structure is given and the task is to tune certain control algorithm parameter until best performance of structure is obtained. There is possibility that tuned parameter gives unnecessary too safety performance. This study has an opinion that installed control device need to be exploited its maximum capability in enhancing structure performance. Then, if unnecessary safety exists, it can be traded off by reducing lateral resisting component of structure since its material cost are more expensive. To apply aforementioned concept, control parameter tuning should consider structure lateral resisting cost and certain safety level should be referenced. This study performs metaheuristic optimization in optimizing not only control parameter but also structural lateral stiffness. Objective of optimization is structure performance in term of displacement to consider serviceability. While reliability as safety measure is put as optimization constraint. Kriging reliability assessment method is utilized as this method require only small portion of sample evaluation in solving reliability problem. This study shows that RBDO (Reliability Based Design Optimization) using Kriging could give efficient number of function evaluation while maintaining high accuracy compared to MCS (Monte Carlo Simulation) result.

Keywords: RBDO, Kriging Reliability, LQR Active Control.

Introduction

To boost efficiency and structural performance responses against wind and earthquakes, technique of structural control has drawn considerable attention in recent years. Originally, to increase structure resistance from earthquake or any vibration loading, engineer adopt passive control device such as damper bracing, tuned mass damper, or base isolation for energy dissipation tool [1-5]. However, this device has fix parameter once construction accomplished in which equipped device only effective for certain vibration characteristic. Once excitation loading behave differently, effectiveness of equipped device is deteriorating. There is no guarantee upcoming earthquake excitation will behave similar with past earthquake experience. In Taiwan, several recent earthquakes such as Meinong and Hualien earthquake surprisingly develops different earthquake dominant frequency from expected frequency in Taiwan design code [6-7]. To address this issue, active and semi-active technology is developed. It termed as active since this device could adapt under different loading excitation characteristic. Instead of only dissipate energy as passive device, active control could generate force to stabilize structure under excitation. Active control strategy has gain attention among researcher from early of 1970. Although implementation still rarely found, significant development in control algorithm technology could be found.

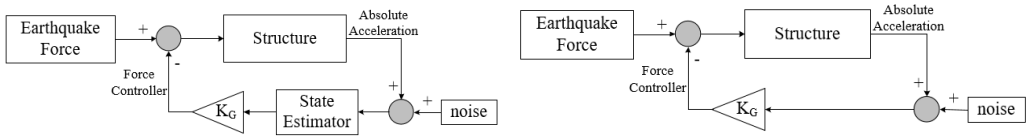

(a)State feedback controller. (b)Output feedback controller.

Figure 1. Active control mechanism.

In general, active control algorithm could be divided into two categories in which state feedback and output feedback controller as shown in Figure 1 (a) and (b) respectively. In active control strategy, generated force is determined based on response output from structure. In state feedback, this force is calculated through K_G (Gain constant) and state information (displacement and velocity). Several state feedback techniques that commonly adopted are LQR [8] and pole placement [9]. Other state feedback technique that considering reliability also developed by researchers [10-12]. State information is not always available due to limited sensor ability. In situation with non-presented state information, output feedback is commonly adopted. Output feedback could be applied either by reconstructing state data using output information (absolute acceleration) or directly using output information and K_G to determine required actuator force. In case state data reconstruction is preferred, state reconstruction method such as Kalman filter is commonly utilized [13]. Direct output feedback also being investigated by several researchers [14-16]. Either state or output feedback, main objective is to obtain K_G parameter. This K_G usually a matrices form with size dependent on state or output size information. No specific rule in determining this parameter. For LQR, several tuning procedure is proposed to determine suitable K_G [17-18]. In several literatures, metaheuristic adopted to determine optimal control parameter [19-21].

Commonly, traditional structure or passive control device is designed based on earthquake site characteristic. For passive device, excessive safety margin offered by device could be traded off with reduced structure column size. As explained earlier, most active control method will tune parameter based on given structural system. High possibility that unnecessary safety will exists caused by oversupplied active control force. This study has intention to use metaheuristic optimization to determine not only optimal control parameter but also structural stiffness at each story. Appropriate stiffness structure at each story combine with tuned control parameter is believed will deliver more optimal result. Also, this study will use statistic reliability approach to create bold threshold line of safety so that excessive safety of structural system could be transferred as stiffness reduction. Reliability will use as constraint in double loop metaheuristic optimization. Challenge rise up when cost to evaluate structural control reliability at every optimization iteration is expensive. In this case, efficient reliability assessment without excessive accuracy sacrifice is required. Reliability assessment using moment method [22-23] is a common reliability method and one of the most efficient. However, its robustness and accuracy is questionable when handling highly nonlinear problem. This study utilizes Kriging method where its assessment cost almost similar to FORM (First Order Reliability Moment) but it has peg accuracy with MCS (Monte Carlo Simulation). Section 2 will describe LQR active control algorithm that will be used in this study. Section 3 explains theory of Kriging method adopted for RBDO (Reliability Based Design Optimization). Section 4 explain the integration of Kriging reliability assessment into metaheuristic optimization. Numerical example will be given in Section 5 and conclusions of this study will be detailed explained in Section 6.

Linear Quadratic Regulator (LQR)

For a structure equipped with base force controller subjected to earthquake disturbances, the equation of motions could be written in a matrix form as shown in Equation (1).

$$M\ddot{u}(t)+C\dot{u}(t)+Ku(t)=-ML\ddot{u}_g(t)+EF(t) \tag{1}$$

where *M*, *C*, and *K* are the mass, damping, and stiffness matrices of a structure system; *E* is the position matrices determine the locations of the force controllers; *L* matrix is an influence vector for determining the disturbance positions; $u(t)$ and $\ddot{u}_g(t)$ represents structural relative displacement and ground acceleration. By defining the state $x=\left[u(t)^T\ \dot{u}(t)^T\right]^T$, Equation (1) could be translated into a state space model as defined in Equation (2).

$$\begin{aligned}\dot{x}(t)&=Ax(t)+BF(t)+H\ddot{u}_g(t)\\ y(t)&=D_1x(t)+D_2F(t)\end{aligned} \tag{2}$$

in which, *A*, *B*, and *H* matrices are the system matrix, control force position matrix, and disturbance location matrix, respectively. *y* is the output matrix contains relative displacements, relative velocities, and absolute accelerations. Matrices *A*, *B*, *H*, D_1 and D_2 are defined in Equations (3) and (4), respectively.

$$A=\begin{bmatrix}0 & I\\ -M^{-1}K & -M^{-1}C\end{bmatrix},B=\begin{bmatrix}0\\ M^{-1}E\end{bmatrix},H=\begin{bmatrix}0\\ -1\end{bmatrix} \tag{3}$$

$$D_1=\begin{bmatrix}I & 0\\ 0 & I\\ -M^{-1}K & -M^{-1}C\end{bmatrix},D_2=\begin{bmatrix}0\\ M^{-1}E\end{bmatrix} \tag{4}$$

A state output feedback force controller is considered in the current study. The structural control process is illustrated in Figure 1(a), where K_G is the controller gain that will generate a required control force ($F(t)$) using the state of structure ($x(t)$). The value of K_G depends on controller type and the corresponding parameters.

LQR controller is one of the most widely and fundamental techniques in control theory. The LQR algorithm aims to reduce the amount of work done by the control systems engineer to optimize the controller. To be specific, LQR in the current study is used to minimize the structural responses and the required control force. The optimal control gain is obtained by minimizing performance index *J* described in Equation (5).

$$J=\int_0^\infty\left[x^T(t)Qx(t)+F^T(t)RF(t)+2x^T(t)NF(t)\right]dt \tag{5}$$

Matrices Q, R and N are the weighting matrices. Here, N is assumed to be zero, and Q and R matrices are symmetric, positive (semi-) definite matrices. The required control force is computed by solving algebraic Ricatti equation described in Equation (6). The control force can be computed using Equation (7) with P obtained in Ricatti equation.

$$A^T P + PA - PBR^{-1}B^T P + Q = 0 \tag{6}$$

$$F(t) = \left[-\frac{1}{2} R^{-1} B^T P \right] x(t) = -K_G x(t) \tag{7}$$

In this paper, matrices Q and R are considered as design variable which are adjusted to minimize the required force with predefined reliability constraints. The LQR algorithm is an approach that automatically finds an appropriate state-feedback controller.

Adaptive Kriging Adopting PSO with Hollow-Hypersphere Space

Reliability assessment method termed as Adaptive Kriging Adopting PSO with Hollow-Hypersphere Space (AK-PSO-HHs). This method implements adaptive Kriging approach as AK-MCS [24] with several advance improvements. First major improvement offered by AK-PSO-HHs is removal of sample pool necessity. This objective attained by applying PSO to find best sample candidate. Besides removing dependency on sample pool, PSO metaheuristic enable lower Kriging evaluation number compared to brute force MCS sample evaluation. Second improvement offered is Hollow-Hypersphere Space (HHs) reduction. Most methods [25-26] restrict and bound its search space into hypersphere with certain radius termed as β_1 as shown in Figure 3(a). In this study, not only outside sphere region is excluded, safety domain formed using β_2 radius inside β_1 sphere also excluded as illustrated in Figure 2(b). Determination of β_2 follow a line search method that can be found in reference [27].

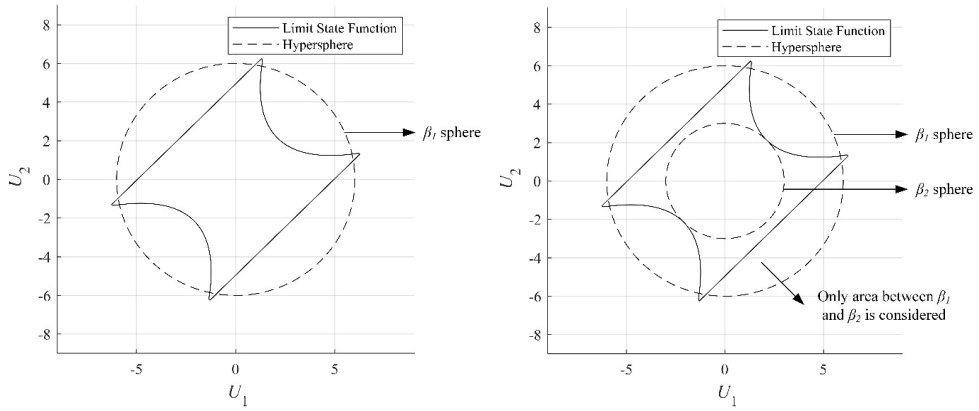

Figure 2. (a) Single hypersphere to bound search space. (b) Hollow Hypersphere space (HHs).

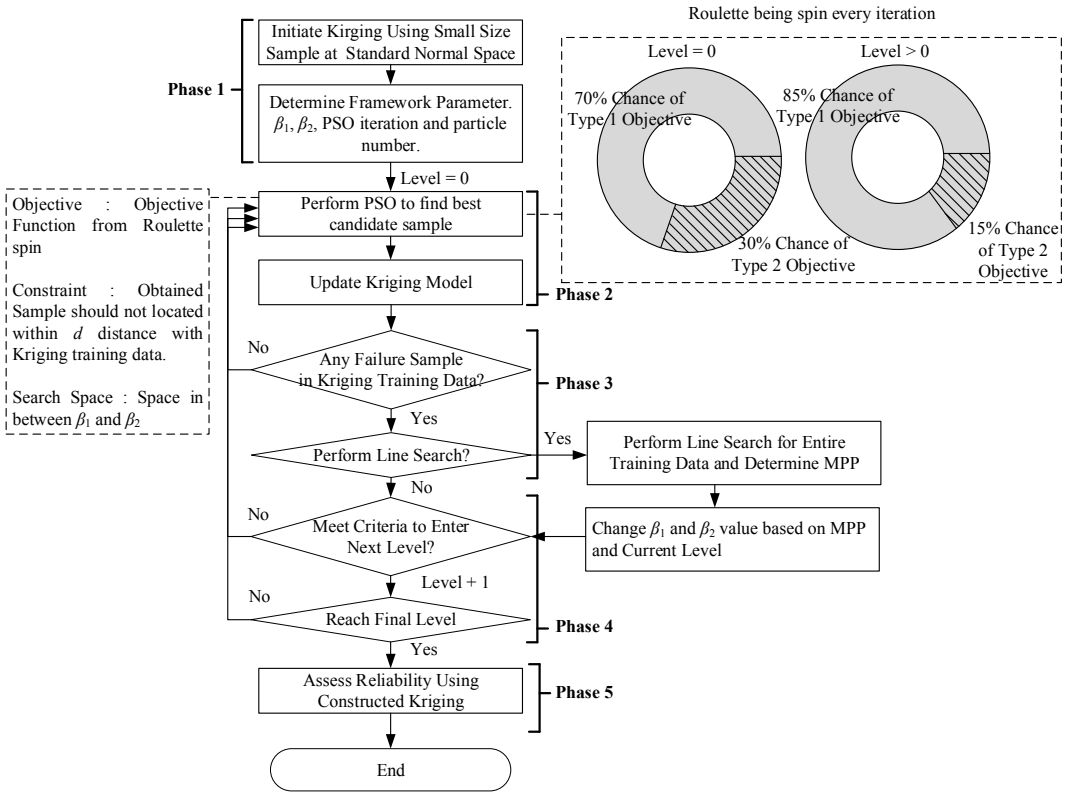

Figure 3. AK-PSO-HHs flowchart.

Only region formed in between β_1 and β_2 is considered. Beside enhancing PSO performance by reducing search space, β_2 information also enable user to perform RBIS (Radial Based Importance Sampling) [25-26] to calculate P_f at the end of Kriging construction. Instead of using MCS for final P_f evaluation, RBIS could be utilized as it is more efficient in termed of function evaluation number. In case that IS (Importance Sampling) with uniform sampling distribution is more preferred, β_2 also helpful in removing uniform sample inside inner sphere β_2. Major flowchart of AK-PSO-HHs is outlined in Figure 2. In this flowchart, PSO, HHs, and stopping criteria feature are included. Proposed method apply a level system for stopping criterion. As shown in Figure 4, level number is started with level = 0. This level keep increased once several requirement is satisfied. Whole process is terminated once final level is reached. Number of level is determined based on random variable number (*nRV*) where number of level equal to 2 x *nRV*. Need to be noted that whole process performed under standard normal space.

This study provide two possible objective function termed as Type 1 and Type 2 as shown in Eq.14 and Eq.15 respectively. Type 1 is REIF-2 objective function adopted from Zhang et al. [26]. To enter next level as described in flowchart Figure 3, two requirements need to satisfy where learning function in Equation 10 should larger than 1.4 and Equation 8 should lower than 0.05.

$$LF_1 = f_x(x)\left\{\mu_k\left[1-2\Phi\left(\frac{\mu_k}{\sigma_k}\right)\right]+\sigma_k\left[2-\sqrt{\frac{2}{\pi}}\exp\left(-0.5\left(\frac{\mu_k}{\sigma_k}\right)^2\right)\right]\right\} \tag{8}$$

$$\begin{aligned}&\mu_k \le 0 \rightarrow LF_2 = -\left|R_x - R_{MPP}\right|\left(w_1 \times \left|\mu_k\right| + w_2\right)\\ &\mu_k > 0 \rightarrow LF_2 = -\infty\end{aligned} \tag{9}$$

$$LF_3 = \frac{\left|\mu_k\right|}{\sigma_k} \tag{10}$$

Reliability Based Design Optimization

This study also performs a double loop RBDO using SOS (Symbiotic Organism Search) [28] metaheuristic optimization algorithm as outer loop and aforementioned Kriging reliability assessment in inner loop. This study utilizes Symbiotic Optimization Search (SOS) Algorithm due to its superiority compared to other optimization algorithms [28]. The flowchart of SOS algorithm is shown in Figure 4. SOS is a nature-inspired algorithm, consisting of three phases: mutualism, commensalism and parasitism. It is inspired by how animal interact with each other. In general, those interaction relations categorized as mutual benefit interaction (mutualism), self-benefit only (commensalism), and parasite interaction (parasitism). Similar to most swarm optimizations, in the process of searching for the optimal solution, SOS also relies on the solution of the best swarm because this interim optimal point dominates the updating of other swarms. At each phase, an existing organism (swarm) is updated with a new organism that has a better objective value. The main difference between SOS and other swarm optimizations is the aforementioned updating is performed at the end of each swarm evaluation as shown in Figure 4. Other conventional swarm optimizations usually update its swarm only when an iteration/generation is finished. Interestingly, mutualism phase gives an option to update two swarms at a time that gives a possibility of a faster convergence toward optimal area. While parasitism phase gives an alternative of randomness to find any better swarm compared to current recorded swarm.

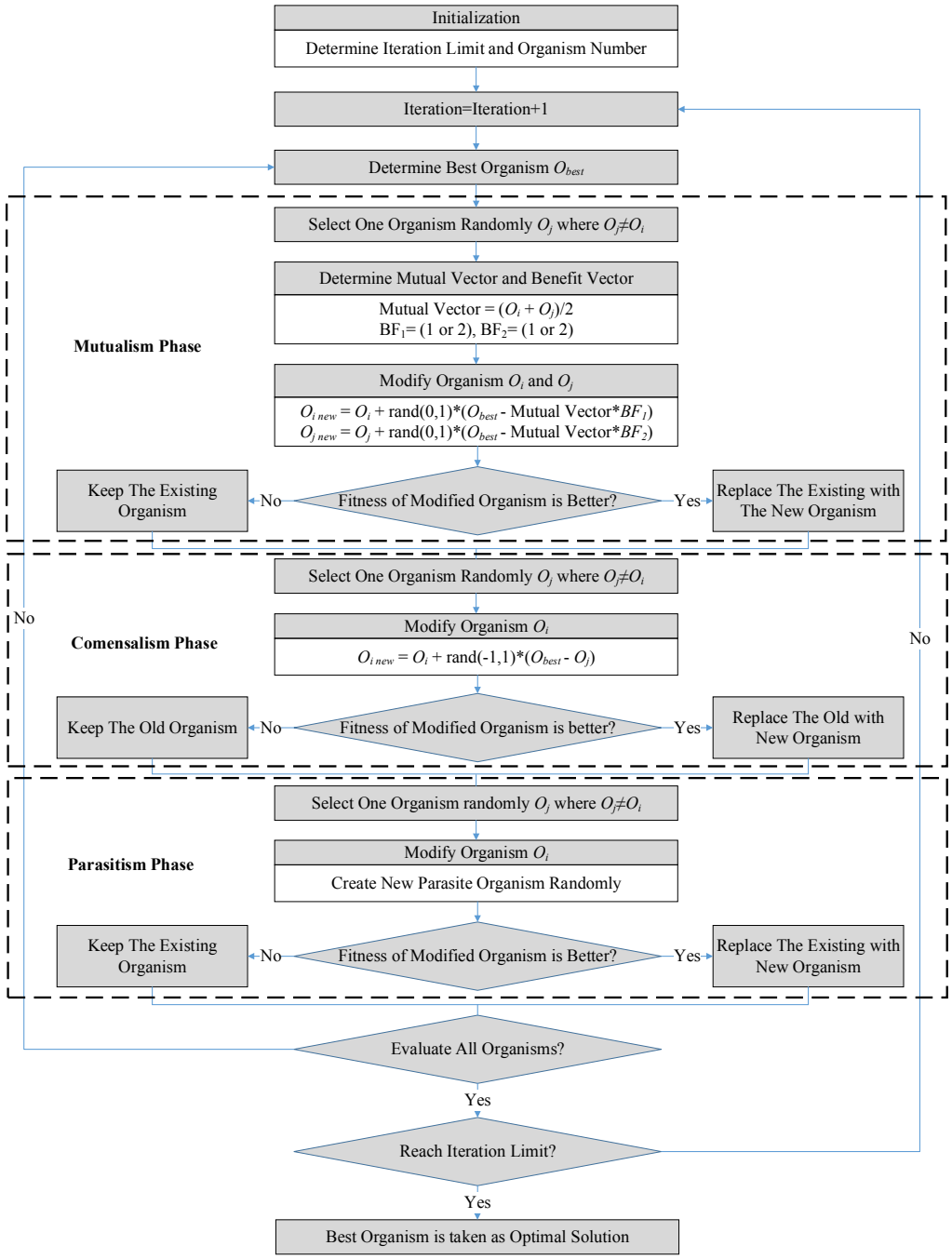

Figure 4. AK-PSO-HHs flowchart.

Other than early explained reasons, reason for SOS being chosen is that parallel computation is not performed for the entire optimization case in this study. Need to be noted, using the flowchart in Figure 4 and updating swarm for each phase, SOS is not suitable for the case where the user can perform parallel computing.

In this RBDO, feasible region will be assumed as set of dimension that could give reliability index of above 1-Φ(β_t) and the rest will be categorized as infeasible region. In determining better organism, the rules will be described below:

1. If feasible candidate compared to infeasible candidate, feasible candidate win.
2. If comparing two feasible candidates, pick the lowest cost function.
3. If comparing two infeasible candidates, pick the one has nearest reliability index to β_t.

Numerical Example

A 4-story structure (Figure 5), adopted from Ramallo et al. [29], is used to demonstrate the proposed methodology. Because they do not consider uncertainties in calculations, to perform an RBDO task, the structure properties such as mass, stiffness, and damping ratio are slightly modified, to be specifically, they are considered as random variables in the current study. Mass-spring stick model is utilized to model the building to save calculation time. Since a structure equipped with active controller is designed to maintain in the elastic range and the considered building is only 4 stories high, rotational difference in each story is not significant. Thus, a mass-stick model is used here.

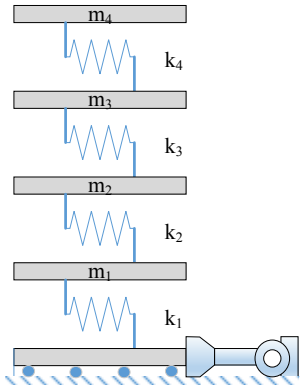

Figure 5. 4-story Structure with Active Controller at the Base.

The objective is to minimize stiffness of structure (k_1, k_2, k_3, and k_4), in which summation of entire stiffness is adopted as the indicator. Top story displacement is the constraint that should be less than 0.015m. To consider the uncertainty in a structural system, probabilistic constraints are applied in this optimization process, in which the target reliability index (β) is assumed to be 3. The control parameter in LQR method, which is also recognized as design variable here, is presented in Equation 11.

$$J = \int_0^\infty \left[x^T(t) Q x(t) + F^T(t) R F(t) \right] dt$$
$$Q = I_{8\times 8} \times \left[q_{a1}, q_{a2}, q_{a3}, q_{a4}, q_{v1}, q_{v2}, q_{v3}, q_{v4} \right] \tag{11}$$
$$R = 10^{-7}$$

Where Q and R matrices are weighting for LQR tuning procedure. Q is identity matrix but diagonally consist of 8 positive number that will be the optimized parameter.

Table 1 Random and Optimized Variable Properties.

Structure Properties	Type	Mean	COV	Unit
m_1, m_2, m_3, m_4	Random Variable	897	0.1	kg
k_1, k_2, k_3, k_4	Random and Optimized Variable	-	0.1	kN/m
ζ	Random Variable	2	0.1	%
q_{a1}, q_{a2}, q_{a3}, q_{a4} q_{v1}, q_{v2}, q_{v3}, q_{v4}	Optimized Variable	-	-	-

In total, there are 8 random variables considered and their statistics are described in Table 1. As seen, all random variables are assumed to follow lognormal distribution with coefficient of variation (COV) of 0.1. While structure stiffness from k_1 to k_4 will also act as optimized variable, its mean value will depend on optimized variable assigned by SOS process. So, there will be 12 optimized parameters consisted by control parameter and structure stiffness. El Centro earthquake with maximum PGA (Peak Ground Acceleration) of 1g is adopted as the external excitation, as presented in Figure 6. The numerical model is constructed using state space formulation, in which Rayleigh damping matrix [30] is adopted for damping matrix construction. The state space formulation is performed using MATLAB SIMULINK and operated by i7 3.2GHz CPU computer.

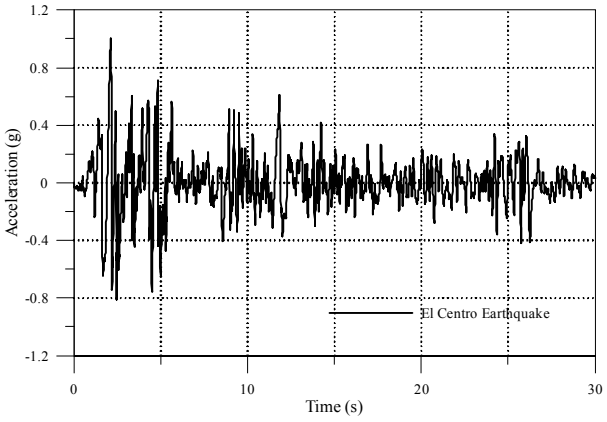

Figure 6. Earthquake used in the Numerical Example.

Two types of RBDO will be performed. First type is RBDO of structure without active control and second type is structure equipped with active control. After obtaining the optimal design that is derived from the proposed algorithm, MCS is used to confirm the obtained solution satisfying the probabilistic constraints. Figure 7 shows convergence of two types RBDO where convergence attained approximately after 30 iterations. Result of RBDO are shown in Table 2 and 3.

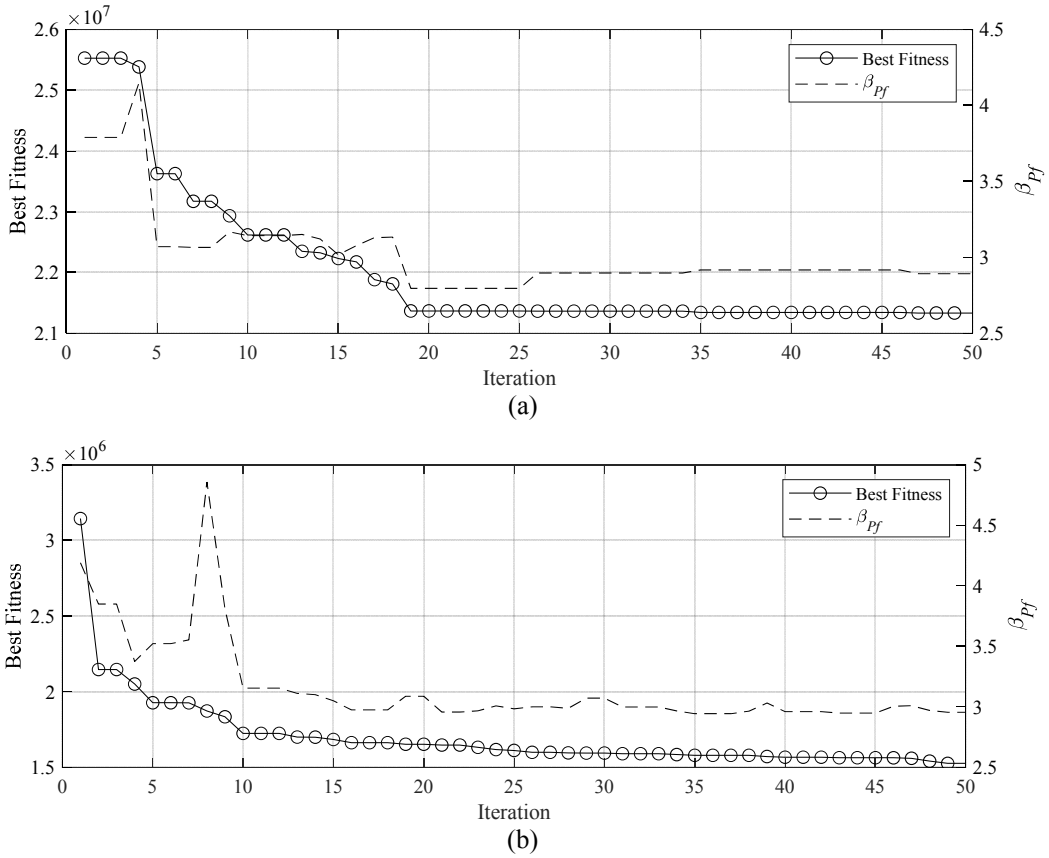

Figure 7. (a) Convergence of RBDO Structure without controller. (b) Convergence of RBDO Structure equipped with RBDO.

Table 2. Brief Result of Ordinary Structure.

Best Organism	Ordinary Structure			
Stiffness (k_1 to k_4)	7043643.4	6322166	5190885.1	2774285
Control Parameter	[655320 7329725 0 6870217 990 659 0 572]			
P_f Kriging	2.89			
P_f MCS	2.64			
Kriging avg FE per RA	102.5			

Table 3. Brief Result of Ordinary Structure.

Best Organism	Structure Equipped with Controller			
Stiffness (k_1 to k_4)	2222.4418	455807.11	453800.879	614317.886
Control Parameter	[0 253382 9651653 9960900 1.7 435 991 355]			
P_f Kriging	2.95			
P_f MCS	2.99			
Kriging avg FE per RA	102.5			

Verification between Kriging assessment and MCS also provided in Table 2 and 3 for ordinary and controlled structure. It shows that error between kriging and MCS is acceptable. Number of FE (Function Evaluation) per RA (Reliability Analysis) also very efficient with only 102.5 function call at each reliability assessment. Uniquely, it can be seen from stiffness result, structure equipped with controller prefer lower stiffness at low level position. It is against result from ordinary structure where higher stiffness required at base level.

Conclusion

To attain optimal control design, this study optimizes not only controller parameter but also stiffness of structure. This optimal design not only resulting efficient control parameter but also efficient stiffness that could minimize construction cost. Excess safety from active control is traded with stiffness reduction of structure. While safety measure itself determined through reliability analysis. To have efficient reliability assessment, Kriging based adaptive method is employed. Two types of analysis are performed in which ordinary structure and active controlled structure. Several conclusions from analysis result are drawn as follow:

1. Kriging based adaptive reliability assessment offer efficient method that only occupy 102.5 function call per reliability analysis. Furthermore, its accuracy also maintained under tolerable error margin compared to MCS result.
2. The use of metaheuristic able to deliver optimal result although it is not exact solution. Complex mathematical derivation in finding control parameter could be avoided although computation time in processing metaheuristic is required.
3. Unique phenomena occur between ordinary and active controlled structure. Ordinary structure has optimal result where high stiffness column is preferable at lower level of structure with gradual decrease of stiffness at higher level. However, controlled structure delivered its optimal result with lower stiffness at base level and gradual increase to top level of structure.

References

Kelly JM. Aseismic base isolation: review and bibliography. Soil Dynamics and Earthquake Engineering. 1986;5:202-16.

Ikago K, Saito K, Inoue N. Seismic control of single-degree-of-freedom structure using tuned viscous mass damper. Earthquake Engineering & Structural Dynamics. 2012;41:453-74.

Peng Y, Ma Y, Huang T, De Domenico D. Reliability-based design optimization of adaptive sliding base isolation system for improving seismic performance of structures. Reliability Engineering & System Safety. 2021;205:107167.

Gluck J, Ribakov Y. The influence of dampers on earthquake response of tall buildings. Civil and structural engineering computing: 2001: Saxe-Coburg Publications; 2001. p. 387–406.

Zhao B, Lu X, Wu M, Mei Z. Sliding mode control of buildings with base-isolation hybrid protective system. Earthquake Engineering & Structural Dynamics. 2000;29:315-26.

Henry, R. S., Lee, B.-Y., McGuigan, D., Finnegan, J., & Ashby, G. (2017). The 2016 Meinong Taiwan earthquake: Learning from earthquakes report. *Bulletin of the New Zealand Society for Earthquake Engineering*, *50*(3), 436–468. https://doi.org/10.5459/bnzsee.50.3.436-468

Lin, J. L., Kuo, C. H., Chang, Y. W., Chao, S. H., Li, Y. A., Shen, W. C., ... & Hwang, S. J. (2020). Reconnaissance and learning after the February 6, 2018, earthquake in Hualien, Taiwan. *Bulletin of Earthquake Engineering*, *18*, 4725-4754.

Shaiju AJ, Petersen IR. Formulas for Discrete Time LQR, LQG, LEQG and Minimax LQG Optimal Control Problems. IFAC Proceedings Volumes. 2008;41:8773-8.

Kinnaert M, Peng Y. The Design of Digital Pole Placement Controllers. In: Leondes CT, editor. Control and Dynamic Systems: Academic Press; 1995. p. 25-65.

Guo SX. Non-Probabilistic Robust Reliability Method and Reliability-Based Performance Optimization for Active Vibration Control of Structures and Dynamic Systems with Bounded Uncertain Parameters. Journal of Vibration and Control. 2016;22:1472-91.

Breitung K, Casciati F, Faravelli L. Reliability Based Stability Analysis for Actively Controlled Structures. Engineering Structures. 1998;20:211-5.

Spencer BF, Sain MK, Won CH, Kaspari DC, Sain PM. Reliability-Based Measures of Structural Control Robustness. Structural Safety. 1994;15:111-29.

Kalman RE. A New Approach to Linear Filtering and Prediction Problems. Journal of Basic Engineering. 1960;82:35-45.

Lin CC, Lu KH, Chung LL. Optimal discrete-time structural control using direct output feedback. Engineering Structures. 1996;18:472-80.

Arfiadi Y, Hadi MNS. Optimal direct (static) output feedback controller using real coded genetic algorithms. Computers & Structures. 2001;79:1625-34.

Wang W-Y, Leu Y-G, Lee T-T. Output-feedback control of nonlinear systems using direct adaptive fuzzy-neural controller. Fuzzy Sets and Systems. 2003;140:341-58.

Alavinasab A, Moharrami H, Khajepour A. Active Control of Structures Using Energy-Based LQR Method. Computer-Aided Civil and Infrastructure Engineering. 2006;21:605-11.

Amini F, Hazaveh NK, Rad AA. Wavelet PSO-Based LQR Algorithm for Optimal Structural Control Using Active Tuned Mass Dampers. Computer-Aided Civil and Infrastructure Engineering. 2013;28:542-57.

Hassani K, Lee WS. Multi-Objective Design of State Feedback Controllers Using Reinforced Quantum-Behaved Particle Swarm Optimization. Applied Soft Computing. 2016;41:66-76.

Liao K-W, Thedy J. Probabilistic optimal control parameters with incomplete information on design variables using a heuristic algorithm. Applied Soft Computing. 2021;110:107586.

Howimanporn S, Thanok S, Chookaew S, Sootkaneung W. Design and implementation of PSO based LQR control for inverted pendulum through PLC. 2016 IEEE/SICE International Symposium on System Integration (SII)2016. p. 664-9.

Zhao Y-G, Ono T. A general procedure for first/second-order reliability method (FORM/SORM).

Structural Safety. 1999;21:95-112.
Zhao Y-G, Lu Z-H. Applicable Range of the Fourth-Moment Method for Structural Reliability. Journal of Asian Architecture and Building Engineering. 2007;6:151-8.
Echard B, Gayton N, Lemaire M. AK-MCS: An active learning reliability method combining Kriging and Monte Carlo Simulation. Structural Safety. 2011;33:145-54.
Kim J, Song J. Probability-Adaptive Kriging in n-Ball (PAK-B^n) for reliability analysis. Structural Safety. 2020;85:101924.
Zhang X, Wang L, Sørensen JD. REIF: A novel active-learning function toward adaptive Kriging surrogate models for structural reliability analysis. Reliability Engineering & System Safety. 2019;185:440-54.
Thedy J, Liao K-W. Multisphere-based importance sampling for structural reliability. Structural Safety. 2021;91:102099.
Cheng MY, Prayogo D. Symbiotic Organisms Search: A New Metaheuristic Optimization Algorithm. Computers & Structures. 2014;139:98-112.
Ramallo JC, Johnson EA, Spencer BF. "Smart" Base Isolation Systems. Journal of Engineering Mechanics. 2002;128:1088-99.
Liu M, Gorman DG. Formulation of Rayleigh Damping and Its Extensions. Computers & Structures. 1995;57:277-85.